Lecture Notes in Civil Engineering

C. N. V. Satyanarayana Reddy
A. Murali Krishna
Neelima Satyam *Editors*

Dynamics of Soil and Modelling of Geotechnical Problems

Proceedings of Indian Geotechnical Conference 2020 Volume 5

Springer

Lecture Notes in Civil Engineering

Volume 186

Lecture Notes in Civil Engineering (LNCE) publishes the latest developments in Civil Engineering—quickly, informally and in top quality. Though original research reported in proceedings and post-proceedings represents the core of LNCE, edited volumes of exceptionally high quality and interest may also be considered for publication. Volumes published in LNCE embrace all aspects and subfields of, as well as new challenges in, Civil Engineering. Topics in the series include:

- Construction and Structural Mechanics
- Building Materials
- Concrete, Steel and Timber Structures
- Geotechnical Engineering
- Earthquake Engineering
- Coastal Engineering
- Ocean and Offshore Engineering; Ships and Floating Structures
- Hydraulics, Hydrology and Water Resources Engineering
- Environmental Engineering and Sustainability
- Structural Health and Monitoring
- Surveying and Geographical Information Systems
- Indoor Environments
- Transportation and Traffic
- Risk Analysis
- Safety and Security

To submit a proposal or request further information, please contact the appropriate Springer Editor:

– Pierpaolo Riva at pierpaolo.riva@springer.com (Europe and Americas);
– Swati Meherishi at swati.meherishi@springer.com (Asia - except China, and Australia, New Zealand);
– Wayne Hu at wayne.hu@springer.com (China).

All books in the series now indexed by Scopus and EI Compendex database!

More information about this series at https://link.springer.com/bookseries/15087

C. N. V. Satyanarayana Reddy · A. Murali Krishna · Neelima Satyam
Editors

Dynamics of Soil and Modelling of Geotechnical Problems

Proceedings of Indian Geotechnical Conference 2020 Volume 5

Springer

Editors
C. N. V. Satyanarayana Reddy
Geotechnical Engineering Division
Department of Civil Engineering
Andhra University College of Engineering
Visakhapatnam, Andhra Pradesh, India

A. Murali Krishna
Department of Civil Engineering
Indian Institute of Technology
Tirupati, Andhra Pradesh, India

Neelima Satyam
Discipline of Civil Engineering
Indian Institute of Technology
Indore, Madhya Pradesh, India

ISSN 2366-2557 ISSN 2366-2565 (electronic)
Lecture Notes in Civil Engineering
ISBN 978-981-16-5604-0 ISBN 978-981-16-5605-7 (eBook)
https://doi.org/10.1007/978-981-16-5605-7

Contents

About the Editors

Dr. C. N. V. Satyanarayana Reddy is a Professor of Civil Engineering at College of Engineering, Andhra University, Visakhapatnam, India, and has 28 years of teaching, research, and consultancy experience. His expertise and research interests are in the areas of reinforced soils, ground improvement, landfills, soil retention in excavations, deep foundations, and forensic geotechnical engineering. He obtained B.Tech. in Civil Engineering from Nagarjuna University, M.Tech. in Geotechnical Engineering from Indian Institute of Technology (IIT) Madras, M.E. (Structures) from Andhra University, and Ph.D. from National Institute of Technology (NIT) Warangal, India. He has guided 8 Ph.D. scholars and 92 M.Tech. dissertations. He has more than 110 publications in various national and international journals and seminars/conference proceedings. He has organized more than 30 seminars, workshops, and training programs. He is fellow of Indian Geotechnical Society, The Institution of Engineers (India) and Life member of Indian Roads Congress, Indian Concrete Institute, Indian Society for Technical Education, Indian Society for Rock Mechanics and tunneling Technology. He handled several research projects funded by DST, UGC and AICTE. He received the Engineer of the Year 2006 Award from Govt. of Andhra Pradesh and The Institution of Engineers (India) A.P. State Centre, Best Academician Award for the year 2014 from Andhra University and Andhra Pradesh Scientist Award 2020 in Civil Engineering Discipline from A.P. State Council of Science and Technology, Govt. of A.P. He served as National Executive Committee member of Indian Geotechnical Society during the period 2013–2020. He served as a member in H-4 Committee on Embankment, Ground Improvement and Drainage Committee of Indian Roads Congress (IRC) for the term 2018–2020. He is serving as member of TC 213 on "Scour and Erosion" of International Society for Soil mechanics and Geotechnical Engineering (ISSMGE).

Prof. A. Murali Krishna is currently a faculty member in the department of Civil Engineering, Indian Institute of Technology (IIT) Tirupati. Dr. Krishna obtained his Ph.D. from Indian Institute of Science Bangalore, M.Tech. degree from IIT

Kanpur and B.Tech. degree from Sri Venkateswara University College of Engineering, Tirupati. His research interests include earthquake geotechnics, geosynthetics and ground improvement, site characterization, and numerical and physical modelling of geotechnical structures. He was a recipient of BRNS Young Scientist Research award, BOYSCAST fellowship and HERTAGE fellowship. He was a visiting fellow at Bristol University (UK), Surrey University (UK) and University de Torino (Italy). He supervised 7 Doctoral students and 24 Masters students; co-authored nearly 180 publications of technical papers in international/national Journals and conference/seminar proceedings, including book chapters.

Dr. Neelima Satyam is currently Associate Professor and Head in Discipline of Civil Engineering at Indian Institute Technology (IIT) Indore. She obtained her Ph.D. and M.Tech. from IIT Delhi and B.Tech. from SV University, Tirupati. She is actively engaged in teaching, research, and consultancy in the field of geotechnical engineering, particularly in geotechnical earthquake engineering, microzonation and site response studies, landslide hazard and monitoring, liquefaction modeling, microseismic data processing, and rock engineering. She received research grants from DST, MHRD, AICTE, ITRA, DAE, NIOT, NRDMS, ISRO, and MoES. She has 97 papers published in journals and conferences of national and international repute. She was Recipient of IEI Young Engineers Award 2011, AICTE Career Award 2012, JSPS fellowship in 2013, and INWES Young Woman Engineer Award in 2012. She is elected National Executive Member of Indian Geotechnical Society (2018–2020) and Indian Society of Engineering Geology (2020–2021).

Forensic Analysis of Retaining Wall Failure

P. S. Aravind and Neerad Mohan

1 Introduction

Forensic investigations involve field and laboratory tests apart from the collection of all available data as well as distress measurements. The test parameters and design assumptions in the forensic analysis will have to be representative of the actual conditions encountered at the site [11]. It often includes a collection of data, characterization of distress, development of failure hypothesis, diagnostic tests, and back analysis [12]. In the present case, forensic geotechnical analysis of the gravity retaining wall is performed to determine the possible causes of the failure of the wall.

1.1 Description of Gravity Wall

The gravity wall is located in Muringoor village, Chalakudy, Trichur district, India, on the banks of the Chalakudy river. It is situated adjacent to Bridge no. 132 of Indian railways (Fig. 1). The 15 m × 1.5 m × 3.0 m wall is a non-monolithic construction joined to the abutment of the bridge by ashlar masonry. The base of the retaining wall is located at a depth of 7.92 m below the track level. The site has a history of slope stability problems on both east and west sides. When a major crack was observed, the tilt is kept under observation, and measurements are taken. Gradually, the tilting increased, and the entire 15 m long retaining wall collapsed into the river (Fig. 2). Unsatisfactory packing of ashlar masonry, insufficient drainage facility, and few dowel bars could be seen. The retaining wall provided is a rigid one having been constructed in a continuous length. During the inspection, it is observed that the soil

P. S. Aravind · N. Mohan (✉)
Thejus Engineering College, Trichur, Kerala, India

C. N. V. Satyanarayana Reddy et al. (eds.), *Dynamics of Soil and Modelling of Geotechnical Problems*, Lecture Notes in Civil Engineering 186,
https://doi.org/10.1007/978-981-16-5605-7_1

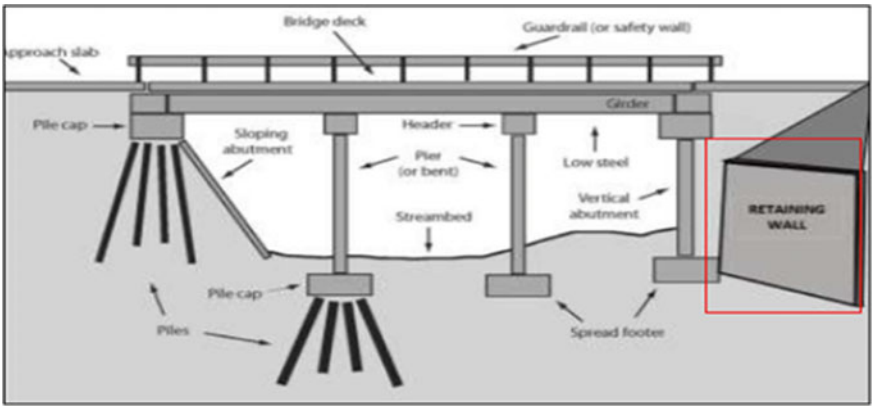

Fig. 1 Retaining wall located adjacent to the bridge abutment

Fig. 2 Collapsed retaining wall

becomes very slushy having very little shear strength after encountering water. Weep holes are provided on the retaining wall but are found to be clogged.

2 Characterization of Distress

The distresses that are observed in the field are in the form of lateral movements and vertical settlements. The abutment wall of bridge no. 132 is taken as the reference point (0, 0) for the measurement of the horizontal lateral displacement of the gravity wall. Maximum lateral displacement of 90 mm is observed as shown in Fig. 3. It also shows the vertical settlement of the wall measured to track level. From field

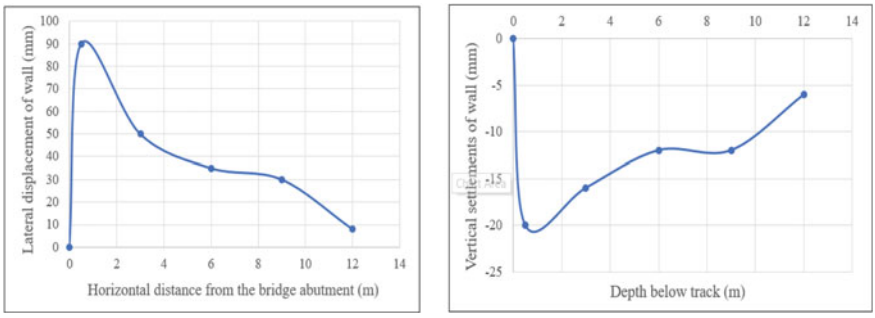

Fig. 3 Collapsed retaining wall

measurements, a maximum vertical displacement of 20 mm is observed at 0.5 m from the bridge abutment. The maximum distress due to lateral movement and vertical settlements is found in the region where the retaining wall joins the bridge abutment. Figure 4 shows the magnitude of distress patterns of lateral deformation. Figure 5 shows visual cracks (more than 60 mm wide) on the inclined slope due to excessive vertical settlement of both backfill and foundation soil beneath the gravity wall. The measured values are compared with deformation values obtained from both displacement analysis and numerical analysis.

Fig. 4 Laterally displaced retaining wall

Fig. 5 Cracks due to vertical settlement

3 Collection and Interpretation of Test Data

A standard penetration test is done to determine geotechnical properties, relative density, and penetration resistance of soil layers. Trial pit-1 excavated at 2.69 m below the track level consists of backfill soil and trial pit-2 located at 7.92 m below the track level consists of natural foundation soil at the site. The trial pit soil samples are used to determine the basic and engineering properties of the soil. Shear strength properties are determined by the undrained unconsolidated triaxial test, and the coefficient of permeability is determined by the constant head permeability test. Tables 1, 2, and 3 present the geotechnical properties of soil samples.

3.1 Soil Profile

Backfill is clayey SAND and it is present until a depth of 7.5 m. The zone's geology features poorly graded SAND from 7.5 to 19.5 m. Underneath them, the lower stratum

Table 1 Properties of trial pit soil samples

Location	Natural moisture content (%)	Specific gravity (G)	Gravel (%)	Sand (%)	Fines (%)	LL (%)	PL (%)	PI
T.P 1	19	2.66	5	57	38	33	16	17
T.P 2	10	2.65	0	70	30	41	N.D	N.D

Table 2 Permeability characteristics of soil samples

Soil	Coefficient of permeability (mm/s)	Drainage property	USBR Classification
SC	1×10^{-4}	Poor	Semi pervious
SP	1.59×10^{-3}	Fair	Pervious
SM	4.14×10^{-2}	Good	Pervious

Table 3 Engineering properties of soil

Location	T.P.1	T.P.2
Cohesion (kPa)	5	0
Frictional Angle (°)	29	30
Young's Modulus (kPa)	7500	7000
Shear Modulus (kPa)	2885	2692
MDD (kPa)	18.4	18.0
OMC (%)	24.0	12.5
Bulk density (kN/m^3)	17.6	17.7
Dry density (kN/m^3)	14.7	16.4
Saturated density (kN/m^3)	19.2	20.3

consists of silty SAND till a depth of 22.5 m beyond which bedrock is present. The rock samples obtained are Charnockite Gneiss and Granite, a common type of hard geological rock found in the Chalakudi district. Relative density values obtained show the presence of loose to medium dense followed by very dense soil strata. The SPT test results show that the site has weak soil at shallow depth. It also reveals that proper compaction is not provided before construction. The RQD of the rock varies from 70 to 80%. The rock samples show good recovery indicating the presence of firm good bedrock strata at 22.5 mt from the ground level. The groundwater level is encountered at 9.52 m with a dip meter. The water level in the river rises during the monsoon season when the nearby dam shutters are opened. As a result, the water level rises to 6 m, and the gravity wall is partially submerged underwater.

4 Field Instrumentation for Measurement of Ground Vibration

MEMS-based triaxial accelerometer ADXL 335 is used for the measurement of the train-induced ground vibrations. Accelerometers are sensors that usually detect accelerations by utilizing inertial force. The ADXL 335 circuit performs signal measurement and amplification to obtain a low amplitude signal. Here, the amplified signal is collected by Arduino micro-controller, and these acquired data are sent via a serial communication protocol to third-party devices, i.e. the laptop. The extension of the railway line was considered for the study and the numerical model has a length of 11 m. An area considered incorporates the railway track, the bridge abutment, the backfill slope, and the retaining wall. The site has a stepped arrangement post slope failure. The entire site is divided into gridlines. Due to the stepped arrangement of the site, the gridlines 1, 2, and 3 are normal to the track and at certain points located at different levels below w.r.t the ground/track level. Gridlines A, B, and C are located at distances of 1.5, 6.5, and 11.5 m from the edge of the railway track. It intersects the gridlines 1, 2, and 3 at A1, A2, A3, B1, B2, B3, C1, C2, and C3. Points B3 and

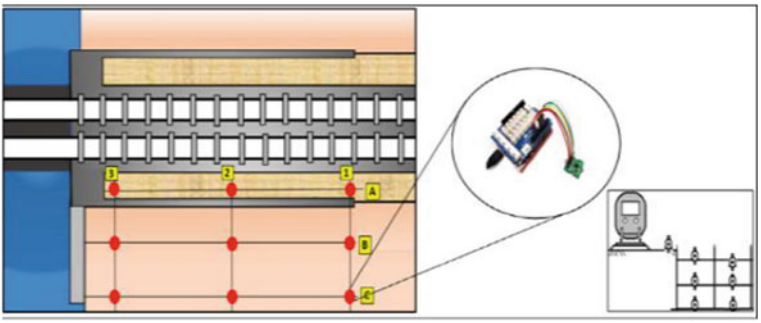

Fig. 6 Field Instrumentation setup

C3 are located closest to the collapsed retaining wall. These points of intersection of gridlines give the measurement points where the triaxial accelerometers are placed. The arrangement is orientated in both the longitudinal and transverse directions of the vibration source and the proximity of the railway track and collapsed gravity wall. The following schematic diagram Fig. 6 shows the instrumentation setup.

5 Time-and Frequency-Domain Parameters

The ground vibration data obtained during the movement of the train are acquired and processed. The typical time-histories of vertical, longitudinal, and lateral acceleration of vibration produced in the soil during train movement for locations B2 and C1 are shown in Figs. 7 and 8. The maximum peak vertical acceleration is about 0.17 g which occurs at a distance of 1.5 m from the track lane.

The time-domain parameters are transformed into frequency-domain parameters using the Fourier transform technique (Fig. 9). Acceleration signals are processed by doing numerical integration to get corresponding peak particle velocity. A Digital filter (IIR—infinite impulse response filter) was used to eliminate noise. Peak ground acceleration, peak particle velocity, frequency, and displacement are determined. The results of vibration analysis (Table 4) are used to determine the influence of train-

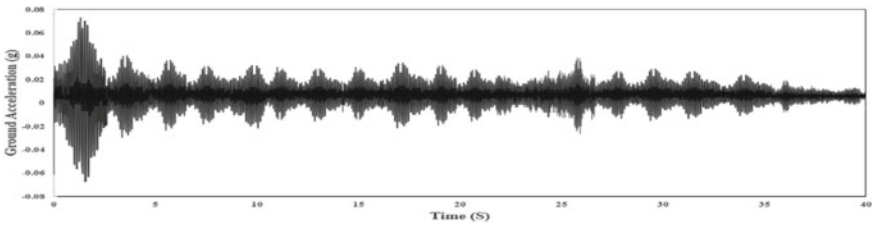

Fig. 7 Acceleration versus time graph for location B2

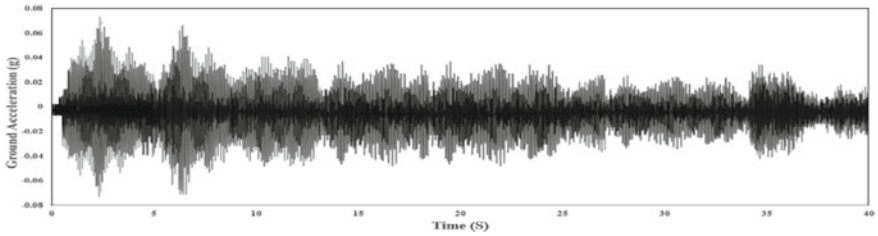

Fig. 8 Acceleration versus time graph for location C1

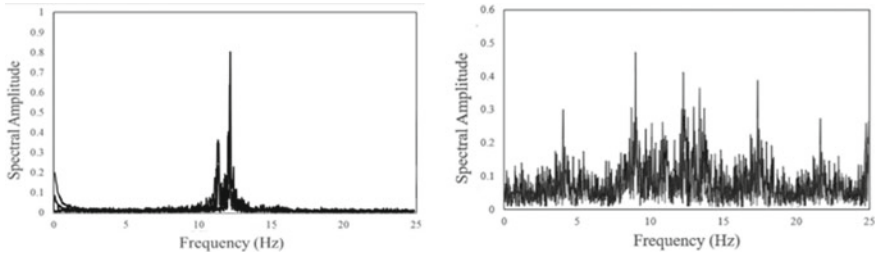

Fig. 9 Spectral amplitude versus frequency

induced ground vibration on producing resonance conditions in the soil and related liquefaction.

6 Characteristics of the Soil Layers

For the estimation of eigenfrequencies of subsoils, a horizontal layered ground is considered, and the frequency is dependent on two factors in the soil, the shear wave velocity and thickness of the subsoil. The subsoils expected eigenfrequency is calculated as follows:

$$f_o = \frac{V_s}{4H} = \sqrt{\frac{G/\gamma}{4H}}$$

H: Total layer thickness of soil layers.
G: Shear modulus of the soil layer.
γ: Density of the soil layer.
V_s: Shear wave velocity.

Using the free-vibration decay method [2], the damping ratio ξ (fraction of critical damping) from the ratio of two peaks a_n and a_{n+m} over m consecutive cycles in the selected area of the acceleration-time curve history is determined with the following equation

Table 4 Ground vibration parameters

Location	Distance from source			Ground acceleration			Frequency	Peak particle velocity
	Damping Ratio	Depth/Level below track (m)	X_{max} Longitudinal (g)	Y_{max} Lateral (g)	Z_{max} Vertical (g)	Peak ground Acceleration (g)	Dominant Frequency (HZ)	SSRS (mm/s)
A1	0.3	0	0.12	0.13	0.17	0.17	22	15.43
A2	0.3	0	0.14	0.12	0.15	0.15	18	15.89
A3	1.5	0	0.13	0.08	0.11	0.13	14	11.90
B1	6.5	1	0.10	0.05	0.08	0.10	17	7.91
B2	6.5	4	0.01	0.07	0.02	0.07	16	5.47
B3	6.5	8	0.02	0.03	0.01	0.03	12	2.59
C1	11.5	2	0.07	0.06	0.03	0.07	13	6.19
C2	11.5	4	0.06	0.06	0.03	0.06	13	5.45
C3	11.5	8	0.03	0.02	0.02	0.03	9	2.40

$$\xi = \frac{\ln\left(\frac{a_n}{a_{n+m}}\right)}{2\pi m}$$

The attenuation coefficient α is used as a measure of the decrease in measured vibration with increasing distance from the track using the following [3] equation:

$$\alpha = \frac{-\ln\left[\frac{V_2}{V_1}\left(\frac{R_1}{R_2}\right)^{-0.5}\right]}{R_2 - R_1}$$

α is the attenuation coefficient (m^{-1}).
V_1 is the vibration velocity nearer to the source (mm/s).
V_2 is the vibration velocity further from the source (mm/s).
R_1 is the nearer distance to the source (m).
R_2 is the further distance to the source (m).

The saturated cohesionless soils are mostly affected by the vibrations. From attenuation values (Table 5), the foundation soil is classified as weak [1].

The natural frequencies of the wall are determined by Nandakumaran et. al solution for pure translation method and are presented in Table 6. It can be noticed from Table 6 that the measured eigenfrequency/dominant frequency of ground vibration is very close to the estimated/expected eigenfrequency for the foundation soil.

Table 5 Ground vibration parameters

Soil layer	Damping ratio	Attenuation coefficient 'α'	Soil characteristics
Soil layer 1 (Backfill 0–4 m)	0.3	0.0002	Competent
Soil layer 2 (Backfill 0–4 m)	0.3	0.002	Weak
Soil layer 3 (Foundation soil 7.5–19.5 m)	0.5	0.001	Weak

Table 6 Ground vibration parameters

System	Expected eigenfrequencies (Hz)	Measured eigenfrequencies (Hz)
Train	40–60	–
Backfill soil	1–10	13–17
Foundation soil	6–10	9–12
Retaining wall	4–9	2

7 Development of Failure Hypothesis

Assumptions are made regarding the possibility of the collapse of the retaining wall. To determine the cause of the collapse of the wall, the site conditions are selected to represent the 'worst possible' scenario, i.e. where it was considered that under the combination of high vibration levels induced by train, unfavorable soil, and backfill conditions along with various static and dynamic forces are acting on the wall are responsible for the collapse of the wall. The following failure hypothesis is developed such as high stresses induced due to ground vibrations, unfavorable soil conditions, the susceptibility of soil to undergo liquefaction, an increase in lateral thrust on the wall, and unscientific design and construction.

8 Back Analysis

The back analysis is conducted on the distressed retaining wall using vibrational analysis, conventional methods, and finite element analysis using PLAXIS 3D.

8.1 Vibrational Analysis

Ground-borne vibrations are generated by dynamic loads that induce energy into the soil and cause wave propagation in the ground [4, 5]. Liquefaction is defined as the transformation of granular material from a solid to a liquefied state because of increased pore water pressure and reduced effective stress [8]. Dynamic loads such as train-induced ground vibration can lead to resonance conditions in the soil which causes liquefaction in saturated cohesionless soils [7, 10]. The loose soil compacts and densifies due to the train-induced ground vibrations. Increased pore water pressure is induced by the tendency of granular materials to compact when subjected to cyclic shear deformations. Therefore, the ability of compaction of the soil is a factor that determines the liquefaction potential [10]. The change of state occurs mostly in loose to moderately dense granular soils with poor drainages, such as silty sands or sands and gravels capped by or containing seams of impermeable sediment. As liquefaction occurs, the soil stratum softens, allowing large cyclic deformations to occur [6]. In loose materials, the softening is also accompanied by a loss of shear strength that may lead to large shear deformations or even flow failure under moderate to high shear stresses, such as beneath a foundation or sloping ground. Resonance impact on soil leads material deterioration to occur followed by an increase of fine-grained material between larger particles causing degradation of shear modulus, shear strength, and bearing capacity which leads to settlements [7]. Loose soils also compact during liquefaction and reconsolidation, leading to differential settlement

and consequent structural damage. Liquefaction, through analysis, is confirmed. This would cause the subsoil to lose its bearing capacity which would lead to settlements.

Also, due to excessive rainfall and flood conditions frequently occurring, there will be a risk that the pore water pressure is built up in the soil which becomes high due to poor impermeable backfill and lack of proper drainage conditions. The possible consequence of this pore water pressure built up is the soil loses its bearing capacity and undergoes settlement. The low permeability backfill present also leads to water retention and adds up to the problem. In the project, the measurements of vibrations for soil layers and an analysis method focusing on the frequency content of the soil layer are performed, and the Eigenfrequencies/dominant frequency of the soil layer is determined. This measured highest amplitude peak for frequencies gives resonance frequencies/dominant frequency of the train-induced ground vibration for that soil layer. The values of the dominant frequency of the ground vibration give the resonance condition of different soil layers occuring. The expected Eigenfrequencies are obtained by empirical formulas. The expected eigenfrequencies are similar to the measured dominant frequencies, and the soil layer is said to undergo resonance at that frequency conditions which lead to liquefaction. Thus, an assessment of the dynamic loadings influences on various soil layers due to train-induced vibrations is performed. The vibrational analysis is a back analysis technique that is compared with the liquefaction resistance ratio which confirms the susceptibility of foundation soil to undergo liquefaction.

8.2 Conventional Analysis

In the conventional analysis, the seismic analysis of the retaining wall was performed to determine the various static and dynamic earth pressures acting on the wall. The design was performed for static condition and dynamic condition with zero and some allowable displacement using Coulomb's theory, the Mononobe-Okabe method, and the Richard-elms method, respectively. Hydrodynamic pore water pressure acting on the wall due to the river is determined by equations of Matzuo and O'Hara [9]. The displacement was determined for the wall for pure translation by the Nandakumaran et al. method. The dynamic bearing capacity was calculated by Richard et al. along with corresponding settlements. The section of the retaining wall was analyzed by stability check against sliding, overturning, and bearing capacity failure. Figure 10 shows forces acting on the gravity wall. Seismic analysis of retaining wall design is performed to determine the translation of the wall. The results of displacement analysis and settlement calculations which showed deformation in the form of translation and vertical settlements are presented. Using conventional methods, the stability of the retaining wall is checked for four prominent failure modes like overturning, sliding, and bearing capacity failure.

Table 7 shows the obtained values of earth pressure for the static and dynamic conditions with various methods. The lateral thrust in case 2 is more than case 1, which shows active lateral thrust increases when soil is saturated.

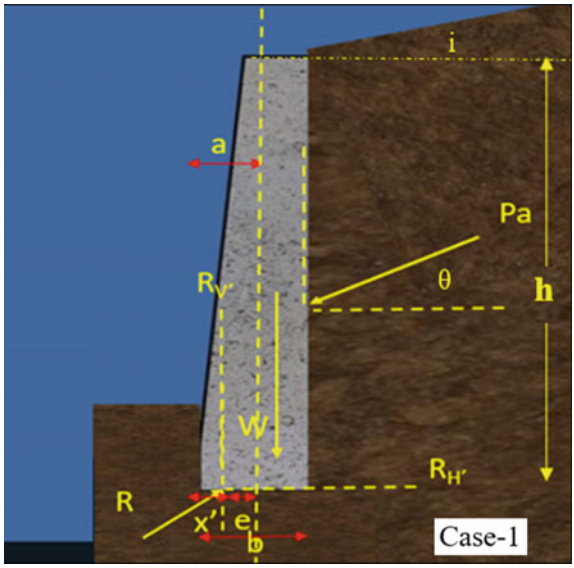

Fig. 10 Forces acting on gravity retaining wall

Table 7 Total lateral active thrust on the wall in static and dynamic conditions

Field condition	Specification	Method	Total Lateral active thrust on the wall, kN/m^2
Case 1–Field condition with dynamic active earth pressure acting on the wall	Static pressure acting on the gravity wall. Design based on force equilibrium	Coulomb theory	22.09
	Seismic pressure on gravity wall. Design based on seismic pressure	Mononobe-Okabe method	48.55
	Seismic displacement of gravity wall. Design based on allowable displacements	Richard-Elms method	34.77
Case 2–Saturated condition with dynamic active earth pressure and hydrodynamic loads acting on the wall	Static pressure acting on the gravity wall Design based on force equilibrium	Coulomb theory	27.67
	Seismic pressure on gravity wall. Design based on seismic pressure	Mononobe-Okabe method	56.54
	Seismic displacement of gravity wall. Design based on allowable displacements	Richard-Elms method	41.51

Table 8 Weight of wall under both static and dynamic conditions

Condition	Existing weight of wall (kN/m)	Safe weight of wall required (kN/m)	Remark
Static	150	124.64	Unsafe
Dynamic	150	150.69	Unsafe

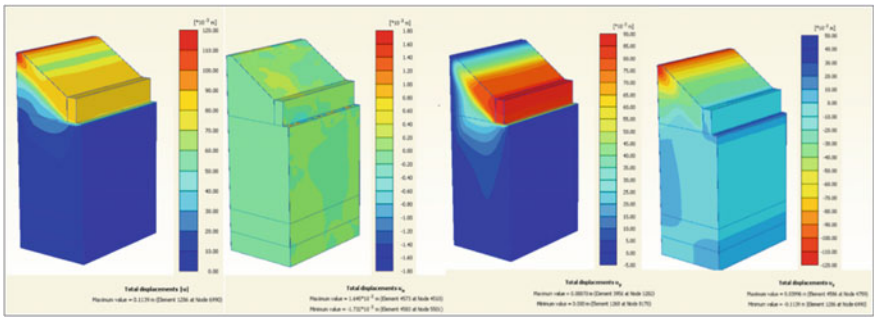

Fig. 11 Numerical analysis using PLAXIS 3D

Table 8 shows that the weight of the wall designed to resist movement due to static loads is quite high than required. Since the wall is founded on weak soil, it will not be able to bear the additional weight of the wall and collapse. Similarly, the weight of the wall provided to resist the movement due to dynamic loads is not sufficient. Hence, the wall is unsafe in both cases.

8.3 Numerical Analysis

The numerical analysis of the gravity retaining wall using FEM software Plaxis 3D is performed (Fig. 11). The deformations are obtained.

9 Comparison of Back Analysis Results

The foundation soil is loose and saturated. The results of conventional back analysis and numerical analysis are found to produce comparable results with the site deformations. The factor of safety obtained from conventional back analysis and numerical analysis is compared. The wall collapsed as a result of bearing capacity failure. Unscientific design and construction of the wall on weak soil led to this kind of failure. The soil present below the wall is already susceptible to liquefaction. The train-induced vibrations accelerated the liquefaction in the foundation soil

Table 9 Comparison of deformations

Method	Lateral displacement (mm)	Vertical displacement (mm)
Seismic displacement analysis and settlement calculation	100	28
Numerical analysis	80	30
Distress measurement at the site	90	20

Table 10 Comparison of results of back analysis

Conventional back analysis (by stability check)			
FS	Overturning	Sliding	Bearing capacity failure
	5.4	2.5	2.4
Numerical analysis using PLAXIS 3D			
Global FS	1		

and backfill. This led to the loss of bearing capacity of the soil and the wall underwent differential settlement leading to collapse. In addition to this, the presence of poor backfill material and lack of drainage led to water retention during rain and floods. The train-induced vibrations caused a rearrangement of the fine-sized particles, which increased the pore water pressure and effective stress decreased which resulted in liquefaction of the foundation soil. This induced additional lateral thrust on the wall resulting in its collapse. In Table 9, the deformations obtained from the site are compared with the conventional back analysis results and numerical PLAXIS 3D software results. The deformations conform with the numerical and conventional back analysis results. The factor of safety is obtained and the mechanism of failure of retaining wall design is presented (Table 10).

10 Conclusions

The vibrations were found to be very weak to cause any significant damage to the structure. The foundation soil is susceptible to liquefaction. The train-induced vibrations act as a trigger mechanism leading to liquefaction and differential settlement of foundation soil. The backfill soil has poor permeability which leads to water retention and exerts the additional lateral thrust on the wall. Stability checks performed show that the mechanism of failure is bearing capacity failure. The weight of the wall designed to resist movement due to static loads is quite high than required. Since the wall is founded on weak soil, it will not be able to bear the additional weight of the wall and undergo bearing capacity failure. The deformations obtained from conventional and numerical methods are compared with the deformations at the site. They are found to produce comparable results. A cantilever retaining wall on a pile foundation is the possible solution to the problem.

References

1. Amick H.: Frequency-dependent soil propagation model. Proc SPIE. 72–80. https://doi.org/10.1117/12.363836 (1999)
2. Chopra A..K.: Dynamics of Structures: Theory and Applications to Earthquake Engineering, Pearson Education Limited (2014)
4. Chouw, N., R. Le, G. Schmid: "Vibration transmitting behavior of the soil", Proc. of the Europ. Conf. on Struct. Dyn. (Eurodyn '90), Univ. of. Bochum, Germany, A.A. Balkema (1991)
3. Dowding C.H.: Construction Vibrations, 2nd Edition, Intl Society of Explosives (2000)
5. Hall L.: Simulations and analyses of train-induced ground vibrations in finite element models. Soil Dynamics and Earthquake Engineering, 23, 403–413 (2003). https://doi.org/10.1016/S0267-7261(02)00209-9.
6. Kramer, S.L.: Geotechnical Earthquake Engineering. Prentice-Hall, Upper Saddle River, New Jersey (1996)
7. Lichtberger, B.: Track Compendium, Eurail Press. Tetzlaff-Hestra GmbH & Co., Hamburg, Germany (2005)
8. Marcuson, W.F.: Definition of Terms Related to Liquefaction, Journal of Geotechnical Engineering Division, ASCE, 104(9), 1197–1200 (1978)
9. Matsuo, H., O'hara. S.: Dynamic pore water pressure acting on quay walls during earthquakes Proceeding of the Third WorkI Conference on Earthquake Engineering. I ol. 1, New Zealand pp. 130–140 (1965)
10. Richart, R.E., Hall, J.R, Woods, R.D.: Vibrations of Soils and Foundations, Prentice Hall Inc., New Jersey (1970)
11. Robert, D.: Forensic Geotechnical and Foundation Engineering. McGraw Hill Education (1997)
12. Sivakumar Babu, G.L. et al.: Forensic analysis of failure of retaining wall. In: 15th Asian Regional Conference on Soil Mechanics and Geotechnical Engineering, Japanese Geotechnical Society (2015)

Numerical Analysis of Laterally Loaded Pile Near Sloping Ground

Rajeswari Botcha, Teja Munaga, and Kalyan Kumar Gonavaram

1 Introduction

1.1 Laterally Loaded Piles

Laterally loaded piles (LLP) are frequently used for the support of bridge abutment, retaining walls, stabilized fabricated embankment and natural slopes, offshore structure, etc. [1–3]. In the case of high-rise structures and chimneys, 20% of the vertical load is expected in the form of horizontal loads due to wind [4, 5]. The soil–pile system behavior is primarily nonlinear, and a laterally loaded pile derives its load carrying capacity through soil-pile system. The performance of the pile-soil system depends on soil properties, material and diameter of pile, type of loading, and bed slope of the ground [6, 7]. Due to the inherent variability of soils in nature, soil properties vary spatially and pile properties and load systems possess different degrees of uncertainty. In coastal regions, the terrain of the ground is more likely to be made of slope. Piles embedded near slopes have to resist both lateral and axial loads subjected due to the superstructure [8–10]. The available literature mostly considers the pile situated on horizontal ground without giving much attention to pile located on sloping ground. The work pertaining to piles located near sloping ground is very limited, and its behavior is not clearly understood so far.

The existing mechanism for load transfer in case of laterally loaded pile proves to be effective in case of horizontal ground. The mechanisms available earlier cannot be applied in case of piles embedded in sloping grounds. Mathematical modeling proves to be an economical way to analyze the response of piles embedded in sloping

R. Botcha · T. Munaga · K. K. Gonavaram (✉)
Department of Civil Engineering, NIT Warangal, Warangal, Telangana 506004, India
e-mail: kalyan@nitw.ac.in

T. Munaga
e-mail: mteja@student.nitw.ac.in

C. N. V. Satyanarayana Reddy et al. (eds.), *Dynamics of Soil and Modelling of Geotechnical Problems*, Lecture Notes in Civil Engineering 186,
https://doi.org/10.1007/978-981-16-5605-7_2

grounds. Numerical and experimental studies are performed for embedded in dry sloping ground to investigate the effect of ground slope and edge distance on pile response.

1.2 Finite Element Method

PLAXIS 3D is a finite element method used for the three-dimensional deformation analysis of all type of structures. It is suitable for all types of geotechnical structures such as shallow footing, deep footing, retaining walls, pile raft, and pile groups with different loading conditions. Foundations form the interaction between an upper structure and the soil. Settlements depend upon native soil conditions and on the development technique. Pile group will be analyzed effectively by means of three-dimensional finite component to simulate soil behavior and soil-structure interaction.

The overall dimensions of the model boundaries is composed of 21D along horizontal plane (where D is the pile diameter) and a height of 1.7L (where L is the length of the pile). These dimensions were assumed to be adequate to eliminate the influence of boundary effects on the pile performance [11]. Pile, soil, and pile-cap are discretized into 20 node isoparametric continuum elements. Interface between pile/pile cap and soil is modeled using 16 node isoparametric surface elements with zero thickness. Numerical model is extended for analysis for group of pile in sloping ground. A parametric study is conducted to examine the effect of slope angle, pile configuration, and soil properties.

2 Methodology

2.1 Pile and Soil Properties

Free-head concrete pile is considered for the current research. The pile diameter varying from 0.15 to 1.0 m with a length of 10 m is considered for current study. The elastic modulus of pile is considered as 22.5×10^6 kPa. The piles are considered to be embedded in the soil at the edge of the slope as shown in schematic diagram (Fig. 1).

The soil strata for analysis was selected based on the bore hole data. The detailed parameters used in layered soil are given in Table 1.

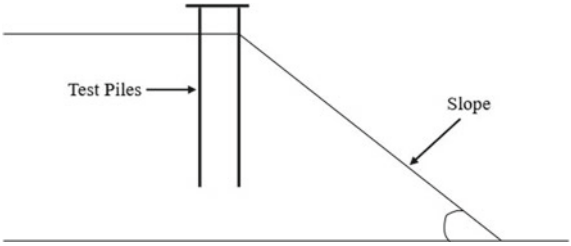

Fig. 1 Schematic diagram of test piles located at the edge of the slope

Table 1 Properties of layered soil

Depth (m)	Soil	Safe bearing capacity (kPa)	Young's Modulus of soil (kPa)	Poisson ratio	K_h (kN/m^2)
0–1.7	Clay	90	11,000	0.45	12,000
1.7–3	Sand	SPT = 24 (175)	36,000	0.35	40,000
3–5.7	Clay	210	21,000	0.45	24,000
5.7–15.45	Sand	SPT = 45–50 (250–275)	60,000	0.35	70,000

2.2 *Validation*

PLAXIS 3D was validated using the experimental work related to [8]. The variation of load vs. deflection was plotted for both experimental and finite element analysis in Fig. 2. It can be inferred from the figure that the results are similar at every stage of load increment. The deviation of finite element analysis results with experimental

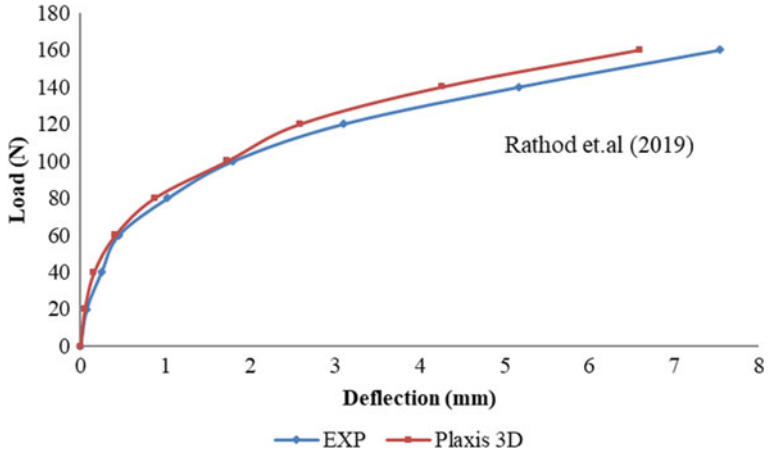

Fig. 2 Schematic diagram and validation of PLAXIS 3D

results is found to be negligible. It indicates that PLAXIS 3D results are in good agreement with experimental results.

2.3 Modeling

PLAXIS 3D enables for modeling of structures with desired properties. The soil stratification is defined using the bore hole. The structural components of model are defined in structure mode. The mesh properties are defined, and the geometry model is discretized and transformed to finite element model. The excavation, activation of various structural components, defining the water level can be achieved in staged construction mode.

3 Results

To analyze the lateral capacity of single and group pile under static lateral load, different diameter of piles and different sloping grounds are used. All single piles are analyzed under free head condition. A concrete pile of diameter 0.15 m and embedded length of 9.5 m below the ground level and 0.5 m above the ground level were used. A concrete pile cap of 20 cm thickness was used for pile groups. Load was applied at the pile head in case of single pile. The model analysis of single pile on sloping ground is shown in Fig. 3. In group pile embedded length of pile was 9.5 m below the ground level, and the pile cap was constructed 0.3 m above the ground

Fig. 3 PLAXIS 3D model for single pile

to avoid the frictional resistance and passive resistance of the pile cap. A line load was applied on the cap at 0.3 m above the ground level in case of pile group. Top deformation was measured exactly on the horizontal and sloping ground level.

3.1 Load Deflection Behavior

The lateral capacity of single pile in layered soil was determined by applying incremental load, and the corresponding deformation was measured for each load increment. The obtained load vs. deflection is plotted in Fig. 4. The load deflection curve was found to be initially linear. With further increase in load, deformation increased due to soil weakening. The curves also show that, at any stage of load increment, the variation in the load carried by the pile in the horizontal ground is higher than that of the piles embedded on other slopes. Load capacity was measured corresponding to pile head deflection of 0.1D [12–14]. The variation of lateral load with increase in the slope of the ground is studied. The lateral load corresponding to a pile head deflection of 0.1D for horizontal ground, 1 V:5H, 1 V:3H, and 1 V:2H, is found to be 25 kN, 23 kN, 17 kN, and 15 kN respectively. It can inferred that with change in slope of ground from horizontal to 1 V:2H, the lateral load decreased by 40%.

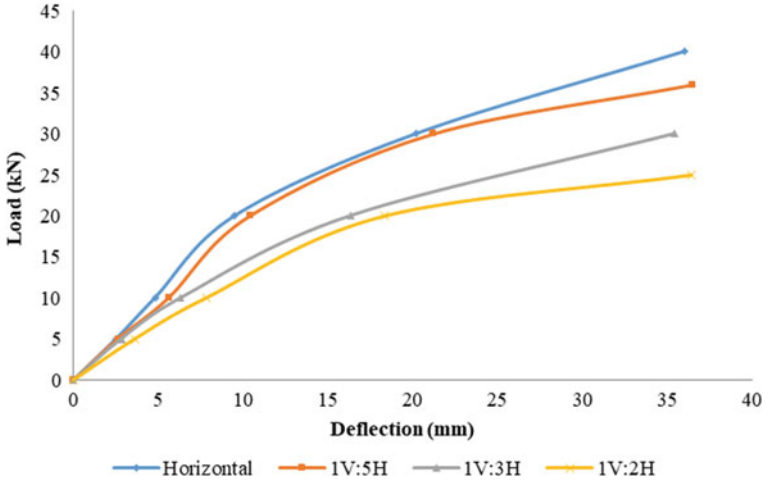

Fig. 4 Effect of Slope on Load vs Deflection behavior of Single Pile

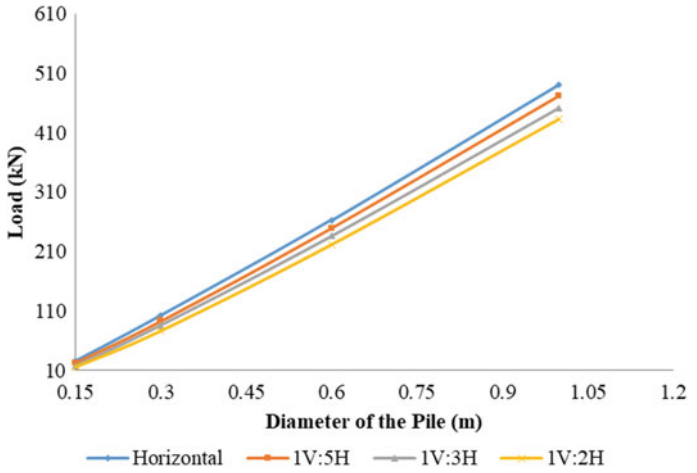

Fig. 5 Slope effect on diameter of Pile

3.2 Combined Effect of Slope and Diameter of the Pile

The variation of lateral load corresponding to 0.1D with an increase in pile diameter and slope of the ground is shown in Fig. 5. It can be observed that for a considered pile diameter, with an increase in the slope from horizontal to 1 V:2H, the lateral load decreased. This is due to reduction in the size of the passive wedge thus leading to reduction in the passive soil resistance offered to the pile. For a considered slope of the ground, with an increase in the diameter of the pile, the lateral load corresponding to 0.1D increased. However, the magnitude of variation in lateral load for change in slope is greater for pile of diameter 1.05 m than that of 0.15 m. It can be inferred that increase in pile diameter results in relatively increased performance of piles in sloping grounds.

3.3 Effect of Spacing on Behavior of Pile Groups

The variation of load vs. deflection for 3 × 3 pile group is shown in Fig. 6. For the considered pile configuration, with an increase in the spacing from 3 to 7D, the lateral load corresponding to a pile head deflection of 0.1D increased. This is due to reduction of overlapping stress zones between the piles in the pile groups.

The influence of pile spacing on the load carrying capacity is estimated in terms of pile group efficiency. The efficiency of pile group is computed using the following expression:

$$\text{Efficiency, } \eta = Q_g/(n_g Q_s), \text{ [14]}$$

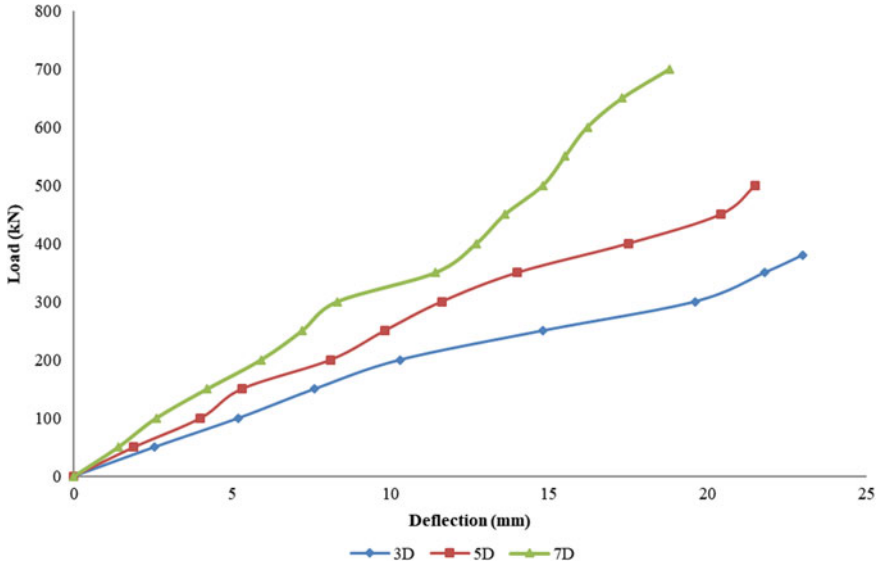

Fig. 6 Load vs deflection curve with varying spacing from 3 to 7D

Q_g = Pile group capacity corresponding to 0.1D pile head deflection.
n_g = No of piles in Pile Group.
Q_s = Single pile capacity corresponding to 0.1D pile head deflection.

Correspondingly the efficiency of pile groups is calculated for considered pile configurations and plotted against the slope of the ground for different pile spacing in Fig. 7. It can be observed that pile groups embedded in horizontal ground has an efficiency of more than 90% for all the spacing considered. However, with the change

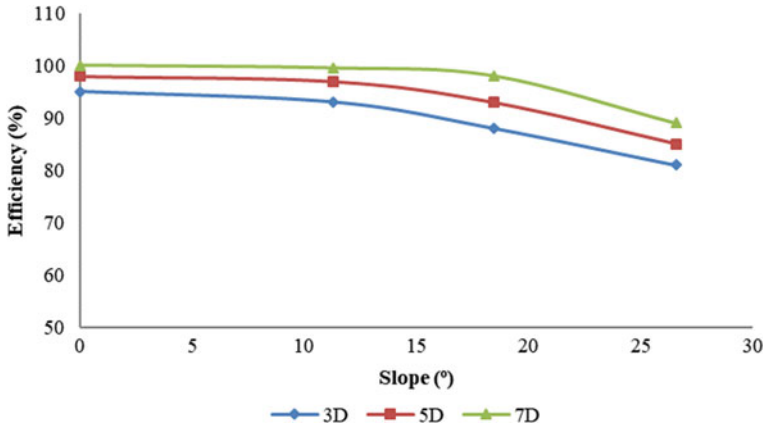

Fig. 7 Effect of Pile spacing and Slope on efficiency of Pile groups

in the slope from horizontal to 1 V:2H, the efficiency of pile groups decreased for all the spacing considered. This is due to the reduction in the passive soil wedge in front of the pile groups.

4 Conclusions

1. With an increase in slope from horizontal to 1 V:2H, the load carried by the pile decreased by 40% due to decrease in passive resistance offered by soil.
2. With an increase in diameter of pile, the effect of slope on load carrying capacity is found to be significantly increasing due to passive wedge on the side of slope.
3. With an increasing spacing from 3 to 7D, the effect of slope on efficiency pile group is decreasing due to passive wedge of soil and decreasing shadowing effect on pile.

References

1. Madhusudan Reddy, K., Ayothiraman, R.: Experimental studies on behavior of single pile under combined uplift and lateral loading. J. Geotech. Geoenviron. Eng. **141**(7), 04015030 (2015)
2. Rollins, K.M., Peterson, K.T., Weaver, T.J.: Lateral load behavior of full-scale pile group in clay. J. Geotech. Geoenviron. Eng. **124**(6), 468–478 (1998)
3. Prakash, S.: Behavior of pile groups subjected to lateral loads. University of Illinois (1962)
4. Matlock, H., Reese, L.C.: Generalized solutions for laterally loaded piles. J. Soil. Mech. Found. Div. **86**(5), 63–94 (1960)
5. Matlock, H., Reese, L.C.: Generalized solutions for laterally loaded piles. Trans. Am. Soc. Civ. Eng. **127**(1), 1220–1247 (1962)
6. Reese, L.C., Welch, R.C.: Lateral loading of deep foundations in stiff clay. J. Geotech. Geoenviron. Eng. **101** (1975)
7. Poulos, H.G.: Behavior of laterally loaded piles I. Single piles. J. Soil. Mech. Found. Div. **97**(5), 711–731 (1971)
8. Rathod, D., Muthukkumaran, K., Thallak, S.G.: Experimental investigation on behavior of a laterally loaded single pile located on sloping ground. Int. J. Geomech. **19**(5), 04019021 (2019)
9. Muthukkumaran, K., Sundaravadivelu, R., Gandhi, S.R.: Effect of slope on py curves due to surcharge load. Soils Found. **48**(3), 353–361 (2008)
10. Deendayal, R., Muthukkumaran, K., Sitharam, T.G.: Analysis of laterally loaded group of piles located on sloping ground. Int. J. Geotech. Eng. **14**(5), 580–588 (2020)
11. Kim, Y., Jeong, S.: Analysis of soil resistance on laterally loaded piles based on 3D soil–pile interaction. Comput. Geotech. **38**(2), 248–257 (2011)
12. Broms, B.B.: Lateral resistance of piles in cohesionless soils. J. Soil Mech. Found. Div. **90**(3), 123–156 (1964)
13. Chandrasekaran, S.S., Boominathan, A., Dodagoudar, G.R.: Experimental investigations on the behaviour of pile groups in clay under lateral cyclic loading. Geotech. Geol. Eng. **28**(5), 603–617 (2010)
14. Chandrasekaran, S.S., Boominathan, A., Dodagoudar, G.R.: Group interaction effects on laterally loaded piles in clay. J. Geotech. Geoenviron. Eng. **136**(4), 573–582 (2010)

Development of Equivalent Lattice Beam Model for Support System in Tunnels and Caverns Using FEM Analysis

Rishabh Tiwari and U. K. Singh

1 Introduction

In tunneling, lattice girder poses some similar function as steel arch support, as it serves as an element of temporary lining to support excavation initially and sometime as a part of permanent lining, offers an extremely prudent alternative to other support technique for an extensive variety of ground condition [1–3]. Lattice girder is utilized as a NATM support to prevent the development of initial deformation until the point when it is completely cured; shotcrete is poured instantly after drilling. It is a combination of truss and beam element, and it transfers load to the lower bar through the bending and axial force. Lattice girder has a three-dimensional structure and length/width ratios can be 10–15. They can be fully integrated with the shotcrete lining and form optimum bond to the ground supported. LG acts as immediate and reliable ground support in the excavation area. The main advantages of lattice girder over conventional steel arch supports are its low weight per meter length of the girder and a more efficient bond with shotcrete making it economical than other supports [4].

The objective of this paper is to rule out the most reliable method for determination of equivalent stiffness of lattice girder, which is a primary rock support system employed in tunnels and caverns, comparing some techniques available in the literature. The equivalent stiffness of lattice girder was determined by four continuum modeling techniques namely, equivalent moment of area based on simply supported condition or fixed end condition, method of parallel axis theorem, Burgardt and Cartraud' method, and direct energy approach method [5]. The equivalent stiffness so obtained was used as input parameter in numerical analysis tool STRAND 7.0 for analysis of equivalent lattice beam. The maximum deflection and bending stress at center of equivalent lattice beam were calculated and compared with central deflection and bending stress in case of original lattice girder using this analysis tool

R. Tiwari (✉) · U. K. Singh
Department of Mining Engineering, Indian Institute of Technology (ISM), Dhanbad 826004, India

C. N. V. Satyanarayana Reddy et al. (eds.), *Dynamics of Soil and Modelling of Geotechnical Problems*, Lecture Notes in Civil Engineering 186,
https://doi.org/10.1007/978-981-16-5605-7_3

STRAND 7.0 The results obtained from FEM analysis using four techniques given by researchers are used to determine equivalent stiffness and also used for simulating the results obtained from FEM analysis of lattice girder and equivalent lattice beam. In this paper the design of a simple beam equivalent to a lattice girder has been done and its performance to the actual lattice structure is being compared.

1.1 Continuum Modeling Techniques

The purpose of a computer model is to accurately represent a structure mathematically. However, limitations exist that inhibit the ability to achieve an "exact" mathematical model. One such limitation is the number of nodes/members that the computer program can utilize. To help alleviate this problem for structures with trusses, a method has been developed to replace trusses with beam elements thereby reducing the size of the computer model required for analysis. The equivalent beam to a lattice structure (Fig. 1) shown in Fig. 2 is calculated by three basic methodologies in which the equivalent stiffness of the beam is calculated based on the deflection of

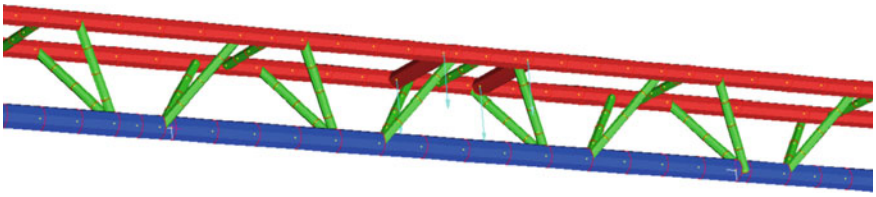

Fig. 1 Lattice girder (LG) under consideration

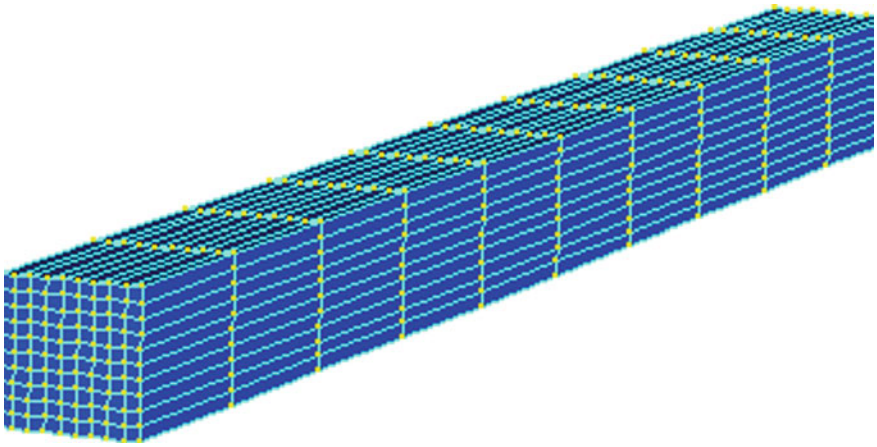

Fig. 2 Equivalent beam

the loaded lattice girder (3D truss), the equivalent stiffness 'I' is calculated based on the truss cross-sectional area using parallel axis theorem, and the equivalent stiffness of the beam is calculated based on strain energy stored in the beam as an action of application of load. The stiffness of continuum lattice beam equivalent to lattice structure is estimated with available techniques proposed by these researchers [5]. The four continuum modeling techniques are equivalent moment of area based on simply supported condition or fixed end condition, method of parallel axis theorem, Burgardt and Cartraud' method, and direct energy approach method.

2 Design of Equivalent Beam Using Continuum Modeling

The calculation of equivalent properties for beam model using all the four techniques is carried out [6]. The calculation has been carried out for lattice girder LG1: 25 × 20 × 10 @170 × 152. The equivalent moment of inertia and area of cross section are calculated for sections LG1 and given in Table 1.

2.1 Finite Element Numerical Modeling of Actual Lattice Girder

A finite element analysis program Strand 7.0 was utilized, for the three dimensional numerical testing of the Lattice Girder and equivalent beam. The Strand 7.0 has a user interface to interact with software and for the analysis broadly; two types of models were developed. One type of model was developed to represent the actual lattice girder, and the other types of models were developed to represent equivalent beam. This actual lattice girder model was developed using beam element geometry, and the equivalent beam was developed using brick elements. The straight bar components, with circular cross section area of measurements S1, S2, and d, are utilized to represent the lower furthermore, the upper arcing bars, and the diagonal bars of the LG individually. An adequate number of elements are utilized to precisely display

Table 1 Summary of properties of equivalent beams obtained from methods A, B, C, and D

Method	Method name	Eauivalent beam LG1 25 × 20x20@100 × 170	
		MoI, m^4	Side of square beam, mm
A	MOI by parallel axis theorem	2 790 666	78
B	Back analysis from deflection results of FE analysis	1,046,901	60
C	Burgardt and Cartraud method	1 914 634	69.3
D	Direct energy approach	1 914 634	69.2

the arched geometry of the structure. The standard strengthening steel, grade S500, is utilized in the experiment, and the yield stress of the reinforcing steel 500 MPa, Young's modulus 200 GPa, and Poisson's proportion 0.3 are used for the inelastic investigations.

Kinematics constraints were provided at both the end of support of the lattice girder model. The left end support of LG Model, pin support was provided only z rotation allowed and translation was restrained in all directions while on the right end of LG Model, roller support was provided only x translation, and in plane z rotation were allowed. The attribute was applied along the chord length of the LG arc model, and deflection was measured at center of lower bar and plotted load versus deflection curve and compared with the experimental data. The material property of reinforcing bar used in numerical analysis and sectional properties of lattice girder is shown in Table 2.

FEM Analysis of Equivalent Lattice Beam

The dimensions of the equivalent lattice beam being estimated using four continuum techniques. The equivalent lattice beam shape assumed square, and material was chosen as mild steel. The material properties and sectional properties for numerical evaluation are listed in Table 3.

Numerical modeling of equivalent beam was done using the finite element method (FEM) based software STRAND7.0. The geometry of equivalent beam created, material and sectional properties are assigned to beam.

The vertical downward concentrated point load on center of lattice beam was applied till the yield point of beam. Kinematics constraints were provided at both the end of support of the lattice girder model. The left end support of LG Model, pin support provided only z rotation restrain, and translation was restrained in all direction while on the right end of LG Model, roller support allowed only x translation and in plane z rotation restrained. Attribute was applied along the chord length of LG arc model. The maximum central deflections of beam in vertical and transverse directions were measured. The contour diagram of deflections in x and y directions is generated using the numerical tool.

All the results from analysis of numerical models of actual lattice girder and equivalent lattice girder obtained by all four methods are summarized in Table 4. This summary enlists calculated value of moment of inertia, value of vertical displacement corresponding to the load of 40 KN.

Table 2 Material properties for analytical evaluation and sectional properties

		Elastic modulus (MPa)	Unit weight (kN/m^3)	Poisson ratio	MOI (mm^4)	Centroid (mm)
Triangular		200,000	7,850	0.3	3219.497	67.02
Lattice girder	Upper, Diagonal, and Lower chord					

Table 3 Material properties for analytical evaluation and sectional properties lattice beam (Square shape)

Method used for estimating equivalent stiffness	Size of square Beam (mm)	Elastic modulus (MPa)	Unit weight (kN/m3)	Poisson ratio
Method-A: Equivalent moment of inertia by parallel axis theorem	78.2	200,000	7,850	0.3
Method-B: Deflection of The loaded lattice girder	60	200,000	7,850	0.3
Method-C: Burgardt en method	69.24	200,000	7,850	0.3
Method-D: Direct energy approach	69.24	200,000	7,850	0.3

Table 4 Summary of central deflections in lattice girder and equivalent beam

S no	Method of analysis of Equivalent Beam	LG 1: MoI, mm^4	Load, kN	Mid-point vertical displacement, mm
1	**Actual LG**	**2 790 666**	**40**	**3.98**
2	**Four Methods (Equivalent LG Beam.)**			
A	Moment of Inertia Method	2 790 666	40	2.005
B	Back analysis using standard formula (Using value of deflection for back analysis from actual numerical model)	1 046 901	40	3.98
C	Burgardt and Cartraud	1 914 634	40	3.356
D	Direct energy approach	1 914 634	40	3.356

The calculations have been carried out for lattice girders, LG 1, and equivalent beam, and deflection results are shown in Table 4.

3 Conclusions

1. The observations from Table 4 show that vertical deflections derived from FEM analysis of lattice girder structure and equivalent lattice girder beam by four methods are comparable, and Method–B gives exact simulating result.
2. The Method–A is least accurate, and Methods C and D give similar deflection values. The techniques given by Methods C and method D show the results, second best close to results of numerical analysis.

3. The size of equivalent lattice beam has been designed, and dimensions of beam show that technique given by method B: Back analysis method provides the most conservative cross section of the beam. Similarly, the method A: Moment of inertia by parallel axis theorem method estimates the most economical cross section of the beam.

References

1. Mitelman, A., Elmo, D.: Analysis of tunnel-support interaction using an equivalent boundary beam. Tunn. Undergr. Space Technol. **84**, 218–226 (2019). ISSN 0886-7798. https://doi.org/10.1016/j.tust.2018.11.021
2. Baumann, T., Betzle, M.: Investigation of the performance of lattice girders in tunneling. Rock Mech. Rock Eng. **17**(2), 67–81 (1984)
3. Braun, W.M.: Lattice girders offer economy and performance for tunnel support. Tunn. Tunn. Int. **15**(5), 19–21(1983)
4. Kim, S.J., Han, T.H., Back, J.S., Kang, Y.J.: Evaluation of the structural performance of tetragonal lattice girders. Int. J. Steel Struct. **13**(1), 31–47 (2013)
5. Teughels, A., De Roeck, G.: Continuum models for beam-and platelike lattice structures. In: Fourth International Colloquium on Computation of Shell & Spatial Structures IASS-IACM, 5–7 June 2000, Chania–Crete, Greece (2000)
6. Tiwari, R.: M.Tech. Thesis, Department of Mining Engineering, Indian Institute of Technology (ISM), Dhanabad, Jharkhand, India (2020)

Earth Pressures of Soils Partially Replaced with Building Derived Materials for Narrow Backfill Condition

Jayatheja Muktinutalapati and Anasua GuhaRay

1 Introduction

Soil or water at different elevations is retained by structures like cantilever sheet piles, anchored sheet piles, and reinforced cantilever walls. The backfill soil is crucial portion, and earth pressures induced in backfill are shear stresses which disturb the stability and performance of retaining wall and backfill as whole. It is very difficult to interpret the earth pressures of soil when the retaining wall is constructed near rock faces and slopes which offers narrow width for backfill. For retaining walls with limited backfill space, the coefficient of active earth pressures decreases with ratio of height of wall and width of backfill [1]. Classical earth pressure theories of Coulomb and Rankine assume that the slip surface of the backfill soil is linear planar and develops across the heel of their taining wall with an inclination angle of $(45° + \varphi/2)$ from the horizontal. When the interface friction angle between the backfill soil and the back of retaining wall is less, this assumption is found to yield satisfactory results [2]. Many analytical solutions assume that failure in narrow backfills are planar and occurs in segmental pattern [3]. The shape of pressure profiles is non–linear and not a triangular distribution in case limited backfill widths; one reason for non–linear distribution of lateral earth pressures is arching of soils [4]. The pressure distribution mainly depends on wall–soil interaction, angle of internal friction, and aspect ratio of backfill.

In general, the failure surfaces are designed based on the assumption that the backfill extends to a sufficient distance from the wall to allow the failure plane to fully develop across the heel of the retaining wall and into the backfill soil behind the wall. This assumption is found to be valid most of the time when retaining walls are built. However, retaining walls at times must be built adjacent to an existing

J. Muktinutalapati · A. GuhaRay (✉)
BITS-Pilani Hyderabad Campus, Secunderabad 500078, India
e-mail: guharay@hyderabad.bits-pilani.ac.in

C. N. V. Satyanarayana Reddy et al. (eds.), *Dynamics of Soil and Modelling of Geotechnical Problems*, Lecture Notes in Civil Engineering 186,
https://doi.org/10.1007/978-981-16-5605-7_4

stable wall to widen existing highways or near the foundations of existing buildings in urban areas [4] or constructed near rigid rock faces in mountainous regions [5], causing the space of backfill to be constrained and limited to a narrow distance from the wall. If the backfill aspect ratio (B/H) is less than 0.55, traditional theories like Coulomb or Rankine cannot estimate lateral earth pressures with the desired accuracy [6]. An analytical solution based on trapezoidal thrust failure wedge was proposed by researchers, which assume linear planar slip surface [7]. Planar and bilinear slip surfaces were assumed in limit equilibrium analysis on mechanically stabilized earth retaining walls with narrow geosynthetic-reinforced backfill soil [8, 9]. Nonlinear slip surfaces are observed by some researchers [5, 10] to be formed in narrow backfill.

The past literature indicates that very few analytical and experimental studies are available on retaining walls with narrow backfills. To the best of author's knowledge, no studies are available on laboratory model scale studies of earth pressures of backfill soil replaced with construction and demolition wastes. The present study proposes a sustainable and eco-friendly usage of Building Derived Materials (BDM) mixed with locally available red soil (R) and sand (S) as a backfill for these retaining walls. The BDM content is varied from 0–30% by weight of soil. Results of the tests demonstrate that the failure surfaces are limited by the width of narrow backfills. The cantilever retaining wall is also modeled using commercially available finite element software PLAXIS 2D. The force–based analysis is carried out by incorporating Hardening Soil (HS) model. A series of consolidated undrained triaxial tests are conducted on soil-BDM blends in order to obtain Duncan Chang's hyperbolic parameters. The soil parameters obtained from hyperbolic modeling is used for modeling the soil in Hardening Soil model in Plaxis. The analysis carried out on retaining walls are explained in subsequent sections.

2 Materials and Methodology

2.1 Soil

Two different types of soils are used in the present study. The first type of soil is red soil (R), collected from Medchal district in the state of Telangana, India. This is the main type of soil available in Hyderabad and surrounding areas. The soil used in the present study is found to be fine-textured. It shows a quick reaction to dilatancy test. The soil is classified as Silty Sand (SM) following Unified Soil Classification System (USCS). A plasticity index value of seven signifies that the soil contains less clayey particles. Also, the soil is found to be almost free from swelling. Wet sieve analysis of red soil is carried out according to IS: 2720 (Part 4)–1985. The grain size distribution curve of red soil is provided in Fig. 1. From Fig. 1, it can be observed that value of C_u is less than 5 and that of C_c is 0.11, and the red soil is gap graded.

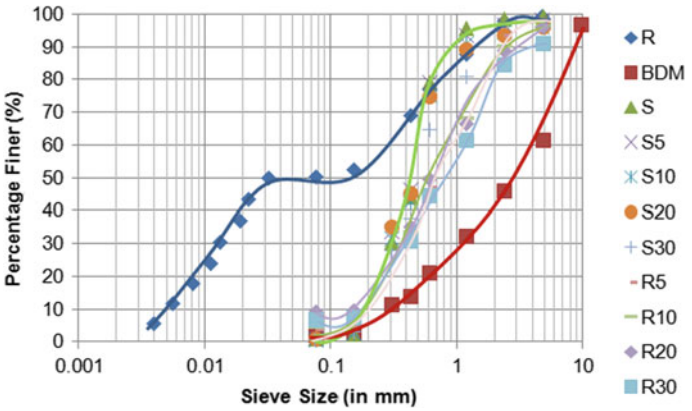

Fig. 1 Particle size distribution of soils blended with building derived materials

The sand (S), used in the present study, is collected from west Godavari river basin near Telangana state of India. The sand is classified as poorly graded sand (SP) according to USCS. A constant relative density of 40% is maintained by rainfall pouring method to achieve medium dense condition. It has a maximum dry unit weight of 18.43 kN/m^3, as obtained through vibratory table method. The minimum dry unit weight is 17.24 kN/m^3 obtained by pouring in its loosest state. From grain size distribution curve (Fig. 1), it is observed that C_u and C_c of sand are 2.5 and 0.9 respectively, indicating a poorly graded soil. The sand particles, as observed through stereomicroscopic images, are mostly angular in shape, with smaller percentages of rounded and sub-rounded particles.

2.2 Building Derived Material (BDM)

The BDM is collected from two local construction and demolition sites near Shameerpet area in Telangana, India. The construction and demolition wastes consist of concrete, brick, ceramic tiles, glass, wood, plastic, concrete, and brick. According to Bhattacharya et al. (2013), CDW consists of 65% concrete, 25% brick, 5% wood, and 5% miscellaneous materials like metals and plastic. The concrete and brick component of this CDW is separated manually and used as BDM for this study. The collected BDM is crushed with the help of a mechanical jaw crusher to less than 10 mm, 10–30 mm, and 30–50 mm. The grain size distributions of each of these sizes are analyzed before and after compaction. It is observed that more than half of larger sized particles tend to get crushed under the action of load. Hence, particles in the range of 2.36–10 mm are utilized in the present study. Grain size distribution curves of locally available soils blended with BDM are presented in Fig. 1.

2.3 Model Retaining Wall Apparatus

The laboratory scale model retaining wall apparatus is designed in a tank of length 1.2 m and height of 0.9 m. The front side of tank is fitted with acrylic sheet of 25 mm, and three sides are built with mild steel (Fig. 2). The retaining wall is instrumented with earth pressure sensors to capture pressure distribution and an inclinometer to monitor the rotations. This setup represents plane strain boundary conditions with rigid, non–yielding wall of dry backfill. The wall is arranged at 0.65 m position to create narrow backfill condition; when L/D is less than 0.4, it resembles a narrow backfill conditions [10]. Rotation is enabled with hinged attachment provided at the bottom base of tank. Active and passive conditions are created by pulling the wall from backfill or pushing the wall into the backfill with jack attached to it. The hydraulic jack of capacity 150 kN is arranged at 0.75 m height to hold the plate in up–right position and also to rotate the plate. To ensure uniform load distribution on to plate element, a bar element is fastened on non–backfilled side in contact with hydraulic jack. Three earth pressure cells of embedded type are arranged on the backfill side to assess pressures at three different conditions of rotation. Diameter of EPC is 200 mm with 7 mm thickness with compressible fluid in pressure pad. The accuracy of sensor is (+) or (−) 0.5% and can measure up to 500 kPa. A LVDT is arranged on the non–backfill side to calculate displacements of wall from mean position. A rough interface is created by sticking emery paper on backfill side. The

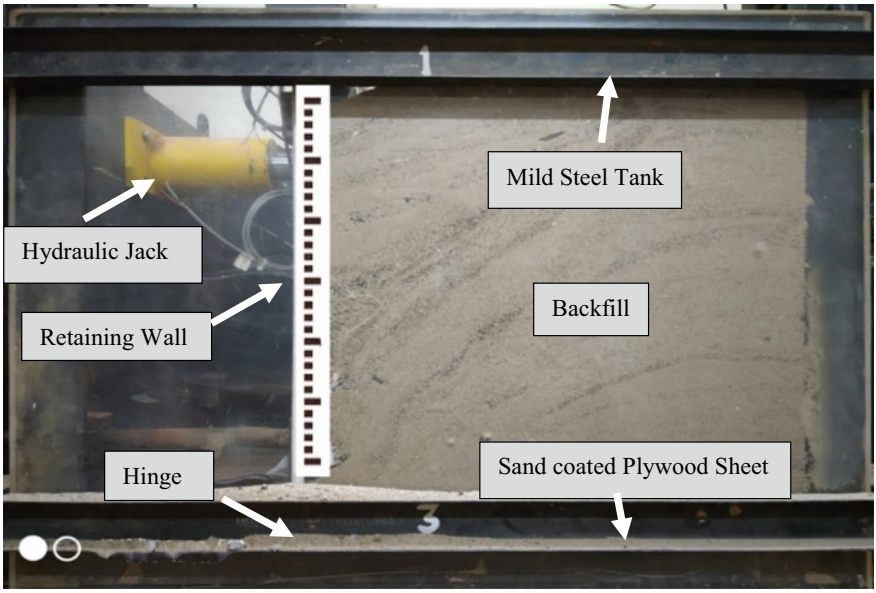

Fig. 2 Model retaining wall test apparatus

interface angle (δ) is calculated by shear box tests and found out to be 13.2° for R–BDM and 13.6° for S–BDM blends respectively. This interface angle also depends on grit size of emery paper and type of soil utilized for the study.

2.4 Numerical Modeling

A numerical modeling is carried out in PLAXIS 2D to validate the experimental results using plane strain conditions. 15 noded triangular elements called as cubic triangle are selected with very fine meshing (Fig. 3). The material properties of numerical model are tabulated in Table 1. Hardening soil model is used as constitutive relation to analyze stress–strain response of soil elements. Hardening soil is formulated based on Duncan–Chang hyperbolic postulates [11], which is utilized for soils in elastoplastic and perfectly plastic states as backfill soils will achieve plastic state when subjected to rotations.

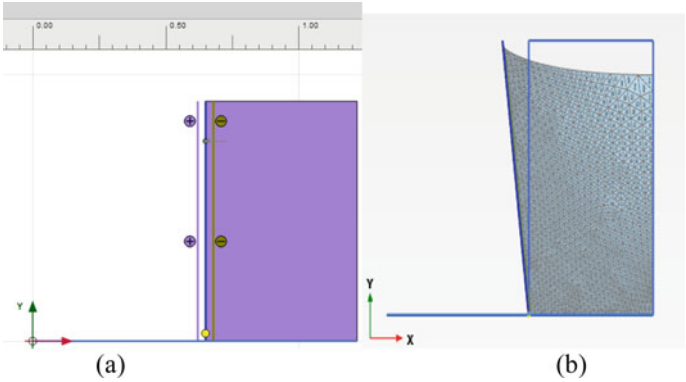

Fig. 3 **a** FEM model of retaining wall **b** Deformed Mesh in K_a case

Table 1 Input parameters of numerical model

Element	Values
(1) Plate element	
EA (kN/m) EI (kN m^2/m) Weight (w) (kN/m/m) Poisson's ratio (υ)	1.25×10^7 1.15×10^5 8.2 0.15
(2) Hinge element	Free to rotate at top
(3) Interface element	
$R_{inter\ (R–BDM)}$ $R_{inter\ (S–BDM)}$ Interface Strength	0.7 0.8 Rigid

3 Results and Discussions

Variation of maximum dry unit and optimum moisture content with BDM content is presented in Fig. 4 a and b respectively. It is observed that the unit weight of soil composite is increasing proportionally with increase in BDM content. This is because void spaces in soil mass are occupied by BDM particles till 20% of replacement. After 20% replacement, unit weight is decreased due to increment in void spaces. When soil mass is replaced by 30% BDM, major quantity of load is taken by BDM particles which leads to improper densities. Optimum values of dry unit weight and optimum moisture content of sand are reported as 19 kN/m^3 and 8.5%, while that of red soil are 18 kN/m^3 and 7.5% respectively on addition of 20% of BDM. Sand–BDM (S–BDM) content exhibited more unit weight values than red soil–BDM (R-BDM). Addition of coarse (BDM) particles increases the gradation parameters and increases the unit weight upon compaction. This in turn increases the shear strength till optimum content of BDM is replaced.

Figure 5 a, b, and c present the variation of at-rest, active, and passive earth pressures along the height of the wall respectively. From Fig. 5a, it is observed that

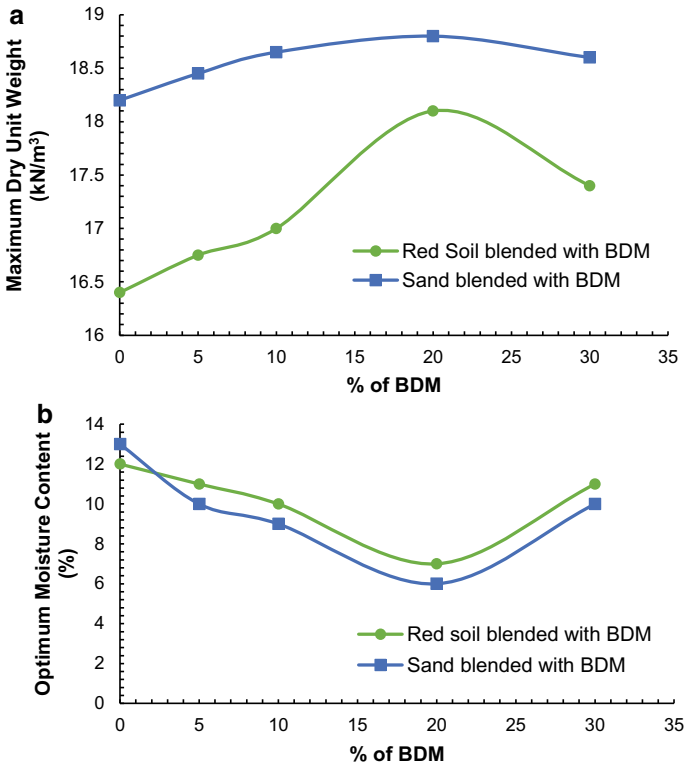

Fig. 4 **a** Variation of MDD with % of BDM. **b** Variation of OMC with % of BDM

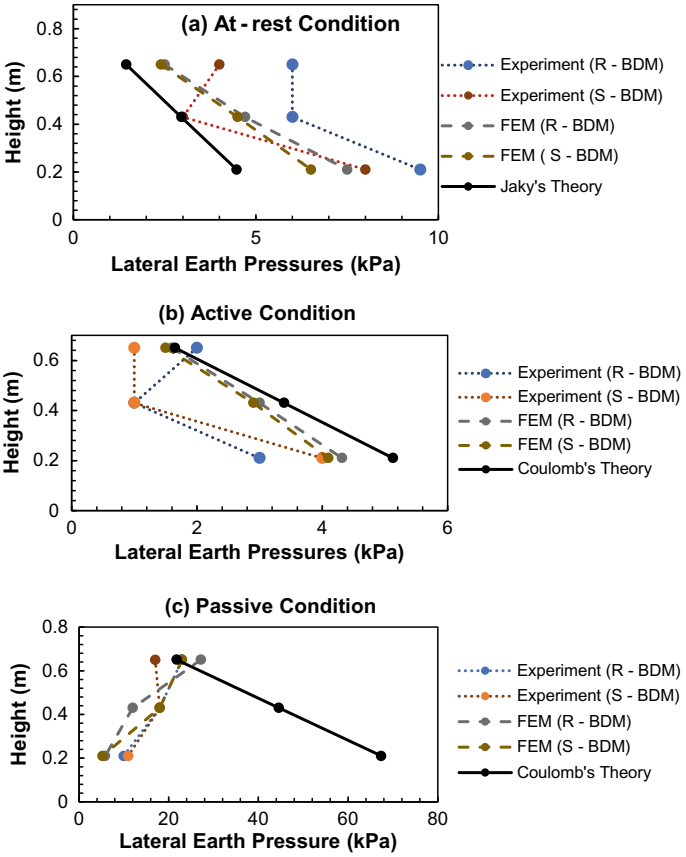

Fig. 5 Variation of **a** at-rest, **b** active, and **c** passive earth pressures with height of wall

observations from experimental investigations are discrete and following a non–continuous distribution with wall height. Jaky's theory and readings recorded from numerical methods are indicating triangular distribution. At–rest earth pressures are dependent on unit weight of soil and its angle of internal friction. In K_0 case, Jaky's theory underpredicted the earth pressures for R–BDM and S–BDM blends. At–rest earth pressures are in range of 2.5–10 kPa for both blends while numerical method predicted a triangular distribution with pressures ranging from 2.4 to 7.5 kPa.

Active case (K_a) which is created from rotating the wall away from backfill is important in designing a retaining structure. Active earth pressures are lower in terms of magnitude when compared with at–rest case. Experimental observations are compared with Coulomb's theory equation as the wall–soil interaction is rough. Non–continuous nature is observed in experimental outcomes, and deviation is observed in middle sensor points. This is due to loss of contact between soil and sensor as wall is made to rotate away from backfill. Active earth pressures are dependent of unit weight

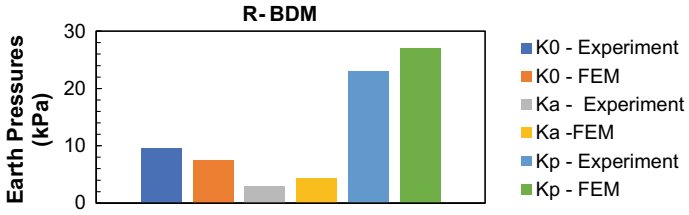

Fig. 6 Comparison between experimental and numerical results for R–BDM blend

of soil, shear strength offered by backfill material, and interaction. Coulomb's theory has over predicted the pressure readings subtended by experiment and numerical outcomes. Numerical and theoretical values are following a triangular distribution with pressures increasing linearly with wall height. Experimental readings are in range of 1–4 kPa for both blends in active case.

Passive case, which is created by rotating the wall into backfill, is crucial in stability calculations of retaining structures. Passive earth pressures are resisting forces offered by backfill soil against rotation of wall which are presented in Fig. 7. Greater magnitude of pressures is observed for backfills which possess higher unit weights. From the figure, it is observed that reverse trend is noted in contrast with traditional theories. Passive pressures are in magnitude of 5–27 kPa with greater magnitudes of pressures in the upper part of wall. This is due to the fact that the top of the wall is rotated into the backfill with the help of hydraulic jack.

Figures 6 and 7 present the comparison between experimental and numerical results of both R–BDM and S–BDM blends. Values from numerical modeling under predicted experimental results in K_0 case, whereas in K_a, K_p case numerical modeling values over predicted experimental outcomes. Error percentages in all three cases for two blends are less than 20%. This study suggests that hardening soil model based on hyperbolic theory can be useful in assessment of earth pressures at field conditions.

In any case of rotation, slip surfaces cannot be developed fully in backfill at narrow backfill position. Hence, physical modelling followed by numerical analysis can present the critical parameters and failure surfaces with appropriate outputs.

The present study is limited to dry backfill condition with zero surcharge loading. Only three EPCs are used to measure the lateral earth pressures. More number of

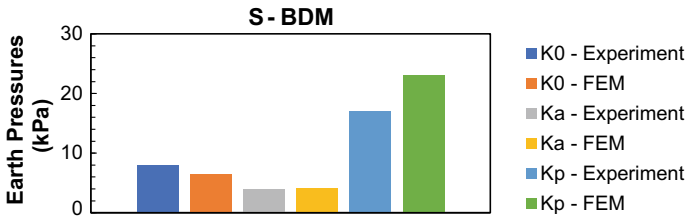

Fig. 7 Comparison between experimental and numerical results for S–BDM blend

EPCs will give a better understanding of the distribution of earth pressures. Care is taken during the experiment so as the model steel retaining wall does not bend under the action of lateral pressure. The soil is considered to be homogenous and compacted at a relative density of 40%. However, in some cases it is difficult to maintain a constant relative density. The presence of BDM particles in backfill sand renders it to be non–homogenous. In the finite element model, plane strain condition is assumed. Ideally two more EPCs needs to be placed on the transverse side of the wall in order to check whether the earth pressures are coming out to be the same in the transverse direction. However, in addition to the measurements of lateral pressure at various locations, a visual observation of the backfill movement from the top further confirms that the boundary effects were negligible. It is observed that the backfill soil moves and settles uniformly in the transverse direction, indicating that the potential boundary effects due to both the transverse dimension and side wall frictions are negligible. As a result, the retaining wall model can be categorized as a plane-strain model and backfill movements can be observed and characterized from its sides. This observation is consistent with the studies of Yang and Tang [10].

4 Conclusions

Precise estimation of earth pressures acting on retaining walls mainly depends on slip surface developed in backfill. The present study proposes an eco–friendly and sustainable usage of Building Derived Materials (BDM) admixed with locally available soils as backfill materials. A narrow backfill condition is considered when the ratio between the backfill width and height of the retaining wall falls below 0.4 and the slip surface intersects with the back wall. The following conclusions can be drawn based on the findings of the present study.

1. The maximum dry density is to attain edits peak value on mixing 20% BDM with soil.
2. In passive case, greater values of earth pressure are observed near the top of the wall and decreased with depth, in contrast to the classical earth pressure theories as the wall is rotated about its base.
3. In active case, earth pressures from experimental investigations exhibited lesser values than the earth pressures calculated from Coulomb's Equation; Jaky's theory under predicted the experimental results in K_0 case.
4. An increase in backfill width decreases the rotation of wall, thus reducing the probability of rotational failure. Hence narrow backfills are more prone to rotational failure.
5. Hardening soil model based on Duncan–Chang hyperbolic relation can capture the stresses and displacements induced in backfill soil for R–BDM and S–BDM blends.

6. The numerical results suggest a good agreement with that of experimental results, for all three positions of the wall, the variations in at-rest, active and passive earth pressure values are in the range of 20–25% as seen from the plots.

Funding This work is supported by the Department of Science and Technology, Science and Engineering Research Board (SERB), Govt. of India, through the Early Career Research Award (Project ID: ECR/2016/000522).

References

1. Leshchinsky, D., Hu, Y., Han, J.: Limited reinforced space insegmental retaining walls. Geotext. Geomembr. **22**(6), 543–553 (2004)
2. Terzaghi, K., Peck, R.: Soil Mechanics in Engineering Practice, 2nd edn. John Wiley, New York (1967)
3. Greco, V.R.: Seismic active thrust on cantilever walls with short heel. Soil Dyn. Earthq. Eng. **29**(2), 249–252 (2009)
4. Yang, K.H., Ching, J., Zornberg, J.: Reliability-based design for external stability of narrow mechanically stabilized earth walls: calibration from centrifuge tests. J. Geotech. Geoenvironmental Eng. **137**(3), 239–253 (2011)
5. Frydman, S., Keissar, I.: Earth pressure on retaining walls near rock faces. J. Geotech. Eng. **113**(6), 586–599 (1987)
6. Greco, V.R.: Active thrust on retaining walls of narrow backfill width. Comput. Geotech. **50**, 66–78 (2013)
7. Chen, J-J., Li, M-G., Wang, J-H.: Active earth pressure against rigid retaining walls subjected to confined cohesionless soil. Int. J. Geomech. **17**(6), 06016041-1-6 (2017)
8. Lawson, C. R., Yee, T. W.: Reinforced soil retaining walls with constrained reinforced fill zones. In: Proceedings of GeoFrontiers 2005, ASCE, Reston, VA, pp 2721–2734 (2005)
9. Leshchinsky, D., Hu, Y., Han, J.: Limited reinforced space in segmental retaining walls. Geotext. Geomembr. **22**, 543–553 (2004)
10. Yang, M., Tang, X.: Rigid retaining walls with narrow cohesionless backfills under various wall movement modes. Int. J. Geomech. **17**(11), 04017098-1-8 (2017)
11. Duncan, J.M., Chang, C.Y.: Nonlinear analysis of stress and strain in soils. J. Soil Mech. Found. Div. **96**(5), 1629–1653 (1970)

Development of a Full-Scale Retaining Wall Model to Evaluate Lateral Earth Pressure Reduction Using EPS Geofoam

Vikas Patil, Mrunmay Junagade, and Dasaka S. Murty

1 Introduction

Retaining walls are designed to withstand pressures from retained materials, surcharge pressures due to movement of vehicular traffic or loads from foundations of adjacent buildings on their backfills, seismic loading, etc. They may also be vulnerable to catastrophic failures during earthquakes due to sudden increase in lateral loads, increase in pore pressures, etc., thus making the appropriate estimation of earth pressures critically important for safe and cost-effective designs. Controlling the cross section of retaining walls successfully requires reducing the total lateral thrust acting on the walls. This can be achieved by placing compressible inclusion between the wall and the backfill and for this purpose, various materials have been examined including EPS geofoam, tire chips, granulated rubber–soil mixture, soil bags, glass fiber, cardboard and hay. However, their material behavior is often unpredictable; glass fiber is seen to be over-compressible; cardboard and hay are biodegradable with time. Expanded Polystyrene Geofoam is a material with predictable stress–strain behavior, possesses high strength to density ratio, is weather-resistant, lightweight, environmentally safe, inexpensive and can be easily shaped or prefabricated [9]. One of the possible methods for lateral thrust mitigation is the Controlled Yielding Technique with Geofoam as a compressible inclusion (Figs. 1 and 2).

As shown in Fig. 1, the controlled yielding technique involves the installation of a vertical layer of a compressible medium abutting retaining wall and between the wall

V. Patil (✉) · M. Junagade · D. S. Murty
Department of Civil Engineering, IIT Bombay, Mumbai 400076, India

M. Junagade
e-mail: mrunmay@iitb.ac.in

D. S. Murty
e-mail: dasaka@iitb.ac.in

C. N. V. Satyanarayana Reddy et al. (eds.), *Dynamics of Soil and Modelling of Geotechnical Problems*, Lecture Notes in Civil Engineering 186,
https://doi.org/10.1007/978-981-16-5605-7_5

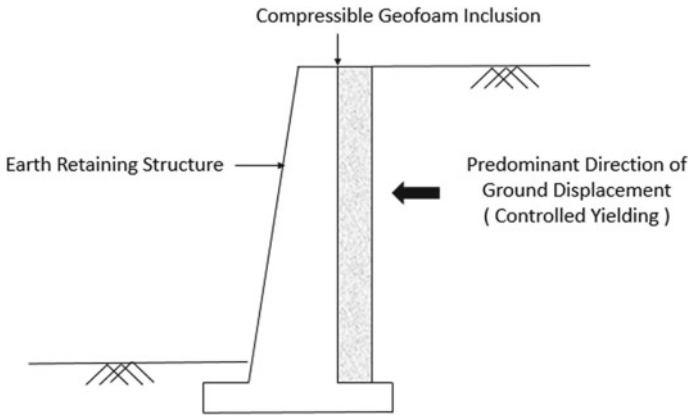

Fig. 1 Illustration of Reduced Earth Pressure Concept (After Horvath [10])

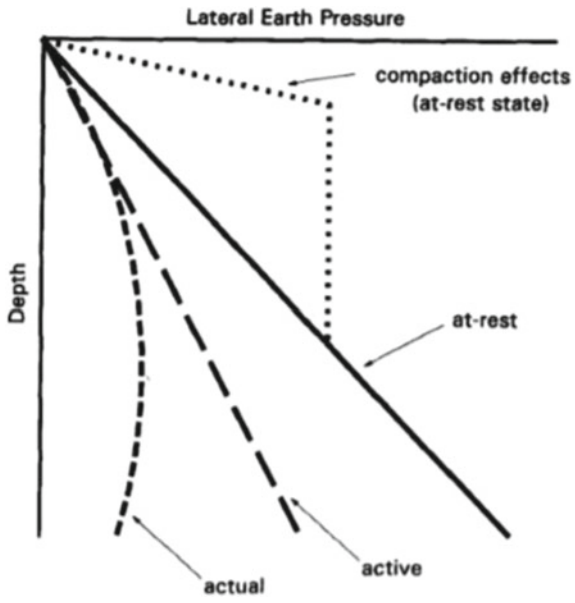

Fig. 2 Illustration of physical behavior of reduced earth pressure (After Horvath [10])

and backfill so as to allow soil to undergo lateral expansion and bring down lateral pressures to active earth pressures [10, 11]. The lateral expansion of soil depends on stiffness, stress–strain relations and the thickness of the inclusion. The presence of compressible inclusion allows arching to develop within retained soil and consequent mobilization of shear strength of soil, thus causing a reduction in lateral thrust. As a result, nonlinear distribution of earth pressures is seen with a peak near mid-height of the wall, as shown in Fig. 3.

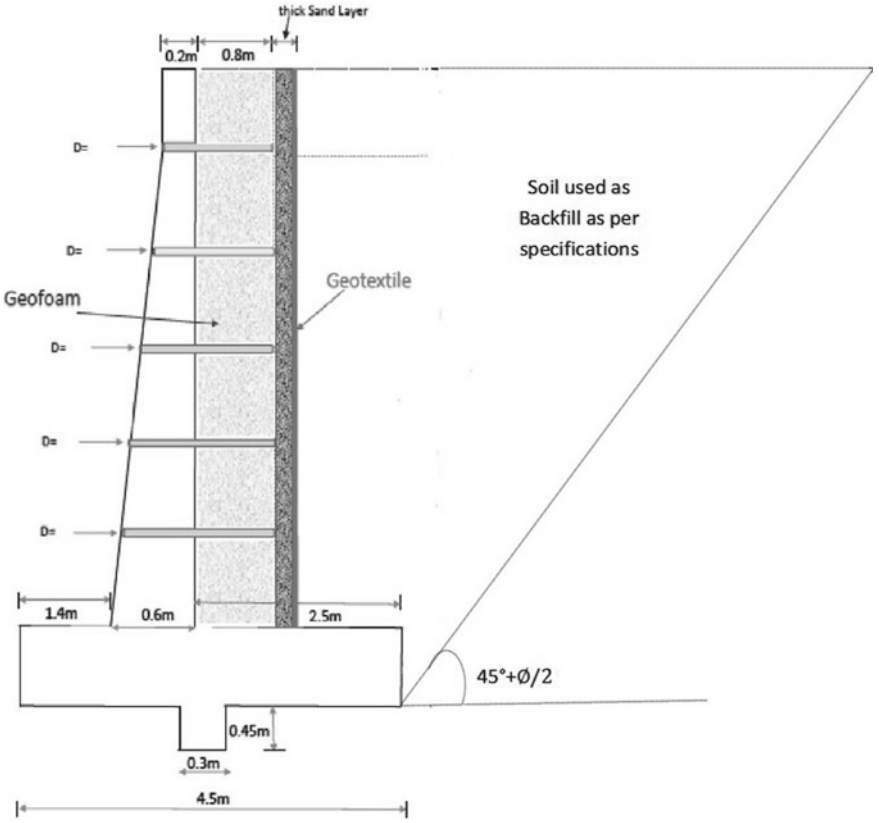

Fig. 3 Sectional view of retaining wall

Small-scale studies and numerical studies of using EPS Geofoam as inclusion in backfill have been documented by numerous researchers. Numerical analysis using the FEM approach for different ratios of the thickness of geofoam inclusion and wall height has shown that an increase in the thickness of compressible layers decreased lateral earth pressures [12]. Seismic performance analysis of both yielding and non-yielding retaining walls with geofoam using dynamic finite-element analysis suggests that permanent wall displacement under seismic load decreased steadily with increasing EPS buffer thickness [4, 5]. Based on their numerical analysis of yielding, Athanasopoulos et al. [1] and Zisimatou [26] reported that the inclusion of geofoam in gravity retaining walls has resulted in reduced lateral thrust due to backfill both in static and dynamic conditions [26]. They further noted that seismic isolation efficiency increased in general with an increase in geofoam thickness up to a certain limit. Shake table tests on a small-scale non-yielding retaining wall with geofoam backfill show that an increase in geofoam thickness leads to a higher reduction of earth pressure but becomes constant at higher accelerations [8]. Similarly, for a scaled gravity retaining wall model with combined surcharge and seismic loading,

it was noted that seismic earth pressure was reduced by more than 28.25% with the use of geofoam of density 10 kg/m^3 [3]. Comparison of different geofoam densities in shake table tests shows that the lower the EPS Geofoam modulus, the greater is the seismic load attenuation [2].

Available literature reveals that the controlled yielding technique significantly reduces earth pressure on retaining walls under static as well as dynamic loading conditions. However, most of the studies were limited to short-term behavior, i.e., the long-term efficiency of this technique is still under question. Further, the effect of subsequent changes in the mechanical properties of EPS geofoam on the lateral earth thrust is yet to be investigated thoroughly. Murphy [17] indicated that geofoam creep can have an important influence on compressible inclusion performance as lateral stress was seen to be highest under rapid loading conditions and decrease with time as creep effects become prominent. Secondly, results of scaled experimental and numerical model studies are valid for defined boundary conditions and scaling effects are always possible. Only limited field studies are available on the scaling effects and the creep of geofoam. However, their influence on the performance of geofoam as an inclusive in gravity retaining walls needs to be explored. Thus, keeping in mind the importance of field verification using large-scale walls, this study describes the development of a full-scale model with a cantilever retaining wall of height 6 m, constructed at the Indian Institute of Technology Bombay.

2 Field Setup

2.1 Cantilever Retaining Wall

An RCC cantilever retaining wall of 6 m height, 10 m length completely underground was constructed with 4 m without geofoam, 4 m with geofoam and remaining 2 m for carrying out parametric studies. The wall is designed to act as a rigid non-yielding retaining wall presumably subjected to at-rest lateral earth pressures. The height of the superimposed load is taken as 1.2 m, and the extent of backfill is as per the guidelines of IRC 78-2014. Figure 3 shows the sectional representation of the wall. It is proposed to provide a geotextile filter as an alternative to traditional granular material as it may pierce the geofoam inclusion. Sufficient weep holes are provided to ensure dissipation of excess pore pressure. The shear key is provided for provision against sliding along the base.

2.2 Instrumentation Setup for Wall Monitoring

Key aspects of the study involve measuring lateral earth pressures on the retaining wall, quantifying deformation of the geofoam inclusion and finding the tilt of the

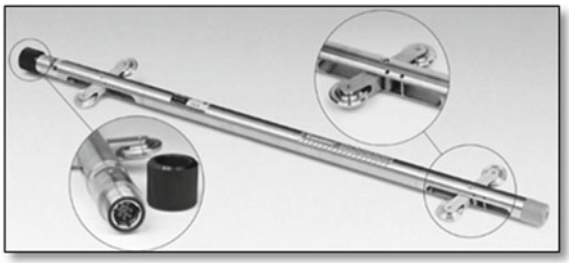

Fig. 4 Slope inclinometer (After Kyowa Elect. Instruments)

wall. For the above-mention goals, earth pressure sensors, laser-based displacement transducers and slope inclinometers are to be used, respectively.

For the wall to be subjected to at-rest lateral earth pressures, it is necessary to ensure that the wall does not deform. Thus, obtaining the slope profile of the wall becomes indispensable for which slope inclinometers are used. Slope inclinometers are geotechnical instruments used to measure horizontal displacements along various points on a borehole; these consist of the main components—grooved casings and the probe. In the field model, the casings are to be installed in boreholes within the stem of the wall. These boreholes extend from the top to the bottom of the wall and are constructed by placing vertical pipes of suitable diameters within the wall at the concrete-pouring stage itself. Wall tilt profile can then be obtained by lowering the probe along the casing. Placing the pipes substantially larger in diameter than the outer diameter of the inclinometer is necessary, as the casings can then be grouted firmly into place while ensuring their verticality. Figure 4 shows a typical inclinometer probe [13].

Measuring the deformation of geofoam in small-scale models can be done conveniently with the use of potentiometers, strain gauges, etc. However, in a full-scale model, physical contact to the geofoam section is extremely difficult; thus, quantifying the deformation along the section is a major challenge. The authors have envisioned using laser-based displacement sensors for this purpose. Laser distance sensors are optoelectronic sensors for non-contact displacement and distance measurements. Most commonly, laser displacement sensors operate either according to the time-of-flight measuring principle or phase comparison principle. A typical Laser-based Displacement Sensor [16] can be seen in Fig. 5. In the study, lasers from the devices will be targeted on a reflective screen placed at the end of the geofoam layer through already provisioned holes with a clear line of sight, and based on the transducer output the distance from the sensor to the end of the geofoam can be obtained. Successive readings over a period of time from holes along the height of the retaining walls will then give information on the deformation of geofoam at different locations.

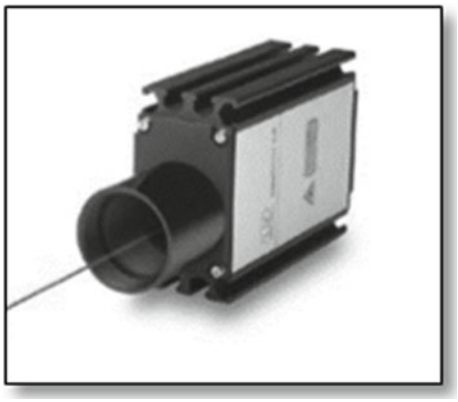

Fig. 5 Laser-based displacement transducer (After Micro-Epsilon)

2.3 Provisions for Instruments in Wall

In the present standard model of the RCC cantilever retaining wall, accounting for all possible parametric studies, a typical arrangement of weep holes, holes for pressure sensor and laser-based displacement transducer are proposed as per guidelines proposed by Lazebnik [15] for full-scale instrumentation as shown in Fig. 6. These holes are created during the casting stage itself by placing PVC pipes of respective diameters. The diameters of holes are chosen such that the cables and the connector

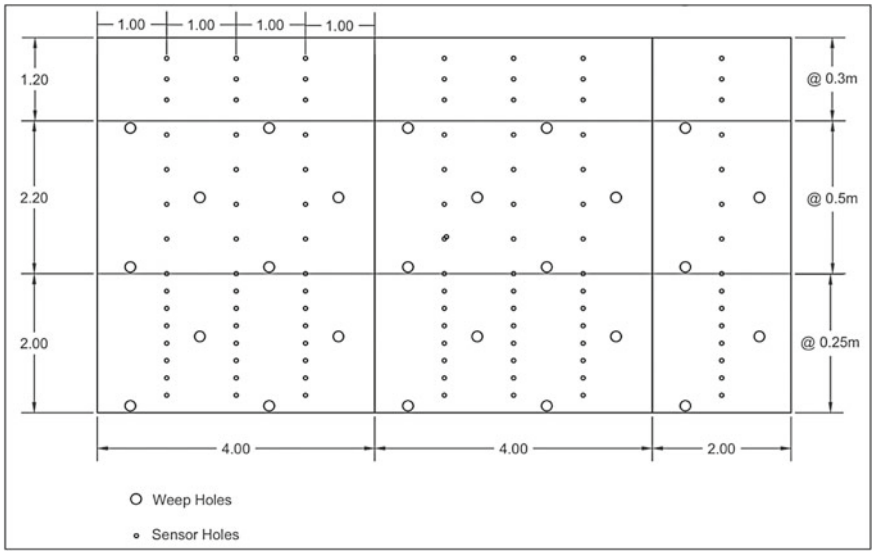

Fig. 6 Arrangement of weep holes, pressure sensors and displacement transducers along the length of retaining wall

pins for earth pressure sensors can be easily extended through the section of the wall. All the instruments including data loggers and computer are installed in a portable cabin adjoining the wall to facilitate reliable and continuous data acquisition.

3 Material Characterization

3.1 Geofoam

Significant properties of geofoam that influence the selection of its appropriate thickness and density include Young's modulus (E), compressive strength (σ_c), yield strength (σ_y) and elastic limit of geofoam. Geofoam of densities 15, 20 and 25 kg/m^3, designated as EPS15, EPS20 and EPS25 are to be used. Cube specimens are used for evaluating the geofoam properties by static compression test, as suggested by ASTM D7180-05. Typical stress–strain behavior of geofoam and definitions of some of the salient properties from static tests are schematically shown in Fig. 7. In the present study, the compressive load is applied using a Servo-hydraulic actuator. The setup of static test of EPS geofoam is shown in Fig. 8.

Axial stress corresponding to 10% axial strain from the stress–strain curve is defined as compressive strength. Static compression tests were performed on three specimens of size 100 mm × 100 mm × 100 mm of samples of different densities. Average values are reported as specimen properties. Figure 9 represents a sample axial stress–strain response of geofoam sample of density 20 kg/m^3. The average compressive strength of EPS 20 was found to be 87.5 kPa.

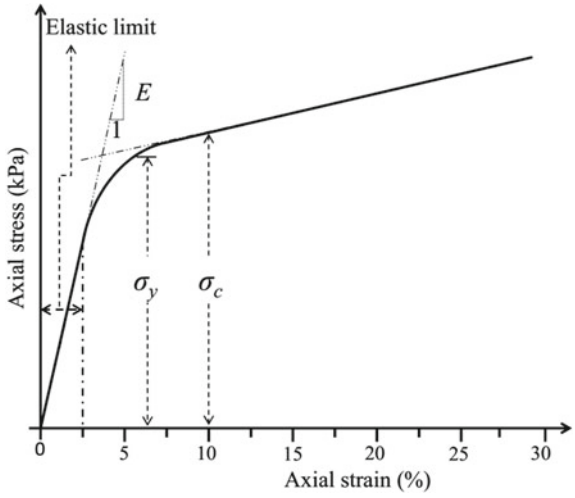

Fig. 7 Mechanical properties of EPS geofoam

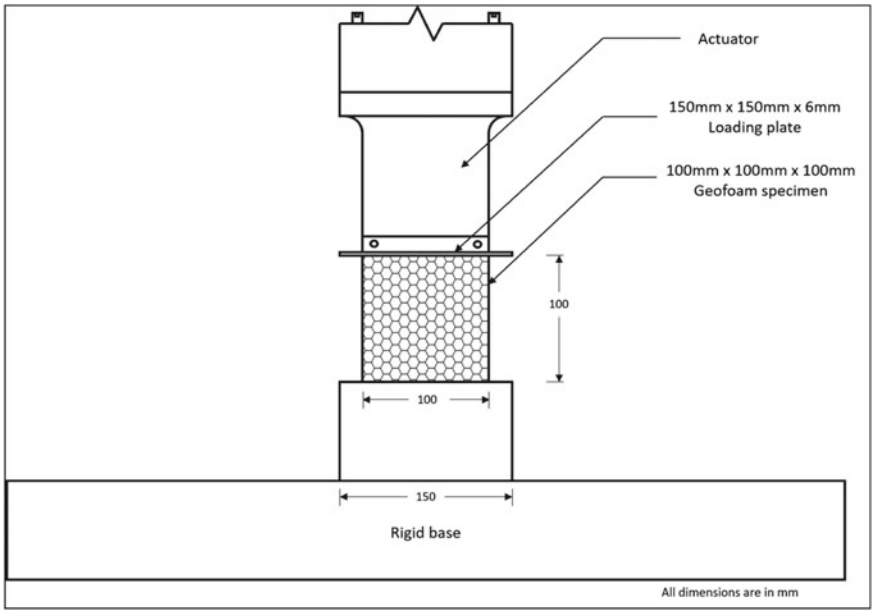

Fig. 8 Experimental static test setup of geofoam

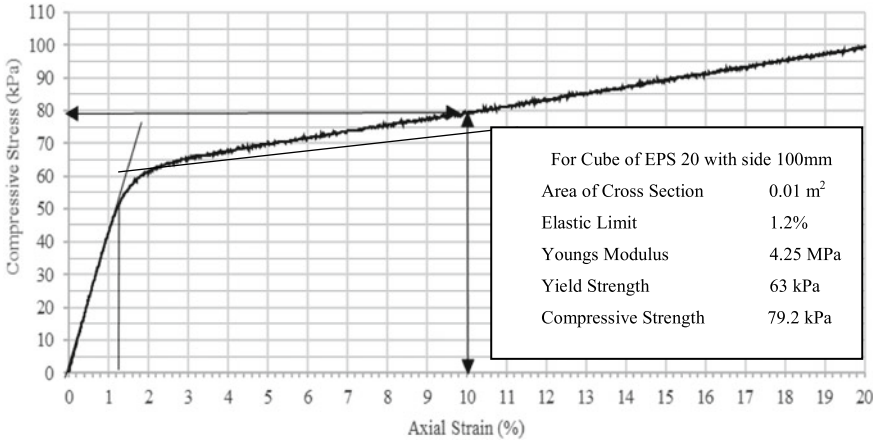

Fig. 9 Axial stress–strain response of EPS 20

3.2 Backfill Material

For the experimental study, the logical choice is to use standardized backfill material, for example, river sand. However, their use on large scale is a costly affair, and they may not be used in high embankments as it increases the cost of the project. Thus,

Table 1 Properties of proposed backfill

Liquid limit	51%
Plastic limit	39%
Free swell index	0
Field density	1580 kg/m^3
Water content	17.44%
Optimum moisture content	22.20%
Maximum dry density	1620 kg/m^3
Specific gravity of soil solids	2.62
Gravel	≈ 1.2%
Sand	≈ 70%
Fines	≈ 22%
IS classification	MH (Silt with high porosity)

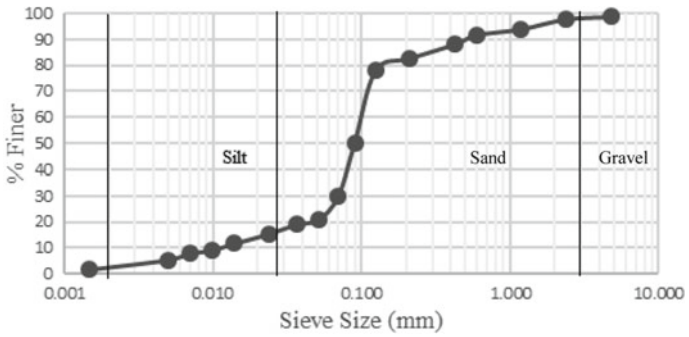

Fig. 10 Particle size distribution curve of backfill

to simulate the field conditions, locally available soil fulfilling the specifications of IRC 78-2014 is decided as a sound and more relevant option for backfilling. The soil is identified as Murum/Powai silty soil with cohesion = 54 kPa and angle of internal friction = 20° obtained from direct shear tests on samples prepared at O.M.C and M.D.D. Properties of the soil are listed in Table 1. As per guidelines listed in IRC 78-2014 on selection for backfill material, the soil is found to be fair to good for backfilling purposes (Fig. 10).

4 Calibration of the Earth Pressure Sensors

Earth pressure sensors are widely used for measuring earth pressure on the surface of a structure or in soil, and they need to be calibrated near to their intended application conditions [18, 20, 25]. The relation between applied pressure and sensor output

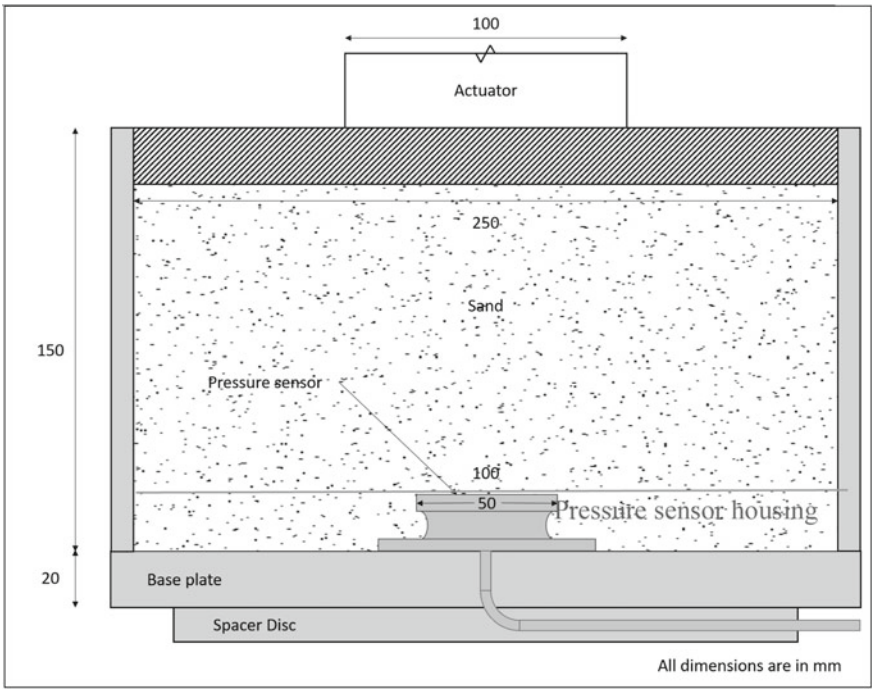

Fig. 11 Deadweight calibration setup used for pressure sensor calibration (After Gade, 2018)

varies with soil type, soil density and location of the sensor, either embedded or boundary [6]. The calibration of the pressure sensor involves the investigation of the unique relationship between the applied pressure and EPC output response [14]. Strain gauge-based sensors of capacity 200 kPa are considered for this study. A deadweight calibration setup (as shown in Fig. 11) previously developed by Gade [7] was used for the calibration of sensors.

The sensors are kept in a calibration chamber which is then filled with the soil from the field and compacted to the field density. Load is applied on the soil using a Hydraulic Actuator with a loading plate such that maximum pressure of 170 kPa with a displacement rate of 0.01 mm/s is reached in the chamber. The response of the earth pressure sensors versus pressure applied by the actuator gives a unique voltage–pressure relationship for each sensor. The sample is loaded and unloaded three times so as to obtain average calibration factors. A sample graph is shown in Fig. 12.

The literature reveals that strain gauge-based sensors pose certain problems, which make them unsuitable for long-term use due to a drift in zero reference point in strain gauges with the passing of time. Furthermore, these sensors respond differently

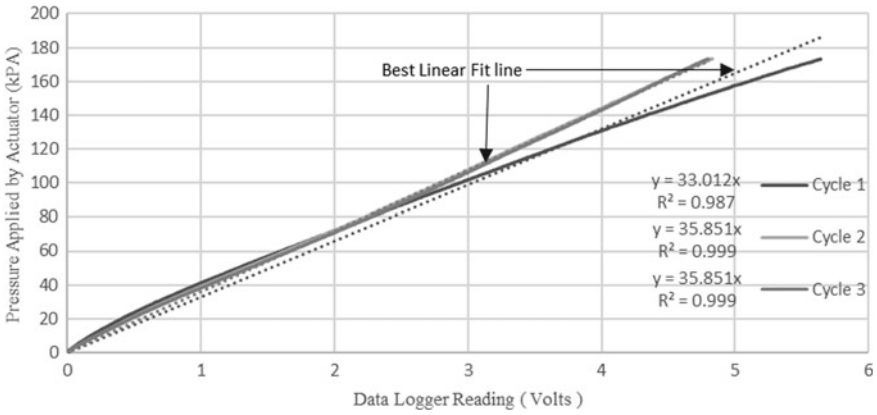

Fig. 12 Response of earth pressure cell versus pressure applied by actuator

to different soils and densities as well as external temperatures. Hence, it was decided to further use vibrating wire-based earth pressure sensors in conjunction with strain gauge-based sensors. These sensors consist of two welded plates with a cavity between them filled with de-aired fluid. Under external pressure, these plates squeeze the fluid inside. The pressure is then recorded by Vibrating Wire Transducers connected to the cavity. The key benefit of these sensors is a very small aspect ratio (typically $t/D < 0.1$) where t is the thickness and D is the diameter of the sensor. Tory and Sparrow [22] noted that for cells with aspect ratios below 0.1, constant over-registration of stresses allows for constant calibration factors. Another advantage over conventional strain-based gauge sensors is that Vibrating Wire-based sensors are not Susceptible to zero drift over a long period of time and also provide for auto compensation of temperatures due to in-built thermistors.

5 Summary

An overview of the establishment of the full-scaled retaining wall model is presented. The model described in this paper will be deployed for achieving the objectives including the following: to evaluate the scale effects on the earth pressure reduction through full-scale field testing of different heights of retaining walls, to evaluate the long-term creep of the geofoam, and its effect on the earth pressure reduction, to evaluate deformation pattern of retaining wall with and without geofoam, to evaluate the distribution of compressive strains in geofoam, to develop design charts for optimum density and thickness of geofoam for achieving maximum earth pressure reduction.

Acknowledgements The authors would like to thank Indian Institute of Technology Bombay, Ministry of Human Resources Department, Ministry of Earth Sciences, Govt. of India and SAVI Infrastructures, Pune, for their support in the project titled "Design and development of advanced yielding technique for static and dynamic earth pressure reduction on retaining structures using compressible geo-inclusions".

References

1. Athanasopoulos, Z.A., Lamote, K., Athanasopoulos, G.A.: Use of EPS geofoam compressible inclusions for reducing the earthquake effects on yielding earth retaining structures. Int. J. Soil Dyn. Earthq. Eng. **41**, 59–71 (2012)
2. Bathurst, R.J., Zarnani, S., Gaskin, A.: Shaking Table testing of Geofoam seismic buffers. Int. J. Soil Dyn. Earthq. Eng. **27**, 324–332 (2007)
3. Dasaka, S.M., Dave, T.N., Khan, N., Murali Krishna, A.: Evaluation of seismic earth pressure reduction using EPS Geofoam. In: Proceedings of the 18th International Conference on Soil Mechanics and Geotechnical Engineering, Paris (2013)
4. Ertugrul, O.L., Trandafir, C.T.: Reduction of lateral Earth Forces on yielding Flexible Retaining Walls by EPS geofoam Inclusions. ASCE, Geocongress, pp. 2068–2077 (2012).
5. Ertugrul, O.L., Trandafir, A.C.: Reduction of lateral earth forces acting on rigid non-yielding retaining walls by EPS geofoam inclusions. J. Mater. Civ. Eng. **23**(12), 1711–1718 (2011)
6. Gade, V.K., Dasaka, S.M.: Influence of contacting material on calibration response of diaphragm earth pressure cells. Indian Geotech. J. **50**, 133–141 (2019)
7. Gade, V.K., Dasaka, S.M.: Calibration of earth pressure sensors. Indian Geotech. J. **48**(1), 142–152 (2018)
8. Hazarika, H., Okuzono, S., Matsuo, Y.: Seismic stability enhancement of Rigid Nonyeilding Structure. In: Proceedings of the 13th, International Offshore and Polar Engineering Conference, pp. 697–702 (2003)
9. Horvath, J.S.: Expanded polystyerene (EPS) geofoam: an introduction to material behavior. Int. J. Geotext. Geomembr. **23**, 263–280 (1994)
10. Horvath, J.S.: The compressible inclusion functions of EPS geofoam: an overview of concepts, Applications and products. Res. Rpt. No. CE/GE-98–1, Manhattan College Civil Engineering Department, Bronx, NY. (1998)
11. Horvath, J.S.: The compressible inclusion functions of EPS geofoam. Int. J. Geotext. Geomembr. **15**, 77–120 (1997)
12. Karpurapu, R., Barthurst, R.J.: Numerical investigation of controlled yielding of soil retaining wall structure. Int. J. Geotext. Geomech. **11**, 115–131 (1992)
13. Kyowa Electronic Instruments, Manual on Insertion Type Inclinometer, Japan.
14. Labuz, J.F., Theroux, B.: Laboratory calibration of earth pressure cells. Geotech. Test J. 28(2):1–9 (2005). https://doi.org/10.1520/GTJ12089
15. Lazebnik, G.E.: Monitoring of Soil-Structure Interaction. Instruments for measuring soil pressures (1998). ISBN 978-1-4613-7740-5. https://doi.org/10.1007/978-1-4615-5979-5
16. Micro-Espilon, Manual on Laser Based Displacement Sensor
17. Murphy, G.P.: The Influence of Geofoam Creep on the Performance of a Compressible Inclusion. Geotext. Geomembr. **15**, 121–131 (1997)
18. Peattie, K.R., Sparrow, R.W.: The fundamental action of earth pressure cells. J. Mech. Phys. Solids **2**, 141–155 (1954). https://doi.org/10.1016/0022-5096(54)90021-6
19. Selig, E.T.: Soil stress gage calibration. Geotech Test J. **28**(2), 12089 (1980)
20. Tory, A.C., Sparrow, R.W.: The influence of diaphragm flexibility on the performance of an earth pressure cell. J. Sci. Instrum. **44**(9), 781–785 (1967)

21. Weiler Jr W., Kulhawy, F.H.: Factors affecting soil stress cell measurement in soils J. Geotech. Eng. Div. **108**(12), 1529–1548 (1982)
22. Zisimatou, E.: Seismic isolation of earth retaining walls using EPS Geofoam compressible inclusions-FE numerical analyses. MSc dissertation. Department of Civil Engineering, University of Patras, Greece (2009)

Prediction of Ultimate Bearing Capacity of Eccentrically Inclined Loaded Strip Footing Resting Over Dense and Medium Dense Sand Using Generalized Regression Neural Network

Vaibhav Chaudhary and Jitendra Singh Yadav

1 Introduction

The evaluation of bearing capacity is the major criterion in the construction of any infrastructure like buildings, dams, bridges, etc. There are several empirical, semi-empirical formulas or methods to estimate the ultimate bearing capacity of footing like Terzhaghi, Meyerhoffs, plate load method, etc. But these are conventional methods that are both time-consuming and less accurate and even sometimes the field methods are less applicable in a remote area as well. These laboratory and field methods are also limited to simpler problems and could not easily manipulate complexities that are generated mostly during performing these conventional methods. There are several geotechnical calculations that require complexities to attain a final result like settlement, slope failure, estimation of bearing capacity, etc. The estimation of bearing capacity of eccentrically inclined loaded strip footing by field methods is itself a challenging task. Therefore, the neural network technique is used to eliminate these complications. With the help of this technique, a well-trained and tested software model can be prepared.

The neural network works on the learning of the experimental or theoretical data. It relates the data with the output in the form of "activation functions". It provides the approximate result or output as compared to the desired output by minimizing errors through iterations. The objective of the current study is to develop a GRNN-General regression neural network prediction model using experimental datasets from laboratory model tests performed by Patra [1] over dense sand and medium dense sand. Three input parameters (Df/B, e/B, and α/ϕ) are used to predict a single output in the form of reduction factor (RF). The results found by GRNN are then

V. Chaudhary (✉) · J. S. Yadav
National Institute of Technology, Hamirpur, Himachal Pradesh, India

C. N. V. Satyanarayana Reddy et al. (eds.), *Dynamics of Soil and Modelling of Geotechnical Problems*, Lecture Notes in Civil Engineering 186,
https://doi.org/10.1007/978-981-16-5605-7_6

compared with the empirical as well as ANN results [2]. The software used to apply GRNN in the present study is DTREG, the results of which are further compared with the results of ANN prediction.

2 Literature Review

2.1 Laboratory Model Test

Laboratory model test was conducted by Patra [1] to determine the ultimate bearing capacity of shallow strip footing subjected to eccentrically inclined load resting over dense and medium dense sand. Reduction factor (RF) value is defined as a ratio of ultimate bearing capacity considering eccentrically inclined load to the bearing capacity centrally loaded with no inclination. The poorly graded dense sand having a coefficient of curvature (Cc), coefficient of uniformity (Cu), and effective size of 1.15, 1.45, and 0.325 mm, respectively, was used in the investigation. The embedment ratio (Df/B), eccentricity ratio (e/B), and inclination ratio were varied from 0 to 1, 0 to 0.15, and 0 to 20°, respectively. Empirical equations were also used to calculate the value of reduction factor and treated as calculated RF which was further compared with the experimental values of RF. A variation of around 15% or less was seen and in some cases deviation was about 30% or less. The experimental value of RF is given by

$$\mathrm{RF} = \left[q_{u(\mathrm{Df/B,e/B},\alpha/\phi)}\right] / \left[q_{u(\mathrm{Df/B,e/B=0},\alpha/\phi=0)}\right] \tag{1}$$

2.2 ANN Modeling

The experimental datasets were utilized for training and testing ANN. A total of 120 datasets were used for model preparation out of which 70% was utilized for training data and 30% was utilized as testing or validation data. Embedment ratio, Eccentricity ratio, and inclination ratio were used as predictor variables, and a single output as reduction factor (RF) which was further utilized to get the bearing capacity. MATLAB software was used for ANN modeling, the training function utilized in this model building was TRAINLM, the adaptation learning function was LEARNGDM, and the performance function was MSE. The number of hidden layers used in the model was one. Figure 1 shows the connection strength of several inputs in the neural network diagram.

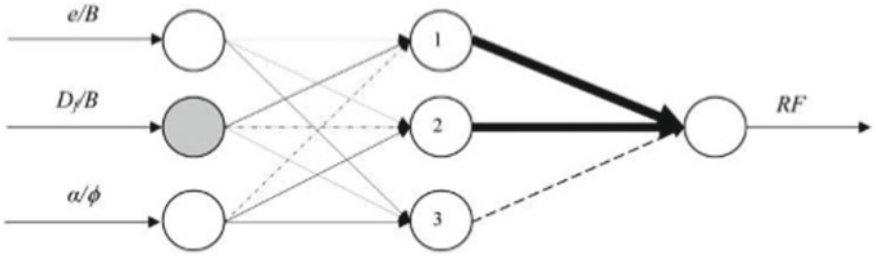

Fig. 1 Neural network diagram showing connection strength of several inputs [2]

3 Methodology

Probability density function used in GRNN is a normal distribution function with each training sample. In the GRNN modeling network, the output is calculated on the basis of weight adjustment mechanism with the help of "Euclidean distance" which is approximately the square of the difference between the training data sample and the testing data sample. If the Euclidean distance of a certain variable is large, then it means that the weight will be less and connection strength will be less for that variable. But if the Euclidean distance is small for certain variables, it will have a large amount of weight and connection strength. The equation used in GRNN is

$$Y(x) = \frac{\sum Y_i e^{-\left(\frac{d_i^2}{2\sigma^2}\right)}}{\sum e^{-\left(\frac{d_i^2}{2\sigma^2}\right)}} \tag{2}$$

Input sample is denoted as "X" and input sample in training as "Xi". Yi is the output sample regarding the input sample of Xi. Euclidean distance is denoted as di^2 which is the distance between X and Xi. The activation function which actually denotes the weight of that input sample is given by $e^{-\left(\frac{d_i^2}{2\sigma^2}\right)}$.

The activation function utilized is the Gaussian type which comes under the type of radial basis function. The normal distribution is widely described by the Gaussian function. It is the best kernel function whose equation is given by

$$g(x) = \frac{1}{\sigma\sqrt{2\pi}} e^{-\frac{1}{2}\left(\frac{x-\mu}{\sigma}\right)^2} \tag{3}$$

3.1 Architecture of GRNN Model

The network model is divided into four layers starting from the input layer and ending at the output layer.

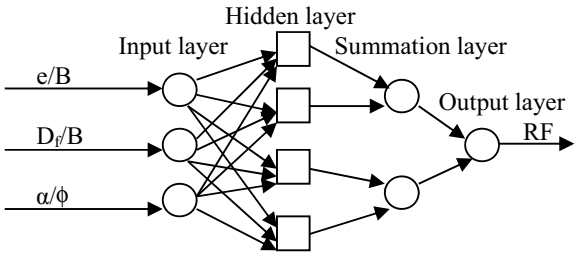

Fig. 2 GRNN architecture model

Input Layer: Each input layer is provided with one neuron in the input layer. The range of input neurons is standardized by the subtraction of median and division of interquartile range. At the end of the layer, the value of each neuron is then provided to the next hidden layer neurons for further processing.

Hidden Layer: The hidden layer neurons are fed values by the input layer neurons. Then comes the hidden layer which is provided with a single neuron for each case in the training data set. The values of predictor and target variables for similar case are stored by the neuron. The input values are presented over the X-axis, the distance from the neurons center point known as Euclidean distance, and is computed by the hidden layer after which using sigma values radial basis activation function is applied. This layer is mainly provided to compute the Euclidean distance which helps in adjusting the weightage of certain predictor variables and in the application of suitable activation function. The output of the hidden layer is then fed to the next layer known as the Pattern layer.

Pattern Layer or Summation Layer: This layer takes values from the hidden layer as input. It contains only two neurons, one is the Numerator neuron and the other is the Denominator neuron. The value of the denominator is computed by the summation of all values of activation function. The value for numerator neuron is computed by summation of multiplicative values of activation function and output data set values. The output values of both numerator and denominator are fed to the next layer known as the decision layer.

Output or Decision Layer: This layer contains only a single neuron. This layer ultimately predicts the target variable by simply computing its value from the division of the Numerator neuron and Denominator neuron values which are fed from the Pattern layer. Figure 2 shows the GRNN architecture model used.

3.2 Training Principle

The primary work in training with generalized regression neural network technique is to select the optimum value of sigma (σ) which helps to control the spread of radial basis function (RBF). The conjugate gradient algorithm is used by the DTREG

software for the computation of optimum sigma values. Separate sigma (σ) values for each predictor variable are used. The software uses the leave one out method for evaluation of σ values during optimization.

4 Database and Preprocessing

The laboratory model test conducted by Patra [1] over shallow strip footing subjected to eccentrically inclined load resting over dense and medium dense sand was used. Data sets are divided into two categories: training and testing, around 70% of data sets are used as training data, whereas 30% of data sets are utilized as testing data. Total 120 data sets are available, so the first 90 sets are taken as training sets, whereas the last 30 sets are used as testing sets.

Table 1 shows the soil characteristics and parameters used by Patra [1] in the investigation. Eccentricity ratio was varied from 0 to 0.15, inclination ratio was varied from 0 to 20° and embedment ratio was varied from 0 to 1 for dense and medium dense type sand. Experimental datasets are used to model the training and testing process given in Table 2.

In this study, a trial version of DTREG software was used which helps in providing results but is unable to generate an equation for the required output. After the selection of the type of model to be built, values of sigma are selected or decided for the model. In this model preparation, sigma for each variable is used. The minimum and maximum sigma value is kept as 0.0001 and 10, respectively and 20 search steps are set for the model. Leave one out method is used in model testing and validation. The target variable is the reduction factor and three input variables are used for prediction. The validation method applied in the modeling is "Leave one out method" in which cross validation is performed by leaving one row out for each model built.

Table 1 Soil parameters and its characteristics [1]

Sand type	Unit weight of compaction (Kg/m^3)	Relative density of sand (%)	Friction angle (ϕ) degree	D_f/B	e/B	Load inclination (α) degree
Dense	14.36	69	40.8	0 0.5 1.0	0 0.05 0.1 0.15	0 5 10 15 20
Medium dense	13.97	51	37.5	0 0.5 1.0	0 0.05 0.1 0.15	0 5 10 15 20

Table 2 Experimental model datasets [1]

Data type	Expt. No.	e/B	Df/B	α/ϕ	Experimental q_u (kN/m^2)	Experimental RF	Calculated RF
Training	1	0.05	0	0	133.42	0.8	0.9
	2	0.1	0	0	109.87	0.659	0.8
	3	0.15	0	0	86.33	0.518	0.7
	4	0	0	0.123	128.51	0.771	0.77
	5	0.05	0	0.123	103.01	0.618	0.693
	6	0.1	0	0.123	86.33	0.518	0.616
	7	0	0	0.245	96.14	0.576	0.57
	8	0.05	0	0.245	76.52	0.459	0.513
	9	0.15	0	0.245	51.99	0.312	0.399
	10	0	0	0.368	66.71	0.4	0.4
	11	0.1	0	0.368	44.15	0.265	0.32
	12	0.15	0	0.368	35.12	0.211	0.28
	13	0.05	0	0.49	34.83	0.209	0.234
	14	0.1	0	0.49	29.43	0.176	0.208
	15	0.15	0	0.49	23.54	0.141	0.182
	16	0	0.5	0	264.87	1	1
	17	0.05	0.5	0	226.61	0.856	0.9
	18	0.1	0.5	0	195.22	0.737	0.8
	19	0	0.5	0.123	223.67	0.844	0.822
	20	0.05	0.5	0.123	193.26	0.73	0.74
	21	0.15	0.5	0.123	140.28	0.53	0.575
	22	0	0.5	0.245	186.39	0.704	0.656
	23	0.1	0.5	0.245	137.34	0.519	0.525
	24	0.15	0.5	0.245	116.74	0.441	0.459
	25	0.05	0.5	0.368	129.49	0.489	0.453
	26	0.1	0.5	0.368	111.83	0.422	0.402
	27	0.15	0.5	0.368	94.18	0.356	0.352
	28	0	0.5	0.49	115.76	0.437	0.364
	29	0.05	0.5	0.49	98.1	0.37	0.328
	30	0.15	0.5	0.49	72.59	0.274	0.255
	31	0	1	0	353.16	1	1
	32	0.1	1	0	278.6	0.789	0.8
	33	0.15	1	0	245.25	0.694	0.7
	34	0.05	1	0.123	277.62	0.786	0.79
	35	0.1	1	0.123	241.33	0.683	0.702

(continued)

Table 2 (continued)

Data type	Expt. No.	e/B	Df/B	α/ϕ	Experimental q_u (kN/m^2)	Experimental RF	Calculated RF
	36	0.15	1	0.123	215.82	0.611	0.614
	37	0	1	0.245	264.87	0.75	0.755
	38	0.05	1	0.245	239.36	0.678	0.679
	39	0.1	1	0.245	212.88	0.603	0.604
	40	0	1	0.368	225.63	0.639	0.632
	41	0.1	1	0.368	179.52	0.508	0.506
	42	0.15	1	0.368	155.98	0.442	0.443
	43	0.05	1	0.49	166.77	0.472	0.459
	44	0.1	1	0.49	143.23	0.406	0.408
	45	0.15	1	0.49	126.55	0.358	0.357
	46	0	0	0	101.04	1	1
	47	0.05	0	0	84.37	0.835	0.9
	48	0.15	0	0	54.94	0.544	0.7
	49	0	0	0.133	79.46	0.786	0.751
	50	0.1	0	0.133	52.97	0.524	0.601
	51	0.15	0	0.133	42.18	0.417	0.526
	52	0.05	0	0.267	47.09	0.466	0.484
	53	0.1	0	0.267	38.46	0.381	0.43
	54	0.15	0	0.267	31.39	0.311	0.376
	55	0	0	0.4	38.26	0.379	0.36
	56	0.05	0	0.4	32.37	0.32	0.324
	57	0.1	0	0.4	26.98	0.267	0.288
	58	0	0	0.533	24.03	0.238	0.218
	59	0.05	0	0.533	19.62	0.194	0.196
	60	0.15	0	0.533	13.34	0.132	0.152
	61	0	0.5	0	143.23	1	1
	62	0.1	0.5	0	103.99	0.726	0.8
	63	0.15	0.5	0	87.31	0.61	0.7
	64	0.05	0.5	0.133	103.99	0.726	0.726
	65	0.1	0.5	0.133	90.25	0.63	0.645
	66	0.15	0.5	0.133	72.59	0.507	0.565
	67	0	0.5	0.267	98.1	0.685	0.628
	68	0.05	0.5	0.267	84.86	0.592	0.565
	69	0.1	0.5	0.267	72.59	0.507	0.502
	70	0	0.5	0.4	79.46	0.555	0.465

(continued)

Table 2 (continued)

Data type	Expt. No.	e/B	Df/B	α/ϕ	Experimental q_u (kN/m^2)	Experimental RF	Calculated RF
	71	0.05	0.5	0.4	67.89	0.474	0.418
	72	0.15	0.5	0.4	48.07	0.336	0.325
	73	0	0.5	0.533	58.27	0.407	0.319
	74	0.1	0.5	0.533	43.16	0.301	0.255
	75	0.15	0.5	0.533	36.3	0.253	0.223
	76	0.05	1	0	193.26	0.925	0.9
	77	0.1	1	0	175.6	0.84	0.8
	78	0.15	1	0	156.96	0.751	0.7
	79	0	1	0.133	186.39	0.892	0.867
	80	0.05	1	0.133	168.73	0.808	0.78
	81	0.1	1	0.133	153.04	0.732	0.693
	82	0	1	0.267	160.88	0.77	0.733
	83	0.05	1	0.267	144.21	0.69	0.66
	84	0.15	1	0.267	112.82	0.54	0.513
	85	0	1	0.4	133.42	0.638	0.6
	86	0.1	1	0.4	106.93	0.512	0.48
	87	0.15	1	0.4	94.18	0.451	0.42
	88	0.05	1	0.533	92.21	0.441	0.42
	89	0.1	1	0.533	84.37	0.404	0.373
	90	0.15	1	0.533	75.54	0.362	0.327
Testing	1	0	0	0	166.77	1	1
	2	0.15	0	0.123	65.73	0.394	0.539
	3	0.1	0	0.245	62.78	0.376	0.456
	4	0.05	0	0.368	53.96	0.324	0.36
	5	0	0	0.49	43.16	0.259	0.26
	6	0.15	0.5	0	164.81	0.622	0.7
	7	0.1	0.5	0.123	165.79	0.626	0.658
	8	0.05	0.5	0.245	160.88	0.607	0.59
	9	0	0.5	0.368	151.07	0.57	0.503
	10	0.1	0.5	0.49	85.35	0.322	0.291
	11	0.05	1	0	313.92	0.889	0.9
	12	0	1	0.123	313.92	0.889	0.877
	13	0.15	1	0.245	188.35	0.533	0.528
	14	0.05	1	0.368	206.01	0.583	0.569
	15	0	1	0.49	183.45	0.519	0.51

(continued)

Table 2 (continued)

Data type	Expt. No.	e/B	Df/B	α/ϕ	Experimental q_u (kN/m^2)	Experimental RF	Calculated RF
	16	0.1	0	0	68.67	0.68	0.8
	17	0.05	0	0.133	63.77	0.631	0.676
	18	0	0	0.267	55.92	0.553	0.538
	19	0.15	0	0.4	20.6	0.204	0.252
	20	0.1	0	0.533	16.68	0.165	0.174
	21	0.05	0.5	0	123.61	0.863	0.9
	22	0	0.5	0.133	120.66	0.842	0.807
	23	0.15	0.5	0.267	60.82	0.425	0.44
	24	0.1	0.5	0.4	56.9	0.397	0.372
	25	0.05	0.5	0.533	50.03	0.349	0.287
	26	0	1	0	208.95	1	1
	27	0.15	1	0.133	137.34	0.657	0.607
	28	0.1	1	0.267	129.49	0.62	0.587
	29	0.05	1	0.4	118.7	0.568	0.54
	30	0	1	0.533	98.1	0.469	0.467

5 Results and Discussions

Best performance analysis is done by using correlation coefficient (Cr), determination coefficient (R^2), mean square error (MSE), root mean square error (RMSE), and mean absolute error (MAE).

Table 3 reveals the training and testing parameters of the experimental model test conducted by Patra [1]. 70% of data sets are used as training data and a GRNN model is built. 30% of datasets are used in the testing data. The coefficient of correlation for training and testing data was 0.998 and 0.994, respectively. It shows the linearity between the value predicted and the actual output with greater precision. More close the value to 1 shows higher linearity. The values of statistical parameters for GNN for all continuous variables are shown in Table 4. As RF is the target variable and the other three are predictor variables. The maximum value for RF was 1, whereas its minimum value was 0.132, and the mean value was 0.65229. The value of standard deviation was 0. 19,833. The statistical parameters from ANN are shown in Table 5. In the statistical analysis, the maximum value of output was 1 and its minimum value was 0.132. Whereas as mean or the average value was set as 0.555. The standard deviation of the output variable was 0.217.

Figure 2 shows the relative importance of the variable in the prediction model. It can be easily seen in Fig. 2 that the inclination variable shows 100% importance or impact over the target variable while the eccentricity ratio variable shows 33.946% impact and embedment ratio makes the least impact or least important as compared

Table 3 Experimental model datasets [1]

Parameters	Training	Testing
Mean target value for input data	0.652293	0.652293
Mean target value for predicted values	0.6530206	0.6544816
Variance in input data	0.0393364	0.0393364
Residual (unexplained) variance after model fit	0.000158	0.0005374
Proportion of variance explained by model (R^2)	99.598%	98.634%
Coefficient of variation (C_v)	0.019267	0.035538
Normalized mean square error (NMSE)	0.004015	0.013661
Correlation between actual and predicted	0.998156	0.994194
Maximum error	0.492199	0.089428
Root mean square error (RMSE)	0.012568	0.0231815
Mean squared error (MSE)	0.000158	0.0005374
Mean absolute error (MAE)	0.0090726	0.0177511
Mean absolute percentage error (MAPE)	0.0179782	0.0323818

Table 4 Statistical parameters from GRNN

Variable	Rows	Minimum	Maximum	Mean	Standard deviation
Df/B	120	0	1	0.66956	0.37450
A	120	0	20	7.98676	6.80215
e/B	120	0	0.15	0.06603	0.05531
RF	120	0.132	1	0.65229	0.19833

Table 5 Statistical parameters from ANN [2]

Parameter	Maximum	Minimum	Average	Standard deviation
e/B	0.15	0	0.075	0.056
Df/b	1	0	0.5	0.408
α/ϕ	0.533	0	0.256	0.181
RF	1	0.132	0.555	0.217

to the other two variables with around 22.112% importance over the target variable. Figures 3 and 4 show the variation of experimental RF (Actual) versus predicted RF value from GRNN and experimental RF versus empirically calculated RF(CRF), respectively. Higher variation can be seen, but still, the graph proceeds in the linear direction but less linearity is shown as compared to the GRNN prediction model graph which is shown in Fig. 3.

Figure 5 shows the variation of actual target variable and AN N predicted output variable for training and testing data. It can be seen from Fig. 5 that the model built was providing good results, which were analyzed with the help of coefficient of

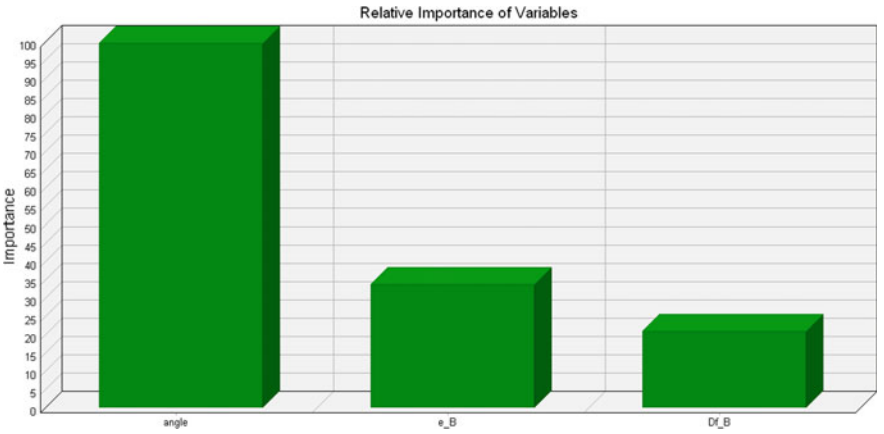

Fig. 3 Relative importance of input variables on output variable RF

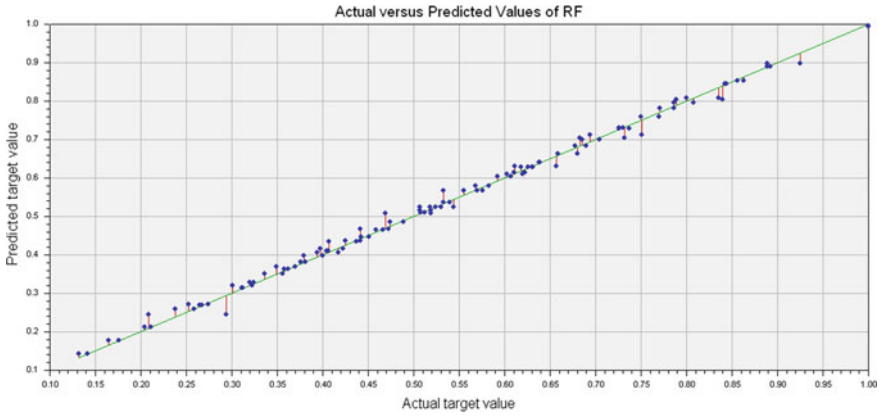

Fig. 4 Plot between experimental RF (Actual) and predicted RF value from GRNN

correlation. The value of Cr for training was 0.997 which is much closer to the value 1, whereas the Cr value for testing was 0.996 which represents a good prediction according to this model.

The comparison between ANN and GNN with different indices is shown in Table 6. No such variation in results was seen between the GRNN network model and the ANN model. The mean square error was less in GRNN prediction work. There was a slight difference between the correlation coefficient like for training work was 0.998 for GRNN model, whereas 0.997 for ANN model, and for testing it was 0.994 for GRNN and 0.996 for ANN. Results of both GRNN and ANN show higher accuracy than empirically calculated results, which are also shown in Figs. 3, 4, 5.

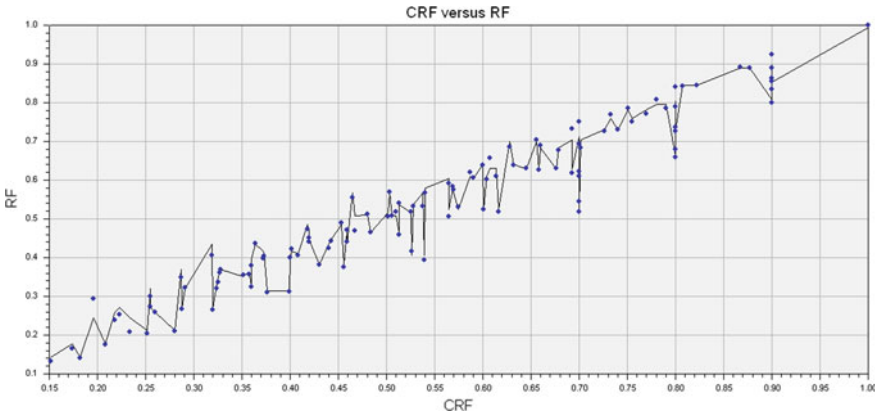

Fig. 5 Plot between Experimental RF and Empirically calculated RF(CRF)

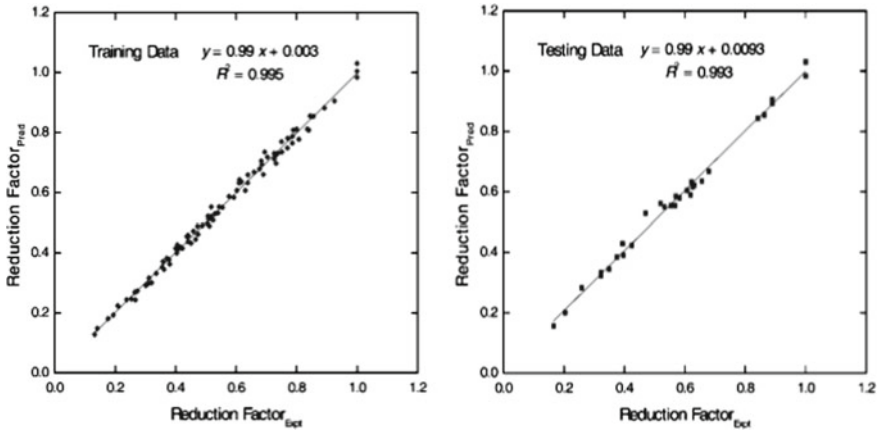

Fig. 6 Plot of experimental RF and predicted RF from ANN [2]

Table 6 Comparison between ANN and GRNN with Mathematical indices

Type of model	GRNN (present study)		ANN (results from [2])	
	Testing	Training	Testing	Training
MSE	0.0005	0.00015	0.0019	0.001
RMSE	0.0231	0.0125	0.043	0.032
R^2	0.986	0.996	0.992	0.994
Cr	0.994	0.998	0.996	0.997

6 Conclusions

Highlights of the present study are shown below:

1. No such variations in results between ANN and GRNN were spotted, both models were equally accurate.
2. The data available was never enough for backpropagation neural network, this GRNN neural network technique founds to be advantageous because of the ability of this technique in utilizing fewer data samples efficiently to converge the function.
3. The standard deviation found in the output reduction factor (RF) was lesser in the GRNN model as compared to the ANN model.
4. In the GRNN model, the inclination ratio was provided higher importance as compared to other two input variables like embedment ratio and eccentricity ratio (α/ϕ as 100%, e/B as 33.946% and Df/B as 21.112%), whereas in the ANN network model, as per Garson's algorithm, the inclination ratio (α/ϕ) was given more importance as compared to other two followed by embedment ratio (Df/B) and then eccentricity ratio (e/B).

References

1. Patra, C., Behara, R., Sivakugan, N., Das, B.: Ultimate bearing capacity of shallow strip foundation under eccentrically inclined load part I. Int. J. Geotech. Eng. **6**(3), 343–352 (2012). https://doi.org/10.3328/IJGE.2012.06.03.343-352
2. Behera1, R.N., Patra1, C.R., Sivakugan, N., Das, B.M.: Prediction of ultimate bearing capacity of eccentrically inclined strip footing resting over dense sand, part-1. Int. J. Geotech. Eng. **7**(1), 36–34 (2012)

Optimization of Piled Raft on Sand for Plaza-Type Structures

B. Sharmila, V. Balakumar, and S. S. Chandrasekaran

1 Introduction

The Exponential Growth in the demand of occupational spaces has resulted in the increase of tall and super-tall structures. The geotechnical site conditions are no more a constraint and so the foundation designers face the challenge of designing an economical foundation system that will satisfy safety and serviceability requirements. Optimization of pile length, pile diameter, and layout along with an appropriate raft thickness form the major features in the economics of foundation design. In this combined foundation system, the total load coming from the superstructure is transferred by means of a complicated three-dimensional interaction among the constituent elements, namely, raft, soil, and the pile group. Zeavert (1957) was perhaps the earliest researcher to introduce the concept of using piles with the raft as a settlement reducer. The observational study had indicated that the pile group takes the major portion of the load. In general, large pile groups are designed with piles of uniform length and diameter having uniform spacing which may result in an uneconomical raft design. The uniform pile length is used to maximize the overall stiffness or minimizing the differential settlement. The intensity of loading and the settlement requirement decides an optimum pile layout keeping the economy in the design of the raft and the pile.

Most of the structures have been supported on piles of uniform length and same diameter. The pile groups were capped with a raft of uniform thickness. Till now, to the best of our knowledge, the optimized design of pile group, depending on the column

B. Sharmila (✉) · S. S. Chandrasekaran
School of Civil Engineering, Vellore Institute of Technology, Vellore, India

S. S. Chandrasekaran
e-mail: chandrasekaran.ss@vit.ac.in

V. Balakumar
Simplex Infrastructures Limited, Chennai, India

C. N. V. Satyanarayana Reddy et al. (eds.), *Dynamics of Soil and Modelling of Geotechnical Problems*, Lecture Notes in Civil Engineering 186,
https://doi.org/10.1007/978-981-16-5605-7_7

loads, appears to the scarce. Although extensive studies have been carried out on the behavior and performance of piled raft through analytical and numerical modeling (Clancy 1993; Russo 1998), 1 g model tests [1] centrifuge modeling (Horikoshi 1995) and observational studies (Katzenbach et al. 2000). Very little work had been done on the optimization work with the use of piles in the case of structures with varying stiffness (Cunha et al. 2001, Leung et al. 2009), [2]. In the present study, Plaza-type structures have been analyzed in E-tabs and the obtained support reactions are taken for the pile group design. According to the column load, the length of pile is varied. Therefore, it becomes necessary to study the performance of raft–soil foundation system reinforced with piles and the behavior of raft contact pressure distribution by the introduction of different lengths of piles in the combined foundation system.

2 Numerical Modeling

Finite element modeling is a method for dividing up a very complicated problem into a small element. It is due to ease in modeling and arranging the elements in the desired shape and pattern. The interface idealization is the essential aspect to be considered for the numerical study of soil–structure interaction.

Any numerical analysis needs a certain level of dilution to reduce the computational efforts. Therefore, the analytical model must be chosen amendable in the sense that the level of the result is not sacrificed. Hence, the plane strain model is chosen as a key equipment for analyzing the present study. Prakoso and Kulhway (2001) performed a piled raft problem by assuming plane strain conditions. The plane strain condition involves a fundamental simplification wherein a finite-sized piled raft is simplified into a strip piled raft provided by Desai et al. (1974) and established that this type of model can provide good results and can be used to analyze a relatively large piled raft without any excessive modeling and computing time. The piles in the plane are converted into plain strain walls and its equivalent pile young's modulus can be calculated by using the below Eq. 1, which is given by (Prokoso 1991).

$$E_{eq} = \frac{n_{p-row} A_p E_p}{L_r B} \tag{1}$$

where $n_{p\text{-}row}$*: Number of piles in a row.*
A_p*: Area of each pile.*
E_p*: Young's modulus.*
L_r*: length of the raft.*
B: Width/Diameter of pile.

3 Super-Structure Modeling

The commercial building adapted in this study carries twelve stories at the center of the building and the rest of the sides carries four stories as shown in Fig. 1. The shape of the building is irregular. The width of the building is 32 m and the length of the building is 96 m along the largest span. The building is designed for a flat-slab system. The building lies on a raft–soil foundation system reinforced with piles. The piles are placed exactly below the column.

The commercial building was modeled using E-tabs for the physical properties. The spacing of the column provided as 8 m and the outer wall was modeled as reinforced concrete walls. M_{35} Grade of concrete and Fe_{500} Grade of steel has been assigned for the structure. The structure has been modeled using E-tabs. The material and section properties are defined for all the structural elements. All the columns are fixed to the base. The static and dynamic loadings are calculated based on IS 875 part 1 and 2 1987 and IS 1893–2002. The self-weight of the building is calculated automatically by E-tabs with their loading combination. After modeling the building, the structure is analyzed. The shear force, bending moment, Storey drift, and displacement values have been extracted from E-Tabs after analysis. The support reaction, i.e., column load obtained from the analysis is used for the further design of foundation elements (Fig. 1).

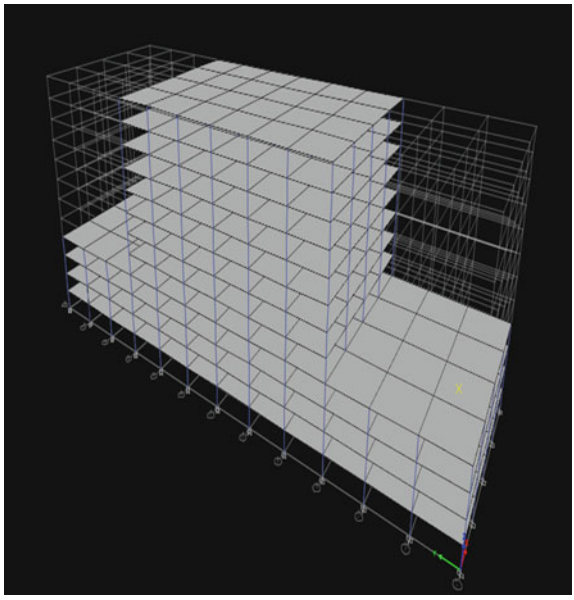

Fig. 1 Modeled Structure

4 The Foundation System

The Raft, soil, and pile are modeled as solid components under material and geometry properties are mentioned in Table 1 Circular piles were modeled are introduced beneath the raft in the combined foundation system (Table 2).

The piled acted as reinforcement in the raft–soil system. In the piled raft foundation system, piles were located below the column under the raft. The total number of columns in the structural frame was 65 as in Fig. 2a. Since the structure is symmetric to each other, so the pile naming in Fig. 2b C1 to C7 has been taken for the analyses and the properties of the pile are tabulated in Table 1. Figure 2a and b are to be read in configuration with each other. The length of the long pile is 20 m and is provided under the tower area simultaneously for shallow area provide the shorter pile of length 16 m. The same procedure is repeated by keeping the longer length pile constant by changing the shorter length of the pile has 10 m.

A uniform dense sand block was modeled around the pile-raft system. Since the influence of the imposed structural load on the raft in an unpiled raft, the system is transferred to the soil. The load that is imposed on the foundation is obtained from the structural analysis of the plaza-type structures in E-Tabs. The concentrated loads are converted into the equivalent uniformly distributed load. This equivalent UDL

Table 1 Properties of foundational element

Property	Raft	Pile	Sandy soil
Material	Concrete	Concrete	Medium dense sand
Shape	Rectangle	Circle	Rectangle
Elastic Modulus (kN/m^2)	3.1 X 10^{10}	3.1 X 10^{10}	4.4 X 10^7
Density (Kg/m^3)	2400	2400	1442
Poisson ratio	0.2	0.2	0.25
Shear angle	–	–	33^0
Size	Thickness = 900 mm	Depth = 20 m, 16 m, 10 m	Depth = 50 m
	Width = 50 m	Diameter = 0.7 m, 0.8 m, 0.9 m	Width = 100 m

Table 2 Deflection results

D/t ratio	Maximum deflection (mm)		
	Piled raft		
	$L = 20$ m	$L = 10$ m	$L = 16$ m
0.8	68.08	65.73	69.14
0.9	65.76	63.73	66.75
1	63.52	60.59	63.52

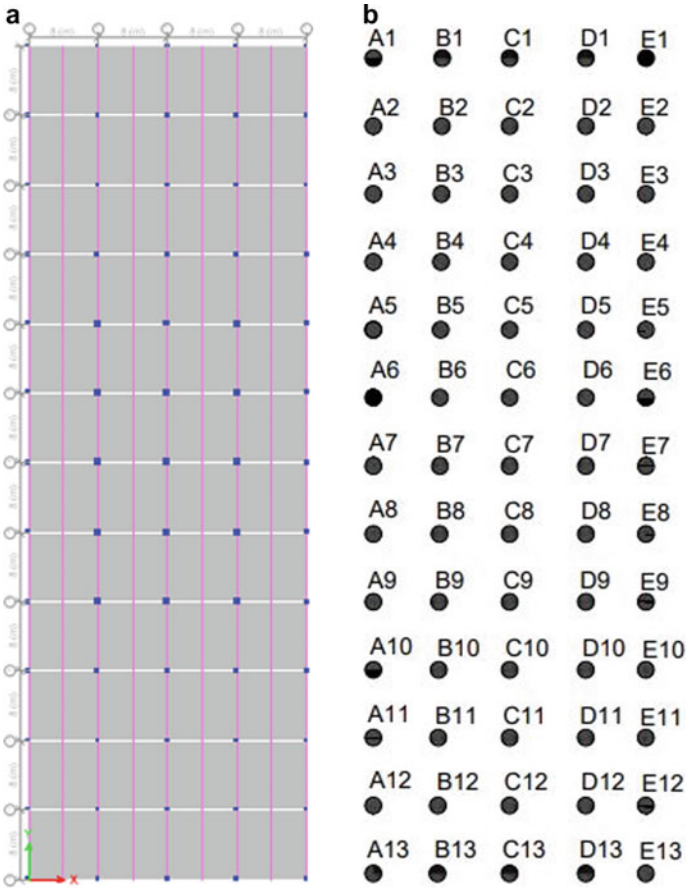

Fig. 2 **a**. Column Layout. **b** Pile Layout

was imposed on the raft surface in the combined foundation system in the form of pressure. The fixity condition act as bounding limits to the soil (Fig. 3).

After completing the model and meshing of the structure, analysis is completed assigning each phase of construction and results are obtained and interpolated. Total deformation and equivalent stress are the two output parameters required in the present study. The numerical analysis is performed after the required output is selected. Total deformation and stress contours are obtained as the end results of the analysis. These displacements and stress contours denote the pattern of the displacement and the stress that undergoes in the combined raft, soil, and pile foundation system, respectively.

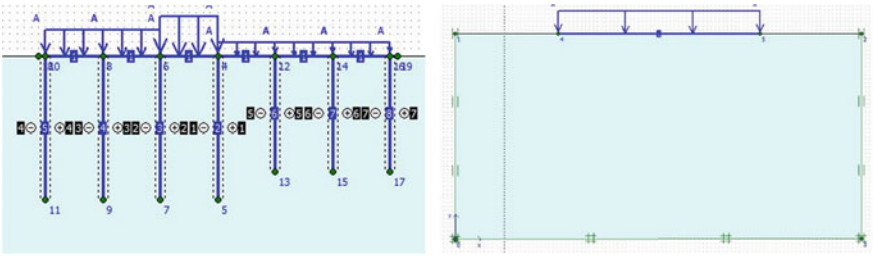

Fig. 3 Piled and un-piled raft model with structural loading

5 Discussion

The present study as said earlier examines this behavior of the pile group of piled raft supporting a plaza-type building. In general, such buildings have column loads varying widely. In particular, the shallow portion transits a much lesser load when compared to the tower on the columns. The present study tries to evaluate the effectiveness of piled raft with varying pile length (keeping the diameter constant) or varying the pile diameter and keeping the pile length constant.

5.1 Effect of Varying Pile Length

In the present cases, the numerical analyses are performed on the combined raft, soil, and pile foundation system for the *D/t ratios*, where

D – Diameter of the pile.

t – thickness of the raft.

Two different pile length has been used, namely, 10 m and 16 m. the raft thickness has been kept as 900 mm. From the below graph images, it clearly explains that:

i. When the length of the pile was kept as 20 m, it clearly shows that the load-carrying capacity of a pile at **d/t** ratio unity was 15% higher than the **d/t** ratio of 0.8.
ii. When the length was increased to 16 m, the load taken by the system having a **d/t** ratio of unity was higher only by 25% compared to the system having a **d/t** ratio of 0.8.
iii. With the **d/t** ratio of unity, and pile length as 10 m, for a settlement of 50 mm the carrying capacity of the system was found to be higher by 40% than the capacity corresponding to a **d/t** ratio of 0.8.

From the above comparative statements, it can be seen that for a given thickness of the raft, the increase in the pile length beyond a certain level does not produce appreciable settlement reduction. This may be due to the enhancement of confining pressure may not occur over the entire length of the pile. It shows that the maximum

settlement reduces with the reduction of the pile length of 50%. This reflects the fact that when the pile length increases the enhancement of the confining pressure might not have been effective over the entire length of the pile.

5.2 *Effect of Variation in Pile Diameter*

The parametric study was further continued to study the effect of variation in the pile length for three different diameters, namely, 700, 800, and 900 mm. The pile naming from C1 to C3 has been taken from the Shallow portion and the remaining C4 to C7 pile taken from the tower area for further analyses. The pile length in the shallower part of the building was varied from 20 m to 16 m and 10 m. For the result discussion, the maximum stress for the piles C1(Shallow portion pile), C4(Intermediate Pile), and C7(Tower area Pile) has been taken to plot the graph.

5.3 *Pile Diameter 700 mm*

The interaction between the soil and pile remains the same by using the same length of the pile. It can be seen that the trend in the shaft stress distribution remains the same irrespective of pile location. Further, in all three cases, the considered shaft stress falls rapidly beyond the pile length of 0.6 l to 0.7 l, namely, 14 m in the case of 20 m long pile and 6 m in the case of 10 m long pile. In the same manner, in the case of 16 m long pile, this value corresponds to 0.65 l to 0.75 l (where l is the overall length of the pile considered) (Figs. 4, 5, and 6).

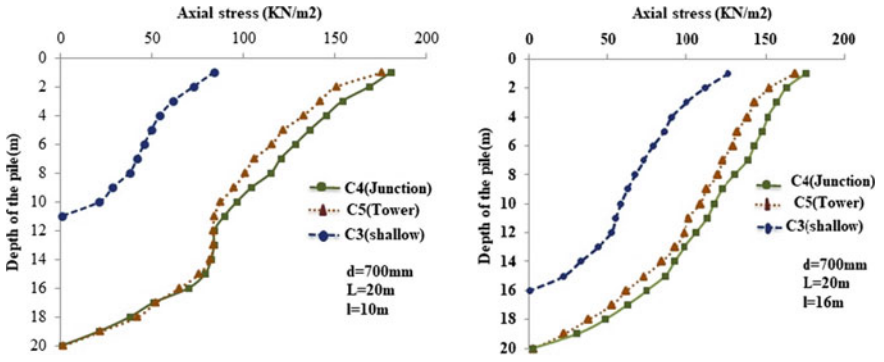

Fig. 4 Shaft stress (d = 700 mm and l = 10 m and 16 m)

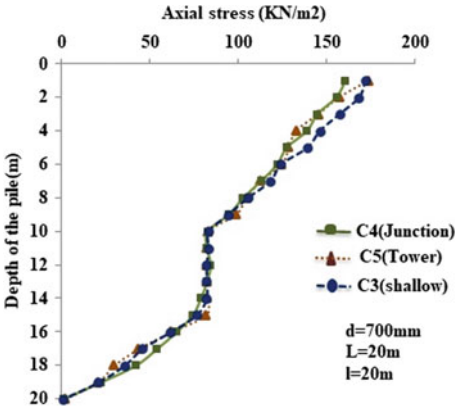

Fig. 5 Shaft stress—piled raft with piles of equal length

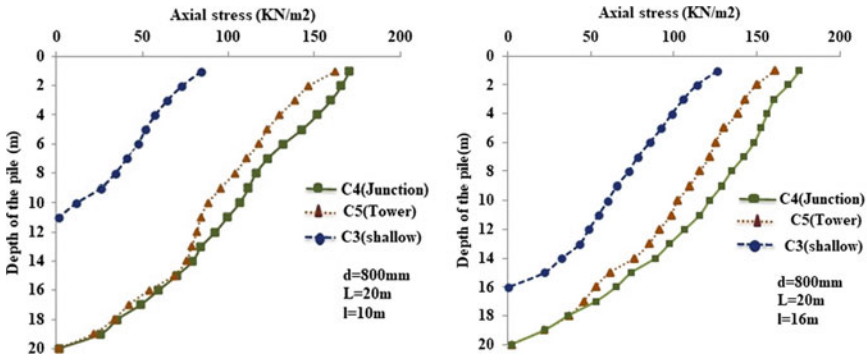

Fig. 6 Shaft stress distribution with depth

5.4 Pile Diameter 800 mm

While the trend remains the same, the rate of fall of shaft stress appears to be more rapid from the beginning. At the point corresponding to 50% of the pile length, the shaft stress falls by 40%, but at 0.8 l, it is 60%. Therefore, it can be said that the rate of fall of shaft stress between 0.5 l to 0.8 l is more gradual. At higher diameter the effective pile length becomes 0.8l where l is length of the pile.

5.5 Pile Diameter 900 mm

It is shown that the shaft stress curve remains unique. The C4 (intermediate Pile) pile stress is maximum because the loading is high due to the combination of Tower

area loading and Shallow portion loading. But the stress remains equal when we use the equal length of the pile for both the area portion. At the point corresponding to 0.5 l, the shaft stress falls by 0.65 l to 0.7 l. Similarly, at 0.8 l, the shaft stress falls by 0.65 l to 0.75 l. The shaft stress is more gradual at a point of 0.65 l to 0.75 l for a greater diameter (Fig. 8).

Figure 9 shows that the shaft stress decreases with the decrease of pile length even the loading is the same. The diameter and length of the central area pile are kept as a constant of 900 mm and 20 m. the maximum interaction occurs at the shorter pile length when compared with using 60% and equal length of the pile. The interaction varies 68–85% with the pile length decreases (Fig. 10). Figure 11 shows that when the pile diameter increases, the shaft stress remains the same at the tip of the pile but gradually decreases at a certain point of 8 m, after that certain point, the shaft stress value increases gradually (Fig. 12).

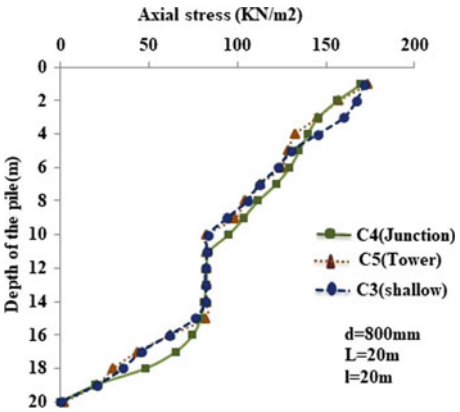

Fig. 7 Stress curve of equal length of Piled raft

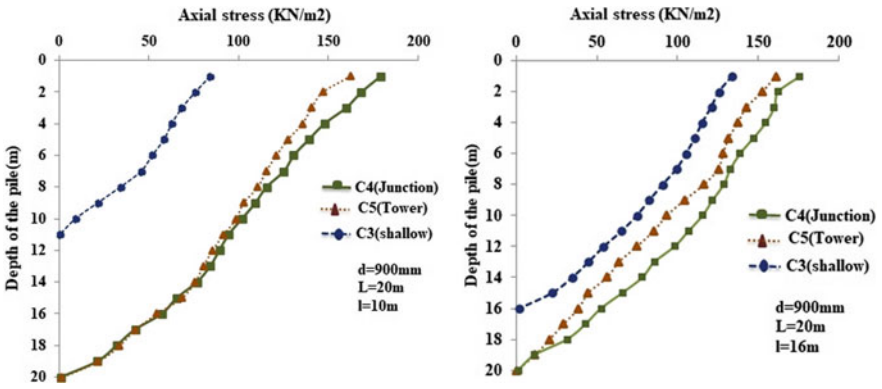

Fig. 8 Shaft stress distribution (d = 900 mm and l = 10 m and 16 m)

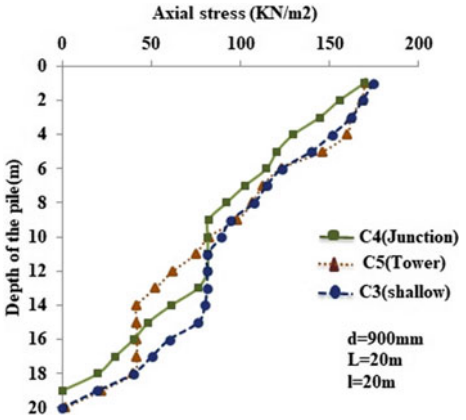

Fig. 9 Stress curve of equal length of Piled raft

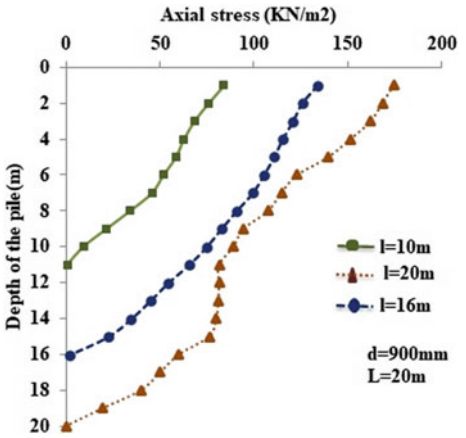

Fig. 10 Effect of if pile length on shaft stress distribution

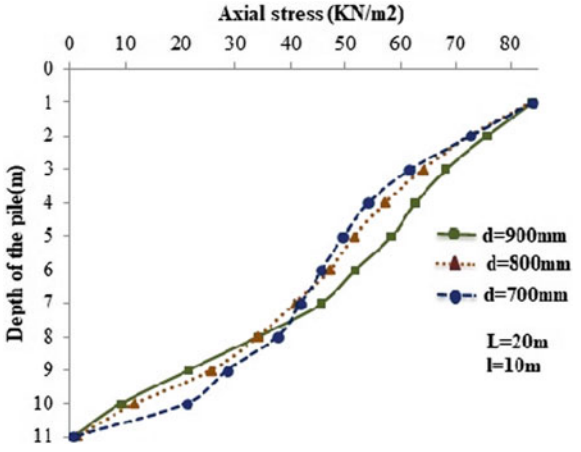

Fig. 11 Effect of changing pile diameter

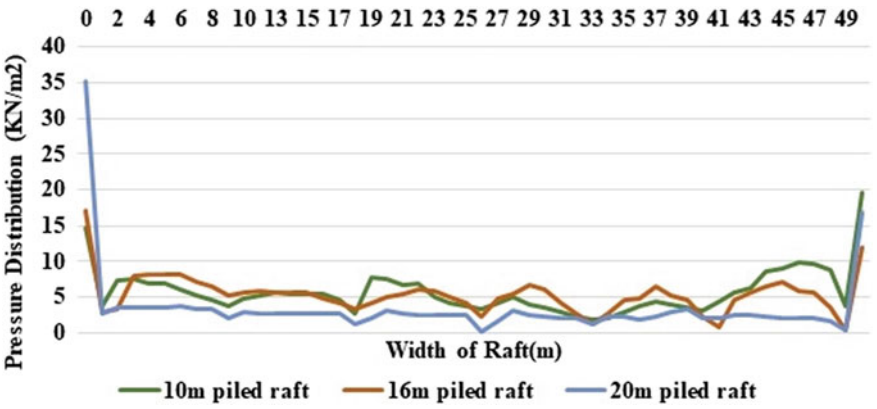

Fig. 12 Contact pressure distribution below the raft of piled raft

The load-carrying capacity of the raft increases with the usage of a small length of the pile. Then the more settlement is observed for a small length of piles. By using different lengths of the pile, the contact pressure distribution of the raft carries 70% of load when compared to the same length of the pile.

6 Conclusions

It was observed from the present study that the introduction of the piles reduced settlement in the foundation by about 80–90% for the present layout of piles. Further reduction in settlement can be achieved by changing the length of the pile. It was observed that the introduction of piles has not only reduced the raft settlement, but also bought out a considerable change in the stress level along the area of the raft. From this study, the following conclusions were made:

1. Although there is an increase in the pile diameter and reduction in the pile length, in the case of piles located in the shallow area, the shaft stress reduces rapidly over the length.
2. The load from the superstructure is directly applied to the piled raft foundation. From the applied load, the pile carries nearly 2–3rd of the load applied on the combined foundation system.
3. The behavior of the raft on the piled raft foundation shows that the contact pressure on the raft gradually decreases at the pile location.
4. By using the different lengths of the pile, the contact pressure distribution of the raft carries 70% of load when compared to the pile using the same length in all portions of the building.
5. The percentage of load carried by raft increases for a small length of the pile. Also, relatively more settlement is observed for small lengths of piles.

6. The interaction effect remains the same when the length of the pile reduces to 80% even when the diameter increases. But when the pile length is reduced to 50%, the interaction increases with an increase in the diameter.

The raft contact stresses obtained from the numerical analysis show uniform distribution and gradually decrease at the pile location and the edges. The shaft stress distribution obtained from the analysis indicated that the stress is higher at the pile head and reduces towards the pile tip.

References

1. Balakumar, V.: Experimental studies of model piled raft on sand and field study of prototype behavior. PhD thesis, Anna University, Chennai (2008)
2. Sawwaf, M.E.I.: Experimental study of eccentrically loaded raft with connected and unconnected short piles. J. Geotech. Geoenviron. Eng. **136**(10), 1394–1402 (2010)
3. Balakumar, V., Ilamparuthi, K.: Performance monitoring of a piled raft foundation of twelve storied building and analytical validation. Indian Geotech. J. **37**(2), 94–115 (2007)
4. Balakumar, V., Anirudhan, I.V.: Piled Raft behavior-model studies and field performance. In: Proceedings of Indian Geotechnical Conference, pp 947–950 (2011)
5. Balakumar, V., Oh, E., Bolton, M., Balasubramaniam, A.S.: A design method for Piled Raft foundations. In: Proceeding of the 18th International Conference on Soil Mechanics and Geotechnical Engineering, Paris, pp. 2671–2674 (2013)
6. Burland, J.B.: Piles as settlement reducer. In: 18th Italian Congress on Soil Mech., Pavia (1995)
7. Rabiel, M., Choobbasti, A.J.: Innovative Piled Raft Foundation design using artificial neural network. Front Struct. Civ. Eng. **14**, 138–146 (2019)
8. Huang, M., Oh, E., Balasubramaniam, A.S., Balakumar, V.: A critical and comparative study on 2D and 3D analyses of Raft and Piled Raft Foundations. Geotech. Eng. J. SEAGS AGSSEA **49**(1) (2018)
9. Padmanaban, M.S., Sreerambabu, J.: Issues on design of Piled Raft Foundation. J. Mech. Civil Eng. **14**(2), 36–40 (2017)
10. Poulos, H.G.: Piled raft foundations: design and applications. Geotech **51**(2), 95–113
11. Vamsi Krishna, B., Ayuluri, S.R.: Settlement analysis of Piled Raft Foundation System (PRFS) in soft clay. Int. J. Mech. Civil Eng. **14**(2), 62–68 (2017)
12. Xie, Y., Chi, S.: Optimization method for irregular Piled Raft Foundation on Layered Soil Media. Advances in Civil Engineering, vol. 2019 (2019)
13. Zeevaert, L.: Compensated Friction Piled Foundation to reduce the settlement of building on highly compressible volcanic clay of Mexico city. In: Proceedings of the 4th international conference of soil mechanics and foundation, vol 2. Eng., London (1957)

Development of Calibration Methodology for Earth Pressure Cells for Installation on Full Scale Retaining Wall

Dinesh Bishnoi, Mrunmay Junagade, and Dasaka S. Murthy

1 Introduction

Earth pressure measurement and its reliability are the necessity for various geotechnical structures such as retaining wall, foundations, and tunnels. These measurements are made to verify the design methodology adopted, for improving the present design methods and for monitoring of the structures. There are various types of earth pressure cells (EPCs) available to measure the earth pressure having different operating principles. Keykhosropur [8] mentioned the types of pressure cells, which are stiff pressure cells, tactile sensors, and fiber optic sensors. Stiff pressure cells are further classified into two types, i.e., force-balance type (hydraulic and pneumatic sensors) and diaphragm pressure cells (strain gage based or vibrating wire based).

There are various factors related to sensors which affects the response of EPCs. Hanon and Jackura [7] covered installation methods and monitoring experience for various types of sensors such as hydraulic, pneumatic, vibrating wire, and electrical resistance type. The authors have cited various factors affecting the response of sensor and some of the important factors such as environmental effects, geometric shape and design, calibration, and installation methods. Environmental effects and geometric factors cause incompliance of sensors with the surrounding and leads to under or over-registration of measurements. The effect of calibration is covered in subsequent section with more details.

The present study is focused on the stiff pressure cells and the various factors which needed to be considered for better understanding of the sensors. The present

D. Bishnoi · M. Junagade (✉) · D. S. Murthy
Department of Civil Engineering, IIT Bombay, Powai, Mumbai 400076, India

D. Bishnoi
e-mail: dinesh_bishnoi@iitb.ac.in

D. S. Murthy
e-mail: dasaka@iitb.ac.in

C. N. V. Satyanarayana Reddy et al. (eds.), *Dynamics of Soil and Modelling of Geotechnical Problems*, Lecture Notes in Civil Engineering 186,
https://doi.org/10.1007/978-981-16-5605-7_8

study is literature review covering sensor types and their modifications, calibration methods available, and their performance.

2 Earth Pressure Cells (Epcs) and Factors Affecting Performance Measurement

There are various types of sensors available for earth pressure measurement, but deflecting diaphragm and vibrating wire sensors are more common so mainly these will be covered. Diaphragm type sensors measure the deflection caused by the earth pressure in electrical outputs such as mV/V or in strains and through sensitivity plots the earth pressure is found out. The deflection causes redistribution of stresses around the sensor, and arching may develop depending on the amount of deflection which leads to erroneous measurement. They are suitable for static as well as dynamic measurement, but their suitability for long-term monitoring is doubtful [4]. The vibrating wire sensors work by measuring the frequency of vibration of a prestressed wire which changes its length and thus frequency of vibration when subjected to pressure. The vibrating wire is suitable for static measurements, and its performance in long term is verified [4].

The EPCs response is affected by the presence of soil, and several researchers studied various factors which affects its performance. Coyle [3] used Terratec pneumatic and Geonor vibrating wire sensor to measure earth pressure behind retaining wall in order to develop more economical design. The effect of grouting and temperature was studied, the grout did not affect the readings, but there was shift in zero-gauge readings with increase in temperature. Felio and bauer [5] used pneumatic EPCs and studied the effect of temperature, contacting material and installation method. It is necessary to monitor the temperature as it has predominant role in earth pressure measurements and needs to be calibrated for determining correction factors. The effect of contacting material and installation method was not much significant. Clayton and bica [2] studied the effect of various soil conditions on diaphragm type EPC. They defined a term CAF (cell action factor) to quantify the measurement error, which is defined as the ratio of normal stress measured by EPC and the stress that would be applied in the absence of cell. The CAF depends on the flexibility ratio, F, which is defined in Eq. 1. The value of CAF should be close to 1, and it is found that flexibility ratio should be less than 0.25 if the CAF is to be greater than 0.95. The ratio of the diameter of the cell diaphragm to the displacement at its center is not less than some threshold value which varies from 1000 to 10,000 to access the performance of cells. It is emphasized that while determining the above, the modulus of soil should be considered especially for dense sands.

$$F = \left(E_{soil} \times R^3\right)/\left(E_{cell} \times t^3\right), \tag{1}$$

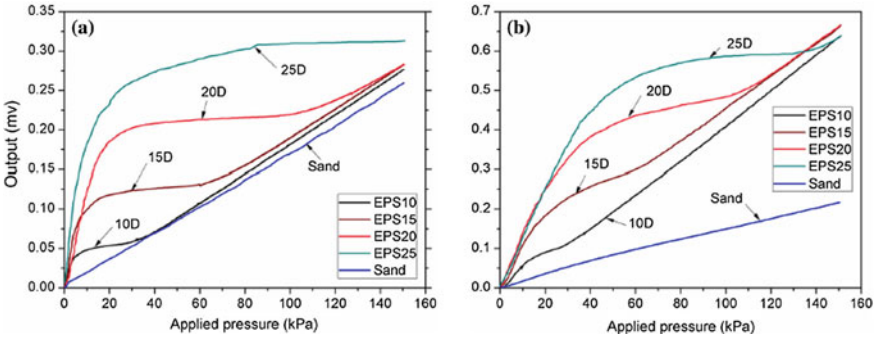

Fig. 1 Response from two different EPCs (**a** KEPC and **b** REPC) makes for geofoam with different densities and sand in contact with the sensor. (Gade and Dasaka [6])

where E_{soil} and E_{cell} are Young's modulus of soil and diaphragm, respectively; R and t are the radius and thickness of diaphragm, respectively.

It is found out that the EPCs should be calibrated for the actual field conditions and it is not always necessary that the contacting material will be soil. The trend of using geosynthetics is increasing such as in drainage and base separation, and the sensors should be calibrated accordingly. Gade and Dasaka [6] used diaphragm based EPCs of different make and studied the effect of grade III sand and geofoam as contact material. Effect of sand thickness, geofoam thickness, geofoam density, and rate of loading was studied. It was found that EPC response depends on the stress–strain behavior of contacting material, and in case of geofoam, the output of EPC resembles the stress–strain behavior of geofoam as shown in Fig. 1. The effect of displacement rate is insignificant for both soil and geofoam. The EPC response of geofoam is higher than the sand, and the effect of geofoam thickness is not significant.

3 Calibration of EPCs

EPCs output is generated in electrical units such as mV/V, strains or in frequency, i.e., Hz, these outputs are correlated with the pressure known as sensitivity plots or calibration plots. Each EPCs is generally provided with calibration charts from the manufacturer, but the calibration is generally done in fluid or air pressure, which may not give accurate results for soil. There are two types of calibration which are fluid calibration and soil calibration. Fluid calibration is generally done in laboratory also to check the response of EPCs to uniform loading and to verify the calibration charts provided by manufacturers. It is essential to calibrate the sensor as close to field conditions as possible for reliable results; thus, soil calibration is required. Researchers developed various calibration chamber to perform soil calibration as it depends on numerous parameters such as side wall friction, effect of particles, and installation type. Selig [10] described an easy to construct and inexpensive calibration

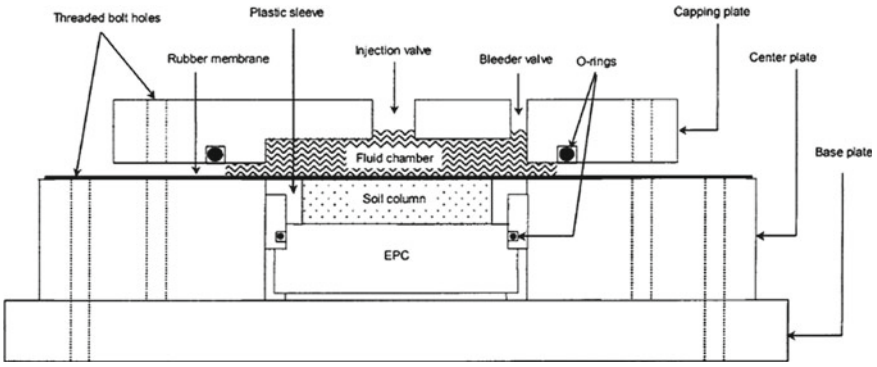

Fig. 2 Uniaxial calibration device (Theroux et al. [15])

chamber which consists of 17 layers of different material and thickness. Pneumatic type and diaphragm type EPCs were used, which were then calibrated with fluid, soil as well as with concrete interface conditions. For pneumatic type over-register, small amount of hysteresis and non-linearity was observed and for electrical type, under registration, significant hysteresis, and non-linearity. It was found that the accuracy of the results is a function of the gage, the installation procedures, the soil properties, and the state of stress. Take and Valsangar [11] used miniature diaphragm type sensor (6.35–7.37 mm) for centrifuge testing, and thus they did fluid calibration, soil calibration at 1 g and 38 g for loose and dense sand. Three types of cells were used, and one is rigid and two are flexibles. For rigid cells, high capacity sensors were used to accommodate scale effects. They found that the stiff subminiature cells can be used successfully to measure earth pressure in centrifuge tests. When flexible sensors are to be used, it is important to calibrate them with soil having stiffness similar to the adjacent zone of cells rather than bulk stiffness.

Uniaxial calibration chamber (Fig. 2) and universal calibration chamber (Fig. 3) are two types of calibration chambers which is used by various researchers for calibration of EPCs [1, 9, 15, 16]. Theroux et al. [15] performed uniaxial calibration tests on Kulite diaphragm type EPCs with silica sand and proposed sand pocket method. A sand pocket container method is for measuring the soil pressure in the field mainly for vertical pressure. The suitability of the sand pocket container was checked in laboratory with universal calibration chamber under static and rapid loading. Field suitability was also checked for pavement under static loading and loads caused by moving trucks.

Wachman and labuz [16] used hydraulic type sensor having diameter of 117 mm and performed fluid calibration as well as soil calibration in universal calibration chamber. Calibration procedure for an EPC is reviewed, and soil-structure interaction model is proposed to understand why soil calibration is necessary. The EPCs were found to over-register by 15–18%. A soil-structure interaction analytical model was developed, and it is found that when the load is distributed over 56% of EPC area, and the over-registration can be 10–20% as observed during calibration of EPCs. It is

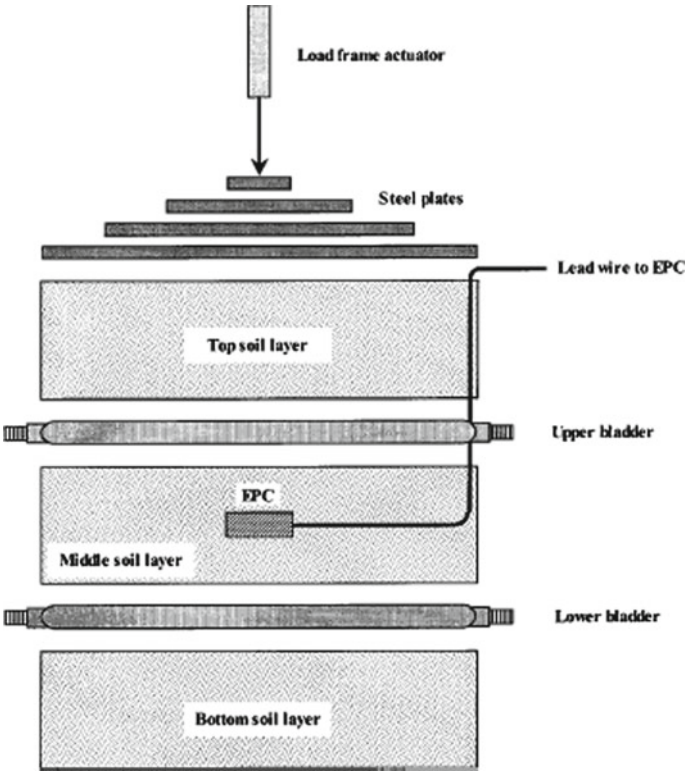

Fig. 3 Universal calibration chamber (Theroux et al. [15])

also mentioned that change in soil density can change contact stress distribution even though the total load remains same. The EPCs may also under-register depending on the distribution of stresses.

4 Development in EPCs

The researchers are coming up with different techniques to improve the performance of the EPCs so that reliable measurements can be made. Traditional EPCs are affected by numerous factors such as material compliance, stress history, contacting material and its size, and temperature. Few researchers used the diaphragm type sensors with hydraulic layer, and this system enhances the resolution of sensor as small variations can be detected easily. Bentler et al. [1] used Kulite diaphragm type EPCs with small fluid chamber under the active face and Geokon hydraulic pressure cells with strain gage transducers to measure soil pressure behind a cantilever retaining wall for a period of 12 months. The study was carried out to better understand the

design process and decrease the cost of construction. Kulite EPCs soil calibration under-registered by up to 25% when compared with the manufacturer calibration factor. The uniaxial calibration factors predicted the stress in the soil to within 5% of the applied stress when checked in the universal chamber. Geokon under-registered by 5–15% mainly because the manufacturer calibration is for transducer and not for whole device. The reading from Geokon EPCs were lower in magnitude than the kulite EPCs caused due to hardware problem with the multiplexer. Labuz and Theroux [9] used diaphragm type with semi-conductor strain gage and a hydraulic oil film and performed fluid calibration (all around, uniaxial on active face only and radial loading around the perimeter) as well as uniaxial calibration and universal calibration for sand. For rigid outer rim, sensitivities computed from soil calibration were 20% lower than the fluid calibration. For fluid calibration, the values agreed well with the manufacturer's value. Arching analysis was also done to understand the behavior of EPC used.

Talesnick [12] proposed a new sensor called as null soil pressure system in which calibration is not required, and the pressure can be measured directly for embedded type. Four types of soil covering mean particle size from 0.2 to 14 mm were used. Three sizes of null sensor were used to check the effect of sensor size on measurement. The response of the null-sensor is not affected by particle size, stress history, and mildly affected by soil stiffness with inherent linear response. The cells are over-registered by 3–4%. The purpose of three different sensor size was to study the effect of particle size by sensor diameter, and it is found that the ratio should not exceed 1:7 for null sensors. Talesnick [13] also used null pressure sensor for soil-structure physical models. The null sensor response is compared with diaphragm type sensor of different thickness for a range of particle sizes. The usage of null sensors in loading conditions involving shear loading is also checked. The response of diaphragm type sensor is different for different size of particles, but the null pressure sensor is not affected by the particle size. It is found that the particle size to sensing diameter can be as small as six particles across the sensor diameter for reliable results and this can be used for physical/centrifuge model testing. The presence of shear stresses does not impede the reliable measurement of normal stresses by null sensors. Drawbacks of null sensor are that the system requires significant peripheral equipment and is more complex, expensive than passive system. The system is difficult to employ in field conditions [14].

Keykhosropur et al. [8] designed a simple, robust, and cost-effective new sensor with large sensing area and homemade assembly for measurement of soil pressure on solid surface. Static calibration with weights and dynamic calibration using linear mass shaker was performed. The sensor is suitable for soils with relatively uniform gradation. The suitability of the sensor is checked in field testing for earth pressure on abutment wall, dynamic shallow foundation footing pressure, and vertical underground structure during shake table testing. The sensor is versatile in the sense that the housing material can be changed to account the compliance issue and capacity can be changed as per our requirement. The sensing area has a benefit of reducing localization effects.

Talesnick et al. [14] developed a sensor which is combination of deflecting diaphragm and fluid filled soil pressure sensor. The new system was implemented in compacted engineered fill of 1.8 m height. The importance of design is to minimize membrane deflection without limiting the resolution of cell. The soil arching does not develop which was shown by lack of hysteresis in load-unload cycle and the system inherently deals with temperature effects. In field, the cells were able to perform satisfactorily for static and dynamic (11 Hz) loading caused due to compaction of fill.

5 Conclusions and Recommendations

For achieving optimized design, it is essential to measure earth pressures in retaining walls, underground structures, etc. using EPC. In this paper, literature related to earth pressure cells (EPCs), factors affecting EPCs, calibration methods, and the development in EPCs is covered. It is found that the response of sensor depends on large number of factors which may cause under-registration or over-registration in the measurements caused due to incompliance in the sensor materials with the surrounding. The fluid calibration chart supplied by the manufacturer is not enough, and proper calibration should be done considering the intended use, installation method, and surrounding soil conditions. Though various improvements in EPCs is done, the use of traditional EPCs is more due to its large user experience and availability of performance record.

Theroux et al. [15] recommended to use sand pocket methods so that the arrangement around sensor remains same and the laboratory curves can be used effectively. It is also recommended by Hanon and Jackura [7] that sometimes users may have to settle for reliable results instead of accurate results irrespective of the type of EPCs and users may be required to rely on alternative measurement system to backup estimate field pressures if feasible.

Acknowledgements Authors thank the financial support received from MHRD (UAY scheme), SAVI Infrastructure Limited, and IIT Bombay.

References

1. Bentler, J.G., Labuz, J.F., Schultz, A.E.: Earth pressure behind a retaining wall. Report no. 2005–14, Minnesoa Department of Transportation, Minnesota (2005)
2. Clayton, C.R.I., Bica, A.V.D.: The design of diaphragm-type boundary total stress cells. Geotechnique **43**(4), 523–535 (1993)
3. Coyle, H.M., Bartoskewitz, R.E., Milberger, L.J., Butler, H.D.: Field measurements of lateral earth pressures on a cantilever retaining wall. Transp. Res. Rec. **517**, 16–29 (1974)
4. Dunnicliff, J.: Geotechnical instrumentation for monitoring filed performance. NCHRP Synthesis 89, Transportation Research Board, Washington, D. C. (1982)

5. Felio, G.Y., Bauer, G.E.: Factors affecting the performance of a pneumatic earth pressure cell. Geotech. Test. J., GTIODJ **9**(2), 102–106 (1986)
6. Gade, V.K., Dasaka, S.M.: Influence of contacting material on calibration response of diaphragm earth pressure cells. Indian Geotech J. **50**(1), 133–141 (2020)
7. Hanon, J.B., Jackura, K.A.: Measurement of earth pressure. Transp. Res. Rec. **1004**, 6–13 (1985)
8. Keykhosropour, L., Lemnitzer, A., Star, L., Marinucci, A., Keowan, S.: Implementation of soil pressure sensors in large-scale soil-structure interaction studies. Geotech. Test. J. **41**, 730–746 (2018)
9. Labuz, J.F., Theroux, B.: Laboratory calibration of earth pressure cells. Geotech. Test. J. **28**(2), 188–196 (2005)
10. Selig, E.T.: Soil stress gage calibration. Geotech. Test. J. GTJODJ **3**(4), 153–158 (1982)
11. Take, W.A., Valsangkar, A.J.: Earth pressures on unyielding retaining walls of narrow backfill width. Can. Geotech. J. **38**, 1220–1230 (2001)
12. Talesnick, M.: Measuring soil pressure within a soil mass. Can. Geotech. J. **50**, 716–722 (2013)
13. Talesnick, M.L., Avraham, R., Ringel, M.: Measurement of contact soil pressure in physical modelling of soil-structure interaction. Int. J. Phys. Model. Geotech. **14**(1), 3–12 (2014)
14. Talesnick, M., Ringel, M., Rollins, K.: Development of hybrid soil pressure sensor and its application to soil compaction. Canad. Geotech. J., manuscript (2020)
15. Theroux, B., Labuz, J.F., Dai, S.: Field installation of an earth pressure cell. Transp. Res. Record 1772, Paper no. 01-3356, 12–19 (2001)
16. Wachman, G.S., Labuz, J.F.: Soil-structure interaction of an Earth Pressure Cell. J. Geotech. Geoenviron. Eng. **137**(9), 843–845 (2011)

Numerical Simulation of Field Vane Shear Test Using Finite Element Method

Anand M. Hulagabali, Pankaj Bariker, C. H. Solanki, and G. R. Dodagoudar

1 Introduction

The vane shear test is one of the most widely used methods for the determination of undrained strength due to its low cost and ease of use. However, despite its common usage, the interpretation of the vane test has been quite often a controversial issue. The following are the main shortcomings of the equipment and the usual sources of error in the estimation of the undrained strength: vane size effects, blade thickness effects, soil anisotropy effects, strain rate effects, and progressive failure. The conventional interpretation of filed vane shear results did not take into account those effects. So far, over more than a half-century of research and application in geotechnical practice, field vane shear testing has been shown to reflect several heavily criticized with the reliability of the undrained shear strength measured with the vane [11]. These criticisms have centered on conventional interpretation of the measurement of the undrained strength due to merely considering the peak torque and diameter of the vane to calculate S_u.

Thus, this paper aims to study some of these effects through a finite element analysis (FEA) with appropriate soil models in PLAXIS 3D.

The field vane shear test consists of four rectangular blades fixed at 90° angles to each other. The analysis is carried out by forcing the vane into the ground to the

A. M. Hulagabali (✉)
National Institute of Engineering (NIE), Mysuru 570008, India
e-mail: anandmh@nie.ac.in

P. Bariker
National Institute of Technology Karnataka, Surathkal, India

C. H. Solanki
Civil Engineering Department, SVNIT, Surat 395007, India

G. R. Dodagoudar
Civil Engineering Department, IIT Madras, Chennai 600036, India

C. N. V. Satyanarayana Reddy et al. (eds.), *Dynamics of Soil and Modelling of Geotechnical Problems*, Lecture Notes in Civil Engineering 186,
https://doi.org/10.1007/978-981-16-5605-7_9

desired depth and manually turning the vane rod from the vane handle located at the upper end until the soil achieves its failure mode to measure the peak torque applied [8]. The peak torque applied to the soil was converted into undrained shear strength, S_u, using the conventional interpretation.

The study addresses the described general objective and tries to investigate the factors influencing the result of filed vane shear test using finite element. The finite element code PLAXIS 3D is used for the numerical simulation with different soil models, the input parameters of each material model derived from the literature work. The result of the numerical analysis was compared with the conventional analysis method.

2 Literature Review

Several researchers have discussed the nature of the disruption caused during vane insertion and measured potential soil disturbance. According to the studies of Wilson et al. [17], strength attained using field vane shear test can be particularly affected by confined soil destruction because of the loss of inter-particle bonds within the soils.

According to Morin [10], the disturbance due to typical blades may result in strength degradation between 10 and 25% of the strength. Insertion disturbance can inconsistently affect both the peak strength and residual strength [3], controlling the accuracy by which soil sensitivity is measured with the vane test.

Cerato and Lutenegger [3] investigated that disturbance induced by inserting a vane should be linked to the geometry of the field vane shear for the same soil. It is reasonable that the more soil that must be displaced to permit the vane to be inserted, the more the amount of disturbed soil. The level of disturbance caused by the field vane shear is measured as shown in Fig. 1. And also at every depth, the undrained shear strength is shown to decrease with increasing blade thickness.

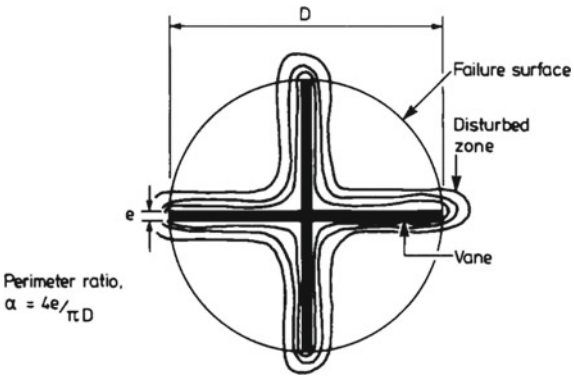

Fig. 1 The disturbance caused by the intrusion of the vane into the clay [3]

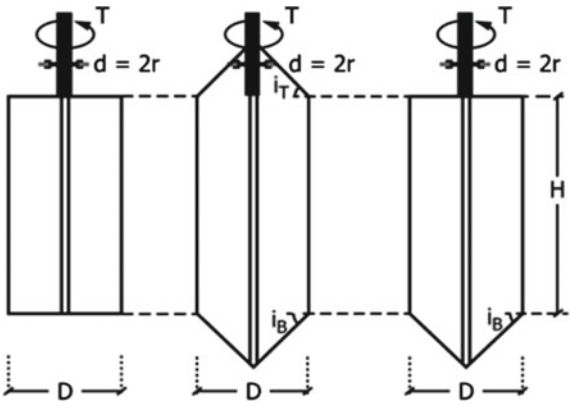

Fig. 2 The geometry of field vane [1]

Variation in geometry vane size and shape can change the rate of soil shearing at constant rotation rate, which has resulted in analysis methods being generalized to consider shear rate in terms of peripheral vane velocity [2]. These methods account for variation in the shear surface (Fig. 2).

Yusoff et al. [18] carried out an experimental program on three vanes, 20 mm in diameter and height 20, 40, and 80 mm. The blades were rotated at a range of peripheral velocities from 0.5 to 400 mm/s to produce correlations of undrained shear strength and applied rate of shear. The outcomes of the investigation highlight that the peak shear resistance recorded increases with increasing peripheral velocity. The magnitude of vane displacement required to achieve full mobilization of soil shear strength was dependent on the applied rate of shear.

Mesri and Huvaj [9] stated that progressive failure affects all laboratory and in situ undrained shear tests. Mainly, undrained shear strength mobilized in a full-scale undrained failure in the field is, in general, not equal to the undrained shear strength measured by laboratory or in situ tests.

Thakur et al. [16] found that strain-softening can happen due to structural geometric instability and material instability. Most of the time, in common geotechnical engineering practice, the structural geometric weakness is ignored. However, softening material can be taken into account, such as fissuring and cracking. Referring to the underlying assumptions on field vane shear test assumes conservatively a fully mobilized cylindrical shear failure around the vane, indicating no progressive failure.

Griffiths and LANE [4] performed two-dimensional and quasi-three-dimensional finite element analysis of VST, considering the only tangential movement of material along with the blades of the vane. The conventional procedure for the mobilization of shear stresses are acceptable for isotropic, non-softening materials, with the peak shear stress distribution on the vane ends adequately modeled using a rectangular assumption. Their study determined that the conventional formula represents the best estimate for the cohesive strength of isotropic and non-softening soils.

Gylland et al. [6] investigated using in situ samples and numerical simulations to detect geometrical failure mode around the shear vane in soft sensitive clay. The global failure geometry is not a full cylinder, but rather a rounded square at the peak global torque. Finite element simulations strengthen these findings. Therefore, the correct assumption regarding the geometrical shape of the failure surface around the vane is essential for interpreting a correct shear strength value.

Gupta et al. [5] performed a numerical model to comprehend the undrained shear strength response of a saturated cohesive soil subjected to the vane shear test. The soil is modeled using the Mohr–Coulomb failure criteria and the response of soil until failure is studied. The result gives a higher value of the cohesive strength of clay from the measured rotation moment in a laboratory test. The respect of the stress distribution pattern in the numerical model shows that the expectations have a significant effect on the cohesive strength of soil as calculated from the maximum rotation moment.

Recently, Rismyhr [13] conducted numerical simulations to examine to which extent progressive failure (softening), anisotropy, and strain rate affect the measured strength from the shear vane test. The material models used were Mohr–Coulomb, Geo future Soft Clay (a user-defined material model developed by NTNU), and the total stress-based NGI ADP model using PLAXIS 2D and PLAXIS 3D.

3 Materials and Methodology

Main Characteristics of the vane apparatus and basic testing procedures design criteria for the device were taken from ASTM D2573–15 (Standard Test Method for Field Vane Shear Test in Cohesive Soil). Here are the common essential technical specifications.

The most commonly used vanes are with rectangular blades measuring 55 mm $\times$ 110 mm and the other with rectangular blades measuring 65 mm $\times$ 130 mm. Both vanes consist of four blades set at right angles. The larger and smaller vanes are capable of measuring undrained shear strength up to 50 kPa and 100 kPa, respectively [1].

Conventionally, it is interpreted that the applied torque is resisted by the shear stress mobilized along the failure surface. Since the test is carried out comparatively fast, undrained conditions can be assumed, and hence, the shear stress at failure is the same as the undrained shear strength, S_u, based on the schematic diagram shown in Fig. 3.

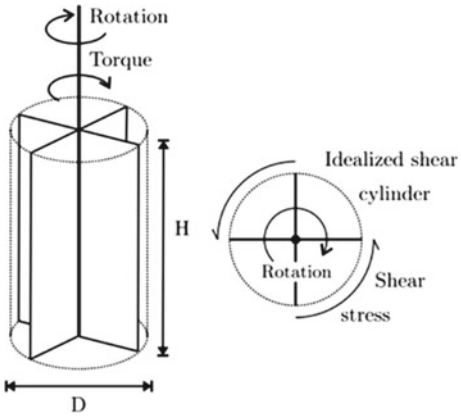

Fig. 3 Illustration of the shear vane (Gylland [6])

4 Finite Element Analysis in PLAXIS

The main features of the vane apparatus and the geometry used in the numerical simulations are based on the standard vane from the standard test method for field vane shear test in cohesive soil (ASTM D2573–15). The standard vane dimension used in this study is the height and diameter of 110 mm and 55 mm, respectively (Table 1).

The thicknesses of blades are also based on the standard to analyze the effect of blade thickness from 0.8 mm up to 3 mm. Soil contour has been defined based on the sensitivity analysis to ensure the boundary surfaces would not affect the results from the numerical simulations. The geometry of the problem is as shown in Fig. 4.

The input parameters of each material parameter were derived from the literature work [14]. The values of each material parameter were based on typical values for soft clay and stiff clay. The Mohr–Coulomb and Hardening soil model material parameters are summarized in Tables 2 and 3, respectively, and material parameters of the plate blades are shown in Table 4.

Undrained (A) is used for calculation of undrained or short-term material behavior in which stiffness and strength are defined in terms of effective properties. A significant bulk stiffness for water is automatically applied to make the soil as a whole incompressible, and (excess) pore pressures are calculated, even above the phreatic surface.

The default boundary conditions were used as in PLAXIS 3D settings as shown in Fig. 5. The horizontal bottom boundary was fully fixed. The vertical boundaries were set in horizontal movement and free in a vertical movement. The top horizontal boundary was free in all directions.

Conditions for cylinder boundaries are also set on; in particular, displacements along all directions are free. Furthermore, conditions about displacements on blades are needed: while vertical displacements on tips are fixed, x and y displacements are

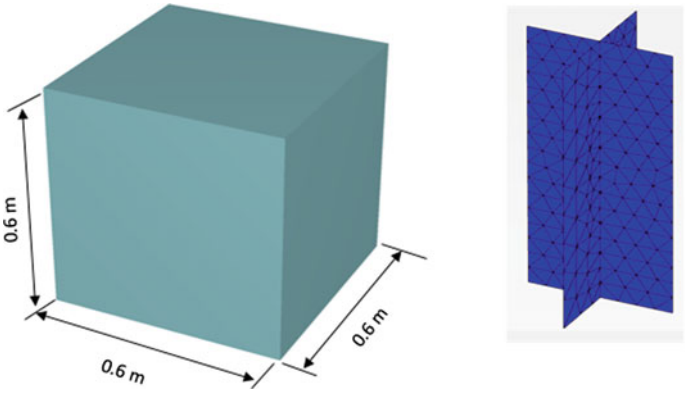

Fig. 4 Soil and Vane model in Plaxis

Table 1 Proposed formulae for estimating lateral soil resistance

Parameters	Standard (ASTM D2573–15)
Vane diameter (D)	35–100 mm
Vane shaft diameter (d)	12.5–16.5 mm
Vane height (H)	$1D \leq H \leq 2.5D$
Blade thickness (e)	$e < 3$ mm
Taper angle (i)	Usually 0 degrees (rectangular) or 45 degrees (tapered)
Vane area ratio	Less than 12%

Table 2 Mohr–Coulomb material parameters used in finite element models

Parameters	Symbol	Soil type	
		Soft clay	Stiff clay
Type of material behavior		Undrained (A)	Undrained (A)
Soil unit weight (kN\m^3)	γ_{unsat}	16	17
	γ_{sat}	18	19
Young's modulus	E_{ref}	3000	4000
Poisson's ratio	ν	0.3	0.3
Cohesion	C_{ref}	1	10
Friction angle	ϕ	15°	28°
Dilatancy angle	ψ	0°	0°

free; displacements are also fixed on the blades' crossing vertical line using the line displacement at the tips of the vane blade as shown in Fig. 6 below.

PLAXIS 3D provides various geometric entities that are the basic components of the physical model. Structures and loads can be assigned to the geometric objects.

Table 3 Hardening soil model material parameters used in finite element models

Parameters	Symbol	Soil type	
		Soft clay	Stiff Clay
Type of material behavior		Undrained (A)	Undrained (A)
Soil unit weight (kN\m^3)	γ_{unsat}	16	17
	γ_{sat}	18	19
Stiffness	E^{ref}_{50}	3000	6000
	E^{ref}_{oed}	3700	6000
	E^{ref}_{ur}	9000	18,000
	Power (m)	1	0.8
	ν_{ur}	0.2	0.2
Strength	C'_{ref}	1	10
	ϕ'	15°	28°
	Ψ'	0°	0°

Table 4 Plate blade material parameters

Parameters	Standard (ASTM D2573–15)
Vane shaft diameter (d)	3 mm
Unit weight (γ)	77 kN/m^3
E1	2.1×10^8
E2	2.1×10^8
ν_{12}	0.495

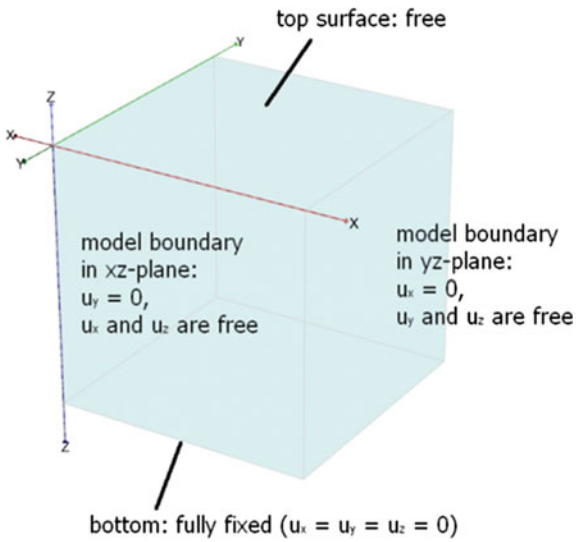

Fig. 5 Boundary conditions in PLAXIS 3D [12]

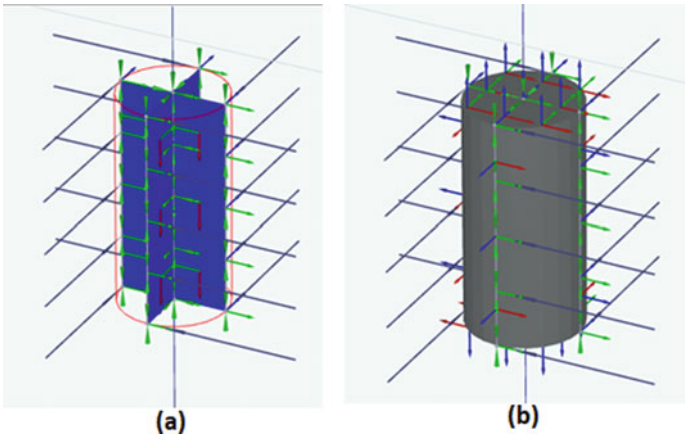

Fig. 6 **a** Creating line displacements at the tip of each blade and the center of the vane; **b** Conditions for cylinder boundaries along all directions are free

The vane blades in PLAXIS 3D can be modeled using plate elements. The material properties of plates are contained in material data sets. The vane blade was modeled in the PLAXIS 3D structure option as a plate with its properties in the material and methods section.

Torque was simulated by applying line loads at the end of each blade. Initially, there were some problems regarding the rotation of the vane. To ensure rotation of the vane, line displacements at the tip and center blade of the vane were created. Each tip was fixed in the x and y direction and free in the z-direction. The center of the vane was fixed in the x, y, and z-direction as shown in Fig. 7.

Fig. 7 Line load at the tip of each blade to simulate the torque at failure

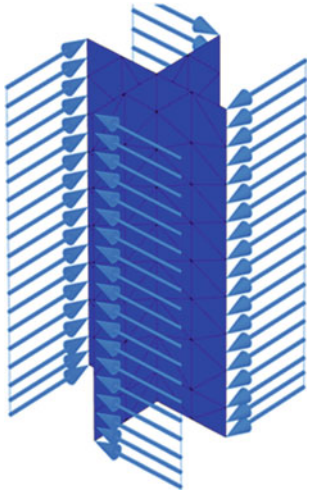

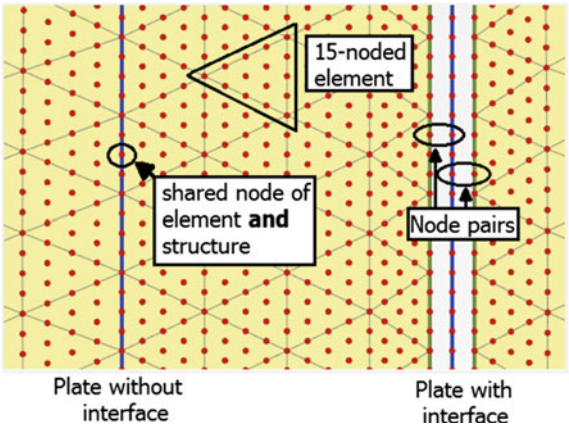

Fig. 8 PLAXIS interface soil-plate layout [12]

To simulate the interaction between the soil and a structure, in this case, the plate, PLAXIS uses interface elements. Without any interface, the structure and the soil are tied together with no relative displacement (slipping/gapping) possible between the structure and the soil. By using an interface, node pairs are created at the interface of structure and soil, one belonging to the soil and the other to the plate. The interaction between the nodes consists of two elastic-perfectly plastic springs, as shown in Fig. 8, the first one models the gap displacement, and the second the slipping displacement.

4.1 Numerical Simulation

The finite element models were modeled having the same dimension as the theoretical calculation used. Both Mohr–Coulomb and Hardening soil material models were considered for both stiff clay and soft clay soils.

As shown in Fig. 9 exported from the PLAXIS 3D tables, the $\sum M_{stage}$, which percentage of the assigned basic load applied on the vane blade tip is 0.119, declares that 11.9% of the primary line load, 25 kN/m, is applied on the vane blade, and it reached its failure using the Mohr–Coulomb material model for the case of stiff clay soil.

The torque at failure for Stiff clay was obtained from PLAXIS simulation via Hardening soil model and Mohr–Coulomb 33.275 Nm and 35.997 Nm, respectively. The hardening soil model fits well with the result from the theoretical calculation 33.275 Nm and 33.53 Nm, respectively. The Percentage of difference for theoretical calculation and numerical simulation using the hardening soil model and Mohr–Coulomb is 0.76% and 8.1%, respectively. Whereas for soft clay, it opts out to be 0.76% and 9.46%, respectively.

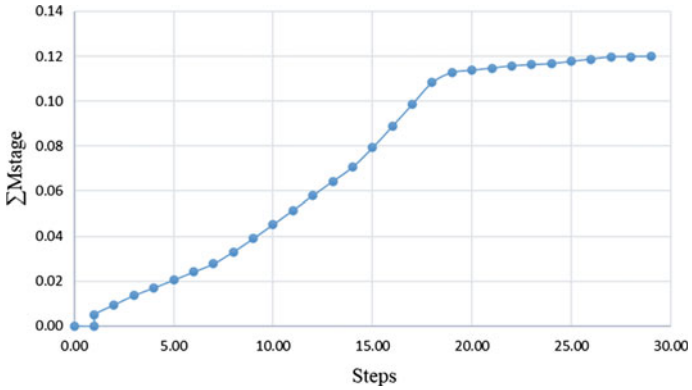

Fig. 9 Ultimate line loading in vane tips

4.2 Effect of Blade Thickness

Four field vane were simulated, having different perimeter ratios ranging from 1.4 to 6.01%. The vanes were rectangular, four-bladed vanes with heights of 110 mm and diameters of 55 mm, given that height to diameter ratios of two. The only difference then was the blade thickness (0.8, 1.4, 2.0, and 2.6 mm). The blade thickness was different to offer different values of α. The diameter of the vanes and height was held constant. Table 3.1 presents the vane dimensions (Fig. 10).

Field Vane test undrained shear strengths are directly interrelated to the thickness of vane blades used within perimeter ratios ranging from 1.4 to 6.01%. The results from four simulations showing that the measured undrained shear strengths are inversely proportional to the perimeter ratio of the vane well agreed with [3,

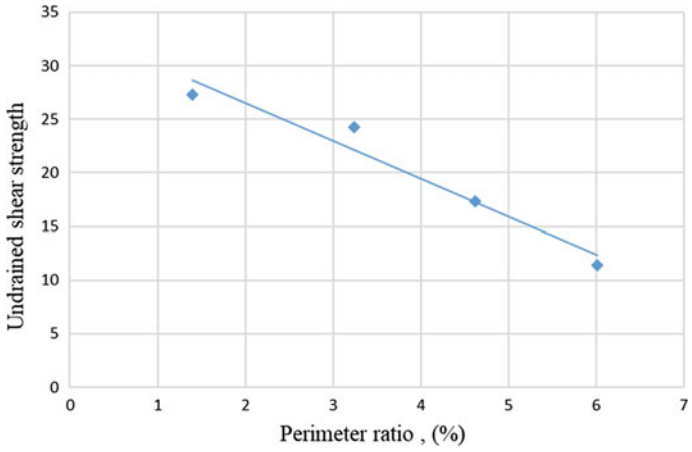

Fig. 10 Result of undrained shear strength versus perimeter ratio

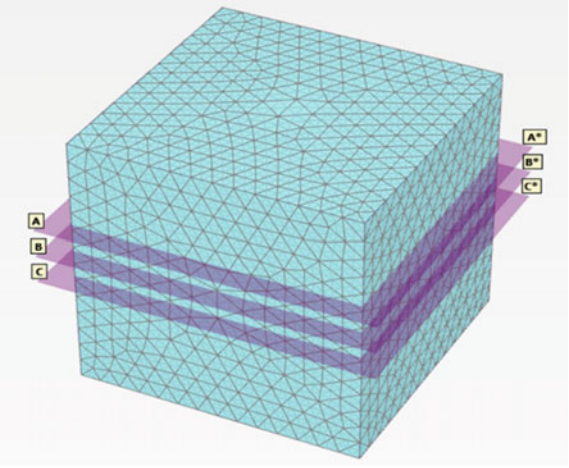

Fig. 11 The sections of the model

15] findings. Undrained strength values approximately 27.28 kN and ($\alpha = 1.4\%$) when compared with Undrained strength 23.4 kN and ($\alpha = 3.24\%$), the percentage of difference is 12.26%. As a result, with the same type of soil but different blade thickness, the undrained shear strength can vary significantly (Fig. 11).

4.3 Further Analysis

The evolution of plastic points increasing rotation close to the peak resistance is presented in Fig. 12. Red plastic points are material regions at the MC line. The evolution of these indicated that elements of progressive failure are present before the peak global resistance is reached.

5 Conclusions

From the Vane shear analysis in PLAXIS, the following conclusions can be drawn.

1. The results for both soft and stiff clay soils using the Mohr–Coulomb gave too large the torque at failure and the big difference between simulated and hand calculation with the percentage of difference for stiff clay soil 8.1% and soft clay soil 9.46%, respectively.
2. The hardening soil model fits well with the result compared to both measured stiff and soft soil between hand calculation and numerical simulation with a percentage of 0.76% for both cases.

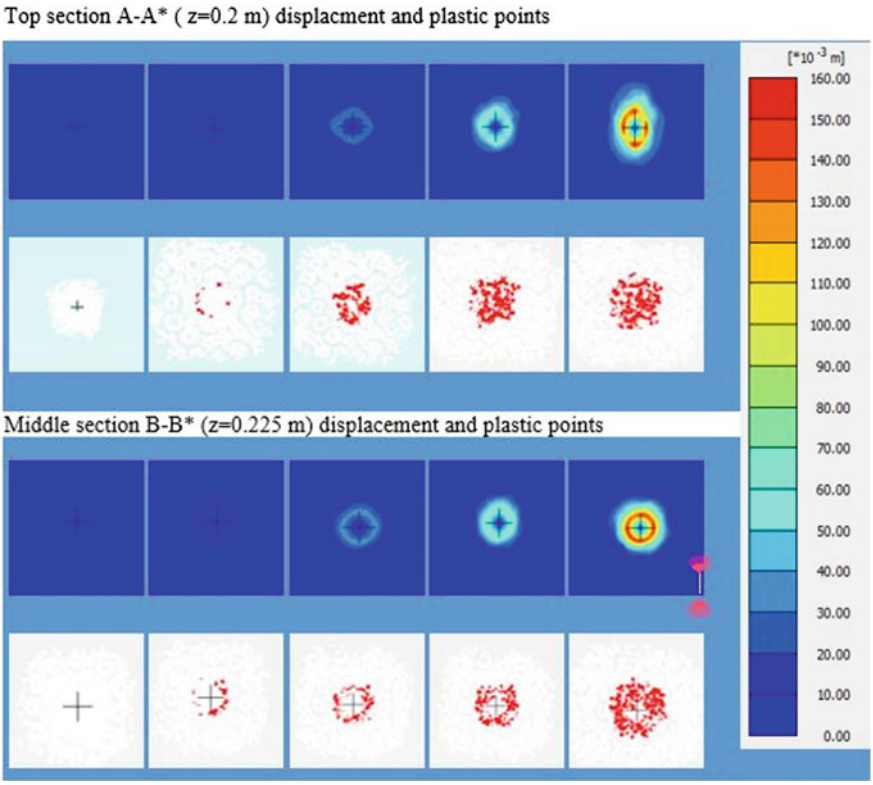

Fig. 12 Results of displacements (u) and evolution of plastic points around the vane during rotation; plastic points refer, respectively, to the top and middle of the vane

3. The result of the four simulations shows for the same type of soil with different blade thickness; the undrained shear strength can vary significantly approximately 27.28 kN for $\alpha = 1.4\%$ and compared with undrained strength 23.4 kN for $\alpha = 3.24\%$ gives the percentage of difference 12.26%.
4. The measured undrained shear strengths are inversely proportional to the perimeter ratio of the vane well agreed with other previous findings.
5. The failure geometry around the blade is recognized in the plastic point's picture, more emphasized at the top than in the middle of the device.

References

1. In Standard Test Method for Field Vane Shear Test in Saturated Fine-Grained Soils, pp. 1–8. https://doi.org/10.1520/D2573
2. Biscontin, G., Pestana, J.: Influence of peripheral velocity on measurements of undrained shear strength for an artificial soil. In: Geotechnical Engineering Report No UCB/GT/99-19 (2000). http://www.ce.berkeley.edu/~pestana/reports/UCBGT99-19 Effect of Peripheral.pdf
3. Cerato, A.B., Lutenegger, A. J.: Disturbance effects of field vane tests in a varved clay. In: Proceedings of the 2nd International Conference on Geotechnical and Geophysical Site Characterization, October, pp. 861–867 (2004). http://faculty-staff.ou.edu/C/Amy.B.Cerato-1/cerdeo.pdf
4. Griffiths, D., Lane, P.A.: Finite element analysis of the shear vane test. **37**(6), 1105–1116 (1990)
5. Gupta, T., Chakraborty, T., Abdel-Rahman, K., Achmus, M.: Large deformation finite element analysis of Vane Shear tests. Geotech. Geol. Eng. **34**(5), 1669–1676 (2016). https://doi.org/10.1007/s10706-016-0048-0
6. Gylland, A.S.: Microstructural Observations of Shear Zones in Sensitive Clay. Norwegian University of Science and Technology (2012)
7. Gylland, A.S., Jostad, H.P., Nordal, S.: Failure geometry around a shear vane in sensitive clay. In: NGM 2012 Proceedings, pp. 103–110 (2012)
8. Jonsson, M., Sellin, C.: Correction of shear strength in cohesive soil (2012)
9. Mesri, G., Huvaj, N.: Shear strength mobilized in undrained failure of soft clay and silt deposits. In: Advances in Measurement and Modeling of Soil Behavior (2007)
10. Morin, P.J.J.: Vane shear strength testing in soils, field, and laboratory studies. ASTM **27**(1), 165–165 (1990). https://doi.org/10.1139/t90-018
11. Peuchen, J., Mayne, P.: Rate effects in vane shear testing. In: Proceedings of the 6th International Offshore Site Investigation and Geotechnics Conference: Confronting New Challenges and Sharing Knowledge, OSIG 2007, pp. 187–194 (2007)
12. PLAXIS.: User's manual (2013)
13. Rismyhr, K.: Effect of Anisotropy, Strain Rate and Progressive Failure in Numerical Simulations of the Shear Vane Test (Issue June) (2017)
14. Susila, E., Apoji, D.: Settlement of a full scale trial Embankment on Peat in Kalimantan: field measurements and finite element simulations. Jurnal Teoretis Dan Terapan Bidang Rekayasa Sipil **19**(0853–2982), 249–269 (2012)
15. Terzaghi, K., Peck, R., Mesri, G.: (1996) Soil Mechanics in Engineering Practice, 3rd edn. Wiley, New York
16. Thakur, V., Nordal, S., Grimstad, G.: Phenomenological issues related to strain localization in sensitive clays. Geotech. Geol. Eng. **24**(6), 1729–1747 (2006). https://doi.org/10.1007/s10706-005-5818-z
17. Wilson, L.J., Kouretzis, G.P., Pineda, J.A., Kelly, R.B.: On the determination of the undrained shear strength from vane shear testing in soft clays. In: Proceedings of the 5th International Conference on Geotechnical and Geophysical Site Characterisation, ISC 2016, pp. 455–460 (2016)
18. Yusoff, N., Black, J.A., Hyde, A.F.: Rate effects and vane shear strength of sandy clay (2018)

Comparison of Flownets for Varying Thickness of Vertical Core Earth and Rockfill Dam Under Rapid Draw-Down and Steady-State Seepage and Its Effect on Stability Using Numerical Modeling

Rajesh Khanna and R. Chitra

1 Introduction

Construction of earth and rockfill dams are most suitable when there is abundance of fine-grained and coarse-grained materials at site [1–4]. Core of earth and rockfill dam provides imperviousness and the shell provides the stability to the dam [11, 13–15]. If there is abundance of fine-grained materials and coarse-grained materials at site, there is a possibility to construct dam with various thicknesses of core depending upon the availability of construction materials. In steady-state and rapid-draw condition of dam, the stability of outer slopes depends upon various factors, i.e., the strength parameters of core and shell materials, imperviousness of core, and flow direction of flow lines in particular condition [5–10].

2 Objective

The objective of the study was to compare variation in the flownet under Steady-State Seepage and Rapid Draw-Down in the core of a dam on account of variation in the thickness of core and its effect on the stability of dam. FEM analysis (Rocscience [12]) was carried out for different thicknesses of core to see how the magnitude and direction of flowlines vary and its effect on stability.

R. Khanna (✉) · R. Chitra
Central Soil and Materials Research Station, New Delhi, India

C. N. V. Satyanarayana Reddy et al. (eds.), *Dynamics of Soil and Modelling of Geotechnical Problems*, Lecture Notes in Civil Engineering 186,
https://doi.org/10.1007/978-981-16-5605-7_10

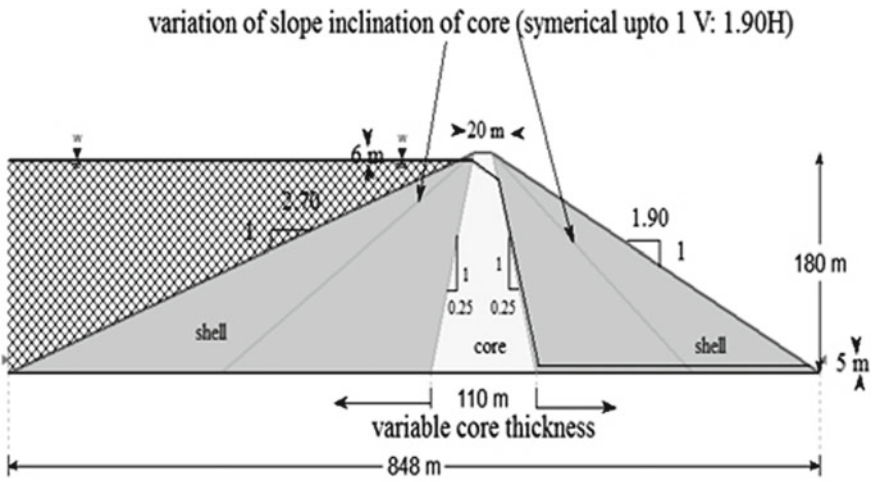

Fig. 1 Simplified section of 180 m high earth and rockfill dam

3 Section of Dam and Parameters Used

A dam section of height 180 m with flat base and founded on strong foundation was selected for the present study. A simplified dam section adopted is shown in Fig. 1. The parameters adopted in the present study are:

Shell materials:

c' = 0 kN/m^2, $\phi = 42°$ (for SSS and RDD).

Core material:

c' = 0kN/m^2, $\phi = 42°$ (for SSS and RDD).

Parametric studies on the following parameters were carried out for:

a. Thickness of core: Starting from 25% of dam height to full base width
b. FEM analysis for various thicknesses of core
c. Levels of draw-down: H/2.

4 Analysis (Comparison of Flownets)

4.1 Variation of Flow Lines Under Steady-State Seepage

The flow lines of earth and rockfill dam were obtained by treating the shell material as highly pervious (without head loss) in comparison to core material. The flow lines were obtained by performing seepage analysis using software (which employs FEM techniques) for different thickness of core under steady-state seepage as shown in Fig. 2 under full reservoir condition. It is inferred from the figure that for all thicknesses of vertical core, the flowlines are directed towards downstream slope of

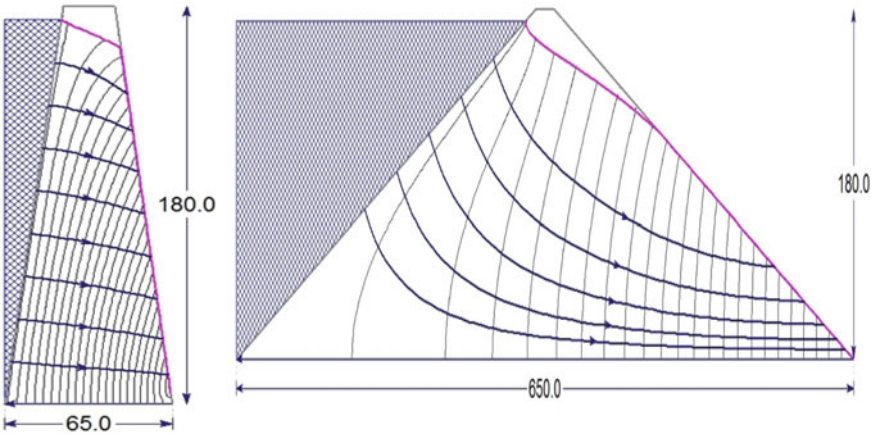

Fig. 2 Flow lines and equipotential lines under steady-state seepage through vertical core of slopes 1 V: 0.125 H and 1 V: 1.00 H

core, and where these flow lines emerge from the core, the flow line is parallel to the outer slope of the core on the downstream side. For the thin core, flow lines are relatively horizontal, and the top line (phreatic line) meets the downstream slope near the top of the downstream face.

4.2 Variation of Flow Lines Under Rapid Draw-Down

The flow lines were obtained by performing seepage analysis using software (which employs FEM techniques) for different thickness of core under rapid-draw-down (H_{dd} = H/2) as shown in Fig. 3. It is observed from the figure that for all cases of rapid-draw-down, when the core is very thin, bulk of the flow lines are toward downstream slope and some are towards upstream slope. As the thickness of the core increases, more flowlines are towards upstream slope including draw-down level. When the vertical core is thick, flowlines in half the flow space are towards downstream face of core and the flowline in other half of space are toward upstream face.

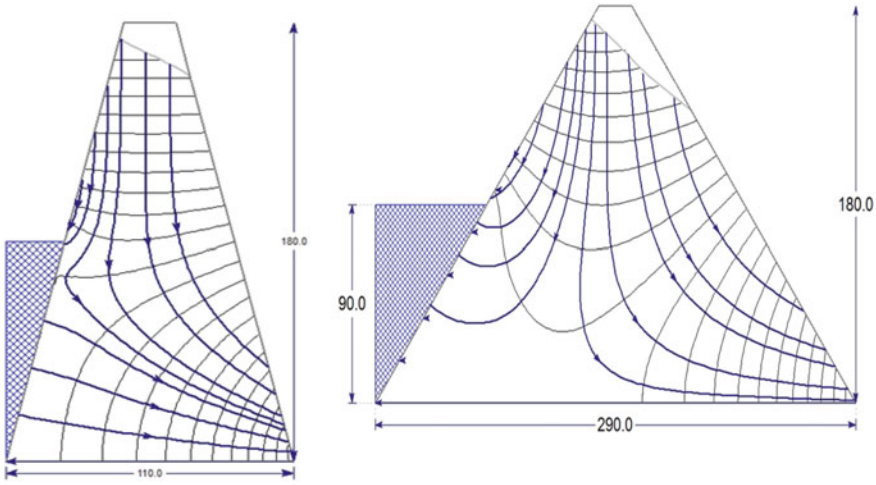

1 V: 0.25H 1 V: 1.00 H

Fig. 3 Flow lines and equipotential lines under rapid draw-down through vertical core of slopes 1 V: 0.25 H and 1 V: 1.00 H

5 Effect Flownet on Stability Analysis

5.1 Effect Flownet on Stability Analysis Under Steady-State Seepage

Stability analysis for downstream slope of dam was carried out for the core thickness of 25% of dam height to full width of dam using numerical modeling. The results from Fig. 4 shows that upto a slope of vertical core from 1 V: 0.125 H to 1 V: 0.50 H (100% thickness of core at bottom), there is no change in factor of safety because failure surface passes through the shell. Beyond U/s and D/s of core slope of 1 V: 0.50 H, the factor of safety begins to decrease as the failure surface passes through the core. The minimum factor of safety is obtained when the D/s slope of the core merges with the outer slope of the core. The factor of safety is close to $\tan\phi/\tan\beta$ (γ_b/γ_t) which is valid for flow parallel to outer slope in infinite slope.

5.2 Effect Flownet on Stability Analysis Under Rapid Draw-Down

Stability analysis for upstream slope of dam was carried out for the core thickness of 25% of dam height to full width of dam using numerical modeling. The results from Fig. 5 shows that upto a slope of vertical core from 1 V: 0.125 H to 1 V: 0.75

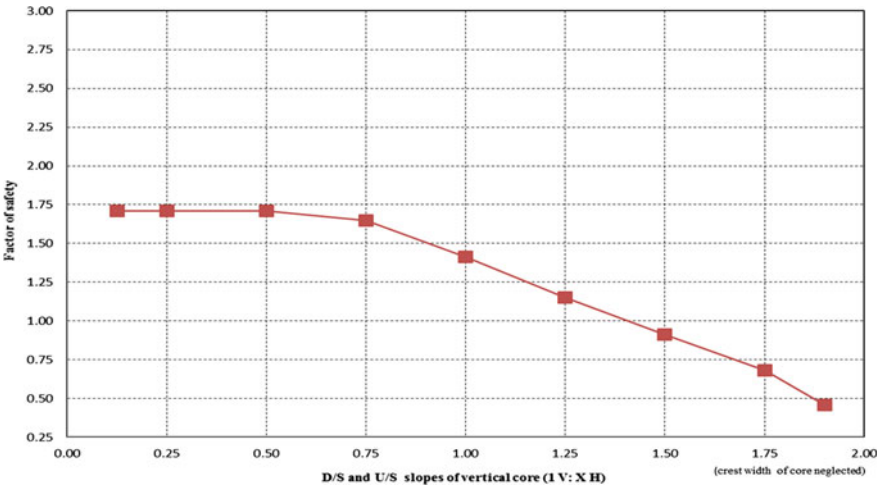

Fig. 4 Influence of vertical core thickness under Steady-State Seepage on stability of downstream slope for 180 m high vertical core earth and rockfill dam for base case ($\phi'_{shell} = 42°$, $\phi'_{core} = 24°$, $c'_{core} = 0$ kPa)

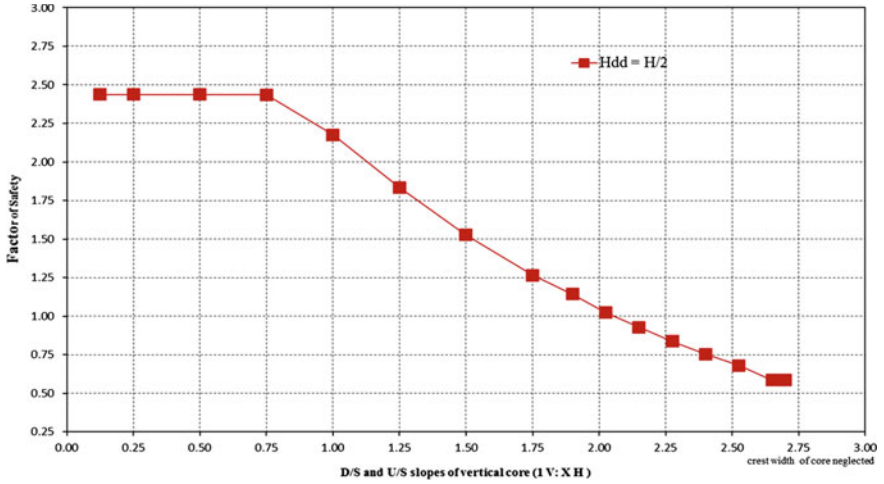

Fig. 5 Influence of vertical core thickness under Rapid Draw-Down on stability of upstream slope for 180 m high vertical core earth and rockfill dam for base case ($\phi'_{shell} = 42°$, $\phi'_{core} = 24°$, $c'_{core} = 0$ kPa)

H (150% thickness of core at bottom), there is no change in factor of safety because failure surface passes through the shell. Beyond U/s and D/s of core slope of 1 V: 0.75 H, the factor of safety begins to decrease as the failure surface passes through the core. The minimum factor of safety is obtained when the U/s slope of the core

merges with the outer slope of the core. The factor of safety is close to $\tan\phi/\tan\beta$ (γ_b/γ_t) which is valid for flow parallel to outer slope in infinite slope.

6 Discussions

It is observed for downstream slope of dam under steady-state seepage condition there is no change in factor of safety as long as the D/s and U/s slopes of vertical core is from 1 V: 0.125 H to 1 V: 0.50 H (100% thickness of core at bottom) because slip surface passes through the shell (highly pervious) and there is not any development of pore water pressure in shell material. Beyond U/s and D/s of core slope of 1 V: 0.50 H, the factor of safety decreases because the slip surface passes through the core and thus there is development of pore water pressure. As the thickness of core increases further, magnitude of flow lines increases towards downstream slope of dam and thus further decreases the factor of safety till the D/s and U/s slopes of vertical core merges with the outer slopes of dam. In a similar manner for upstream slope of dam under Rapid Draw-Down condition, as long as the core thickness is such that the vertical core of slope is steeper than 1 V: 0.75 H, there is no influence of core on stability of upstream slope of dam because the slip surface passes through the shell (highly pervious). Beyond this, the slip surface passes through the core because of that there is development of pore water pressure and thus factor of safety decreases. As the thickness of core increases further, magnitude of flow lines in reverse direction, i.e., towards upstream slope increases and factor of safety continue to decrease till upstream slope of core merges with the upstream slope of dam.

7 Conclusions

Factor of safety under steady-state seepage and rapid draw-down condition depends upon the magnitude and direction of flow lines. Also, after a critical thickness of core when slip circle passes through the core, the factor of safety decreases and continue to decrease till the U/s slope and D/s slope of core merges with the U/s slope and D/s slope of dam.

References

1. Datta, M.: Design of Beas dam embankment. Int. Water Power Dam Constr. J. Lond. **31** (6), 58–63 (1979)
2. Datta, M., Gulhati, S.K.: The influence of core thickness and inclination on stability of dams. In: Proceedings of the 9th Asian Regional Conference on Soil Mechanics and Foundation Engineering, Bankok, Thiland, vol. 1, pp. 227–234 (1991)

3. Datta, M., Kumar, M., Tankha, A.: The effect of core size and position on the slope stability of zoned embankment dams. Ground Eng. J. **27**(9), 29–33 (1994)
4. Gulati, S.K., Datta, M.: Geotechnical Engineering. Tata McGraw- Hill, New Delhi (2005)
5. Khanna, R. et al.: End-of-construction stability of earth and rockfill dams having vertical core. In: Indian Geotechnical Conference, Kakinada, India (2014)
6. Khanna, R., et al.: Influence of thin core on stability of upstream slope of earth and rockfill dams. Electron. J. Geotech. Eng. Bundle U **2014**, 6293–6305 (2014)
7. Khanna, R., et al.: Influence of thickness of vertical core on slope stability of earth and rockfill dams. J. Dams Reserv. **24**(4), 152–167 (2015)
8. Khanna, R. et al.: Influence of core thickness on stability of upstream slope of earth and rockfill dams under rapid-draw-down. In: Indian Geotechnical Conference, Pune, India (2015)
9. Khanna, R. et al.: Influence of core thickness on stability of downstream slope of earth and rockfill dams under steady-state-seepage. In: 19th Southeast Asian Geotechnical Conference and 2nd AGSSEA Conference (19SEAGC & 2AGSSEA). Kuala Lumpur (2016).
10. Khanna, R. et al.: Influence of core thickness on stability of downstream slope of earth and rockfill dams under steady-state-seepage. Int. J. Geotech Eng. (2017)
11. Kutzner, C.: Earth and Rockfill Dams. Oxford and IBH Publishing, New Delhi (1997)
12. Rocscience.: SLIDE 5.0. Manual of SLIDE 5, 2D limit equilibrium slope stability analysis (2006)
13. Sherard, J.L., et al.: Earth and Rockfill Dams. Willy, New York (1963)
14. Singh, B., Varshney, S.R.: Engineering for Embankment Dams. Oxford and IBH Publishing Company, New Delhi. (1995).
15. Singh, B., Sharma, H.D.: Earth and Rockfill Dams. Sarita Parkashan, Meerut (2004)

Numerical Analysis of Ring Foundation Fixed with Geogrid

Rahul P. Shende, Dipendra C. Swarnkar, and A. K. Singh

1 Introduction

The foundation of the top-heavy tower-like structure and self-supporting vertical cantilever structures like a chimney, silos, overhead water tank, telecommunication tower, etc. are usually axisymmetric. The foundation of these structures is frequently subjected to vertical load along with overturning moments caused due to lateral loads (wind). For such structures, a ring foundation is used due to economic advantages. Ring footing varies from a narrow circular beam to a circular footing. The central radius (R_c) is the radius that divides the ring surface into two equal areas. The ring radii ratio is the ratio of inner ring radius to outer ring radius, i.e., $n = R_i/R_o$ and the performance of ring foundation depends on the n value.

Geosynthetic material holds a number of functions like separation, filtration, reinforcement, stiffening, confinement sealing, lateral drainage, and barrier. Geogrid is generally used with earth, soil, rock, and different peripheral substance as reinforcement. Geogrid has openings ranges from 10 to 100 mm in size and has relatively extended power, improved modulus, and low rupture potential. Geogrid is a geosynthetic material that can be used as tensile reinforcement.

In this study, the three-dimensional finite-element method is used to know the responses of ring foundation fixed with geogrid. Many researchers investigated the ring foundation in the past and some of them utilized specific three-dimensional finite-element models. Textbooks and design manuals suggest different approaches to analyze and design the ring foundation. Compared to strip and circular footings, only limited studies are available that deal exclusively with ring footings. Bowels [2] has given FEM model for ring foundation that is divided into 20 nodal elements.

R. P. Shende (✉) · D. C. Swarnkar · A. K. Singh
NIT Jamshedpur, Jamshedpur, India

A. K. Singh
e-mail: aksingh.civil@nitjsr.ac.in

C. N. V. Satyanarayana Reddy et al. (eds.), *Dynamics of Soil and Modelling of Geotechnical Problems*, Lecture Notes in Civil Engineering 186,
https://doi.org/10.1007/978-981-16-5605-7_11

Winterkorn and Fang [12] have given the solution of ring foundation resting on an elastic foundation using the finite differences method. IS: 11,089 [5] has given empirical formula for the determination of radial moment and tangential moment under different loading conditions. Timoshenko and Krieger [11] have given the relationship between the different cases of axisymmetric loading on circular as well as ring plate with the vertical direction. Benmebarak et al. [3] calculated values of bearing capacity factors N_γ of soil in case of rough and smooth ring footings, for values of high and low friction angle for associated as well as non-associated soils of Mohr–Coulomb type. Kumar and Chakrobarty [6] analyzed bearing capacity factors by the usage of finite-element analysis. The effect of foundation embedment, rigidity, and soil non-homogeneity on the elastic vertical settlement of a ring foundation was evaluated by Naseri and Hosseininia [8] using the FDM technique. Hosseinimia [4] investigated the bearing capacity of ring footings by numerical simulations applying the FDM. Sharma and Kumar [9] studied the behavior of ring footing resting on reinforced sand influenced by eccentric-inclined loading. Azzawi and Daud [1] have done a numerical analysis of ring foundation for different loading conditions. In addition to the analytical and numerical solutions, some experimental investigation has been also carried out on ring foundations. Laman and Yildiz [7] investigated the behavior of ring foundation above sand bed with geogrid as reinforcement. Sawwaf and Nazir [10] investigated the behavior of ring footings loaded eccentrically which rests on geogrid reinforced compacted layered sand on a loose extended sand layer. Most of the studies conducted on ring foundations focused on the behavior of ring foundation on reinforced soil and bearing capacity factors. No one has tried to found out the behavior of ring foundation by fixing geogrid with the circumference of ring foundation.

In this study, the behavior of ring foundation fixed with geogrid at outer circumference and ring foundation without geogrid has been investigated. The behavior of ring foundation is also investigated by changing parameters like n value, sub-grade reaction, central radius, and number of loaded columns. Simulations are performed by ANSYS software for a ring foundation with and without geogrid.

2 Application of Numerical Method

2.1 Problem Description

Wind acting on the body of tall structures creates an overturning moment on the ring foundation which tries to topple the structure. From the design point of view, the overturning moment plays a vital role in the design of the ring foundation. In order to counterbalance the effect of lateral load on ring foundation, research has been carried out.

To reduce the effect of lateral forces, geogrid is fixed on the circumference of the ring foundation and it is spread in the lateral direction. Geogrid is fixed at the middle of the thickness of ring footing. One end of geogrid is fixed with ring footing and the other end is taken as fixed in the model to utilize the tensile strength of geogrid. The concept behind this is that the geogrid will create an anchorage against the overturning force. The geogrid is attached at 90° and 45° and the result is compared with ring foundation without geogrid. The behavior of the ring foundation is investigated by changing parameters such as sub-grade reaction, n value (Ri/Ro ratio), number of loaded columns (N_C), and central radius of ring foundation. The analysis has been carried out using ANSYS software. In this study, static structural analysis is performed that works on Newton–Rapson approximation method.

2.2 Geometry and Model Creation

Ring Foundation Model

Ring foundation model is created in ANSYS design modular. The ring is divided into 20 segments/parts as in Winterkorn and Fang [12] approach. A total of 20 points are made on the central radius spaced at an equal distance. The values of deflections are considered on these 20 points. The load is applied on four columns on a central radius equally spaced. In this study, three n values 0.2, 0.3, and 0.4 have been considered. Ring foundation of outer diameter 300 and 400 mm has been considered. The thickness of the ring foundation is kept at 70 mm.

Soil and Geogrid Model

Soil is modeled in a steel test box on which the ring foundation rests. The cross-section of the soil box is taken as 2 m × 2 m, keeping at least a distance of five times the ring diameter. The depth of soil is taken as 1.0 m below ring foundation and 33 mm above the base of the ring foundation.

Geogrid is placed on the surface of the soil model. The geogrid is fixed at 45° and 90°. The width of the geogrid modeled is 100 mm and thickness is taken as 4.0 mm. The length of geogrid is kept at 800 mm (greater than 2.5 times of ring diameter). The length is kept equal in all directions.

2.3 Finite-Element Mesh, Boundary Condition, and Contacts

In numerical modeling, the selection of boundary conditions plays an important role. The bottom boundary of soil is considered to be fixed, and all side boundaries can only move vertically (vertical displacement). The Z–X plane's displacement is restricted in the y-axis in the lateral direction. Likewise, in the Z–Y plane displacement is restricted in the x-axis in the lateral direction. One end of geogrid is connected with

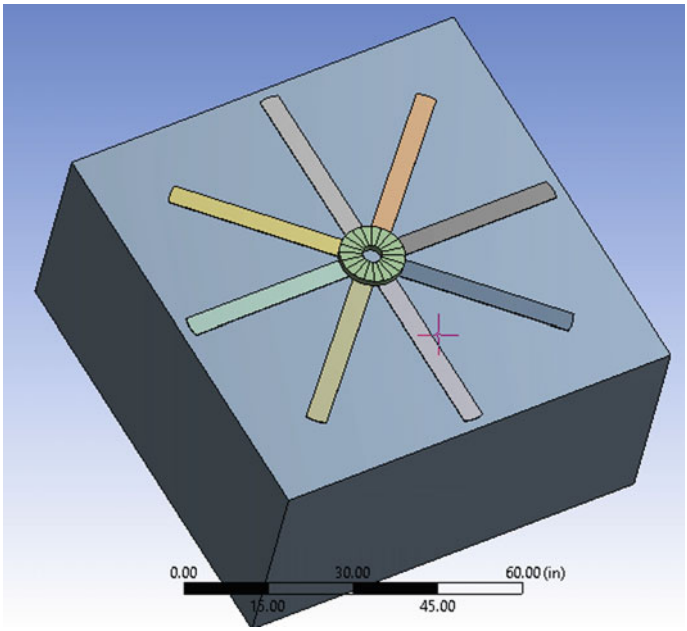

Fig. 1 Ring foundation resting on cohesion-less soil fixed with geogrid at 45°

the ring foundation and the other end is fixed and restricted from all displacements. The top surface of the soil is assigned as elastic support with a sub-grade reaction value of 86.4 kcf (13,573 kN/m^3).

The contact is provided between interfaces of two surfaces in ANSYS software. By default, ANSYS select bounded contact. The contact provided between ring foundation and soil is rough contact. The contact provided between ring foundation and geogrid is bounded contact with beam formulation. Frictionless contact is provided between geogrid and soil.

For instance, default meshes were specified for the model in numerical analysis. In cases where the stress and displacement are higher, a refined mesh was used around the loaded points (i.e., finer meshes under loads). Figure 1 shows the geometry of ring foundation resting on cohesion-less soil fixed with geogrid at 45°.

2.4 Properties of Material

The material used for the ring foundation model is concrete with a modulus of elasticity of 20,684 MPa. Tables 1 and 2 show the properties of the soil and the geogrid used in the finite-element models.

Table 1 Parameters used for the soil

S. no.	Properties	Value
1	Type	Mohr–Coulomb
2	Modulus of elasticity (MPa)	43
3	Friction angle (degree)	40°
4	Density (kg/m^3)	1600
5	Poisson's ratio	0.35
6	Dilatancy angle	10°
7	Cohesion	0

Table 2 Parameters used for the geogrid

Sl. No	Properties	Value
1	Density (kg/m^3)	950
2	Modulus of elasticity (MPa)	2e5
3	Poisson's ratio	0.3
4	Tensile yield strength (MPa)	200
5	Tensile ultimate strength (MPa)	230

2.5 Loading

The load is applied on four columns on the central radius equally spaced. Stepwise incremental loading is provided to know load versus settlement characteristics. In case of overturning moment versus settlement, an overburden load of 10 kN is applied as a load of the structure and then the overturning moment is increased stepwise.

To know the effect of sub-grade reaction, the number of columns and central radius, ring foundation of size 300 mm, and ring radii ratio n = 0.3 are used, and a total load of 50 kN is applied on four columns at equal spacing on central radius. The settlement on 20 segments on central radius is found and maximum settlement among them is considered.

3 Results and Discussion

3.1 Numerical Analysis of Ring Foundation Fixed with Geogrid

Effect of geogrid

The ring foundation with 300 mm outer diameter and n value 0.3 are used. The geogrid is attached at 45° and 90°. The comparison is carried out between ring foundations without geogrid and fixed with geogrid at 45° and 90°and shown in Figs. 2 and 3.

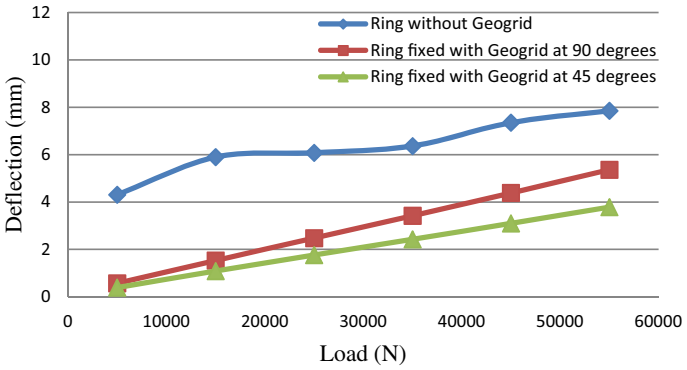

Fig. 2 Load versus deflection for ring foundation

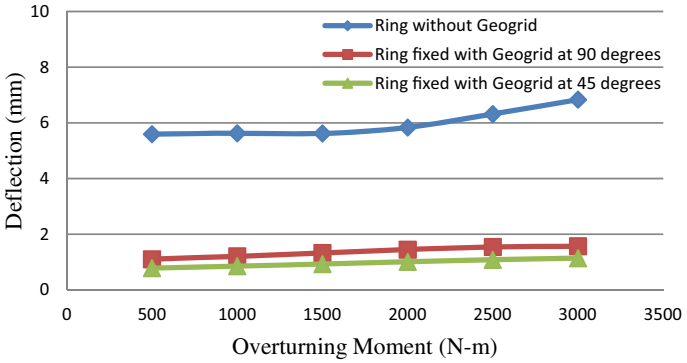

Fig. 3 Overturning moment versus deflection for ring foundation

From Figs. 2 and 3, it is observed that if geogrid is fixed with ring foundation, the load-carrying capacity and overturning moment resisting capacity increases, and as the amount of geogrid (90–45°) is increased, it will further increase.

Optimization of Ring Foundation

The ring foundation of the larger diameter without geogrid is compared with the ring foundation fixed with geogrid of smaller diameter. For comparison, 400 mm size ring foundation and 300 mm size ring foundation of the same ring radii ratio and thickness are considered. The 300 mm ring foundation is fixed with geogrid at 90°.

For the same loading, deflection in 400 mm ring foundation without geogrid is more than 300 mm ring foundation fixed with geogrid, as shown in Figs. 4 and 5. The load-carrying capacity and overturning moment resisting capacity in 300 mm ring foundation with geogrid is more than 400 mm ring foundation without geogrid. Hence, in this way, the optimization of the ring foundation is done.

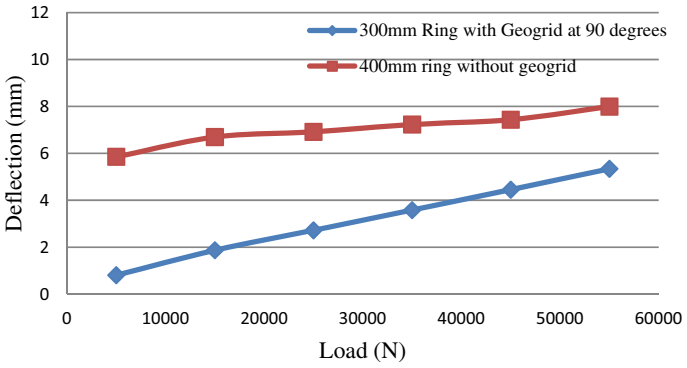

Fig. 4 Load versus deflection for the optimization of ring foundation

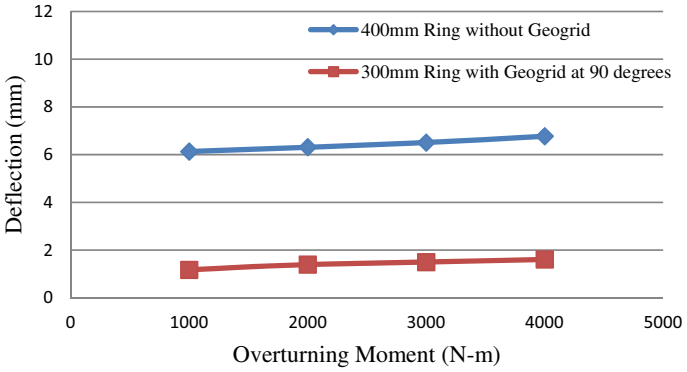

Fig. 5 Overturning moment versus deflection for the optimization of ring foundation

3.2 Numerical Analysis Ring Foundation with Different Parameters

Effect of n Value

The ring foundation of 300 mm outer diameter is used with changing n values of 0.2, 0.3, and 0.4 and presented in Figs. 6 and 7. From these figures, it is observed that with the increase in n value, the load-carrying and overturning moment resisting capacity decreases.

Effect of Sub-grade Reaction

Stepwise increment of sub-grade reaction is applied and maximum deflection is considered. From Fig. 8, it can be concluded that when the sub-grade reaction increases the settlement of ring foundation decreases.

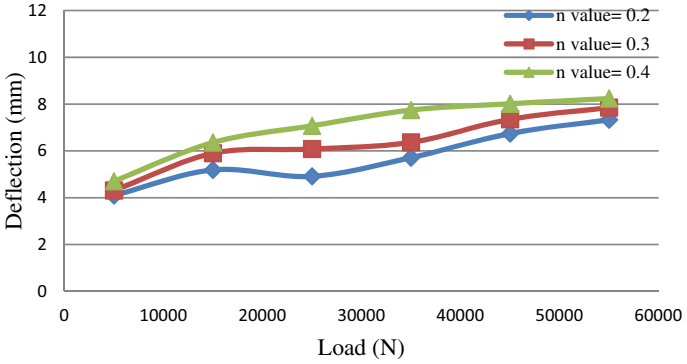

Fig. 6 Load versus deflection for the effect of n value

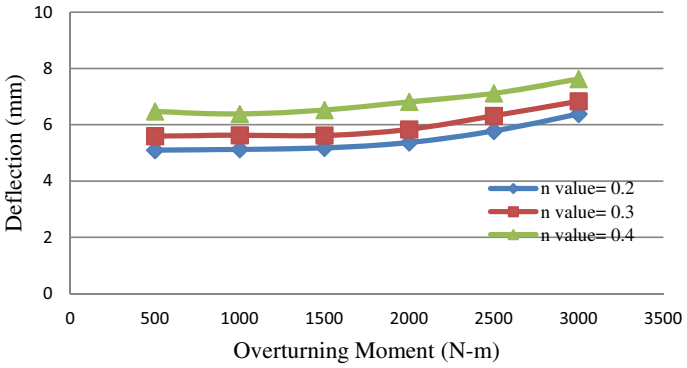

Fig. 7 Overturning moment versus deflection for the effect of n value

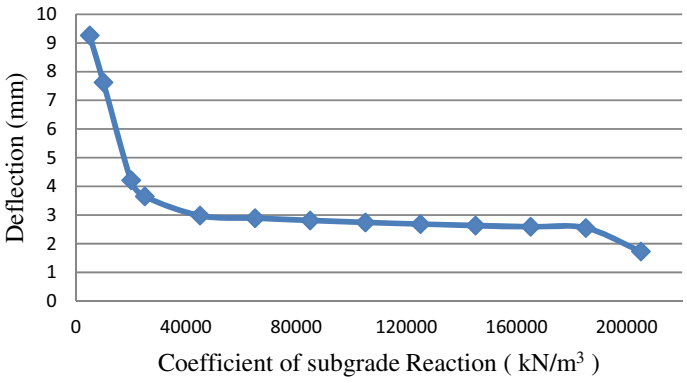

Fig. 8 Coefficient of sub-grade reaction versus deflection

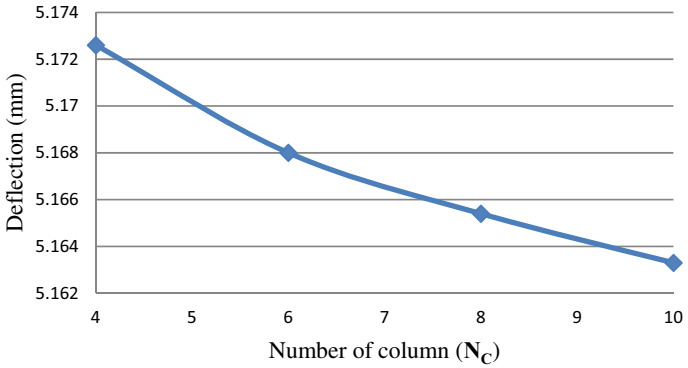

Fig. 9 Number of column versus deflection

Effect of Number of Columns

The number of loaded column (Nc) has an effect on deflection behavior and also on tangential and radial moments. The load is applied on 4, 6, 8, and 10 numbers of columns, respectively, which are located on a central radius equally spaced. Deflection versus Nc is shown in Fig. 9. From Fig. 9, it is evident that when the N_C is increased, the deflection is decreased. Deflection is rapidly decreased when the number of columns increased from 4 to 6 and 8 and after that decreases slowly. It means deflection decreases when concentrated load moves toward a uniform load.

Effect of Central Radius

The effect of central radius on ring foundation is studied in this case. Here the ring radii ratio is kept at 0.3 (constant). The inner radius is increased in a stepped manner and accordingly the outer radius is changed. For changed conditions, the central radius is calculated.

From Fig. 10, it can be recognized that as the central radius increased keeping all other parameters constant, the deflection is reducing.

4 Conclusions

1. It is found that settlement in the ring foundation without geogrid is significantly more than settlement in the ring foundation with geogrid fixed with ring foundation. Settlement is reduced if eight numbers of the geogrid strip are fixed at 45° as compared to the settlement when four numbers of the geogrid strip are fixed at 90°.
2. Overturning moment-resisting capacity of ring foundation fixed with geogrid has high value than without geogrid. It is also concluded that the overturning resistance increases if the number of geogrid strip increases.

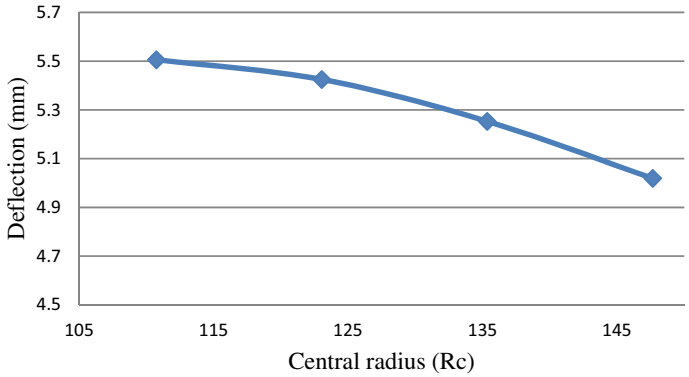

Fig. 10 Central radius versus deflection

3. The size of the ring foundation can be optimized and the material can be saved if the ring foundation of small diameter (300 mm) is fixed with geogrid at 90° or 45° as compared to a large diameter (400 mm) without geogrid.
4. As the n value increases, the load-carrying capacity along with overturning moment-resisting capacity decreases.
5. As the value of the sub-grade reaction of soil increases, the settlement of the ring foundation decreases.
6. Settlement decreases if the number of loaded column (N_C) increases.
7. Settlement of the ring foundation decreases as the central radius increases keeping constant load.

References

1. Azzawi, A., Daud, K.: Numerical analysis of thin ring foundations under different loading conditions. In: International Conference on Civil and Environmental Engineering Technologies (2019)
2. Bowles, J.E.: Foundation analysis and design, 5th International edition. Tata Macgraw-Hill, New Delhi (1996)
3. Benmebarek, S., Remadna, M.S., Benmebarek, N., Belounar, L.: Numerical evaluation of bearing capacity factor Nγ of ring footings. Comput. Geotech. **44**, 132–138 (2012)
4. Hosseinimia, S.: Bearing capacity factors of ring footings. IJST (2016)
5. IS: 11089: Code of practice for design and construction of ring foundation, Part 1, Reaffirmed 2008 (1984)
6. Kumar, J., Chakrobarty, M.: Bearing capacity factors for ring foundations. ASCE (2015)
7. Laman, M., Yildiz, A.: Model studies of ring foundations on geogrid-reinforced sand. Geosynt. Int. **10**, 142–152 (2003)
8. Naseri, M., Hosseininia, E.: Elastic settlement of ring foundations. J. Soils Found. **2**(55), 284–295 (2015)
9. Sharma, V., Kumar, A.: Numerical study of ring and circular foundations resting on fibre-reinforced soil. IJGE (2018)

10. Sawwaf, M.E.I., Nazir, A.: Behaviour of eccentrically loaded small-scale ring footings resting on reinforced layered soil. ASCE **138**(1), 376–384 (2012)
11. Timoshenko, S.P., Woinowsky, K.S.: Theory of Plates and Shells, 2nd ed. McGraw- Hill, Newyork (1959)
12. Winterkorn, H.F., Fang, Y.H.: Foundation Engineering Handbook, 1st edn. Galgotia Book-source, India (1970)

Numerical Analysis of Bearing Capacity and Settlement Reduction of Bamboo Reinforced Sand Beds

M. Ajesh Sankar, K. S. Akhil, N. Sankar, and S. Chandrakaran

1 Introduction

1.1 Bamboo-Reinforced Soils

Rapid population growth and industrialization demand more and more ideal land to meet the demand. This results in an acute shortage of ideal land for construction. So, the development in the soft ground has almost become unavoidable for civil engineers. In such cases, the soil needs to be improved to increase its mass density and thus the shear strength and bearing capacity. Soil reinforcement techniques have been used to improve the bearing capacity of foundation soil.

Reinforcing soil with locally available materials is quite common and cost-effective. The use of sustainable and naturally accessible substances as reinforcing materials has become popular nowadays. Bamboo is one of the most abundantly available natural materials for reinforcing soil because of its excellent mechanical and engineering properties. Several researchers reported [1–5] that the use of bamboo-reinforced soil bed gave improved results in bearing capacity and settlement reduction compared with soil without any reinforcements. Small-scale laboratory model experiments on soil reinforced with bamboo coated with bitumen yielded about 24% of settlement reduction [3]. The green or dry state of bamboo requires different preservation techniques to be adopted [2]. Steeping, diffusion and sap displacement are the commonly adopted methods for treating bamboo obtained in a fresh condition.

M. Ajesh Sankar (✉) · K. S. Akhil · N. Sankar · S. Chandrakaran
Department of Civil Engineering, NIT Calicut, Kerala 673601, India

N. Sankar
e-mail: sankar@nitc.ac.in

S. Chandrakaran
e-mail: chandra@nitc.ac.in

C. N. V. Satyanarayana Reddy et al. (eds.), *Dynamics of Soil and Modelling of Geotechnical Problems*, Lecture Notes in Civil Engineering 186,
https://doi.org/10.1007/978-981-16-5605-7_12

Soaking, pressure impregnation, hot and cold processes, etc. are used to treat dry bamboo. In soaking, the air-dried bamboo grids are immersed in the preservative solution (copper-chrome-arsenic) for a certain period. The chemical composition test was carried out to ascertain the effectiveness of the preservation method adopted [2]. They reported that the treatment of bamboo reduces the tensile strength by 15%. However, the tensile strength is more for treated bamboo than geotextiles and geogrids. The surface roughness was found reduced to 20% by treatment. Boucherie–Mourisco principle includes a preservative solution of borax with water into bamboo with air pressure [4].

Several researchers [6–8] reported that to simulate the behaviour of foundation soil, the "Mohr–Coulomb model" is the most appropriate model since it assumes the soil as elastoplastic. The Mohr–Coulomb model requires five parameters, namely Young's modulus (E), Poisson's ratio (υ), cohesion (C), angle of friction (φ) and angle of dilatancy (ψ). Young's modulus and Poisson's ratio present the elastic behaviour of soil. Cohesion and angle of internal friction define the failure criteria. The angle of dilatancy describes the flow rule. Gamal et al. [8] studied the effect of first geogrid reinforcement depth, the spacing between the reinforcement and its extension relative to the footing length on the mobilized bearing capacity. The laboratory results were simulated, and the results were validated using the commercial finite element package (PLAXIS v8.2). The authors reported the comparison between experimental and model studies through bearing capacity ratio (BCR).

Akhil et al. [1] conducted an experimental study to understand the performance of sand beds reinforced with bamboo mats in improving the bearing capacity and settlement characteristics. They reported that when the number of layers was increased, bearing capacity and settlement reduction were also increased. In the present investigation, an attempt has been made to simulate the bamboo mat reinforced soil foundation numerically.

2 Numerical Modelling

Numerical modelling technics are powerful tools that have been used to study the behaviour of various structures under a variety of loading conditions. Numerical models are particularly useful in situations where the prototype is huge to be tested in the laboratory.

Plate load tests were conducted to study the effect of bamboo reinforcements on sand beds, and the properties of the sand bed are shown in Fig. 1.

Test tank of 750 mm × 750 mm × 750 mm size and steel plate of thickness 25 mm representing the model footing was used. The same dimensions and experimental setup were used for the modelling. However, because of the symmetry and to reduce the computation time and effort, only a quarter portion of the test tank was modelled. The soil was modelled as elastoplastic Mohr–Coulomb model and the reinforcement

Property	Value
Effective size (D_{10})	0.265
D_{30}	0.46
D_{60}	0.70
Coefficient of uniformity (C_u)	2.66
Coefficient of curvature (C_c)	1.13
Specific gravity, G	2.65
Maximum dry density, kN/m^3	16.3
Minimum dry density, kN/m^3	14.4
Angle of internal friction (ϕ) at relative density of 60%, degrees	39.5
Classification of soil as per Unified Soil Classification System (USCS)	SP (Poorly graded sand)

Fig. 1 Basic properties of sand bed (after Akhil et al. [1])

as a linear-elastic model. The boundary conditions were fixed such that the horizontal boundaries which represent the vertical walls of the test tank were restrained in the horizontal direction while the bottom boundary was restrained in both vertical and horizontal directions. Table 1 shows the soil properties assigned in the material data set of PLAXIS 2D.

The shear strength parameters (C and φ) calculated by direct shear test and reported by Akhil et al. [1] were used in the present study. Young's modulus of sand bed modelled was directly taken from the load–settlement response of the plate load test conducted on unreinforced sand beds. Latha and Somwanshy [9] and Makkar et al. [7] also used the same procedure to determine the elastic modulus of sand. Ghazavi and Lavason [10] showed that the best results of the numerical analysis were achieved when the angle of dilatancy (ψ) was considered as two-thirds (2/3) of

Table 1 Soil properties for modelling

Material	Symbol	Assigned value
Material model	–	Mohr–Coulomb
Drainage type	–	Drained
Unsaturated unit weight	$\gamma_{unsat,}$	15.44 kN/m^3
Saturated unit weight	γ_{sat}	19.42 kN/m^3
Young's modulus	E	3500 kPa
Poisson's ratio	υ	0.3
Cohesion	C	1 kPa
Angle of internal friction	Φ	39.5^0
Dilation angle	Ψ	28^0

the angle of internal friction (φ). A typical value for the angle of dilatancy for dense sand is 15°. The value of ψ used in this study is 28°.

Tensile tests on bamboo strips were conducted by several researchers [1, 2], which showed that the tensile strength of bamboo was about nine times more than that of the geogrid and geocell materials [2]. A mean value of 205 MPa as the tensile strength and a mean secant modulus of 6350 MPa [1] were used to determine the axial stiffness of the reinforcement material for numerical modelling.

Depth to the first reinforcement layer was kept as 0.3 times the width of the footing, the width of the bamboo mat was kept three times the width of the footing, and the subsequent layers were kept at 0.3 times the width of the footing each. All these parameters were reported as optimum parameters for reinforcement placing in the referred journal paper [1].

A uniformly distributed load was applied on top of the footing. As mentioned earlier, the horizontal and vertical boundaries were fixed.

A non-dimensional parameter was introduced to evaluate the degree of improvement of bearing capacity.

$$IF = \frac{BC}{BCu} \tag{1}$$

where IF = improvement factor
BC = bearing capacity of bamboo reinforced sand
BCu = bearing capacity of unreinforced sand

3 Results and Discussions

The load–settlement curve obtained from numerical modelling of unreinforced sand is shown in Fig. 2. A maximum bearing pressure of 361.1 kPa and a maximum settlement of 40.87 mm were obtained.

With the increase in the number of layers, the applied pressure is distributed over a more significant depth, thereby contributing to higher bearing capacity and settlement reduction. The trend observed in the current study is shown in Fig. 3. When the number of layers increases the bearing capacity also increases. Beyond a certain depth, the inclusion of reinforcements has no significant effects on bearing capacity. When N = 4 and N = 5 the load–settlement curves are almost the same. Considering the economic aspects, three layers of reinforcement are sufficient for optimum performance. Figure 4 shows the improvement achieved for the different number of layers.

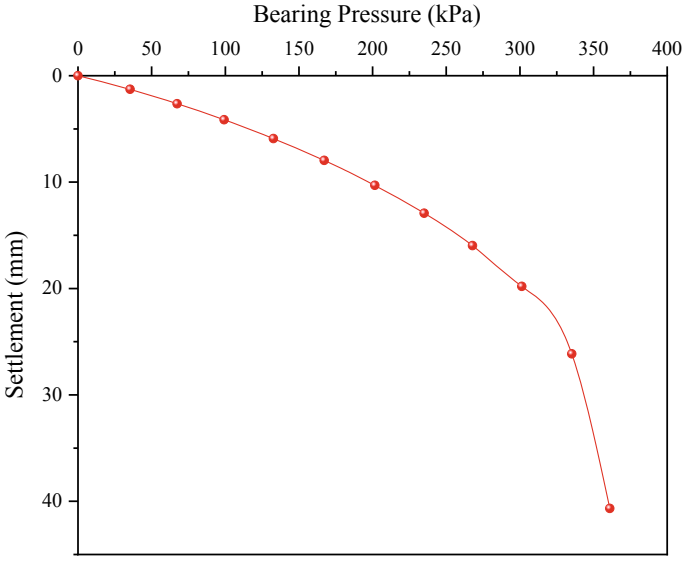

Fig. 2 Load–settlement curve for unreinforced sand

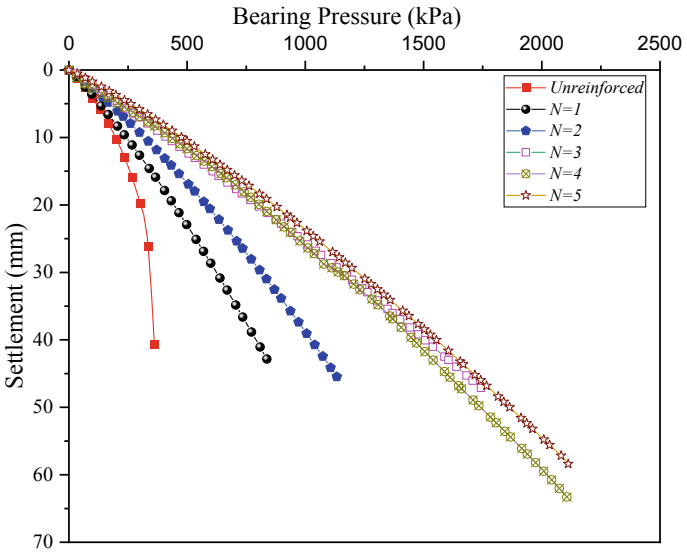

Fig. 3 Load–settlement curve for different number of layers

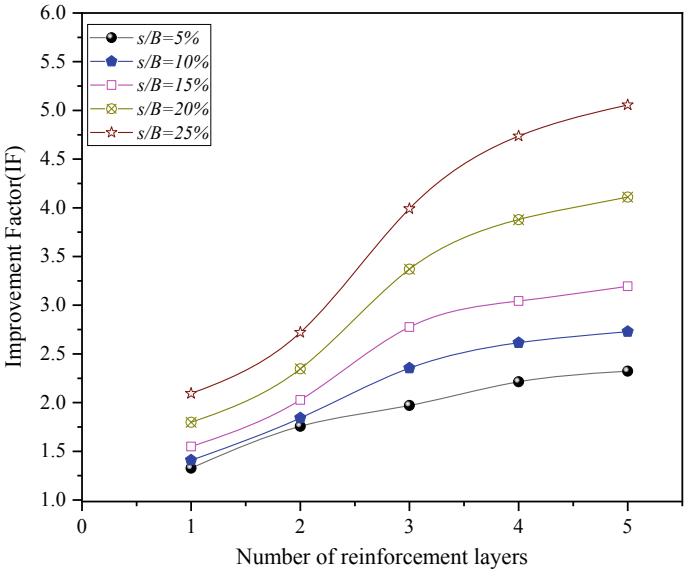

Fig. 4 Improvement factors for different number of layers of reinforcement

Figure 5 (a–e) shows the vertical displacement contours for different layers of bamboo reinforcement. It is observed that settlement is more for four number of layers compared with five number of layers. Considering the economic aspects, three layers of reinforcement are sufficient for optimum performance.

4 Conclusions

Numerical analyses were carried out to understand the behaviour of bamboo-mat-reinforced soil systems using PLAXIS 2D. From the numerical study, the following conclusions have been made:

1. Bearing capacity of the soil was increased when reinforced with bamboo grids of a rectangular pattern.
2. When the number of layers is more, the bearing capacity was also found to be more. There is no significant increase in bearing pressure from layer 4–5. So by considering the economic aspects we can say that optimum results were obtained at four layers of reinforcement.

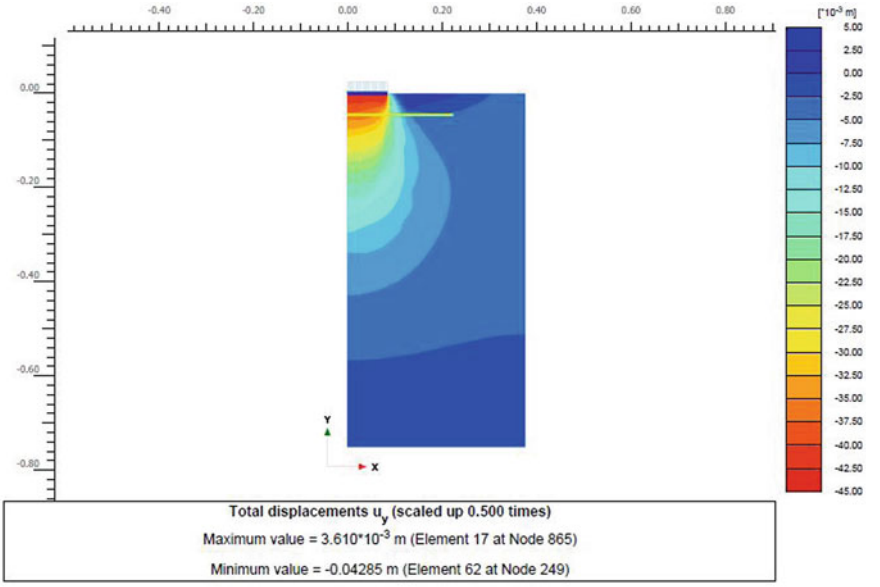

(a) N=1

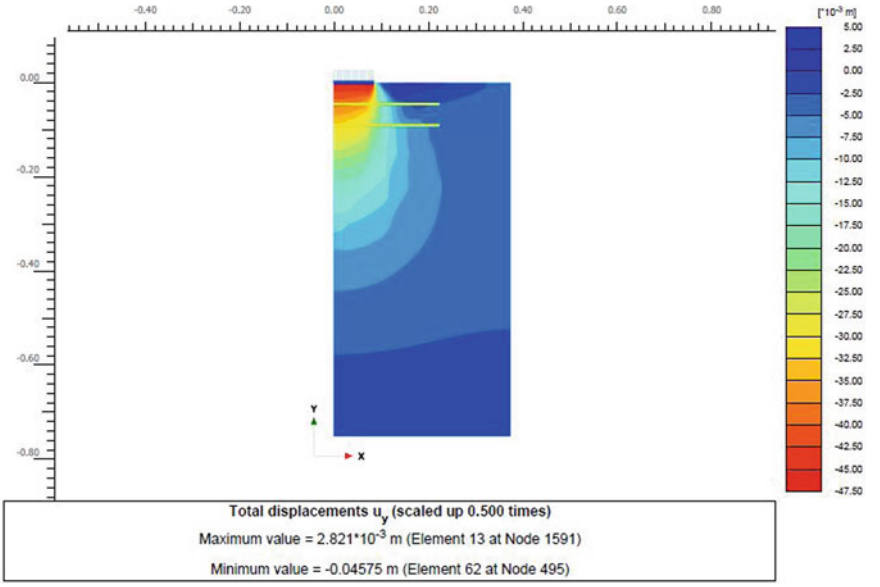

(b) N=2

Fig. 5 Vertical displacement contours for different layers of bamboo reinforcement

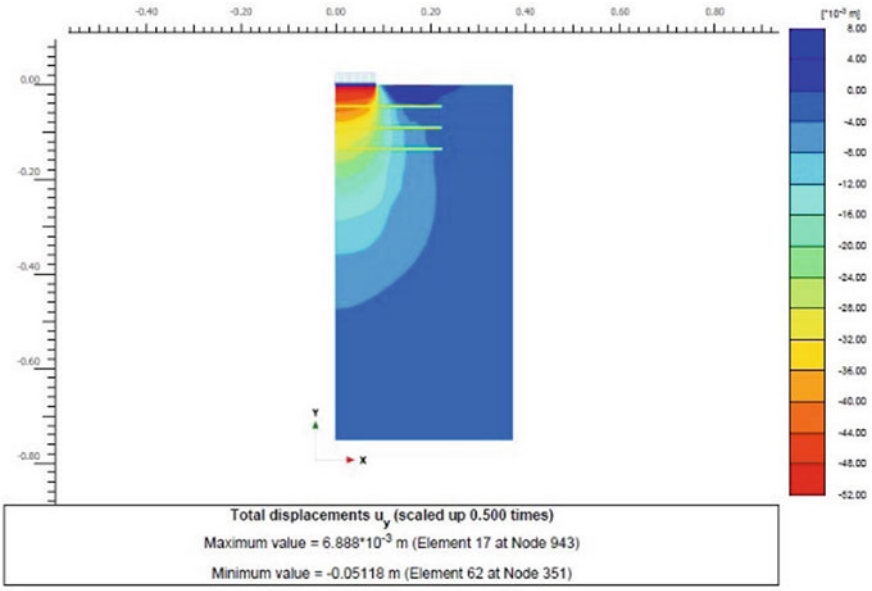

(c) N=3

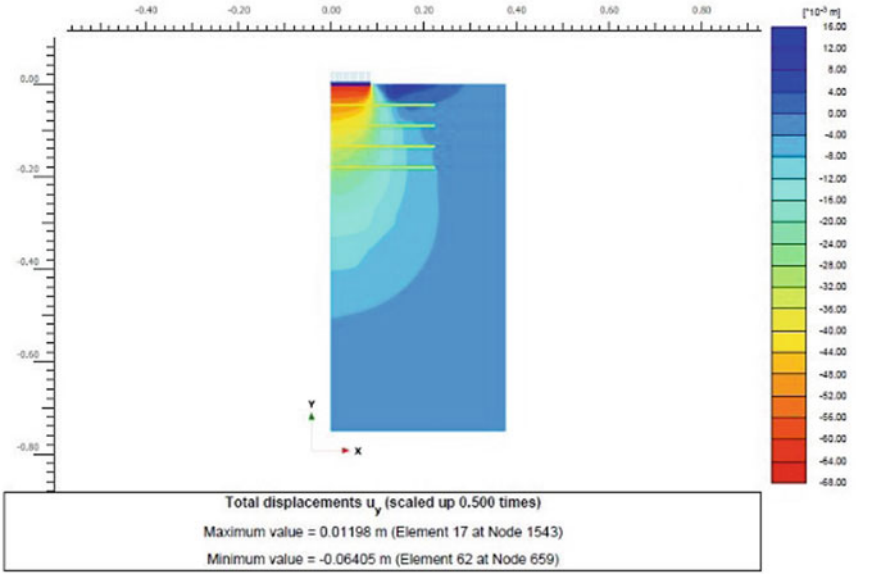

(d) N=4

Fig. 5 (continued)

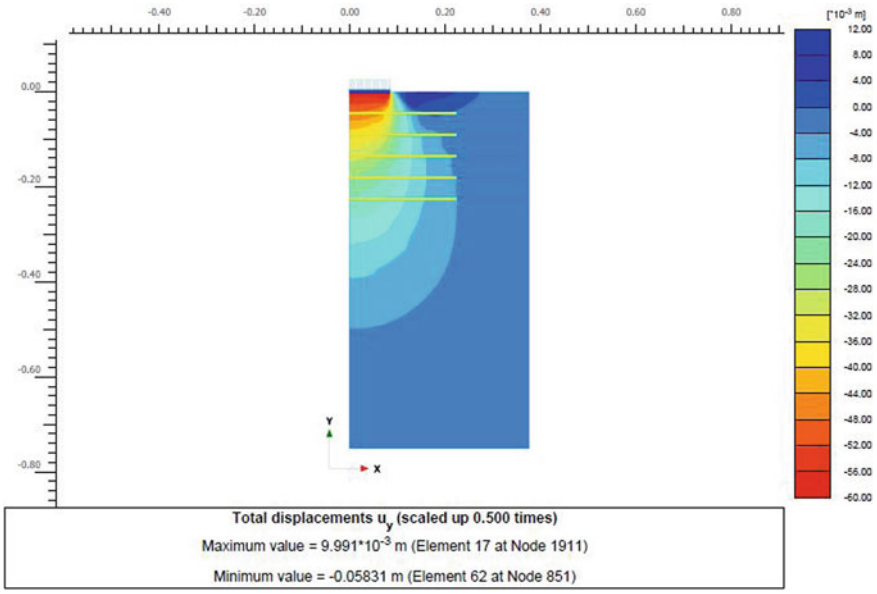

(e) N=5

Fig. 5 (continued)

References

1. Akhil, K.S., Sankar, N., Chandrakaran, S.: Behaviour of model footing on bamboo mat-reinforced sand beds. Soils Found. **59**, 1324–1335 (2019)
2. Hegde, A., Sitharam, T.G.: Three-dimensional numerical analysis of geocell-reinforced soft clay beds by considering the actual geometry of geocell pockets. Can. Geotech. J. **52**(9), 1396–1407 (2015)
3. Sara, C.S., Shyla, J.A.: Experimental investigation on soil reinforced with bitumen coated bamboo. Int. Res. J. Eng. Technol. **3**(9), 66–68 (2016)
4. Waruwu, A., Susanti, R.D.: Behavior of soil peat with reinforcement of bamboo grid. IOSR J. Eng. **5**(11), 29–36 (2015)
5. Asaduzzaman, Md., Islam M.I.: Soil improvement by using bamboo reinforcement. Am. J. Eng. Res. **B**(8), 362–368 (2014)
6. Balakumar, V., Huang, M., Erwin, O., Balasubramaniam, A.S.: Critical and comparative study on 2D and 3D analyses of raft and piled raft foundations. In: SEAGS 50th Anniversary Symposium Proceedings 14, pp 15–26 (2017)
7. Makkar, F. M., Sreya, M. V., Chandrakaran, S., Sankar, N.: 3-dimensional numerical modelling of sand bed reinforced with 3D geogrids of triangular form. Aust. Geomech. **54**(2), 99–110 (2019)
8. Gamal, A.M., Belal, A.M., Elsoud, S.A.: Numerical modeling of geogrid reinforced soil bed under strip footings using finite element analysis. Int. J. Civ. Environ. Eng. **10**(1), 37–38 (2016)
9. Latha, G.M., Somwanshi, A.: Bearing capacity of square footings on geosynthetic reinforced sand. Geotext. Geomembr. **27**(4), 281–294 (2009)
10. Ghazavi, M., Lavasan, A.M.: Interference effect of shallow foundations constructed on sand reinforced with geosynthetics. Geotext. Geomembr. **26**, 404–415 (2008)

Reliability Analysis of Settlement of a Foundation Resting Over a Circular Void

Kumar Shubham, Subhadeep Metya, and Gautam Bhattacharya

1 Introduction

The bearing capacity of the foundation soil is the main factor that affects the structural stability of any structure. The presence of any type of excavation or void underneath the foundation of a structure is one of the major factors that affect the stability and may cause extreme damage to the structure. The factors affecting the bearing capacity and settlement of foundation are soil properties, operational conditions, void size, location of the void, number of voids and depth of foundation. Due to rapid urbanization and growing population, the construction technology has evolved and shifted towards a new phase where underground buried conduits and utility tunnels have become popular for installing electricity cables, water supply pipes, wire communications, gas supply, etc., and the foundation of new construction may exist in the vicinity of the existing buried conduits or utility tunnel due to land scarcity issues. There are various geological studies that show that the presence of voids or cavities may be due to man-made activities (mining, construction of tunnels, aqueducts, conduits and underground water tanks) or natural activities (the dissolution of minerals salts, dolomite, gypsum etc., the formation of tension cracks and the presence of organic materials in the stratified soil). Thus, the existence of underground cavities for significant and immense structures affects the serviceability of the structure.

K. Shubham (✉) · S. Metya
Civil Engineering Department, NIT Jamshedpur, Jharkhand, India

K. Shubham
Arka Jain University, Jamshedpur, Jharkhand, India

G. Bhattacharya
Civil Engineering Department, IIEST, Shibpur, West Bengal, India

C. N. V. Satyanarayana Reddy et al. (eds.), *Dynamics of Soil and Modelling of Geotechnical Problems*, Lecture Notes in Civil Engineering 186,
https://doi.org/10.1007/978-981-16-5605-7_13

In recent years, there has been a development of interest among the researchers and also the increased dependability on the probabilistic approach or reliability analysis in the field of geotechnical engineering because geotechnical parameters are highly uncertain or random. Foundation stability analysis is one of the important areas where the recent trend is to determine the probability of failure instead of, or complementary to, the conventional methods based on determining the settlement. Many researchers have worked on developing a probabilistic model for the progressive failure of slopes [1, 7]. It has been found in some research that the stability of footing can be significantly affected when the void is located within the critical region under the footing using upper bound limit analysis [2, 10]. A calculation formula can also be used for estimating the critical conditions of foundation placed above the voids using 2D finite element analysis and then using the reliability techniques to analyze the data [4, 5, 9]. Construction of underground voids like tunnels inevitably induces varying degrees of ground movement towards the excavation resulting in ground surface settlement. This ground settlement is likely to affect adjacent buildings and leads to environmental hazards. Some methods have been developed to determine surface settlement and lining stresses induced by tunnelling based on field measurements [8]. Other than studies on green-field settlement prediction due to tunnelling and its control, there are several numerical studies, which investigated the effect of tunnelling on foundations. This paper shows an analysis of the effect of excavation below the shallow foundation on its stability and a reliability approach to study the same. Finite Element Analysis package PLAXIS 2D is used for the analysis of the performance of footing over a void under different boundary conditions.

2 Formulation

The most common empirical method is the Gaussian curve to predict ground movements. The Gaussian curve has been used for long to predict settlement in case of excavation under the foundation [8] as shown in Fig. 1. The ground loss (GL) and the standard deviation 'i' of the Gaussian curve are the two parameters that need to match with the surface settlement. The finite element method is used for analysing the bearing capacity and settlement of footing over the void using the data available in the literature. The design of experiments can be performed using full factorial design and then the trail sets are analyzed using the finite element method. A linear surface method is then used to analyze these sets of input and output parameters, which is further used to develop a limit state function and thus the reliability index is determined using the first-order reliability method. The first-order model with controlled input parameters x_1 and x_2 to get a simple response y using the response surface method is shown in Eq. (1).

$$y = \beta_0 + \beta_1 x_1 + \beta_2 x_2 + \beta_{12} x_1 x_2 + \in \tag{1}$$

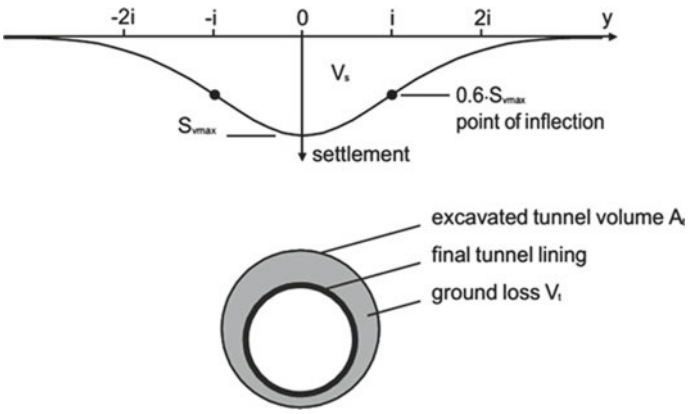

Fig. 1 Gaussian curve for settlement in the presence of void [6]

In the polynomial equation, ϵ represents error due to uncontrolled parameters and experimental error. The coefficients β_1 and β_2 are the main effects, while β_{12} is a two-way interaction effect. In an experiment, the coefficients β_0, β_1, β_2 and β_{12} were calculated accurately by changing x_1 and x_2 to get a response y. The load of a system is 'S' and resistance is 'R', these values are uncertain. These values have mean–variance and covariances. Margin of safety that represents the performance of the function is $M = R - S = 0$. The probability of failure is $P_f = P\,[(R - S) \leq 0]$.

Cording and Hansmire [3] defined the ground loss as the volume of soil that is displaced across the perimeter of a tunnel. It is often defined in terms of volume lost per unit length of the tunnel constructed. The percentage ground loss (GL) is defined as follows:

$$GL = \frac{\text{Vi}}{\text{Vo}} \times 100 \tag{2}$$

where Vi = trough volume, Vo = tunnel opening volume (p r2) and r = radius of the tunnel. Based on the shape of the normal distribution curve, Peck [8] showed that the maximum settlement $S_{v,\,max}$ can be given by

$$Sv, max = \frac{0.314 \times \text{GL} \times D^2}{\text{i}} \tag{3}$$

where 'D' = diameter of the tunnel and *Sv*, max = maximum settlement occurring above the tunnel axis. The settlement at various points of the trough is then given by,

$$Sv(y) = Svmax.exp.\left(\frac{-y^2}{2i^2}\right) \tag{4}$$

where 'y' = horizontal distance from the tunnel axis and 'i' = horizontal distance from the tunnel axis to the point of inflexion. Some researchers suggested that 1–2% of ground loss (GL) is usually found for stiff clay, 2–5% for soft clay and less than 1% for sandy soil [8]. It was also suggested that Gaussian distribution could be helpful to approximate subsurface settlement profiles [6].

3 Methodology

3.1 Materials, Structure and PLAXIS Model

The presence of voids under the foundation affects bearing capacity and settlement of footing. Many studies have been carried out to know the significant effect on the footing. Wang et al adopted three failure mechanisms to formulate equations for the collapse load of footing over the circular void. Figure 2 shows failure mechanisms considered by Wang and Hsieh [10] in which it was observed that the failure under the footing with the void is punching shear failure in which shear planes are confined to soil mass causing the collapse of soil into the void just below the footing.

The settlement analysis has been done by considering the effect of change in depth, the horizontal distance from the centre of the foundation and the loads. The same is modelled and simulated in PLAXIS 2D as shown in Fig. 3, and results are compared. In the present study, the foundation soil mass was represented by the finite number of discrete elements interconnected by nodal points, Triangular element with 15 nodes were used as soil element. In the later section, the footing was analyzed for different conditions. Figure 3 shows the geometrical model of footing and the values of the various associated parameters are mentioned in Table 1.

In this study, the depth of the shallow foundation (D_f) and width of the footing (B) have been considered as per the general construction practice as 2 m and 1.5 m, respectively. Then the load and the void position within the pressure bulb is varied.

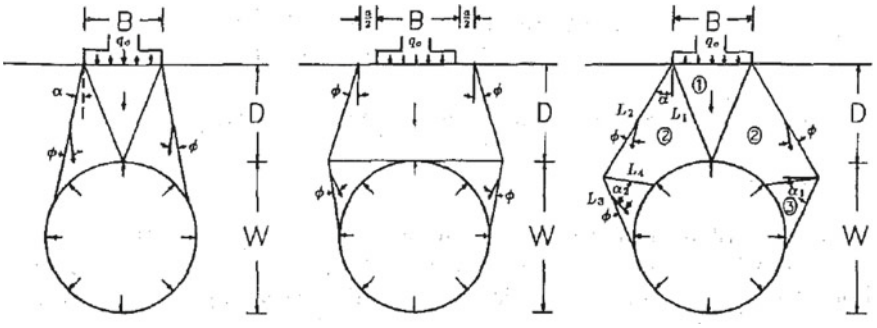

Fig. 2 Failure mechanism of footing collapse [10]

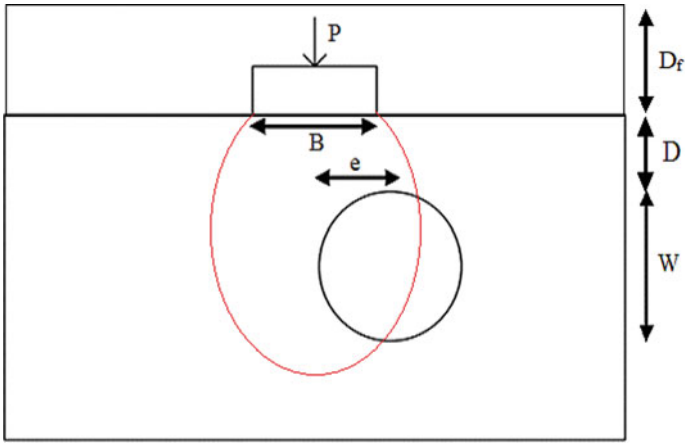

Fig. 3 Definition sketch of the model used in PLAXIS 2D

Table 1 Values of parameters used in the PLAXIS 2D model

Parameters	Description (Soil)	Description (Void lining)	Description (Concrete)
Material	Mohr–Coulomb	Linear elastic	Linear elastic
Material behaviour	Undrained	Non-porous	Non-porous
γ_{unsat}[kN/m^3]	16	22	24
E_{ref} [kN/m^2]	26,604,000	–	5000
c_{ref} [kN/m^2]	5	–	–
ν	0.35	0.15	0.2
ϕ[°]	20	–	–
EI [kN m^2]	–	6.25×10^6	–
EA [kN m^2]	–	3.20×10^4	-

In the first case, depth of void (D) from the base of footing is gradually increased from 0.5 to 3 m keeping an interval of 0.25 m. Then, for each vertical position, i.e. specific depth, horizontal position (e) is varied from 0 to 10 m keeping an interval of 2 m. At last, the load of the structure acting on the footing (P) is varied from 50 to 300 kN/m^2 keeping other parameters constant.

3.2 Reliability Analysis

For carrying out the analysis, Design of Experiment is used at a two-level with three factors at full factorial design. The vertical depth of void, horizontal distance of the void and the load from the structure are considered as the variables. The mean settlement is calculated for different cases. The corresponding values of reliability index and probability of failure are then calculated.

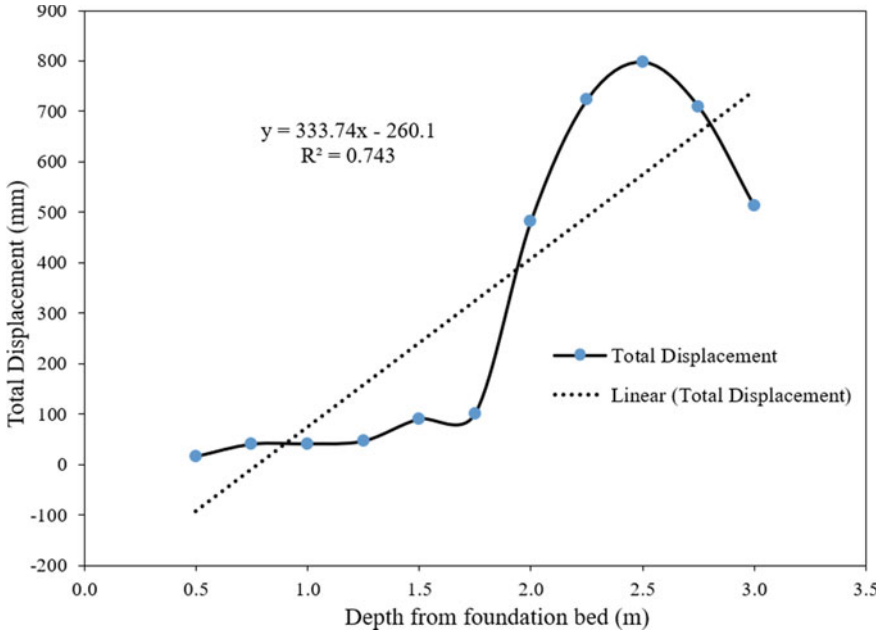

Fig. 4 Variation of total displacement with depth from foundation bed

4 Results

4.1 Effect of Depth

The settlement profile was observed in different cases by varying the depth of tunnel location varying from 0.5 to 3 m. The graph shown in Fig. 4 is the Gaussian distribution curve for tunnel location from 0.5 to 3 m. The vertical settlement reduces from the depth of 2.5–3 m. It can be inferred that the settlement when the void is present within the pressure bulb increases minimally up to a depth of 1.75 m but takes a sudden pattern curve up to 2.5 m.

4.2 Effect of Horizontal Distance

The settlement profile was observed in different cases by varying the horizontal distance of tunnel varying from 0 to 10 m from the centre of the foundation. The graph shown in Fig. 5 is the Gaussian distribution curve for tunnel location from 0 to 10 m. The settlement of the foundation within the 1.75 m of depth is within the permissible limit while there is an abrupt increase in the settlement.

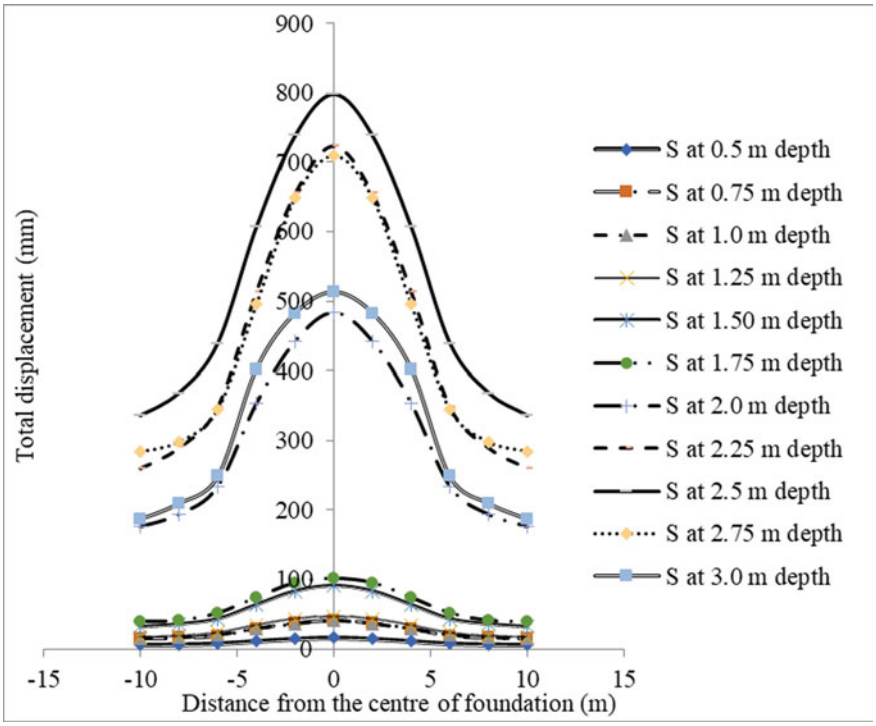

Fig. 5 Variation of total displacement with the horizontal distance from the centre of the foundation

4.3 Effect of Load Variation

The settlement profile was observed in different cases by varying the load from the structure from 50 to 350 kN/m^2. The graph shown in Fig. 6 is the Gaussian distribution curve for tunnel location from 50 to 350 kN/m^2. The settlement of the foundation is more or less having a common gradual increasing pattern. With the increase in the load, it can be observed that the total vertical displacement also increases.

4.4 Regression Equation

If the factors are analyzed and a correlation equation between the vertical position of void from foundation bed (W + D), horizontal position of void from the centre of foundation (e) and the vertical load (P) is obtained as mentioned in Eq. (5):

$$\begin{aligned}\text{Settlement} = 112.9 - 11.74V - 0.000350H + 0.3597P + 0.0007V \times H \\ - 0.04657V \times P + 0.000001H \times P - 0.000002V \times H \times P \quad (5)\end{aligned}$$

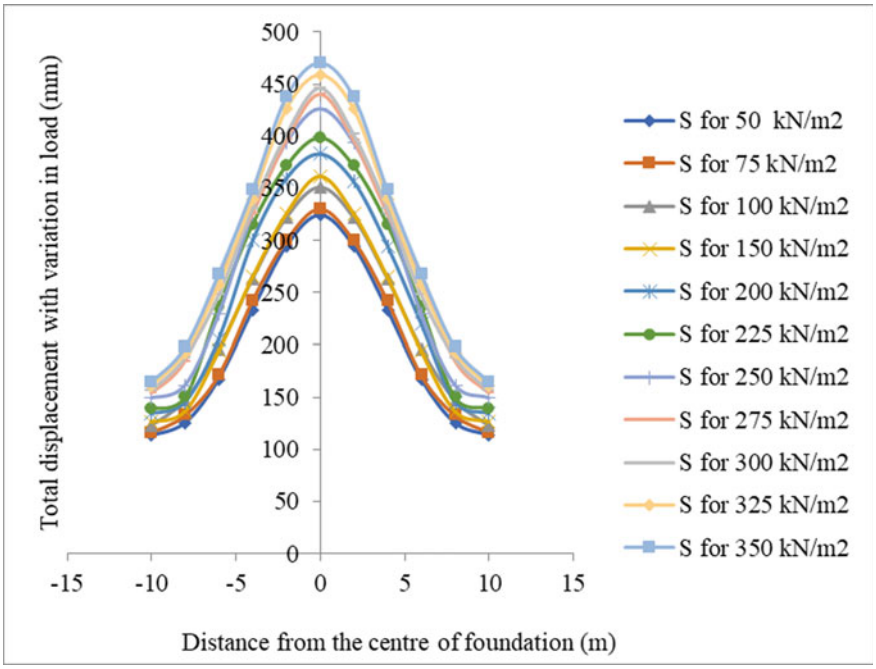

Fig. 6 Variation of total displacement with the distance from the centre of the foundation with a change in load

It can be inferred from the regression equation in Eq. (5) that the vertical depth of void and the variation in the load has a predominant effect on the settlement of the foundation. The interrelation of the factors can be observed in Figs. 7, 8.

4.5 Reliability Index and Probability of Failure

The DOE is used to develop a two-level three factored full factorial design to obtain the different cases of analysis through the MINITAB software. These conditions were further analyzed using PLAXIS 2D software to determine the settlement of the foundation as shown in Fig. 9. This is then processed through EXCEL-XSTAT to obtain the reliability index (β), which is calculated as 0.894, and the probability of failure (P_f) comes to be 0.185. Also, the value of Cronbach alpha obtained is 0.965, which shows a consistency in the data observed through the various steps of calculation. The value of the reliability index and the probability of failure shows hazardous condition if we consider the risk according to the settlement of the foundation.

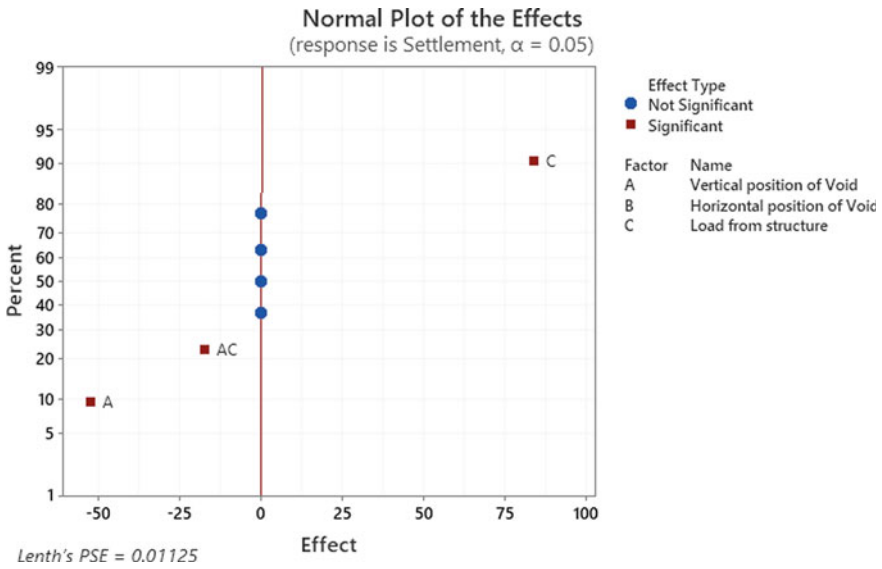

Fig. 7 Effects of various factors and their interrelations

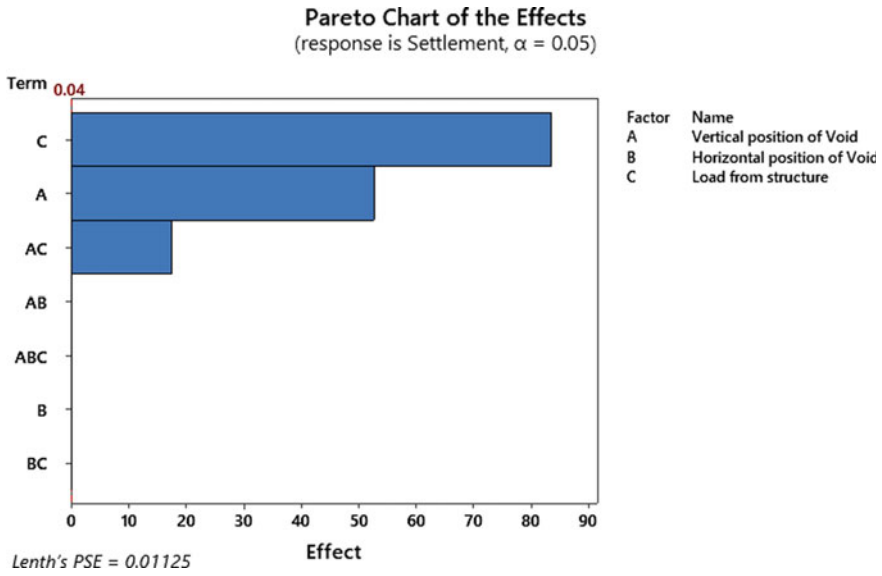

Fig. 8 The Pareto chart of the effects

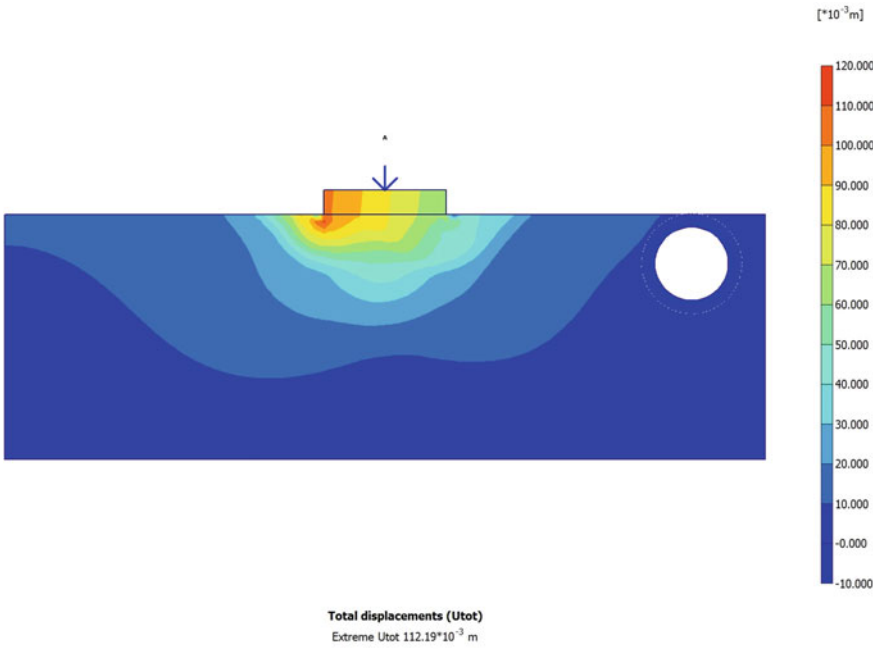

Fig. 9 One of the cases obtained through DOE

5 Conclusions

Based on the present study, the following concluding remarks can be made:

1. The behaviour of void depth from 0 to 3 m in given soil conditions is studied with the help of Plaxis 2D software to generate a graph of vertical settlement versus depth of the tunnel and hence, the ground surface settlement is demonstrated by Gaussian distribution curve. As the depth of the centre of tunnel increases from 0 to 3 m, the surface settlement first increases and then decreases, it means the influence of tunnel location on ground settlement decreases as the depth of void increases after a certain depth. It can be concluded that within a certain range of vertical location, the effect of depth of void is maximum.
2. Due to an increase in depth of void, the overburden pressure increases and simultaneously values of axial force, bending moment and shear force on tunnel lining also get increased.
3. Due to an increase in the building load (from 50 to 350 kN/m^2), the values of extreme total displacement on the ground surface, axial force, bending moment and shear force on tunnel will also increase. There is no phenomenon observed that demarcates the inverse effect of loading on the settlement. However, it has been observed that with an increase in horizontal distance from the centre of foundation, the settlement decreases.

4. The inconsistencies in the results of the failure of the structure cannot be found using a deterministic approach. Therefore, reliability analysis was performed, using the first-order reliability method, the reliability index for footing over single void is found as 0.894, and the probability of failure of structure is found as 0.185. From USACE (1997) chart, the structure is hazardous under standard conditions.

References

1. Babu, G.L.S., Srivastava, A.: Reliability analysis of allowable pressure on shallow foundation using response surface method. Comput. Geotech. **34**, 187–194 (2007). https://doi.org/10.1016/j.compgeo.2006.11.002
2. Badie, A., Wang, M.C.: Stability of spread footing above void in clay. J. Geotech. Eng. **110**, 1591–1605 (1984). https://doi.org/10.1061/(ASCE)0733-9410(1984)110:11(1591)
3. Cording, E.J., Hansmire, W.H.: Displacement around soft ground tunnels. In: 6th Pan-American Conference of Soil Mechanics and Foundation Engineering. Buenos Aires, pp. 571–633 (1975)
4. Fenton, G.A., Zhou, H., Jaksa, M.B., Griffiths, D. V.: Reliability analysis of a strip footing designed against settlement. In: ICASP9, Int. Conf. on Applications of Statistics and Probability in Civil Engineering, pp. 1271–1277 (2003)
5. Kiyosumi, M., Kusakabe, O., Ohuchi, M.: Model tests and analyses of bearing capacity of strip footing on stiff ground with voids. J. Geotech. Geoenviron. Eng. **137**, 363–375 (2011). https://doi.org/10.1061/(asce)gt.1943-5606.0000440
6. Mair, R.J., Taylor, R.N.: Theme lecture: bored tunnelling in the urban environment. Soil. Mech. Found. Eng **14**, 2353–2386 (1997)
7. Metya, S., Bhattacharya, G.: Probabilistic critical slip surface for earth slopes based on the first order reliability method. Indian Geotech J 44. (2014) https://doi.org/10.1007/s40098-013-0089-8
8. Peck, R.B.: Deep excavations and tunneling in soft ground. In: 7th ICSMFE, pp 225–290 (1969)
9. Schweiger, H.F., Peschl, G.M.: Reliability analysis in geotechnics with the random set finite element method. Comput. Geotech. **32**, 422–435 (2005). https://doi.org/10.1016/j.compgeo.2005.07.002
10. Wang, M.C., Hsieh, C.W.: Collapse load of strip footing above circular void. J. Geotech. Eng. **113**, 511–515 (1987)

Behaviour of Buried Pipelines in Geosynthetics Reinforced Soil Slopes

Soumen Naskar and Awdhesh Kumar Choudhary

1 Introduction

Buried pipelines are one of the most critical parts of any urban infrastructure and smooth functioning of it can be helpful in deciding the economical development of a nation. In recent years, scarcity of suitable horizontal land has forced engineers to place these buried pipelines under sloping terrain. Also at times, these pipelines have to pass below an existing embankment. The bearing capacity of these pipelines gets significantly reduced and settlement increases as compared with the pipelines lying below a horizontal land under loading. In such cases, the promising performance of geosynthetics owing to its high tensile strength can be utilized to stabilize the embankments or existing slopes. This will help in increasing the stability of the buried pipelines by increasing their bearing capacity and decreasing their settlement under heavy loads. An understanding of the behaviour of buried pipelines located in reinforced slopes under loading is of much practical importance to geotechnical engineers.

Many researchers such as [2, 3, 6, 8] have investigated the use of geosynthetics reinforcement and reported that the ultimate bearing capacity as well as load settlement behaviour of a footing placed near the slope can be considerably improved by incorporating the use of geosynthetic reinforcement.

Recently, the behaviour of buried pipelines located on the horizontal surface has been clearly demonstrated by several investigators [4]. Also, the use of geosynthetics such as geocell mats, EPS blocks etc. to improve the stability of buried pipelines by decreasing the upcoming vertical pressure on pipe's crown has been extensively reported by several researchers [1, 7, 9, 11].

S. Naskar (✉) · A. K. Choudhary
Department of Civil Engineering, NIT Jamshedpur, Jamshedpur, Jharkhand 831014, India

A. K. Choudhary
e-mail: awdhesh.ce@nitjsr.ac.in

C. N. V. Satyanarayana Reddy et al. (eds.), *Dynamics of Soil and Modelling of Geotechnical Problems*, Lecture Notes in Civil Engineering 186,
https://doi.org/10.1007/978-981-16-5605-7_14

Bildik and Laman [5], in particular, performed the parametric study and investigated the stress behaviour of buried pipelines located under a strip footing on the horizontal surface. The results indicated a serious increase in bearing capacity and decrease in hoop stress when embedment ratio and horizontal distance of pipe to footing were increased. Also, increase in bearing capacity and decrease in pipe hoop stress were observed in case of perpendicular installation of pipeline than parallel installation with respect to footing.

Although other researchers have studied the role of geosynthetics on the behaviour of buried pipelines lying beneath horizontal surfaces, but there is still a lack of investigations in case of buried pipelines located near the slopes. This paper seeks to aid understanding the role of geosynthetics in increasing the stability of buried pipelines located on slopes.

The main purpose of this investigation is to examine the role of geosynthetics in increasing the stability of buried pipelines located on slopes.

2 Methodology

2.1 Numerical Investigation

Finite element analysis was performed to model the response of footing on buried PVC pipelines for different embedment depths, relative density of sand, slope angle and setback distance of the footing. Analysis was carried out for both reinforced and unreinforced slopes. In the present problem, five calculation phases are defined in total. They are initial phase, pipe simulation phase, footing simulation phase, geogrid simulation phase and loading phase. The initial phase is automatically generated and contains initial stress and model geometry details. Except for soil, all other structural elements and loadings are deactivated in this phase. The K0 procedure is used for initial stress calculation and staged construction is selected as the type of loading. The second phase is added after the initial phase and named as pipe simulation phase. In this phase, pipe is activated. Similarly, footing and geogrid are simulated in the following phases and activated respectively. Finally, loading phase is added after the geogrid simulation phase. In this phase, loading is activated along with all other structural elements. After successfully assigning each calculation phase, the finite element model is analyzed for the existing loads and boundary conditions.

2.2 Modelling Using Finite Element Mesh and Boundary Condition

Finite element analysis using PLAXIS^{3D} is done in this research. The parametric study is performed on different models and compared with both reinforced and

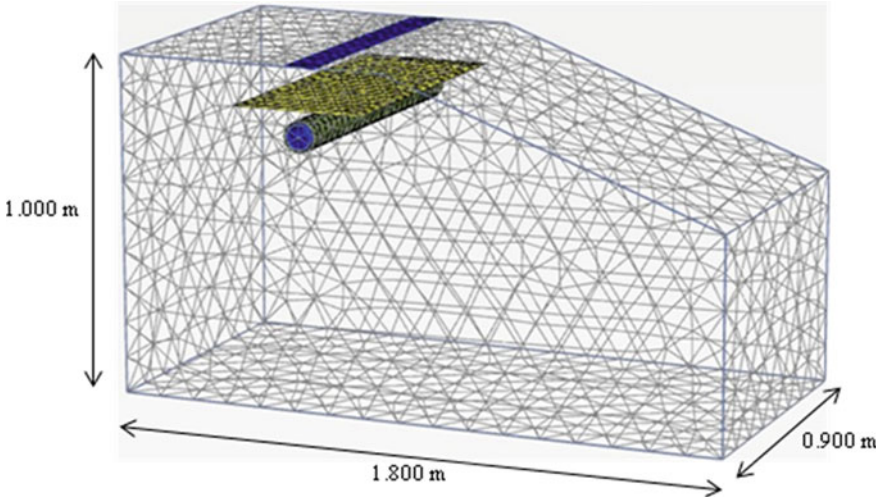

Fig. 1 Distribution of nodes and elements in the generated mesh

unreinforced slope in order to investigate the role of geosynthetics in increasing the stability of buried pipelines. Experimental work reported by Lee and Manjunath [8] was chosen to validate the finite element model in this study. The numerical model consists of a single sand layer with an initial slope of 20°, geosynthetics in the form of geogrid, rectangular strip footing and buried PVC pipe. The size of the test tank is kept the same as that of the experimental analysis carried out by Lee and Manjunath [8]. The model was fully fixed (both horizontal and vertical movement restricted) at the base and normally fixed (horizontal movement restricted) at the sides. The dimension of the soil model is shown below (Fig. 1).

In the present study, the soil is modelled as hardening soil (HS) model. The desired relative density is achieved by varying different soil parameters as shown (Tables 1 and 2).

3 Results and Discussion

3.1 Validation of Numerical Model

Initially, the present numerical model has been validated with the existing experimental work reported by Lee and Manjunath [8]. Subsequently, the detailed numerical analysis has been carried to investigate the behaviour of buried pipe under reinforced soil slope. Typical load–displacement response obtained from numerical analysis has been compared with experimental results [8] as shown in Fig. 2. The model dimensions and the properties of the material were adopted the same as reported in

Table 1 Soil parameters used in the present study

Parameter	Relative density 85%	Relative density 65%	Relative density 45%
Unsaturated unit weight, γ_{unsat} (kN/m^3)	18.20	17.52	16.85
Saturated unit weight, γ_{sat} (kN/m^3)	21.02	20.50	19.98
Material model	Hardening soil	Hardening soil	Hardening soil
Drainage type	Drained	Drained	Drained
E_{50}^{ref} (kPa)	60,000	42,000	24,000
E_{oed}^{ref} (kPa)	60,000	42,000	24,000
E_{ur}^{ref} (kPa)	180,000	126,000	72,000
Power in stiffness laws (m)	0.8	0.8	0.8
Unloading–reloading Poisson's ratio (υ)	0.3	0.3	0.3
Cohesion, c (kN/m^2)	1.0	1.0	1.0
Friction angle, φ (°)	38	35	30
Angle of dilatancy, ψ (°)	8.0	5.0	0.0
Interface reduction factor, R_{inter}	1.0	1.0	1.0

Table 2 Material properties used in numerical analysis

Parameter	Model footing	PVC pipe	Geogrid
Unit weight, γ(kN/m^3)	78.50	13.83	–
Material type	Elastic	Elastic	–
Young's modulus, E (kN/m^2)	210×10^6	93.3×10^4	–
Shear modulus, G (kN/m^2)	80.77×10^6	35.61×10^4	–
Poisson's ratio (υ)	0.30	0.31	–
Axial stiffness (kN/m)	–	–	68

the experimental model tests by Lee and Manjunath [8]. From Fig. 2, it can be seen that the present result is well comparable to experimental results with marginal error. This error is possibly due to the error that occurred in simulating the soil properties reported. Therefore, it can be said that the present model can be used to simulate the behaviour of buried pipe in reinforced soil slope.

The response of the footing in terms of its load-carrying capacity is observed for varying slope angle, relative density of soil and edge distances of the footing. The soil model providing the safest values in terms of load-carrying capacity of the footing as well as conforming to the actual analysis in consideration is fixed before introducing pipeline and geogrid into the system.

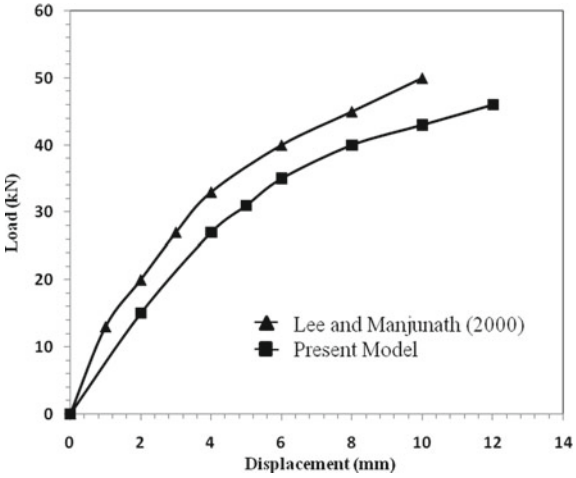

Fig. 2 Validation of numerical results with experimental work

3.2 Response of Footing for Different Parameters

Influence of slope angle on footing placed at different edge distances

The response of footing is observed for varied footing position (i.e. b/B ratio) and slope angle ($\beta = 20°$, 26.5° and 30°) through the numerical model. In total, six different positions of the footing is considered in this study starting from b/B = 0, 1, 2, 3, 4 and 5 where b/B = 0 denotes that footing is located on the edge of the slope. The response of the footing at b/B = 2 for different slope angles is shown in Fig. 3. It can be seen that the load carrying capacity is maximum for level ground ($\beta = 0°$) and gradually reduces with an increase in slope angle. However, the slope having $\beta = 20°$ is found to be safest as compared with other slope angles. Hence, $\beta = 20°$ has been considered for further analysis.

Influence of relative density of soil on footing placed at different edge distances

The behaviour of footing is observed for varied footing positions (i.e. b/B ratio) and relative density (85%, 65% and 45%) through the numerical model. Soil parameters such as unit weight, angle of internal friction, dilatancy angle etc. are varied in order to simulate different relative densities of soil. For each relative density, analysis is done for fixed slope angle ($\beta = 20°$) and varied b/B ratios of 0.0, 1.0, 2.0, 3.0, 4.0 and 5.0. The response of the footing at b/B = 2 for different relative densities is shown in Fig. 4. It is observed that the load-carrying capacity is maximum when relative density is 85% and gradually reduces with a decrease in relative density. Therefore, sand having a relative density of 85% has been considered for further parametric study.

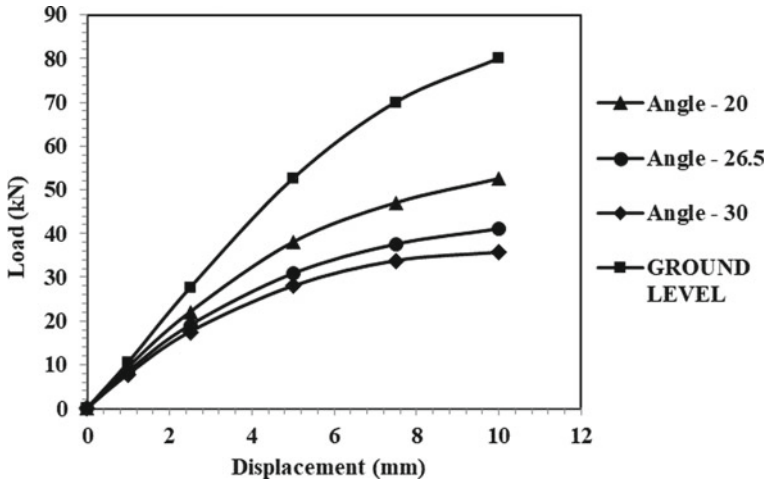

Fig. 3 Response of footing at different slope angles

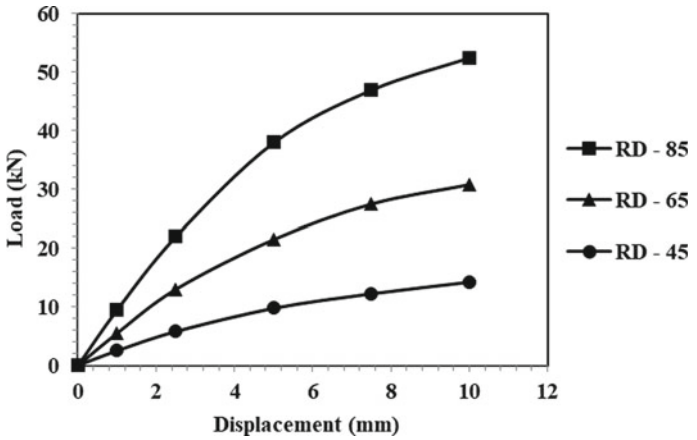

Fig. 4 Response of footing at different relative densities of soil

Response of footing placed at different edge distances

The behaviour observed for varied footing positions (i.e. b/B ratios) is discussed in this section. The slope angle and relative density are kept constant ($\beta = 20°$ and RD = 85%). Analysis is also carried out with strip footing lying in level sand surface for comparison. The response of the footing placed at different edge distances is presented in Fig. 5. An increasing trend in bearing capacity is observed when the position of the footing is shifted away from the slope crest. This increase in bearing capacity with increasing edge distance is attributed due to the diminishing effect of the slope. This explanation seems to be consistent with the experimental results of Lee and Manjunath [8].

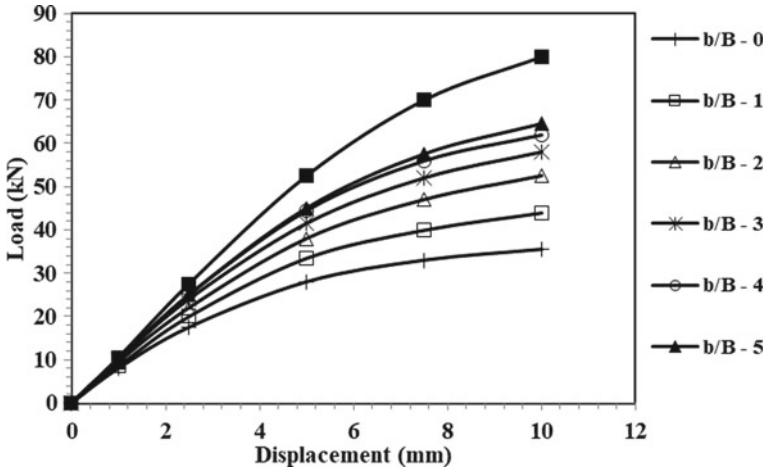

Fig. 5 Response of footing at different edge distances

When the position of the footing is at b/B = 5, the BCR value nearly achieves 80% of the value of case of footing placed on a level surface. This shows that if the edge distance is further increased, then footing will start to behave as if placed on a level surface. Therefore to stay with the actual analysis of considering the slope effect in monitoring the role of geosynthetics on buried pipe, the position of the footing is fixed at b/B = 2.

Once the slope angle, relative density and footing position are decided, PVC pipe is introduced in the model and placed under the footing. Also before carrying out the analysis with reinforced slope, the optimum position of the reinforcement needs to be fixed.

Influence of reinforcement embedment depth on footing

The load-carrying capacity of the footing due to different embedment depths of geogrid is observed in this study. A series of analysis is carried out for various embedment depths to footing width ratio (u/B) of 0.25, 0.50, 0.75, 1.00, 1.25, 1.50 and 1.75 by keeping the edge distance of the footing (b/B = 2) and slope angle ($\beta = 20°$) constant. Load settlement curves for seven different u/B ratios as mentioned earlier are shown in Fig. 6. Also, the ultimate load-carrying capacity of the footing is tabulated in Table 3. From Table 3, it is observed that load-carrying capacity of the footing increases with an increase in embedment depth of reinforcement till u/B = 1.25. For u/B > 1.25, a reduction in load-carrying capacity of the footing is observed due to the reduced performance of the geogrid. Therefore, the optimum depth of reinforcement is considered to be u/B = 1.25.

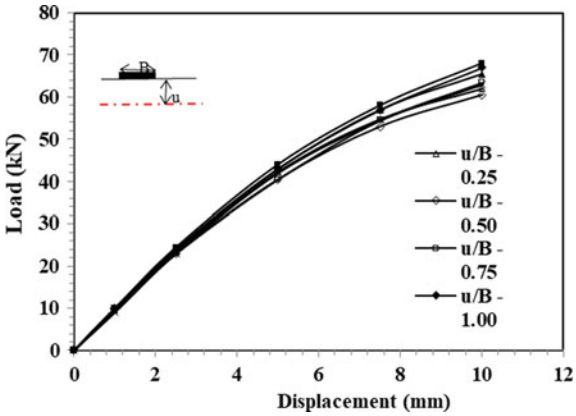

Fig. 6 Response of footing at different reinforcement embedment depths

Table 3 Ultimate load-carrying capacity of footing at different u/B ratios

u/B	Ultimate load-carrying capacity of the footing (kN)
0.25	47.50
0.50	49.20
0.75	52.30
1.00	58.70
1.25	60.00
1.50	58.00
1.75	57.00

3.3 Response of Footing Due to Vertical Movement of Pipe

Unreinforced slope

The response of footing in the form of bearing capacity ratio is observed for different vertical positions of the pipe in unreinforced sand. The position of the pipe is varied from d/B ratios equal to 0.5, 1.0, 1.5, 2.0, 2.5, 3.0 and 3.5. Analysis is also carried out with strip footing lying on sand without pipe for comparison. Load settlement curves for seven different d/B ratios are presented in Fig. 7. It is observed that the BCR value of footing goes on increasing as the pipe moves in vertically downward direction. The BCR value reached 96% of case of without pipe at d/B = 3.5. This implies that if the pipe is placed beyond d/B = 3.5, the BCR value is reached the same BCR value of case of without pipe. The results show that the bearing capacity of the footing is directly affected when pipe is buried within the stress bulb. Also, the effect of load on pipe is almost negligible when it is placed beyond d/B = 3.5. This explanation seems to hold a reasonable agreement with the experimental work conducted by Bildik and Laman [5]. Figures 8 and 9 show the displacement contour of the model without pipe and with pipe in unreinforced slope respectively. Upon

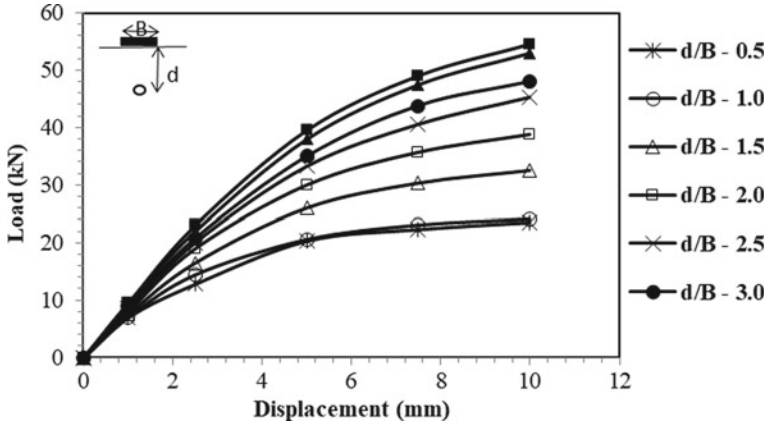

Fig. 7 Response of footing for different embedment depths

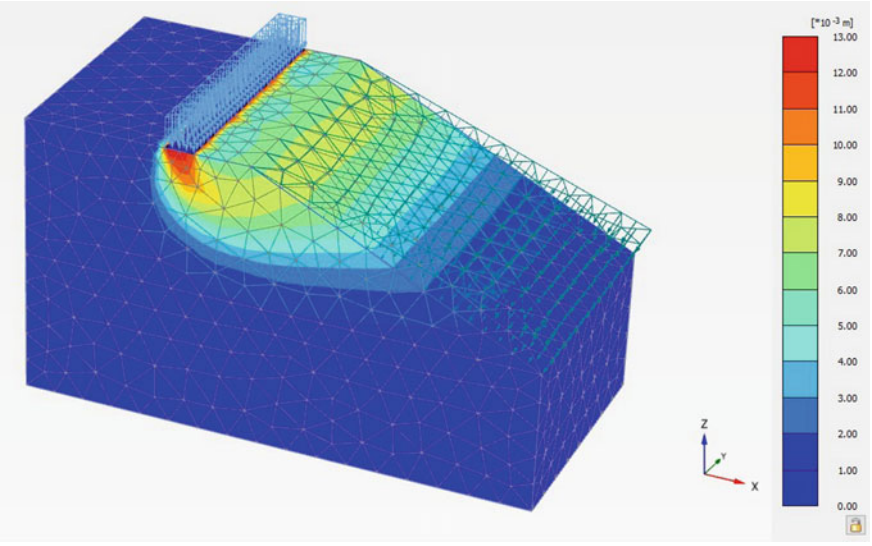

Fig. 8 Displacement contour of model without pipe in unreinforced slope

comparing with no pipe case, the safety of the buried pipe can be ascertained as it is lying between less displaced contours. Therefore, the vertical position of the pipe (embedment depth) is fixed at d/B = 3.5 in case of unreinforced sand.

Reinforced slope

The response of footing in the form of bearing capacity ratio is observed for different embedment depths of the pipe in reinforced sand. Since the buried pipe needs to be protected by geogrid, therefore, it should be placed at least below the optimum depth

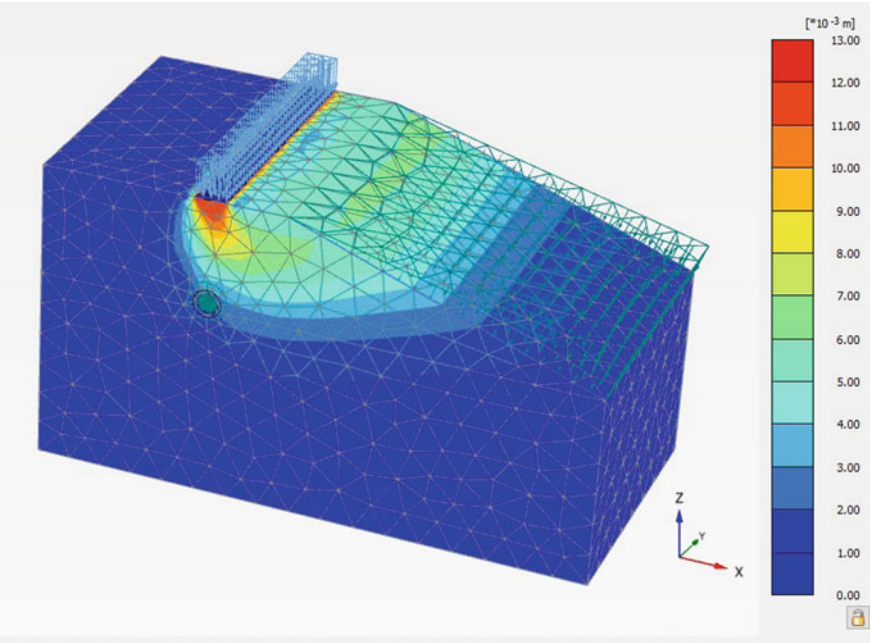

Fig. 9 Displacement contour of model with pipe in unreinforced slope (d/B = 3.5)

of the reinforcement, i.e. u/B = 1.25. Analysis is carried out for d/B ratios of 2.0, 2.5 and 3.0 and compared with strip footing lying on sand without pipe. Load settlement curves for three different d/B ratios are presented in Fig. 10. Also, the ultimate load-carrying capacity of the footing is tabulated 4.1. From Table 4, it is observed that the BCR value of footing goes on increasing as the embedment depth of pipe increases. The BCR value reached 97% with pipe at d/B = 3.5 as compared with without pipe.

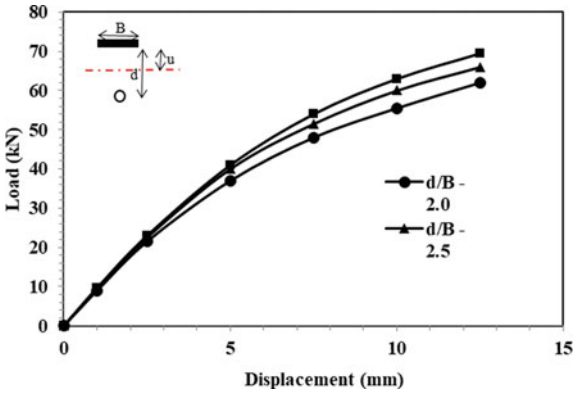

Fig. 10 Response of footing for different embedment depths in reinforced sand

Table 4 Ultimate load carrying capacity of footing for different *d/B* ratios

d/B	Ultimate load of footing with pipe (kN)	Ultimate load of footing without pipe (kN)	BCR
2.0	50.0	56	0.89
2.5	53.0	56	0.94
3.0	54.5	56	0.97

When compared with unreinforced sand, similar BCR value is achieved when d/B = 3.5. Improvement in BCR value at a lesser depth signifies the performance of geogrid. Also the displacement contours of the model without pipe and with pipe in reinforced slope are shown in Figs. 11 and 12. The safe position of the buried pipeline can be justified as it can be seen lying in between less displaced contours when compared with no pipe condition. Therefore, the embedment depth of pipe is fixed at d/B = 3.0 in case of reinforced sand. Hence, with reinforcement, the depth of pipe can be reduced by 0.5 times of B.

From Sects. 3.2 and 3.3, the following statements can be justified with respect to unreinforced and reinforced slope.

- The bearing capacity of the footing is directly affected when pipe is buried within the stress bulb in case of both unreinforced and reinforced slopes.

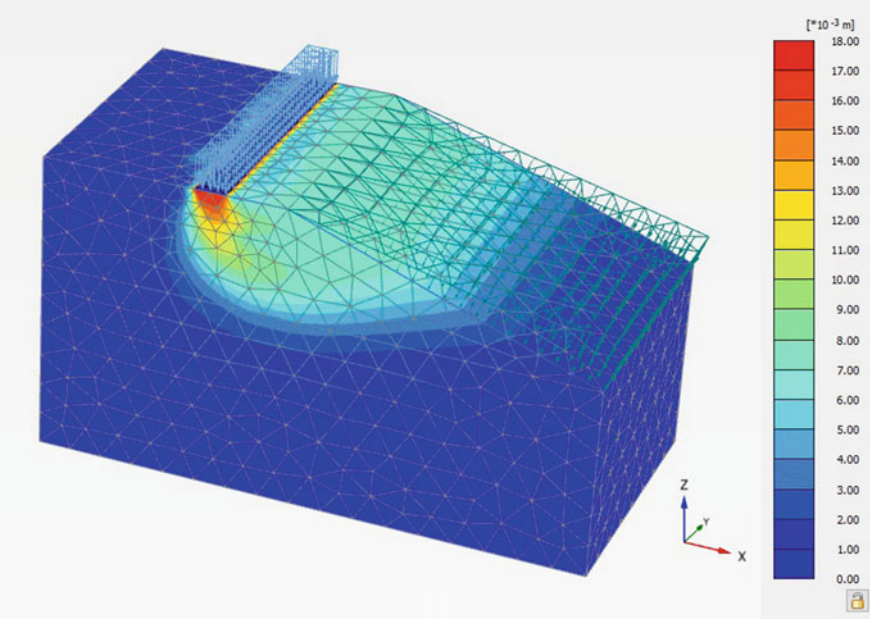

Fig. 11 Displacement contour of model without pipe in reinforced slope

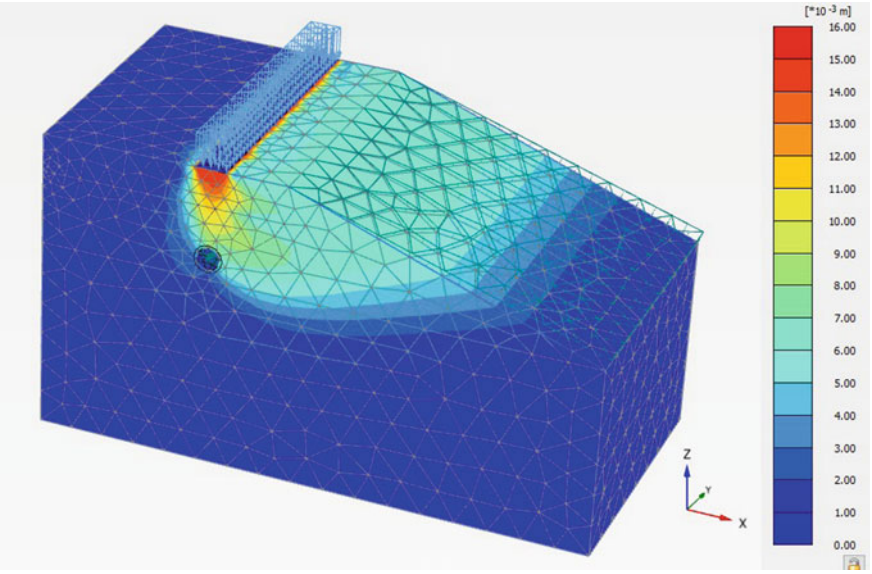

Fig. 12 Displacement contour of model with pipe in reinforced slope (d/B = 3.0)

- The effect of load on pipe is almost negligible when it is placed beyond d/B = 3.5 in case of unreinforced slope and d/B = 3.0 in case of reinforced slope.
- Improvement in BCR value at a lesser depth in case of reinforced slope signifies the performance of geogrid.

4 Conclusions

1. Load carrying capacity of the footing can be improved by the inclusion of geosynthetics.
2. Embedment depth of pipe lying on soil slope can be reduced with the use of geogrid. This will help in reducing the extra cost of trenching during the laying of buried pipelines in soil slopes.
3. Geosynthetics in the form of geogrid is helpful in improving the overall stability of buried pipelines in soil slopes.

Acknowledgements The authors sincerely acknowledged the financial support provided to the third author by Technical Education Quality Improvement Programme (TEQIP-III), India in the form of minor research (seed) grant (NITJSR/DCE/2019-20/023) at the Department of Civil Engineering, NIT Jamshedpur.

References

1. Almohammed, W.H., Fattah, M.Y., Rasheed, S.E.: Numerical analysis of the effect of geocell reinforcement above buried pipes on surface settlement and vertical pressure. Int. J. Geotech. Geolog Eng **12**(3) (2018)
2. Altalhea, E.B., Tahaa, M.R., Abdrabboa, F.M.: Bearing capacity of strip footing on sand slopes reinforced with geotextile and soil nails. Jurnal Teknologi (Sci. Eng.) **65**(2), 1–11 (2013)
3. Alamshahi, S., Hataf, N.: Bearing capacity of strip footings on sand slopes reinforced with geogrid and grid-anchor. Geotext. Geomembr. **27**, 217–226 (2009)
4. Amit Srivastava, Chaitanya R. Goyal and Abhishek Raghuvanshi: Load Settlement Response of Footing Placed over Buried Flexible Pipe through a Model Plate Load Test, International Journal of Geomechanics, Vol. 13, No. 4 (2013)
5. Bildik, S., Laman, M.: Experimental investigation of soil-structure-pipe interaction. KSCE J. Civil Eng (2019)
6. El Sawwaf, M.: Strip footing behavior on pile and sheet pile-stabilized sand slope. J. Geotechnol. Geoenviron. Eng. **131**(6), 705–715 (2005)
7. Hegde, A.M., Sitharam.T.G.: Experimental and numerical studies on protection of buried pipelines and underground utilities using geocells. Geotext. Geomembr. (2015)
8. Lee, K.M., Manjunath, V.R.: Experimental and numerical studies of geosynthetic-reinforced sand slopes loaded with a footing. Can. Geotech. J. **37**, 828–842 (2000)
9. Mehrjardi, G.T., Tafreshi, S.N.M, Dawson, A.R.: Numerical analysis on Buried pipes protected by combination of geocell reinforcement and rubber-soil mixture. International J. Civ. Eng. **13**(2) (2015)
10. Tafreshia, S.N.M., Darabia, N.J., Dawson, A.R.: Combining EPS geofoam with geocell to reduce buried pipe loads and trench surface rutting. Geotext. Geomembr. (2019)

Parametric Study of Stone Column Using PLAXIS 2D

Shruti Roy and A. K. Sinha

1 Introduction

When we discuss the problem in dealing with soil, Clay is named to be the most obnoxious one. The low undrained shear strength of soft soils makes it difficult for them to serve the purpose of the structure. This may lead to failure of structure or lack of serviceability of the structure. Both conditions are highly undesirable. In pursuit of finding the solutions to these situations, many techniques have been developed, known as Ground Improvement techniques. Nowadays, ground improvement has proven to be way more economical than shifting location due to the mammoth surge in land prices. The ground improvement technique known as Granular Column, also known as Sand Column, Stone Column or Granular Pile has been serving as a life saviour as a panacea to the problems created by soft soil. It can be practiced by three methods: "Reinforcement", "Improvement", "Treatment" or a combination of these. Previously, only aggregate used to be used as fill, hence granular fill or granular column are also known as stone column. But nowadays, various cohesionless materials are getting used.

Balaam and Booker [1] observed that the stone column reduces settlement to 40% and the rate of settlement also increases. Alamgir et al. [2] observed that the shear stress was maximum at the top and at the soil column interface, and decreasing with depth and radial distance. stress in column and soil was the same at the surface. Poorooshasb and Meyerhof [3] concluded that most governing parameters in the stone column are area replacement ratio and the compaction of column material which ultimately leads to providing stiffens and strength to the soil. Fattah et al. [4] concluded that area replacement ratio is the most influential parameter on bearing capacity. Madun et al. [5] conducted a numerical analysis using PLAXIS 2D and Response Surface Methodology (RSM). Numerical modelling was done by scaling

S. Roy (✉) · A. K. Sinha
NIT Jamshedpur, Jamshedpur, India

C. N. V. Satyanarayana Reddy et al. (eds.), *Dynamics of Soil and Modelling of Geotechnical Problems*, Lecture Notes in Civil Engineering 186,
https://doi.org/10.1007/978-981-16-5605-7_15

down 25 times and observed that bearing capacity increases with the diameter of the stone column and settlement reduces with the increasing length of the stone column. One of the major conclusions achieved was desirability for optimum design. Since the effectiveness of the column depends on various parameters, hence for an optimized design, the effect of key parameters must be understood well.

2 Numerical Modelling

In this study, numerical analysis has been carried out by using PLAXIS 2D having an axisymmetric model. Dimension of soil model is considered to be 300 mm x 300 mm to analyze the load-deformation curve of stone column. As there is no undulation in the ground surface, hence the number of boreholes was used as one. The boundary condition for the sides was set to restrained in the x-direction, while the bottom was restrained in x and y-direction both.

In order to analyze the settlement performance and deformation of surrounding soil and stone column, respectively, five variables are taken into consideration. These five variables are Slenderness ratio (L/D Ratio), Undrained Shear strength, Modular Ratio (Ratio of modulus of elasticity of materials of stone column to modulus of elasticity of surrounding soil, i.e. soft soil), Area Replacements Ratio in %, and Loading area. To analyze the model, the unit cell concept is used. Settlement at surface and failure was observed. For assuming Elasto-Plastic behaviour, Mohr–Coulomb model is adopted for analysis. The granular column is assumed to be drained and soft soil as undrained. For the calculation and specifications, IS 15284(Part 1):2003 is used. The arrangement of stone columns is assumed in square pattern with 4 mm diameter of each column and 32 mm spacing between columns. Equivalent diameter is calculated using the following formula

$$de = 1.03S \tag{1}$$

where de = equivalent diameter of single column and S = spacing between columns. From the above equation, the equivalent diameter of a single column is calculated to be 37 mm. The output is generated by the addition of two phases in the staged construction mode of the model. Constant parameters in structure mode to analyze the deformation of stone columns were the diameter of the stone column (which is taken as 37 mm) and line load (500 kN/m). The variable parameters in the stone column for the consideration of different curve plots were length to diameter ratio (L/D ratio = 3, 4, 5 and 6), Modulus of elasticity of sand in stone column (E_s = 12,000 kPa, 20,000 kPa, 28,000 kPa) and angle of friction of sand in stone column (26, 35 and 40 degrees).

The following Table 1 gives a summary of all properties used in numerical modelling.

Table 1 Material properties used in modelling

Parameters	Soft soil	Sand
γ_{dry}(kN/m^3)	14.4	15.50
γ_{sat}(kN/m^3)	24.4	25.5
C_u (kPa)	30, 40 and 50	–
μ	0.4	0.3
E (kPa)	4600	12,000, 20,000 and 28,000
Φ (degree)	–	26, 35 and 40
Ψ (degree)	–	0, 5 and 10

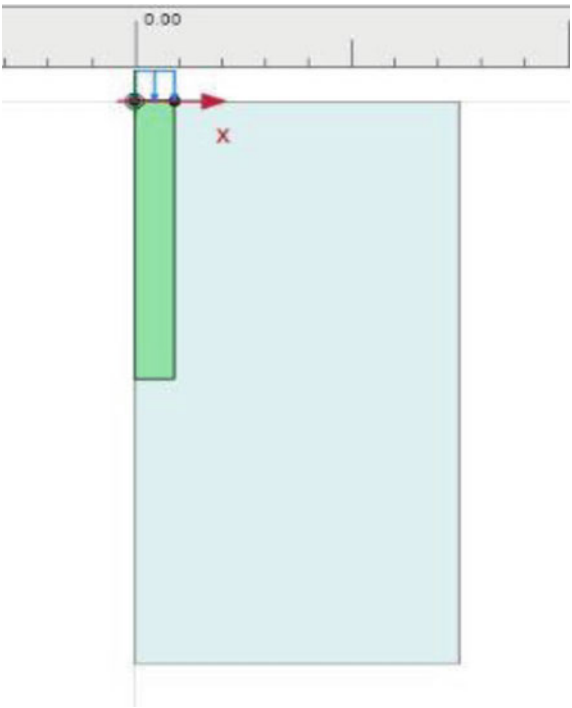

Fig. 1 Pictorial representation of soil stratigraphy used as a soft soil and stone column with line load

Model taken as axisymmetric model in PLAXIS 2D, element 15 noded and element size is 8.943 × 10^{-3} (see in Figs. 1 and 2).

3 Validation

Validation has been done with the model used by Naseer et al. [6]. A single column with a diameter of 37 mm and height of 150 mm was tested in a cylindrical tank of diameter 0.3 m and height of 0.3 m. A uniformly distributed load of 500 kN/m is

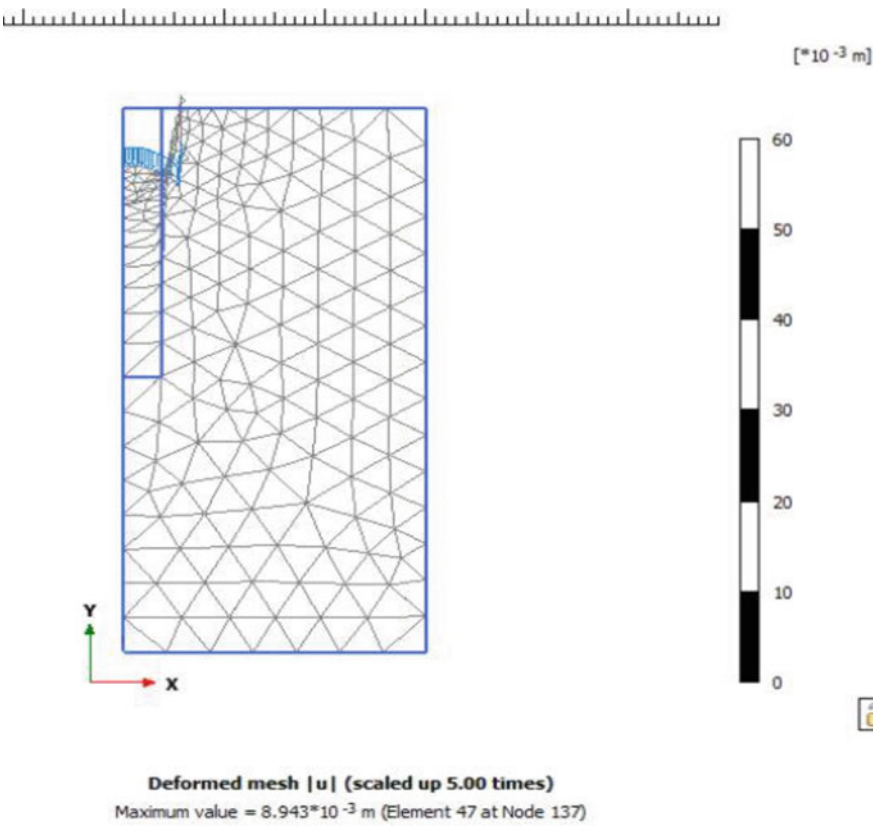

Fig. 2 Deformation of the axially loaded stone column after calculation analysis in staged calculation

applied. Application of load was assumed to be on column only. A schematic diagram of the setup is presented in Fig. 3. Present modelling results are in well agreement with the author as shown in Fig. 4.

Material properties used are listed in the table below (Table 2).

4 Results and Discussion

4.1 Influence of Shear Strength of Soft Soil (Cu)

Undrained shear strength of soft soil is changed for a value of 30, 40 and 50 kPa. Simultaneously, Esc = 12 MPa and $\phi = 26^{\circ}$ is kept constant. Figure 5 shows the effect of undrained shear strength of soft soil on maximum load and maximum settlement.

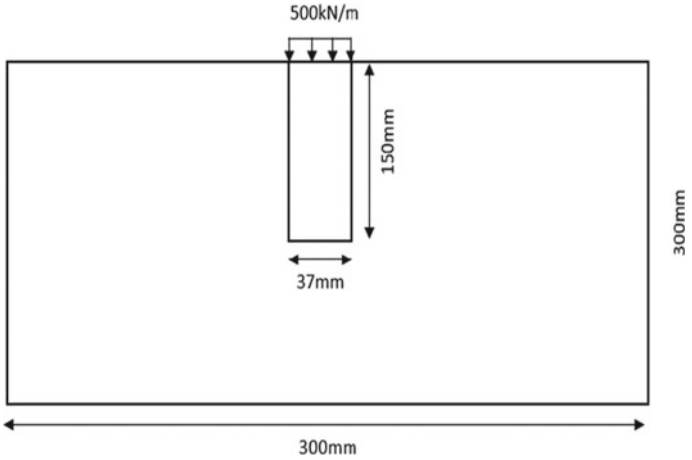

Fig. 3 Schematic diagram of setup by Naseer et al. [6]

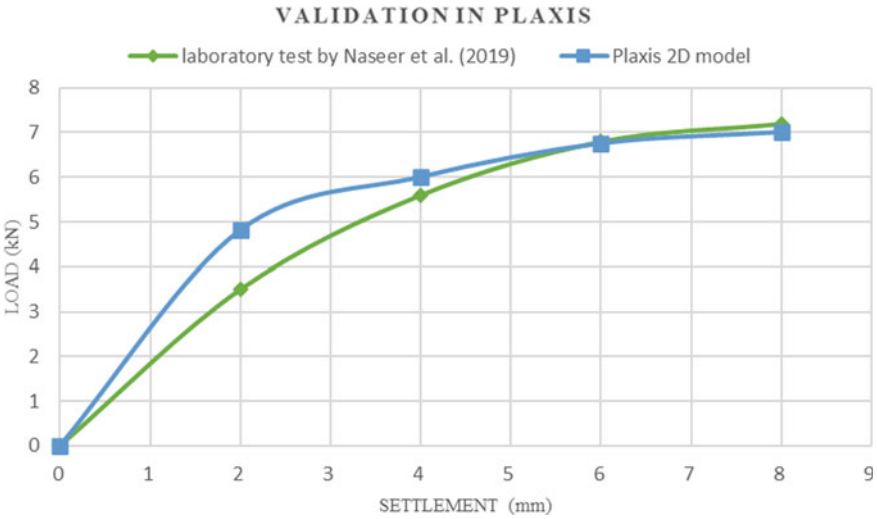

Fig. 4 Validation of the numerical model

Table 2 Material properties used in the model by Naseer et al. [6]

Parameters	Soft soil	Sand
γ_{dry}(kN/m^3)	14.4	15.50
γ_{sat}(kN/m^3)	24.4	25.5
C_u (kPa)	30	–
M	0.4	0.3
E (kPa)	4600	12,000
Φ (degree)	–	26

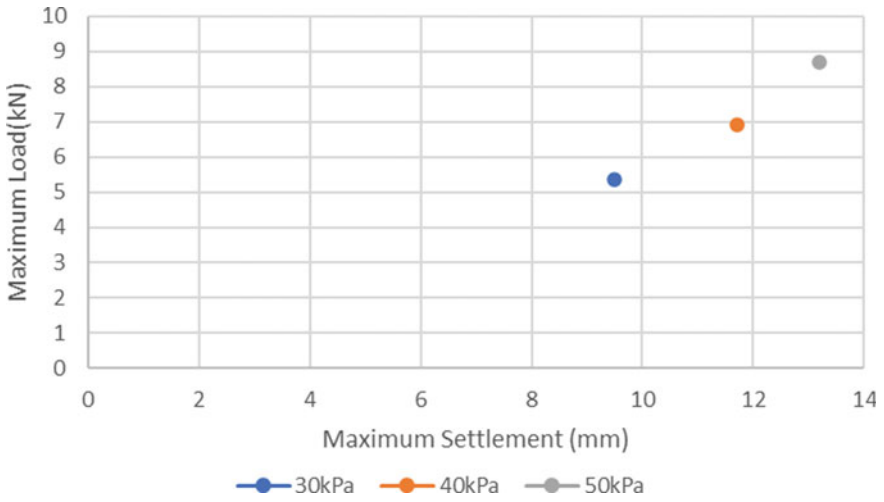

Fig. 5 Effect of undrained shear strength of soft soil on maximum load and maximum settlement

It is observed that with an increase in undrained shear strength of soil, load-carrying capacity of the column increases. It may be because of passive resistance offered to the radial bulging of the column. More shear strength of soil will offer more resistance to radial bulging, hence more stiffness to the column and leading to higher load-carrying capacity. Also, lesser radial bulging of the column will lead to more transfer of vertical stress and vertical deformation leading to more ultimate settlement. At higher value of undrained shear strength of soft soil maximum passive resistance is offered to the column which increases load-bearing capacity increases. An increasing area of the column also doesn't make much difference at a normal loading value when Cu is high.

4.2 Influence of Slenderness Ratio of Column

To investigate the influence of slenderness ratio, the L/D ratio has to be changed and the rest of the parameters has to be unchanged. When the only column assumed to be loaded, for Cu = 30 kPa of soft soil, L/D ratio of the column is varied as 3, 4, 5 and 6.

Also, stress analysis has been done and quantified with the term Stress Concentration Ratio (SCR), denoted as n. SCR is defined as the ratio of stress taken by column to stress taken by the surrounding soil. It is observed that the stress concentration ratio increased rapidly between L/D ratio 4 to 5. Though peak is observed between 5 to 6, it can be concluded that L/D ratio is optimum between 4 to 5. Also, the maximum SCR value obtained is around 2.8. Figure 6 shows the SCR behaviour with varying L/D ratios of the system.

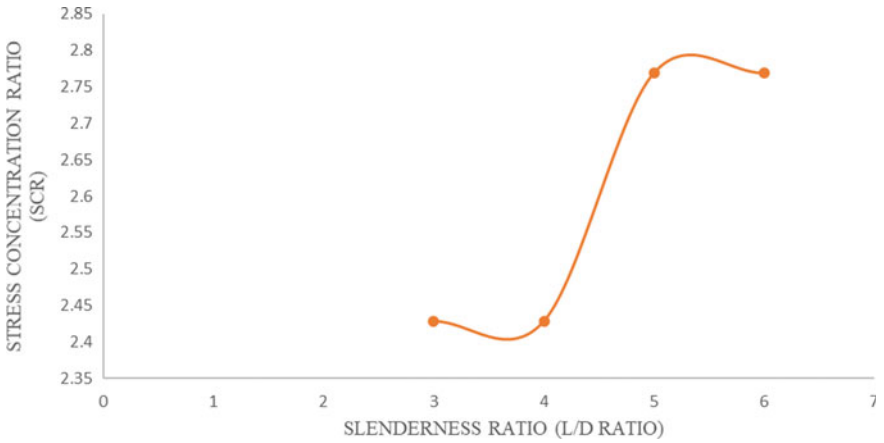

Fig. 6 Effect of L/D ratio on SCR when Cu = 30 kPa and Ar = 0.38%

4.3 Influence of Internal Friction Angle of Stone Column (Φ)

The angle of internal friction of the column directly relates to the strength of the column. It signifies the interlocking, and hence the shear strength of the column. Since stone columns are not bonded by any adhesive, internal friction angle is key to the effectiveness of stone column. It is dependent on compaction during installment, grain size distribution and arrangement of grains.

To study the influence of ϕ on a column, rest parameters were kept constant. Meanwhile, ϕ is changed as 26 degrees, 35 degrees and 40 degrees. L/D ratio is adopted as 4, Ar = 1.5%, Cu = 30 kPa, Esc = 12 MPa and $\psi = 1 - \phi$. Figure 7

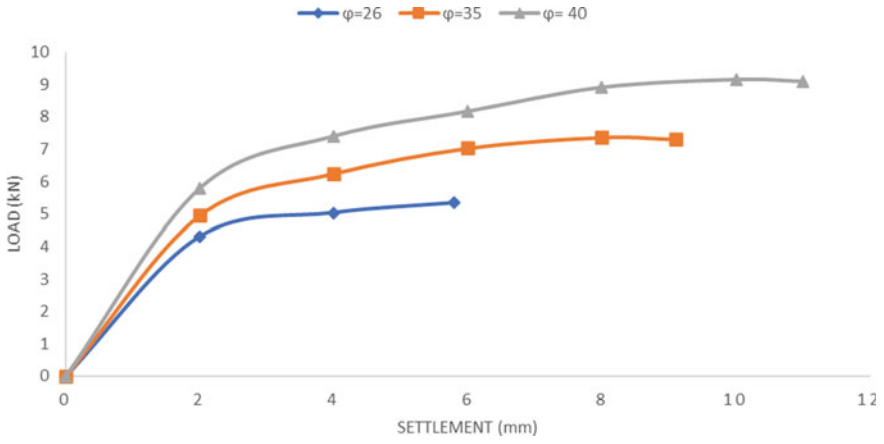

Fig. 7 Effect of ϕ, when L/D ratio = 4 and Cu = 30 kPa with Ar = 1.5%

shows the effect of internal friction angle.

It is observed that the increment of ultimate settlement is quite linear with an increase of ϕ (Fig. 8). Also, with an increase in ϕ, ultimate load carrying capacity has also increased initially with mild slope and the later slope becomes steeper (Fig. 9).

It is known that as the load is applied to the column, grains of the column undergo a vertical deformation which triggers radial bulging. This bulging is prevented by passive resistance provided by soil. Depth up to which axial load transfers, tends to move radially. When ϕ increases, the transfer of load will be more, because of more interlocking and shear strength. Hence, passive resistance will appear to be deeper with more ϕ.

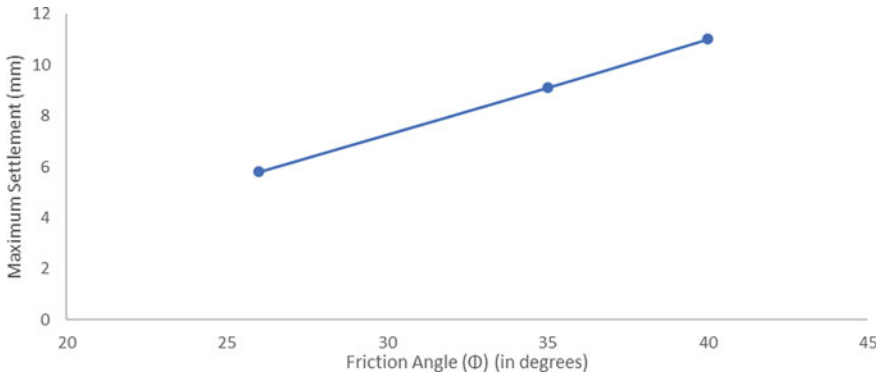

Fig. 8 Effect of ϕ on maximum settlement when L/D ratio = 4 and Cu = 30 kPa with Ar = 1.5%

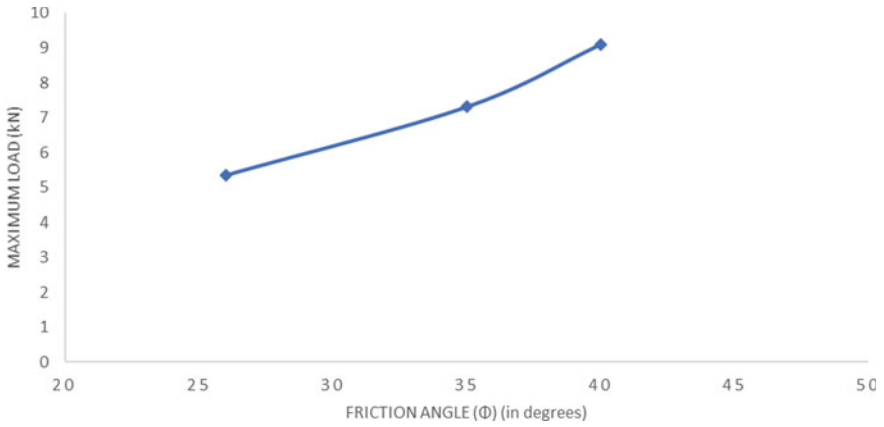

Fig. 9 Effect of ϕ on maximum load when L/D ratio = 4 and Cu = 30 kPa with Ar = 1.5%

4.4 Influence of Modular Ratio (m)

To understand the effect of the modular ratio, all the parameters were kept constant and the modular ratio kept on varying to the value 2.6, 4.34 and 6.08. Parameters kept constant are L/D ratio = 4, Cu = 30 kPa, Es = 4600 kPa, $\phi = 26^{\circ}$ and Ar = 1.5%. While Modulus of elasticity of stone column (Esc) is varied to a value of 12,000, 20,000 and 28,000 kPa.

The modular ratio is the ratio of Young's modulus of elasticity of grain used in the column to the modulus of elasticity of soft soil.

$$m = \frac{E_{granular\ column}}{E_{soft\ soil}} \tag{2}$$

It is observed that with an increase in Esc, the ultimate settlement corresponding to a load also get increased. This may be due to the reason that, when Esc increases, the self-weight of the column will also increase, which ultimately adds up to the axial loading. Due to this reason, vertical settlement will increase for the unchanged value of load when Esc will increase. It is observed that for the first 8000 kPa increment in Esc, settlement increased by 18.96%, while for the next 8000 kPa, stress increased by 9.13% only (Fig. 10). Also, ground heaving is seen occurring at 2.7D away from the column while radial bulging. But ground heaving can be seen reducing with increasing Esc, which means radial bulging is also reduced to some extent. But maximum vertical deformation can be seen increasing with increasing Esc, which means punching is also playing role in the failure. Hence, an interesting conclusion came here is that with increasing Esc, radial bulging decreases and punching starts to become active.

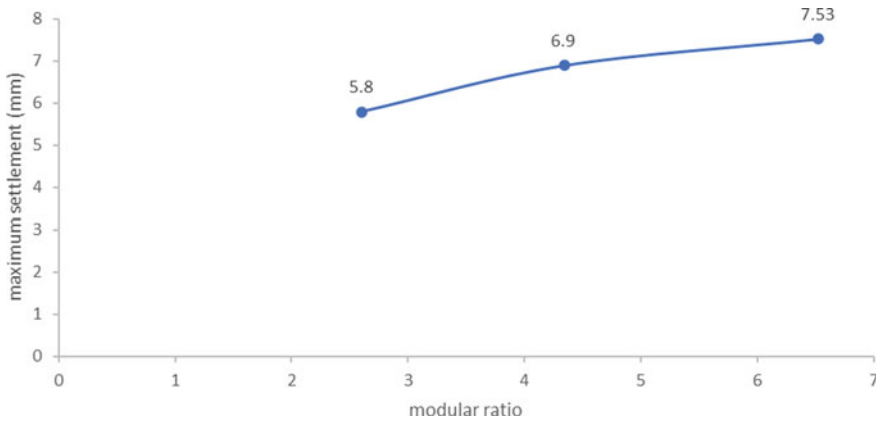

Fig. 10 Effect of modular ratio on settlement

5 Conclusions

1. For Cu = 30, 40 and 50 kPa, the SCR increased rapidly between L/D ratio 4 to 5. Also, increase in the Cu increases load-carrying capacity of the column.
2. With the increasing value of ϕ, the depth at which passive resistance becomes zero, also deepens. While increment of ultimate settlement is quite linear and ultimate load carrying capacity has also increased initially with mild slope and later slope becomes steeper.
3. It is observed that for the first 8000 kPa increment in Esc, settlement increased by 18.96%, while for the next 8000 kPa, stress increased by 9.13% only.
4. When Esc increases, the vertical settlement at any instant and the ultimate settlement corresponding to a load increases. Though maximum load isn't much affected, ground heaving (occurring at 2.7D away) kept on reducing and punching was seen to be arising.

References

1. Balaam, N.P., Booker, J.R.: Analysis of rigid rafts supported by granular piles. Int. J. Numer. Anal. Meth. Geomech. **5**, 379–403 (1981)
2. Alamgir, et al.: Deformation analysis of soft ground reinforced by columnar inclusions. Comput. Geotech. **18**(4), 267–290 (1996)
3. Poorooshasb, H.B., Meyerhof, G.G.: Analysis of behavior of stone columns and lime columns. Comput. Geotech. **20**(1), 47–70 (1997)
4. Fattah et al.: Stress concentration ratio of model stone columns in soft clays. Geotech. Test. J. ASTM **34**(1), 61–71. Paper ID GTJ103060 (2011)
5. Madun, A., Meghzili, S.A., Tajudin, S.A.A., Yusof, M.F., Zainalabidin, M.H., Al-Gheethi, A.A., Md Dan, M.F., Ismail, M.A.M.: Mathematical solution of the stone column effect on the load bearing capacity and settlement using numerical analysis. J. Phys: Conf. Ser. **995**, 012036 (2018). https://doi.org/10.1088/1742-6596/995/1/012036
6. Naseer, S., Sarfraz Faiz, M., Iqbal, S., Jamil, S.M.: Laboratory and numerical based analysis of floating sand columns in clayey soil. Int. J. Geo-Eng. **10**(1) (2019). https://doi.org/10.1186/s40703-019-0106-6

Time-Dependent Response of Soft Soil Under Tilted Storage Tanks

Suhit Chakraborty and Amit Kumar Das

1 Introduction

Cylindrical storage tanks are often considered as one of the most important structures for continuing the proper functioning of the industries. Most of these storage tanks are cylindrical in shape. Storage tanks are often built in coastal regions, where, in general, soft marine clay soils are found. Many times, it was noticed that there was a differential settlement, distortion of the tank, and tilting of the structure occurred due to the poor soil condition. So, the design and construction of storage tanks are not only limited to superstructure but also need proper soil investigation. Moreover, since such kind of structure is operational for a long period so even after the construction of such structure, proper monitoring is required.

Many researchers have studied the behavior of a circular raft foundation considering the steel storage tanks. Brown and Paterson [1] investigated the failure history of oil storage tanks founded on sensitive marine clay to determine the suitable bearing capacity. D'Orazio and Duncan [2] studied the settlement of the steel tank and made an effort to determine the tolerable limit of differential settlement. Also, they defined three different settlement profiles of the steel tank. Berardi and Lancellotta [3] conducted a study on oil tank settlement due to the yielding of soil. For this they considered the Critical State concept and plasticity model to incorporate soil behavior. Zanjani et al. [4] performed numerical analysis and compared the settlement of the steel tanks with available codes by keeping the ratio of tank diameter to height of order four and by varying slenderness ratio. Mistrikova and Jendzelovsky [5] performed the analysis of the circular symmetric tanks resting on elastic subsoil. The authors considered concrete storage tanks and simulated foundation soil with different constitutive models to observe the effect on the deformation of soil. Ramdane et al. [6]

S. Chakraborty · A. K. Das (✉)
Department of Civil Engineering, NIT, Silchar, Assam 788010, India
e-mail: amitkdas@civil.nits.ac.in

C. N. V. Satyanarayana Reddy et al. (eds.), *Dynamics of Soil and Modelling of Geotechnical Problems*, Lecture Notes in Civil Engineering 186,
https://doi.org/10.1007/978-981-16-5605-7_16

performed the case study of the settlement of oil storage tanks located in the marine terminal of Bejaia. Hotala and Ignatowicz [7] studied the settlement under steel tanks with different foundation arrangements. Deb and Das [8] and Das and Deb [9, 10] also addressed soft soil engineering related to concrete rafts and storage tanks.

Most of this research work was performed considering the steel storage tanks. Also, a study was conducted to check for the differential settlement of steel tanks on the untreated ground. But alongside differential settlement, it is also required to study the tilting phenomenon of the tanks. Moreover, it is also very important to find the reason behind the tilting as well as to analyze the changes in the response of soft soil with time. Thus, the present study investigates the time-dependent behavior of soft foundation soil under tilted cylindrical storage tanks considering the foundation of the storage tank as a circular raft.

2 Modeling

In the present work, a hypothetical soil profile is considered for the numerical analysis to study the tilting and differential settlement of storage tanks. Numerical analysis is performed using finite element software package Plaxis 3D. Details of the soil layers and soil properties of each layer considered for the numerical model are shown in Table 1.

The diameter of the circular raft is assumed as 20 m and it is made of concrete with unit weight, $\gamma = 25$ kN/m^3 and Young's Modulus, $E = 31 \times 10^6$ kN/m^2. The Height of the tank is assumed as 6 m. The overall surcharge acting on the raft due to stored material is considered as 60 kN/m^2. Ultimate bearing capacity of footing resting on stratified soil layer is determined for the case considering top soil is dense sand and bottom soil layer is saturated soft clay [11]. It is found to be safe. There may be different reasons for tilting of structures of which one of the main reasons is expected to be variable soil layer thickness beneath the structure. In the case of large structures like storage tanks, there is a high possibility of change in soil layer thickness beneath the structures. If this soil layer of variable thickness is weak and

Table 1 Soil profile and properties used in the present study

Layers	Soil	Parameters
First	Sand	$c = 0$ kN/m^2, $\phi = 30^\circ$, $E = 30{,}000$ kN/m^2, $\gamma = 16$ kN/m^3, $e = 0.7$, $\mu = 0.3$, $k = 8.64$ m/day, $S = 0$
Second	Soft clay	$c_u = 10$ kN/m^2, $\phi = 0^\circ$, $E = 300c_u$ kN/m^2, $\gamma = 17$ kN/m^3, $e = 1.2$, $\mu = 0.4$, $k = 0.000864$ m/day, $S = 1$
Third	Rock	$c = 20$ kN/m^2, $\phi = 45^\circ$, $E = 150{,}000$ kN/m^2, $\gamma = 21$ kN/m^3, $e = 0.15$, $\mu = 0.15$, Non-Porous

c = cohesion of soil, ϕ = friction angle, E = modulus of elasticity, μ = Poisson's ratio, e = void ratio, γ = unit weight of soil, k = permeability, S = saturation of soil

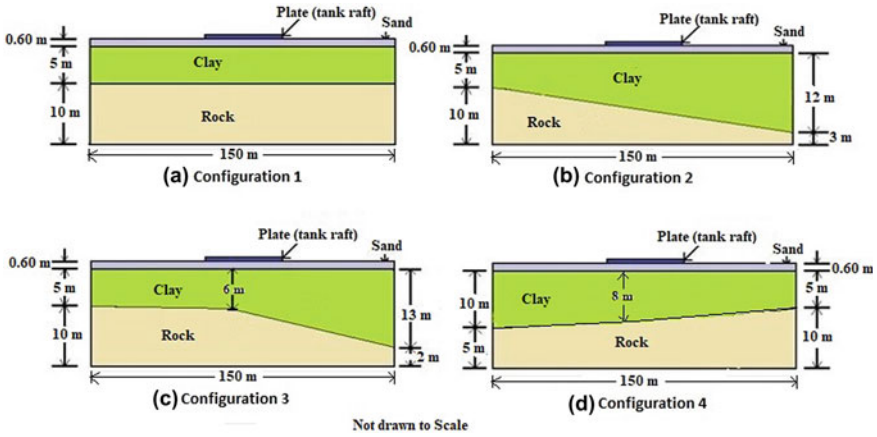

Fig. 1 Cross-sectional view of four different soil profiles

compressible, then differential settlement and tilting are expected to occur. Four different cases of soil profiles with or without variation in thickness are configured, as shown in Fig. 1, for numerical analysis to evaluate the tilting of the structure.

Initially, convergence study is performed using coarse, medium, and fine meshing and medium meshing is found satisfactory enough. The medium meshing technique is adopted for the analysis with 133,630 elements and 208,254 nodes. Ten-noded tetrahedral elements for the 3D soil model and 6-noded triangular elements for raft simulated by plate are used in the numerical model. Soil layers in the numerical models are simulated using Mohr–Coulomb constitutive model. In all the numerical models, side boundaries are partially fixed, while the bottom is fully fixed and the top surface is free. The numerical modeling in Plaxis 3D is performed in five steps: gravity loading, placing of sand layer, construction of tank raft, loading, and consolidation. All the steps, excluding gravity loading, are kept under the consolidation stage considering consolidation of soil a continuous process starting from the construction of tank to loading with surcharge. Among the four configurations mentioned in Fig. 1, configuration 3 is selected for the study of the time-dependent behavior of the tilted structure. The model prepared in Plaxis 3D for time-dependent study with configuration 3 is shown in Fig. 2.

3 Validation of Numerical Model

In order to validate the numerical model developed in Plaxis 3D, a case study is selected from Ramdane et al. [6] and the results obtained are compared. Ramdane et al. [6] presented a case of the settlement of hydrocarbon liquids storage tanks located in the marine terminal of Bejaia. After 25 years of construction of tanks, a differential settlement, ovalization, and tilting occurred in few tanks. Figure 3 shows

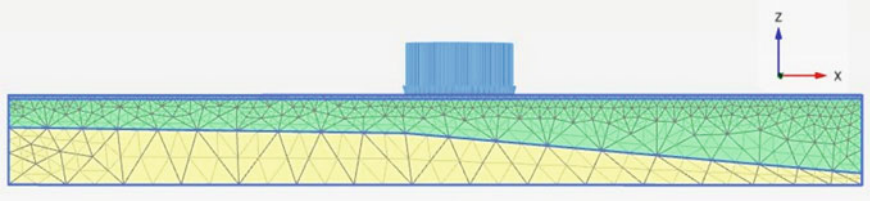

Fig. 2 Numerical model developed in Plaxis 3D with configuration 3 soil profile for time-dependent analysis

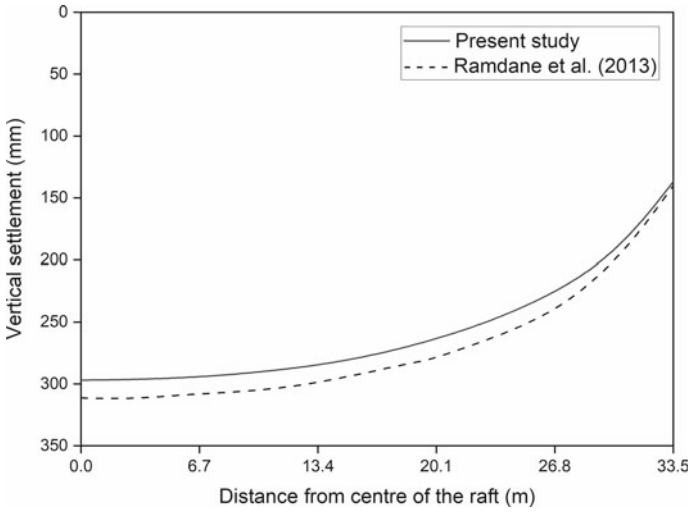

Fig. 3 Comparison of vertical settlement between results obtained from the present study and Ramdane et al. [6]

the vertical settlements reported by Ramdane et al. [6] and the same obtained from the numerical model developed in Plaxis 3D. The results show good agreement.

4 Results and Discussion

Figure 4 shows the vertical settlement profile of raft for different soil profile configurations (as shown in Fig. 1) just after the application of surcharge load. Further settlement takes place with the consolidation of soil. The tilting behavior of storage tanks under different configurations is observed, excluding configuration 1, even at this stage, when major consolidation is yet to occur. In the case of configuration 1, where each layer has a uniform thickness, only differential settlement is observed. This differential settlement is measured as the difference in the vertical settlement

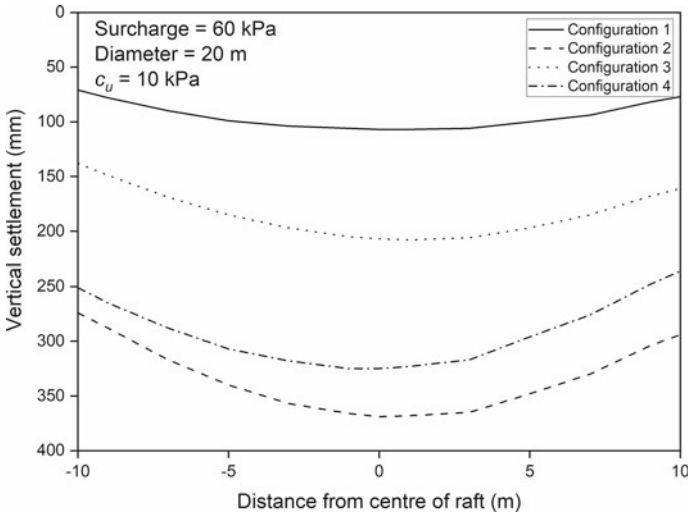

Fig. 4 Vertical settlement profile of raft for different soil profile configuration

between the edge and center of the raft, which is expected if the raft is flexible. At this stage, in configuration 2–4, the amount of tilting (difference in the vertical settlement between two opposite edges) is 20 mm towards the right side, 23 mm towards the right side, and 15 mm towards the left side, respectively. It may be noted that the tilting is higher in the case of configuration 3 despite the settlement is lower than configurations 2 and 4.

Figure 5 shows vertical settlement for configuration 3 soil profile at different times after application of the surcharge load. The results of the time-dependent analysis show that the raft is tilted by 23 mm up to the loading step of the analysis. The analysis is then continued for further consolidation. Consolidation steps are further subdivided into different steps in order to monitor the settlement behavior of the raft. Finally, settlement up to 90% consolidation data is noted. It is observed that there is an increase in tilting of the tank with further consolidation and after 90% consolidation tilting of the raft is 105 mm. Therefore, ultimate tilting is almost 4.5 times the initial tilting observed just after the application of the surcharge.

Parametric studies are performed to observe the effect of different important factors on the tilting of the structure. In parametric studies, other parameters are kept unchanged, while tilting is studied for variation of any one parameter. Figure 6 shows the effect of undrained cohesion (c_u) of soft clay on time-dependent change in tilting of the structure. The change in undrained cohesion, also indicates a change in stiffness of soil, since the value of modulus of elasticity (E) for clay soil also changes with undrained cohesion considering $E = 300c_u$. It is observed that with the increase in undrained cohesion of soft soil, as well as an increase in stiffness of the soil, tilting of the structure reduces. It is also observed that the tilting of the structure may become insignificant in stiffer soil.

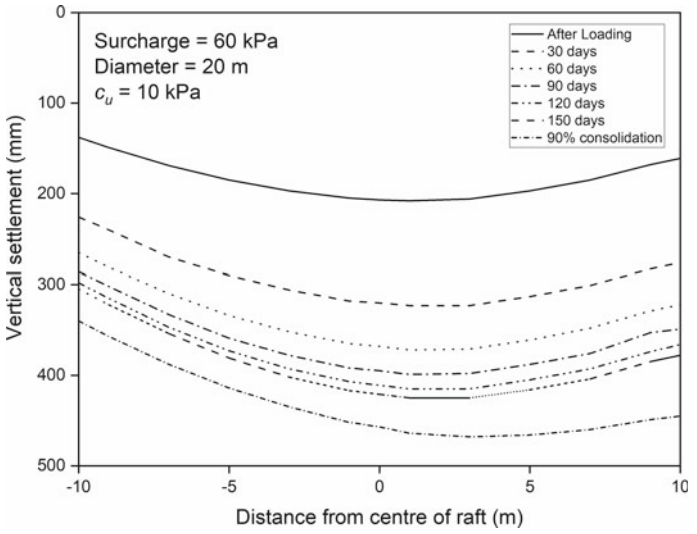

Fig. 5 Vertical settlement profile of the raft at different times after application of surcharge for configuration 3 soil profile

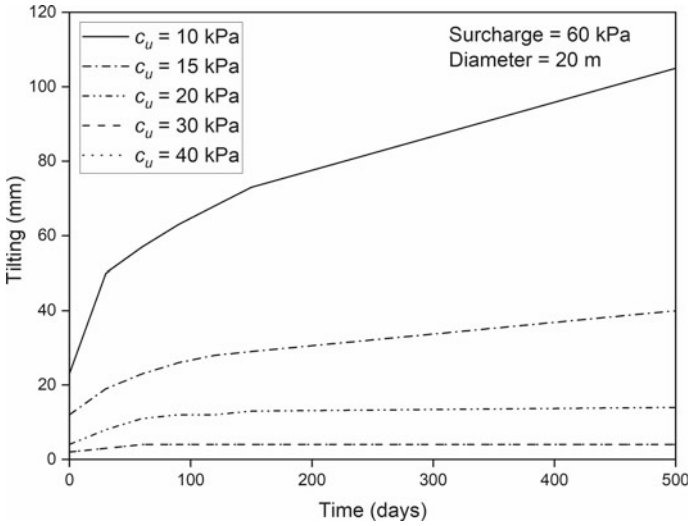

Fig. 6 Tilting of the raft for different undrained cohesion (c_u) of soft soil

The effect of the intensity of surcharge on time-dependent change in tilting of structure is presented in Fig. 7. In this study, undrained cohesion of soft clay (c_u) is considered as 15 kPa to ensure safety against bearing failure. It is observed that the increase in the intensity of surcharge causes an increase in tilting of structure. Tilting

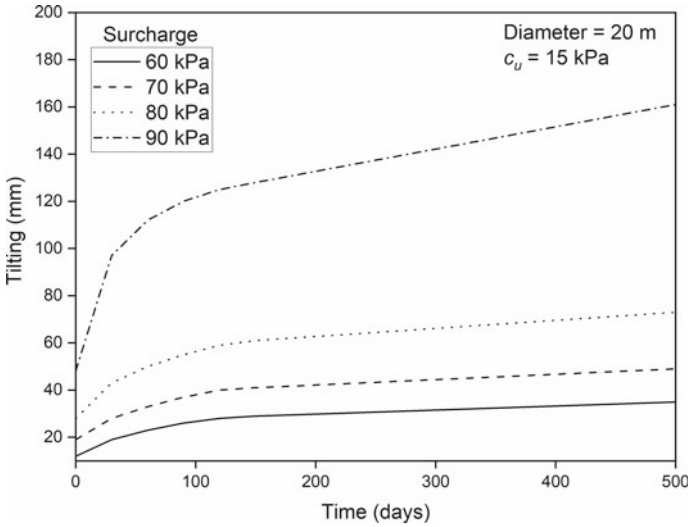

Fig. 7 Time-dependent change in tilting of the structure for different intensity of surcharge

reaches 3 times the initial tilting when the intensity of the surcharge is 60 kPa, but the same is 3.4 times the initial tilting as observed for the 90 kPa surcharge after 500 days. It is also observed that the possibility of ultimate tilting is higher when the intensity of surcharge is higher. In the present study, tilting is a function of the consolidation settlement, which increases non-linearly with surcharge intensity and time. Therefore, tilting is observed to increase disproportionately with an increase in surcharge intensity, because the rate of consolidation settlement increases with surcharge intensity, but decreases with time.

Figure 8 shows the change in tilting with time for different diameters of the raft. It shows that the smaller the raft diameter, the chances of tilting of structure reduces. The percentage decrease in tilting observed after 500 days is about 37% while the diameter of the raft changes from 20 to 15 m and the same for change in diameter from 20 to 10 m is about 80%. It is also observed that the change in tilting of the structure with time is almost linear for rafts of lower diameter, whereas the same is nonlinear when the diameter of the raft is large. Such change in tilting behavior may be attributed to the decrease in relative stiffness of the raft with an increase in diameter, while the thickness of the raft remains constant.

5 Conclusions

The present study shows that the tilting of structure should be studied as a function of time, otherwise the design of appropriate remedial measures may prove to be erroneous or ineffective. The following conclusions are drawn from the present study:

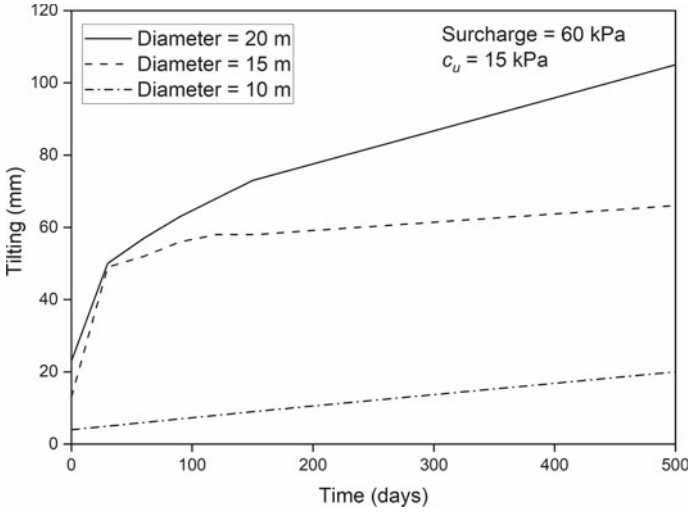

Fig. 8 Tilting of the raft with change in diameter of the raft

(1) Differential settlement may occur even in foundations resting on uniform soft soil, but tilting is governed by a change in thickness of compressible soil layer.
(2) Tilting of the structure increases with time as consolidation of the soil progress.
(3) With an increase in undrained cohesion of soft clay as well as stiffness of the soil, tilting of the structure reduces.
(4) Larger the diameter of the storage tank, the possibility of tilting is higher.

References

1. Brown, J.D., Paterson, W.G.: Failure of an oil storage tank founded on a sensitive marine clay. Can. Geotech. J. **1**(4), 205–214 (1964)
2. D'Orazio, T.B., Duncan, J.M.: Deferential settlement in steel tank. J. Geotech. Eng. **113**(9), 967–983 (1987)
3. Berardi, R., Lancellotta, R.: Yielding from field behavior and its influence on oil tank settlements. J. Geotech. Geoenviron. Eng. **128**(5), 404–415 (2002)
4. Zanjani, A.A., Fakher, A., Maddah-Sadatieh, S.R.: A numerical study on the effect of uneven settlements of oil storage tank. In: 2nd International Conference on New Developments in Soil Mechanics and Geotechnical Engineering, pp. 238–245. Near East University, Nicosia, North Cyprus (2009)
5. Mistrikova, Z., Jendzelovsky, N.: Static analysis of the cylindrical tank resting on various types of subsoil. J. Civ. Eng. Manag. **18**(5), 744–751 (2012)
6. Ramdane, B., Omar, S., Djahid, A.: Differential settlements of cylindrical steel storage tanks: case of the marine terminal of Bejaia. In: International Conference on Case Histories in Geotechnical Engineering, Paper No. 2.26, Chicago (2013)
7. Hotala, E., Ignatowicz, R.: Effect of settlement of foundations on the failure risk of the bottom of cylindrical steel vertical tanks for liquids. Studia Geotechnica et Mechanica **41**(3), 171–176 (2019)

8. Deb, K., Das, A.K.: Distribution of stress on stone column-reinforced soft soil under cylindrical storage tank. Appl. Mech. Mater. **567**, 699–704 (2014)
9. Das, A.K., Deb, K.: Modeling of uniformly loaded circular raft resting on stone column-improved ground. Soils Found. **54**(6), 1212–1224 (2014)
10. Das, A.K., Deb, K.: Response of cylindrical storage tank foundation resting on tensionless stone column-improved soil. International Journal of Geomechanics 17(1), Paper No. 04016035 (2017).
11. Murthy, V.N.S.: Principles and Practices of Soil Mechanics and Foundation Engineering. Marcel Dekker Inc., New York (2002)

Effect of Seepage Barrier in Steady Seepage Below Earthen Dam by Centrifuge Modeling

Smita Tung, Sibapriya Mukherjee, and Gupinath Bhandari

1 Introduction

The effect of seepage water flow causes loss of inter-particle force leading to a decrease in the skeleton stress which triggers dam failures as well as induced slope instability. According to the studies, approximately 41.6% of dam failures are related to internal erosion [1]. A comprehensive discussion on the mechanisms of piping and internal erosion in dams was presented by McCook [2]. Fell and Wan [3] presented methods for estimating the probability of failure of embankment dams by internal erosion, piping within the foundation, and piping from the embankment to the foundation. Cut-off walls are used to prevent seepage in dams as a long-term effective solution.

Approaches of centrifuge modeling have facilitated the evaluation of seepage and deformation in the embankments and are also considered a powerful tool to examine the failure mechanisms. Centrifuge modeling generates the real stress field and at the same time faster seepage flow. Centrifuge modeling is a technique that involves physical modeling to capture the correct failure mechanism in the boundary value problems with the help of digital cameras.

The basic principle of a geotechnical centrifuge is to enhance the gravity field by the same geometric factor N, relative to the normal earth's gravity field. In a

S. Tung (✉)
Assistant Professor, Department of Civil Engineering, GLA University, Mathura 281406, India

S. Mukherjee
Professor, Department of Civil Engineering, Jadavpur University, Kolkata 700092, India
e-mail: sibapriya.mukherjee@jadavpuruniversity.in

G. Bhandari
Associate Professor, Department of Civil Engineering, Jadavpur University, Kolkata 700092, India
e-mail: gupinath.bhandari@jadavpuruniversity.in

C. N. V. Satyanarayana Reddy et al. (eds.), *Dynamics of Soil and Modelling of Geotechnical Problems*, Lecture Notes in Civil Engineering 186,
https://doi.org/10.1007/978-981-16-5605-7_17

centrifuge, small-scale models are tested in a gravity field, which is a linear function of the distance from the center of rotation. Thus, the gravity field varies linearly with radius from the center of rotation and as a square of the angular velocity $\dot{\theta}$ of the centrifuge.

A seepage study was carried out for the western dyke of Wallace dam (Lake Oconee, Georgia, USA) by Aral and Maslia [4]. It was observed that the flow vector to the chimney drain showed that it was very effective in reducing seepage pressures.

Davies and Parry [5] conducted a centrifuge test to check the performance of low embankment founded on soft clay soil during and after the construction. They monitored displacement and pore pressure variation to observe the progressive failure. They carried out total and effective stress analyses of the embankment stability. The pore pressure studied increased as much as 18% after the end of the construction. Perri et al. [6] analyzed the influence of the pore water pressures in the calculated factor of safety of an embankment with and without cut-off wall in steady-state condition of full flooding stage using finite element method. They observed that using cut-off wall there was a significant decrease in seepage gradient and thereby an increase of Factor of Safety.

The present study has taken up a field problem in the Sunderbans region of West Bengal, India, where 3520 km of earthen embankments, used as protective structures of water heads of 3–4.5 m. The Sunderbans along the Bay of Bengal has evolved through quaternary sediments deposited mainly carried by the complex network of tidal rivers. It is part of the tide-dominated lower deltaic plain.

The purpose of this study is to find the effect of cut-off wall beneath an earthen dam for analyzing the failure by the use of centrifuge modeling as a tool. Experimental testing procedures were implemented as part of a recent centrifuge study undertaken to evaluate the performance of slopes at failure. In the experimental simulation, phreatic line, flow net, and stability against steady-state seepage in terms of factor of safety have been obtained. The effectiveness of sheet pile as seepage barrier, varying sheet pile length and position for all cases, have been studied, with the variation of sheet pile length of 5 m, 10 m, 15 m, and 20 m varying the sheet pile position at $B/8$, $2B/8$, and $3B/8$ positions from the downstream end, B being the width of the dam. It has been observed that sheet pile length has a significant effect on pore pressure variation along the sheet pile. It also evaluated by experimental modeling that seepage failure is more likely to occur at the bottom of cut-off walls because of the magnitude of high seepage velocity. The average seepage gradient of the embankment foundation decreases with the increase of the height of cut-off walls, and the seepage gradient at the bottom of cut-off walls is always maximum along the seepage contour line.

2 Model for the Study

The stratification of the subsoil of the selected area of South 24 Parganas, West Bengal, has been obtained from the study of bore log data sheets of different locations.

The cross-sectional details of the existing embankment of the typical model dam have been presented in Fig. 1. The study has been done for working head of 3.0 m in steady-state condition. Table 1 presents sheet pile properties for steady seepage and transient condition.

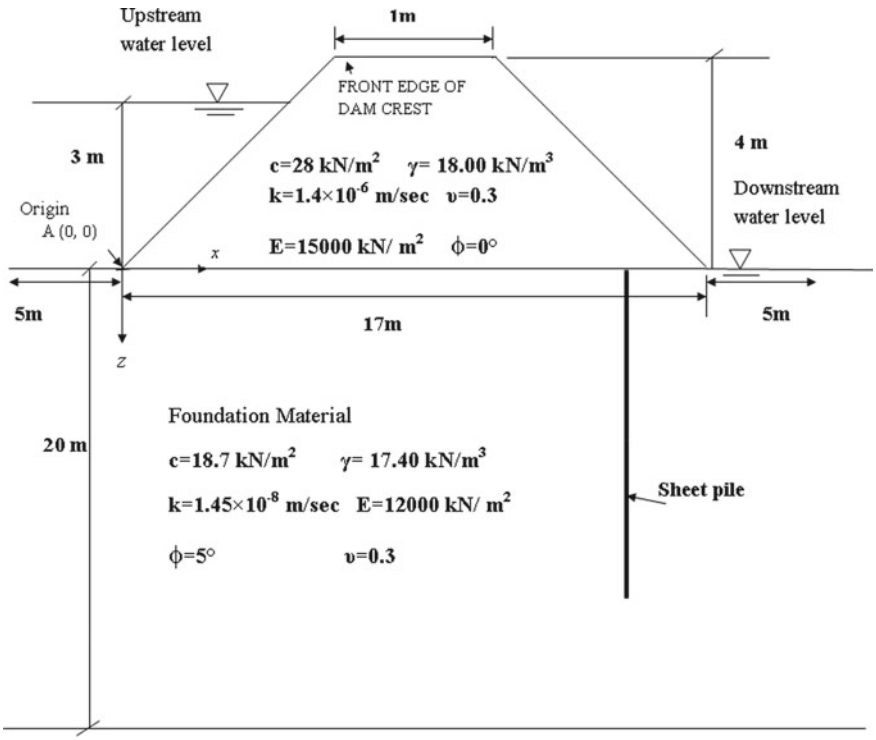

Fig. 1 Schematic diagram of the model embankment for centrifuge modeling

Table 1 Properties of sheet pile material

Area of cross-section per meter	0.03
Moment of Inertia per meter (N-m/m)	0.00225
E_{steel} (N/m^2)	2×10^{11}

3 Centrifuge Modeling

3.1 Description of Centrifuge

This geotechnical centrifuge at the Geotechnical Engineering Laboratory, Civil Engineering Department, Jadavpur, is a 4 pole 500 Hz induction motor with 3 phase system and of a 1.5 m radius with a maximum payload capacity of 8.5 tons at 400 g. The diameter of the centrifuge is 0.55 m. The turner beam carries a scaled model at one end and a counterweight at the other, each mounted on a swing platform has been described in Fig. 2. In the geotechnical centrifuge considering 100 g the calculated rpm is 404 rpm using Eq. (1).

$$\omega^2 R = ng \tag{1}$$

$$\omega = \sqrt{\frac{100 \times 9.81}{0.55}} = 42.23 \text{ rad/s} = 404 \text{ rpm} = 400 \text{ rpm (say)}$$

In centrifuge modeling, a rotating soil body is mounted on a geotechnical centrifuge to represent a scale model of a given prototype that is to be modeled.

The ratio of linear prototype dimension to the centrifuge model when N, then the ratio of area is N^2 and volume N^3. It has been indicated from the scaling relation that the forces in the prototype are N^2 times and moments N^3 of the corresponding model. In the experiment, it was necessary to design model wall to a similar stiffness of prototype per unit width (EI). The ratio of stiffness of the prototype is N^3 times that of the model. In the present study, N has been adopted as 100. The model was

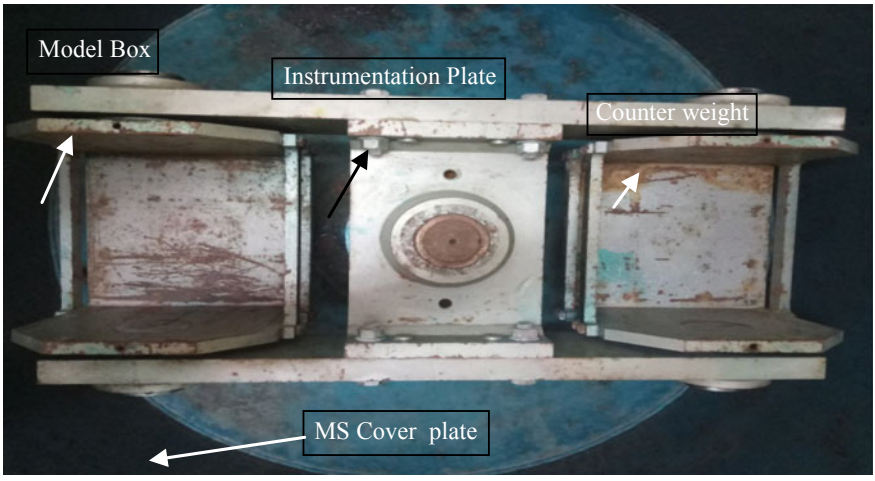

Fig. 2 Top view of the geotechnical centrifuge with component details

1/100 of the prototype linear dimension, and the model acceleration was 100 times of normal terrestrial gravity. In order to determine the true stiffness (EI) of the modeled sheet pile wall, $EI_{\text{model}} = EI_{\text{prototype}}/N^3$.

Steel sheet pile has been considered as prototype structure. Modulus of Elasticity of Steel Sheet pile ($E_{\text{prototype}}$) $= 2 \times 10^{11}$ N/m^2. Moment of Inertia per meter of steel sheet pile ($I_{\text{prototype}}$) $= 0.00225$ m^3. In the present seepage study, Perspex sheet has been used as modeled sheet pile. Modulus of Elasticity (E_{model}) of the Perspex $= 2.0 \times 10^9$ Pa. Moment of Inertia per unit width (I) of a rectangular cross-section is $\frac{(h')^3}{12}$, where h' is the section depth. In the present experimental study, 20 cm length of Perspex when modeled as sheet pile, Moment of Inertia per unit width (I_{model}) $= 2.49 \times 10^{-7}$ m^3/m.

$$EI_{\text{model}} = 2.0 \times 10^9 \times 2.49 \times 10^{-7} = 498 \text{ N-m/m}.$$

3.2 Experimental Setup

3.2.1 Test Box

The scaled model and the counterweight have been mounted at two ends of a swing platform. A seepage square tank has been fabricated with a steel frame, supporting a 10 mm thick transparent Perspex sheet on all sides to simulate three-dimensional conditions. The test box has dimensions of 26.7 cm (Length) by 26.7 cm (Width) by 26.7 cm (Height).

Water Supply Arrangement Using Valve

The reservoir has been placed above the top of the tank and the flow from reservoir to tank has been taken by virtue of centrifugal acceleration. In this study, Arduino ATMEGA 2560 board has been used to control the inlet and outlet valve. An artificial tide control circuit to provide an interface to complete the experimental work. The circuit has been processed by providing an internal energy source and has been controlled by an infrared remote.

Digital Image Processing

With the help of digital cameras, it has been possible to capture the digital image of the centrifuge model by mounting the camera on the model and viewing the cross-section through the transparent side. To fulfill the objective, Raspberry Pi 3B model has been used with a preinstalled Wi-Fi hardware module.

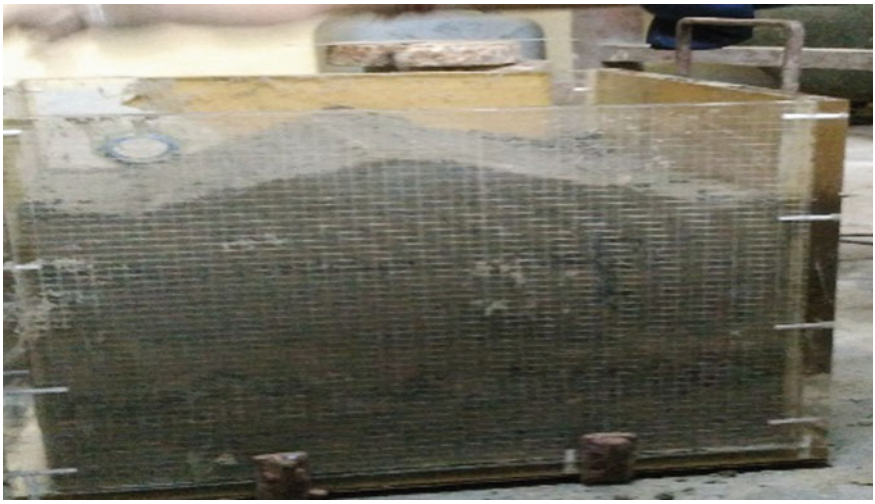

Fig. 3 Top view of the geotechnical centrifuge with component details

Construction of Model Embankment

Embankment model was formed as a typical earthen embankment with desired dimensions and properties and a centrifuge scale of $N = 100$ has been shown in Fig. 3.

A 20 cm thick bed was constructed in five layers was achieved by blows from a Standard Proctor Hammer of 4.5 kg falling over a height of 300 mm. The number of blows was adjusted as per the density requirement. The targeted density was 95% of Standard Proctor density. The Soil properties of the embankment as per IS classification is ML. The side slopes were kept at 2(H):1(V). Sheet piles were used as a cutoff in the experimental model in the centrifuge. Table 2 represents numerical analysis for the current study considering a variation of parameters of sheet pile length and positions under steady-state conditions.

4 Results and Discussion

During steady-state tests with a working head of 3.0 m, the flow net pattern has been shown in Fig. 4 for the embankment. The variation of the flow net in the upstream side with respect to the working head condition has also been shown in the respective figures. Points A, B, C, D, E have been marked with the progress of time to illustrate the propagation of flow.

Table 2 List of centrifuge modeling cases under steady state

Sl. no	Sheet pile length in meter	Sheet pile position from the downstream end
1	N.A	N.A
2	5	*B*/8
3	10	
4	15	
5	20	
6	5	2*B*/8
7	10	
8	15	
9	20	
10	5	3*B*/8
11	10	
12	15	
13	20	

Where B = Base width of dam. Based on the images obtained from the experiments, phreatic line and flow net has been obtained for each experimental model against steady-state seepage condition

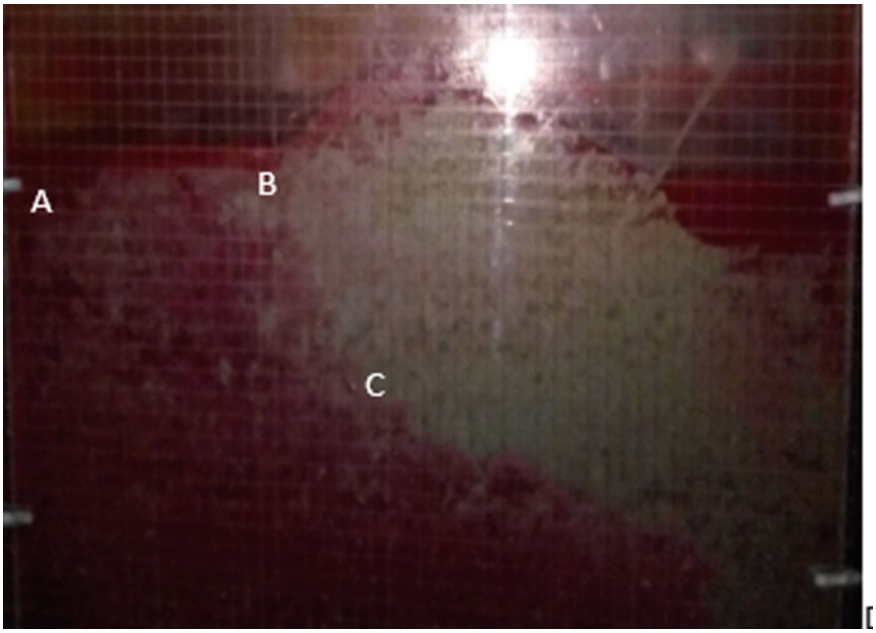

Fig. 4 Experimental output of embankment during steady-state condition without cutoff

4.1 Flow Net Pattern

An attempt has been made to observe the effect of location and length of sheet pile, used, as seepage cutoff. The results of the tests have been obtained by processing the captured image through MATLAB programming PIV High-resolution images that can be obtained from centrifuge model tests have been processed to give the fluid flow vector by Particle Image velocimetry (PIV) technique. PIV is a non-intrusive velocity field mapping technique that makes use of captured optical images to produce instantaneous vector measurements. Furthermore, PIV allows for the visualization of magnitudes and gives values the x–y components of velocity for the flow at different points, at different times in matrix form. The flow net has been developed for different cases under steady seepage conditions and also in different time intervals by image processing through PIV. The experimentally obtained phreatic surface, flow net, and pattern of fluid flow vector of an embankment has been shown in Fig. 5. The experimentally obtained typical phreatic surface, flow net, and pattern of fluid flow vector in an embankment for *B*/8 position 10 m length and 15 length sheet pile has been shown for in Fig. 7 and Fig. 8, respectively. A typical phreatic surface and flow net have been shown in Fig. 6 for the sheet pile at 3*B*/8 position 10 m length.

It has been observed from Figs. 6, 7, and 8 that that sheet pile acts as a fluid barrier effectively. It has been observed that as the Sheet pile moves away from the

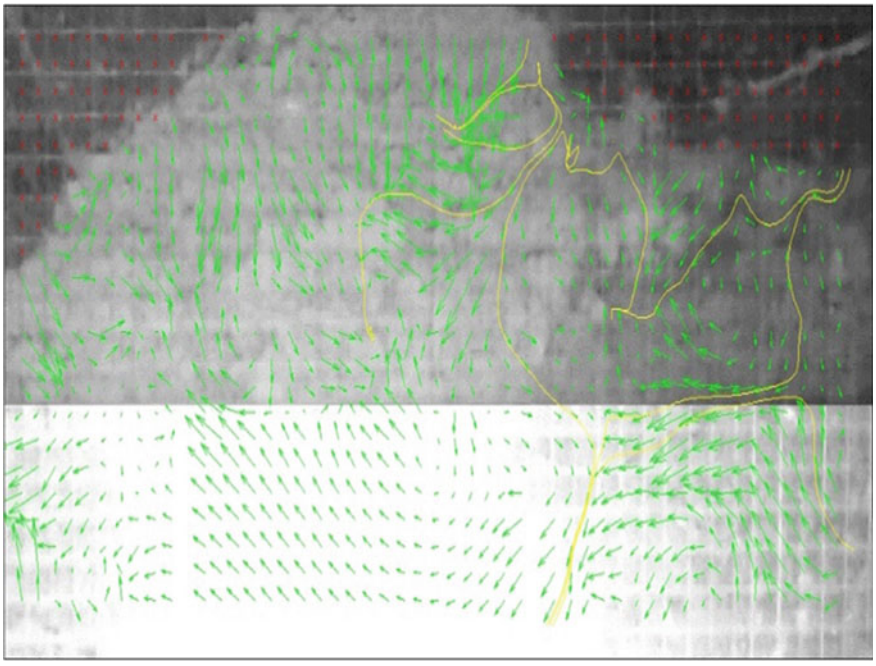

Fig. 5 Phreatic surface and flow net for steady-state condition

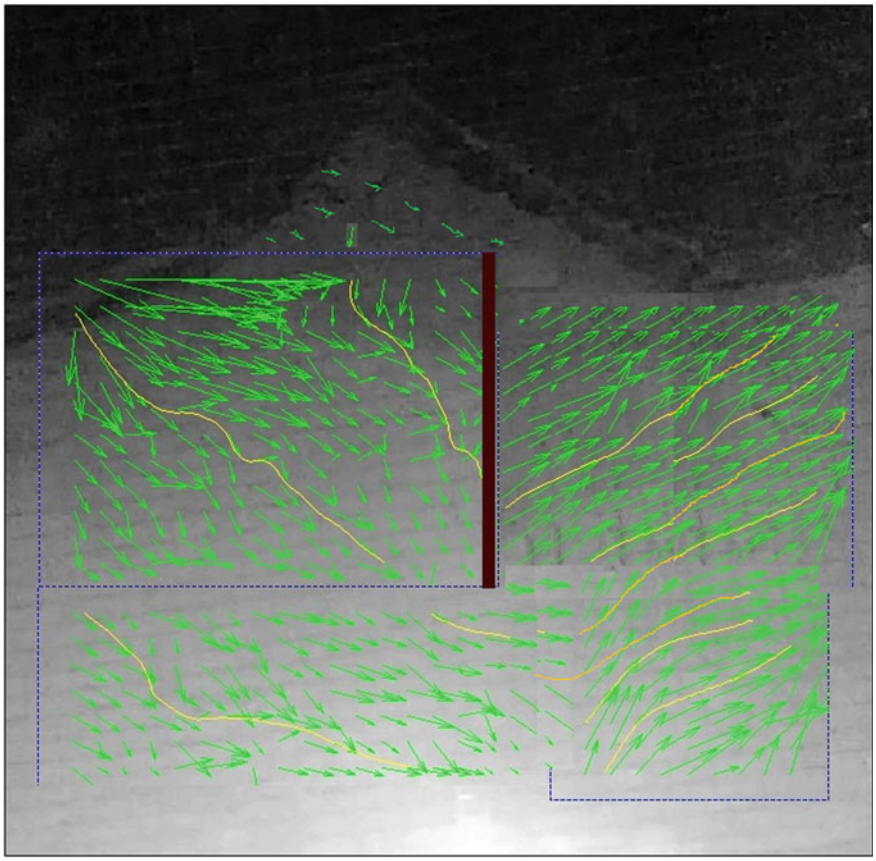

Fig. 6 Flow net and fluid flow vector for 3*B*/8 position 10 m long sheet pile

downstream end the field of the flow net near the downstream end is becoming more or more effective. When the sheet pile is shifted toward the downstream end, then the average dimension of the last element of the flow line is decreased. It also observed that for any fixed position when sheet pile length increases seepage path increases. It has been observed that for any fixed position of sheet pile exit gradient reduces with sheet pile length for any particular position of sheet pile. As sheet pile length increases seepage path increases which reduces the exit gradient. It has been observed when sheet pile length increases by 30% of the bottom width of the dam the exit gradient decreases to 9.97%. Furthermore, it evaluated that, If the sheet pile length increases 59% of bottom width of dam the exit gradient decreases by 18.16%. Therefore, from the modeling of seepage analysis, it is evaluated that if the sheet pile length increases 30–59% of the bottom width of the dam the exit gradient decreases of exit gradient is almost proportional to the pile length. From experimental modeling of seepage

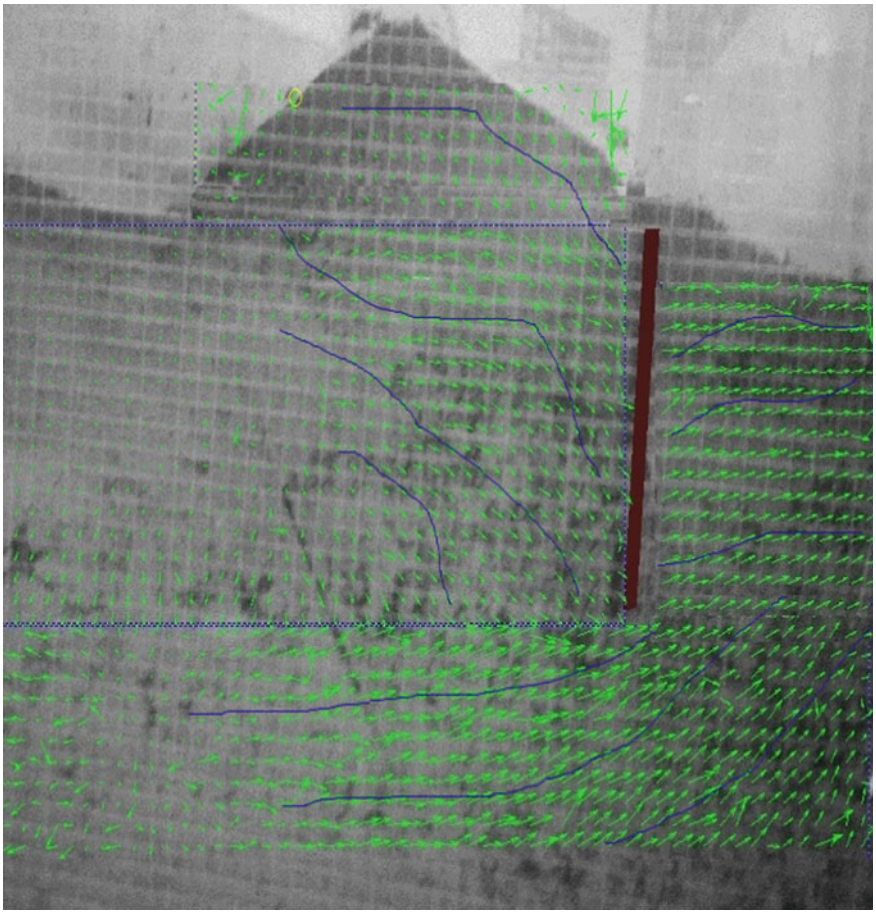

Fig. 7 Flow net and fluid flow vector for *B*/8 position 15m long sheet pile

analysis, it is evaluated that exit gradient decreases by 8.17% if the sheet pile position is shifted from 14.25% of the bottom width of the dam from the downstream end.

4.2 Fluid Flow Vector

An attempt has been made in this section to study the development of fluid flow vector with a variation of time without and with sheet pile depending on sheet pile lengths and positions. In each case, fluid flow vectors have been plotted along the horizontal profile at distances of 5 m from the top of the dam to study its variation within the dam body as well as the foundation of the dam. The purpose of this fluid flow vector study is to investigate the effectiveness of sheet piles against erosion

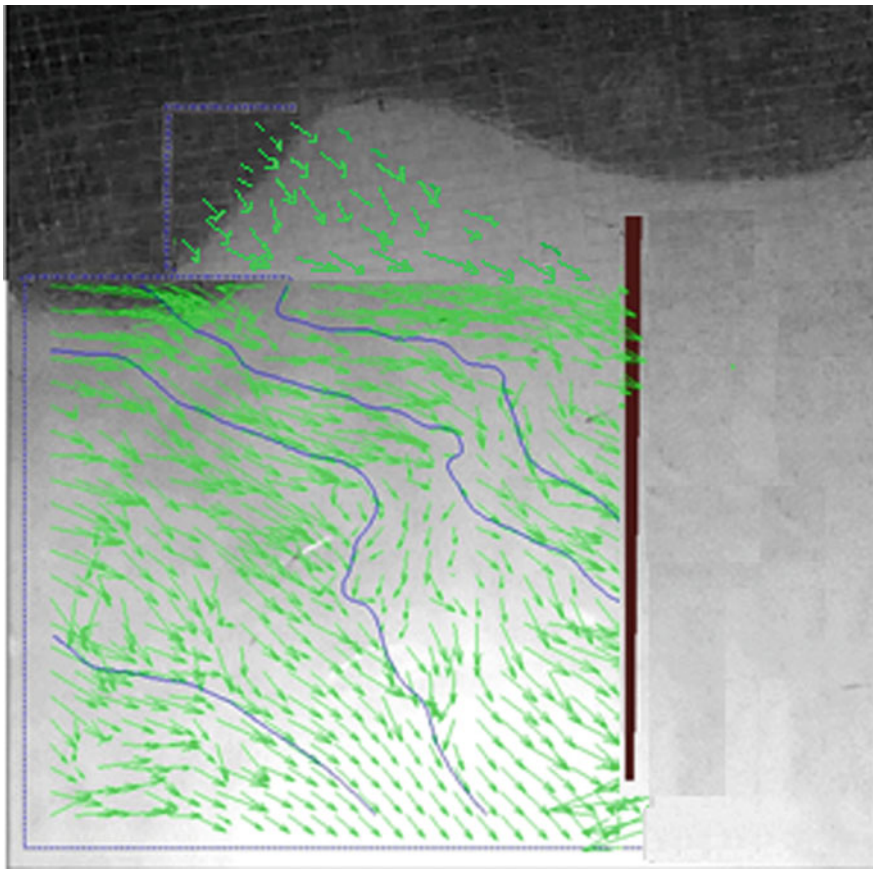

Fig. 8 Flow net and fluid flow vector *B*/8 position 10 m long sheet pile

caused by piping. Distance and velocity components in vertical direction have been plotted in the form of pixel/frame through PIV analysis.

Figure 9 represents a typical figure of fluid flow vector in pixel form analyzed by PIV for 10 m length of sheet pile positioned at *B*/8 position from downstream end along the horizontal direction. Figure 10 represents a typical figure of fluid flow vector analyzed by PIV for different length of sheet pile positioned at 3*B*/8 position from downstream end along the horizontal direction.

It is observed from Figs. 9 and 10 that maximum flow vector occurs at sheet pile position. This maximum value is highest for the 3*B*/8 position of sheet pile from the downstream end. For each case, the flow vector is increased at the sheet pile position indicating vertical flow along the sheet pile. The negative signs arise due to fluid flow in the downward direction along the length of the sheet pile. At the position of sheet pile, there is an abrupt jump of the fluid flow vector. At the upstream side of sheet pile, the fluid flow vector decreases along the length and at the downstream side of

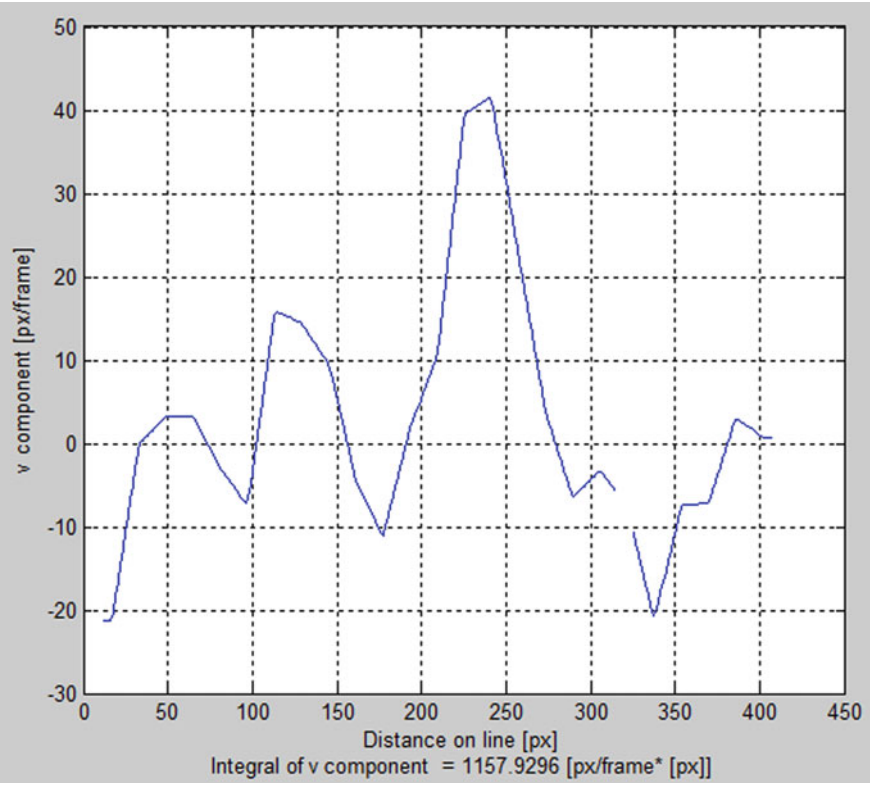

Fig. 9 Fluid flow vector in the vertical direction for sheet pile length 10 m at a fixed position of *B*/8

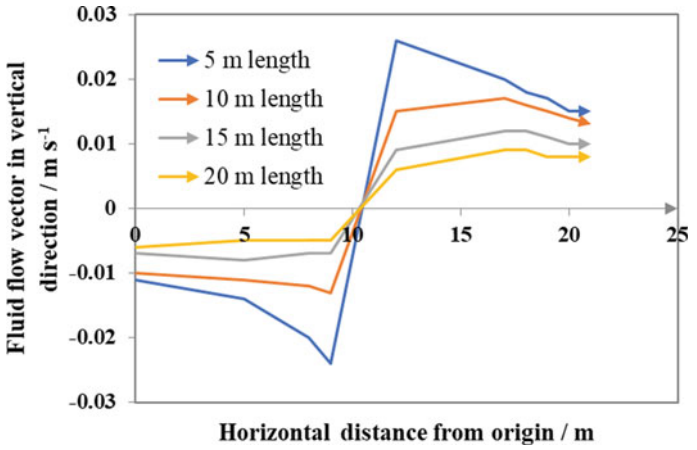

Fig. 10 Fluid flow vector in the vertical direction for different sheet pile lengths at a fixed position of 3*B*/8

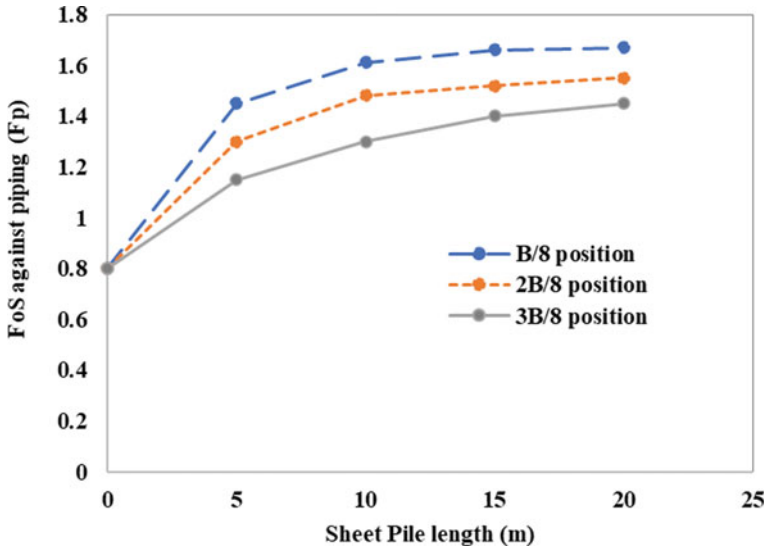

Fig. 11 Variation of the factor of safety with sheet pile position and length

sheet pile it increases with length. It has also been observed from Fig. 10 that the decrease of fluid flow vector for 20 m length of sheet pile on the downstream end is 30% less compared to 5 m length of sheet pile and 13% less compared to 15 m length of sheet pile at 3*B*/8 position. It has also been observed that the effect of sheet pile position on fluid flow vector on the downstream end is minimal.

4.3 Stability Against Piping

Figure 11 shows the variation of factor of safety against piping with sheet pile lengths at different positions.

It is observed that for a fixed sheet pile length, the factor of safety against piping decreases when the sheet pile position moves away from the downstream end. When sheet pile moves from downstream end, exit gradient increases and the chance of piping is reduced. As sheet pile position is shifted toward the downstream end, the average flow length of the extreme field of flow net at downstream end increases which causes a reduction in exit gradient. Thus, the factor of safety against piping increases. As sheet pile length increases seepage path increases, reducing the exit gradient and thus also reducing the chance of piping failure. A similar observation was made by Perri et al. [6]. For increase of the length of sheet pile, as creep length increases, exit gradient reduces and thereby factor of safety against piping increases. It has been seen that at 5 m of sheet pile at *B*/8 position factor of safety against piping increases up to 22.00% compared to 3*B*/8 position whereas this is approximately

18.18% for 2*B*/8 position, compared to 3*B*/8 position. It is also observed that factor of safety against piping increases by 20–30% due to increase in sheet pile length.

5 Conclusions

The following conclusions may be drawn from this present study:

1. Effectiveness of seepage cut off has been appropriately studied in centrifuge modeling through image-based analysis.
2. Sheet pile length increases the seepage path, which reduces the exit gradient. In case of an increase of sheet pile length by 30% of the bottom width of the dam the exit gradient decreases 9.97%. Furthermore, when sheet pile length increases 59% of the bottom width of the dam, the exit gradient decreases 18.16%.
3. Exit gradient decreases by 8.17% if the sheet pile position is shifted from 14.25% of bottom width of the dam from the downstream end.
4. For any fixed position when sheet pile length increases seepage path increases. Fluid flow vector decreases as sheet pile moves toward downstream end and it is maximum for least length and flow vector reduces with the increase of sheet pile length studied through experimental modeling.
5. Fluid flow vector for 20 m length of sheet pile on the downstream end decreases 30% less compared to 5 m length of sheet pile and 13% less compared to 15 m length of sheet pile for any particular position of sheet pile.
6. Factor of safety against piping decreases 18% when sheet pile position moves away from downstream end for a fixed sheet pile length. As the length of the sheet pile increases the factor of safety against piping also increases. In the case of piping, it is more predominant due to the increase in creep length. The factor of safety against piping increases by 20–30% due to an increase of sheet pile length.

References

1. Foster, M., Fell, R., Spannagle, M.: The statistics of embankment dam failures and accidents. Canadian Geotech. J. **37**(10), 1000–1024 (2000)
2. McCook, D.: A Comprehensive discussion of piping and internal erosion failure mechanisms. In: Proceedings of the 2004 Annual Association of State Dam Safety Officials, 1–6 (2004)
3. Fell, R., Wan, C.F.: Methods for estimating the probability of failure of embankment dams by internal erosion and piping-piping through the foundation and from embankment to foundation. UNICIV Report No R-436, The University of New South Wales, Sydney, 2052, Australia. ISBN: 85841 403 1 (2005)
4. Aral, Mustafa M., Maslia, Morris L.: Unsteady seepage analysis of Wallace dam. J. Hydraul. Eng. **109**, 809–826 (1983)

5. Davies, M.C.R., Parry, R.H.G.: Centrifuge modelling of embankments on clay foundations. Soils Found. **25**(4), 19–36, December 1985, Japanese Society of Soil Mechanics and Foundation Engineering (1985)
6. Perri, J.F., Shewbridge, S.E., Cobos-Roam D.A., Green, R.K.: Steady state seepage pore water pressures influence in the slope stability analysis of levees. In: GeoCongress, ASCE (2012)

Analysis of 3D Consolidation Settlement of C-ϕ Soil Using PLAXIS 3D Under Different Drainage Conditions

Arpan Laskar and Sujit Kumar Pal

1 Introduction

As the process of consolidation is governed by the different behaviors of soil, significant effort has been made to understand better how soils consolidate and what factors influence the process of consolidation. Karl von Terzaghi was the first to develop the analytical theory to explain and predict the process of one-dimensional consolidation in 1923 [1]. In his theory, he made use of several assumptions which may be applicable for many applications in geotechnical engineering; but in three-dimensional cases, it may not apply to the actual field conditions. In the consolidation theory of Karl von Terzaghi, there is an assumption that the ratio of the compressibility and hydraulic conductivity remains comparatively constant throughout the process of consolidation. This theoretical assumption is applicable for the soils which are relatively dense at the beginning of the consolidation process, such that their total volumetric strain is relatively small. Consolidation of soil having a high void ratio may not follow the constant material properties throughout the consolidation process.

During the progress of consolidation of soil, the void ratio changed with the change of depth, and so that the horizontal and vertical permeability of that soil gets changed. In the field, the soil under consolidation may have different soil characteristics corresponding to the variation of soil depth. As horizontal permeability and lateral movements of soil particles also have a significant effect on consolidation characteristics of the soil, considering horizontal permeability and lateral movements of soil particles, with vertical permeability and settlement of soil is very important to precisely predict the consolidation characteristics of the soil. So in this part of the study, a commercially available three-dimensional finite element software package called

A. Laskar (✉)
C.E. Department, Techno College of Engineering Agartala, Agartala, Tripura, India

S. K. Pal
C.E. Department, National Institute of Technology Agartala, Agartala, Tripura, India

C. N. V. Satyanarayana Reddy et al. (eds.), *Dynamics of Soil and Modelling of Geotechnical Problems*, Lecture Notes in Civil Engineering 186,
https://doi.org/10.1007/978-981-16-5605-7_18

PLAXIS 3D FOUNDATION is selected to determine the three-dimensional consolidation settlement characteristics of the soil. The linear elastic behavior of soil can be efficiently solved by the conventional method. However, most of the field-oriented problems show non-linear elastoplastic behavior rather than the elastic behavior of soil. A numerical computer program based on FEM is reasonable when the conventional method based on analytical solutions is incapable to solve the elastoplastic behavior of soil.

Over the years, by simulating the field conditions many investigators have presented their studies on the development of concepts for assessing consolidation characteristics. Biot [2] first introduced the general theory of 3D consolidation by considering coupling between solid and fluid. Different researchers had developed a different analytical solution based on Biot's 3D consolidation theory. Edelman [3] studied an analytical solution of consolidation taking the nonlinear characteristics of soil into account by assuming Young's modulus of soil, which varies linearly with depth but the permeability of the soil was assumed constant with depth. Skempton and Bjerrum [4] proposed a correction factor (μ) to bring three-dimensional consolidation effects in one-dimensional consolidation settlement. Hwang and Witczak [5] developed a numerical procedure for the probabilistic solution of consolidation of soils with multidimensional soil variability and water flow. Ai and Cheng [6] performed a numerical 3D consolidation analysis with an anisotropic permeability (k) of a layered soil system and shown the effects of anisotropy of permeability on the consolidation behavior of soil. Ai et al. [7] presented an analytical solution for 3D consolidation of a multi-layered porous medium with anisotropic permeability by using the transfer matrix method and they presented that the anisotropy of permeability had a great effect on the surface settlement. The wide use of computers and the parallel advances of numerical techniques have made possible more precise analyses. The variation of permeability with strain and the nonlinear behavior of the soil skeleton can now be simply taken into account.

2 Aim of the Study

In engineering practice, Terzaghi's [1] one-dimensional consolidation theory is used in most of the cases to calculate the settlement of soil. To determine the settlement of soil, most recently [2], the three-dimensional theory has been used, based on a linear stress–strain constitutive relationship and also a linear form of Darcy's flow rule. The wide use of computers and the parallel advances of numerical techniques have made possible more precise analyses. The variation of permeability with strain and the non-linear behavior of the soil skeleton can now be simply taken into account. The aim of this study is to evaluate the three-dimensional settlement of soil using a 3D consolidation apparatus and a commercially available three-dimensional finite element software package called PLAXIS 3D FOUNDATION and develop the ability for making a predictive simulation. The comparison of the numerical result to the result obtained from the presently developed three-dimensional consolidation apparatus is also bringing out in this study.

Table 1 Basic properties of soil

Soil properties	
Specific gravity (G)	2.60
Liquid limit, LL (%)	53.35
Plastic limit, PL (%)	29.32
Plasticity index, PI (%)	24.03
Sand (4.75 > 0.075 mm), (%) Silt (0.075 > 0.002 mm), (%) Clay (<0.002 mm) (%)	4.86 41.46 53.68
Classification of soil as per IS	CH
Optimum moisture content, OMC (%)	25.75
Maximum dry density, MDD (kg/m^3)	1560
Coefficient of permeability at MDD (m/s)	3.39E-10

3 Soil Properties

A C-ϕ soil is used in this study. Several tests are carried out to analyze this test material. Different properties of this soil are listed in Table 1.

4 Instrumentation

Figure 1 shows the design of a newly developed three-dimensional consolidation apparatus. In the following sections, the different parts of this present consolidation apparatus are discussed. In this study, this apparatus has been used to analyze 3D consolidation settlement of soil. This apparatus has been developed by the authors Laskar and Pal itself [8].

5 Experimental Results and Analysis

Three-dimensional consolidation tests are conducted on the above-mentioned soil, which is compacted at MDD and OMC. Figure 2 shows anisotropic flow directions of pore water through the soil under a three-dimensional consolidation test. Under these different five anisotropic flow conditions, 3D consolidation tests are conducted. The sample preparation and procedure of test are the same as explained in Laskar and Pal [8].

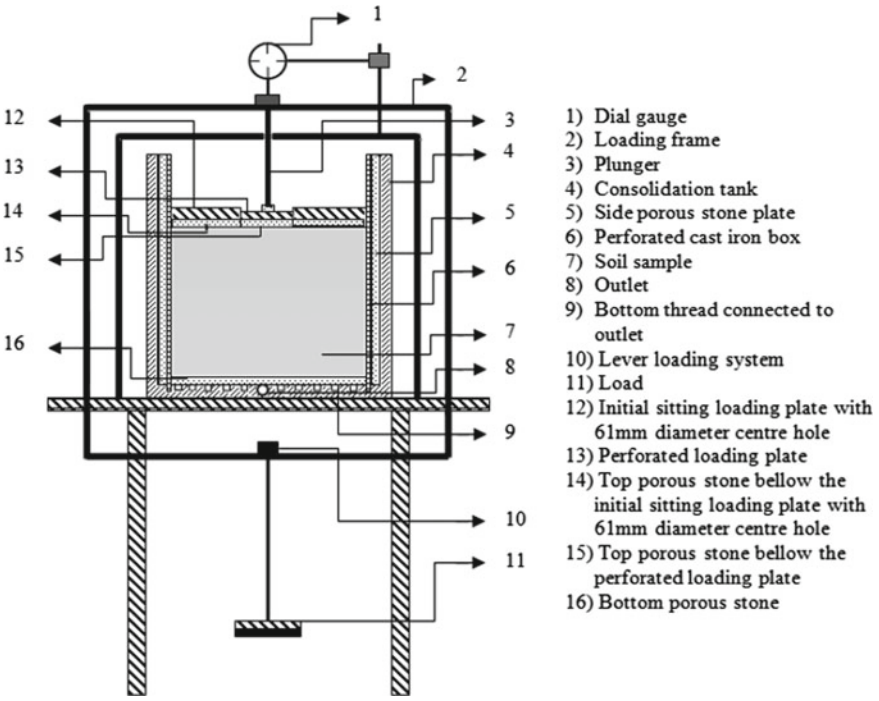

Fig. 1 Schematic diagram of the newly developed three-dimensional consolidation apparatus [8]

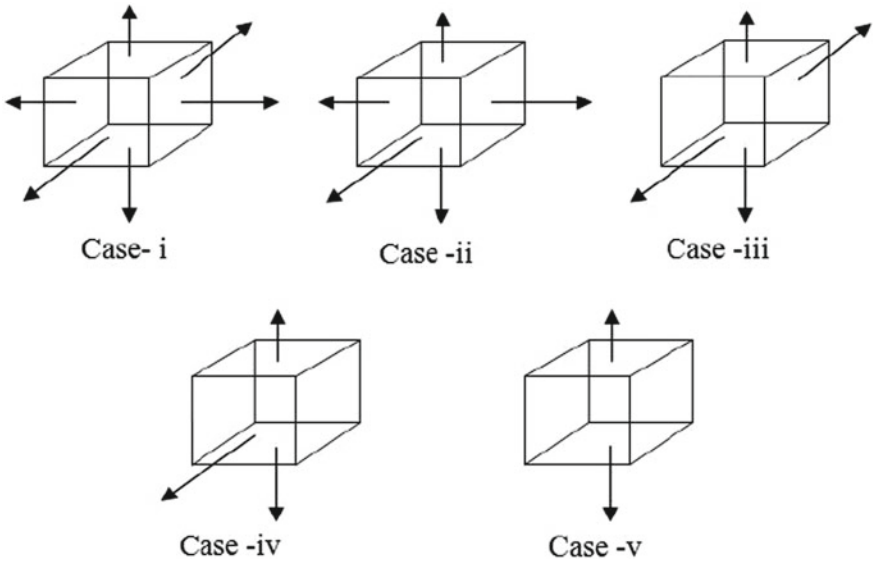

Fig. 2 Anisotropic flow direction of pore water through the soil under three-dimensional consolidation [8]

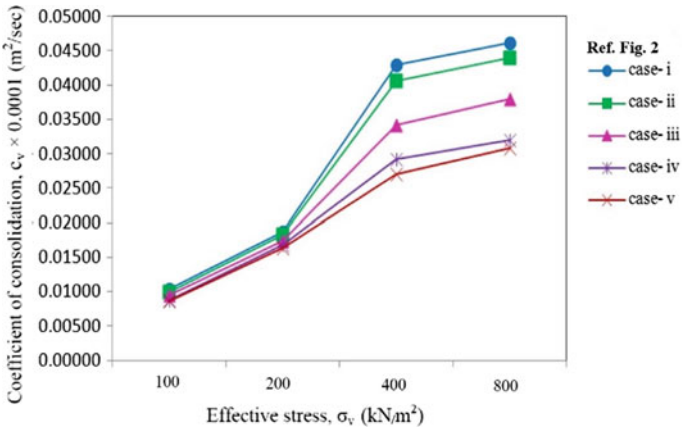

Fig. 3 Coefficient of consolidation of silty-clay soil under different radial flow conditions

5.1 Calculation of Rate of Consolidation Using Three-Dimensional Consolidation Apparatus Under Different Drainage Conditions

The coefficient of consolidation (c_v) has been calculated by three-dimensional consolidation apparatus under different boundary conditions. The evaluation method of the coefficient of consolidation (c_v) is same as Laskar and Pal [8]. The coefficient of consolidation (c_v) has been calculated under the following different drainage conditions as follows.

The coefficient of consolidation of silty-clay soil is measured under different flow conditions as shown in Fig. 2. Different anisotropic flow conditions are created using different consolidation cells. The effects of different flow conditions on the rate of consolidation of silty-clay soil are assessed and presented in Fig. 3.

5.2 Effect of Anisotropic Flow of Water on Three-Dimensional Consolidation Characteristics of Soil

In actual field conditions, in situ soils are not isotropic in all directions. These anisotropic characteristics of the soil, affect the direction of pore water flow. In some of the practical cases, it may have impermeable soil layers or stones on one or several sides of the foundation soil, and it affects the direction of extraction of pore water at the time of the consolidation process. Consideration of the effects of anisotropy radial pore water flow on the consolidation of soil is essential regarding the accurate prediction of consolidation properties. In this study, silty-clay soil compacted

at a maximum dry density (MDD) is used as a consolidative soil, and five numbers of 3D consolidation tests are conducted at different flow conditions as shown in Fig. 2. These 3D consolidation tests under different anisotropic flow conditions are conducted by the three-dimensional consolidation apparatus shown in Fig. 1. Five (5) different consolidation cells are used to generate different flow conditions at the time of the consolidation test. Figure 4 shows the surface settlements of the soil with different time intervals at different radial flow conditions and from this figure, it is observed that the settlements are considerably different during the process of consolidation of soil, but it is the same at the initial and final stages of settlement. As final settlements of the soil in all the 3D consolidation tests under different radial flow conditions are the same, the compression index values are identical for all the pore water flow boundary conditions. The anisotropic flow of water does not have any effect on initial and final surface settlements but has a significant influence on the surface settlement during the process of consolidation, and similar observation was also noticed by Ai and Cheng [6].

The anisotropic flow of water has a significant effect on the rate of consolidation of soil as shown in Fig. 3. From Fig. 3, it is observed that the coefficient of consolidation value is maximum at free flow in radial and vertical directions (Case-i of Fig. 2), but decreases with the increase of restraint in flow at radial directions. The coefficient of consolidation of any soil is purely based on the rate of expansion of pore water from that soil sample. As Case-i of Fig. 2 allows the flow of pore water through all the directions during the consolidation process, it shows a high rate of extraction of pore water compared to other Cases shown in Fig. 2; and that is why, Case-i showing the maximum coefficient of consolidation value and the Case-v showing the lowest coefficient of consolidation value, although the consolidative soil is identical for all the Cases.

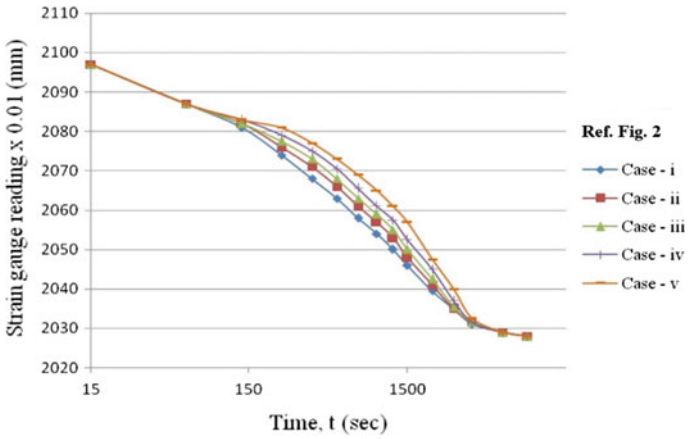

Fig. 4 Comparison of surface settlements at anisotropic radial flow conditions

6 Analysis of Settlement of Soil Using PLAXIS 3D Foundation

6.1 Three-Dimensional Consolidation Modeling Results

Consolidation settlements are calculated for silty-clay soil under the constant load of 200 kN/m^2. After completion of the calculation process, the result can be evaluated in the *output* program. In the output program, the displacement and stresses corresponding to the individual work plans and calculation phases can be viewed. Before applying the 200 kN/m^2 load, an initial seating pressure of 5.0 kN/m^2 is applied. Figure 5 shows the shadings of total displacements at the seating pressure stage under the load 5.0 kN/m^2 and Fig. 6 shows the shadings of total displacements under the load 200 kN/m^2. After the completion of calculation stage, the consolidation settlement under the load 200 kN/m^2 is 5.24 mm.

Elastoplastic Consolidation. When a non-linear material model is used, iterations are needed to arrive at the correct solution. Due to plasticity or stress-dependent stiffness behavior, the simple equilibrium equations are not necessarily satisfied. Therefore, the equilibrium equation is inspected here. Here equilibrium equation is written in the sub-incremental form

$$\underline{K}\delta\underline{v} + \underline{L}\delta\underline{p}_n = \underline{r}_n \tag{1}$$

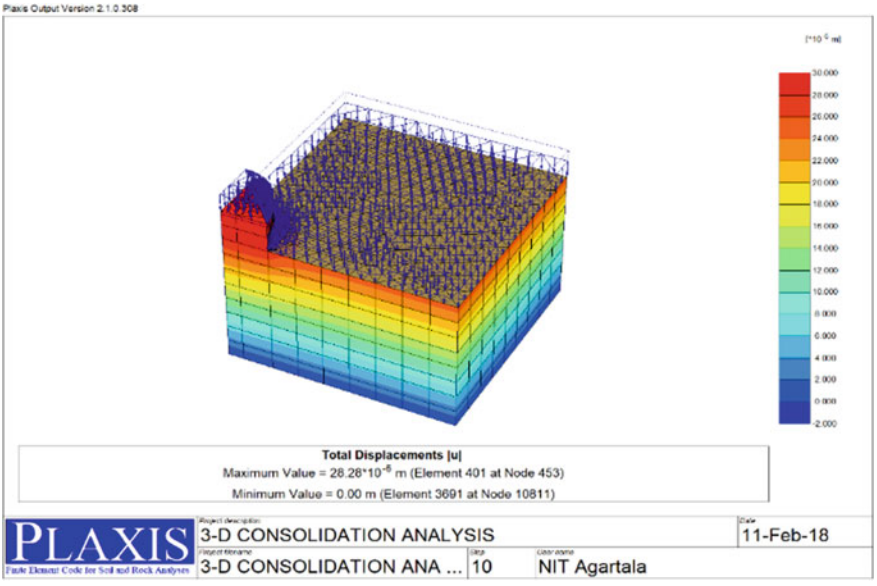

Fig. 5 Shadings of total displacements of silty-clay soil layer under the load 5.0 kN/m^2

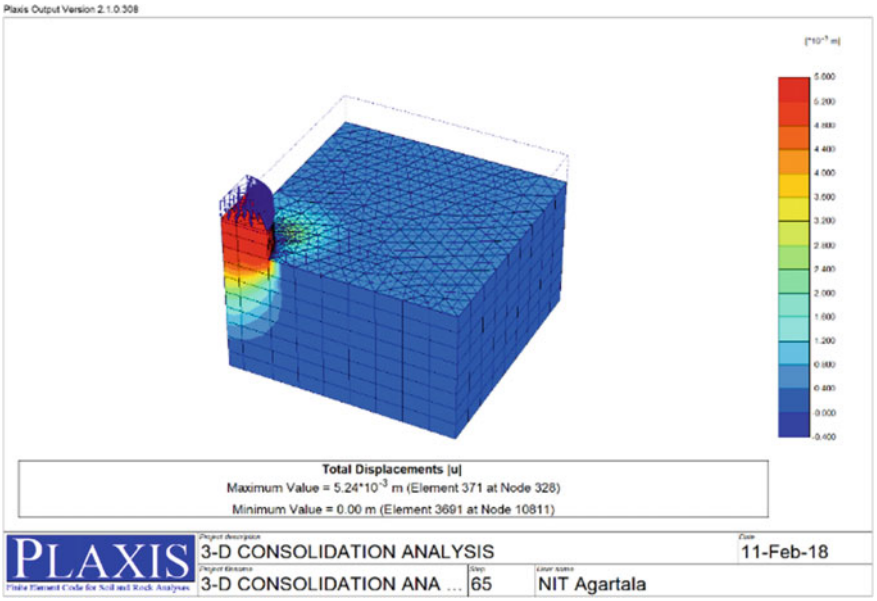

Fig. 6 Shadings of total displacements of silty-clay soil layer under the load 200 kN/m^2

where

$\underline{K}$ = stiffness matrix;
$\underline{v}$ = nodal displacement vector;
$\underline{L}$ = coupling matrix;
$\underline{P}_n$ = excess pore pressure vector;
$\underline{r}_n$ = global residual force vector.

The total displacement increment $\Delta\underline{v}$ is the summation of sub-increments $\delta\underline{v}$ from all iterations in the current step

$$\underline{r}_n = \int \underline{\underline{N}}^T \underline{b} dV + \int \underline{\underline{N}}^T \underline{t} dS - \int \underline{\underline{B}}^T \underline{\sigma} dV \tag{2}$$

With,

$$\underline{b} = \underline{b}_0 + \Delta b; \quad \text{and} \tag{3}$$

$$\underline{t} = \underline{t}_0 + \Delta \underline{t} \tag{4}$$

where

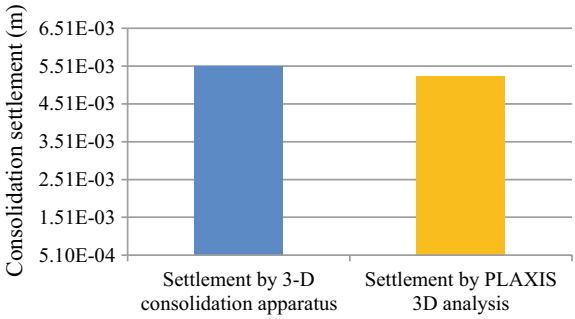

Fig. 7 Consolidation settlement values of silty-clay soil corresponding to 200 kN/m^2 load

$\underline{u}$ = continuous displacement vector within an element,
$\underline{N}$ = matrix contains the interpolation functions,
$\underline{B}$ = strain interpolation matrix,
$\underline{b}$ = body force due to self-weight, and
$\underline{t}$ = surface tensions.

In the first iteration, we consider $\underline{\sigma} = \underline{\sigma}_0$, i.e., the stress at the beginning of the step. Successive iterations are used on the current stresses that are computed from the appropriate constitutive model.

6.2 Comparison of Test Results

In this chapter, three-dimensional consolidation settlements of two different types of soils are analyzed by using FEM. After analyzing the three-dimensional consolidation settlement using PLAXIS 3D FOUNDATION software, a comparison study is performed between consolidation settlement results of different soils, evaluated by the presently developed three-dimensional consolidation apparatus, and numerical analysis by PLAXIS 3D FOUNDATION.

Figure 7 presens the consolidation settlement values of silty-clay soil corresponding to 200 kN/m^2 load. From this figure, it is observed that the consolidation settlement value obtains from FEM analysis is deflected by 4.73% from the settlement value obtained from the presently developed three-dimensional consolidation apparatus.

7 Practical Implications

The success of a study depends on the practical implication of the solution of that study. Following is the different implication of this study.

The conventional method of evaluation of settlement from the result of oedometer tests assumes that the soil only has a vertical strain and there will be no lateral strain, and it also assumes that the pore water dissipation only occurs in the vertical direction and there will be no radial drainage of water. The lateral confinement of the soil sample in the case of a one-dimensional oedometer test is taken to be representative of the actual soil conditions. Presently developed three-dimensional consolidation apparatus allows the vertical as well as horizontal movement of soil particles and it also allows the vertical as well as the radial flow of pore water during the consolidation process. In many practical cases, it was seen that the time taken for actual field soil settlement is much smaller than the predicted time of settlement by traditional oedometer test [9, 10]. In this regard, the newly developed three-dimensional consolidation apparatus is much efficient to predict actual field consolidation settlement.

8 Conclusion

The effects of the anisotropic flow of pore water on three-dimensional consolidation characteristics of the soil are obtained using a three-dimensional consolidation apparatus. Using the three-dimensional consolidation apparatus, the effects of five different anisotropic flow conditions of pore water on three-dimensional consolidation of soil are evaluated. The coefficient of consolidation (c_v) has been determined by comparing the relationship between elapsed time (t) in logarithmic scale and dial gauge readings of the soil sample in the laboratory to the hypothetical relationship (Taylor's method) between T_v and U.

The proposed solution permits to be solved the three-dimensional consolidation problem, with different boundary conditions. Experimental results indicate that the anisotropic permeability does not have any influence on the initial and final surface settlements, but it has a great influence on the surface settlement during the process of consolidation. The rate of consolidation of soil has been immensely affected by the anisotropic flow of water.

In this study, FEM-based numerical analysis of three-dimensional consolidation settlement is also performed. A comparative study is also performed between the resultant consolidation settlement of different soils, obtained by presently developed three-dimensional consolidation apparatus and FEM-based numerical analysis. From the comparison of the consolidation settlement results, it is observed that the deflections of numerical analysis results from experimental results are 4.73%.

References

1. Terzaghi, K.: Die Berechnung der Durchlassigkeitsziffer des Tones aus dem Verlauf der hydrodynamischenSpannungser-scheinungen. Stiz. Wiss. Math.-naturw., Abt. IIa, 132 Bd., 3. U.4.H (1923)
2. Biot, M.A.: General theory of three-dimensional consolidation. J. Appl. Phys. **12**(2), 155–164 (1941)
3. Edelman, T.: The consolidation of a layer which modulus of elasticity is proportional to depth. In: 3rd International Proceedings of the Conference of Soil Mechanics, vol. 1, p. 358, Zurich, Switzerland, August 1953
4. Skempton, A.W., Bjerrum, L.: A contribution to the settlement analysis of foundations on clay. Geotechnique **7**(4), 168–178 (1957)
5. Hwang, D., Witczak, M.W.: Multidimensional probabilistic consolidation. J. Geotech. Eng. **110**(8), 1059–1078 (1984)
6. Ai, Z., Cheng, Y.: 3-D consolidation analysis of layered soil with anisotropic permeability using analytical layer-element method. Acta Mechanica Solida Sinica **26**(1), 62–70 (2013)
7. Ai, Z.Y., Cheng Y.C., Zeng, W.Z., Wu, C.: 3-dconsolidation of multi-layered porous medium with anisotropic permeability and compressible pore fluid. Meccanica. Int. J. Theor. Appl. Mech. **48**(2), 491–499 (2013)
8. Laskar, A., Pal, S.K.: Investigation of the effects of anisotropic flow of pore water and multi-layered soils on three-dimensional consolidation characteristics. Adv. Mater. Sci. Eng. **2017** (2017). https://doi.org/10.1155/2017/8568953
9. Duncan, J.M.: Limitations of conventional analysis of consolidation settlement. J. Geotech. Eng., ASCE **119**(9), 1333–1359 (1993)
10. Leroueil, S.: Recent developments in consolidation of natural clays. Tenth Canadian Geotech. colloquium, Canadian Geotech. J. **25**(1), 85–107 (1988)

Studies on Centrifuge Modelling of Rainfall-Induced Landslides

Dipankana Bhattacherjee and B. V. S. Viswanadham

1 Introduction

Rainfall-induced instability of geotechnical soil structures is a serious global issue and deserves special attention. The problem aggravates if the backfill material of soil slopes, walls, and retaining earth structures is not adequately selected. Koerner and Koerner [1] reported that 68% of the 82 cases of reinforced soil-wall failures in their database were due to improper drainage control during rainwater infiltration. In general, slope failure and associated landslides are recognized as a natural and tangible process in a landscape, involving the rainfall history as well as local geology. Anderson and Sitar [2] reported that the mechanism of rainfall-induced slope failure involves a stress change caused by the hydrologic response of the slope to rainfall. The negative pore-water pressure in unsaturated soil is highly influenced by the external climatic conditions and flux boundary changes involving infiltration, evaporation, and transpiration. As per the findings of Fredlund and Rahardjo [3], the negative pore-water pressure contributes to imparting additional shear strength to unsaturated soils. As water infiltrates into the slope, positive pore water pressure in the slope increases, causing the additional shear strength due to matric suction to decrease and eventually disappear, thereby making the slopes vulnerable to failure. Full-scale modeling of natural and engineered soil slopes subjected to rainfall is warranted in this regard for a comprehensive understanding of the actual physical phenomena involved in the process. However, full-scale physical model tests are expensive, time-consuming, and difficult to replicate in case of a complex natural hazard like rainfall. At the same

D. Bhattacherjee (✉)
Department of Civil Engineering, Indian Institute of Engineering Science and Technology, Shibpur, Howrah, West Bengal 711103, India

B. V. S. Viswanadham
Department of Civil Engineering, IIT Bombay, Powai, Mumbai 400076, India
e-mail: viswam@civil.iitb.ac.in

C. N. V. Satyanarayana Reddy et al. (eds.), *Dynamics of Soil and Modelling of Geotechnical Problems*, Lecture Notes in Civil Engineering 186,
https://doi.org/10.1007/978-981-16-5605-7_19

time, small-scale physical modeling cannot predict the behavior of prototype slopes accurately owing to dissimilarities in stress levels and strains existing between the laboratory 1*g* model and the corresponding prototype. In such situations, geotechnical centrifuge modeling can be used as an effective tool for investigating the response of geotechnical structures during various rainfall events by subjecting the model to a centrifugal acceleration of magnitude *N* times greater (*Ng*) than that of earth's gravitational acceleration (1*g*).

The present study focuses on investigating the mechanism of rainfall-induced landslides in low-permeable soil slopes through a series of centrifuge model tests. The above soil type was selected as model soil in view of the acute scarcity of good-quality permeable granular material in recent times, which leads to the eventual use of low-permeability soils or marginal soils available locally at the site, as per the findings of Yoo et al. [4] and Pathak and Alfaro [5]. Three typical rainfall intensities of 10, 20, and 50 mm/h were simulated on silty sand slopes of 7.2 height with 7.5 m crest width, and 2 V:1H inclination, having an initial water table up to slope base. The results are interpreted in terms of crest settlements, face movement, deformed slope profiles, and phreatic surfaces developed during rainfall based on instrumentation data and digital image analysis.

2 Modelling Considerations

The basic principle of centrifuge modeling for geotechnical purposes is based upon the requirement of achieving identical stress fields in the model and prototype. This is achieved by developing appropriate scaling laws relating the model behavior to the corresponding prototype, as outlined in Schofield [6] and Taylor [7]. The model soil used during slope preparation is assumed to have an identical mass density as that of the prototype. However, unlike 1 *g* laboratory model, the centrifuge model slope is subjected to a high gravitational field (*N*g) during rotation about a vertical axis in a horizontal plane at a desired angular velocity denoted by ω. Thus, the centrifuge model is subjected to an inertial acceleration field of *N* times the earth's gravity, where *N* indicates the gravity level; the same as that of the geometric scale factor. The scale factor (model:prototype) for linear dimensions of the slope is thus 1: *N*. Since the model is a linear scale representation of the prototype, slope displacements will also have a scale factor of 1:*N*, and in accordance, strains are scaled by a factor of 1:1. Therefore, the stress–strain variation of the soil mobilized in a centrifuge model will be identical to that of the prototype. Rainfall is characterized primarily by its intensity and duration, and can be scaled at high gravities based on scaling factors derived for time and water flow under transient unsaturated conditions, as discussed in Caicedo et al. [8] and Bhattacherjee and Viswanadham [9, 10]. The relevant scaling factors involved in the modeling of rainfall-induced landslides in a geotechnical centrifuge is presented in Table 1.

Table 1 Scaling laws adopted in centrifuge modeling of rainfall-induced landslides

Parameter	Unit	Scale factor
Unit weight of soil (γ)	kN/m^3	N
Cohesion (c)	kPa	1
Co-efficient of soil friction (ϕ)	°	1
Co-efficient of soil permeability (k)	m/s	N
Pore water pressure in soil (u); Suction (ψ)	kPa	1
Slope inclination (β)	°	1
Slope height (H)	m	1/N
Duration of rainfall (t)	h	1/N^2
Rainfall intensity (r)	mm/h	N
Amount of rainfall (R)	mm	1/N
Impact pressure on ground (P)	Pa	1

3 Selection of Model Soil

In view of the significance of backfill material in controlling the performance of reinforced soil structures, special emphasis has been given to studies performed in low-permeable soils, and the detrimental effect of water on the performance of these structures. Zornberg and Leshchinsky [11] summarised the design criteria for geosynthetic reinforced walls, slopes, and embankments put forth by various world-wide agencies which limit the percentage of fines in backfill material preferably to within 15%. The Ministry of Road Transport and Highways (MORTH), Government of India specifies up to 10% fines, whereas The Federal Highway Administration (FHWA) allows up to 35% fines (passing 0.075 mm) in the reinforced soil zone. Accordingly, the model soil used in slope preparation was formulated in the laboratory to arrive at 20% fines by blending locally available fine sand and commercially available kaolin. The Goa sand is classified as SP according to USCS, whereas, the kaolin sample is classified as CL as per USCS, and consists predominantly of silt and clay in the ratio of 47% and 53%, respectively.

The blended silty sand is SM as per USCS, and consists of sand and kaolin in the ratio of 4:1 by dry weight with a saturated permeability (k_{sat}) of 1.54×10^{-6} m/s. The model soil is thus representative of the properties of locally available marginal soils which contain fines in excess of 15% and exhibit a saturated coefficient of permeability of $<1 \times 10^{-6}$ m/s, prescribed, respectively, by Christopher and Stuglis [12] and Holtz and Kovacs [13].

4 Model Preparation and Test Program

Centrifuge-based physical modeling was performed at 30 gravities on a representative silty sand slope of 240 mm height, 60 mm base layer, and 2 V:1H inclination, having a crest width of 250 mm. Tests were conducted using the 4.5 m radius beam centrifuge facility of 2500 g-kN capacity available at IIT Bombay, INDIA. The detailed specification of the centrifuge equipment is available in Chandrasekaran [14]. Rainfall was simulated using a custom-designed rainfall simulating assembly consisting of specially designed air-atomizing nozzles, nozzle hanging rods, nozzle assembly attaching plate, water container assembly, and a seepage tank. The water container was designed to act like a modified Mariotte's tube when filled with pressurized water at high gravities. Additionally, a solenoid valve was used to control the duration of rainfall during the centrifuge tests, and the excess water flowing as run-off was collected in a run-off collector. The calibration results discussed in Bhattacherjee and Viswanadham [9] indicate that the simulator is capable of producing fine mist at a uniform rate in-flight condition with intensities of 2–80 mm/h. In the present study, three typical rainfall patterns were simulated on slope models referred to as Model T1, Model T3, and Model T4. Model T1 was subjected to a low intensity but a lingering storm of 10 mm/h persisting for a longer duration, whereas Model T3 was subjected to a medium rainfall event of 20 mm/h similar to seasonal monsoon showers. Model T4 depicted an extreme case of short and intense cloudburst of 50 mm/h intensity, which can be associated with global warming and allied climatic changes. As per the classification system suggested by Llasat [15], the three rainfall events can be regarded as a light drizzle, moderate shower, and torrential rainfall respectively, thereby replicating all possible ranges of natural hazards.

An initial groundwater table was simulated in-flight up to the slope base at the onset of rainfall using the perforated seepage tank mentioned previously. The slopes were instrumented with four commercially available miniature Druck-PDCR-type pore pressure transducers (PPTs) placed above the base layer at distances of 20 mm (PPT4), 125 mm (PPT3), 250 mm (PPT2), and 350 mm (PPT1) from the perforated face of seepage tank in model dimensions. Further, L-shaped plastic markers made from thin transparency sheets of 20 mm $\times$ 10 mm dimensions were embedded within the slope front elevation and slope face to track displacements with the progress of rainfall. The various stages involved in the construction of slope models in the centrifuge are discussed elaborately in Bhattacherjee and Viswanadham [16].

5 Results and Discussion

The seepage and stability aspects of marginal slopes during the simulated rainfall event were analyzed using data recorded by pore-pressure transducers and through image analysis [17] of photographs captured in-flight. The results are discussed in subsequent sections and briefly summarized in Table 2. The results are presented in

Table 2 Summary of centrifuge test results

Parameter	Model T1	Model T3	Model T4
Intensity of rainfall (I) (mm/h)	10	20	50
[a]Time elapsed during rainfall (days)	33.75	9.375	3.75
[b]$u_{max}/\gamma H$	0.636	0.554	0.411
$S_{c,max}/H$	0.354	0.492	0.525
$S_{f,max}/H$	0.141	0.166	0.250

Note: All values are reported in prototype dimensions
[a]Time corresponding to the ultimate stage of the test
[b]$u_{max}/\gamma H$: Normalized pore pressure for PPT 4 placed at 350 mm from the slope toe; *h:* Height of slope; $S_{c,max}$: Max. crest settlement; $S_{f,max}$: Max. deformation along slope face; For all the tests, the water table is at slope base; $\beta = 63°$

this study up to the "ultimate stage" of test, which marks the time frame beyond which the observed slope deformations and recorded pore-water pressure values depicted negligible variations with the progress of rainfall. It thus represents the ultimate state of distress underwent by each individual model slope during rainfall.

5.1 *Deformed Slope Profiles with Progress of Rainfall*

The front elevation of slopes subjected to rainfall intensities of 10, 20, and 50 mm/h captured at various time intervals until the ultimate stage of centrifuge tests are presented in Fig. 1a–c, Fig. 2a–c, and Fig. 3a–c, respectively. Model T1 of 2 V:1H inclination subjected to a light rainfall intensity of 10 mm/h failed progressively, as shown in Fig. 1a–c, and instability occurred at the end of 54 min (33.75 days). A deep-seated face failure was encountered on account of deeper rainwater infiltration into the slope.

On the contrary, Model T3 subjected to a moderate rainfall intensity of 20 mm/h underwent a clear and distinct sliding failure about the toe at an interval of 15 min (9.375 days) of rainfall infiltration into the slope (Fig. 2a–c). Model T4 subjected to

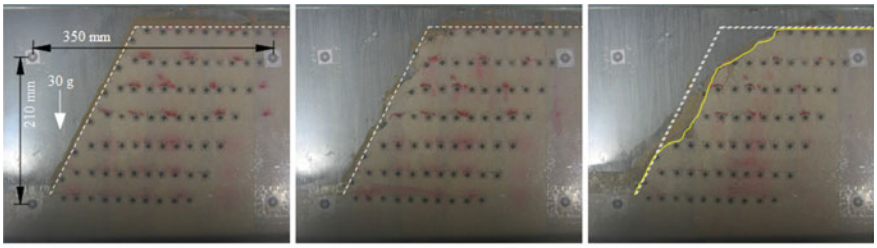

Fig. 1 Front elevation of model T1 [$I = 10$ mm/h] with the progress of rainfall

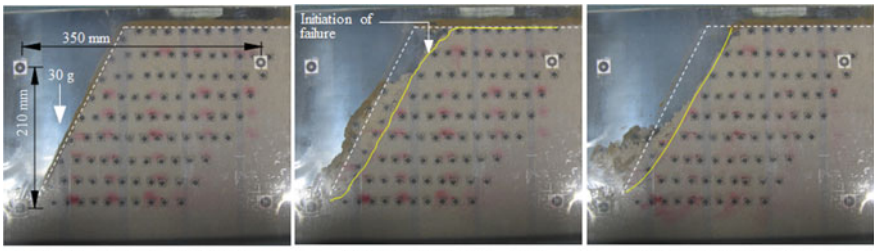

Fig. 2 Front elevation of model T3 [$I = 20$ mm/h] with the progress of rainfall

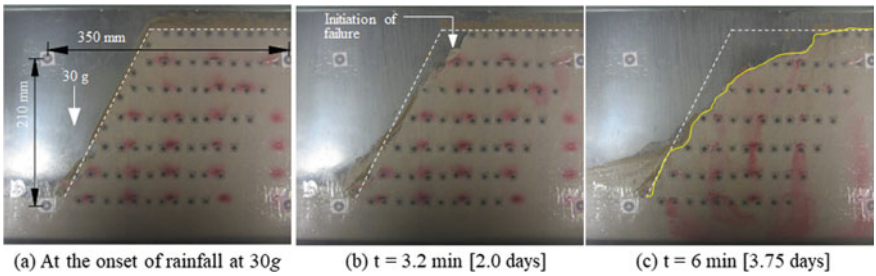

Fig. 3 Front elevation of model T4 [$I = 50$ mm/h] with the progress of rainfall

a heavy torrent of 50 mm/h failed catastrophically and instantaneously within 6 min (3.75 days) of rainfall due to extensive erosion, as depicted in Fig. 3a–c. The failure, in this case, resembled that of mass block sliding. This suggests the existence of a threshold rainfall intensity, beyond which rainwater can no longer infiltrate into the slope and disappears mostly as run-off. The type of slope failure is thus inferred to depend on the ratio of the saturated soil permeability to the input rainfall flux.

5.2 Crest Settlements and Slope Face Movements

Figure 4 presents the variation of crest movement with time for the entire duration of rainfall until the ultimate stage of the test. Model T1 subjected to a light rainfall of 10 mm/h exhibited a slow but steady increase in crest movements with time. In the case of Model T3 and Model T4 subjected to moderate and heavy showers of 20 mm/h and 50 mm/h, respectively (Results of Model T2 are not presented in this paper), the rate of increase in crest settlement was more rapid. The final settlements incurred at the crest for all three slopes are observed to be extremely high, and in the order of about 2.55 m, 3.54 m, and 3.78 m, respectively, in prototype scale for Models: T1, T3, and T4. The above is indicative of the catastrophic failure underwent

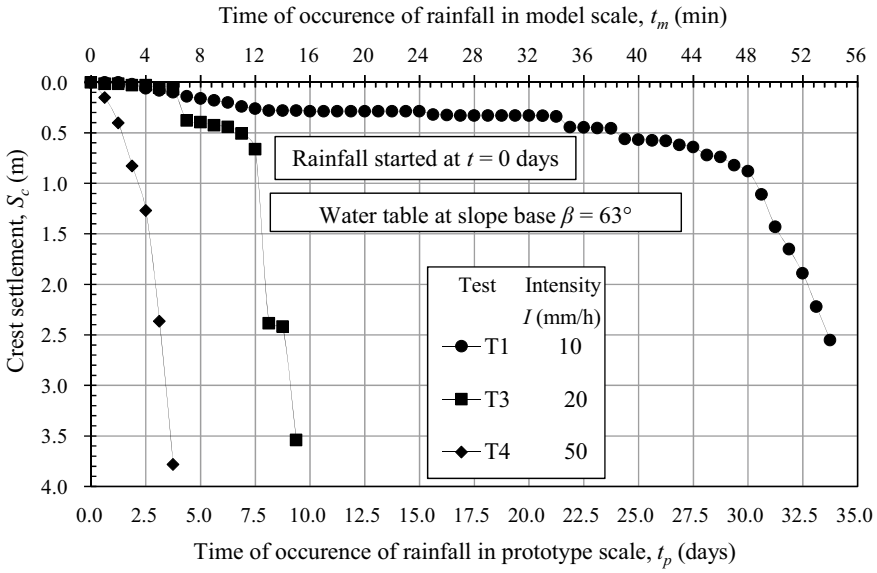

Fig. 4 Variation of crest settlement with time

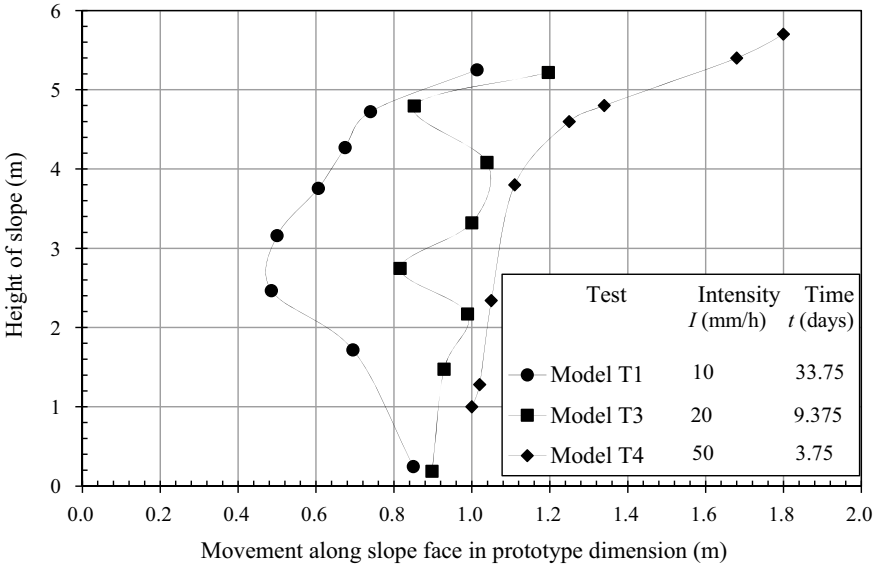

Fig. 5 Slope face movements during rainfall

by each slope model on being subjected to rainfall. A similar observation holds good for the slope face movements depicted in Fig. 5, wherein prototype values of the

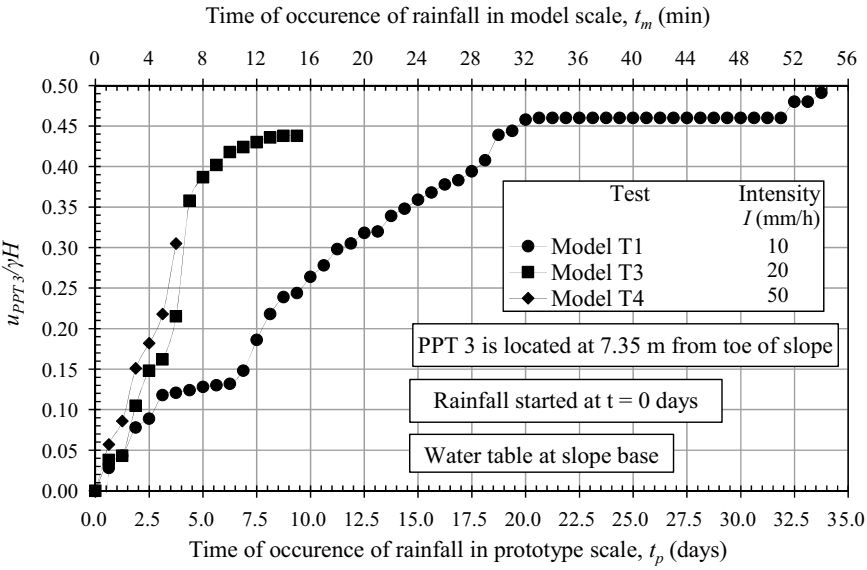

Fig. 6 Variation of normalized excess pore water pressure ($u_{PPT3}/\gamma H$) with rainfall

order of 1.02, 1.19, and 1.8 m were reported at the ultimate stage for Models: T1, T3, and T4, respectively. As expected, the face movements and surface settlements increased with increasing rainfall intensity.

5.3 Pore Water Pressure Developments with Rainfall

The pore water pressure generation during rainfall for the slope models is shown in Fig. 6. The values measured by PPT3 ($u_{PPT3}/\gamma H$) placed vertically below the mid-point of the crest on the base layer are herein presented. The pore pressures (u) are normalized with respect to the unit weight of model soil (γ) multiplied by the slope height (H), and are expressed in prototype dimensions, starting from the time of occurrence of rainfall. As can be observed from Fig. 6, Model T1 subjected to 10 mm/h rainfall exhibited a slow but steady rise in pore water pressure with rainfall resulting in progressive deformations and multiple sliding stages, where each stage of sliding corresponded to a level of increase in excess pore water pressure. However, the pore water pressures increased rapidly for Model T3 and Model T4 subjected to higher intensities of 20 mm/h and 50 mm/h, respectively, resulting in instantaneous slope instability.

6 Conclusions

The present study aims at investigating the mechanism of rainfall-induced landslides in low-permeable soil slopes. Centrifuge-based physical modeling was performed in this regard on prototype silty sand slopes of 7.2 height with 7.5 m crest width and 2 V:1H inclination, having an initial water table up to slope base. Three typical rainfall intensities were simulated, wherein, the first slope model was subjected to a prolonged and light rainfall intensity of 10 mm/h, whereas, the second and third models were subjected to short-span moderate and heavy simulations of 20 mm/h and 50 mm/h, respectively. The intensity of rainfall was observed to play a crucial role in governing the failure mechanism of landslides. A light rainfall intensity of 10 mm/h of longer duration caused a progressive deep-seated face failure on account of deeper rainwater infiltration inside the slope body, where each stage of sliding corresponded to a level of increase in excess pore water pressure. A moderate rainfall intensity of 20 mm/h of medium duration similar to that of seasonal showers corresponded to an abrupt rotational slip originating at the toe and gradually propagating upwards with increasing levels of saturation. In contrast, a short and intense cloudburst of 50 mm/h triggered a major block sliding type of failure due to extensive erosion on account of the rainfall flux exceeding that of the saturated soil permeability.

References

1. Koerner, R.M., Koerner, G.R.: The importance of drainage control for geosynthetic reinforced mechanically stabilized earth walls. J. Geoeng. **6**(1), 3–13 (2011)
2. Anderson, S.A., Sitar, N.: Analysis of rainfall-induced debris flows. Geotech. Eng. ASCE **121**(7), 544–552 (1995)
3. Fredlund, D.G., Rahardjo, H.: Soil Mechanics for Unsaturated Soils. Wiley, New York (1993)
4. Yoo, C., Jung, H. S., Jung, H. Y.: Lessons learned from a failure of geosynthetics reinforced segmental retaining wall. In: Shim, S., Yoo, C., Heon, H.Y. (eds.) Proceedings of the 3rd Asian Regional Conference on Geosynthetics CIIR, pp. 265–274, Seoul, Korea (2004)
5. Pathak, Y.P., Alfaro, M.C.: Wetting-drying behavior of geogrid-reinforced clay under working load conditions. Geosynth. Int. **17**(3), 144–156 (2010)
6. Schofield, A.N.: Cambridge geotechnical operations. Geotechnique **30**(3), 227–268 (1980)
7. Taylor, R.N.: Centrifuges in modelling: principles and scale effects. In: Geotechnical Centrifuge Technology. Blackie Academic and Professional, Glasgow, UK (1995)
8. Caicedo, B., Tristancho, J., Thorel, L: Mathematical and physical modelling of rainfall in centrifuge. Int. J. Phys. Model. Geotech. **15**(3), 150–164 (2015)
9. Bhattacherjee, D., Viswanadham, B.V.S.: Design and Performance of an Inflight Rainfall Simulator in a Geotechnical Centrifuge. Geotech. Test. J., ASTM **41**(1), 72–91 (2018)
10. Bhattacherjee, D., Viswanadham, B.V.S.: Centrifuge model studies on performance of hybrid geosynthetic reinforced slopes with poorly draining soil subjected to rainfall. J. Geotech. Geoenviron. Eng. ASCE **145**(12) 04019108:1–13 (2019)
11. Zornberg, J. G., Leshchinsky, D.: Comparison of international design criteria for geosynthetic-reinforced soil structures. In: Ochiai, J., Otani, Miyata, Y. (eds.) Geosynthetics and Earth Reinforcement, ISSMGE-TC9 Report, pp. 106–117 (2001)

12. Christopher, B.R., Stuglis, R.S.: Low permeable backfill soils in geosynthetic reinforced soil wall: state of the practice in North America. In: Proceedings of North American Geosynthetics Conference (NAGS2005), GRI-19, pp. 14–16, Las Vegas, USA (2005)
13. Holtz, R.D., Kovacs, W.D.: An introduction to Geotechnical Engineering. Prentice Hall, Englewood Cliffs, New Jersey (1981)
14. Chandrasekaran, V.S.: Numerical and centrifuge modelling in soil structure interaction. Indian Geotech. J. **31**(1), 30–59 (2001)
15. Llasat, M.C.: An objective classification of rainfall events on the basis of their convective features. Int. J. Climatol. **21**(1), 1385–1400 (2001)
16. Bhattacherjee, D., Viswanadham, B.V.S.: Effect of geocomposite layers on slope stability under rainfall condition. Indian Geotech. J. **48**(2), 316–326 (2018)
17. Image-Pro Plus: Image-Pro Plus Manual. Ver. 5.1. Media Cybernetics, Inc., USA (2004)

Studies on the Performance of Pipelines Subjected to Differential Settlements: Numerical Study

Vaibhav V. Nirgude, B. V. S. Viswanadham, and S. Chatterjee

1 Introduction

Pipelines are the lifeline for a country and an efficient pipeline network helps in many ways, e.g. economical and reliable transport of oil and gas, water supply, waste management network, etc. Pipeline failures not only cost unnecessary remedial works and huge financial losses but also in some circumstances may lead to gas explosions and spillage, resulting in severe environmental damage and loss of life. Permanent Ground Deformation due to geohazard represents the fourth major cause of pipeline failures [1].

Settlement is one of the types of Permanent Ground Deformation and is defined as, the vertical movement of the ground, generally caused by changes in stresses within the earth. Subsidence is a term often used to describe the caving or sinking of the ground, which may not be associated with changes in soil stresses. Hence, the distinction between subsidence and settlement is not always apparent. In both conditions, the pipeline is primarily subjected to vertical loading along the pipeline length due to soil vertical movement. Most anthropogenic subsidences observed all over the world are caused by the withdrawal of subsurface fluids from porous granular media, mining of coal and minerals, and drainage of organic soils.

A pipeline subjected to differential settlement is a unique loading condition, in which the pipeline is subjected to vertical movement along the pipeline length

V. V. Nirgude (✉) · B. V. S. Viswanadham · S. Chatterjee
Department of Civil Engineering, Indian Institute of Technology Bombay, Powai, Mumbai 400076, India
e-mail: nirgudev@civil.iitb.ac.in

B. V. S. Viswanadham
e-mail: viswam@civil.iitb.ac.in

S. Chatterjee
e-mail: sc@civil.iitb.ac.in

C. N. V. Satyanarayana Reddy et al. (eds.), *Dynamics of Soil and Modelling of Geotechnical Problems*, Lecture Notes in Civil Engineering 186,
https://doi.org/10.1007/978-981-16-5605-7_20

embedded in the soil. Hence, it can be referred to as pipeline subjected to a continuous differential settlement. The effect of the differential settlement on the pipeline can be observed at pipeline traversing hard to soft foundations at pumping station/pipeline interfaces, change in soil strata along pipeline length, crossing of landfill areas, etc. Figure 1 shows the effect of differential settlement on pipeline and structure.

The predominant effect of the differential settlement on the pipeline is in a longitudinal direction. Hence, even though the differential settlement is detrimental for structures, it can be accommodated effectively in the pipeline, by detailed investigation. Proper attention to potential settlement and design is necessary to make pipelines function reliably as a safe, integral part of a conveyance system. Flexibility is important with the design of large diameter pipelines, because they are much stiffer and less tolerant to movements than smaller diameter pipelines. In similar aspects, the number of pipeline parameters (diameter, thickness, material, surface effect, buried depth) and soil parameters (types of soil, saturation condition) affects the pipe soil interaction. Hence, each pipeline possesses unique challenges.

ASCE guidelines are generally used for pipeline design, which is based on an analytical model. To simplify the problem, analytical models are based on certain assumptions on the soil behavior, geometries, and loading conditions. Moreover, the p-y relationship is developed based on 2D soil deformation [2, 3]. Addressing pipe soil interaction with the analytical model becomes challenging due to the presence of geometrical, boundary, and material nonlinearity. Simulation of 1 g physical setup is costly and time consuming, due to the large variation in the input parameters [4].

Finite Element Analysis (FEA) can handle geometric, material, and boundary nonlinearity. With verified pipe soil interaction and soil material modeling approach, 3-D FE analysis can provide better visualization and understanding of soil-structure interaction for pipe subjected to differential settlements.

2 Analysis Approach and FE Model Details

2.1 Mechanical Analysis of the Buried Pipeline

There are three kinds of mechanical models for the buried pipeline. The first one is the beam on elastic foundation model. The second is the soil spring model. The surrounding soil was assumed as a series of springs and the spring stiffness is decided by the soil properties. The third one is the nonlinear contact model. It is usually in numerical calculation [5].

A pipeline subjected to differential settlement is a nonlinear problem involving complex pipe-soil interactions. Therefore, it is challenging to solve the realistic pipeline response by analytic methods.

2.2 Finite Element Model

3D finite element analysis approach using ABAQUS is utilized to study the stress-strain response of the buried steel pipeline under the action of ground settlement. The numerical simulation considers geometric (large strain and displacement), material (nonlinear material behavior of soil and pipeline) and boundary nonlinearities.

Half symmetry FE model is considered based on the symmetric nature of the problem (buried pipeline and soil) and loads acting. Figure 2 shows the finite element model of the buried pipeline and soil stratum. The pipeline is embedded in soil along the x-axis. Four noded reduced integration shell elements (S4R) are used to model the pipeline and eight noded reduced integration brick elements (C3D8R) are used to simulate the surrounding soil. The thickness of backfill soil (h) is 1.5 m. The soil model in the x-direction is equal to at least 60 pipeline diameters, where the dimensions in directions y, z equal to 7.5D and 15D, respectively. A total of 40 shell elements around the cylinder circumference in this central part have been found to be adequate to achieve convergence of the solution, and surrounding soil has meshed with a smaller size [6, 7].

Initially, in situ conditions are simulated followed by settlement loading. The analysis is conducted in two steps. In the first step, gravity loading and internal pressure were applied and subsequently, in the second step, displacement was imposed on the ground settlement zone. The nodes on the bottom boundary plane of the stratum remain fixed in the z-direction. Symmetry constraints are imposed on the symmetry planes of the buried pipeline and stratum. Figure 2 shows details of the boundary conditions applied in the analysis.

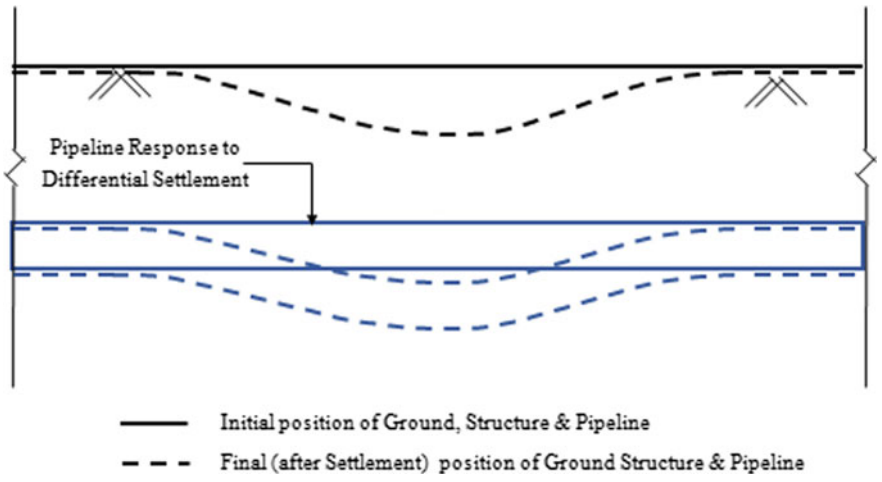

Fig. 1 Effect of differential settlement on pipeline and structure

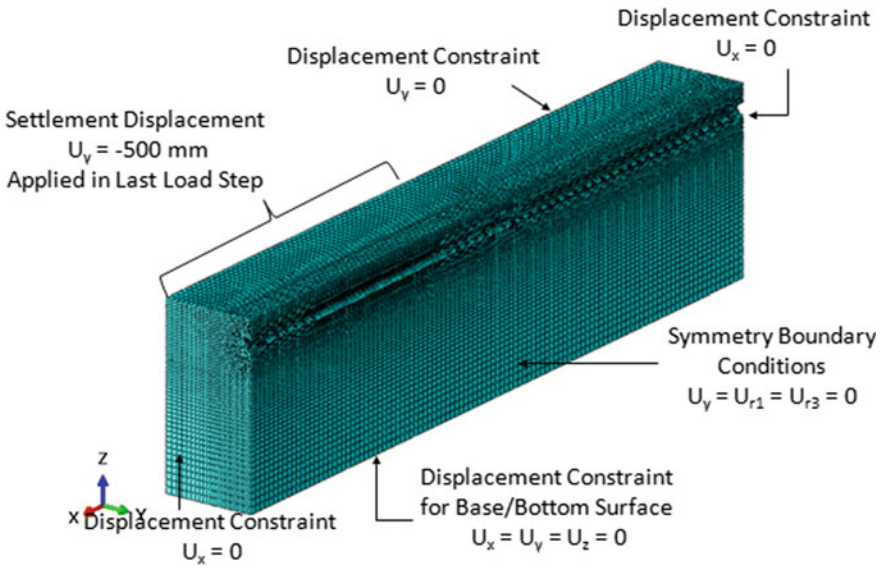

Fig. 2 Finite element model and boundary condition for differential settlement study

Mechanical behavior of the soil material is simulated through an elastic perfectly plastic Mohr–Coulomb constitutive model. Zero friction angle was assumed to essentially consider Tresca failure criteria. Materials of backfill soil and the stratum are the same, with undrained cohesive strength c = 10 kPa at base and 0.02 kPa at top, modulus of elasticity E = 5 MPa at base and 0.01 MPa at top, Poisson's ratio μ = 0.49, and density $\rho = 1510$ kg/m^3.

Steel pipeline of X65 grade is simulated with a large strain von Mises plasticity model with isotropic hardening. The pipeline diameter (D) is 0.762 m, which is a typical size for a hydrocarbon transmission pipeline. The pipeline wall thickness (t) is considered equal to 25.4 mm. Pipeline material yield stress σ_y is 449 MPa. Young's modulus of the steel material is 210 GPa, Poisson's ratio is 0.3 and density is 7800 kg/m^3. The dependency of soil properties (i.e. Young's Modulus and un-drained Cohesion Strength) with depth is considered by defining a field variable.

Deformations behavior of the buried pipeline and surrounding soil influence each other. The interface between the outer surface of the pipeline and the surrounding soil is simulated with a contact algorithm, which allows separation of the pipeline and soil and accounts for contact friction. Isotropic coulomb friction is applied with a value of friction coefficient μ as 0.5.

2.3 Response of the Pipeline Under Settlements

Figures 3 and 4 show displacement plots for soil and pipeline, at the end of the

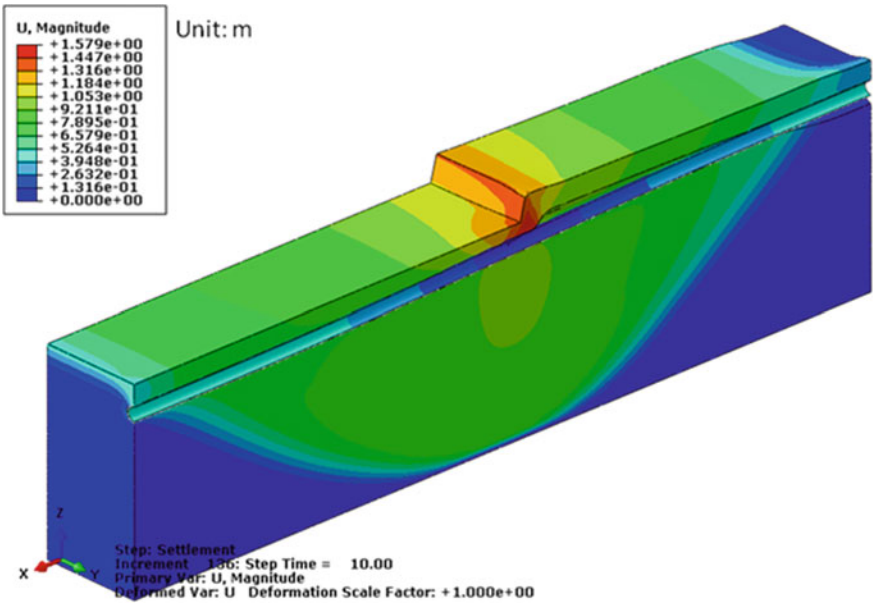

Fig. 3 Displacement plot—at the end of settlement condition

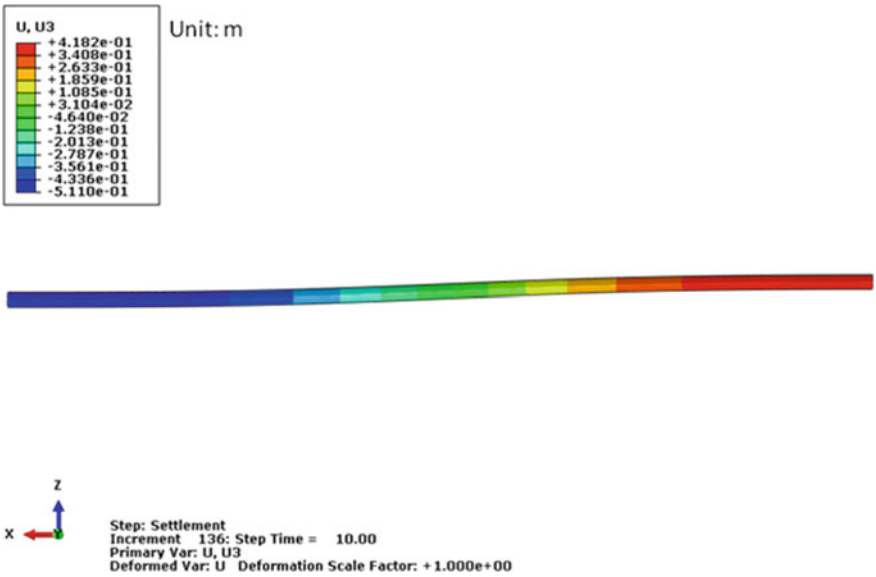

Fig. 4 Displacement plot for the pipeline in the vertical direction—at the end of the settlement

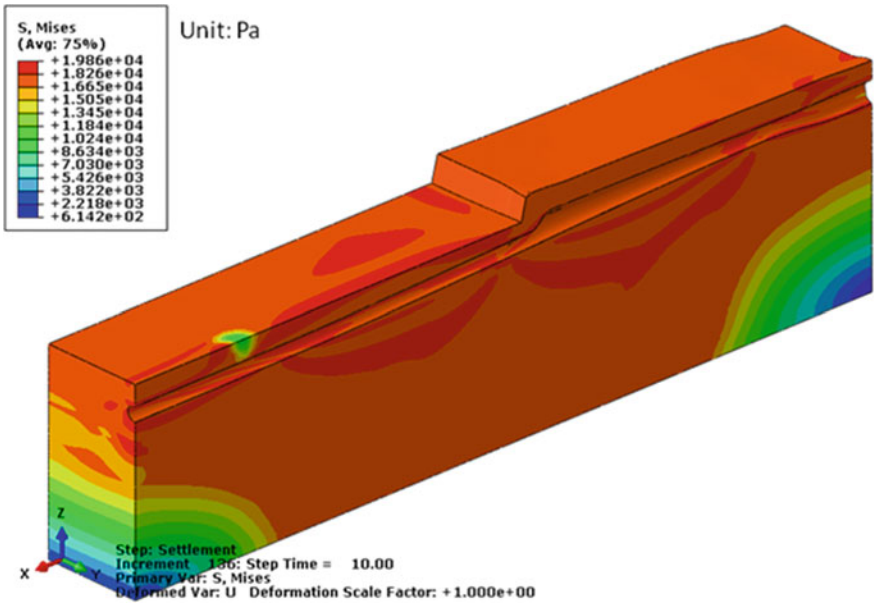

Fig. 5 von Mises stress plot for soil—at the end of settlement condition

soil settlement load step, i.e., settlement displacement of 500 mm. Figures 5 and 6 show von Mises stresses in the soil and pipeline, respectively, at the end of soil settlement–settlement of 500 mm.

The pipeline response to the soil settlement is affected by the pipe soil interaction, which in turn affects the soil deformation surrounding the pipeline. In the no-settlement zone, pipeline shows the upheaval movement and in the settlement zone pipeline compresses the soil. This behavior results in void formation near the dividing plane or soil interface at settlement and non-settlement.

From the analysis, it is observed that the von Mises stress and high-stress area increase with an increasing settlement. There are two oval-shaped high-stress areas near the dividing plane. In the no-settlement zone, the pipeline upper section is in tension (higher stress location) and the bottom section is in compression, inverse behaviour for stress nature and location is observed in the settlement zone. The distance between the high-stress areas is increased with an increase in settlement. The middle section of the pipeline is having low stresses.

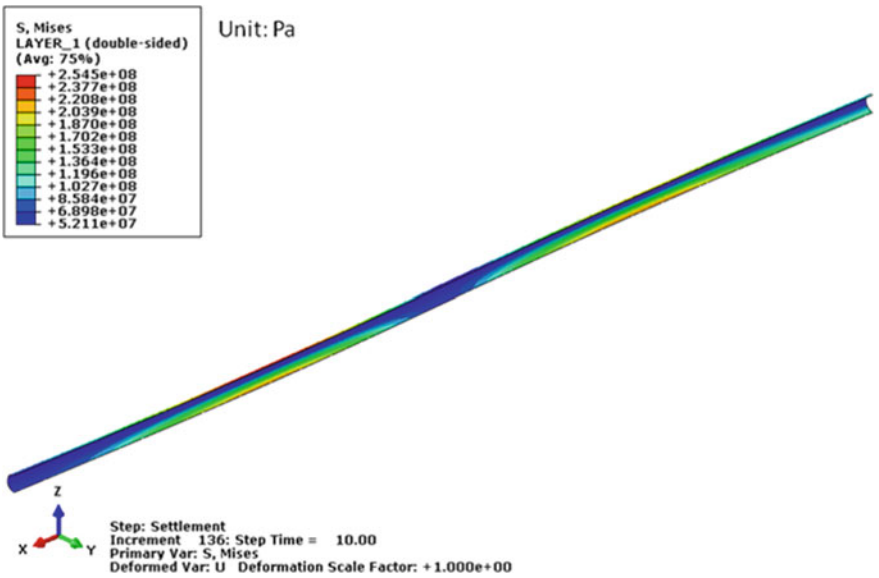

Fig. 6 von Mises stress plot for pipeline—at the end of settlement condition

3 Effect of Pipeline Parameters

3.1 Diameter to Thickness Ratio (D/t)

For the ground settlement of 300 mm and internal pressure is $0.2P_{max}$, stress and axial strain responses of the pipeline under different diameter to thickness ratios are shown in figures. As seen in Fig. 6, von Mises stresses and higher order stress area decrease with decreasing diameter to thickness ratio, because the larger diameter to thickness reduces the pipeline stiffness. Under the joint action of the ground settlement and internal pressure, the overall stress and local stress increase with the increase in diameter to thickness ratio. Figure 7 shows the axial strain of the pipeline, the maximum axial strain increases with the increase in the diameter to thickness ratio.

Figure 8 shows the bending curves of the pipeline. The reduction in curvature radius near the dividing plane in the settlement zone indicates that, thin-walled steel pipeline is prone to buckling under ground settlement near the dividing plane.

3.2 Internal Pressure (P/P_{max})

For the ground settlement of 300 mm, stress-strain responses of the pipeline with increasing P/P_{max} ratios are shown in figures. As shown in Fig. 9, under the joint

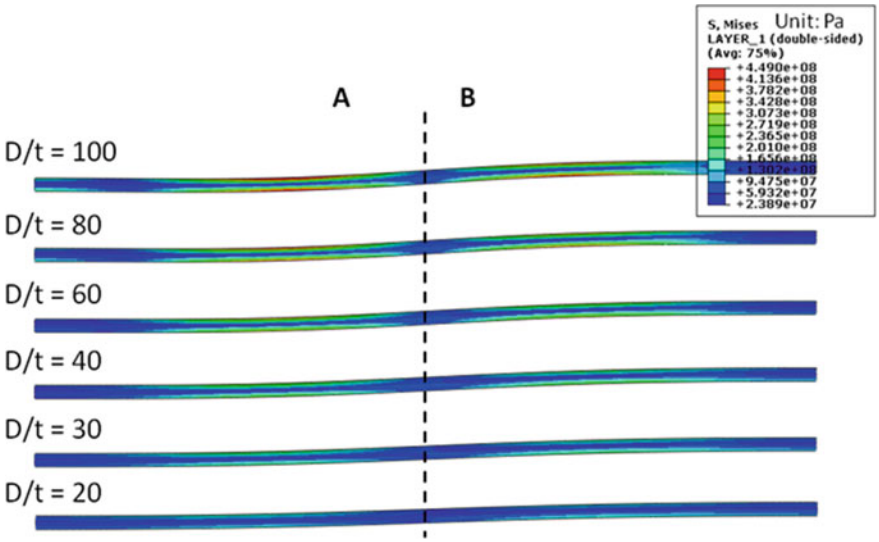

Fig. 7 von Mises stress plot of the pipeline for different D/t ratios

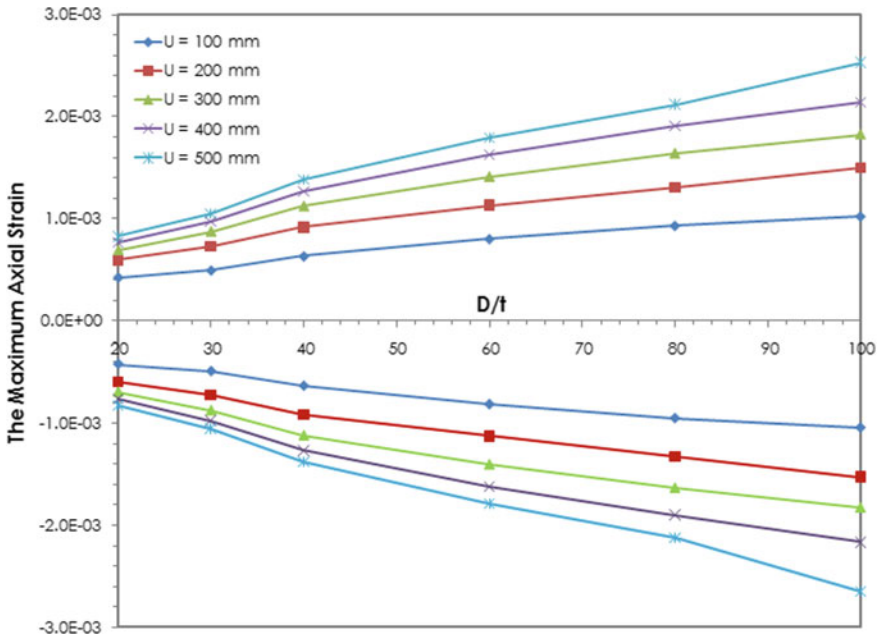

Fig. 8 Axial tensile and compressive strain plot of the pipeline for different D/t ratios

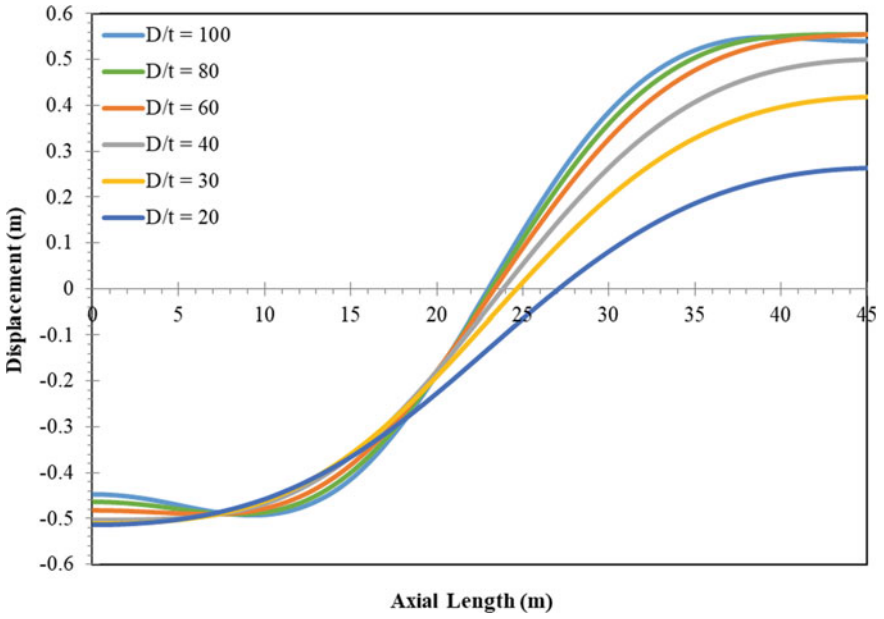

Fig. 9 Pipeline displacement due to settlement load along pipeline length

action of the ground settlement and internal pressure, the overall stress and local stress increase with the increase in the P/P_{max} ratio. The increase in induced stress is directly proportional to the increase in internal pressure. Figure 10 shows the axial strain of the pipeline, the maximum axial strain increases with the increase in the P/P_{max} ratio. With the increase in ground settlement, the change rate of the maximum axial strain decreases. Figure 11 indicates that P/P_{max} ratio doesn't affect the bending deformation of the buried pipeline. No case has shown the plastic strain in the pipeline.

3.3 Normalized Depth of Burial (h/D)

When the ground settlement is 300 mm, internal pressure is $0.2P_{max}$, stress-strain response of the pipeline under different buried depth to pipeline diameter ratios is shown in figures. As shown in Figs. 12 and 13, the overall stress and local stress decrease with the increase in buried depth to pipeline diameter ratios. Figure 14 shows the axial strain of the pipeline, the maximum axial strain decreases with the increase in the buried depth to pipeline diameter ratio. With the increase in ground settlement, the rate of change of the maximum axial strain decreases. Figure 15 shows the considerable upheaval bending deformation of buried pipeline in the no-settlement zone.

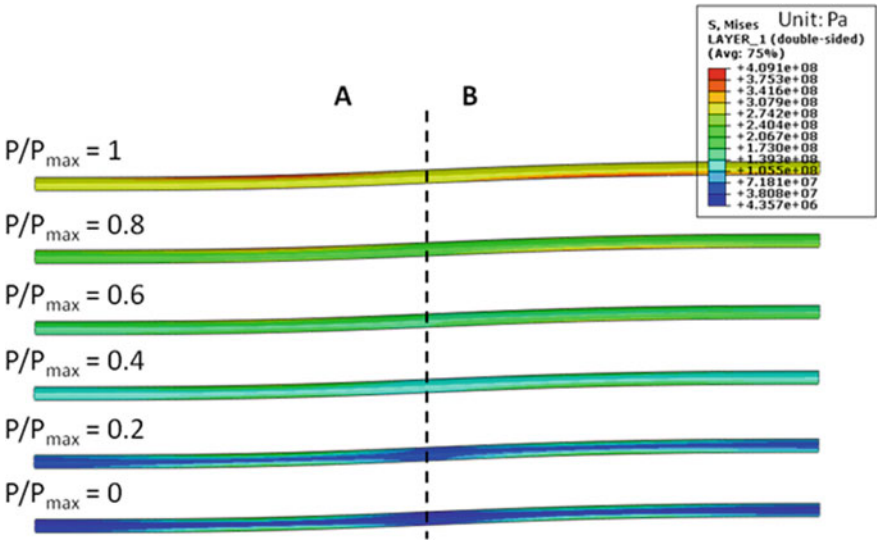

Fig. 10 von Mises stress plot of the pipeline for different D/t ratios

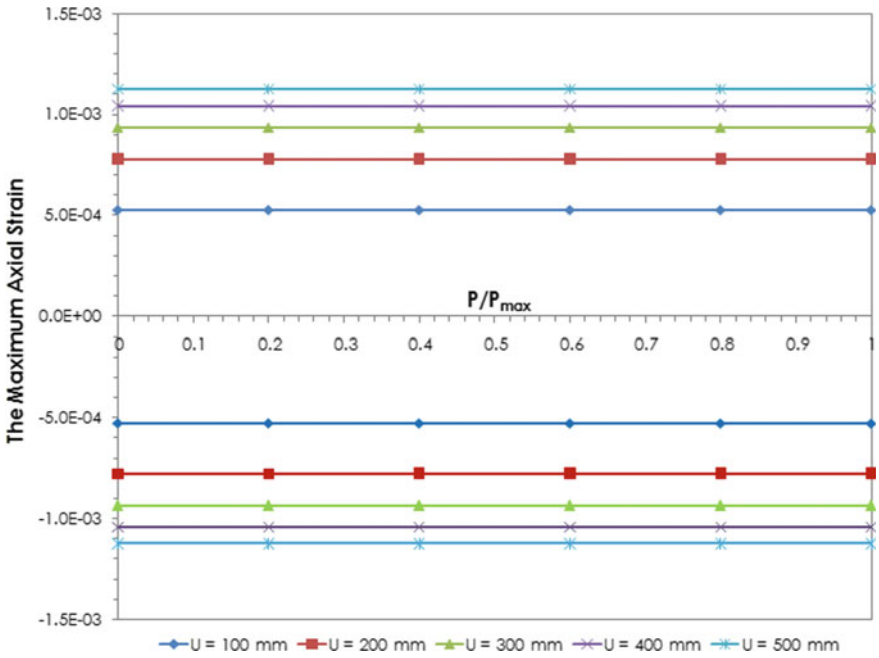

Fig. 11 Axial tensile and compressive strain plot of the pipeline for different D/t ratios

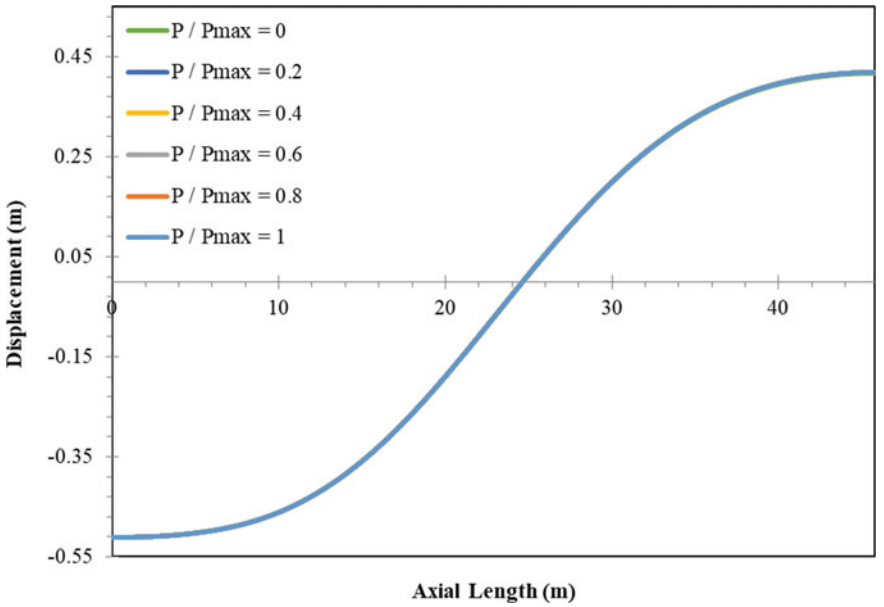

Fig. 12 Pipeline displacement due to settlement load along pipeline length

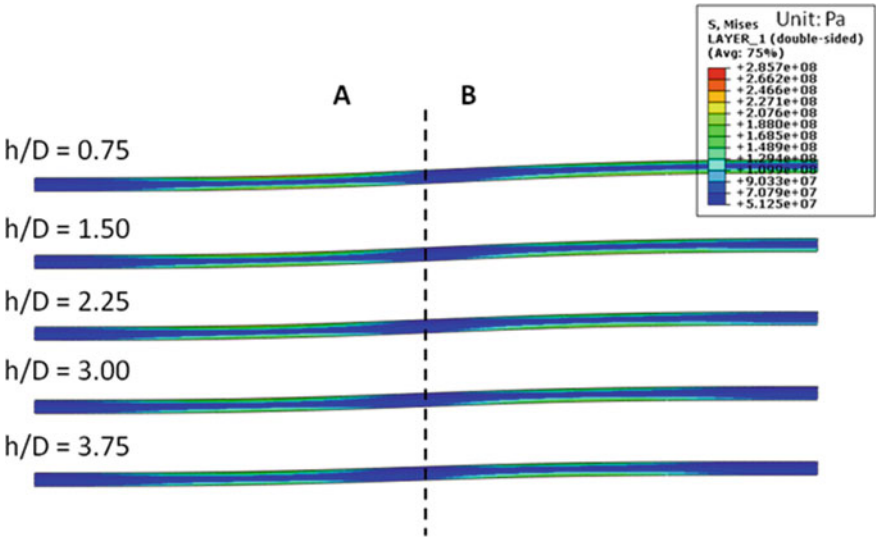

Fig. 13 von Mises stress plot of the pipeline for different D/t ratios

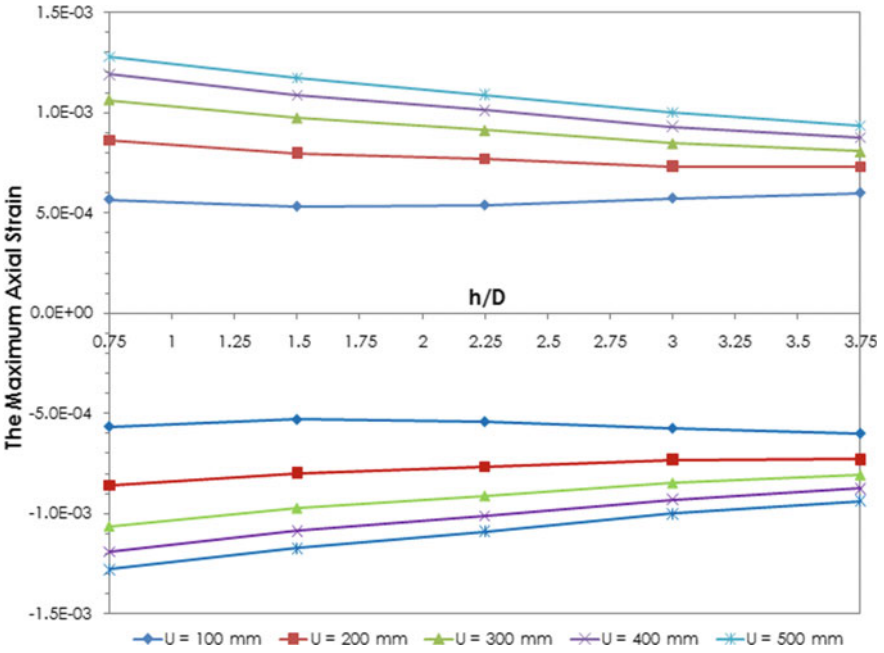

Fig. 14 Axial tensile and compressive strain plot of the pipeline for different D/t ratios

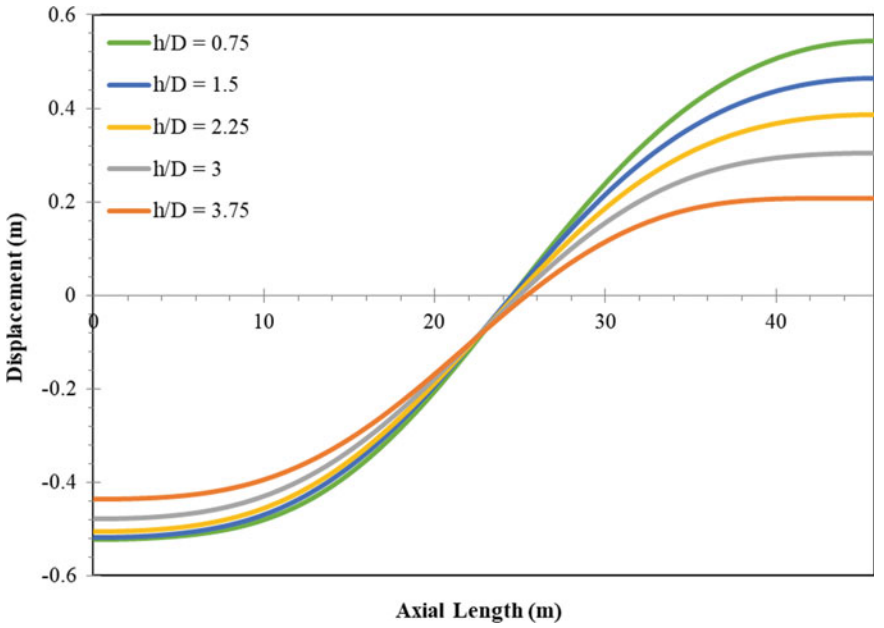

Fig. 15 Pipeline displacement due to settlement load along pipeline length

4 Conclusions

In a pipeline subjected to continuous differential settlements, two higher stress locations are formed each one in settlement and no-settlement zone, near the interface plane. In the no-settlement zone, the pipeline upper section is in tension (higher stress location) and the bottom section is in compression, inverse behavior for stress and location is observed in the settlement zone. The pipe-soil interaction results in soil compression and void formation near the settlement and no-settlement zone, respectively.

From the interpretation of analysis and pipeline parametric studies, the following conclusions can be drawn:

1. With the increase in diameter to thickness ratio, the pipeline becomes prone to local buckling near the dividing plane.
2. Internal pressure variation does not affect the pipeline deformation behavior.
3. With the decrease in buried depth to diameter ratio, the pipeline may get exposed in the no-settlement zone.

References

1. Dash, S.R., Sehgal, S., Nair, G.S.: Seismic vulnerability of pipelines in India. Struct. Eng. Convent. 2949–2959 (2014)
2. Newmark, N.M., Hall, W.J.: Pipeline design to resist large fault displacement. In: Proceeding of the US National Conference on Earthquake Engineering. University of Michigan, Ann Arbor, pp. 416–425 (1975)
3. Kennedy, R.P., Chow, A.W., Williamson, R.A.: Fault movement effects on buried oil pipeline. Transp. Eng. J., ASCE **103**(TE5), 617–633 (1977)
4. Tohda, J., Hachiya, M.: Response and design of buried pipelines subjected to differential ground settlement. In: Proceeding of the 16th International Conference on Soil Mechanics and Geotechnical Engineering, pp. 1659–1662 (2006)
5. Zhang, J., Liang, Z., Han, C.J.: Numerical modeling of mechanical behavior for buried steel pipelines crossing subsidence strata. J. PLoS One **10**(6), 1–16 (2015)
6. Sarvanis, C., Karamanos, S.A., Vazouras, P., Mecozzi, E., Lucci, A., Dakoulas, P.: Permanent earthquake induced actions in buried pipelines numerical modeling & experimental verification. Earthq. Eng. Struct. Dyn. **47**, 966–987 (2017)
7. Zhang, J., Liang, Z., Zhao, G.: Mechanical behaviour analysis of a buried steel pipeline under ground overload. J. Eng. Failure Anal. **63**, 131–145 (2016)

Effect of EPS Geofoam on Lateral Earth Pressure Reduction—A Numerical Study

Neeraj Kumar Burugupelly and Satyanarayana Murty Dasaka

1 Introduction

In most cases of rigid retaining wall systems, wall movements are highly restricted such as basement walls, bridge abutments, box culverts, etc. fall under this category. In designing these walls at-rest lateral earth pressures are generally considered. This results in greater magnitudes of lateral earth pressures, resulting in larger cross-sectional dimensions of the wall, making it highly uneconomical and requires larger volumes of materials.

Horvath (1997) concluded that by placing lightweight compressible material like foam behind the retaining wall, these lateral earth pressures can be reduced significantly. This technique of using compressible inclusion involves placing of a highly compressible material between the soil backfill and retaining wall. By placing the compressible inclusion, room for the lateral movement of soil is created so that, the soil can change its state from at-rest condition to active condition. Expanded Polystyrene (EPS) geofoam material is most widely used material for compressible inclusion purpose because of its wide availability, absence of release of gases such as Formaldehyde post its production (Stark et al. 2004) and it can be manufactured with required stiffness without compromising on its low unit weight. Several researchers (Karpurapu and Bathurst 1992; Zarnani and Bathurst 2008; Athanasopoulus et al. 2012; and Abdelsalam and Azzam 2015) carried out numerical parametric studies to understand the behavior of rigid retaining walls with EPS geofoam compressible inclusions. In the current study PLAXIS 2D software was used to carry out numerical parametric analysis, to quantify the effect of various parameters like height of

N. K. Burugupelly (✉) · S. M. Dasaka
Department of Civil Engineering, IIT Bombay, Mumbai, India

S. M. Dasaka
e-mail: dasaka@civil.iitb.ac.in

C. N. V. Satyanarayana Reddy et al. (eds.), *Dynamics of Soil and Modelling of Geotechnical Problems*, Lecture Notes in Civil Engineering 186,
https://doi.org/10.1007/978-981-16-5605-7_21

retaining wall, density and thickness of geofoam inclusion on the extent of lateral thrust reduction on rigid retaining wall.

The work was carried out in two stages. First stage involves performing set of laboratory experiments to characterize the locally available geofoam material. In the second stage, numerical simulations were carried out to understand the influence of the various parameters on lateral earth pressure reduction.

2 Material Testing and Characterization

This section details the experimental work carried out to obtain the material and interface parameters required for the constitutive modelling and calibration of numerical model. The experimental program includes performing 9 static compression tests on EPS geofoam cubes to obtain its compressive strength parameters, set of 3 UU Triaxial tests on cylindrical EPS geofoam samples to determine its shear strength properties and 9 interface shear tests to determine the interface properties of Geofoam–Sand, Geofoam–Concrete and Sand–Geofoam interfaces.

2.1 Static Compression Tests

Static compression tests were performed to evaluate the initial Young's modulus (E), compressive strength (σ_c), yield strength (σ_y) and elastic limit of EPS geofoam. The slope of tangent to the initial linear region of stress strain curve is the initial Young's modulus (Stark et al. 2004). Yield strength is the stress corresponding to point obtained by intersecting initial tangent and back tangent to linear portion of curve at higher strains. Testing was carried in accordance with ASTM D6817M-17 50 × 50 × 50 mm size cubic samples of EPS geofoam of density 20 kg/m^3 were acquired from INSUPAC Industries LTD, Mumbai, for the testing purpose. A strain rate of 10%/min was adopted. As per ASTM D7180-05, stress level corresponding to 10% axial strain was taken as compressive strength of the EPS geofoam (Fig. 1).

2.2 Unconsolidated Undrained Triaxial Tests

To obtain the shear strength properties of EPS 20 geofoam, Unconsolidated Undrained Triaxial tests were carried out on cylindrical geofoam samples of height 76 mm and diameter 38 mm (height to diameter ratio = 2). Tests were performed as per IS 2720 (Part 11):1993 with a constant displacemnt rate of 1.25 mm/min. Confining pressures of 50 kPa, 100 kPa and 150 kPa were adopted. The results obtained are shown in the Fig. 2.

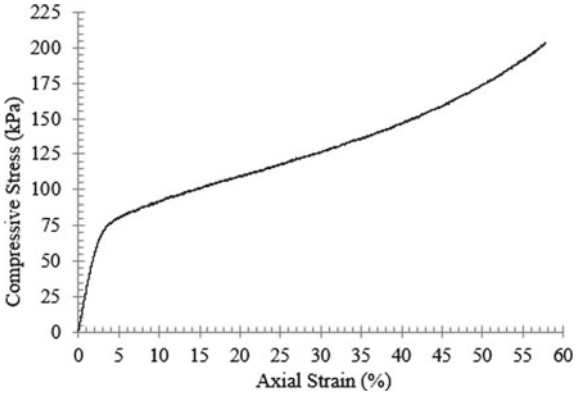

Fig. 1 Compressive stress versus axial strain relationship for EPS 20 geofoam material

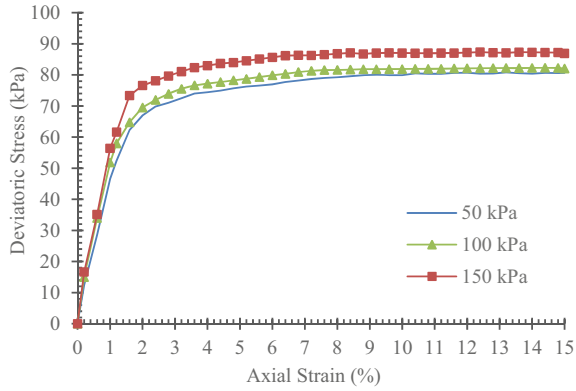

Fig. 2 Unconsolidated Undrained Triaxial test results for EPS 20 geofoam

2.3 Modified Direct Shear Tests

According to Meguid and Khan [11], the surface roughness of various interfaces plays a significant role in providing the shear resistance. To accurately obtain the shear parameters of various interfaces, modified direct shear tests were carried out for determining interface properties of geofoam-concrete, geofoam-sand, and sand-concrete interfaces. Modified direct shear test involves application of shear strain along the interface of two different materials. Two different materials were placed in two different halves of the shearing box, such that the shearing plane coincides with the interface of these two materials.

ASTM D5321-17 was followed in performing the modified direct shear tests. Shear box of size 100 × 100 × 50 mm was used to avoid any possible boundary effect. Sets of three modified direct shear tests were performed at three different normal stress levels of 25, 50 and 75 kPa for each interface. These normal stresses were adopted so as to represent the field conditions to be investigated. M40 Concrete, EPS 20 geofoam and Indian Standard Grade II sand (backfill) were used as the

Table 1 Summary of interface shear test results

Test	Parameter	Value
Concrete—Geofoam	Adhesion (α) (kPa)	1
	ϕ (deg.)	30
Concrete—Sand	Adhesion (α) (kPa)	7
	ϕ (deg.)	32
Sand—Geofoam	Adhesion (α) (kPa)	10
	ϕ (deg.)	27

testing materials. EPS geofoam and concrete samples were accurately cut into blocks of size 99.5 × 99.5 × 25 mm so as to perfectly fit into one half of shear box. According to ASTM D3080/D3080M—11, the failure stress condition is defined as the maximum shear stress attained, or in the absence of a peak condition, the shear stress at 10% relative lateral displacement. Relative lateral displacement is the displacement between the top half and bottom half of the shear box.

A total of nine experiments were performed, three for each interface combination (geofoam-concrete, geofoam-sand, and sand-concrete). In all the experiments sand was placed at a relative density of 65% (15.93 kN/m$^{3)}$. In each interface shear test, harder material was placed in the bottom half of the direct shear box, so as to ensure that the shearing plane exactly coincides with the interface and also it prevents the tilting of shearing plane that may develop due to the differential settlement of geofoam. Dial gauges were used to take vertical and horizontal displacement measurements, proving ring was used to measure the shear force across the shear plane. The test is displacement controlled in nature and horizontal displacement was applied to the lower half of the shear box. A shearing rate of 1.25 mm/min was adopted. No area correction was taken into account (Table 1).

3 Calibration of Numerical Model and Interface Elements

The results obtained from the static compression tests were used to calibrate the Mohr–Coulomb constitutive law used in modelling of EPS geofoam material. Interface shear test results were used to calibrate the interface elements used in the numerical modelling. To calibrate the constitutive law used in modelling of EPS geofoam, static compression tests were numerically simulated and obtained stress–strain relation was compared with that of experimental result (Fig. 3).

For calibration of interface elements interface shear tests were numerically simulated by varying *RInterface* value until the numerical predictions are matched with that of experimental results.

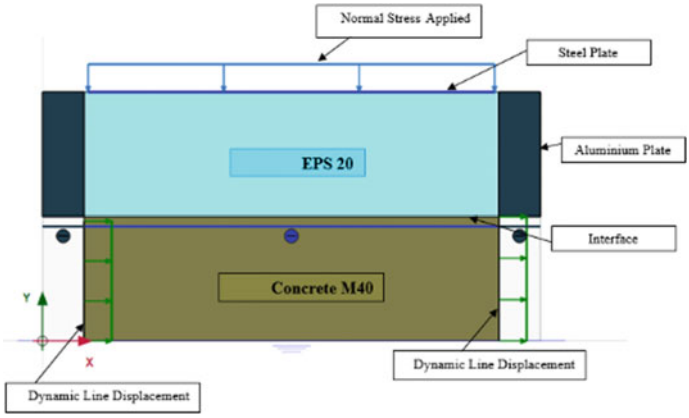

Fig. 3 Plane strain numerical model of interface shear test

4 Development of Numerical Model

4.1 Validation of Numerical Model

Ertugrul and Trandafir [5] carried out small-scale physical model tests on rigid non-yielding wall models with and without EPS geofoam compressible inclusions. The results of these physical model tests were used to validate the numerical model used in the present study (Fig. 4).

Accurate predictions of lateral earth pressures were observed in top two-thirds portion of the wall giving confidence in the elastoplastic Mohr–Coulomb model that

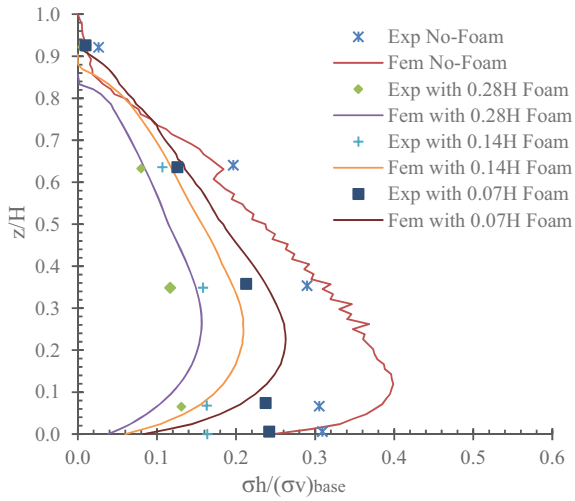

Fig. 4 Comparison of results of numerical model used in current study with small-scale physical model test results by Ertugrul and Trandafir [5]

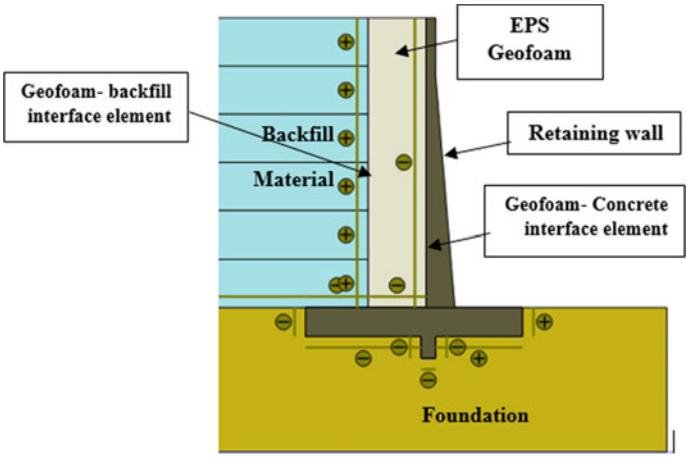

Fig. 5 Detailed view of the 6 m height retaining wall with 0.2H thick EPS 15 geofoam inclusion

was adopted in the current study. Hence same constitutive law was used in predicting the lateral earth pressures on rigid retaining walls of field-scale.

4.2 Numerical Parametric Analysis

Numerical parametric study has been carried out to study the effect of wall height, inclusion thickness and inclusion density on the extent of lateral earth pressure reduction on the rigid retaining wall. The backfill material, foundation soil and EPS geofoam inclusion were modelled using the Mohr–Coulomb constitutive law. The parametric study has been carried out considering five different wall heights, four different geofoam densities and five different (Fig. 5).

geofoam inclusion thicknesses. The material parameters required for foundation material were taken from Ertugrul and Trandafir [5]. Indian Standard Grade II sand was used as backfill material. The properties of various materials used in numerical analysis are shown in Table 2 and 3. The list of various parameters considered in analysis were presented in Tables 4. Boundary conditions of the numerical model were as shown in the Fig. 6. To simulate the on—field conditions, stage wise constriction is carried out in modelling the wall. The extent of foundation soil behind the wall is maintained at 3 m in all the cases. The backfilling is done in six stages for all the wall heights.

The stage wise construction is carried out in the following manner.

Initial Phase: Normal ground condition (No loading).

Phase 1: Construction of retaining wall.

Phase 2: Placing of geofoam behind the retaining wall throughout the wall height.

Phase 3: Placing of first layer of the backfill material.

Table 2 Material parameters of various materials and interfaces

Material	Concrete	Sand	Sand-concrete interface	Sand-Geofoam interface	Concrete-Geofoam interface
Constitutive model	Linear elastic	Mohr–Coulomb	Mohr–Coulomb	Mohr–Coulomb	Mohr–Coulomb
Unit weight, γ (kN/m^3)	25	15.93	15.93	15.93	0.2
Cohesion, c′ (kPa)	–	0	7	10	1
Friction angle, φ′ (deg.)	–	39	32	27	30
Initial modulus, (kPa)	1.4×10^7	13,000	13,000	13,000	3028
Poisson's ratio, ν	0.25	0.25	0.25	0.25	0.1
$\mathbf{R_{Interface}}$	1	0.8	0.785	0.925	0.9

Table 3 Mechanical properties of EPS geofoam inclusion material [12]

Material	Density (kN/m^3)	Initial modulus (kPa)	Cohesion (kPa)	Friction angle φ (°)
EPS 15	0.15	2480.76	33.75	1.5
EPS 20	0.20	4070.55	38.75	2
EPS 22	0.22	5508.16	41.88	2
EPS 30	0.30	7550.28	62.00	2.5

Table 4 Variables used in the present study

Parameter	Value
Wall height (H)	3 m, 4.5 m, 6 m, 9 m, 12 m
Geofoam density	EPS 15, EPS 20, EPS 22, EPS 30
Inclusion thickness (t)	0.05H, 0.10H, 0.15H, 0.20H, 0.25H

Phase 4: Placing of second layer of the backfill material.
Phase 5: Placing of third layer of the backfill material.
Phase 6: Placing of fourth layer of the backfill material.
Phase 7: Placing of fifth layer of the backfill material.
Phase 8: Placing of sixth layer of the backfill material.

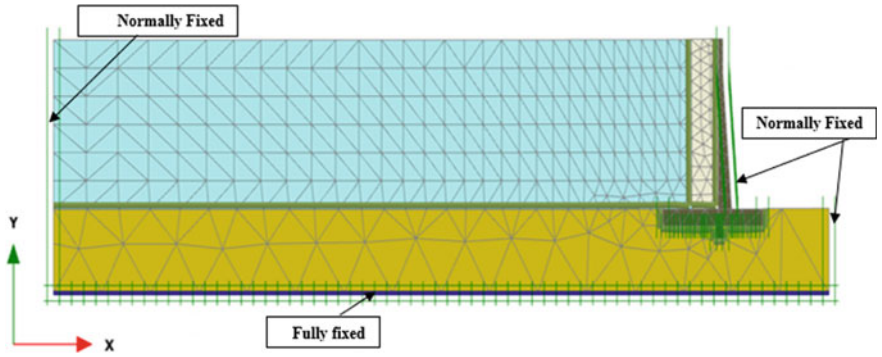

Fig. 6 Deformed mesh of 6 m height retaining wall with 0.20H thick EPS 15 geofoam inclusion

5 Results and Discussion

In total 100 (5 × 4 × 5) numerical simulations were carried out in the present parametric study. Five different wall heights (3 m, 4.5 m, 6 m, 9 m, and 12 m), four different geofoam densities (EPS 15, EPS 20, EPS 22 and EPS 30) and five different geofoam inclusion thicknesses (0.05H, 0.10H, 0.15H, 0.20H and 0.25H) were considered. Total lateral earth force (per unit length), isolation efficiency and maximum lateral earth pressure were calculated for each case and were compared with that of standard control case (without inclusion) to evaluate the influence of various parameters. The total force per unit length (p_x) was calculated using

$$p_x = \int_0^H \sigma_x \mathrm{d}z \tag{1}$$

Isolation efficiency (i_p) was calculated using

$$i_p = \frac{p_o}{p_o} \times 100 \tag{2}$$

where p_o is lateral force per unit length on the wall without the inclusion and p is the lateral force per unit length on the wall with inclusion (Fig. 7).

Considerable lateral movements were observed behind the retaining wall in its lower half-region due to the compression of geofoam inclusion resulting in the lateral movement of backfill material without any retaining wall movement. Even though the EPS geofoam is modelled as Elastoplastic material, the observed strains in majority of the cases in the current study were well within the elastic limit (1.5%) of the geofoam (Fig. 8).

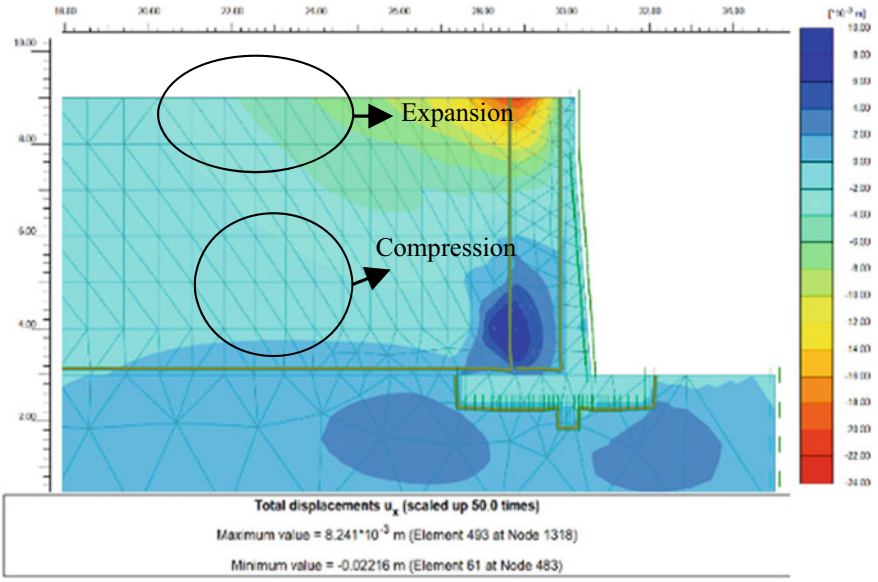

Fig. 7 Total displacement profile of the retaining wall of height 6 m with inclusion thickness of 0.20H

Fig. 8 The variation of lateral earth pressure profile with EPS geofoam density for a 6 m height retaining wall with 0.20H geofoam inclusion relative thickness

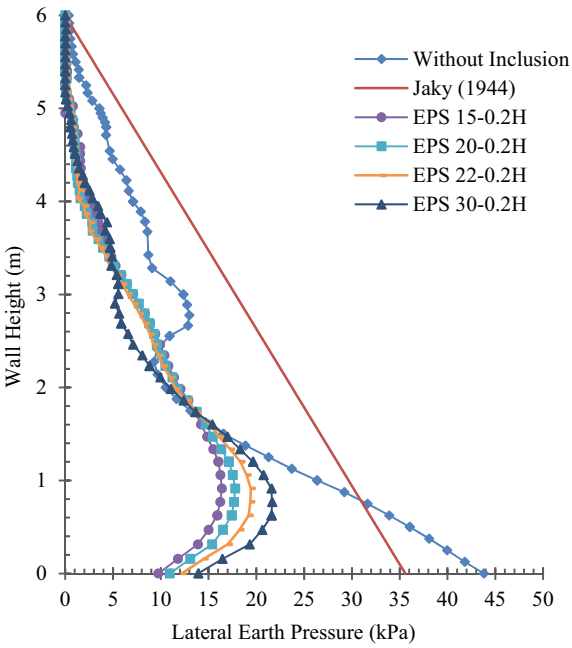

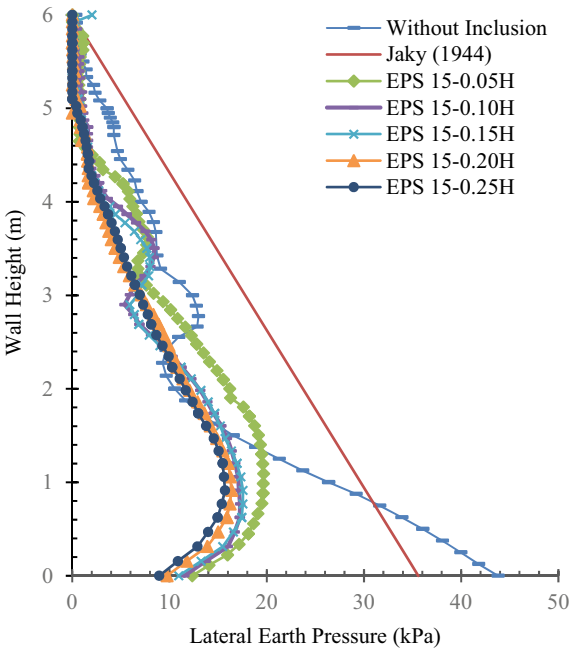

Fig. 9 The variation of lateral earth pressure profile with EPS relative thickness for a 6 m height retaining wall with EPS 15 geofoam inclusion

From the present analysis, among all the cases, highest isolation efficiency of 46.66% was observed for 6 m height retaining wall with EPS 15 geofoam inclusion of 0.25H relative thickness. The isolation efficiency increased with increase in the wall height up to 6 m, beyond which it decreased. The isolation efficiency was also found to increase with the increase in inclusion thickness and decrease with increase in geofoam density provided that the other parameters were kept constant (Fig. 9).

6 Conclusions

1. EPS geofoam density and its relative thickness play a predominant role in the extent of lateral earth pressure reduction.
2. From the calculated lateral displacements of backfill material, considerable magnitude of lateral displacements was observed in the lower-half of the retaining wall with compressible inclusion, thus allowing backfill soil to yield, resulting in the reduction of total lateral earth thrust on the wall.
3. It was noted that for a given relative thickness of geofoam inclusion, with the increase in EPS geofoam density, there is decreasing trend in the isolation efficiency of the compressible inclusion.
4. The isolation efficiency was observed to improve with the increase in the relative thickness of EPS inclusion for a given inclusion density.

5. The isolation efficiency improved with increase in the height of the retaining wall up to 6 m height. Beyond 6 m the isolation efficiency reduced with increase in the wall height.
6. Maximum isolation efficiency of 46.66% was observed for 6 m height retaining wall with EPS 15 geofoam with relative inclusion thickness of 0.25H.

References

1. ASTM D5321: Standard test method for determining the coefficient of soil and geosynthetic or geosynthetic and geosynthetic friction by the direct shear method, American Society of Testing Materials West Conshohocken (2017)
2. ASTM D1621: Standard test method for compressive properties of rigid cellular plastics, West Conshohocken (2010)
3. ASTM D3080: Standard test method for direct shear test of soils under consolidated drained conditions, American Society of Testing Materials, West Conshohocken (2011)
4. ASTM D6817, Standard specification for rigid cellular polystyrene Geofoam. American Society of Testing Materials, West Conshohocken (2006)
5. Ertugrul, O.L., Trandafir, A.C.: Reduction of lateral earth forces acting on rigid non-yielding retaining walls by EPS geofoam inclusions. J. Mater. Civ. Eng. **23**(12), 1711–1718 (2011)
6. Gade, V.K.: Reduction of earth pressure on rigid non-yielding retaining walls subjected to traffic loading using EPS Geofoam. Doctoral dissertation. Indian Institute of Technology Bombay, Mumbai (2018)
7. Horvath, J.S.: Integral-abutment bridges: problems and innovative solutions using EPS geofoam and other geosynthetics. Research. Report. No. CE/GE-00–2, (2000)
8. Horvath, J.S.: An overview of the functions and applications of cellular geosynthetics. In: International e-Conference on Modern Trends in Foundation Engineering: Geotechnical Challenges and Solutions. https://www.ecfg.iitm.ac.in/, India (2003)
9. IS 2720-Part 11: Determination of the shear strength parameters of a specimen tested in unconsolidated undrained triaxial compression without the measurement of pore water pressure, Bureau of Indian Standards, New Delhi (1993)
10. IS 2720-Part 13: Method of test for soils, direct shear test, Bureau of Indian Standards, New Delhi (1986)
11. Meguid, M.A., Khan, M.I.: On the role of geofoam density on the interface shear behavior of composite geosystems. Int. J. Geo-Eng. **10**(1), 6 (2019)
12. Padade, A.H., Mandal, J.N.: Behavior of expanded polystyrene (EPS) geofoam under triaxial loading conditions. Electron. J. Geotech. Eng. **17**, 2542–2553 (2019)

Numerical Study on the Effect of Rock-Socketing on Laterally Loaded Piles in the Proximity of Sloping Ground

Nandhagopal Raja and K. Muthukkumaran

1 Introduction

Pile foundations are designed primarily to transfer the axial loading from the superstructure onto the soil strata. However, in cases of high rise buildings, transmission towers, offshore wind turbines, and other such structures that are susceptible to large lateral loads, the pile foundations are to be designed to sustain lateral loads as well. The structural properties of the pile and the properties of the soil strata at the site are both factors that affect the lateral load capacity of the pile.

The study of laterally loaded piles was first presented by Reese and Matlock [1]. They extended Hetenyi's [2] derivation assuming the pile as a beam and considering a linear increment of the modulus of subgrade reaction with depth. Broms [3] presented solutions for the ultimate lateral resistance of a pile assuming the distribution of lateral soil pressure. Davidson [4] presented the normal stress variation in the soil surrounding the pile subjected to lateral load. This was furthered by Reese and Van Impe [5], who presented two different models for the passive wedge formation in sand and clay soil. Certain modifications to the passive wedge theory for the application of it on slopes were further presented by Reese et al. [6].

Researchers have established that a decrease in the lateral load capacity of piles has been observed when they are tested in the vicinity of a sloping ground [7–11]. This effect has been termed as the effect of edge distance. Therefore, it is necessary to identify appropriate solutions to facilitate the better efficiency of the pile foundations installed in the vicinity of sloping ground.

In general, rock-socketing is a technique that has been adapted when the soil stratum appears considerably weak to take on the design loads. IS 14593:1998 [12] recommends a depth of socketing of the pile in the range of one to four times the pile diameter with respect to the type of rock to improve the lateral load capacity.

N. Raja (✉) · K. Muthukkumaran
National Institute of Technology, Tiruchirappalli 620015, India

C. N. V. Satyanarayana Reddy et al. (eds.), *Dynamics of Soil and Modelling of Geotechnical Problems*, Lecture Notes in Civil Engineering 186,
https://doi.org/10.1007/978-981-16-5605-7_22

Carter and Kulhawy [13] presented parametric solutions from which closed-form solutions may be derived for various loading conditions and rock stiffness. Reese [14] developed for the analysis of a single pile socketed in a weak rock considering the non-linearity of the rock mass surrounding by assuming series of springs of soil or rock along the length of the pile based on the p-y curve approach. Muthukkumaran and Prakash [15] presented based on a parametric experimental study that increasing the depth of socketing significantly increases the lateral load-carrying capacity of the pile. Nandhagopal and Muthukumaran [16] performed model experiments on rock-socketed piles installed in the vicinity of the slope created using single-layered loose sand. Based on the results, it was concluded that rock-socketing of piles produced a significant increase in the lateral load capacity of the pile, in turn negating the decrease of it due to the effect of edge distance.

Desai and Appel [17] first developed a general finite element procedure for the analysis of laterally loaded piles. The soil behaviour was assumed to be linearly elastic, and the pile was modelled as a 1D beam element. The interaction between the pile and the soil was modelled using a thin-layer element. Yang and Jeremi [18] used FE methods to study the behaviour of laterally loaded piles on layered soil. A simple Von-Mises material model and a Drucker–Prager model were concluded to best model the clay and sand soils with acceptable accuracy, respectively. Chae et al. [19] reaffirmed the decrease of lateral load capacity of piles in the vicinity of sloping ground based on model and prototype 3D FEM analyses. Georgiadis and Georgiadis [20, 21] studied laterally loaded piles on cohesive slopes based on 3D FEM tests. They concluded that the piles of L/D = 10–20 on a sloping ground of 45° were unaffected by the effect of the slope beyond a distance of 6 pile diameters. Karthigeyan S et al. [22] studied the influence of depth of socketing on the behaviour laterally loaded short piles using 3D FEM techniques. It was observed that the lateral load capacity attained a constant value after a significant increase. Karthigeyan S and Rajagopal K [23] conducted 3D FEM analysis on rock-socketed piles embedded in cohesionless soil overlying rock. It was concluded that the effect of depth of socketing might not be significant on long piles where the depth of soil is significant to resist the lateral load.

From the literature study, it can be observed that there is very limited published literature related to the laterally loaded rock-socketed piles in the multi-layered soil or the vicinity of sloping ground. Therefore, in this paper, the results of parametric numerical analyses performed on a full-scale laterally loaded rock-socketed pile modelled onto a multi-layered soil in the vicinity of sloping ground have been discussed. The response of the rock-socketed piles has been compared to the same piles tested on undisturbed horizontal ground and un-socketed piles modelled and tested in identical conditions. The position of the pile and the depth of socketing have been used as variable parameters.

Table 1 Properties of the soil-rock stratum

Properties	Soil layer 1	Soil layer 2	Rock
Material model	HS-Small	HS-Small	MC
Material behaviour	Drained	Drained	Drained
Unsaturated unit weight (Υ_{unsat}) (kN/m^3)	18.7	19.5	28
Young's modulus (E) (kN/m^2)	3.5E + 4	5.0E + 4	5.0E + 6
Poisson's ratio ($\surd$)	0.34	0.3	0.21
Cohesion (c) (kN/m^2)	20	0.1	500
Friction angle (Φ)	35	43	27
Dilatancy angle (ψ)	5	13	-
Interface factor (R_{inter})	0.9	0.9	0.9

2 Numerical Model

All finite element analyses in the parametric study were performed by using the 3D finite element program PLAXIS 3D. The pile, soil strata, and their properties have been derived from the full-scale lateral load field test presented by Ismael [24]. The pile was modelled using the embedded beam tool as a linearly elastic body. The embedded beam elements are 3-node line elements with six degrees of freedom. The soil was modelled using the Hardening small strain (HS-small) model as it considers both stress and strain dependency of the soil. The soil model used 15 node-wedge elements having six stress points, which gives an ample number of locations for the accurate measurement of the stress–strain behaviour of the pile along with its embedded depth. The pile-soil interface has been modelled using the interface element (R_{inter}), which recreates the ideal friction in the system. The rock was modelled using a simple Mohr–Coulomb (MC) model. The medium-mesh has been adapted throughout the study based on a convergence study. The properties used for the modelling of this soil-rock stratum are given in Table 1.

3 Parametric Study

In this parametric study, lateral load tests were conducted on a full-scale prototype pile embedded of diameter 0.3 m, embedded depth 5 m, and flexural stiffness of 20.2MN/m^2 onto a two-layered soil stratum. The pile properties are listed in Table 2.

The classification of the pile has been calculated based on IS 2911-Part 1/Sect. 4 [25] according to which, if L $\leq$ 2 T, the pile is short rigid, and if L $\geq$ 4 T, then the pile is long flexible. Therefore, the pile used in this study has been classified as intermediate in all cases, as shown in Table 3.

The soil stratum has been modelled as field pile tests 9 to 12 presented by Ismael [24]. A slope of 1 V: 1.5 H was introduced onto the strata. The position of the pile was

Table 2 Properties of the Pile

Description	Value
Pile diameter (m)	0.3
Pile length (m)	5
Density of pile (kN/m^3)	25
Flexural Stiffness (EI) MN/m^2	20.2

Table 3 Values for Classification of the Pile

Case	Embedded length of the pile (m)	L/D	L/T
+15D to 0D	5	16.67	3.94
−3D	4.4	14.67	3.47
−6D	3.8	12.67	3.00
−9D	3.2	10.67	2.52

considered a varying parameter with positions on both the embankment and sloping ground. The position of the pile on the embankment was modelled and tested at 15 pile diameters from the crest (+15D). Then, the position was moved towards the crest by decrements of three pile diameters. The position was varied until the pile was situated and tested at nine pile diameters from the crest on the sloping ground (−9D). The positions of the pile are shown in Fig. 1.

The depth of socketing was also considered as a variable parameter with starting from 1D (one time the pile diameter) and further improving it to 2D and 3D. The response of the piles is compared to the corresponding pile tested on undisturbed horizontal ground to estimate the decrease in the lateral load capacity due to the position of the pile. The response is also compared to that of the un-socketed piles tested in identical conditions to estimate the improvement of the lateral load capacity attributed to the rock-socketing. The lateral load corresponding to the pile displacement of 4 mm at the ground level was taken as the lateral load capacity of the pile as per IS 14593–1998.

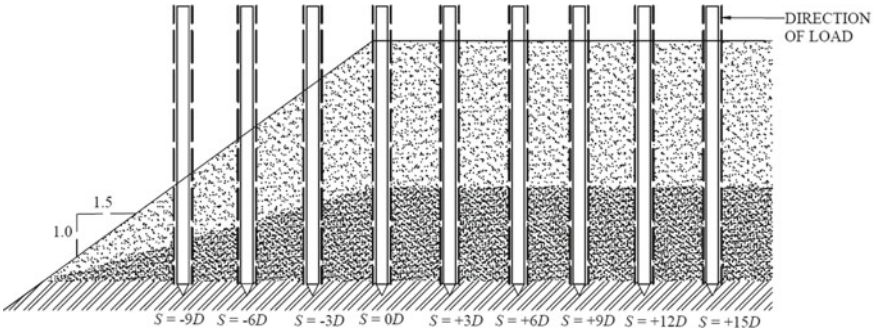

Fig. 1 Positions of the pile

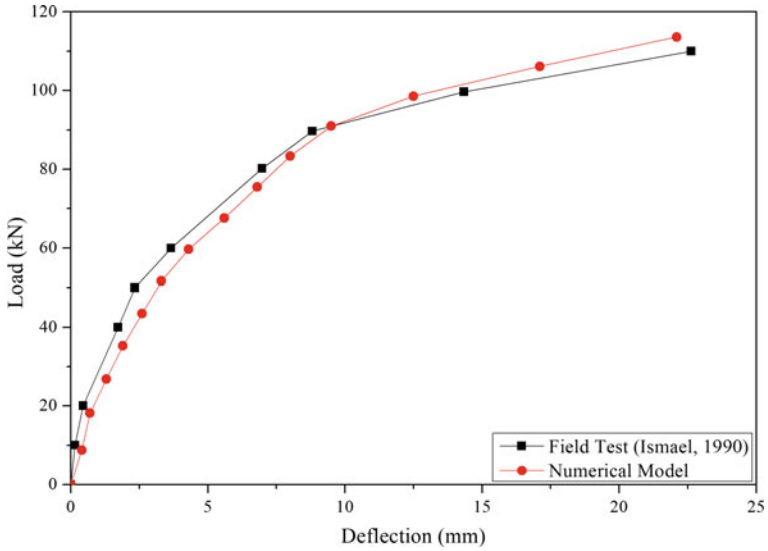

Fig. 2 Validation of the numerical model

4 Validation

Ismael [24] conducted laterally loaded tests on 12 piles, of which piles 9 to 12 are of relevance to the present study. The piles were 5 m long and of 0.3 m in diameter and were situated on two-layered soil strata, a surface layer of cemented sand from 0 to 3.5 m underlain by very dense sand from 3.5 m to 5 m. The average load–deflection response of the four piles was presented and has been considered for comparison of this experimental study.

The full-scale test presented by Ismael [24] was modelled using the model developed on PLAXIS 3D, and the resulting load–deflection curve has been compared with field test results. This is shown in Fig. 2. The curves are found to be in good agreement. Therefore, the experimental model is verified to provide results of the lateral response of the pile with acceptable accuracy.

5 Results and Discussion

In this parametric study, the lateral load corresponding to the pile displacement of 4 mm at the ground level was taken as the lateral load capacity of the pile as per IS 14593–1998. A test for each case of un-socketed and socketed piles was performed on the undisturbed horizontal ground to observe the ideal response of the pile and estimate the lateral load capacity of the pile to compare to other corresponding cases.

The developed load–displacement curves for the different cases in this study are shown in Figs. 3, 4, 5, and 6. The comparison of the observed lateral load capacities for the different piles is shown in Fig. 7.

From the lateral load–displacement curves, it can be observed that the lateral load capacity decreases as the position of the pile move from the extreme embankment position (+15D) towards the extreme position on the sloping ground (−9D) for both un-socketed and socketed piles. This decrease can be attributed to the effect of edge distance for the piles on the embankment. Further, for the piles situated on the crest and the sloping ground, a reduction of the volume of soil resisting the lateral movement of the pile is another factor.

With the increase in depth of socketing, as the effect of the slope is negated, piles further on the embankment tend to replicate the response of the pile tested on undisturbed horizontal ground. Therefore, it can be observed that the lateral load capacities of the piles on embankment lay closer to the pile on the horizontal ground in the case of 2D and 3D socketing.

The increase in lateral load capacity, aided by the effect of rock-socketing, can be observed in Fig. 7. The piles situated on the crest and sloping ground can be observed to have the more significant increments in lateral load capacity attributing to the lesser embedded depth causing the load to be transferred onto the rock. Also, it can be observed the increase in lateral load capacity increases with the increase in depth of socketing. In numbers, the lateral load capacity of the pile situated in the extreme position on the sloping ground (-9D) is improved by 22.50%, 32.21%, and 42.05% under 1D, 2D, and 3D socketed conditions, respectively. Whereas, the

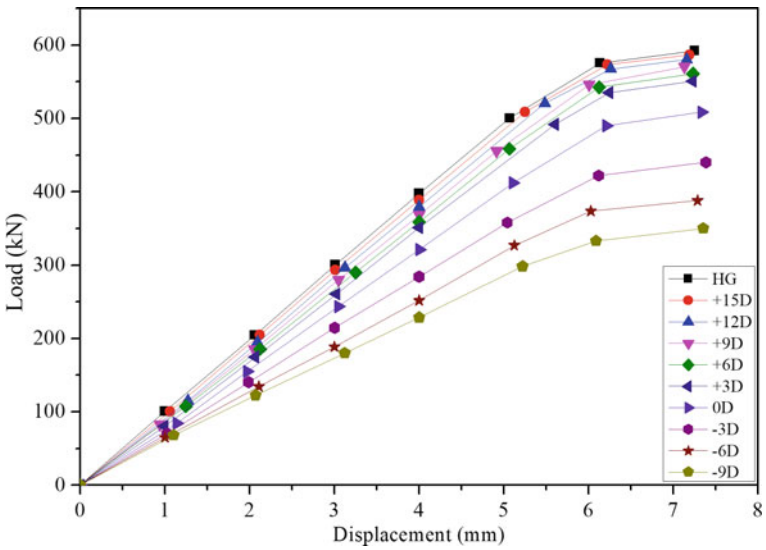

Fig. 3 Lateral Load versus Displacement of un-socketed piles

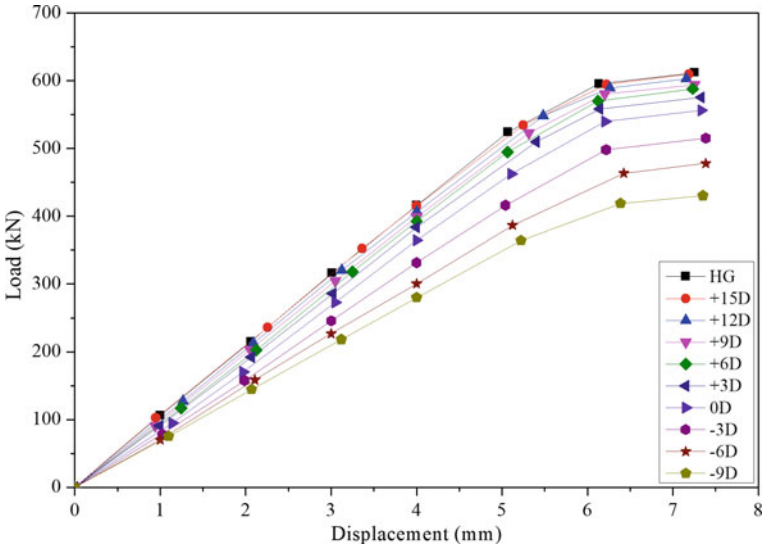

Fig. 4 Lateral Load versus Displacement of 1D socketed piles

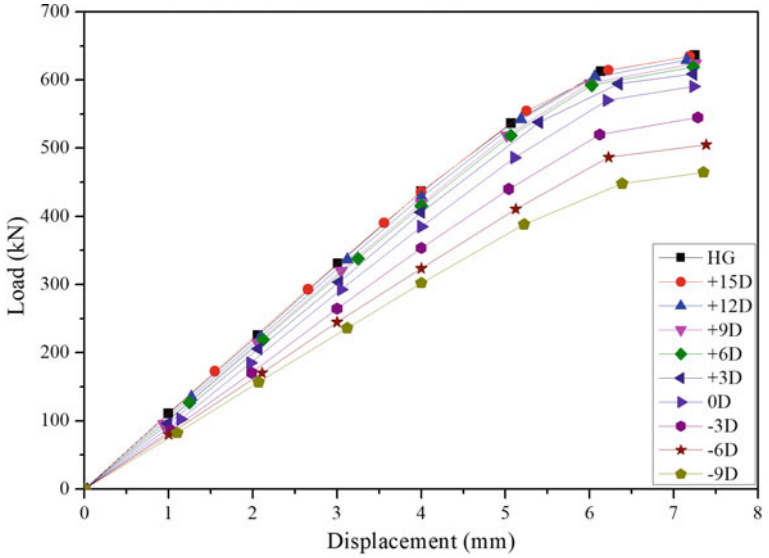

Fig. 5 Lateral Load versus Displacement of 2D socketed piles

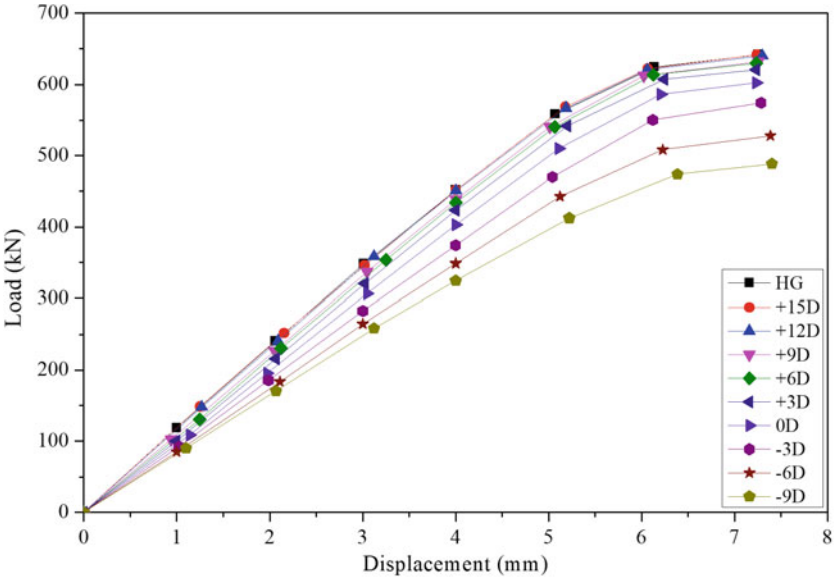

Fig. 6 Lateral Load versus Displacement of 3D socketed piles

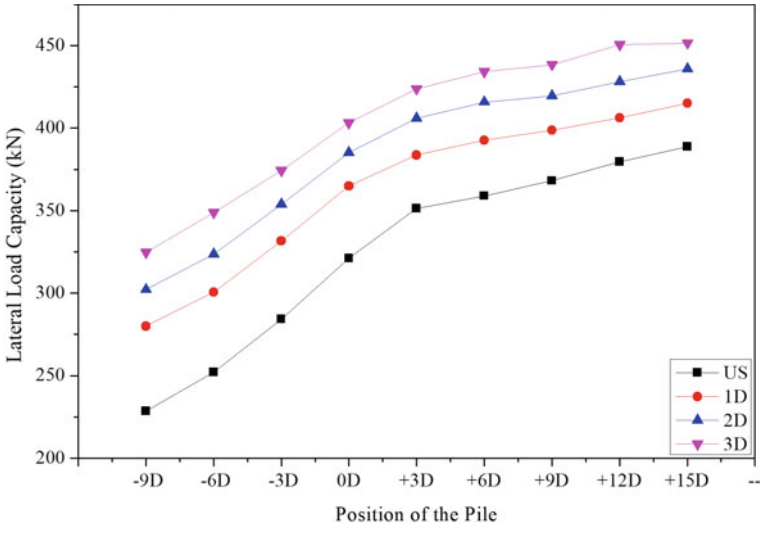

Fig. 7 Comparison of Lateral load capacity of all cases

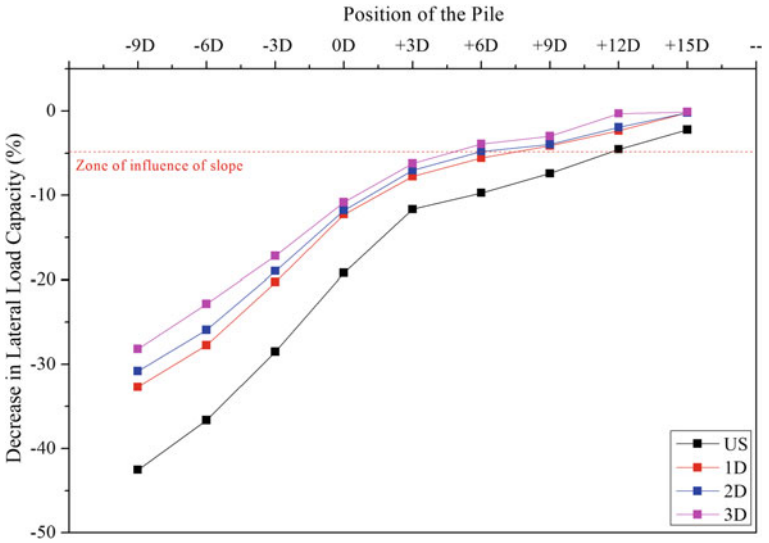

Fig. 8 Comparison of Zone of influence of the effect of slope

improvement of lateral load capacity of the pile situated at the extreme embankment position (+15D) is limited to 6.77%, 12.12%, and 16.15% for the corresponding conditions of rock-socketing.

In Fig. 7, it can be observed that the rate of decrement of lateral load capacity as the position of the piles is moved from extreme embankment position to extreme position on the slope is reduced with the increase in depth of socketing.

It was assuming that a reduction more significant than 5% in the lateral load capacity classifies the pile to be affected by the effect of the slope. Therefore, it implies that the pile is present within the zone of influence. Figure 8 shows the extent of the zone of influence in un-socketed and socketed cases. It can be observed in the figure that the zone of influence of the un-socketed piles (US) lays close to + 12D. Further, as rock-socketing was introduced, the zone of influence can be observed to be less than + 9D in the case of 1D socketing. The zone of influence further decreases with the increase in depth of socketing to + 6D under 2D socketing and lesser than + 6D under 3D socketing.

6 Conclusions

This parametric numerical study was focused on studying the effect of rock-socketing to overcome the effect of slope on piles situated in the vicinity of sloping ground on a multi-layered soil. Based on the results of the numerical analyses performed by varying the position of the pile and depth of socketing, the following conclusions were derived:

1. The increment of lateral load capacity increases with an increase in depth of socketing irrespective of the pile position.
2. The effect of rock-socketing is more effective on the piles situated on the crest and the sloping ground as compared to the piles on the embankment. The improvement of the lateral load capacity of the pile situated in the extreme position on the sloping ground (-9D) was 22.50%, 32.21%, and 42.05%. For the pile on the extreme embankment position (+15D), it was 6.77%, 12.12%, and 16.15% under 1D, 2D, and 3D socketed conditions, respectively.
3. The rate of decrement of lateral load capacity as the position of the piles moved from extreme embankment position to extreme position on the slope is reduced with the increase in depth of socketing.
4. The zone of influence due to the effect of slope decreases with the increase in depth of socketing. The zone of influence lays close to + 12D for un-socketed piles. The zone decreases to less + 9D in 1D socketing, at + 6D in 2D socketing, and lesser than + 6D under the 3D depth of socketing.

References

1. Reese, L.C., Matlock, H.: Non-dimensional solutions for laterally-loaded piles with soil modulus assumed proportional to depth. Proceedings of the 8th Texas Conference on Soil Mechanics and Foundation Engineering, Austin, Texas, pp.1–41 (1956)
2. Hetenyi, M.: Beams on elastic foundation. The University of Michigan Press, Ann Arbor, Michigan (1946)
3. Broms, B.B.: Lateral resistance of piles in cohesion-less soils. J. Soils Found. Div. ASCE **90**(2), 27–63 (1964)
4. Davidson, H.L.: Laterally loaded drilled pier research, Vol 1: Design methodology, Vol. 2: Research documentation. Final Report by GAI Consultants Inc., to Electric Power Research Institute (EPRI) (1982)
5. Reese L.C., Van Impe, W.F.: Single Piles and Pile Groups Under Lateral Loading. CRC Press (2000)
6. Reese, L.C., Isenhower, W.M., Wang, S.T.: Analysis of design of shallow and deep foundations. Wiley, New York (2006)
7. Mezazigh, S., Levacher, D.: Laterally loaded piles in sand: Slope effect on p-y reaction curves. Can. Geotech. J. **35**(3), 433–441 (1998)
8. Muthukkumaran, K., Sundaravadivelu, R., Gandhi, S.R.: Effect of slope on P-Y curves due to surcharge load. Soils Found. **48**(3), 361–369 (2008)
9. Begum, N.A., Muthukkumaran, K.: Experimental investigation on single model pile in sloping ground under lateral load. Int. J. Geotech. Eng. **3**(1), 133–146 (2009)
10. Muthukkumaran, K.: Effect of slope and loading direction on laterally loaded piles in cohesionless soil. Int. J. Geomechanics ASCE **14**(1), 1–7 (2014)
11. Rathod, D., Muthukkumaran, K., Thallak, S.G.: Experimental investigation on behavior of a laterally loaded single pile located on sloping ground. Int. J. Geomechanics ASCE **19**(5), 04019021 (2019)
12. IS 14593–1998, Design and construction of bored cast-in-situ piles founded on rocks—Guidelines. Bureau of Indian Standards, New Delhi
13. Carter, J.P., Kulhawy, F.H.: Analysis of laterally loaded shafts in rock. Geotech. Eng. **118**(6), 839–855 (1992)

14. Reese, L.C.: Analysis of laterally loaded piles in weak rock. J. Geotechn. Geoenvironmental Eng. **123**(11), 1010–1017 (1997)
15. Muthukkumaran, K., Prakash, A.R.: Behaviour of laterally loaded socketed pile in multi-layered soil-rock profile. Japanese Geotechn. Soc. Special Publ. **3**(2), 51–55. https://doi.org/10.3208/jgssp.v03.i07 (2016)
16. Nandhagopal, A.R., Muthukkumaran, K.: Forthcoming. effect of rock-socketing on laterally loaded piles installed in the proximity of sloping ground. Int. J. Geomechanics ASCE (2020)
17. Desai, C., Appel, G.: 3-D analysis of laterally loaded structures. Proceedings of the 2nd International Conference on Numerical Methods in Geomechanics, Blacksburg, pp. 405–418 (1976)
18. Yang, Z., Jeremi, B.: Numerical analysis of pile behaviour under lateral loads in layered elastic–plastic soils. Int. J. Numer. Anal. Methods Geomech. **26**(14), 1385–1406 (2002)
19. Chae, K.S., Ugai, K., Wakai, A.: Lateral resistance of short single piles and pile groups located near slopes. Int. J. Geomechanics ASCE **4**(2), 93–103 (2004)
20. Georgiadis, K., Georgiadis, M.: Undrained lateral pile response in sloping ground. J. Geotechical Geoenviron. Eng. ASCE **136**(11), 1489–1500 (2010)
21. Georgiadis, K., Georgiadis, M.: Development of p-y curves for undrained response of piles near slopes. Comput. Geotech. **40**, 53–61 (2012)
22. Karthigeyan, S, Ramakrishna V.V.G.S.T. Rajagopal, K.: Behaviour of rock socketed short piles under lateral loads. Proceedings of IGC 2004, pp. 386–389 (2004)
23. Karthigeyan, S., Rajagopal, K.: Influence of rock-socketing on the lateral response of single pile. Indian Geotechn. J. **42**(1), 49–55 (2012)
24. Ismael, N.: Behavior of laterally loaded bored piles in cemented sand. J. Geotechn. Eng. Div. ASCE, 1678–1699 (1990)
25. IS 2911—Part 1/ Section 4—2010, Design and construction of pile foundations—code of practice. Bureau of Indian Standards, New Delhi, (2010)

Numerical Analysis on Stability Assessment of Left Bank Rock Slopes, Polavaram Irrigation Tunnel

P. Rajendra Kumar and K. Muthukkumaran

1 Introduction

The evaluation of the stability of slopes becomes essential at the site due to construction activities. When pre-existing geologic features govern the instability like fissures or joints, bedding planes, or faults in rock slopes, the failure will be different cases like plane sliding, wedge sliding, or toppling. A rock slope can fail mostly due to one or a combination of these three mechanisms.

Bolla and Paronuzzi [1] performed geomechanical survey study on a natural rock slope located in Italy. Their study considers the interaction between pre-existing discontinuities internal sub-blocks and evaluates the reason for the collapse of slopes. Basahel and Mitri [2] studied rock mass classification systems to rock slope stability. They use different empirical methods based on their failure mechanism and also their limitations. Naeini et al. [3] studied the parameters like water level, cohesion, and distance of reinforcements numerically investigated on slope stability by using Plaxis 2D Software. Buyuksagis and Goktan [4] studied the effect of Schmidt Hammer type on UCS prediction of rock. Wang and Garga [5] studied numerical models using block spring models for jointed rock mass. They analyse both end—anchored and fully grouted rock bolts for pre-tensioned or untensioned condition. Latha and Garage [6] studied the seismic slope stability analysis of a 350 m high slope using the equivalent continuum approach and the GHB failure criterion. Pain et al. [7] studied the rock slope's static stability analysis using the finite element method (FEM). Griffiths and Lane [8] and Oikawa [9] use the finite element method (FEM) with the strength

P. R. Kumar (✉) · K. Muthukkumaran
Department of Civil Engineering, NIT Tiruchirappalli, Tiruchirappalli 620015, India

K. Muthukkumaran
e-mail: kmk@nitt.edu

C. N. V. Satyanarayana Reddy et al. (eds.), *Dynamics of Soil and Modelling of Geotechnical Problems*, Lecture Notes in Civil Engineering 186,
https://doi.org/10.1007/978-981-16-5605-7_23

reduction technique (Matsui and San) to evaluate the factor of safety (FOS) of soil slope. From literature survey, the design of support is a site specific for slope stability problems.

In this study, stability of slopes of the Polavaram left bank irrigation tunnel has been analysed. It is a multipurpose project, predominantly a significant irrigation project involving the construction of a Rock Fill Dam, Gated Spillway, Powerhouse, Navigation Lock system, Canal, and Tunnel systems on either bank to provide irrigation for 23.20 lakh acres. The longitudinal section, along with the left bank approach and tunnel exit, is shown in Fig. 1. The site photos at left bank approach are shown in Fig. 2 to design support system for stability of slopes.

2 Description of the Study Area

The study area is located on the Godavari River in the East Godavari District of Visakhapatnam Districts, Andhra Pradesh, India. Different field studies were carried out to find structural discontinuities, soil and weathering profile, topographical features and examination of drill cores and core logging. The rock samples were collected for assessing rock mass parameters. This region is covered with thick soil consists of silt, clay and laterite occurs for a depth of 8–20 m and weathered zones of Kondalites varies from 3 to 20 m. It is observed that a stretch of 600 m from the entry portal is of Garnetiferous biotite gneiss (from Ch. 1960 to Ch. 2560) followed by 200 m of charnokite (from Ch. 2560 to Ch. 2760) and 150 m of Kondalites (from Ch. 2660 to Ch. 2825) across the proposed tunnel alignment. It can be seen that the proposed tunnel alignment falls in massive rock formations and the major rock type are biotite gneiss and Kondalites. The general strike of the above formations is NEE-SWW and dip at 40° to 60° towards NW or SE. Although strike joints, dip joints, oblique joints are common in this area, there are no folds and faults noticed in this area (Table 1).

3 Material Properties

To perform the stability analysis, the material properties are evaluated from field data report from Polavaram irrigation tunnel design report from Polavaram Irrigation Project Head Works (PIPHW) and the lab tests results are used in the numerical simulation. In collection of field data, the joints are measured by using compass and Joint Roughness Coefficient (JRC) is measured based on roughness profiles developed by Barton. In Hoek and Brown [10, 11] failure criterion (1997 and 2002) is used for estimating the rock mass properties from intact uniaxial compressive strength test (σ_c), Geological Strength Index (GSI), Rock Quality Designation (RQD), Intact Modulus (E) and Disturbance factor (D). Samples were collected from the field for conducting Brazilian point load test of the available irregular samples of 50 mm dia,

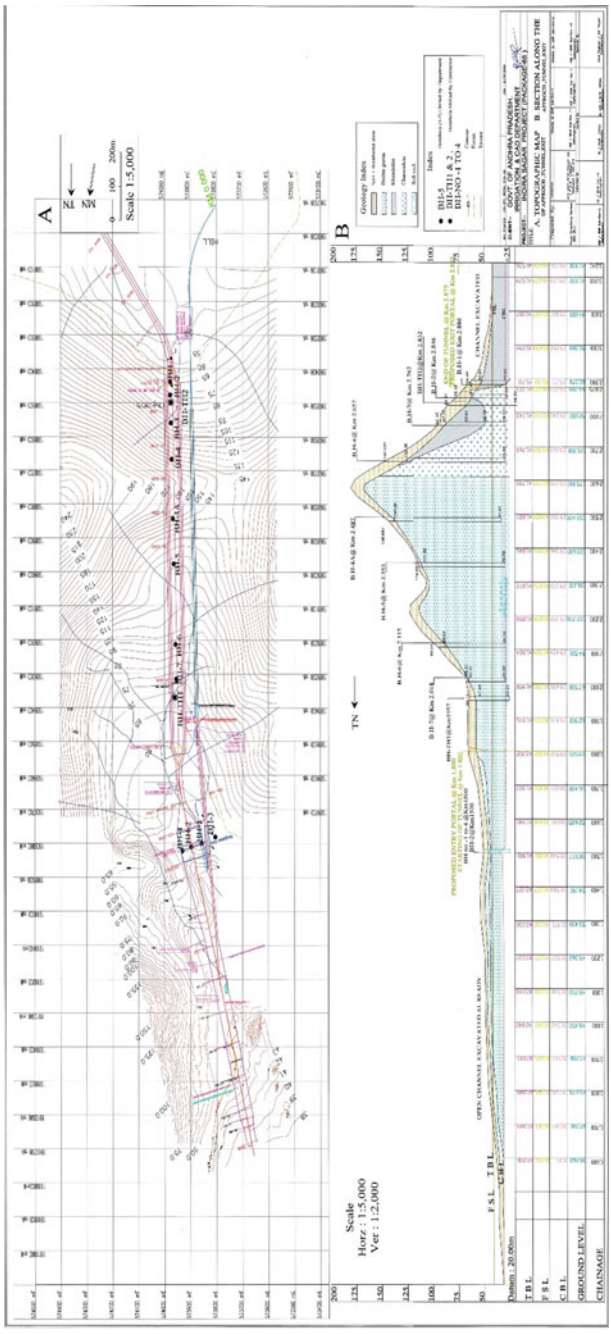

Fig. 1 Longitudinal section along the approach, tunnel exit

Fig. 2 Site Photos at approach of left irrigation tunnel of Polavaram

and the equivalent σ_c values were calculated as per International Society for Rock Mechanics (ISRM) standards. From Roclab, Hoek-Brown Criterion parameters mb, s and a and Mohr–Coulomb parameters cohesion (c) and angle of internal friction (φ) are evaluated. The results are presented in Table 2 and Fig. 3.

The equation used in the analysis in FEM analysis is

$$\tau = c + \sigma_n \tan\Phi, \tag{1}$$

where τ is the shear strength of joint, φ is the friction angle, c is the Cohesion and σ_n is the Normal Stress.

The latest version of the Hoek–Brown failure criterion is expressed as Eqs. (2)–(5)

$$\sigma_1{}' = \sigma_3{}' + \sigma_{ci}\left(m_b \frac{\sigma_3{}'}{\sigma_{ci}} + s\right)^a, \tag{2}$$

Table 1 Rock mass properties

Unit weight (γ) (kN/m^3)	Elastic modulus (E) (GPa)	Poisson's ratio (υ)	Cohesion (c) (kPa)	Tension (kPa)	Angle of internal friction (φ)	GSI
26	0.11	0.3	1290	337	61	70

Table 2 Intact rock properties

Unit weight (γ) (kN/m^3)	Elastic modulus (GPa)	Poisson's ratio (υ)	mi	s	a
26	19.93	0.3	23	0.036	0.501

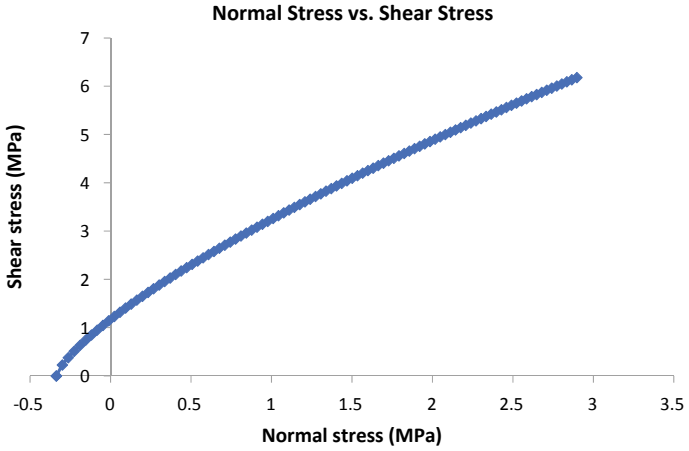

Fig. 3 Normal stress versus shear stress for rockmass

where

$$m_b = m_i exp\left(\frac{GSI - 100}{28 - 14D}\right), \tag{3}$$

$$s = exp\left(\frac{GSI - 100}{9 - 3D}\right)$$

$$a = \frac{1}{2} + \frac{1}{6}\left(e^{-GSI/15} - e^{-20/3}\right) \tag{5}$$

4 Stability Analysis

The FE model discretized into six-nodded triangular element mesh in Phase^2 software. In Phase^2 factor of safety is calculated using shear strength reduction method for finding the critical strength reduction factor. The strength of material is reduced by some factor, and FE solution is evaluated to obtain the critical SRF. The probabilistic analysis carried using Slide2 and the plot for the factor of safety variation with cohesion and the Angle of Internal friction shown in Figs. 4 and 5.

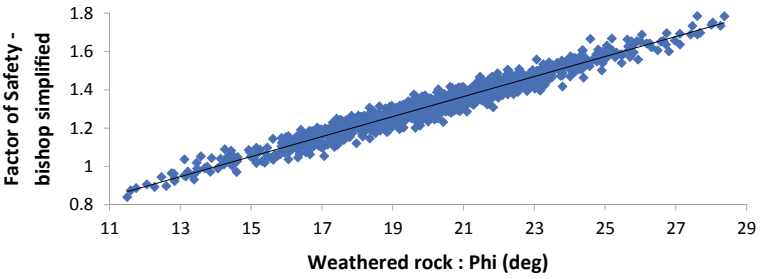

Fig. 4 Factor of safety versus Phi for weathered rock

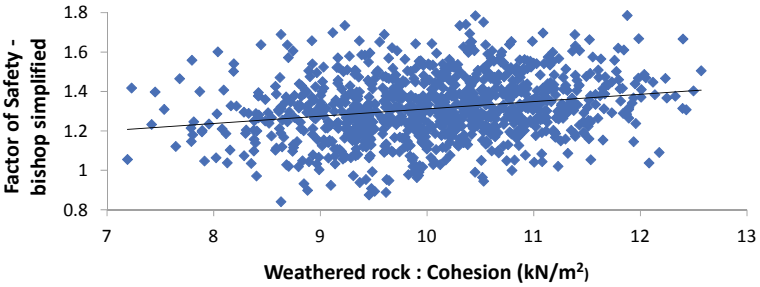

Fig. 5 Factor of safety versus Cohesion for weathered rock

4.1 Static Stability Analysis

Two-dimensional plane strain approach is used for the stability of rock slope. In this model, the rock slope is a continuum model. The effect of discontinuities considered are reducing the properties and strength of intact rock to those of the rock mass. FOS is calculated using the Shear Strength Reduction (SSR) method [12].

4.2 Results of Finite Element Analysis

The results are from numerical simulation of the rock slopes using a continuum model with and without tunnel effect.

4.2.1 Results of Continuum Analysis

The rock slope is evaluated under gravity using the input parameters. Figure 6 shows the discretized Finite Element (FE) model of the rock slope. The FE model has discretized into a deformable 6 noded triangular plane strain finite element. The

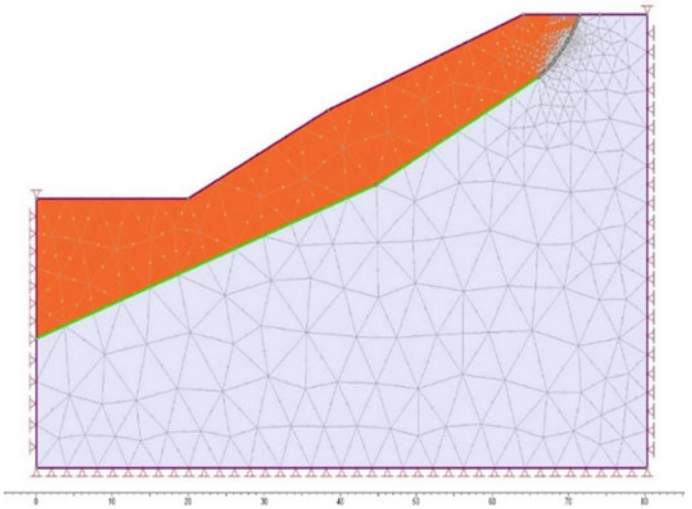

Fig. 6 Discretised FE mesh for continuum analysis

stresses vary linearly with depth, and the ratio of the horizontal to vertical stress in the rock mass was equal to 1.0. For a particular mesh resolution, we perform several trials. The most common method for improving the solution convergence is by successively increasing mesh resolution, i.e., increasing the number of elements. The total displacement contour of the continuum FE model is shown in Fig. 7. The factor of safety is to be 1.29 in continuum analysis. The total displacement contour of continuum FE model with tunnel interface is shown in Fig. 8. The factor of safety

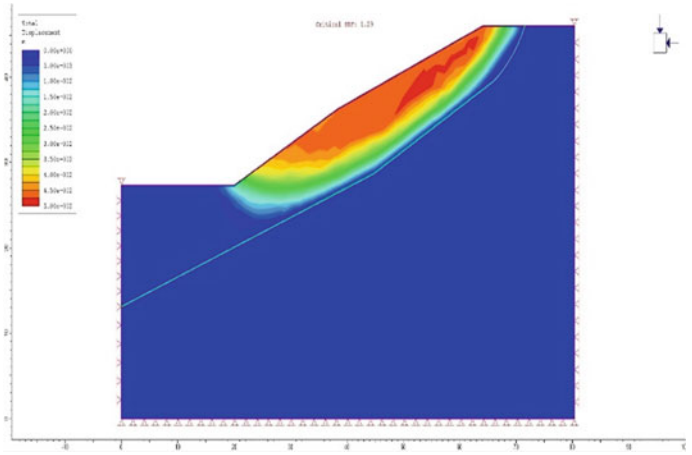

Fig. 7 Total displacement contour

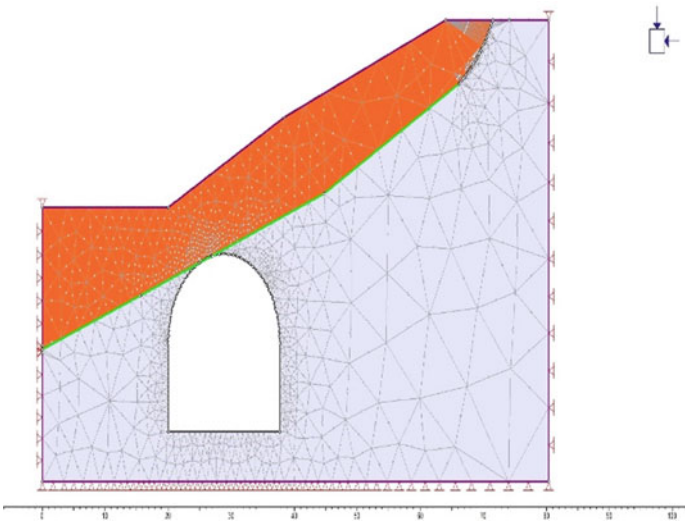

Fig. 8 Rock Slope with tunnel portal

in continuum analysis with tunnel interface is 0.8 due to excavation of tunnel. The total displacement contour of continuum FE model with tunnel interface is shown in Fig. 9. The factor of safety is to be 1.64 in continuum analysis with support (Figs. 10 and 11).

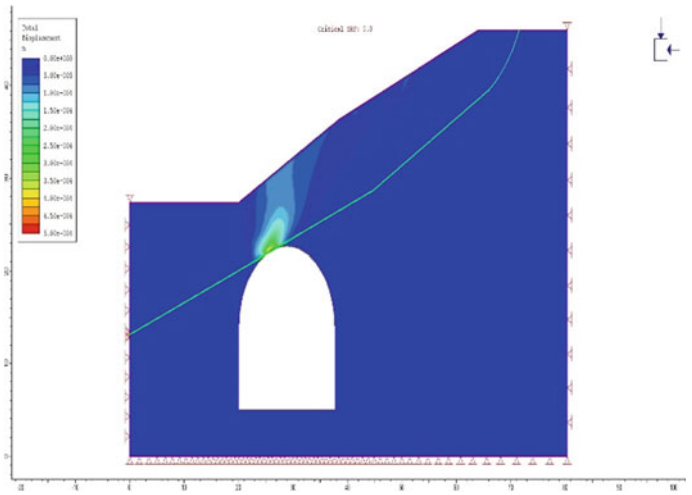

Fig. 9 Displacement contours

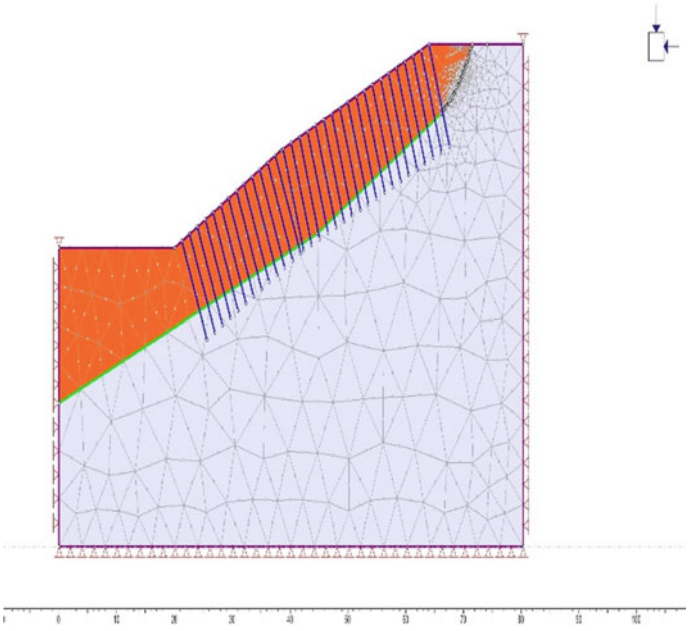

Fig. 10 Rock slope with support

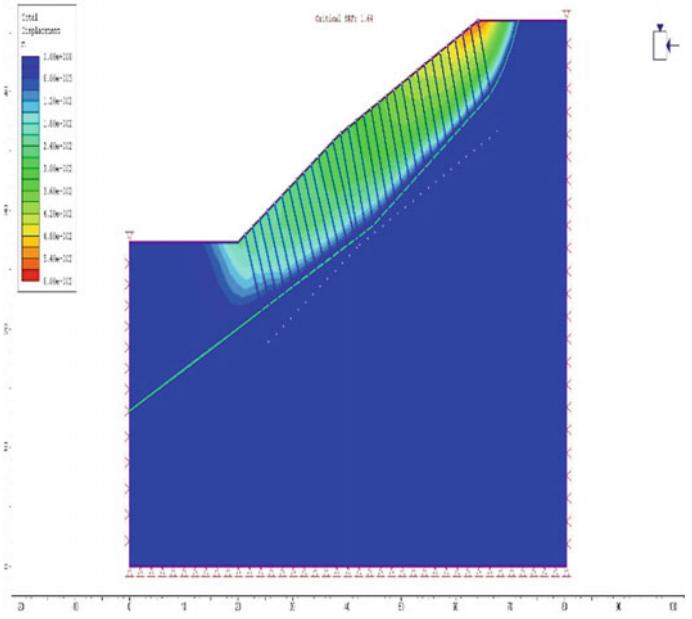

Fig. 11 Displacement contours

5 Conclusions

A continuum model performed the stability analysis of the rock slope with and without a tunnel using Phase^2. The rock mass in these slopes is blocky or very blocky. From the FE analysis, the following significant conclusions are drawn.

1. The critical Strength Reduction Factor (SRF) obtained is 1.29 in model with continuum analysis, and it is decreased further to 0.8 in continuum analysis with a tunnel at slope face.
2. The critical SRF is increased from 0.8 to 1.64 with addition of rock bolts of length 10 m End anchored and 1.5 m spacing and placing normal to the slope face.

Acknowledgements The authors are grateful to Superintending Engineer, Deputy Executive Engineer, Assistant Executive Engineer and Junior Engineer of PIPHW Circle, Dowlaiswaram and M/s Max Infra Manager for his kind permission to do work and provide the field data to publish this work.

References

1. Bolla, A., Paronuzzi, P.: Geomechanical field survey to identify an unstable rock slope: the Passo della Morte case history (NE Italy). Rock Mech. Rock Eng. **53**(4) (2020). https://doi.org/10.1007/s00603-019-01963-w
2. Basahel, H., Mitri, H.: journal of rock mechanics and geotechnical engineering application of rock mass classification systems to rock slope stability assessment : a case study. J. Rock Mech. Geotech. Eng. **9**(6), 993–1009 (2017). https://doi.org/10.1016/j.jrmge.2017.07.007
3. Naeini, S.A., Gholampoor, N., Kashki, R.R.: The effect of reinforcement on stability of slopes. **3**(1), 35–38 (2015)
4. Buyuksagis, I.S., Goktan, R.M.: The effect of Schmidt hammer type on uniaxial compressive strength prediction of rock. Int. J. Rock Mech. Min. Sci. **44**(2), 299–307 (2007). https://doi.org/10.1016/j.ijrmms.2006.07.008
5. Wang, B., Garga, V.K.: A numerical method for modelling large displacements of jointed rocks. I. Fundamentals. Can. Geotech. J. **30**(1), 96–108 (1993) https://doi.org/10.1139/t93-009
6. Latha, G.M., Garaga, A.: Seismic stability analysis of a Himalayan rock slope. Rock Mech. Rock Eng. **43**(6), 831–843 (2010). https://doi.org/10.1007/s00603-010-0088-3
7. Pain, A., Kanungo, D.P., Sarkar, S.: Rock slope stability assessment using finite element based modelling—examples from the Indian Himalayas. Geomechanics Geoeng. **9**(3), 215–230 (2014). https://doi.org/10.1080/17486025.2014.883465
8. Griffiths, D.V., Lane, P.A.: Slope stability analysis by ® nite elements. GeÂotechnique **49**(3), 387–403 (2013)
9. Oikawa, T.: NII-electronic library service. Chem. Pharm. Bull. (43), 2091 (2002). [Online]. Available:http://www.mendeley.com/research/geology-volcanic-history-eruptive-style-yakedake-volcano-group-central-japan/
10. Hoek, E., Brown, E.T.: Practical estimates of rock mass strength. Int. J. Rock Mech. Min. Sci. **34**(8), 1165–1186 (1997). https://doi.org/10.1016/S1365-1609(97)80069-X
11. Eberhardt, E.: The Hoek-Brown failure criterion. Rock Mech. Rock Eng. **45**(6), 981–988 (2012). https://doi.org/10.1007/s00603-012-0276-4

12. Matsui, T., San, K.C.: Finite element slope stability analysis by shear strength reduction technique. Soils Found. **32**(1), 59–70 (1992)
13. Hoek, E., Bray, J.W.: Rock slope engineering, 3rd edn. Taylor & Francis, London (1981)
14. PHASE^2: A 2D finite element program for calculating stresses and estimating support around the underground excavations. Geomechanics Software and Research. Toronto, ON: Rocscience Inc (2012)

Displacement Based Analysis of Retaining Wall with Narrow Backfill Under Rotation About Bottom Mode

Godas Srikar, Satyendra Mittal, and Ankarapu Sindhuja

1 Introduction

Retaining walls are the most common geotechnical structures used in any nation's highway construction. The earth pressure distribution is generally an important factor for estimating point of application of lateral thrust. Though distribution is assumed as linear, many studies have revealed that the realistic distribution is non-linear and mostly curvilinear [1–4]. The construction of retaining wall involves many complications in practical view point. One of the complication is construction of retaining wall in hilly areas where the space of the backfill is constrained [5]. Considering construction methodology of such retaining wall as out of scope, the present paper emphasizes on the analysis. In general retaining walls are analyzed using conventional earth pressure theories namely Coulomb's earth pressure theory or Rankine' theory yields a poor design of retaining wall in economy grounds. Reference [6] is pioneering study that addressed the effect of confinement of backfill material in silos aspect. The earth pressure acting on the retaining wall is majorly affected by arching affect in the backfill [7–10]. This effect is phenomenal in the case of retaining walls with narrow backfill. Researchers in the previous study have addressed the problem in three different approaches namely experimental, analytical, and numerical approach.

Reference [11] adopted limit equilibrium to analyze retaining wall with reinforced backfill in limited space. This study proposes design charts to obtain lateral earth pressure for different height to width ratio of backfill. Reference [12, 13] also proposed analytical solution for retaining wall with narrow backfill width. Reference [13] has divided the problem into different mechanisms based on the width of the

G. Srikar (✉) · S. Mittal
Indian Institute of Technology Roorkee, Roorkee 247667, Uttarakhand, India

A. Sindhuja
Government Polytechnic Korutla, Korutla 505326, Telangana, India

C. N. V. Satyanarayana Reddy et al. (eds.), *Dynamics of Soil and Modelling of Geotechnical Problems*, Lecture Notes in Civil Engineering 186,
https://doi.org/10.1007/978-981-16-5605-7_24

backfill. The study reveals that as width of the backfill reduces, the number of potential failure wedges increases. As width reduces the induced failure plane coincides with the lateral constraint and affects the weight of the soil participating in the failure. As the weight of the soil participating in failure plays an important role in attaining limit equilibrium, it affects lateral pressure acting on the wall.

The available literature has number of studies in analytical approach, and there are very limited number of papers that offer experimental view to study the problem. Reference [14] conducted laboratorial test to study the effect of backfill width on lateral earth pressure acting on the retaining. The study presents centrifugal tests for different widths of the backfill. The study reveals that arching effect in backfill due to lateral confinement plays an important role in reduction in lateral earth pressure acting on the retaining wall. Confinement of backfill is mainly due to rigid retaining wall on one side and lateral constraint like hillock on other side. A virtual arch is formed in the backfill starting from vertical wall and ending on the other side, i.e., on hillock side. The total vertical overburden pressure acting in the soil is reacted by this virtual arch and the friction between backfill and retaining wall, backfill and hillock on the other side. Thereby reducing net vertical pressure in backfill, further reducing the lateral earth pressure acting on the retaining wall. Very recently, [15] conducted laboratorial study to know the behavior of narrow backfill wall for three different modes of yielding of retaining wall namely sliding mode, rotation about bottom, and rotation about top. The study reveals that the measured earth pressure coefficient is much smaller than compared to Coulomb's earth pressure coefficient.

Apart from experimental investigation, numerical analysis also gained enough recognition in the literature. Though the experimental study provides a detailed behavior of retaining wall, the study can only be done to a model. Whereas, in numerical approach it has its own advantage of studying for any scale of the problem. Each approach has its own advantages. References [16, 17] proposed numerical analysis to study the effect of width of the backfill.

The present study considers a narrow backfill retaining wall in a numerical background using PLAXIS-2D software. The study examines the effect of width of the backfill on lateral earth pressure acting on the wall. The type of displacement in the wall adopted in the study is rotation about bottom. The effect of backfill width on the induced potential failure plane is presented. Further, the study presents the influence of aspect ratio of backfill space on the coefficient of lateral earth pressure coefficient.

2 Methodology

The present numerical analysis by varying width of the backfill is carried in PLAXIS-2D software. The present problem deals with retaining wall, and the strains in length direction are assumed to be zero. Hence to reduce computational effort, the present problem is assumed to obey plane strain condition.

Figure 1 shows the model of retaining wall used in the study. The model is analyzed accordingly by varying width of the backfill. The present model has an element with 15 nodal points. This consideration improves the accuracy in the results obtained.

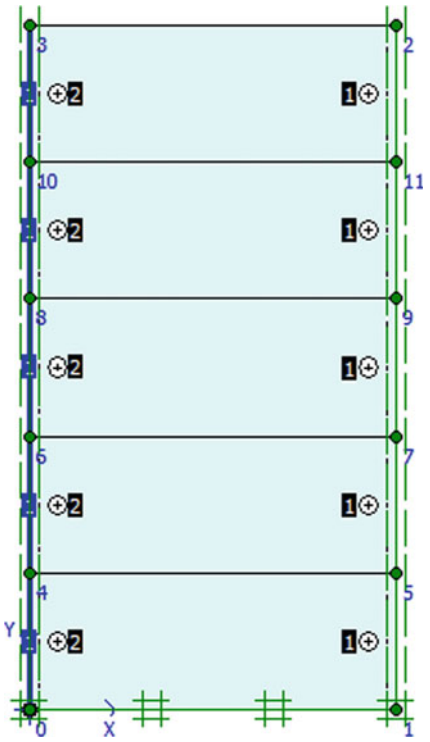

Fig. 1 Finite element model adopted for the study

In the present study, the height of the wall is fixed as 5 m and the width of the back-fill is varied. Mohr–Coulomb failure criterion is adopted for modeling backfill soil. Table 1 shows the different properties considered in the model. Horizontally fixed vertical boundaries are adopted in the study to allow vertical displacement. Whereas horizontally and vertically fixed, bottom horizontal boundaries are adopted in the model. It is recommendable that a reduced value of the shear strength is to be considered at the interface of the wall-backfill. Therefore, separate interface elements are modeled. Staged construction is adopted to simulate the field conditions in the model.

Table 1 Properties used in the numerical analysis

Material	Property	Value
Soil	Unit weight	13.4 kN/m^3
	Friction angle	29^o
	Model	Mohr–Coulomb
Wall	Normal stiffness	1.26E7 kN/m
	Flexural stiffness	4.2E4kN-m^2/m
	Model	Plate-Linear elastic

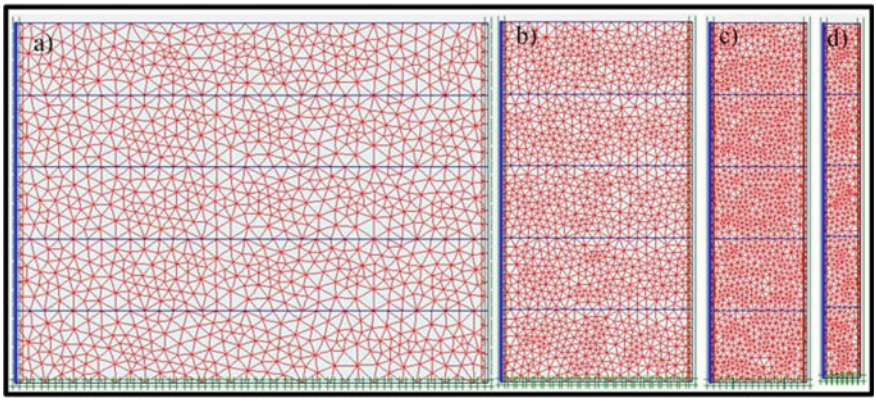

Fig. 2 Finite element mesh generated for four different widths of backfill **a** 6.57 m, **b**. 2.67, **c**. 1.36 m, and **d**. 0.56 m

To conduct a detailed study, the adopted model is validated with an experimental study. For this objective, the model is compared with that of [15] maintaining the same geometrical limitations. Reference [15] performed a centrifugal test to evaluate lateral earth pressure acting on an unyielding wall. The test considers a wall height of 5 m with four different widths of the backfill (6.57 m, 2.67 m, 1.36 m, and 0.56 m). Figure 2 shows the finite element mesh generated in numerical analysis. The soil properties adopted in the analysis are considered from [15]. The lateral earth pressure distribution on the wall is considered as the parameter to validate the present finite element model.

Figure 3 shows the earth pressure distribution acting on the unyielding wall obtained from centrifugal test and numerical analysis for the four considered widths of the backfill.

3 Results and Discussion

Numerical analysis is conducted for the wall rotating about bottom mode. To simulate the rotation about bottom mode, the wall is prescribed with varying displacement. In particular, zero displacement is prescribed at bottom of the wall and a maximum displacement of 20 mm (0.4% of height of the wall) is prescribed at top of the wall as shown in Fig. 4. The displacements in the model is activated after activating the wall elements and soil cluster in construction stage.

Figure 5 shows the maximum shear strain contours which are considered as failure planes in the present study. The potential failure angle is observed to be around 56.4° with respect to horizontal plane. Figure 6 shows the variation of normalized coefficient of lateral earth pressure coefficient with respect to aspect ratio of backfill space (width/height). The normalization of coefficient of lateral pressure is

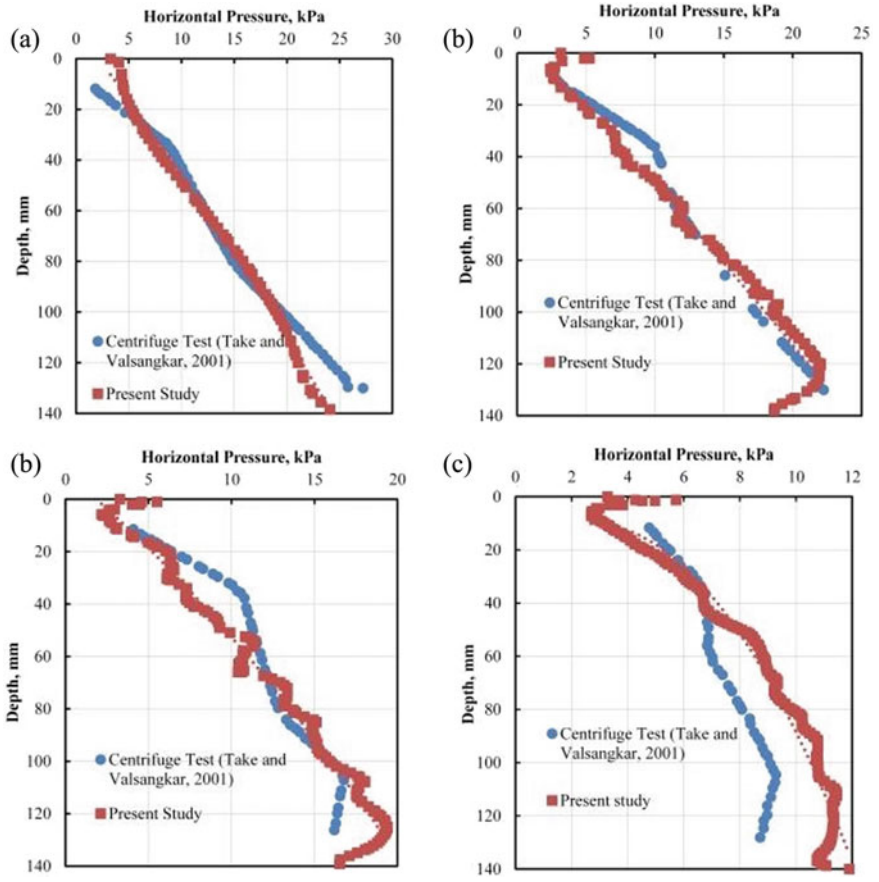

Fig. 3 Earth pressure distribution acting on the retaining wall with different backfill widths **a** 6.57 m, **b** 2.67 m, **c** 1.36 m, and **d** 0.56 m

done by considering the ratio of obtained coefficient of earth pressure from numerical analysis to the coefficient of earth pressure obtained from Coulomb's theory (Ka(FEM)/Ka(Coulomb)) as shown in Fig. 6.

It is observed from Fig. 6 that as aspect ratio of backfill space decreases the coefficient of lateral earth pressure reduces. Though small discrepancy is observed at an aspect ratio of 0.3, the value of coefficient reduces. From Fig. 6 it is evident that the lateral earth pressure ratio (Ka(FEM)/Ka(Coulomb)) remains unity for the aspect ratio greater than unity.

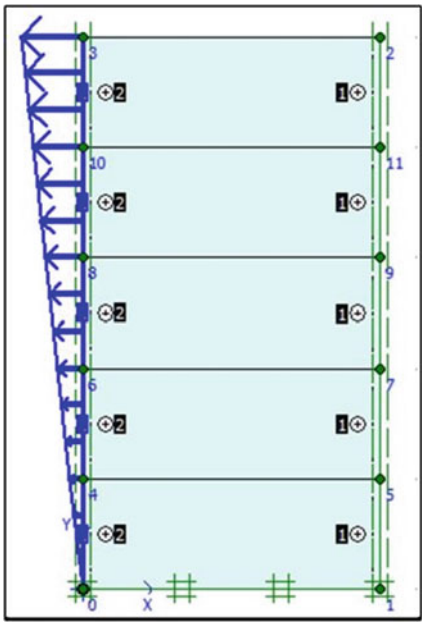

Fig. 4 Geometrical model showing rotation of wall about bottom

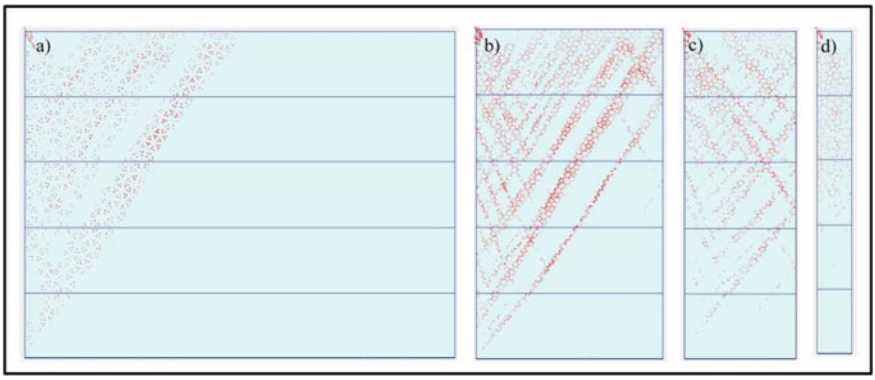

Fig. 5 The failure planes obtained for different depths of backfill **a** 6.57 m, **b** 2.67 m, **c** 1.36 m, and **d** 0.56 m

4 Conclusions

The proposed study considers displacement based numerical approach to investigate the effect of aspect ratio of backfill space on lateral earth pressure coefficient. The rotation about bottom mode is adopted, and the pressure acting on the wall due to backfill soil is estimated. Firstly, the adopted model that used for the study is

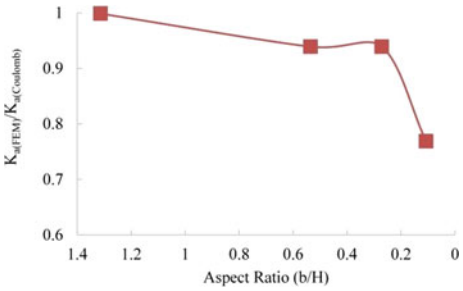

Fig. 6 Variation of lateral earth pressure coefficient with aspect ratio of backfill space

validated by comparing lateral earth pressure obtained from a laboratorial centrifuge test adopted from the literature. The comparison of lateral earth pressure obtained from numerical study and centrifugal study is observed to be in good agreement. The rotation in the wall is applied about bottom. The lateral earth pressure obtained for different widths is estimated. The failure plan for each widths of the back fill is presented in the study. It is observed that the failure plane is contained in the backfill as the aspect ratio of the backfill space is reduced. The reduction in the lateral earth pressure as the aspect ratio of backfill space is reported in terms of coefficient of lateral earth pressure ratio.

References

1. Spangler, M.G., Handy, R.L.: Soil Engineering. Harper and Row, New York (1982)
2. Fang, Y.S., Ishibashi, I.: Static earth pressures with various wall movements. J. Geotechn. Eng. **112**(3), 317–333 (1986)
3. Wang, Y.Z.: Distribution of earth pressure on a retaining wall. Geotechnique **50**(1), 83–88 (2000)
4. Tsagareli, Z.V.: Experimental investigation of the pressure of a loose medium on retaining walls with a vertical back face and horizontal backfill surface. Soil Mechan. Found. Eng. **2**(4), 197–200 (1965)
5. Janssen, H.A.: Versuche uber getreidedruck in silozellen. Z. Ver. Dtsch. Ing **39**(35), 1045–1049 (1895)
6. Paik, K.H., Salgado, R.: Estimation of active earth pressure against rigid retaining walls considering arching effects. Geotechnique **53**(7), 643–653 (2003)
7. Rao, P., Chen, Q., Zhou, Y., Nimbalkar, S., Chiaro, G.: Determination of active earth pressure on rigid retaining wall considering arching effect in cohesive backfill soil. Int. J. Geomech. **16**(3), 04015082 (2016)
8. Singh, S., Sivakugan, N., Shukla, S.K.: Can soil arching be insensitive to ϕ? Int. J. Geomech. **10**(3), 124–128 (2010)
9. Goel, S., Patra, N.R.: Effect of arching on active earth pressure for rigid retaining walls considering translation mode. Int. J. Geomech. **8**(2), 123–133 (2008)
10. Leshchinsky, D., Hu, Y., Han, J.: Limited reinforced space in segmental retaining walls. Geotext. Geomembr. **22**(6), 543–553 (2004)
11. Greco, V.R.: Seismic active thrust on cantilever walls with short heel. Soil Dyn. Earthq. Eng. **29**(2), 249–252 (2009)
12. Greco, V.: Active thrust on retaining walls of narrow backfill width. Comput. Geotechn. **50**, 66–78 (2013)

13. Frydman, S., Keissar, I.: Earth pressure on retaining walls near rock faces. J. Geotechn. Eng. **113**(6), 586–599 (1987)
14. Take, W.A., Valsangkar, A.J.: Earth pressures on unyielding retaining walls of narrow backfill width. Can. Geotech. J. **38**(6), 1220–1230 (2001)
15. Yang, M., Tang, X.: Rigid retaining walls with narrow cohesionless backfills under various wall movement modes. Int. J. Geomech. **17**(11), 04017098 (2017)
16. Fan, C.C., Fang, Y.S.: Numerical solution of active earth pressures on rigid retaining walls built near rock faces. Comput. Geotech. **37**(7–8), 1023–1029 (2010)
17. Yang, K.H., Liu, C.N.: Finite element analysis of earth pressures for narrow retaining walls. J. GeoEng. **2**(2), 43–52 (2007)

Theoretical Simulation of Experimental Results with Barron's Theory for Consolidation of Soft Clay by Radial Flow Using PVD

R. P. Shrivastava and A. V. Shroff

1 Introduction

Beginning with the classical work of Terzaghi on three dimensional consolidation process and thereafter Barron's theory on consolidation due to radial flow which was further extended by Hansbo, number of research workers carried out research and focused the attention on various influencing factors of vertical geodrain on consolidation characteristics of clayey soil due to radial flow either by laboratory model or in the field. Most of the soil deposits have greater permeability in horizontal direction which can be utilized efficiently by the use of prefabricated vertical drains. After the use of sand drains, several new types of geo-drain has come on the horizon, with different shapes and material namely Sand wick Drain, Jute Drain, Polypropylene Drain, Card board drain, Rope Drain, etc.

At first, three dimensional consolidations problem was given by Terzaghi (1923). Prior to this three dimensional consolidation problems were solved using one dimensional approximation to three dimensional problems using Terzaghi's famous consolidation theories. Further modified in Terzaghi (1943) and Barron (1948) reported simplified expression for the design of vertical drains. The theory after Tan (1961) includes stress strain relationship for clays during radial flow as a function of time, which he approximately solved using linear, integrated equation. The fourth theory was propagated and enhanced by workers namely Hansbo (1960), Heinrich and Desoyer (1961), Escario et al. (1961), and Hansbo (1981). They have extended the scope of the theory, considering with respect to variable nature of loads, permeability, compressibility, and structural viscosity. The equations of Barron were also

R. P. Shrivastava
Parul University, Waghodia, Limda, Vadodara, Gujarat, India
e-mail: ruchi.shrivastava@paruluniversity.ac.in

A. V. Shroff (✉)
M.S. University, Vadodara, Gujarat, India

C. N. V. Satyanarayana Reddy et al. (eds.), *Dynamics of Soil and Modelling of Geotechnical Problems*, Lecture Notes in Civil Engineering 186,
https://doi.org/10.1007/978-981-16-5605-7_25

used by Rowe (1959) in analyzing the consolidation of lacustrine, laminated clays. This work was subsequently developed by Horne (1964), which includes and gives for laminated or layered clays having sequence of identical layers.

2 Theoretical Development on Three Dimensional Consolidation

2.1 Terzaghi's Theory

The one dimensional theory given by Terzaghi is

$$\frac{\partial u}{\partial t} = C_{vz}\frac{\partial^2 u}{\partial z^2}, \tag{1}$$

where u = Pore water pressure.

Cv = $k/mv\gamma w$.

k = co-efficient of permeability.

mv = coefficient of volume change.

The basic equation of one dimensional theory of Terzaghi is (Fig. 1)

$$\frac{\partial u}{\partial t} = C_v\frac{\partial^2 u}{\partial z^2} \text{ with initial condions } U(x, y, z, t) = U_o(x, y, z, o) \tag{2}$$

It relates the rate of change of excess hydrostatic pressure to rate of expulsion of excess pore water from a unit volume of soil during the same time interval.

The three dimensional consolidation equation is

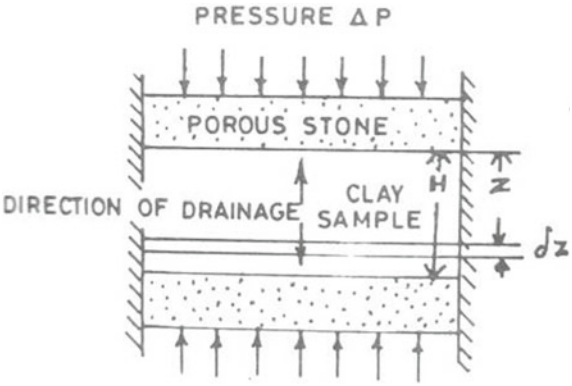

Fig. 1 Three Dimensional Consolidation

$$\frac{\partial u}{\partial t} = C_{vx}\frac{\partial^2 u}{\partial x^2} + C_{vy}\frac{\partial^2 u}{\partial y^2} + C_{vz}\frac{\partial^2 u}{\partial z^2}, \tag{3}$$

where

Cv = Coefficient of consolidation in (cm^2/s) various co-ordinates.
= Kmvγw

$$U(\%) = f(T_v) \tag{4}$$

where

$$T_v = \frac{C_v t}{H_2}$$

is time factor.

In the case of sand drains, where the process of three dimensional consolidation is symmetrical about vertical axis, it is more convenient to express Eq. 3.2 into polar co-ordinates as

$$\frac{\partial u}{\partial t} = C_h\left[\frac{\partial^2 u}{\partial r^2} + \frac{1}{r}\frac{\partial u}{\partial r}\right] + C_v\frac{\partial^2 u}{\partial z^2} \tag{5}$$

If the radial flow takes place in planes at right angle to z axis, the term $\partial^2 u/\partial z^2$ equals to zero and so equation reduces to

$$\frac{\partial u}{\partial t} = C_{vr}\left[\frac{\partial^2 u}{\partial r^2} + \frac{1}{r}\frac{\partial u}{\partial r}\right] \tag{6}$$

In the present investigation mid plane pore pressure is measured. The pore pressure in central drain is found to be zero.

2.2 Barron's Theory (1948)

His theory was based on all of the simplifying assumptions of Terzaghi uncoupled one dimensional consolidation theory. Barron considered two types of vertical strains which might occur in a clay layer.

(1) Free strain case. (2) Equal strain case.

(1) **Free Strain Case**.

If the surcharge load placed over the sand blanket is flexible, free strain case occurs. In this case, there is uniform distribution of surface loads, but the settlements at the surface are uneven. The basic differential equation for radial drainage is given by Eq. 7,

$$\frac{\partial u}{\partial r} = C_{vr}\left[\frac{\partial^2 u}{\partial r^2} + \frac{1}{r}\frac{\partial u}{\partial r}\right] \tag{7}$$

In the case of free strain case, the boundary conditions are as under

$$At\ time\ t = 0, \overline{u} = \overline{u_r},\ At\ time\ t > 0, \overline{u} = 0\ at\ r = rw\ and\ r = R, \frac{\partial \overline{u}}{\partial r} = 0$$

This solution for excess pore water pressure $\overline{u}$ at any time t and at a radial distance r is obtained by the solution of the differential equation as

$$\overline{u} = \sum_{\alpha 1,\alpha 2}^{\alpha=\infty} \frac{-2\mathrm{U1(a)U_0}\left(\frac{\alpha_r}{\alpha_w}\right)}{\alpha\left[n^2\mathrm{U_0^2}(\alpha n) - \mathrm{U_1^2}(\alpha)\right]} e^{-4\alpha^2 \mathrm{n}^2}\mathrm{T_r}, \tag{8}$$

where $n = R/r_w$ and

$$U_1(\alpha) = J_1(\alpha)Y_0(\alpha) - Y_1(\alpha)J_0(\alpha),$$

$$U_0(\alpha n) = J_0(\alpha n)Y_0(\alpha) - Y_0(\alpha n)J_0(\alpha),$$

$$\text{and } U_0\left(\alpha r/r_w\right) = J_0\left(\alpha r/r_w\right)Y_0(\alpha) - Y_0\left(\frac{\alpha r}{r_w}\right)J_0(\alpha),$$

where J_0 = Bessel function of first kind of zero order.
J_1 = Bessel function of first kind of first order.
Y_0 = Bessel function of second kind of zero order.
Y_1 = Bessel function of second kind of first order.
And $\alpha_1, \alpha_2 \ldots$. are roots of Bessel function which satisfy the equation.

$$J_1(\alpha n) = Y_0(\alpha) - Y_1(\alpha n)J_0(\alpha) = 0.$$

Also $T_r = C_{vr}\, t/(2R)^2$,

where

$$C_{vr} = \frac{K_r}{m_v y_w} = \frac{K_h}{m_v y_w},$$

where k_h is co-efficient of permeability in horizontal direction.

The average pore water pressure u_{av} throughout the soil mass may be written as

$$u_{av} = \mathrm{ui}\sum_{\alpha 1,\alpha 2....}^{\alpha=\infty} \frac{4\mathrm{U_1}^2(\alpha)}{\alpha^2\left(\mathrm{n}^2-1\right)\left[\mathrm{n}^2\mathrm{U_0}^2(\alpha \mathrm{n})-\mathrm{U_1}^2(\alpha)\right]} \mathrm{e}^{\left(-4\alpha^2 \mathrm{n}^2 \mathrm{T_r}\right)} \tag{9}$$

The average degree of radial consolidation U_r with the time factor T_r by dotted lines for different values of n (Fig. 2), where $n = R/r_w$.

(2) **Equal Strain case**

This case occurs when the surcharge applied is rigid, such as heavy steel plates. In this case, the settlements are uniform but the distribution of pressure is non-uniform. The problem was solved by Barron, who gave the expression for excess pore pressure $\overline{u}$ as

$$\overline{u} = \frac{4u_{av}}{(2R)^2 F(r)}\left[R^2 \log_e\left(\frac{r}{r_w}\right) - \left(\frac{r^2 - r_w^2}{2}\right)\right], \tag{10}$$

where $\mathrm{F(n)} = \frac{n^2}{n^2-1} log^{(n)}{}_{e^-} \frac{3n^2-1)}{4n^2}$,

U_{av} = Average value of pore water pressure throughout the embankment.

$U_{av} = \overline{u_i} e^{\gamma}$ in which $\gamma = \frac{-8T_r}{F(n)}$.

Formation of Barron's Equation for Consolidation Due to Radial Flow:

The Terzaghi equation for three dimensional consolidation in Cartesian coordinate is

$$\frac{\partial u}{\partial t} = C_{vx}\frac{\partial^2 u}{\partial x^2} + C_{vy}\frac{\partial^2 u}{\partial y^2} + C_{vz}\frac{\partial^2 u}{\partial z^2}. \tag{11}$$

The same in cylindrical coordinate

$$\frac{\partial u}{\partial t} = C_{cvr}\left[\frac{\partial^2 u}{\partial r^2} + \frac{1}{r}\frac{\partial u}{\partial r}\right] + C_v\frac{\partial^2 u}{\partial z^2}. \tag{12}$$

The equation can be split into two parts:

Radial Flow:

$$C_{cvr}\left[\frac{\partial^2 u}{\partial r^2} + \frac{1}{r}\frac{\partial r}{\partial t}\right] = \partial u/\partial t, \tag{13}$$

where

$$C_{vr} = \frac{kr}{mvyw-}$$

This equation is Barron's theoretical equation for radial flow which is similar to the radial flow in Rowe type oedometer used for research work.

Vertical Flow:

$$C_{vz}\frac{\partial^2 u}{\partial z^2} = \frac{\partial u}{\partial t}, \tag{14}$$

where

$$C_{vz} = \frac{kz}{mvyw-}$$

This equation is given by Terzaghi in one dimensional condition.

Considering the radial drainage and applying the boundary condition, solution for excess pore water pressure at any time t and at radial distance r can be obtained.

The degree of consolidation of radial consolidation for equal strain with no smear.

$\mathrm{Ur} = 1-e^{(-8Tvr/f(n)}$, where the value of Tvr and F(n) are explained as follows:

Barron's equal vertical strain theory with no smear and no well resistance has been used to carry out the analysis for radial consolidation. Figure shows the relationship between Tvr and Ur. Using this curve, the time factor, Tvr, for 50% percent consolidation is found out.

The Average degree of consolidation in radial direction is given by $U_r\ with\ T_r\ by\ firm\ lines\ for\ 3\ values\ of\ n$ (Table 1).

It may be observed that the curves for free strain are not much different and they give approximately the same results. Equal strain case is generally preferred as it is more convenient. Figure 2 also gives the value of T_r in a tabular form for the equal strain case.

Table 1 T_r (Equal strain case)

Ur%	n = 5	n = 10	n = 40
10	0.012	0.021	0.039
20	0.026	0.046	0.082
30	0.042	0.070	0.131
40	0.060	0.101	0.188
50	0.081	0.137	0.255
60	0.107	0.180	0.337
70	0.137	0.231	0.431
80	0.188	0.317	0.592
90	0.270	0.455	0.847
95	0.351	0.590	1.102
99	0.539	0.907	1.693

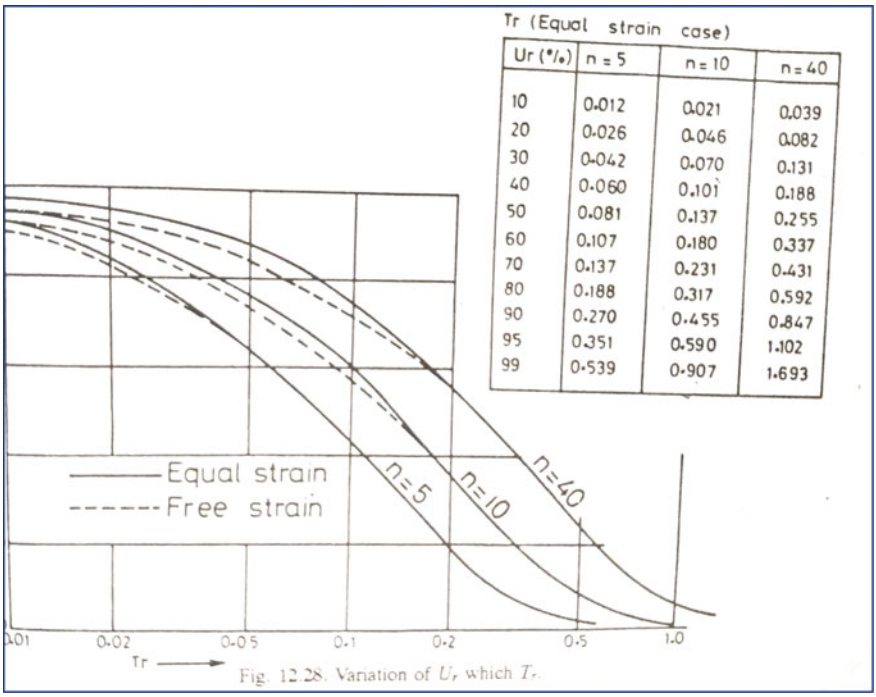

Fig. 2 Variation of U_r with T_v

3 Scope and Objective

The hydraulically pressurized Oedometer (Rowe Type) (Fig. 3) with central geodrain is employed in present investigation and Cvr value is determined for both settlement and pore pressure readings. Measurements of pore pressures are planned to carry out by conventional Bishop's pore pressure setup and extensometer.

It is intended to conduct a series of consolidation tests with radial drainage through vertical geodrain centrally placed and measurement of settlement and pore water pressure at three radial distances will be taken so as to prove efficacy against various physical factors namely type of drain material, shape, aspect ratio, various shapes of drain, 'n' value (i.e. different diameters of drain related to influence zone).

In the present study Sand, Saw dust, Saw dust wick, Jute, Polyamide Polyster Geosynthetics are used to fabricate the vertical geodrains of different diameters. Hydraulically pressurized oedometer (Rowe Type) with special arrangement for measuring pore pressure and settlement during consolidation due to radial flow of water is used in the study. The present investigation will simulate the theoretical values of Degree of Consolidation with experimental values for all n values where n = Radius of Oedometer to Radius of the drain.

Fig. 3 Rowe Type oedometer and self-compensating mercury

4 Laboratory Investigations

4.1 Materials Used

The soil used for this investigation was clay mineral Kaolinite obtained commercially in the form of powder. To ensure full saturation of the sample the clay was mixed to form slurry with twice the liquid limit using de-aired distilled water.

4.2 Properties of PVD Drain Material

In present investigation, Saw dust wrapped with Whatman filter paper (SD), Saw dust wrapped with Geosynthetics (SDW), Sand Drain, and Jute wrapped with polyamide polyster (JPPG) is used for investigation. The properties of the drain material are shown in Tables 2, 3, 4 and 5. The Saw Dust is treated chemically and then used as a drain by encasing it with Whatman filter paper (Tables 6 and 7).

Table 2 Property of Kaolinite soil

Type of clay	Kaolinite
Specific Gravity	2.456
Liquid Limit (LL)	59.6%
Plastic limit (PL)	33.33%
Plasticity Index (PI)	26.27%
Classification by A-line Casagrande Chart	CH
Co-efficient of Permeability	0.6 × 10–6 cm/sec

Table 3 Property of Saw dust wrapped with Whatman Filter Paper

Sr. No	Properties of saw dust	Value
1	D_{10} mm	0.29
2	D_{30} mm	0.52
3	D_{60} mm	1.05
4	Co-efficient of uniformity, c_u	3.620
5	Co-efficient of curvature, c_c	0.888
6	Maximum compressive stress, kg/cm^2	0.138
7	Coefficient of permeability, cm/sec	1.502×10^{-3}

Table 4 Properties of Geotextile used in sawdust wick drain

Sr. No	Description	Value
1	Type of Geotextile	Non-woven
2	Mass per unit area	250gm/m2
3	Tensile strength	14 KN/m
4	Permeability by falling head	3.6 × 10–3 cm/sec
5	Opening size	85 microns
6	Puncture strength (CBR)	1940 N

Table 5 Properties of sand used in sand drain

1	Specific gravity	2.645
2	Co-efficient of permeability	8.45 × 10–3 cm/sec
3	Co-efficient of uniformity, cu	2.023
4	Co-efficient of curvature, cc	1.295
5	Fineness moduli	2.2–2.3
6	Sand classified	SW

Table 6 Properties of prefabricated vertical circular Jute wrapped with Polyamide Polyster Geosynthetics

Sr. No	Properties of newly developed jute wrapped with Polyamide Polyster drain	Unit	Value
1	Weight	gms	5
2	Diameter	Cm	2.1
3	Height	Cm	5.1
4	Peak unconfined stress for flexibility measurement	Kg/cm^2	0.8
5	A.O.S. (0_{95})—filter	μm	<75
6	Permeability—filter	Cm/sec	1.1 × 10–1
7	Grab tensile strength—filter	KN	0.6
8	Elongation at break—filter	%	25

Table 7 Properties of Jute used in JPPG drain

Sr. No	Description	Value
1	Mass per unit area	388 gm/m^2
2	Tensile strength	250–350 N
3	Permeability by falling head	3 × 10–2 cm/s
4	Jute thickness single layer and double layer	1.08 mm & 2.06
5	Grab tensile strength	800–900 N
6	Length of fibers in mm	10–200 (highly variable)
7	Elongation percentage at break	5%

4.3 Experimental Setup

The experimental setup used in the present investigation consists of the following:

(i) Hydraulic Pressure System.
(ii) Oedometer.
(iii) Pore pressure measurement system.
(iv) Settlement measurement system.

The hydraulically pressurized Oedometer (Rowe Type) with central geodrain is employed in present investigation, and Cvr value is determined for both settlement and pore pressure readings. Measurements of pore pressures are planned to carry out by conventional Bishop's pore pressure setup.

4.4 Method of Soil Preparation

The soil used for this investigation was clay mineral Kaolinite obtained commercially in the form of powder. To ensure full maturation of the sample the clay was mixed to form slurry with twice the liquid limit using de-aired distilled water. Density was sufficiently low to allow the removal of entrapped air when the sample in the consolidation cell was vibrated. The slurry was transferred into the Oedometer after the cell body had been lightly coated with a thin layer of silicon grease to minimize side friction; the Oedometer was then placed on a handle operated vibrator and vibrated for approximately one hour after which only occasional air bubbles could be seen on the surface. The clay was then scribed level. And a filter paper followed by a porous stone was placed at the top. The sample was then preconsolidated under gradually applied static dead load of 10 kPa, with $\Delta p/p = 1$ kPa, 2 kPa, 4 kPa, 8 kPa, 10 kPa) so that the consolidation occurring is normal. (Where 1 kPa = 0.01 kg/cm^2).

These increments are given by means of dead load with porous stone on the top of the clay sample topped by filter paper so that sample during consolidation water

gets removed through porous stone. These increments of dead loads are to be kept for a longer period of time (at least 48 h). Representative sample for determination of water content was taken and measured. Initial strength was measured by Vane shear in separate crucible of vane shear apparatus by dead loading in same fashion by small weights. To avoid the soil structure disturbance of soil cake prepared, initial height was measured with pointer arrangement with stand and the extra soil was trimmed.

Filter paper is kept on the surface of the trimmed soil and rigid Perspex plate was laid on it to create the equal strain condition while loading.

4.5 Installation Stages of Vertical Drain

The axial hole was formed with a thin walled mandrel, having an area ratio of 0.8 to 1.6 attached with template and guide frame. Circular filter paper of size PVD is lowered in the bore hole. A drain hole was then flooded with water from the central connection to the reservoir. The drain was filled with de-aired saturated PVD drain material with the aid of small diameter flexible tubing by syphoning action without any smear and without any intrusion of clay in PVD to avoid blockage. The top cover is then seated into position.

4.6 Test Procedure

After the cell is sealed, settlement dial gauge and Bishop pore pressure measuring apparatus were connected at their respective location. The first pressure increment is applied through the flexible convoluted jacket after closing the drainage control valve, and settlement gauge reading is recorded. After completion of consolidation process, drainage control valve was closed, then the next increment of load is applied, and the same process is repeated for a series of various pressure increments, with $P/P = 1.0$. The loading was done in the increment of 20, 40, 80, 160, and 320 kPa keeping $\Delta P/P = 1$.

After the completion of the test, vane shear test was performed at three locations to determine the gain in strength due to dissipation of water. The value of settlement and pore water pressure is measured with respect to time, and the co-efficient of radial consolidation is calculated.

5 Tests and Result Analysis

Experimental curves will be compared with Barron's Theoretical curve.

Settlement.

- Degree of Consolidation (Ur) % versus Theoretical Time factor
- Degree of Consolidation (Ur) % (as obtained from experimental results) versus Theoretical Time factor (as obtained from Experimental results)

5. (A) Settlement

(i) ***Degree of Consolidation (Ur) % versus Theoretical Time factor.***

Calculation of theoretical Time factor for Barron's theory 254 mm diameter oedometer.

Keeping n = 10 for Settlement.

R_e = Radius of Oedometer = 254/2 = 127 mm.

R_w = Radius of Drain = 25.4/2 = 12.7 mm.

$$n = R_e / R_w = 10.$$

$$\mathbf{F(n)} = \left(\mathbf{n^2}/\mathbf{n^2} - 1\right)\mathbf{ln(n)} - \frac{3\mathbf{n}^2 - 1}{4\mathbf{n}^2} \tag{15}$$

$$F(n) = 1.5783.$$

$$\mathbf{U_r} = 1 - \mathbf{e}^{(-8\mathbf{Tr}/\mathbf{F(n)})}.$$

$$\mathbf{Tvr} = \mathbf{ln}(1 - \mathbf{U_r}) * \mathbf{F(n)}/-8. \tag{16}$$

$$Tvr = \frac{\ln(1 - U_r)}{-5.068}.$$

By substituting the value of Ur, we can get the theoretical value of time factor Tvr.

Calculation of experimental Time factor using Barron's theory 254 mm diameter oedometer keeping n = 10 for Settlement.

R_e = Radius of Oedometer = 254/2 = 127 mm.

R_w = Radius of Drain = 25.4/2 = 12.7 mm.

$$n = R_e / R_w = 10.$$

$$F(n) = \left(n^2/n^2 - 1\right) ln(n) - \frac{3n^2 - 1}{4n^2}.$$

$$F(n) = 1.5783.$$

$$U_r = 1 - e^{(-8Tr/F(n))}.$$

$$Tvr = ln(1 - U_r) * F(n) / -8.$$

$$Tvr = \frac{\ln(1 - U_r)}{-5.068}.$$

By substituting the value of Ur calculated from log fitting method from the graph of DGR versus Log t we get experimental values of Tvr from Eq. 1.

Values of Tvr for different values of U_r are calculated as shown in table for n = 10. Typical fitting of experimental and theoretical curve is as shown in figure.

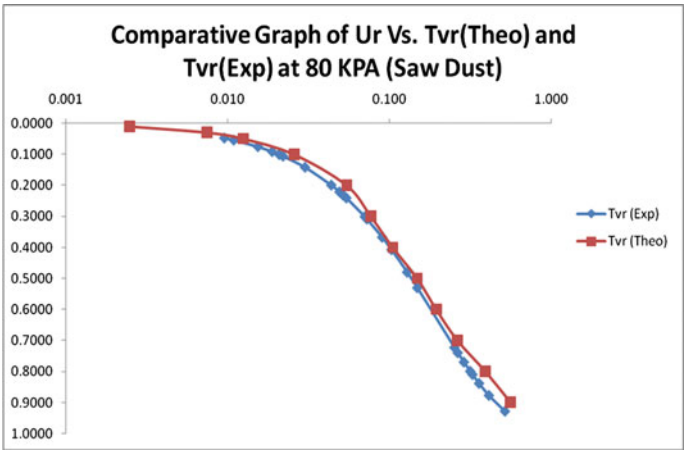

- The theoretical Ur% and Tvr for settlement for SD circular drain is plotted.
- It is compared with experimental values at 80 kPa, and it is observed that up to 20% degree of consolidation slight variation is observed in experimental and theoretical value.
- Then from 20 to 92% of degree of consolidation, the theoretical and experimental curve for settlement is coinciding and again a slight variation is observed after 92%.

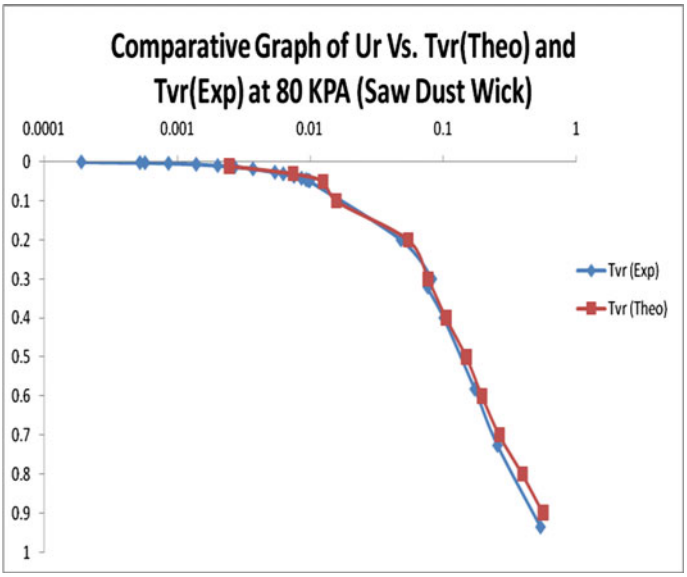

- The theoretical Ur% and Tvr for settlement for SD circular drain is plotted.
- It is compared with experimental values at 80 kPa, and it is observed that up to 20% degree of consolidation 5% variation is observed in experimental and theoretical value.
- Then from 20 to 94% of degree of consolidation, the theoretical and experimental curve for settlement is coinciding and again a 6% variation is observed after 99%.

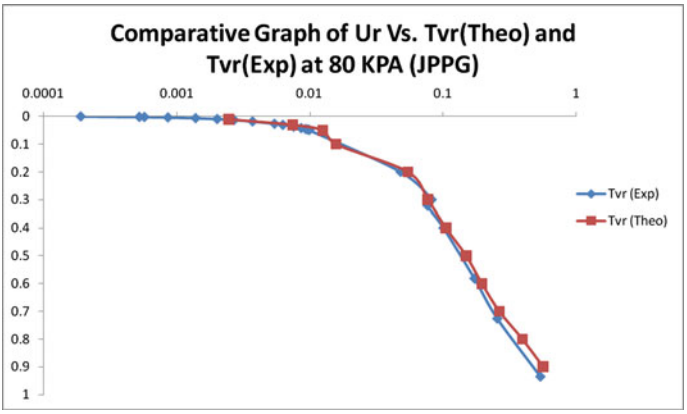

- The theoretical Ur% versus Tvr graph for settlement for JPPG drain is plotted.
- It is compared with experimental values at 80 kPa, and it is observed that up to 4% degree of consolidation slight variation is observed in experimental and theoretical value.

- Then from 4 to 82% of degree of consolidation, the theoretical and experimental curve for settlement is coinciding and again a slight variation is observed after **90%.**

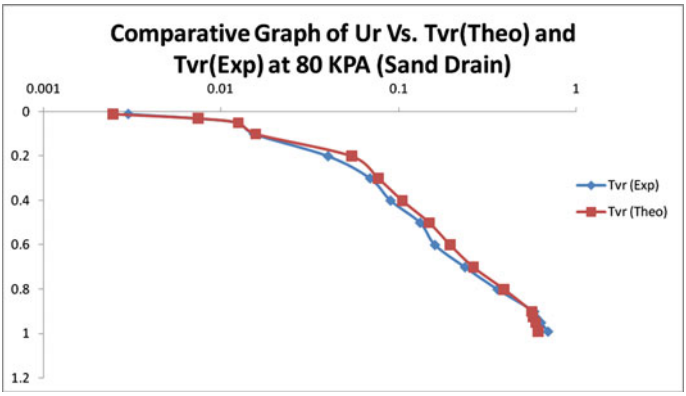

- The theoretical Ur% versus Tvr graph for settlement for sand drain for n = 14.76 is plotted.
- It is compared with experimental values at 80 kPa, and it is observed that up to 8% degree of consolidation slight variation is observed in experimental and theoretical value.
- From 8 to 90% of degree of consolidation, the theoretical and experimental curve for settlement is coinciding and again a slight variation is observed after 90%.

6 Conclusions

(i) The theoretical Ur% and Tvr for settlement for SD circular drain is plotted. It is compared with experimental values at 80 kPa, and it is observed that up to 20% degree of consolidation slight variation is observed in experimental and theoretical value. Then from 20 to 92% of degree of consolidation, the theoretical and experimental curve for settlement is coinciding, and again a slight variation is observed after 92%.

(ii) The theoretical Ur% and Tvr for settlement for SDW drain is plotted. It is compared with experimental values at 80 kPa, and it is observed that up to 20% degree of consolidation 5% variation is observed in experimental and theoretical value. Then from 20 to 94% of degree of consolidation, the theoretical and experimental curve for settlement is coinciding and again a 6% variation is observed after 99%.

(iii) The theoretical Ur% versus Tvr graph for settlement for JPPG drain is plotted. It is compared with experimental values at 80 kPa, and it is observed that up to 4% degree of consolidation slight variation is observed in experimental

and theoretical value. Then from 4 to 82% of degree of consolidation, the theoretical and experimental curve for settlement is coinciding and again a slight variation is observed after 90%.

(iv) The theoretical Ur% versus Tvr graph for settlement for sand drain for n = 14.76 is plotted. It is compared with experimental values at 80 kPa, and it is observed that up to 8% degree of consolidation slight variation is observed in experimental and theoretical value. From 8 to 90% of degree of consolidation, the theoretical and experimental curve for settlement is coinciding and again a slight variation is observed after 90%.

Thus it is observed that for all drain material there is slight variation in degree of consolidation up to 4 to 6% in theoretical and experimental values for Ur% versus Tvr. This is because of the physiochemical effect of clay minerology.

It is also observed that variation in theoretical and experimental values is observed at 84 to 86% of Degree of Consolidation. This is due to the secondary compression in the soil structure. The depression of the adsorbed layer results in the secondary compression.

Consolidation due to radial drainage using PVD is one of the ground improvement techniques in which the consolidation is accelerated by reducing drainage path.

Among various drain materials viz. sand, SD, and SDW used in the investigation JPPG drain expedite the dissipation of water efficiently resulting in faster rate of consolidation and strength of treated mass. The hydraulically pressurized Rowe-type oedometer is employed in present investigation is found to be efficient to measure settlement and pore pressure.

It is observed that for all drain materials viz. SD, SDW, and Sand, there is slight variation of 4% to 6% initially and 6 to 10% at end of primary consolidation in theoretical and experimental curve plotted for Degree of Consolidation (Ur%) and Theoretical and experimental Time Factor (Tvr). JPPG curve fits well compared to other drains.

Initial variation is due to hydrodynamic lag in consolidation while end portion variation is because of secondary compression of soil due to depression of adsorbed water in clay water system.

References

1. Abid, M.M., Pyrah, I.C.: Consolidation behavior of finely laminated clays. Comput. Geotech. **10**(4), 307–323 (1990)
2. Balasubramanian A.S.: Experiences with sand drains and prefabricated vertical drains in ground improvement of soft clays. Seminar on Eng. for Coastal Development, Singapore, pp. 29–40 (1995)
3. Barron, R.A.: Consolidation of fine-grained soils by drain wells. Trans. ASCE **113**, 718–754 (1948)
4. Bergado, D.T., Brenner, R.R., Balasubramaniam, A.S., Chotivittayathanin, R., Pananookooln, R.: Improvement of soft Bangkok clay using vertical geotextile band drains compared with granular piles. Geotext. Geomembr. **9**(3), 203–231 (1990)

5. Bergado, D.T., Cheung, Y.K., Lee, P.K.K., Xie, K.H.: Smear effects of vertical drains on soft Bangkok clay. J. Geotechn. Eng. **117**(10), 1509–1529 (1991)
6. Bergado D.T.: Improvement of soft Bangkok clay using vertical drains. Geotextiles Geomembranes **12**(7), 615–663 (1993a)
7. Bergado, D.T., Mukherjee, K., Alfaro, M.C., Balasubramaniam, A.S.: Prediction of vertical-band-drain performance by the finite-element method. Geotext. Geomembr. **12**(6), 567–586 (1993)
8. Bergado, D.T., Balasubramaniam, A.S., Fannin, R.J., Holtz, R.D.: Prefabricated vertical drains (PVDs) in soft Bangkok clay: a case study of the New Bangkok International Airport project. Can. Geotech. J. **39**, 304–315 (2002)
9. Chu, J., Bo, M.W., Choa, V.: Practical Considerations for using vertical drains in soil improvement projects. Geotext. Geomembr. **22**, 101–117 (2004)
10. Dhar, A.S., Siddique, A., Syed, A.F.: Investigation of smear zone around vertical drain. Proceedings of the Third International Conference on Ground Improvement Techniques, Singapore, pp. 109–114 (2000)
11. Escario, V. and Uriel, V.:. Determining the coefficient of consolidation and horizontal permeability by radial drainage, Proc. 5th Int Conf. on 'SM and FE', 83-87, Paris, Dunod Press.(1961)
12. Hansbo, S.: Consolidation of Clay with Special Reference to the influence of vertical sand drains. Diss. Chalmers Univ. of Technology, Swedish Geotechnical Institute, Proc. No. 18 (1960)
13. Hansbo, S.: Consolidation of Fine-Grained Soils by Prefabricated Drains. In 10th ICSMFE,12–22. Stockholm, Rotterdam : A.A.Balkema (1981)
14. Hansbo: Aspects of vertical drain design: Darcian or non-Darcian flow. Geotechnique **47**, 983–992 (1997)
15. Heinrich, G. and Desoyer, K.: Theorie dreidimensionaler setznugsvorgänge in Tonschichten, Ing. Arch. 30:4 , 225–253 (1961)
16. Holtz, R.D., Jamiolkowski, M., Lancellotta, R., Pedroni, S.: Performance of prefabricated band-shaped drains. Construction Industry Research and Information Association (CIRIA), London, England; Report RPS 364 (1987)
17. Horne, M. R.: The consolidation of stratified soil with vertical and horizontal drainage. Int. J. Mech. Sci. 6, 187-197 (1964)
18. Madhav, M.R., Khan Ayub, P.: Consolidation of soft ground with drains with no (PVDs) and finite stiffness (granular piles). Proceedings of Indian Geotechnical Conference, December 15–17 (2011)
19. Naga, A.H.M., Bouazza: Equivalent diameter of a prefabricated vertical drain. Geotextiles Geomembranes (2009)
20. Rowe, P., W.: Measurement of the consolidation of Lacustrine Clay, Geo-technique 9, 107-118 (1959)
21. Shah, M., Shroff, A.V.: Consolidation of soft clay through Radial drainage using vertical sand Drains of various diameter and geometry. Proceedings of ASCGE, Vol-1 (2009)
22. Shah, M., Shroff, A.V.: Non-linear theory of consolidation through radial Drainage for soft soils using vertical drains. Proceedings of XIII-Danube-European Conference on Geotechnical Engineering, Vol. I, pp. 349–354 (2006)
23. Tan, T. K.: Consolidation and Secondary Time Effect of Homogeneous, Anisotropic, Saturated Clay Strata. Proceedings, Fifth International Conference on Soil Mechanics and Foundation Engineering, pp. 367–373 (1961)
24. Terzaghi, K.: Mathematisch-naturewissenschaftliche Klasse', Akademie der Wissenschaften in Wien, **132**, (3–4), 125–138 (1923)
25. Terzaghi, K.: "Theoretical Soil Mechanics", John Wiley & Sons, New York (1943)

Effect of Strain-Rate on Stress–Strain Behavior of Dredged Material at Different Moisture Contents—An Experimental Study

Tehseena Ali and B. A. Mir

1 Introduction

The primary requirement of the design of sustainable and resilient infrastructures is that engineering structure must withstand economically and efficiently any anticipated and unanticipated force, and whenever subjected to extreme loads, these structures should work within a reasonable time and with minimum repair capacity. Natural causes in the form of a tsunami, tornado, and earthquake and human activities like bomb blast, rocket attack, and collision are the main reasons for extreme loadings. Blasts, missile penetration, and sudden landslides are among such loading events which may generate strain-rates of the order of 10^4/s in the soil [1] and may also prompt catastrophic failures. Effect of strain-rate on the shear strength of soil was first studied in 1948 [2]. Triaxial compression tests were performed on sand at a strain-rate up to 115%/s and confining pressures varying from 30 to 90 kPa. The conclusions drawn from the experiments were a 10% increase in shear strength of dry sand when tested at higher strain-rates. Consolidated-undrained (CU) triaxial compression tests conducted on compacted boulder clay shows a log-linear increase in undrained shear strength with increasing strain-rate [3] in both conditions (saturated and unsaturated). A research was conducted on the time-dependent behavior of dense Toyoura sand with strain-rates ranging from 0.00000417 to 0.0021%/s [4, 5]. It was concluded that, at low strain rates, there was not a large effect of strain-rate when sheared at different but constant rates. However, a much more significant effect was noticed when changing rates during shearing. Being among the weakest of all civil engineering materials, soil often plays a critical role in the failure of the structures under catastrophic events. In the study of soil behavior under loading such as explosions, earthquakes, mine blasts, vehicle and aircraft loading, and dynamic

T. Ali (✉) · B. A. Mir
National Institute of Technology, Srinagar, J&K 190006, India

C. N. V. Satyanarayana Reddy et al. (eds.), *Dynamics of Soil and Modelling of Geotechnical Problems*, Lecture Notes in Civil Engineering 186,
https://doi.org/10.1007/978-981-16-5605-7_26

compaction, consideration of the impact of strain-rate on soil behavior is important. It is widely accepted in the solid mechanic's community that the strength, constitutive behavior, and overall response of soils are highly dependent on the strain-rate.

The rate of loading or strain-rate is found one among the most important factors influencing the shear strength parameters of soil. However, another dominant factor of soil failure or deformation is moisture content. Various conditions that result in change of moisture content of soil are groundwater rising, surface water infiltration, precipitation, etc. which subsequently decreases the resilient modulus and strength of soil. A comparison was made between stress–strain properties of unsaturated specimens that were prepared at different molding water contents by different preparation techniques [6]. It was noticed that statically compacted specimens have a stiffness value larger than dynamically compacted ones, while with increasing water content, a decrease in the stiffness occurs. An increase in cohesion component with decreasing molding water content was also observed. The constrained modulus, which is the ratio of axial stress to axial strain in one-dimensional compression, is consistently higher when soil is compacted on the dry side of optimum than when compacted on wet side [7]. Triaxial compression tests on compacted specimens were performed, and it was concluded that unsaturated specimens compacted at different water contents should be treated as different materials [8]. At saturated conditions, there is a slight change in secant modulus with change in confining pressure [9], whereas a significant increase in secant modulus is observed at moisture content less than 20%. From the stress–strain curve, a strain-softening behavior of loess can be seen with increase in the moisture content. When the moisture content is less than plastic limit, there is a slight increase in cohesion with increase in moisture content, while a significant decrease is observed when moisture content exceeds plastic limit. However, no such change was observed in internal friction angle.

This paper characterized the variation of deviator stress at failure during triaxial tests under different strain-rates and moisture content. The moisture content influence on deviator stress of soil under different confining pressures is also analyzed. The results are utilized to gain a better understanding of the strain-rate effects and water content on stress–strain behavior of soil.

2 Material

The soil selected for the purpose of this study was collected from the disposal site "Brain" area of Nishat Jammu and Kashmir. The soil was a dredged material from "Dal", a lake in Srinagar, the summer capital of Jammu and Kashmir. The city's lake, which is the second-largest lake in the country, is an integral part of tourism and recreation in Kashmir and is called "Jewel of the Kashmir Crown" or "Jewel of Srinagar". A huge amount of dredged material is generated from various basins of Dal Lake due to the movement of large volumes of sediment into Dal. This material can be an important reserve for many viable purposes. The material excavated may constitute gravel, soft clays, or silt depending upon the kind of environment. Based

on its classification, the material can be put to different uses like foundation material, construction of subgrade, reclamation, landscaping, landfill covers, and constructing wetlands for water quality improvement, bank stabilization, and creation of islands, etc. Therefore, for the utilization of dredged material in mass in different geotechnical applications, an attempt was made to examine the mechanical and physical properties. This material is difficult for certain projects due to its high moisture content and low processability. Nonetheless, treated dredged material can be used as a resource for various engineering applications and a stabilizer for improving the behavior of fine-grained soils.

Figure 1 shows a particle size distribution (PSD) curve for the test soil. As per the Indian Standard Soil Classification System (ISSCS) the processed soil is classified as medium compressible silt (MI). Standard Proctor Compaction curve for soil is shown in Fig. 2. Corresponding to optimum conditions, the dry unit weight and compaction water content has a value of 14.8 kN/m^3 and 22.2% respectively for the standard proctor compaction effort.

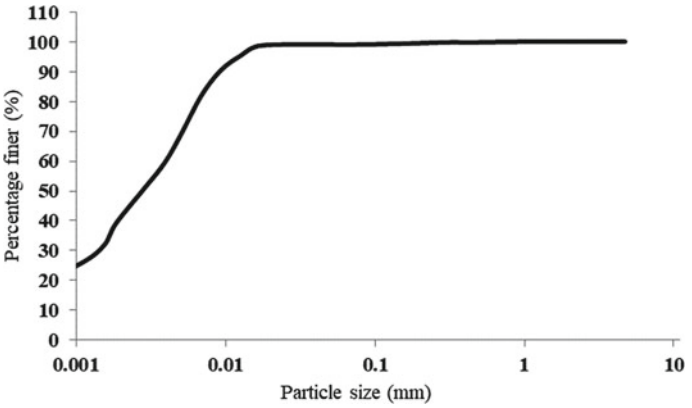

Fig. 1 Particle size distribution (PSD) curve of the test soil

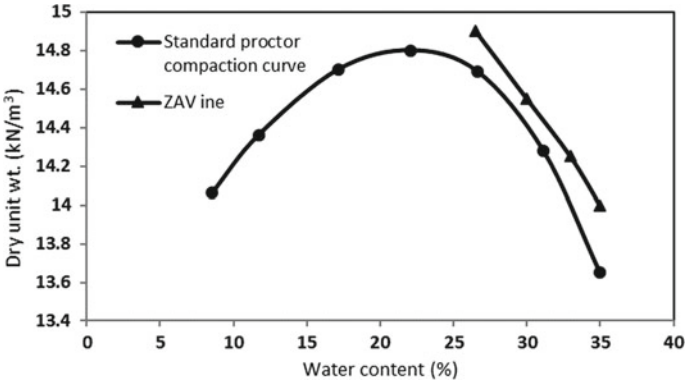

Fig. 2 Standard proctor compaction curve of the test soil

Table 1 Basic test results of soil sample

Parameter	Value	Unit
Field moisture content	54.62	%
Specific gravity	2.4	–
D_{30}	0.0015	mm
D_{50}	0.0028	mm
D_{60}	0.004	mm
Sand fraction	1	%
Silt fraction	57	%
Clay fraction	42	%
Particle size range	< 0.001 – 0.6	mm
Liquid limit	39.5	%
Plastic limit	26.1	%
Plasticity index	13.4	%
PI (A-line)	14.24	%
PI (U-line)	28.35	%
Clay mineral type	Kaolinite	–
Classification	MI	–
Optimum Moisture Content (OMC)	22.2	%
Maximum Dry Unit Wt. (MDU)	14.80	kN/m^3

All tests were performed in accordance with the corresponding Indian standards [10–14]. The physical properties of the materials used are listed in Table 1.

3 Experimental Approach

A series of Unconsolidated Undrained (UU) triaxial compression tests were performed on the test soil for three different strain-rates. The rate of strain was studied from 6 mm/min to 0.24 mm/min. Cylindrical specimens of diameter 38 mm were prepared with a height equal to twice of diameter (H/D = 2). The cylindrical mold consists of a length of steel tube with the diameter and length of the desired specimen. Figure 3 shows the different extruded soil specimens at OMC. The three different cell pressures used for the study are 50 kPa, 100 kPa, and 150 kPa. The failed soil specimen is shown in Fig. 4.

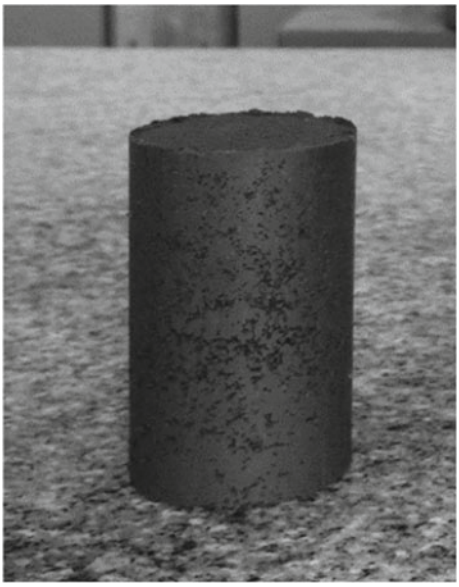

Fig. 3 Extruded soil specimens

Fig. 4 Sheared soil specimen (at OMC)

4 Experimental Results

The deviator stress (σ_d) which is the principal stress difference ($\sigma_1 - \sigma_3$) is plotted as a function of axial strain for specimen at various OMCs. The deviator stress is given by

$$(\sigma_1 - \sigma_3) = \sigma_d,$$

where σ_1 is the major principal stress (axial stress), σ_3 is the minor principal stress (cell pressure), and σ_d is the deviator stress.

In this study, deviator stress at failure $(\sigma_1 - \sigma_3)_f$ is used to present the undrained shear strength of the soil. During the evaluation of stress–strain curves, the deviator stress at failure $(\sigma_1 - \sigma_3)_f$ is taken as either the maximum value of deviator stress from stress–strain curve in case where peak is observed or the value of deviator stress at an axial strain of 20% in case where no peak is observed.

The influence of strain-rate on the undrained deviator stress is summarized in Figs. 5, 6 and 7. The figures compare the variation of undrained deviator stress by

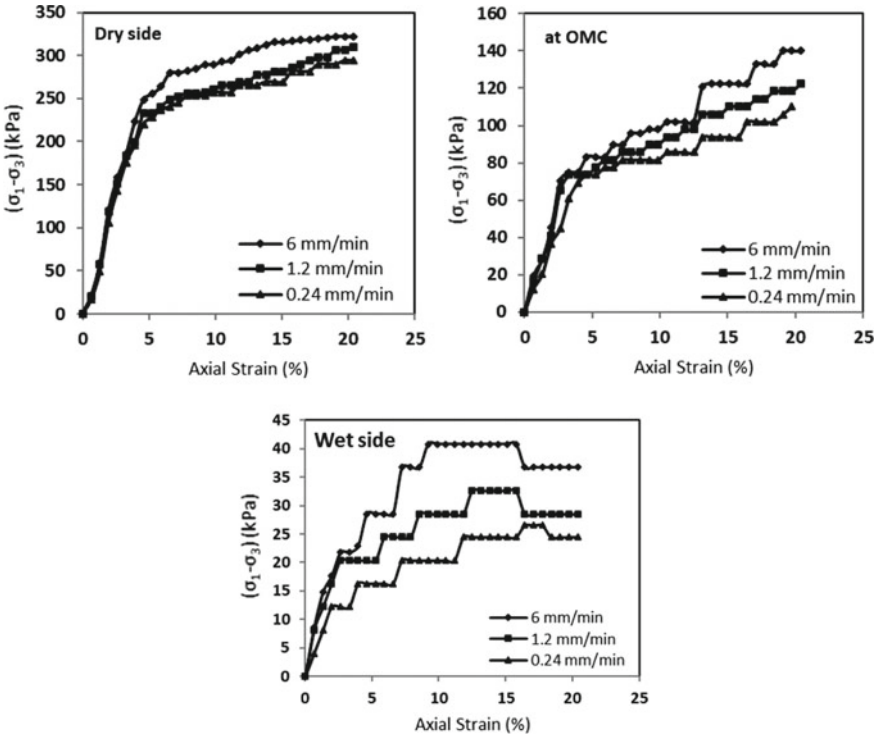

Fig. 5 Behavior of deviator stress under UU triaxial compression tests at different strain-rates and moisture content ($\sigma_3 = 50$ kPa)

varying axial strain from the triaxial compression tests at different moisture content. The variation of deviator stress with varying strain-rate and for same confining pressure (50 kPa) but different moisture content is shown in Fig. 5. It is observed that with increasing strain-rate, an increase in failure deviator stress occurs. The value of deviator stress at failure is maximum for highest strain-rate (6 mm/min) and minimum for lowest one (0.24 mm/min). Also, it is observed that at failure the value of deviator stress is more at the dry side of optimum, less at OMC, and even lesser at the wet side of optimum. No peak is observed when the specimen is sheared at dry of optimum and at optimum, but the significant peak is observed when sheared at the wet side of optimum.

Similarly, deviator stress variation at a cell pressure of 100 kPa for different moisture content with varying strain-rates is shown in Fig. 6. Similar results were observed as observed for cell pressure of 50 kPa. The deviator stress is found to be more for highest strain-rate (6 mm/min) and minimum for lowest one (0.24 mm/min). Also, it is observed that at failure the value of deviator stress is more at the dry side

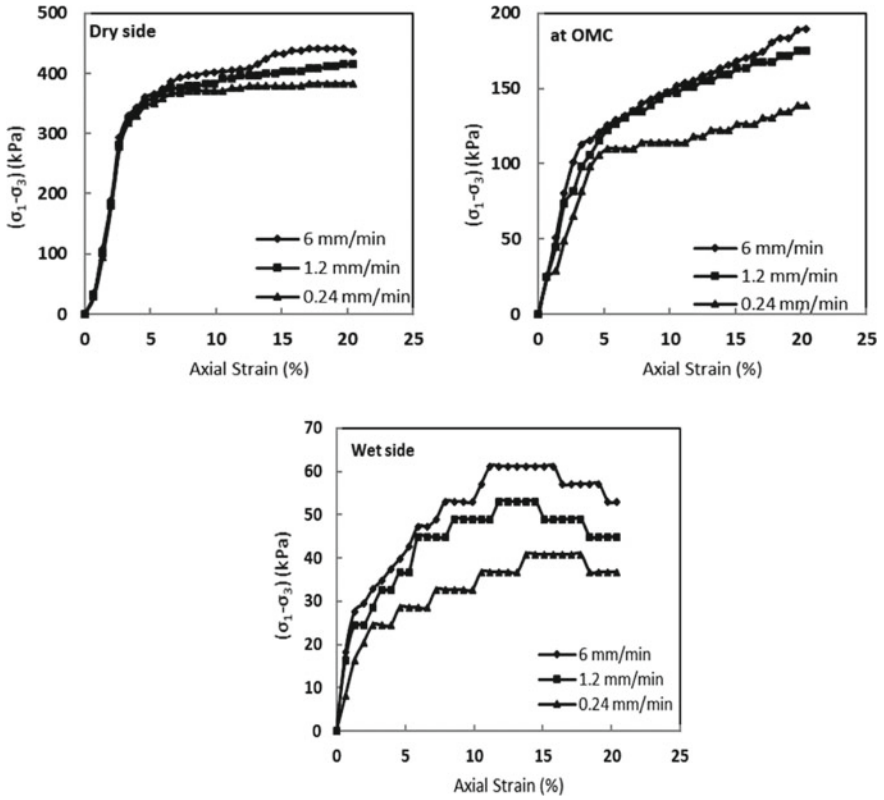

Fig. 6 Behavior of deviator stress under UU triaxial compression tests at different strain-rates and moisture content ($\sigma_3 = 100$ kPa)

of optimum, less at OMC, and even lesser at the wet side of optimum. No peak is observed when the specimen is sheared at dry of optimum and at optimum, but the significant peak is observed when sheared at the wet side of optimum.

Similarly, the variation of deviator stress at a cell pressure of 150 kPa for different moisture content with varying strain-rates is shown in Fig. 7. Similar results were observed as observed for cell pressure of 50 and 100 kPa. The deviator stress is found to be more for highest strain-rate, and with decreasing strain-rate a decrease in deviator stress is observed. Also, it is observed that at failure the value of deviator stress is more at the dry side of optimum, less at OMC, and even lesser at the wet side of optimum. No peak is observed when the specimen is sheared at dry of optimum and at optimum, but the significant peak is observed when sheared at the wet side of optimum.

The effect of strain-rate on the cohesion of soil is presented in the form of a graph (Fig. 8). It can be seen from the figure that cohesion increases as the strain-rate increases. The cohesion mobilizes more at high strain-rate (6 mm/min) and less at low strain-rate (0.24 mm/min). Again, it is observed that at dry side of optimum cohesion obtained is higher and with increase in moisture content cohesion decreases.

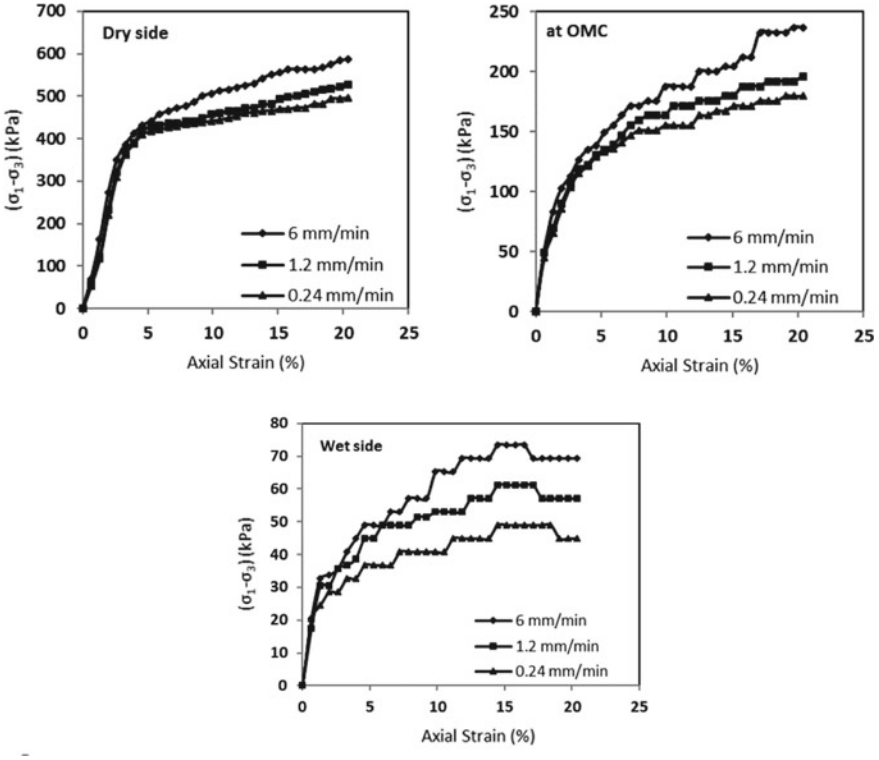

Fig. 7 Behavior of deviator stress under UU triaxial compression tests at different strain-rates and moisture content ($\sigma_3 = 150$ kPa)

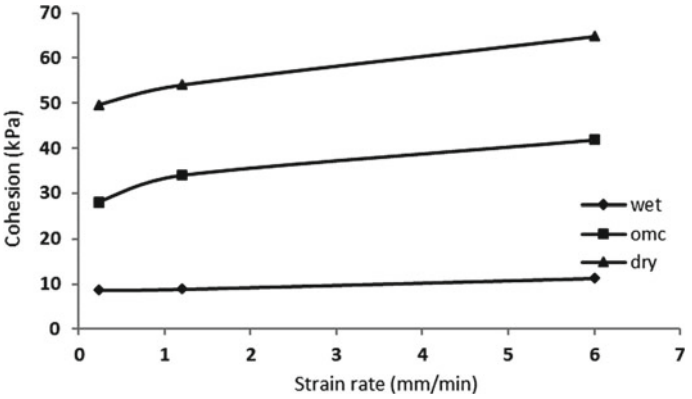

Fig. 8 Variation of cohesion (c) with strain-rate at different moisture contents

5 Conclusions

The conclusions that were drawn from the series of experiments are as follows:

1. The strain-rate variation leads to the shear strength variation of the soil. With increasing strain-rate, an increase in $(\sigma_1-\sigma_3)_f$ was observed in the stress–strain curves. The maximum value for $(\sigma_1-\sigma_3)_f$ was observed for the highest strain-rate (6 mm/min) and minimum value for the lowest strain-rate (0.24 mm/min).
2. Throughout the tests, the deviator stress mobilizes largely at dry side of optimum and with increase in moisture content it decreases.
3. By examining stress curves, it is seen that the $(\sigma_1-\sigma_3)_f$ increases with increasing confinement pressure. The maximum value of $(\sigma_1-\sigma_3)_f$ was observed for 150 kPa and minimum for 50 kPa.
4. An increase in cohesion (c) of soil with decreasing moisture content was also observed.
5. Clear shear bands were observed at the dry side of OMC while no bands were observed at OMC and dry side of OMC.
6. Based on these tests, it must be concluded that to obtain significant increases in strength takes a rate of strain equivalent to a fast-transient test.

References

1. Ngo, T., Mendis, P., Gupta, A., Ramsay, J.: Blast loading and blast effects on structures—an overview. EJSE (2007)
2. Casagrande, A., Shannon, W.L.: Strength of soils under dynamic loads. Proc. ASCE **74**(4), 591–608 (1948)
3. Svoboda, J.S., McCartney, J. S.: Shearing rate effects on dense sand and compacted clay. In: Conference Proceedings of the Society for Experimental Mechanics Series. pp. 389–395 (2014)

4. Tatsuoka, F., Uchnimura, T., Hayano, K., Di Benedetto, H., Koseki, J., Siddiquee, M.S.A.: Time-dependent deformation characteristics of stiff geomaterials in engineering practice. In: Proc., 2nd Int. Conf. on Pre-Failure Deformation Characteristics of Geomaterials, M. Jamiolkowski, and R. Lancellotta, eds., Vol. 2, Balkema, Rotterdam, The Netherlands, 1161–1262 (2001)
5. Matsushita, M., Tatsuoka, F., Koseki, J., Cazacliu, B., Di Benedetto, H., Yasin, S. J. M.: Time effects on the pre-peak deformation properties of sands. In: Proc., 2nd Int. Conf. on Pre-Failure Deformation Characteristics of Geomaterials, M. Jamiolkowski, R. Lancellotta, and D. Lo Presti, eds., Vol. 1, Balkema, Rotterdam, The Netherlands, 681–689 (1999)
6. Kouassi, P., Breysse, D., Girard, H., Poulain, D.: A new technique of kneading compaction in the laboratory. Geotech. Test. J. **23**, 72–82 (2000). https://doi.org/10.1520/gtj11125j
7. Carrier, W.D.: Compressibility of a compacted sand. J. Geotech. Geoenviron. Eng. **126**, 273–275 (2000). https://doi.org/10.1061/(ASCE)1090-0241(2000)126:3(273)
8. Sivakumar, V., Wheeler, S.J.: Influence of compaction procedure on the mechanical behaviour of an unsaturated compacted clay Part 1: Wetting and isotropic compression. Geotechnique **50**, 359–368 (2000). https://doi.org/10.1680/geot.2000.50.4.359
9. Wang, Y., Xie, W., Gao, G.: Effect of different moisture content and triaxial test methods on shear strength characteristics of loess. **07007**, 1–5 (2019)
10. IS 2720 – Part 2: Methods of test for soils: determination of water content. Bureau of Indian Standards, New Delhi (1973)
11. IS 2720 – Part 4: Methods of test for soils: Grain size analysis. Bureau of Indian Standards, New Delhi (1985)
12. IS 2720 – Part 5: Methods of test for soils: determination of liquid limit and plastic limit. Bureau of Indian Standards, New Delhi (1985)
13. IS 2720 – Part 7: Methods of test for soils: determination of water content-dry density relation using light compassion. Bureau of Indian Standards, New Delhi (1980)
14. IS 2720 – Part 12: Methods of test for soils: determination of shear strength parameters of soil from consolidated undrained triaxial compression test with measurement of pore water pressure. Bureau of Indian Standards, New Delhi (1983)

Effect of Liquefaction on Behavior of Strip Footings on Sands in Roorkee

Manendra Singh and B. K. Maheshwari

1 Introduction

Effect of liquefaction on shallow foundations is very interesting topic for research point of view. Generally on liquefied soils, deep foundation is to be provided and lot of research works have been done on earthquake resistant design of deep foundation on liquefied soils. But in residential buildings, it is not advisable to provide deep foundation. So if any liquefaction susceptible site exists in residential area then shallow foundation is required.

Estimation of seismic response of shallow foundation during a strong earthquake has been proven a difficult task throughout the years. This is due to the fact that soil behaves in a highly non-linear manner when subjected to large cyclic strains. It can deform substantially and then, when saturated, may develop high pore pressures and finally liquefaction occurs in it. The soil strength may reduce under seismic loading depending on the type of soil and seismic motion. Due to earthquake, pore pressure builds up and undrained conditions may result in decrease in strength and an increase in settlement. Failures of shallow foundations by earthquake occur due to increase in settlement. However, bearing capacity failures have also been observed during Niigata earthquake (1964) in Japan and Izmit earthquake (1999) in Turkey [1].

Liquefaction leads to severe loss of bearing capacity and increase settlements which lead to serious damage to the superstructures. Construction of shallow foundation upon the liquefiable soil is possible when a sufficient thick non-liquefiable soil

M. Singh (✉)
Department of Civil Engineering, National Institute of Technology Hamirpur, Hamirpur, HP 177005, India
e-mail: manendra@nith.ac.in

B. K. Maheshwari
Department ofEarthquake Engineering, IIT Roorkee, Roorkee, Uttarakhand 247667, India
e-mail: bk.maheshwari@eq.iitr.ac.in

C. N. V. Satyanarayana Reddy et al. (eds.), *Dynamics of Soil and Modelling of Geotechnical Problems*, Lecture Notes in Civil Engineering 186,
https://doi.org/10.1007/978-981-16-5605-7_27

Table 1 Unit weights and N value of DEQ, IIT Roorkee [2]

Depth (m)	Dry unit weight, γ (kN/m^3)	Saturated unit weight, γ_{sat} (kN/m^3)	Uncorrected N value
1.5	14.5	–	5
3.0	14.5	–	11
4.5	–	16.93	5
6.0	–	16.18	8
7.5	–	15.46	8
9.0	–	17.89	11
10.0	–	17.85	12

crust (such as clay, dense sand, dry sand, and improved soil), between the foundation and liquefiable soil, exists. In this paper, liquefaction performance of a strip footing is discussed considering various parameters such as PGA, relative density of soil medium and location of liquefiable soil below the footing.

2 Problem Definition

2.1 SPT Data

Analysis is carried out assuming a strip footing of width 4 m. Depth of footing is 1.5 m below the ground surface. Water table is located at 4.5 m below the ground surface, and Avg. load on the footing is assumed to be 100 kPa. The soil data for analysis was obtained from Department of Earthquake Engineering, IIT Roorkee. Table 1 shows unit weights and SPT (N) values for DEQ campus [2].

2.2 Shear Strength Parameters of Soil

From grain size distribution curves, it can be observed that the soil type is sand at all depth. So cohesion of soil is zero for this site. Friction angle (ϕ) is calculated by SPT number N and unit weights. For this corrected N values are used. For correction of SPT N value overburden pressure and dilatancy corrections are to be applied. Corrected N values are determined and shown in Table 2.

Overburden correction factor is calculated from Eq. (1) [3].

$$N_1 = C_N N_m \tag{1a}$$

Where,

Table 2 Calculation of corrected N values

Depth (m)	N	σ_v' (kN/m^2)	C_N	N_1	N_2
1.5	5	21.75	1.5	7.5	7.5
3.0	11	43.5	1.28	14.08	14.08
4.5	5	68.895	1.12	5.6	5.6
6.0	8	78.165	1.08	8.64	8.64
7.5	8	86.355	1.05	8.4	8.4
9.0	11	98.19	1.0	11	11
10.0	12	106.04	0.98	11.76	11.76

$$C_N = 0.77 \log_{10}\left(\frac{2000}{\sigma_v'}\right) \tag{1b}$$

.

N_m is the measured N value. σ_v' is the vertical effective stress in kN/m^2.

Dilatancy correction is calculated using Eq. (2) [4].

$$N_2 = (N_1 + 15)/2 \qquad \text{for } N_1 > 15 \tag{2a}$$

$$N_2 = N_1\ , \qquad \text{for } N_1 \leq 15 \tag{2b}$$

Depth of influence below the footing level is taken as 2.1 times of width of footing. From Table 1, Avg. saturated unit weight below the footing is calculated as 6.86 kN/m^3. From Table 2, Avg. corrected N value below the footing is obtained as 10. From IS 6403:1981 [5], for corresponding corrected N value, friction angle from comes out as 30°. From above calculation, we summarized the problem and this is shown by Fig. 1.

2.3 Earthquake Loading

Sinusoidal motion of earthquake was taken for the analysis. Since Roorkee city lies in Zone IV of the seismic zone of India; therefore, following earthquake properties were adopted for simulation.

Maximum peak ground acceleration, $a_{max} = 0.24$ g, Number of cycle N = 10, Time period = 0.4 s.

Magnitude = 7.0.

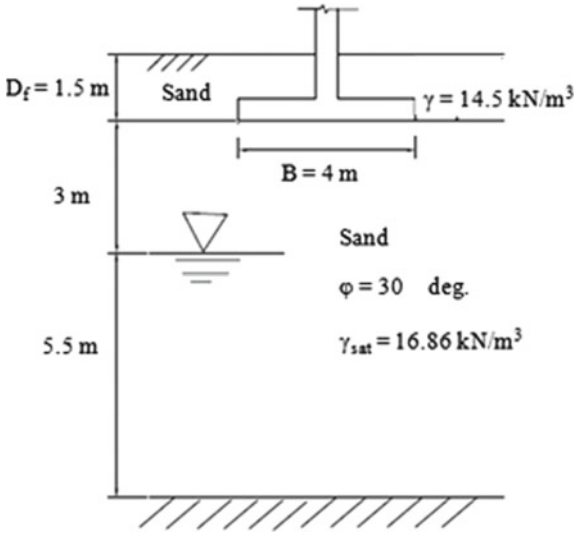

Fig. 1 Strip footing resting on sand layer

3 Methodology

3.1 Static Bearing Capacity, Settlement, and Liquefaction Potential

Static bearing capacity is determined as per IS 6403:1981 [5]. For sandy soil static settlement is calculated using IS 8009 (Part1): 1976 [6]. Liquefaction potential is calculated by the method given by Seed and Idriss (1971) [7].

3.2 Dynamic Bearing Capacity and Settlement Due to Liquefaction

Analysis consists of three steps: (a) evaluation of excess pore pressure, (b) dynamic bearing capacity, and (c) dynamic settlement.

Evaluation of excess pore pressure. A parameter, i.e., excess pore pressure (EPP) ratio is defined which is represented for the entire sand layer. Since excess pore pressure ratio developing in the region under the footing remain less than the EPP ratio under the free field. It has been taken in consideration that an active failure zone forms under the footing, forcing the soil in the free field into passive failure. Following this logic, a weighted average of the excess pore pressure ratios underneath the footing (r_{foot}) and in the free field (r_{ff}) was taken for the analytical solution. For strip footing, average excess pore pressure is calculated as $r_u = (r_{foot} + r_{ff})/2$ [8, 9].

Excess pore pressure in free field condition ($\Delta u_{ff,c}$) and under the footing ($\Delta u_{footing,c}$) due to earthquake are calculated by finite element method using Cyclic 1D software and Cyclic TP Software, respectively [10]. EPP for both cases is calculated at characteristic point which lies at a certain depth below the center line of footing. This depth is calculated from Eq. 3 [8, 9].

$$Z_c = H + \left[1.0 - 0.5\left(\frac{B}{L}\right)^3\right]B \tag{3}$$

For strip footing $Z_c = H + B$, where H is the thickness of non-liquefiable layer, B is the width of footing, and L is the length of footing. Further, $\Delta u_{foot,c}$ is EPP under the footing and $\Delta u_{ff,c}$ is the EPP under the free field at characteristic depth. The $\Delta\sigma_{v,c}$ is the additional vertical stress imposed to the characteristic point by the foundation load and $\sigma'_{v,c}$ is the geostatic vertical effective stress [9].

Subsequently EPP ratio under the footing (r_{foot}) and free field (r_{ff}) are calculated from Eqs. 4 and 5, respectively [9].

$$r_{foot} = \frac{\Delta u_{foot,c}}{\sigma'_{v,c} + \Delta\sigma_{v,c}} \tag{4}$$

$$r_{ff} = \Delta u_{ff,c} / \sigma vc' \tag{5}$$

Dynamic Bearing Capacity. A simple failure mechanism which may be used to calculate the degraded bearing capacity of shallow foundations at the end of shaking, while the soil below the soil crust is still in a liquefied state, is shown in Fig. 2. The footing punches through the crust forcing the development of a wedge-type failure mechanism within the liquefied subsoil [11].

In the failure mechanism of Fig. 2, it is assumed that the shear strength of the liquefied soil is expressed in terms of a degraded friction angle ϕ_d and it is calculated from Eq. 6 [11].

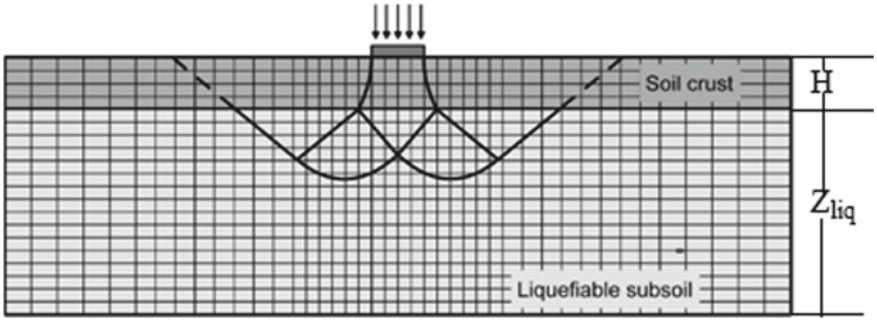

Fig. 2 Composite mechanism for end-of-shaking failure of shallow foundations resting on a soil crust over liquefied subsoil [11]

$$\tan \phi_d = (1 - r_u) \tan \phi \tag{6}$$

where ϕ is the actual friction angle of the sand and r_u is the excess pore pressure ratio induced by ground shaking, taken as uniform over the entire liquefied layer. From Eq. 6, increase in pore pressure ratio leads to decrease in friction angle. Therefore, excess pore pressure ratio is most important parameter for liquefaction analysis. Ultimate degraded bearing capacity of strip footing is given by Eq. (7) [11].

$$(q_u)_{\text{deg}} = \gamma_1'\left(D_f + H\right)N_{q2} + 0.5\gamma_2' B N_{\gamma 2} + \left(\gamma_1' H^2/B\right)\left(1 + 2D_f/H\right)K_s \tan \phi_1 - \gamma_1' H \tag{7}$$

Bearing capacity degradation factor is determined from Eq. (8) [11].

$$\zeta = (q_u)_{\text{deg}}/qu \leq 1 \tag{8}$$

where H is thickness of non-liquefiable sand layer, D_f is the depth of foundation below the ground surface, N_{q2} and $N_{\gamma 2}$ are the bearing capacity factors of the liquefied layer for the degraded friction angle ϕ_d, γ_1' is the submerged unit weight of non-liquefiable sand layer, γ_2' is the submerged unit weight of liquefied layer, ϕ_1 is the friction angle for non-liquefiable sand layer, and K_s is the coefficient of punching shear resistance on the vertical plane through the footing edges. K_s is determined from Fig. 4. K_s depends on approximate bearing capacity ratio which is determined from Eq. (9) [12].

$$q_2/q_1 = \left(\gamma_2 N_{\gamma 2}/\gamma_1 N_{\gamma 1}\right) \tag{9}$$

If H = 0, i.e., footing is directly on liquefiable sand then Eq. (7) can be written as follows:

$$(q_u)_{\text{deg}} = \gamma_1' D_f N_{q2} + 0.5'_{\gamma 2} B N_{\gamma 2} \tag{10}$$

Dynamic Settlement. Dynamic settlement is calculated from Eq. 11 [13].

$$S_{dyn} = c a_{\max} T^2 N \left(\frac{Z_{liq}}{B}\right)^{1.5} \left(\frac{1}{F S_{\text{deg}}}\right)^3 \tag{11}$$

Coefficient c is equal to 0.008 and 0.035 for square and strip foundations, respectively. Here a_{max} is the seismic peak ground acceleration, T is the predominant excitation time period, N is the number of cycles corresponding to PGA (a_{max}), Z_{liq} is the thickness of liquefiable layer, B is the width of foundation, and q is the average footing load [13].

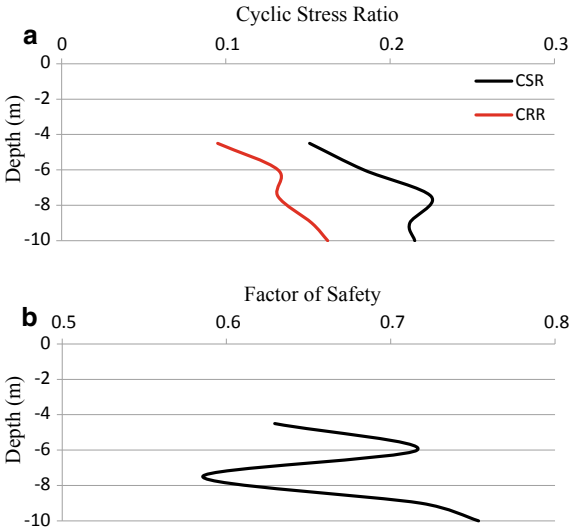

Fig. 3 **a** Evaluation of liquefaction potential for sand. **b** Factor of safety against the liquefaction

4 Results and Discussions

4.1 Static Bearing Capacity and Settlement

Static ultimate bearing capacity strip footing shown in Fig. 1 was found to be 481.16 kN/m^2 whereas settlement of footing was 40.91 mm.

4.2 Evaluation of Liquefaction Potential

Liquefaction potential was calculated by the method given by Seed and Idriss [7]. Figure 3 shows the variation of cyclic stress ratio with the depth. It can be seen from Fig. 3a that cyclic stress ratio of earthquake excitation (CSR) was found to be greater than the cyclic resistance ratio of soil (CRR) for all the depth below the water table. From Fig. 3b it can be seen that factor of safety against the liquefaction was found to be less than unity. Therefore soil below the water table is susceptible to liquefy under the earthquake loading.

4.3 Excess Pore Pressure

Excess pore pressure ratio under the footing is measured at characteristic depth and given by Eq. (12) [9].

$$r_{foot} = \frac{A}{1 + \Delta\sigma_{v,c}/\sigma'_{v,c}} \tag{12}$$

where $\Delta\sigma_{v,c}$ is the additional vertical stress imposed to the characteristic point by the foundation load and $\sigma'_{v,c}$ is the geostatic vertical effective stress. $\Delta u_{ff,c}$ is the excess pore pressure at characteristic depth under the free field condition. Subsoil dilation effect may be conservatively overlooked, assuming a correction factor A = 1.

For free field excess pore pressure ratio is assumed to unity at characteristic depth. Characteristic depth ($Z_c = H + B$) is calculated as 7 m below the footing. Subsequently effective stress at this characteristic point was calculated as 94.245kN/m^2.

Avg. excess pore pressure ratio $r_u = (r_{foot} + r_{ff})/2 = 0.74$.

4.4 Dynamic Bearing Capacity and Dynamic Settlement

Following values are obtained by the methods as discussed in Sect. 3.

Degraded bearing capacity	$q_{ultd} = 172.97$kN/m^2.
Degradation factor	$\zeta = 0.36$.
Dynamic settlement	$S_{dyn} = 40.34$ mm.
Total settlement	S = 81.25 mm.

.

Effect of liquefaction is summarized in Table 3. It can be observed from Table 3 that bearing capacity was found to reduce 36% due to liquefaction as compared to static condition whereas total settlement has increased almost two times as compared to static condition.

Table 3 Effect of liquefaction

	Static condition	Dynamic condition
Ultimate bearing capacity (kN/m$^{2)}$	481.16	172.97
Settlement (mm)	40.91	81.25

Table 4 Properties of sand

Type of soils	Shear wave velocity V_s(m/s)	N	Friction angle ϕ (°)	Unit weight γ_{sat} (kN/m^3)
Loose sand	185	9	29	17
Medium sand	205	11	31.5	19

5 Parametric Studies

5.1 Effects of Relative Density of Sand

In this section strip footing of width 5 m is taken. Depth of footing is 1 m below the ground surface. Water table is assumed to be located at the ground surface. Two cases are taken for the soil properties:

Case 1: Footing is resting on loose sand.

Case 2: Footing is resting on medium sand.

Properties of soils are given in Table 4. N is determined from Seed and Idriss formula by Eq. 13 [7].

$$V_s = 61.4N_{0.5} \tag{13}$$

For both the cases Poisson's ratio (0.4) and coefficient of permeability are the same (6.6×10^{-5} m/s). Average load on footing for both cases is 125 kPa. Effects of liquefaction are found out for both cases. Figure 4 describes the above problem.

Static Bearing capacity and static settlement are calculated as per IS 6403:1981 [5] and IS 8009:1976 [6], respectively and shown in Table 5.

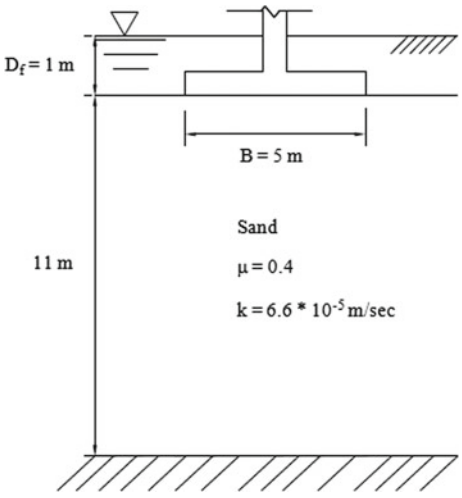

Fig. 4 Problem diagram of a footing resting on loose or medium sand

Table 5 Calculations of bearing capacity and settlement

Type of soil	q_{ult} (kN/m^2)	Settlement (mm)
Loose sand	200.47	165
Medium sand	459.79	82.5

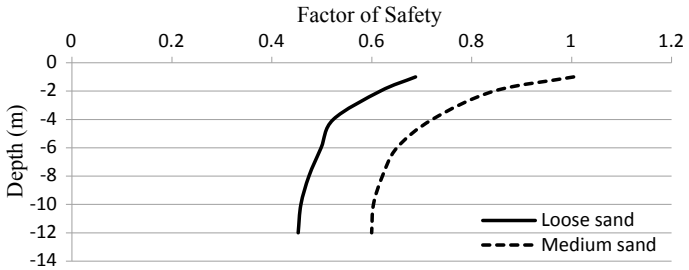

Fig. 5 Factor of safety against liquefaction for loose and medium sand

Evaluation of liquefaction potential. Factor of safety against the liquefaction has been determined as discussed in Sect. 3, and it has been shown in Fig. 5. From Fig. 5, it can be observed that liquefaction occurs at all depths for both loose and medium sand.

Excess pore pressure

Under the Free Field. EPP is determined from CYCLIC 1D software. CYCLIC 1D is a nonlinear finite element program for execution of one dimensional site amplification and liquefaction simulation. Following properties were taken for analysis:

$a_{max} = 0.2$ g, T = 0.25 s, N = 10 or f = 4 Hz.

Rayleigh Damping parameters: $A_m = 0.215423$, $A_k = 0.0009094557$.

Under the Footing. EPP under the footing is determined by CYCLIC TP software by nonlinear analysis. CYCLIC TP is a finite element program for two dimensional (2D) analysis of shallow foundations, under liquefaction-induced seismic excitation scenarios. Following footing parameters were adopted for analysis:

B = 5 m, $D_f = 1$ m, Ht. above the G.S. = 1 m, $E_s = 25$ GPa, $\mu = 0.25$, Mass density = 2500 kg/m^3.

Excess pore pressure calculated from software CYCLIC 1D and CYCLIC TP is shown in Figs. 6 and 7 for loose sand and medium sand respectively. Similarly EPP ratio for both cases has been shown in Figs. 8 and 9.

From Figs. 6 and 7, it can be noticed that epp under the free field is less than the epp under the footing, but from Figs. 8 and 9, it can be concluded that epp ratio is quite high under the free field than the under the footing. Characteristic depth (Z_c) is 6 m below the ground level. Avg. EPP ratio is calculated at this depth and given in Table 6.

Dynamic bearing capacity and settlement. Calculated degraded bearing capacity and dynamic settlement are shown in Table 7.

Effects of liquefaction are shown in Table 8.

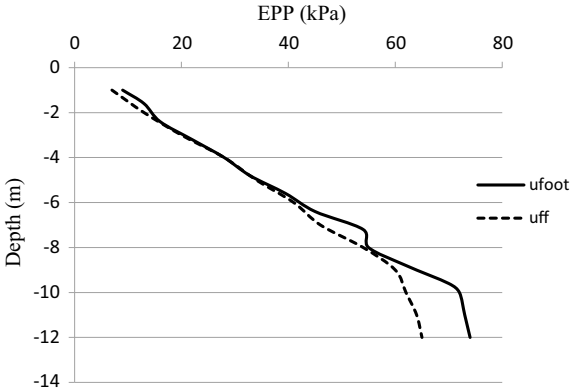

Fig. 6 Excess pore pressure for loose sand

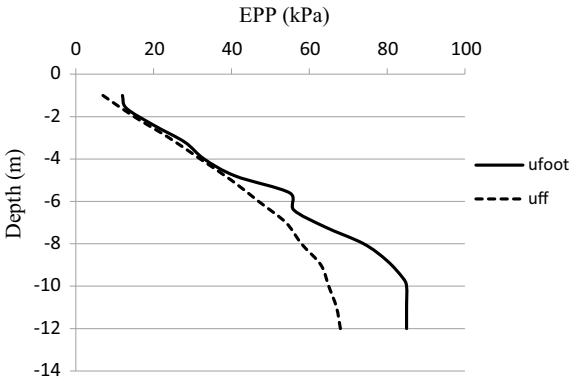

Fig. 7 Excess pore pressure for medium sand

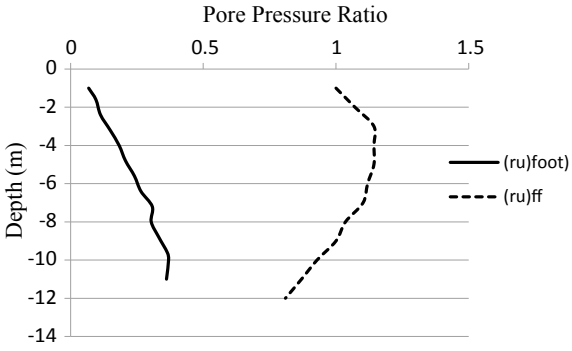

Fig. 8 EPP ratio for loose sand

It can be observed from Table 8 that effect of liquefaction is significantly greater for loose sand as compared to medium sand.

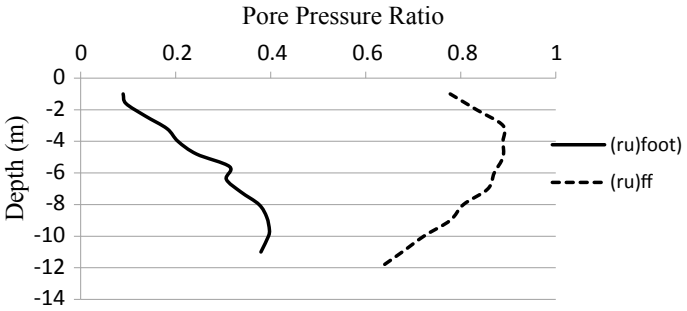

Fig. 9 EPP ratio for medium sand

Table 6 EPP Ratio for loose and medium sand

Type of soil	r_{ff}	r_{foot}	r_u
Loose sand	0.98	0.25	0.615
Medium sand	0.87	0.31	0.59

Table 7 Analysis with seismic forces for loose and medium sand

Type of soil	r_u	ϕ_d (deg.)	q_{ultd} (kN/m^2)	FS_{deg}	$S_{dyn}(2)$
Loose sand	0.615	12.05	56.96	0.456	1.5 m
Medium sand	0.59	14.10	87.55	0.70	41.55 cm

Table 8 Effects of liquefaction for loose and medium sand

Type of soil	q_{ult} (kN/m^2)	q_{ultd} (kN/m^2)	ζ	S_{static}	S_{dyn}	Total S
Loose sand	200.47	56.96	0.28	165 mm	1.5 m	1.66 m
Medium sand	459.79	87.55	0.19	82.5 mm	45.69 cm	53.94 cm

5.2 Varying Maximum Acceleration

Peak ground acceleration (PGA) is the most important parameter for liquefaction. In this section effect of PGA on liquefaction is discussed. There is a footing of width 4 m, resting on sand layer. The properties of footing and sand layer are shown in Fig. 10. Water table is located at the footing level. And depth of footing is 1 m below the ground surface. In this section, parametric studies are carried out by varying PGA (a_{max}) and all other properties are kept constant.

Input motion: a_{max} is varying, T = 0.25 s, N = 10.

Footing properties: E_s = 25 GPa, μ = 0.25, Mass density = 2500 kg/m^3.

Load on footing = 100 kPa.

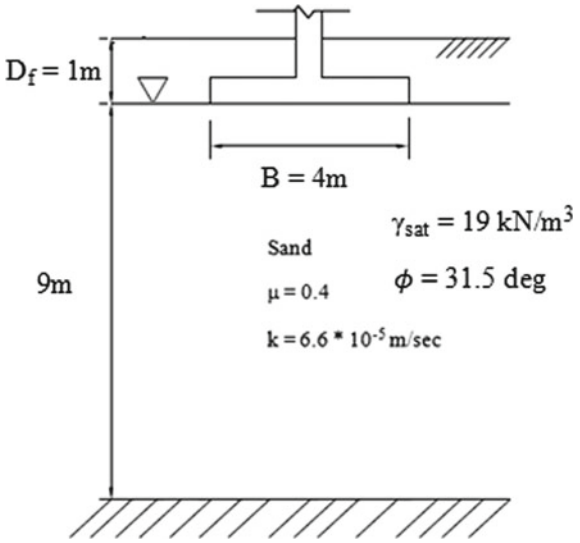

Fig.10 Strip footing on sand for different PGA

Figure 11 shows the liquefaction analysis for different PGA. Liquefaction does not occur for PGA 0.1 g, but it occurs below the depth 2 m from the footing for PGA 0.2 g and at all depth below the footing for PGA 0.5 g and 1 g.

For analysis with seismic forces, same procedure is used as in Sect. 5.1, then following values are obtained as shown in Table 9.

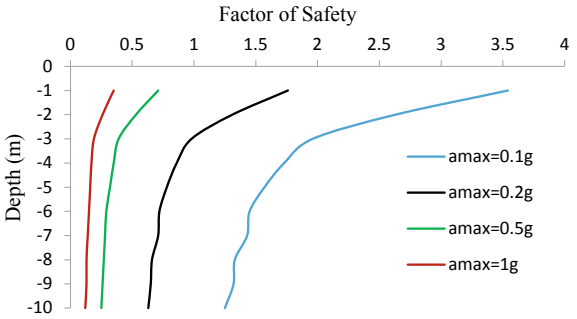

Fig. 11 Factor of safety against liquefaction for different PGA

Table 9 Effects of PGA

a_{max}	r_u	ϕ (deg.)	q_u (kN/m^2)	ζ	S_{static}	S_{dyn} (mm)	Total S(mm)
0.1 g	-	31.5	518.70	-	71.6	-	71.6
0.2 g	0.55	15.4	167.54	0.25	71.6	41.19	112.79
0.5 g	0.56	15.09	126.19	0.24	71.6	149.67	221.27
1 g	0.57	14.76	121.53	0.23	71.6	233.08	304.68

For PGA 0.1 g, there is no liquefaction. Table 9 shows that increase in PGA, increases settlement drastically and increase in PGA also leads to result in reduction in bearing capacity.

5.3 *Varying the Location of Liquefiable Layer*

Shallow foundation cannot be constructed directly on liquefiable soil. Thickness of unliquefiable layer play a significant role in this case. In this section the role of this layer explained by taking various depth of liquefiable layer.

There is a footing of width 3 m resting in soil. Water table is located at ground surface. Depth of footing is 1 m below ground surface. Other properties are shown in Fig. 12.

Input motion: $a_{max} = 0.4$ g, T = 1 s of f = 1 Hz, N = 10.

Footing properties: $E_s = 25$ GPa, $\mu = 0.25$, Mass density = 2500 kg/m^3.

Load on footing = 75 kPa.

Thickness of liquefiable layer $Z_{liq} = 3$ m.

Same methodology used as explained in Sect. 5.1.

It can be observed from Table 10 that change in location of unliquefiable layer has affected the excess pore pressure ratio. Friction angle decreases as H increases,

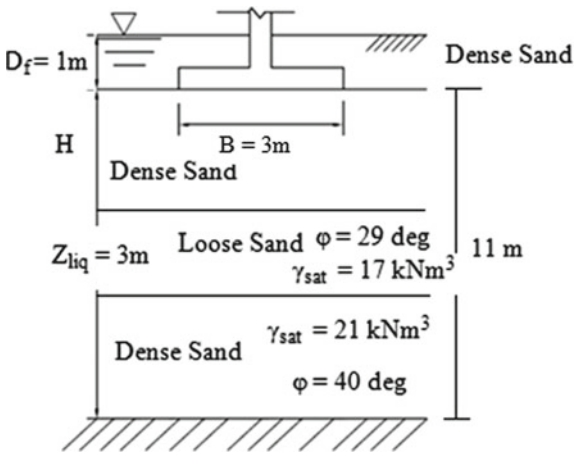

Fig. 12 Strip footing resting for different location of liquefiable sand

Table 10 Effect of location of liquefiable layer

case	r_u	ϕ_d (deg)	q_{ultd} (kPa)	FS_{deg}	S_{dyn} (mm)
H = 2 m	0.45	16.96	222.76	2.96	53.43
H = 4 m	0.48	16.07	375.68	5.0	11.14
H = 6 m	0.58	14.4	499.18	6.6	4.85

but there is decrease in coefficient of punching shear. Therefore increase in H result in increase in bearing capacity and factor of safety and also decrease the dynamic settlement. So increase in thickness of unliquefiable layer reduces the effects of liquefaction.

6 Conclusions

Based on work, following conclusions are summarized.

1. Liquefaction induced settlement and degraded bearing capacity are affected by type of soil, dimension of foundation, and seismic excitation parameters.
2. When PGA increases, there is drastic increase in dynamic settlement but bearing capacity first increases after that marginally affected by PGA. This is because that dynamic settlement is directly related to PGA. Bearing capacity does not greatly influenced by PGA because it is mainly directly related to excess pore pressure.
3. The location of liquefiable layer below the footing affects the liquefaction performance, if depth below increases then there is decrease in dynamic settlement and increase in bearing capacity.

References

1. Day, R. W.: Geotechnical Earthquake Engineering Hand Book. McGraw Hill (2002)
2. Datta, M. K., Kamble, S., et.al.: Project Report on Liquefaction Potential of DEQ Campus using SPT and Design of Pile Foundation. Department of Earthquake Engineering, IIT Roorkee, India (2006)
3. Peck, R.B., Hanson, W.E., Thornburn, T.H.: Foundation Engineering. Wiley, New York (1974)
4. Terzaghi, K., Peck, R.B.: Soil Mechanics Engineering practic. John Wiley & Sons, New York (1967)
5. Indian Standard (IS) 6403: Code of Practice for Determination of Bearing Capacity of Shallow foundation. Bureau of Indian Standards (1981)
6. Indian Standard (IS) 8009-Part I: Code of Practice for calculation of Settlements of foundation", Bureau of Indian Standards, New Delhi, (1976)
7. Seed, H.B., Idriss, I.M.: Simplified Procedure for Evaluating Soil Liquefaction Potential. Journal of Geotechnical Engineering Division, ASCE **97**(9), 1249–1273 (1971)
8. Karamitors, D.K., Bouckovalas, G.D., Chaloulos, Y.K., Andrianopoulos, K.I.: Numerical analysis of liquefaction-induced bearing capacity degradation of shallow foundations on a two-layered soil profile. Soil Dyn. Earthq. Eng. **44**, 90–101 (2012)
9. Karamitors, D.K., Bouckovalas, G.D., Chaloulos, Y.K.: Insight into the Seismic Performance of Shallow Foundations. Journal of Geotechnical Geoenvironmental Engineering, ASCE **194**(4), 599–607 (2013)
10. Cyclic 1 D and Cyclic TP: Softwares for ground response analysis and seismic analysis of shallow foundation. Version 1.2
11. Bouckovalas, G., Dakoulas, P.: Liquefaction performance of Shallow Foundations in peresence of a clay crust. Earthq. Geotech. Eng. Springer **6**, 245–276 (2007)

12. Meyerhof, G.G., Hanna, A.M.: Ultimate bearing capacity of foundations on layered soils under inclined load. Can. Geotech. J. **15**(4), 565–572 (1978)
13. Karamitors, D.K., Bouckovalas, G.D., Chaloulos, Y.K.: Seismic settlements of shallow foundations on liquefiable soil with a clay crust. Soil Dyn. Earthq. Eng. **46**, 64–76 (2013)

A Case Study of Liquefaction-Induced Damage to a Port Building Supported on Pile Foundation

Monirul Mallick, Kalyan Kumar Mandal, and Ramendu Bikas Sahu

1 Introduction

Pile foundations are extensively used to support the high-rise structures when the top soil is weak and results in bearing capacity and settlement problems. Soil liquefaction is a great concern for design of pile foundation in seismically active areas. Indian standard seismic design code IS 1893–2002, Part-I [1] provides various guidelines mainly for seismic design of superstructures. However, this code does not provide detailed guidelines for seismic design of pile foundation in liquefiable soil. So, it is a challenging job for geotechnical earthquake engineers to ensure safe and economical design of pile foundation and pile-supported high-rise structures in liquefiable soil. A significant number of damages and/or collapses of pile foundations and pile-supported structures are observed in liquefiable soils during past major earthquakes. The lateral spreading was reported the main factor causing bending failure of piles [2–7]. However, pile foundations are also vulnerable due to bending-buckling interaction in liquefiable soil [8–10].

Port structures are more vulnerable to seismic damages when built in seismically active area like Gujarat in India [11]. The foundation of Port Structures is often constructed on reclaimed land which are potentially liquefiable. During the 2001 Bhuj earthquake, the liquefaction of intermediate sandy layer, ground settlement, lateral spreading and resulted damages of Kandla port building have been reported [12]. The damages of pile foundation in liquefiable soil during seismic event may be due to structural failure, geotechnical failure or combination thereof depending up on the relative thickness and position of liquefiable soil layer. The non-liquefied crust overlying on liquefiable soil layer is mainly responsible for bending or shear failure of pile foundation. If top non-liquefiable crust is absent, the pile may loss the

M. Mallick (✉) · K. K. Mandal · R. B. Sahu
Department of Civil Engineering, Jadavpur University, Kolkata 700032, India

C. N. V. Satyanarayana Reddy et al. (eds.), *Dynamics of Soil and Modelling of Geotechnical Problems*, Lecture Notes in Civil Engineering 186,
https://doi.org/10.1007/978-981-16-5605-7_28

lateral support and prone to buckling failure under large axial load. However, if the top and bottom non-liquefiable crust is not present, pile may fail due to excessive settlement [12].

Liquefaction-induced damage to building supported on Pile foundation during earthquake is presented in this study using a reported case study on damages to the Kandla Port building during the 2001 Bhuj earthquake in India [12]. The effective stress-based ground response analysis (GRA) of the port site has been carried out using nonlinear finite element program Cyclic1D [13] considering nonlinearity of soil. The foundation system has been analysed by using beam on nonlinear Winkler foundation (BNWF) model to study the lateral spreading of the port building site, and the results obtained are found to be in line with the post-earthquake observations.

2 Kandla Port Building: Liquefaction-Induced Damage During Bhuj Earthquake

2.1 The Earthquake

The 2001 Bhuj earthquake (Mw = 7.7) was the most devastating seismic hazard causing tremendous damages of lives and properties in urban area of India. It struck the Kutch area of Gujarat state of India on January26, 2001. The epicentre of the earthquake was situated at 23.419°N, 70.232°E located at a distance of 20 km North East of Bhuj in Gujrat. The maximum bedrock level acceleration (MBRA) was 0.106 g. The acceleration time-history of the earthquake is shown in Fig. 1a.

2.2 The Structural Details of the Kandla Port Building

Kandla Port is located in the Kandla Creek and is 50 km from the epicentre of the earthquake. The Kandla Port tower, a 22.0 m high six-storied building supported on combined pile-raft foundation is located proximate to waterfront. The building was supported by 12 numbers of column (0.45 × 0.45 m and 0.25 × 0.25 m) and 32 numbers RCC piles of diameter 0.4 m and length 18 m. The 0.5 m thick foundation mat was provided as a rigid pile cap.

2.3 The Geotechnical Properties of the Port Site

The Kandla port is built on inherent ground consisting of recent unconsolidated layer of clay, silt and sand. The ground slope is about 1.5–2.0% towards seaside. The ground water table (GWT) is located at 1.2–3.0 m below ground surface. The soil

of the site composes of 10 m deep soft clay underlain by 12 m deep fine to medium dense sand and 10 m deep hard clay [12]. The top clay layer having water content 42–47% is highly plastic in nature. The SPT-N values of the upper fine sand layer is below 15, whereas the deep coarse sand layer is below 50. The fine content of sandy soils is in the range of 1–32%. The N-value below 15 and fine content 1–32% below GWT of intermediate sandy layer are prone to liquefaction under strong to moderate earthquake vibration.

2.4 Post-earthquake Observations

The top of the considered pile-supported building was tilted about 0.30 m towards sea side. The ground adjacent to the building was settled about 0.3 m. Ejaculation of sand through ground cracking was observed near the building site which indicates the widespread liquefaction. A successive pattern of lateral spreading was noticed after earthquake. The maximum magnitude of lateral spreading reported was 0.80 to 1.0 m [12]. Very little damage of superstructure was noticed and significant damages observed in the foundation. Figure 1b shows the tilted building, schematic drawing of the building before and after earthquake respectively [12].

3 Nonlinear Ground Response Analysis of the Port Building Site

1D nonlinear GRA has been carried out for predicting the layered soil response of Kandla port building site using 2001 Bhuj earthquake input ground motion at bedrock level. The present study utilizes the nonlinear methods of analyses through computer program Cyclic1D [13]. Cyclic1D has been developed for 1D wave propagation analysis using pressure-dependent and pressure-independent soil constitutive models. The constitutive model of soil in Cyclic1D has the capability to narrate the development and dissipation of pore water pressure. The liquefaction model within Cyclic1D is built under multi-yield-surface plasticity framework. The soil models available in Cyclic1D have also been implemented in OpenSees [14], a software framework for developing applications to simulate the performance of structural and geotechnical systems subjected to earthquakes. Incremental plasticity model is used to simulate the nonlinearity of soil. The finite elements are assigned for saturated soil strata under formulation of fully-coupled fluid-soil system. In time domain based nonlinear analysis the dynamic equation of motion is solved at every time step with the help of Newmark time integration method by specifying two user defined coefficients Beta (β) and Gama (γ).

A finite element model in the present study is defined in Cyclic1D by specifying the total height of soil profile of 40 m. The multi-layered soil profile layer has been

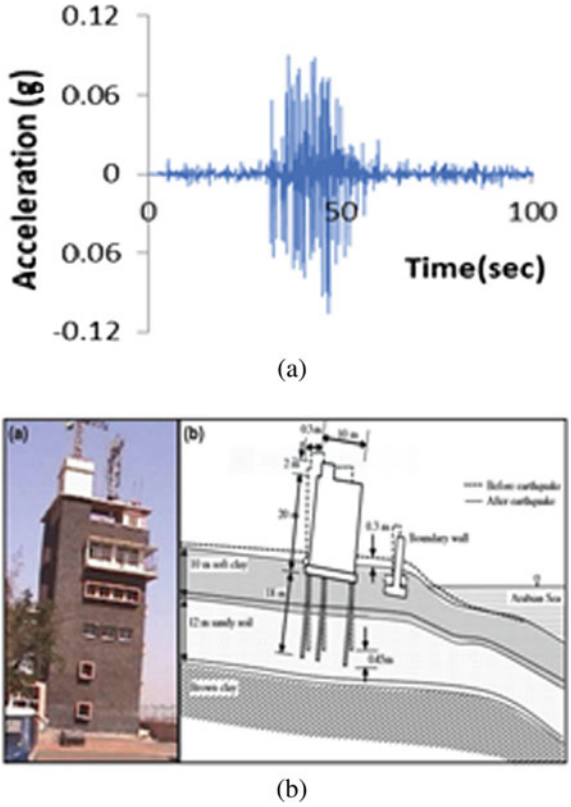

Fig. 1 **a** Acceleration time-history of Bhuj earthquake and **b** Tilting of Kandla Port Building along with building configuration before and after the 2001 Bhuj earthquake [12]

divided into total 80 numbers of elements, each of 0.50 m thick after convergence analysis. Predefined material models of clayey and sandy soils are chosen to define the soil profile of the site as shown in Table 1. A rigid bedrock base is considered for soil layer. Location of GWT is assumed at 1.50 m below ground surface. Mass and stiffness proportional Rayleigh-type damping (5%) has been considered. In current study, average acceleration method ($\gamma = 0.50$ and $\beta = 0.25$) has been used in Cyclic1D.

3.1 Assessment of Liquefaction Potential

Figure 2a, b show the profile of PGA and peak shear strain. The PGA at surface level for Bhuj earthquake motion is 0.107 g against MBRA 0.106 g. It is seen that surface acceleration is almost same with respect to MBRA for the Kandla port site. The soil strata at 10.0 m to 22.0 m depth consisting of fine to medium dense sand undergoes large strain. The peak strain value obtained is 1.05% at 13.25 m depth from surface.

Table 1 Parameter values for the soil materials models of Kandla Port soil [13]

Depth (m)	SPT-N value	Material model	Unit weight (kN/m$^{3)}$	V_s (m/sec)	Poisson's ratio	Co-eff. of permeability (m/s)	Φ (degree)	C_u (kN/m^2)
0.0–10.0	5	Cohesive soft	13.00	100	0.4	1.0E-09	-	18
10.0–22.0	14	Medium, sand permeability	19.00	205	0.4	6.6E-05	31.5	-
22.0–32.0	35	Cohesive stiff	18.00	300	0.4	1.0E-09	-	75
32.0–40.0	50	Medium-dense, sand permeability	20.00	225	0.4	6.6E-05	35	-

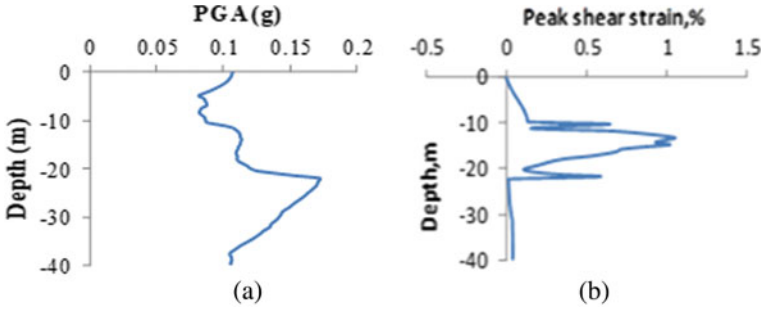

Fig. 2 Profile of **a** PGA and **b** peak shear strain

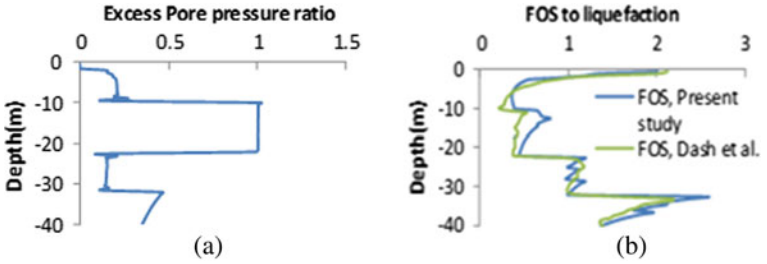

Fig. 3 Profile of **a** Excess pore pressure ratio and **b** Factor of safety for liquefaction potential (FOS)

Amplification of PGA reduces significantly at that strata due to higher shear strain. Higher strain value indicates the liquefaction susceptibility of the site. The profile of excess pore pressure (EPP) ratio is evaluated at each depth of Kandla Port site as shown in Fig. 3a. The EPP ratio is almost 1 for soil layer of 10.0–22.0 m depth under the Bhuj earthquake. So, the intermediate fine to coarse sandy strata is prone to liquefaction.

Simplified deterministic method [15–17] is used to assess the liquefaction susceptibility of the port site as shown in Fig. 3b. The factor of safety to liquefaction (FOS) which is ratio of cyclic resistance ratio (CRR) to cyclic stress ratio (CSR) is evaluated along depth. CRR is evaluated from corrected SPT-N value and fine content (FC) percentage. The PGA at surface and shear stress reduction co-efficient profile (R_d) obtained from nonlinear GRA has been utilized for evaluating the CRR. The FOS evaluated from the results obtained using Cycic1D software is compared with that obtained using SHAKE 2000 computer program [12], which uses equivalent linear analysis. Figure 3b shows the comparison of FOS along depth using both the codes. It is found that the results of Cyclic1D are co-relates well with the results of SHAKE 2000. The slight deviation in results at intermediate depth may be reasonable due to different analysis procedures and soil model which are estimated based on soil descriptions by two authors.

It is clear from graph that the FOS is less than 1 for top clay (1.5–10.0 m) and intermediate sandy layer (10.0–22.0 m) under Bhuj motion. So, the upper clay stratum experiences ground deformation and cracking due to cyclic failure. Moreover, intermediate sand layer (10.0–22.0 m) suffers ground settlement and lateral spreading due to liquefaction. So, the results of GRA argue the ejaculation of liquefiable fine sand through ground cracking near the building site.

3.2 Evaluation of Post-liquefaction Settlement

Post liquefaction settlement of saturated sand depends on a number of factors such as relative density, maximum volumetric strain and excess pore pressure. Figure 4a, b show the profile of volumetric strain and settlement of the port site under Bhuj earthquake motion. The peak value of volumetric strain obtained is 0.49% at 10.25 m depth. The post-liquefaction settlement profile of port site is evaluated using Cyclic1D. The total post-liquefaction settlement calculated using present model, previous study [12] and field observation are illustrated in Table 2. The settlement values obtained from the present analysis (0.288 m) are matching well with the previous author as well as post-earthquake observed settlement of 0.3 m. Hence, the present study justifies the liquefaction phenomenon of the port site at Kandla.

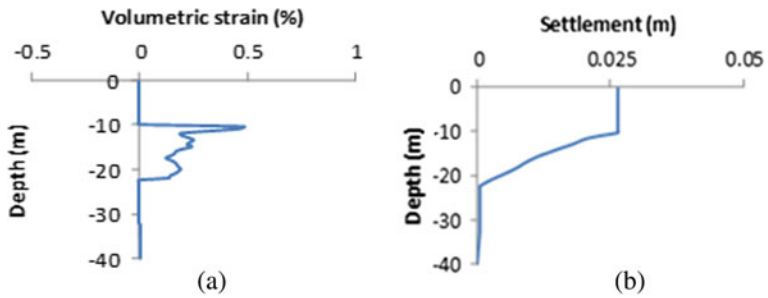

Fig. 4 Profile of **a** volumetric strain and **b** post-liquefaction settlement

Table 2 Post-liquefaction settlement

Depth(m)	Settlement (m)	Settlement (m) [12]		Observed settlement (m) [12]
		Method-I	Method-II	
10–22	0.283	0.241	0.345	
32–40	0.005	0.070	0.028	
Total settlement	0.288	0.311	0.373	0.300

3.3 *Lateral Spreading of the Site*

Lateral spreading is generally defined as permanent lateral displacement of gently sloping ground due to earthquake-induced liquefaction. Various empirical and semi-empirical methods are available in the literature [18–21] for predicting the amount of lateral spreading. In this study, simplified semi-empirical relationship [20] is used to estimate the amount of lateral spreading for probability of exceedance of 16% and 84% respectively. The value of yield co-efficient of soil slope considered is 0.052 assuming 5% ground slope. Additionally, the following values have been considered for evaluation of lateral spreading: earthquake magnitude Mw = 7.7, Average shear wave velocity = 175 m/sec, Initial time period of ground Ts = 0.23 s, and spectral acceleration at 1.5Ts = 0.44 g. The amount of lateral spreading evaluated in the present study is presented in Table 3 along with the values calculated by Dash et al. [12] and observed post-earthquake observation. The obtained value is comparable with the estimated value [12] and post-earthquake observed value.

The peak ground displacement (PGD) is almost uniform for depth 10.0 m from ground surface as shown in Fig. 5a. The PGD below depth 10.0 m decreasing linearly and becomes negligible at the bottom of liquefiable layer. Figure 5b represents the displacement time-history of the site under Bhuj motion. It is noticed that soil shows residual displacement at the end of loading cycle indicating probability of earthquake-induced lateral spreading under strong motion. The PGD at surface of soil are 0.590 m.

Table 3 Liquefaction-induced lateral spreading

	Present study		Dash et al. [12]		Observed value [12]
	16% probability of exceedance	84% probability of exceedance	16% probability of exceedance	84% probability of exceedance	
Lateral spreading (cm)	18.43	73.73	24	91	80–100

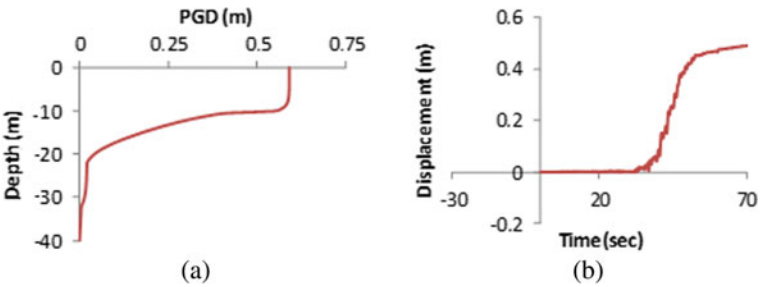

Fig. 5 **a** PGD profile and **b** Displacement time-history

4 Modelling and Analysis of Foundation System

The foundation of Kandla Port building consisted of 32 number 0.4 m diameter and 18.0 m long piles. The laterally loaded single pile is analysed using BNWF model subjected to a kinematic loading simulating lateral spreading as shown in Fig. 6. The open source finite element-based code, OpenSees [14,] is used to conduct the analysis. The undermost 8.0 m of the pile was founded in liquefiable soil and top 10.0 m were embedded in non-liquefied soft clay layer as shown in Fig. 2b. Pile and soil are simulated by displacement-based beam element and nonlinear spring element respectively. p-y curves based on API [22] procedures are used for simulating nonlinear behaviour of soil. The PGD profile as shown in Fig. 5 is employed to the soil end of the p-y springs to simulate lateral spreading [23]. The displacement profile is almost uniform for top 10.0 m soil layer. The same is varying linearly over liquefiable layer and is zero at the bottom layer.

The model is developed with three different sets of nodes: fixed spring nodes, slave spring nodes and pile nodes. The finite element mesh is generated using element length of 0.5 m. The three-dimensional spring nodes having three translational degrees of freedom are generated. Zero-length elements are used to define soil springs. The p-y springs oriented in lateral direction represent lateral resistance of soil-pile interface. The p-y springs are defined using the PySimple1 uniaxial materials. The input parameters for defining PySimple1 material are ultimate lateral resistance of soil (p_{ult}) and initial stiffness (k). p_{ult} values of clay and sand are calculated using procedure proposed by Matlock [24] and Brinch Hansen [25] respectively. Initial stiffness values (k) are computed as recommended by the API [22]. The modification of stiffness values for depth are done using procedure proposed by Boulanger et al. [26].

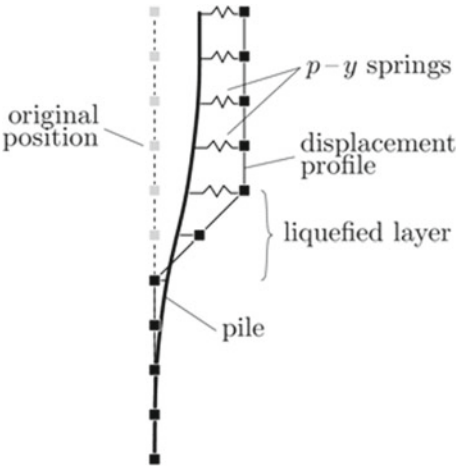

Fig. 6 BNWF Lateral spreading modelling approach adopted for soil-pile interaction [14]

The three-dimensional pile nodes are created with six degrees of freedom. Both translational and rotational degrees of freedom of pile nodes are considered. The base of the pile is considered as fixed. The pile nodes are connected with slave nodes of soil springs using equal degrees of freedom. Here the pile nodes are considered as master nodes. Both the nodes share equal degrees of freedom in lateral direction. The pile is modelled as displacement-based beam-column elements with elastic behaviour. The value of Young modulus and Poisson's ratio of pile used in the study are 30,000 MPa and 0.3 respectively [12]. Pseudo-static analysis has been conducted applying incremental displacement.

The profile of shear force and bending moment obtained from the analysis are shown in Fig. 7a, b respectively. Table 4 summaries the results obtained from the present lateral spreading analysis of single pile. From Table 4, it is observed that the maximum bending moment (233.38 kN.m) exceeds the capacity of the pile in seismic condition. But shear force demand is less than shear capacity of pile. Hence, the pile is unsecured on account of kinematic bending failure. Formation of plastic hinge is anticipated at the interface between liquefiable and non-liquefiable crust as shown in Fig. 7a. However, no structural failure is expected. The pile supported Kandla Port building was tilted mainly due to liquefaction-induced ground failure.

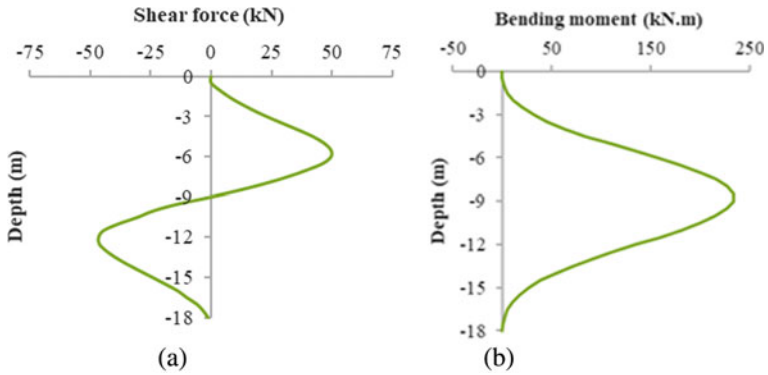

Fig. 7 **a** Shear force diagram and **b** Bending moment diagram of pile

Table 4 Bending moment and shear force of pile foundation

Bending moment (kN.m)			Shear force (kN)		
Demand (present study)		Capacity [12]	Demand (present study)		Capacity [12]
233.38		120–144	49.51		459.3–473.3

5 Conclusions

In the present study, a case study of liquefaction-induced damage to Kandla Port Building (Gujarat) supported on pile foundation during 2001 Bhuj earthquake is presented. The 22.0 m high six-storied RCC frame building supported on combined pile-raft foundation was tilted towards sea side after this earthquake. The key conclusions from the present analysis are as follows:

1. The acceleration at the ground surface does not magnify significantly with respect to MBRA for the Kandla port site under Bhuj earthquake.
2. 12.0 m thick intermediate loose to medium dense saturated sand below soft clay strata is potentially liquefiable under 2001 Bhuj earthquake motion.
3. The post-earthquake observed ground settlement of 0.3 m is matching well with the evaluated post-liquefaction settlement of 0.288 m obtained from present study.
4. The field-observed lateral spreading of 0.8 to 1.0 m is also consistent with the present results of lateral spreading analysis.
5. There is no possibility of structural failure of the foundation of the Kandla port building under 2001 Bhuj earthquake. The foundation was failed mainly due to geotechnical failure (i.e., excessive settlement).
6. The pile foundation travel through non-liquefiable layer and terminated in liquefiable soil can experience undue settlement. This exercise can be avoided as far as possible in practical situation.

References

1. IS 1893-Part 1: Criteria for earthquake resistant design of structure. Bureau of Indian Standards, New Delhi, India (2002)
2. Ishihara, K.: Geotechnical aspects of the 1995 Kobe earthquake: Terzaghi Oration. In: Proceedings of the 14th International Conference on Soil Mechanics and Foundation Engineering, Hamburg, Germany (1997)
3. Tokimatsu, K., Oh-oka, H., Satake, K., Shamoto, Y. and Asaka, Y.: Effects of lateral ground movements on failure patterns of piles in the 1995 Hyogoken-Nambu earthquake. In: Proceedings of Geotechnical Earthquake Engineering and Soil Dynamics III, pp. 1175–1181.ASCE geotechnical special publication, Reston (1998)
4. Berrill, J.B., Christensen, S.A., Keenan, R.P., Okada, W., Pettinga, J.R.: Case studies of lateral spreading forces on a piled foundation. Geotechnique **51**(6), 501–517 (2001)
5. Abdoun, T.H., Dobry, R.: Evaluation of pile foundation response to lateral spreading. Soil Dyn. Earthq. Eng. **22**(9–12), 1051–1058 (2002)
6. Finn, W.D.L., Fujita, N.: Piles in liquefiable soils: seismic analysis and design issues. Soil Dyn. Earthq. Eng. **22**(9–12), 731–742 (2002)
7. Abdoun, T., Dobry, R., O'Rouke, T.D., Goh, S.H.: Pile foundation response to lateral spreads: centrifuge modelling. J. Geotech. Geoenviron. Eng. ASCE **129**(10), 869–878 (2003)
8. Bhattacharya, S.: Pile instability during earthquake liquefaction. Ph.D. Thesis, University of Cambridge (2003)

9. Dash, S.R., Bhattacharya, S., Blakeborough, A.: Bending-buckling interaction as a failure mechanism of piles in liquefiable soils. Soil Dyn. Earthq. Eng. **30**(1–2), 32–39 (2010)
10. Knappett, J.A., Madabhushi, S.P.G.: Effects of axial load and slope arrangement on pile group response in laterally spreading soils. J. Geotech. Geoenviron. Eng. ASCE **138**, 799–809 (2012)
11. Rajaram, C. and Kumar, R.P.: Vulnerability assessment of coastal structure: a study on port buildings. Int. J. Educ. Appl. Res. **4**, Issue SPL-2 (2014)
12. Dash, S.R., Govindaraju, L., Bhattacharya, S.: A case study of damages of the Kandla Port and customs office tower supported on a mat–pile foundation in liquefied soils under the 2001 Bhuj earthquake. Soil Dyn. Earthq. Eng. **29**(2), 333–346 (2009)
13. Elgamal, A., Yang, Z. and Lu, J. Cyclic1D: A Computer Program for Seismic Ground Response. Report No. SSRP-06/05, Department of Structural Engineering, University of California, San Diego, La Jolla, CA (2006)
14. Mazzoni, S., McKenna, F., Scott, M.H., Fenves, G.L., et al.: OpenSees Command Language Manual. University of California, Berkeley, PEER (2006)
15. Seed, B., Idriss, I.M.: Simplified procedure for evaluating soil liquefaction potential. J. Geotech. Eng. Div., ASCE **97**(9), 1249–1273 (1971)
16. Seed, H.B., Tokimatsu, K., Harder, L.F., Chung, R.M.: The influence of SPT procedures in soil liquefaction resistance evaluations. J. Geotech. Eng. **111**(12), 1425–1445 (1985)
17. Boulanger, R.W. and Idriss, I.M.: CPT and SPT based liquefaction triggering procedures. Report No. UCD/CGM-14/01, Center for Geotechnical Modeling, University of California, Davis (2014)
18. Kramer, S.L., Smith, M.W.: Modified Newmark model for seismic displacements of complaint slopes. J. Geotech. Geoenviron. Eng. **123**(7), 635–644 (1997)
19. Bray, J.D., Rathje, E.M., Augello, A.J., Merry, S.M.: Simplified seismic design procedures for geosynthetic-lined, solid waste landfills. Geosynth. Int. **5**(1–2), 203–235 (1998)
20. Bray, J.D., Travasarou, T.: Simplified procedure for estimating earthquake-induced deviatoric slope displacements. J. Geotech. Geoenviron. Eng. **133**(4), 381–392 (2007)
21. Escudero, J.L.M.: Simplified Procedures for Estimating Earthquake-Induced Displacements. Ph.D. Thesis, University of California, Berkeley (2017)
22. American Petroleum Institute (API): Recommended Practice for Planning, Designing and Constructing Fixed Offshore Platforms. API Recommended Practice 2A(RP–2A), Washington, D.C., 17th edition (1987)
23. Brandenberg, S.J., Boulanger, R.W., Kutter, B.L., Chang, D.: Static pushover analyses of pile groups in liquefied and laterally spreading ground in centrifuge tests. Journal of Geotechnical and Geoenvironmental Engineering, ASCE **133**(9), 1055–1066 (2007)
24. Matlock, H.: Correlations for design of laterally loaded piles in soft clay. In: Proceedings of the II Annual Offshore Technology Conference, pp. 577–594. Houston, Texas (1970)
25. Brinch Hansen, J.: The ultimate resistance of rigid piles against transversal forces. *Bulletin No. 12*, Geoteknisk Institute, Copenhagen 5–9 (1961)
26. Boulanger, R.W., Kutter, B.L., Brandenberg, S.J., Singh, P., and Chang, D.: Pile Foundations in Liquefied and Laterally Spreading Ground During Earthquakes: Centrifuge Experiments and Analyses. Center for Geotechnical Modeling, University of California at Davis, Davis, CA. Rep. UCD/CGM-03/01 (2003)

Behavior of Single Pile Embedded in Multi-layered Soil Subjected to Dynamic Excitation

Bidisha Borthakur and Arup Bhatacharjee

1 Introduction

1.1 Response of Pile Foundation Due to Earthquake

Past earthquake case histories show that structures supported by different types of foundations is affected in a different manner depending upon the type of earthquake and the type of foundation. The failure patterns of piles have been seen to be different for each case depending on the peak ground acceleration, geometric configuration of pile foundation, and surrounding soil layers. Pile foundations consisting of concrete piles were seen to crack at pile head and at different depths after the Kobe earthquake in 1995, which had different peak ground acceleration in different routes [2]. Also, excessive lateral ground movement resulted in very large kinematic load on the piles which further lead to collapse of the piles. The Niigata earthquake in 1964 resulted in collapse of many bridges due to lateral spreading of the soil caused by liquefaction, which resulted in cracks not only at the top of the foundation, but also at the bottom [3]. Since the reason of failure of pile may be different in different cases, it is important to study the behavior of pile embedded in soil. However, prediction of the dynamic response of foundation-ground system is quite challenging due to complexity of soil-foundation interface mechanisms. Lack of advanced nonlinear soil behavior tools along with difficulty in soil-structure interaction modeling also lead to inaccurate prediction of response of pile. Since soil-structure interaction (SSI) during an earthquake has shown great impact on the seismic response of structure, it is mandatory to incorporate the SSI during analysis for better assessment of the performance of the structure. From various investigations conducted on liquefying soil, it was stated that progressive build-up of pore water pressure result in loss of strength and stiffness which result in large bending moments and shear force on pile

B. Borthakur (✉) · A. Bhatacharjee
Department of Civil Engineering, Jorhat Engineering College, Jorhat, Assam, India

C. N. V. Satyanarayana Reddy et al. (eds.), *Dynamics of Soil and Modelling of Geotechnical Problems*, Lecture Notes in Civil Engineering 186,
https://doi.org/10.1007/978-981-16-5605-7_29

[4]. Thus it is extremely important to conduct proper seismic analysis for foundations surrounded by liquefiable as well as non-liquefiable soil to obtain reliable results for design of such foundations. The objective of this paper is to study the influence of multilayered soil on pile in terms of pile head displacement and maximum bending moment on pile due to dynamic seismic analysis.

1.2 Finite Element Analysis Using OpenSees PL

Earthquake engineering simulations are performed using Finite Element Analysis program which can incorporate element formulation, material relations, analysis algorithms, and solution strategies. Finite Element Analysis software utilizes object-oriented design principles and programming approach which has brought revolution in the way software is written. One such software framework was created by Pacific Earthquake Engineering Research (PEER) Center for developing applications that could be used to simulate the performance of structural and geotechnical systems subjected to seismic loading. This framework was named as OpenSees (Open System for Earthquake Engineering Simulation). The main feature of OpenSees is that it is a finite element code for non-linear static as well as dynamic structural analyses that was developed under the paradigm of object-oriented programming. OpenSees allows usage of object oriented programming language C++, as well as Tcl (Tool Command Language), which is a pre-Java scripting language.

Using the pre- and post- processing efforts of OpenSees, a user-friendly interface known as OpenSees PL was created for 3D foundation-ground analyses such that the complicated soil-structure interaction mechanism could be incorporated while analyzing the foundation under seismic loading in order to represent the actual geometric configuration that is involved due to soil-structure interaction. OpenSees PL is a FE graphical user-interface for 3D ground-structure interaction response which allows conducting pushover analysis as well as seismic simulations [6].

1.3 Validation of Seismic Analysis Using OpenSees PL

To validate the use of OpenSees PL for obtaining desired results of seismic analysis of pile foundation, pile-soil configuration of single pile embedded in soil is modeled as per Lu et al. [5]. Lu et al. [5] validated the use of OpenSees PL by verifying with analytical results obtained by Abedzadeh et al. [1]. As per the modeling by Lu et al. [5], a circular free-head pile of 10.15 m length and radius 203.20 mm, fully embedded in a 20.12 m soil domain of submerged unit weight 9.87 kN/m^3 is modeled in OpenSees PL. The pile is modeled using linear beam-column elements so that bending moment, axial loads, and shear force could be viewed easily with rigid beam-column elements representing the diameter and interface with the surrounding soil elements. The soil is modeled using 8-node brick elements with *MultiYield* material

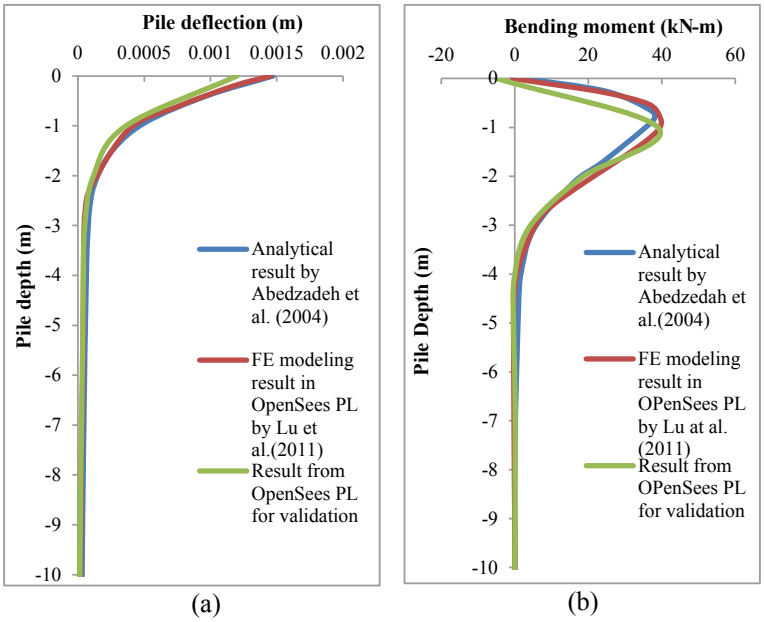

Fig. 1 Deflection and bending moment of pile due to pushover loading

to capture seismic events accurately. Lateral incremental pushover loading is applied monotonically at the pile head up to a total load of 140.12 kN. Figure 1 shows the pile deflection and the bending moment experienced by the pile throughout its length due to pushover loading. From the results, it is seen that pile response in terms of deflection and bending moment obtained from pushover analysis in OpenSees PL is similar to the analytical results of pushover analysis obtained by Abedzadeh et al. [1]. Thus, for conducting seismic analysis of pile foundation in OpenSees PL for this research work, pile-soil system is modeled as per Lu et al. [5].

2 Seismic Analysis of Pile Foundation

Dynamic analysis and pushover analysis is conducted on pile-soil system using OpenSees PL. A 0.4 m and 0.8 m diameter fixed pile is considered to be embedded in soil consisting of different layers of soil. Combination of cohesionless soil and cohesive soil is considered to be placed at different positions to study the impact of the surrounding soil on the pile subjected to seismic loading.

2.1 Numerical Modeling of Pile-Soil System

Similar pile and soil elements used by Lu et al. [5] have been used for modeling the pile-soil system for this research work. The 10 m long circular pile is modeled using linear beam-column elements. Rigid beam-column elements, which are 10^4 times stiffer than the pile elements axially and flexurally, are used for representing the cross-sectional diameter and the interface with the soil elements surrounding the pile. The pile is considered to be fixed at the top and bottom with water table up to the pile head. The mass density of the considered pile is taken as 2400 kg/m^3. The Young's modulus and the shear modulus are 3×10^7 kPa and 1.154×10^7 kPa respectively. For 0.4 m diameter pile, the moment inertia of the pile and torsion constant is 0.00125 m^4 and 0.00251 m^4 respectively. For 0.8 m diameter pile, the moment inertia of the pile and torsion constant is 0.02010 m^4 and 0.040212 m^4 respectively.

The 10 m soil domain consists of layers cohesionless very loose sand and cohesive medium soil in three different combinations. The non-linear soil modeling is done by modeling the soil domain with 8-node brick elements using *MultiYield* material. Sand is modeled using *PressureDependMultiYield* soil model and cohesive medium soil is modeled using *PressureIndependMultiYield* model. The details about the soil elastic properties, soil nonlinear properties, fluid properties, dilatancy properties, and liquefaction properties for the saturated cohesionless soil and cohesive soil are given in Table 1. The water table is considered up to the pile head so as to consider liquefaction analysis while conducting dynamic or static analyses. The soil combinations are as follows:

1. Cohesive medium soil (5 m) + Cohesionless very loose sand (5 m)
2. Cohesionless very loose sand (5 m) + Cohesive medium soil (5 m)
3. Cohesive medium soil (2 m) + Cohesionless very loose sand (6 m) + Cohesive medium soil (2 m).

The boundary condition is rigid box type and is considered to be fixed at the bottom in all directions. The plane of symmetry for half mesh configuration is fixed in Y direction while keeping it free in Z and X direction to model 3D full mesh scenario.

2.2 Dynamic Analysis Results of Single Pile

Dynamic analysis of single pile embedded in each type of soil combination is conducted by applying dynamic excitation in the form of sinusoidal wave of 0.3 g peak ground acceleration having frequency of 2 Hz for 10 cycles at the base of the pile. Figure 2 shows the displacement profiles of 0.4 m and 0.8 m diameter piles due to dynamic analysis. Pile surrounded by cohesive medium soil layer placed above cohesionless very loose sand layer results in high displacement throughout the pile length. Maximum displacement of 0.0242 m is experienced by the pile at the

Table 1 Soil properties of cohesionless very loose sand and cohesive medium soil

	Cohesionless very loose sand	Cohesive medium soil
Soil elastic properties		
Saturated mass density (Mg/m3)	1.7	1.5
Reference pressure (kPa)	80	100
Reference Shear modulus (kPa)	55,000	60,000
Reference Bulk modulus (kPa)	150,000	300,000
Soil nonlinear properties		
Friction (deg)	29	0
Cohesion(c) multiplied by((sqrt(3))/2)	0.2	37
Fluid properties		
Fluid mass density (Mg/m3)	1	1
Horizontal permeability (m/s)	6.6E-05	1.00E-0.9
Vertical permeability (m/s)	6.6E-05	1.00E-0.9
Dilatancy/liquefaction properties		
Phase transformation angle (deg)	29	–
Contraction parameter	0.21	–
Dilation parameter 1	0	–
Dilation parameter 2	0	–
Liquefaction parameter 1	10	–
Liquefaction parameter 2	0.02	–
Liquefaction parameter 3	1	–

beginning of the sand layer. The displacement of pile at the pile head is 0.0192 m. Interchanging of soil layers result in high pile displacement of 0.0103 m at the pile head where cohesionless very loose sand is present. For cohesionless very loose sand sandwiched between cohesive medium soil layers, 0.0196 m displacement is experienced by the pile at the beginning of the sand layer. The displacement at the pile head is 0.0171 m which is surrounded by cohesive medium soil layer. However, for the same pile surrounded by cohesive medium soil layer at the bottom of the pile, witnesses negligible displacement. 0.8 m diameter pile is seen to witness the highest pile displacement at the pile head for all the soil combinations irrespective of the location of cohesionless very loose sand layer. Pile surrounded by cohesive medium soil placed above cohesionless very loose sand displaces the pile head by 0.0182 m, which is the maximum displacement witnessed by the pile. Interchanging of soil layer position reduces the pile head displacement to 0.0143 m. For this soil combination, pile witnesses negligible displacement beyond 6 m depth at the cohesive medium soil layer. Pile surrounded by cohesionless very loose sand sandwiched between cohesive medium soil layers result in pile head displacement of 0.0180 m.

Figure 3 shows the bending moments experienced by 0.4 and 0.8 m diameter pile due to dynamic analysis. From the graphs it can be seen that 0.4 m diameter pile

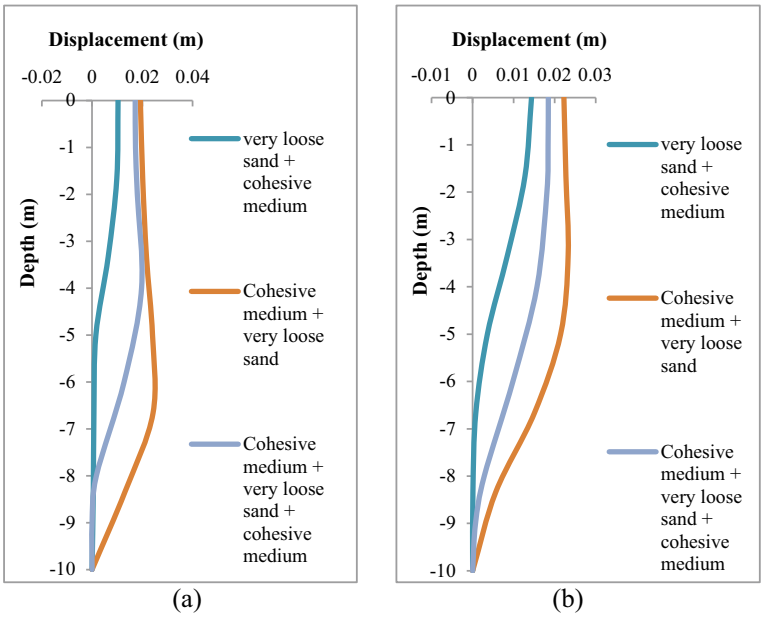

Fig. 2 Displacement results of **a** 0.4 m and **b** 0.8 m diameter pile subjected to dynamic analysis with PGA 0.3 g

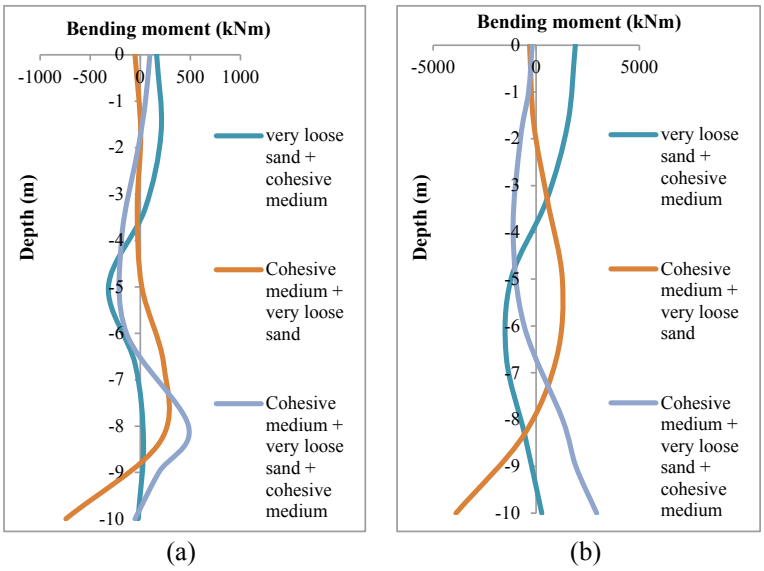

Fig.3 Bending moment results of **a** 0.4 m and **b** diameter pile subjected to dynamic analysis with PGA 0.3 g

witnesses change in bending behavior at more locations than 0.8 m diameter pile. For 0.4 m diameter pile, cohesive soil placed above cohesionless very loose sand layer results in the maximum magnitude of bending moment 742.39 kN-m. On interchanging the soil layers, the maximum magnitude of bending moment experienced by pile reduces to 317.72kN-m. This shows the influence of positioning of soil layers on response of pile. For cohesionless very loose sand sandwiched between cohesive soil layers, the maximum bending moment acting on pile is 481.53kN-m. Similar influence of positioning of soil layers is seen to occur for 0.8 m diameter pile as well. The maximum magnitude of bending moment experienced by pile surrounded by cohesive medium soil placed above cohesionless very loose sand is 4291.9kN-m. For pile surrounded by cohesionless very loose sand layer placed above cohesive medium soil layer, the maximum bending moment experienced by pile is 1897.81kN-m. Sandwiching cohesionless very loose sand between cohesive medium soil result in maximum bending moment of magnitude 3334.06 kN-m.

From the dynamic analysis results of 0.4 and 0.8 m diameter pile, it is seen that the type of surrounding soil present along with the positioning of soil layers affect the response of piles. Lower diameter piles are seen to be affected more than higher diameter piles. Different positions of soil layers result in different pile displacements for 0.4 m diameter pile throughout its length. Presence of cohesionless very loose sand at any layer results in higher displacement of pile within that layer. However, 0.8 m diameter pile witness high pile displacement at the pile head for all soil combinations even though there is difference among the displacement values for each soil combination. The magnitude of maximum bending moment is seen to depend on the positioning of soil layers and the type of soil present for both the diameters of pile. Presence of cohesionless very loose sand at the top layer results in low magnitude of maximum bending moment witnessed by the pile.

2.3 Pushover Analysis Results of Single Pile

Further, pushover analysis of the same piles embedded in the same soil conditions is conducted. The pile is pushed by applying incremental monotonic horizontal loading at the pile head. The load is applied until the pile head displacement is same as that obtained from dynamic analysis. Table 2 shows the magnitudes of maximum bending moment witnessed by piles due to pushover analysis.

2.4 Comparison of Dynamic Analysis and Pushover Analysis Results

As per Fig. 4, the magnitude of maximum bending moment witnessed by each pile is comparable for both the analyses for all the soil combinations. Of the three soil

Table 2 Maximum magnitude of bending moment due to pushover analysis

Soil combination	0.4 m diameter pile	0.8 m diameter pile
Cohesive medium soil + Cohesionless very Loose sand	861.5 kN-m	4798 kN-m
Cohesionless very loose sand + Cohesive medium soil	302.4 kN-m	1964 kN-m
Cohesive medium soil + Cohesionless very loose sand + Cohesive medium soil	561.5 kN-m	3564 kN-m

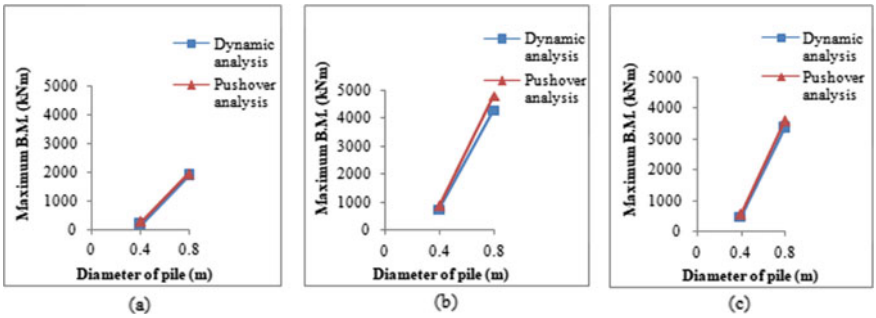

Fig.4 Magnitudes of maximum bending moment of piles surrounded by **a** Cohesionless very loose sand + Cohesive medium soil, **b** Cohesive medium soil + Cohesionless very loose sand, and **c** Cohesive medium soil + Cohesionless very loose sand + Cohesive medium soil

combinations considered, cohesive medium soil layer placed above cohesionless very loose sand results in the highest magnitude of maximum bending moment for both the analyses. For this soil combination, 0.4 m diameter pile witnesses 742.68 kN-m and 861.5 kN-m for dynamic and pushover analyses respectively. 0.8 m diameter pile witnesses maximum bending moment of magnitudes 4291.9 kN-m and 4798 kN-m for dynamic and pushover analyses respectively. Interchanging position of soil layers result is lower magnitudes of maximum bending moment. 0.4 m diameter pile witnesses 208.01 kN-m and 302.4 kN-m for dynamic and pushover analyses. For this soil combination, 0.8 m diameter pile results in maximum bending moment of magnitudes 1897.81 kN-m and 1964 kN-m for dynamic and pushover analyses. However, the triple layered soil combination containing cohesionless very loose sand sandwiched between cohesive medium soil layers, result in maximum bending moments of magnitude 481.53 kN-m and 561.5 kN-m for dynamic and pushover analyses for 0.4 m diameter pile. For 0.8 m diameter pile, the maximum bending moment for this soil combination is 3334.06 kN-m and 3564 kN-m for dynamic and pushover analyses.

3 Conclusions

From the seismic analysis conducted on piles of different diameter each surrounded by different soil combinations, it can be concluded that

1. The type of soil surrounding pile, along with the positioning of soil layer in different layered soil combinations, influences the behavior of pile subjected to seismic loading.
2. Lower diameter piles are affected more than higher diameter piles due to different surrounding soil conditions.
3. On conducting pushover analysis up to the pile head displacement obtained from dynamic analysis, comparable results of maximum bending moment magnitudes are achieved for both the analyses, thus confirming the results of pile behavior obtained from dynamic analysis due to various surrounding soil conditions.

References

1. Abedzadeh, F., Pak, R.Y.S.: Continuum Mechanics of Lateral Soil-Pile Interaction. J. Eng. Mech. **130**(11), 1309–1318 (2004)
2. Amiri, S.K.: The earthquake response of bridge pile foundations to liquefaction induced lateral spread displacement demands. Ph.D. Thesis, University of South California, Los Angeles (2008)
3. Bhattacharya, S., Madabhushi, S.P.G.: A critical review of methods for pile design in seismically liquefiable soils. Bull Earthq. Eng. **2008**(6), 407–446 (2008). https://doi.org/10.1007/s10518-008-9068-3,Springer
4. Inqualabi, K.Q., Garg, R.K. and Rao, K.B.: Seismic vulnerability of urban bridges due to liquefaction using nonlinear pushover analysis and assessing parameters for damage detection. In: 11th International Symposium on Plasticity and Impact Mechanics, IMPLAST 2016. Elsevier. Proc. Eng. **173**(2017), 1739–1746 (2016)
5. Lu, J., Elgamal, A., Yang, Z.: OpenSees PL: 3D Lateral Pile-Ground Interaction. User Manual. University of California, San Diego (2011)
6. Wang, N.: Three-Dimensional Modeling of Ground-Pile Systems and Bridge Foundations. Ph.D. Thesis. University of California, San Diego (2015)

Analysis of Laterally Loaded Single Pile in Cohesionless Soil Considering Nonlinear Soil-Structure Interaction Effects

Monirul Mallick, Kalyan Kumar Mandal, and Ramendu Bikas Sahu

1 Introduction

Foundation is a substructure built below the superstructure to transfer the structural loads safely to the underlying soil. Piles are slender member primarily used to transfer vertical load from superstructure to deep soil strata or rock. Pile foundations are also required to carry both vertical and lateral loads in high rise buildings, bridges, chimney, transmission towers, port and harbour structures. The major causes of lateral loads are wind action, lateral earth pressure, impact load, water pressure, and seismic forces. Ultimate lateral resistance of soil and maximum allowable lateral displacement of pile are the two principal criteria for design of laterally loaded pile (LLP) foundation. The ultimate lateral resistance of a single pile depends on both geotechnical properties of soil and structural properties of pile. The pattern of failure of short and long piles is also different. The failure of short pile is due to rigid body translation or rotation whereas that of long pile is by forming one or more plastic hinges. Hence, slenderness ratio of pile has a profound influence on lateral response of single pile.

Lateral response of single pile has been analysed by several researchers in the past using analytical, numerical and experimental methods [1–11]. The response of LLP in layered soil has been evaluated considering constant but different modulus of subgrade reaction for each layer [12]. Liyanapathirana and Poulos [13] proposed pseudo-static approach for analysis of LLP. The effects of vertical load on LLP foundation has also been evaluated by several researchers [14–16]. The solution of LLP is complex problem and involves nonlinear soil-structure interaction (SSI) effects. The exact solution of LLP foundation is not well established unlike vertically loaded piles (VLP). Only approximate solutions based on theoretical analysis are presented in Indian standard code of pile foundations IS-2911 [17]. The effects of SSI

M. Mallick (✉) · K. K. Mandal · R. B. Sahu
Department of Civil Engineering, Jadavpur University, Kolkata 700032, India

C. N. V. Satyanarayana Reddy et al. (eds.), *Dynamics of Soil and Modelling of Geotechnical Problems*, Lecture Notes in Civil Engineering 186,
https://doi.org/10.1007/978-981-16-5605-7_30

are neglected in conventional design practice assuming fixed base condition to avoid complexity of the problem. However, this assumption is valid for low rise structures resting on stiff soil. The consideration of SSI becomes compulsory for laterally loaded high rise structures resting on soft soil. The flexibility of the supporting soil medium affects the time period and damping properties of the structure. So, the seismic response of structure may not be accurate by neglecting or oversimplifying the SSI effects. The effects of nonlinear SSI on free and fixed head single pile under lateral load in cohesionless soil is investigated in the current study using Beam on nonlinear Winkler foundation (BNWF) model. The simplified BNWF model is capable to incorporate nonlinear SSI effects accurately with less computational operation. The effects of various soil types on pile and soil response are investigated for single pile considering nonlinear SSI effects. The effects of slenderness ratio (L/D) and pile head fixity condition are also studied for loose sand.

2 Model Description

A 3D soil-pile model has been built using open source finite element-based code, OpenSees [18]. BNWF model is used to model the interaction between pile and soil as shown in Fig. 1. Pile and soil are simulated by displacement-based beam element and nonlinear spring element respectively. p-y curves based on API procedures [19] are used for simulating nonlinear behaviour of soil. The model is developed with three different sets of nodes: fixed spring nodes, slave spring nodes and pile nodes. The finite element mesh is generated using element length of 0.5 m. The three-dimensional spring nodes having three translational degrees of freedom are generated. Zero-length elements are used to define soil springs using fixed and slave-nodes. Distinct uniaxial material objects are used in the lateral and vertical directions. The p-y springs oriented in lateral direction represent lateral resistance of soil-pile interface. On the other hand, vertically oriented t-z and Q-z springs represent skin friction along pile length and end

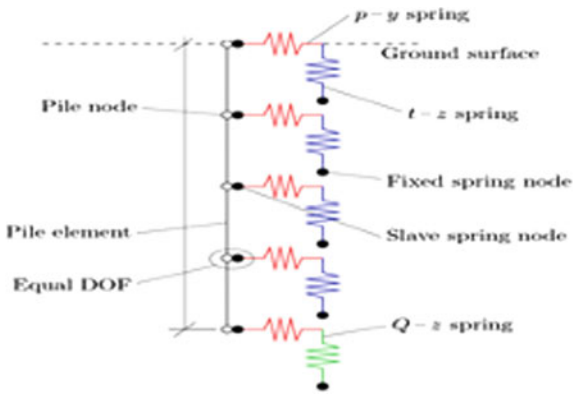

Fig. 1 BNWF modelling approach adopted for soil-pile interaction [18]

bearing at pile base, respectively. The p-y, t-z and Q-z springs are defined using the PySimple1, TzSimple1 and QzSimple1 uniaxial materials, respectively. The detail backbone equations and parameters of these springs are presented by Boulanger et al. [20] and Boulanger [21]. The three-dimensional pile nodes are created with six degrees of freedom. Both translational and rotational degrees of freedom of pile nodes are considered. Orientation of the pile is done by specifying a linear coordinate transformation object. The topmost pile head node is simulated as free head condition to apply lateral load. The pile nodes are connected with slave nodes of soil springs using equal degree of freedom command. Here the pile nodes are considered as master nodes. Both the nodes share equal degrees of freedom in lateral and vertical direction. Elastic behaviour of pile is considered using elastic section object.

3 Validation of the Present Numerical Model

The reliability of the present finite element based numerical model is verified by comparing results with the theoretical solution of Reese and Matlock [22]. A laterally loaded single pile of length 10 m and diameter 0.5 m resting in loose sand is analysed using present model. The modulus of subgrade reaction is taken as 6800 kN/m3 [1]. Lateral load of magnitude 150 kN is applied at pile top. Figure 2a, b present the comparison of lateral displacement and bending moment profile of pile using the present model and theoretical solution [22]. The present results are matching well with the theoretical solutions available in the literature. The slight deviation in results may be equitable due to different analysis methodology and soil model which are considered based on soil descriptions. Hence, the BNWF model implemented in OpenSees can be efficiently used for lateral response of pile foundation.

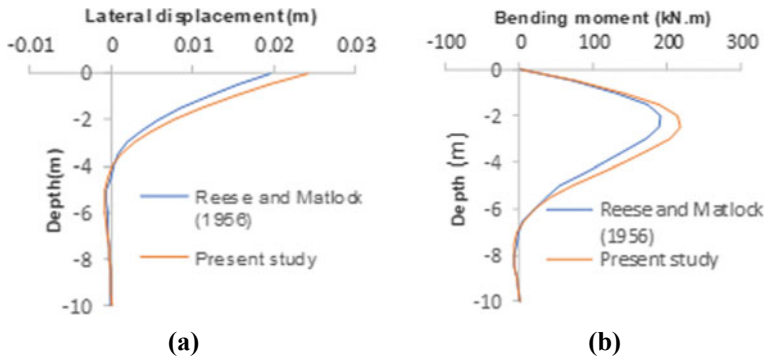

Fig. 2 Comparison of **a** lateral displacement and **b** bending moment response of pile obtained from present study with Reese and Matlock [22]

4 Results and Discussions

The behaviour of LLP foundation depends on a number of parameters. The effects of various soil types on pile and soil response are investigated using present model for single pile. The effects of slenderness ratio (L/D) of pile and pile head fixity are also studied. The length of pile is varied from 5.0 m to 15.0 m keeping diameter constant (0.5 m) for parametric study. Tables 1 and 2 summarise the properties of pile and soil used in the study respectively. The properties of pile and soil are taken from IS 456–2000 [23] and Das, BM [24] respectively. Single layer cohesionless soil is considered, and the ground water table is considered well below the tip of the pile. Pile head is located at ground surface. Lateral load of 150 kN is applied linearly from 0 to 150 kN over a 10 s at topmost pile node using plain pattern with elective time-series parameters. The load-controlled integrator is used to conduct the analysis.

4.1 Influence of Soil Type on Pile and Soil Response

Static analysis for 15.0 m long pile (L/D = 30) has been performed for loose, medium and dense soil types, and the results are presented. Variation of lateral displacement profile of pile is presented in Fig. 3a for various soil types. It is observed that the maximum lateral displacements at free end for loose, medium and dense sand under same lateral load of 150 kN are 24.12, 9.33 and 4.22 mm respectively. Maximum

Table 1 Pile parameters considered in the present study [23]

Particulars	Values
Length of pile (L)	15 m
Diameter of pile (D)	0.5 m
Lateral load (P)	150 kN
Grade of concrete	M30
Young's modulus of pile (Ep)	27,400 MPa
Poisson's ratio of pile (μ)	0.2
Moment of inertia of pile (Ip)	0.003066 m4

Table 2 Soil parameters considered in the present study [24]

Soil type	Unit weight, γ (kN/m^3)	Young's Modulus,Es (MPa)	Poisson's ratio,μs	Friction angle, ϕ (°)
Loose sand	17	18	0.25	29
Medium sand	19	25	0.30	33
Dense sand	21	50	0.35	40

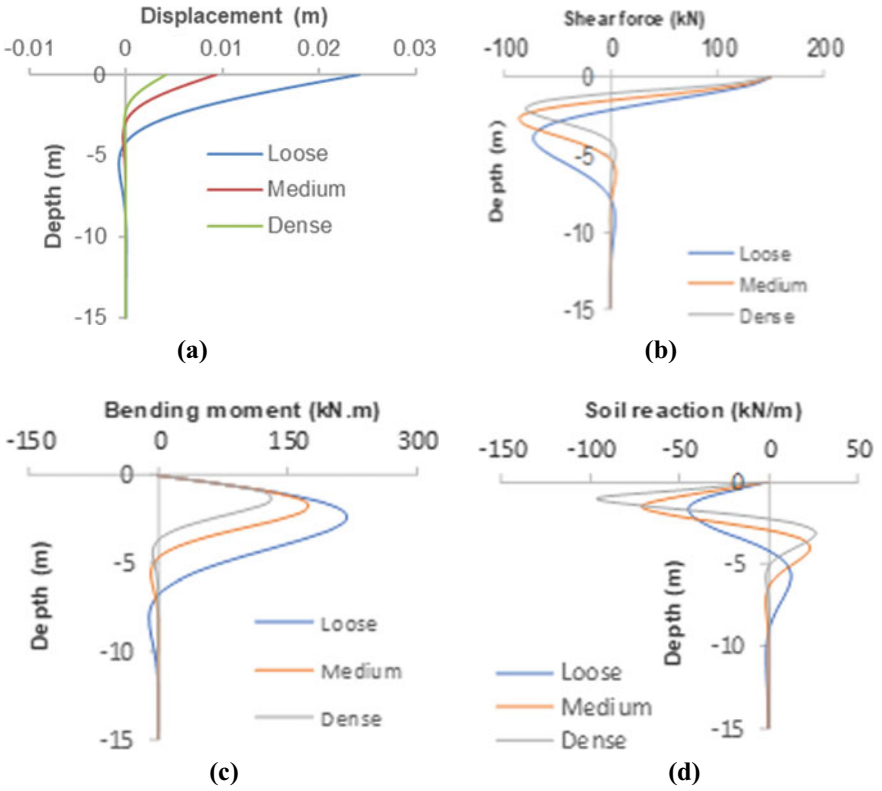

Fig. 3 Profile of **a** lateral displacement, **b** shear force, **c** bending moment of pile and **d** soil reaction response for various soil types

lateral displacement is reduced by 82.50% when the soil type changes from loose to dense sand. So, the significant reduction of lateral displacement of pile is observed with the increase of stiffness of soil.

The variation of shear force and bending moment of the pile along depth are shown in Figs. 3b, c respectively. The peak value of shear force obtained is 150 kN at free head of the pile. The depths corresponding to point of inflection are 2.5 m, 1.5 m, and 1.5 m for loose, medium and dense sand respectively. The maximum values of bending moment are also affected by the stiffness of soil. The maximum bending moments are 218.18 kN-m, 170.33 kN-m and 128.58 kN-m for loose, medium and dense sand respectively. The depth corresponding to peak bending moment is dependent on soil type. The peak value of bending moment of pile is reduced by 41.10% when the soil type changes from loose to dense sand. The depth of point of contraflexure from ground surface decreases with the increase of relative density of soil.

Figure 3d presents the soil reaction profile for various soil types. The response is negative from the ground surface to about 4.5 m, 3.0 m and 2.5 m depth, then

transitions to positive until about 9.0 m 6.0 m and 5.0 m depth, for loose, medium and dense sand have a second smaller negative section and then is nearly zero near the tip of the pile. The peak value of soil reaction obtained for loose, medium and dense sand are 44.12, 70.87 and 95.98 kN/m respectively. Also, the soil reaction of dense sand is 35.40% more than loose sand under same lateral load.

4.2 *Influence of Pile Slenderness Ratio (l/d) on Pile and Soil Response*

The behaviour of pile as short rigid or long flexible, response of pile and soil are highly influenced by L/D ratio of pile. Figure 4a shows the impact of L/D on lateral displacement of pile in loose sand. The pile having L/D ratio 10 behaves like short rigid pile and tends to rotate with respect to point of inflection. The peak opposite displacement appeared at the bottom of short pile as shown in Fig. 4a. The piles having L/D ratio 15, 20 and 30 behave like long flexible piles and the maximum

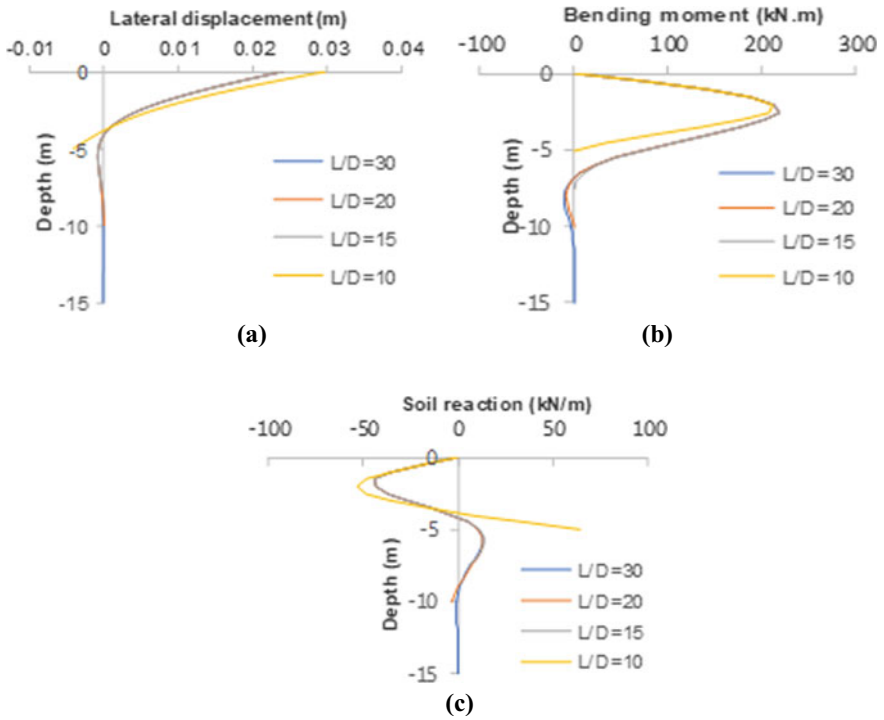

Fig. 4 Profile of **a** lateral displacement, **b** bending moment of pile and **c** soil reaction response in loose sand for various pile slenderness ratio

negative displacement occurred in between inflection point and the base of pile. Also, the negative tip displacement is more for short pile with compared to long pile.

It is observed that the maximum bending moment is 211.55 kN-m for L/D ratio 10 and 218.18 kN-m for L/D ratio more than 10 in loose sand. Also, the maximum bending moment of pile decreases along length for L/D ratio 10 and 15. However, the negative bending moment occurs near the point of contraflexure and finally becomes zero at base of pile for L/D ratio 20 and 30 as shown in Fig. 4b.

The soil reaction profile for various L/D ratio of pile in loose sand is presented in Fig. 4c. The soil reaction is 46.80% more for short pile (L/D = 10) than long piles (L/D more than 10) resting in loose sand. Also, soil reaction for the pile having L/D ratio 10 transitions to positive and becomes maximum at the pile tip. When L/D ratio exceeding 10 the reaction changes to positive and has a second smaller negative and tends to zero near the base of pile.

4.3 Influence of Pile Head Fixity Condition on Pile and Soil Response

The effects of pile head fixity on lateral displacement response of short and long pile for loose and dense sand are presented in Fig. 5a, b respectively. The rigid behaviour showing rigid body rotation is noticed for short free and fixed head pile (L/D = 10) in loose sand. But, in dense sand the flexible type behaviour was observed for same pile for both free and fixed head condition. However, the behaviour of long pile (L/D = 30) is always flexible type for all types of soils and pile head fixity condition as shown in Fig. 5b. Also, it is overserved that the lateral displacement of pile decreases significantly when the pile head fixity changes from free head to fixed head condition. The lateral displacement of long pile (L/D = 30) for loose and dense sand is decreased by 69.75% and 73.90% respectively when the pile head fixity changes from free to fixed head condition.

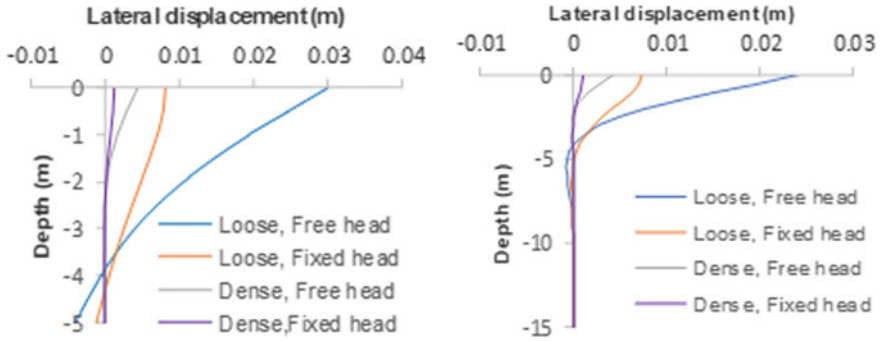

Fig. 5 Lateral displacement profile for **a** short pile (L/D = 10) and **b** long pile (L/D = 30)

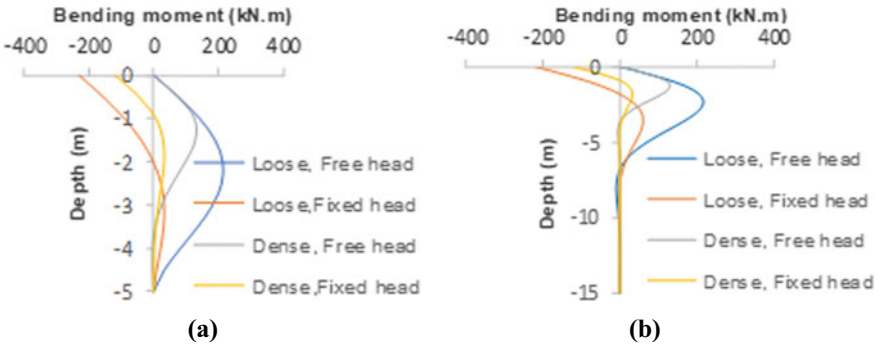

Fig. 6 Bending moment profile for **a** short pile (L/D = 10) and **b** long pile (L/D = 30)

The bending moment profiles of short and long pile for different pile head condition and soil type are presented in Fig. 6a, b respectively. The pile head fixity condition and slenderness ratio have profound influence on bending moment profile. The depth corresponds to maximum bending moment are also different for free and fixed head pile. The maximum bending moment of free head and fixed head long pile is reduced by 41.10% and 45.60% respectively for changes of relative density of soil from loose to dense.

The soil response is also dependent on pile head fixity condition for both short and long pile. Figure 7a, b illustrate the soil reaction profile for short and long pile embedded in loose and dense sand. The pattern of soil reaction of short free and fixed head pile in loose sand is completely different with that of long pile.

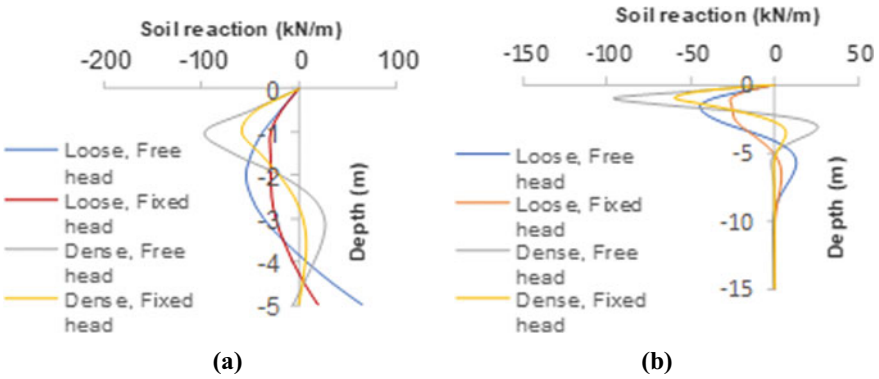

Fig. 7 Soil response profile for **a** short pile (L/D = 10) and **b** long pile (L/D = 30)

5 Conclusions

A three-dimensional finite element BNWF model has been developed using the open-source software platform OpenSees to study the static response of single pile in cohesionless soil. The key conclusions from the results of present study are as follows:

1. The relative density of soil has profound influence on pile response. The maximum bending moment of free head and fixed head long pile is reduced by 41.10% and 45.60% respectively for changes of relative density from loose to dense.
2. The depth of point of contraflexure from ground surface decreases with the increase of relative density of soil.
3. The rigid or flexible nature of pile is extremely dependent on slenderness ratio and pile head fixity. Pile of L/D less than 10 behaves like short rigid pile and more than 10 behaves like long pile.
4. Short pile undergoes significant negative displacement. The maximum negative displacement occurred at the base of the pile for short pile. The same is occurred in between inflection point and the base of pile for long pile in loose sand. The soil reaction is 46.80% more for short pile than long piles resting in loose sand.
5. The lateral displacement of long pile for loose and dense sand is reduced by 69.75% and 73.90% respectively when the pile head fixity changes from free to fixed head condition.

References

1. Matlock, H., Reese, L.C.: Generalized solution for laterally loaded piles. J. Soil Mech. Found. Div. ASCE **86**(SM5), 63–91 (1960)
2. Broms, B.B.: Lateral resistance of piles in cohesive soils. J. Soil Mech. Found. Div. ASCE **90**(2), 27–63 (1964)
3. Broms, B.B.: Lateral resistance of piles in cohesionless soils. J. Soil Mech. Found. Div. ASCE **90**(3), 123–156 (1964)
4. Poulos, H.G., Davis, E.H.: Pile Foundation Analysis and Design. Wiley, New York (1980)
5. Randolph, M.F.: The response of flexible piles to lateral loading. Geotechnique **31**(2), 247–259 (1981)
6. Murthy, V.N.S., Subba Rao, K.S.: Prediction of nonlinear behavior of laterally loaded long piles. Foundation Engineer, vol. 1, no 2, New Delhi (1995).
7. Comodromos, E.M.: Response prediction for horizontally loaded pile groups. J. Geotech. Eng. Southeast Asian Geotech. Soc. 122–123 (2003)
8. Phanikanth, V.S., Choudhury, D., Reddy, G.R.: Response of single pile under lateral loads in cohesionless soil. Electron J. Geotech. Eng. **15**(H), 813–830 (2010a)
9. Phanikanth, V.S., Choudhury, D., Reddy, G.R.: Behavior of fixed head single pile in cohesionless soil under lateral loads, Electron. J. Geotech. Eng. **15**(M), 1243–1262 (2010b)
10. Phanikanth, V.S., Choudhury, D.: Single piles in cohesionless soils under lateral loads using elastic continuum approach. Indian Geotech. J. **44**(3), 225–233 (2014)

11. Abbas, J.M., Chik, Z., Taha, M.R.: Modelling and Assessment of a Single Pile Subjected to Lateral Load. Studia Geotechnica et Mechanica **40**(1), 65–78 (2018)
12. Davisson, M.T., Gill, H.L.: Laterally loaded piles in layered soil system. J. Soil Mech. Found. Div. ASCE **89**(3), 63–94 (1963)
13. Liyanapathirana, D.S., Poulos, H.G.: Pseudo-static approach for seismic analysis of piles in liquefying soil. J. Geotech. Geoenviron. Eng. ASCE **131**,1480–1487 (2005b)
14. Karthigeyan, S., Ramakrishna, V.V.G.S.T., Rajagopal, K.: Influence of vertical load on the lateral response of piles in sand. Comput. Geotech. **33**, 121–131 (2006)
15. Chatterjee, K., Choudhury, D.: Analytical and numerical approaches to compute the influence of vertical load on lateral response of single pile. In: The 15th Asian Regional Conference on Soil Mechanics and Geotechnical Engineering (2015)
16. Hazzar, L., Hussien, M.N., Karry, M.: Influence of vertical loads on lateral response of pile foundations in sands and clays. J. Rock Mech. Geotech. Eng. **9**(2017), 291–304 (2017)
17. IS 2911- Part1 Section 4: Indian standard code of practice for design and construction of pile foundations, Bureau of Indian Standards, New Delhi (1984)
18. Mazzoni,S., McKenna,F., Scott,M.H., Fenves,G.L. et al.: OpenSees (Open System for Earthquake Engineering Simulation) Command Language Manual, Pacific Earthquake Engineering Research Center (PEER), University of California, Berkeley (2006)
19. API: American Petroleum Institute Recommended practice for planning, design and constructing fixed offshore platforms. RP 2A-WSD, Washington, DC (2007)
20. Boulanger, R.W., Curras, C.J., Kutter, B.L., Wilson, D.W., Abghari, A.: Seismic soil-pile-structure interaction experiments and analyses. ASCE J. Geotech. Geoenviron. Eng. **125**(9), 750–759 (1999)
21. Boulanger, R.W.: The PySimple1, TzSimple1 and QzSimple1 Material Models. Documentation for the OpenSees platform (2000). http://opensees.berkeley.edu
22. Reese, L.C., Matlock, H.: Non-dimensional solutions for laterally loaded piles with soil modulus assumed proportional to depth. In: Proceedings Eighth Texas Conference on Soil Mechanics and Foundation Engineering, Special Publication No. 29, Bureau of Engineering Research, University of Texas, Austin, TX (1956)
23. IS 456: Indian standard on plain and reinforced concrete-code of practice. Bureau of Indian Standards, New Delhi (2000)
24. Das, B.M.: Advanced Soil Mechanics. Taylor and Francis Publisher (1983)

Evaluation of Liquefaction Potential of Class F Fly Ash and Calibration of Numerical Model

Sangeeta Yadav and Sumanta Haldar

1 Introduction

Fly ash is the finely divided residue that results from the combustion of pulverized coal. India has the fifth largest coal reserve in the world, and over 70% of the nation's power generation is coal-based. Globally 41% of electricity is produced from the thermal electric plants producing a considerable amount of fly ash, about which only 43% is used in cement, concrete, or brick manufacturing, and the rest is placed in the landfills. According to the Global Fly Ash Industry Analysis, fly ash production is expected to increase by 2.6% by the year 2033 and a production of 131 million tons of fly ash per year in the USA only. The plenitude of fly ash presents remarkable use in structural fills and other geotechnical applications. Since fly ash mainly consists of non-plastic silt size particles of relatively low permeability than sand, it is prone to liquefaction during earthquakes [1, 2]. Hence it is essential to predict the liquefaction potential of the fly ash before using it in seismically active areas.

Jakka et al. [2] carried out a detailed study on liquefaction resistance of pond ash by conducting an undrained cyclic triaxial test and found that liquefaction resistance of pond ash varies significantly within the same pond from inflow to outflow point. The strength deformation behavior of the pond ash shows that the relative density and the level of cyclic stress amplitude are the crucial parameters in the liquefaction potential of the pond ash, and its behavior is comparable with the granular soil containing 20% fines [3]. A similar observation is made by Kim and Prezzi [4] on class-F Indiana (US) fly ash. Observation made by Boominathan and Hari [1] and Vijayasri et al. [5] on reinforced pond ash shows good friction angle, better

S. Yadav (✉) · S. Haldar
School of Infrastructure, Indian Institute of Technology Bhubaneswar, Bhubaneswar, India
e-mail: sy15@iitbbs.ac.in

S. Haldar
e-mail: sumanta@iitbbs.ac.in

C. N. V. Satyanarayana Reddy et al. (eds.), *Dynamics of Soil and Modelling of Geotechnical Problems*, Lecture Notes in Civil Engineering 186,
https://doi.org/10.1007/978-981-16-5605-7_31

drainage properties, and improved liquefaction resistance of pond ash compared to the unreinforced ash material. It indicates that the pond ash, with reinforcement, can be used as an economical material in the seismic prone areas. Further liquefaction potential and post-liquefaction shear strength of impounded fly ash is reported by Zand et al. [6] and concluded that the liquefaction potential of fly ash is a stronger function of the initial dry density as well as low level effective confining stress as reported by Jakka et al. [2].

The performance of the structures with ash is influenced by several factors; hence, it is important to carry out site-specific response studies. Jakka et al. [7] studied the performance of the ash embankments constructed by the upstream and downstream methods of construction to assess the suitability of ash as a geotechnical construction material. The influence of various factors on the dynamic properties of ash is investigated by Chattaraj and Sengupta, and correlations are proposed for predicting maximum Shear Modulus (G_{max}) and damping for the fly ash [8].

During the most recent couple of years, numerical investigations have too concentrated on the behavior of pond ash material under static and dynamic loadings. The effect of gradation on the dynamic response of pond ash has studied by Rahitya and Patra [9] using *OpenSees*. Vijayasari et al. [10, 11] performed a two-dimensional dynamic response analysis using a fully coupled effective stress nonlinear approach on the Renusagar pond ash embankment in India, and the further extension of the study has focused on the mode shapes, fundamental period, acceleration intensification, horizontal and vertical displacement, nonlinear stress–strain behavior, cyclic stress ratio, and liquefaction potential. A similar study has been carried out on the Talcher pond ash embankment in India, considering the existing water table and full saturation condition [12].

It is evident that past studies mostly addressed the liquefaction potential of fly ash based experimental observation. However, limited studies have been carried out on the evaluation of the appropriate constitutive model for numerical analysis of the potentially liquefiable material. The constitutive model involves several material constants. Calibration of the model parameters is a time-consuming trial and error procedure; hence, sensitivity analysis of the input parameters can be helpful to identify the relative importance of each parameter. This in turn helps to expedite the calibration process. In this study, the liquefaction triggering of the fly ash is simulated using nine node quadrilateral plane-strain elements with solid–fluid, fully coupled material that uses a pressure-dependent elastoplastic constitutive model in *OpenSees*.

2 Methodology

The present study adopted the test results of liquefaction potential assessment of class-F fly ash using stress-controlled cyclic triaxial tests from the literature [2]. The physical properties of pond ash are summarized in Table 1. The undrained cyclic

Table 1 Physical properties of the fly ash [2]

Material properties	Value
Specific gravity	2.18
Initial density (kN/m^3)	10.84
Coefficient of permeability (m/s)	9.4×10^{-7}
Friction angle (degrees)	37
Void ratio	0.97

triaxial test was conducted at an effective confining pressure of 106 kPa, a cyclic stress ratio of 0.3, and a loading frequency of 0.1 Hz, and for the applied deviator stress, axial strain and excess pore water pressure were measured.

2.1 Numerical Model

Numerical models have proven to be an essential tool for solving practical problems. OpenSees is a software framework for simulation applications in earthquake engineering using Finite Element (FE) methods. The constitutive model, which can describe the essential features of the material behavior, has been implemented in this FE model.

From geotechnical classification, the above-mentioned pond ash is classified as silt; hence, *PressureDependentMultiYield02 (PDMY02)* material model for cohesionless soil is utilized for the numerical modeling. *PDMY02* is an elastic–plastic material for simulating the essential response characteristics of the pressure-sensitive material whose shear behavior is dependent on the confining pressure. To simulate the undrained behavior of pond ash, a solid–fluid fully coupled *u-p* element named *9_4_QuadUP* element is considered, and its configuration along with the boundary condition is shown in Fig. 1.

It has 9 nodes for solid deformation (u) and 4 nodes for pore water pressure (p). Four corner nodes have three degrees of freedom (two translations and one pore water pressure), while the intermediate nodes have only two translational degrees of freedom. Base nodes are fixed in the horizontal and vertical directions, whereas the PWP degree of freedom is restricted for nodes 3 and 4.

The loading is given in two stages. In the first stage, the hydrostatic condition is generated by incorporating gravity in the analysis, having a magnitude equal to the components of gravity in horizontal and vertical directions. In the second stage, cyclic loading is given by applying a sinusoidal wave of a particular frequency. Material behavior is considered to be linear elastic during the gravity loading stage, and in the subsequent loading phase, the stress–strain response is ensured plastic by updating the material stage. The formulation of plasticity is done using a multi-surface concept, and the Drucker-Prager yield surfaces are used. The flow rule is non-associative, in which the rate of plastic strain increment vector is not normal to the yield surface. For the numerical integration in the transient analysis, Newmark's

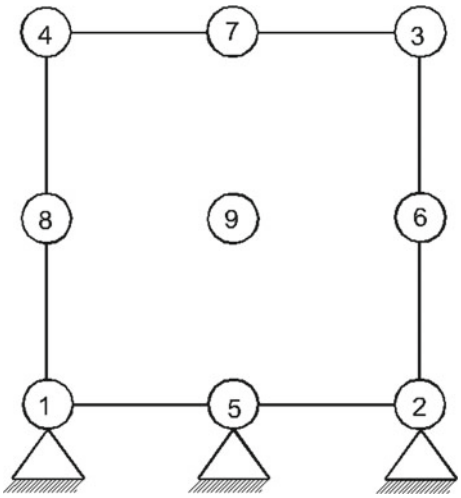

Fig. 1 Schematics of nine node solid–fluid fully coupled u-p element, 9_4_ QuadUP element

integrator has been used with integration parameters gamma and beta as 0.6 and 0.3, respectively. The maximum number of iterations and tolerance is set as 50 and 10–3, respectively.

PDMY02 model requires a total of 23 parameters comprising 3 additional parameters, namely, Contrac2, Contrac3, and Dilate3. Some of the material parameters used in the model are shown in Table 2. Contrac1 defines the rate of contraction. Stronger is the contraction; larger is the reduction in effective vertical stress. Contrac2 is a constant reflecting dilation history on contraction tendency, and stronger dilation results in a higher contraction in the subsequent unloading cycle. Dilate1 and Dilate2 reflect the rate of shear-induced dilation. Contrac3 and Dilate3 are the new parameters introduced in the model *PDMY02,* to account for the overburden stress

Table 2 Input parameters used in the model

Input parameters	Value	Remarks
Maximum shear modulus (kPa)	40,000	–
Effective confining pressure (kPa)	106	–
Pressure dependent coefficient	0.5	–
Phase transformation angle (deg.)	27	–
Contrac1	0.013	Determines the shear-induced decrease in volumetric strain to develop pore water pressure
Contrac2	5.0	
Contrac3	0.1	
Dilate1	0.2	Determines the shear-induced increase in volumetric strain or dilation
Dilate2	3.0	
Dilate3	0.1	

effect. Parameters Liquefaction1 and Liquefaction2 are related to the accumulation of permanent shear strain as a function of dilation and load reversal history, respectively.

Pore water pressure, shear stresses, and shear strains are recorded using the *OpenSees* Element Recorder commands. The displacements and pore water pressure are recorded at the nodes. The stresses and strains are the most accurate at Gauss points; it is measured at different integration points instead of the nodes; thereafter, it is extrapolated to the rest of the element. The recorded outputs have been utilized for further analysis.

3 Results and Discussion

3.1 Model Validation

Plots obtained from the result of finite element analysis are superimposed with that of the cyclic triaxial test performed by Jakka et al. [2]. The stress–strain response and the pore water pressure recorded is used for the validation of the numerical model and shows the typical stress–strain response, which matches reasonably well with the experimental result. *PDMY02* material model is capable of capturing many aspects of the soil response. In Fig. 3, pore water pressure is plotted in terms of excess pore pressure ratio with the number of cycles, and it is assumed that liquefaction is initiated at the point where excess pore pressure becomes almost equal to the initially applied confining pressure, i.e., pore pressure ratio equals to one. Similar to the results reported by Jakka et al. [2], the finite element result shows that material reaches the state of initial liquefaction, and thereafter, pore pressure falls to the lower levels with the gradual development of strain exhibiting cyclic mobility type of liquefaction (Fig. 2).

3.2 Sensitivity Analysis

After calibration of the numerical model, sensitivity analysis is performed by varying only one parameter at a time and keeping the rest of the parameter constant. The result of sensitivity analysis is shown in Fig. 4. The number of cycles required for initial liquefaction is considered as output. For the change in the input parameter, the corresponding change in output is recorded in percentage. A parameter that gives a higher slope is considered as sensitive. The recommended range of parameters for the *PDMY02* model can be found in the *OpenSees* manual [13].

Contrac1 in the dense state is found marginal sensitive parameter; a 100% change in the input caused only a 13% change in the number of cycles. However, in a loose state, there is a significant change, which indicates the faster development of the PWP in the loose state as compared to the dense state. Figure 5 shows the effect of

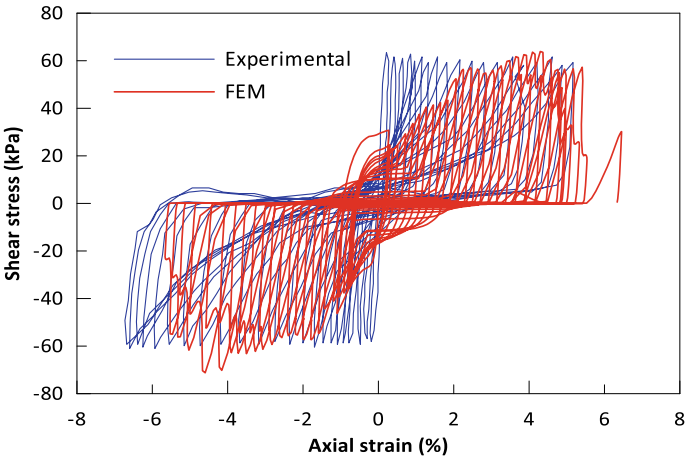

Fig. 2 Shear stress versus axial strain plot

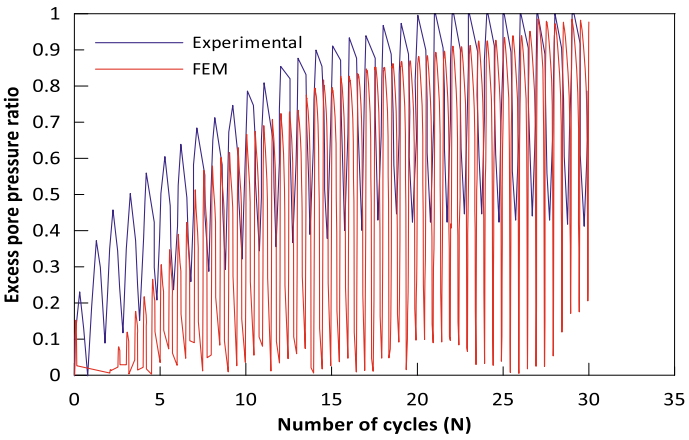

Fig. 3 Excess PWP ratio versus number of cycles

the Contrac1 parameter on the development of excess PWP. A small circle is used to indicate a point where liquefaction occurs (i.e., EPWPR = 1.0) for the different values of the input parameter. From Fig. 5 it is clear that the higher contraction value results in faster volumetric reduction.

For the PDMY02 model, Contrac2 shall be fixed as 5, which represents a point where fabric damage is activated, at which accumulated volumetric strain in the first dilation results in the more contractive behavior in the unloading cycle.

From the sensitivity plot, Dilate1 is found to be the most sensitive. Figure 6 shows the effect of the Dilate1 parameter on the initiation of liquefaction. Even a small increase in the Dilate1 results in stronger dilation, as a result of which the material

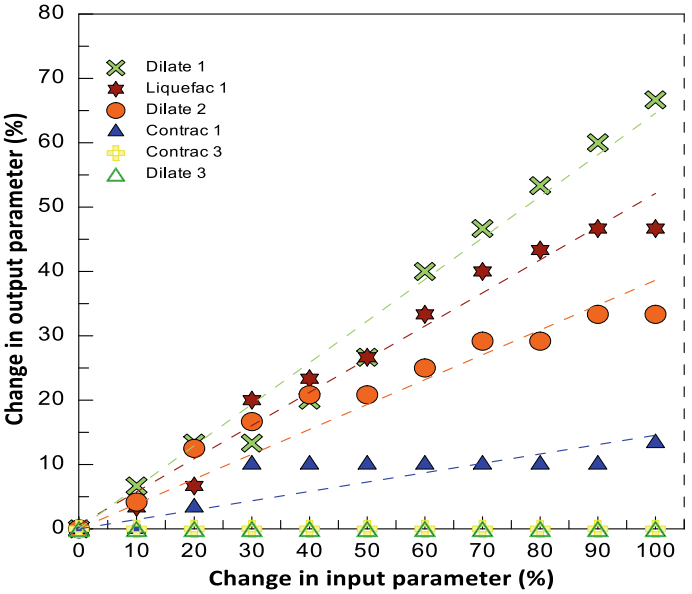

Fig.4 Sensitivity of input parameters

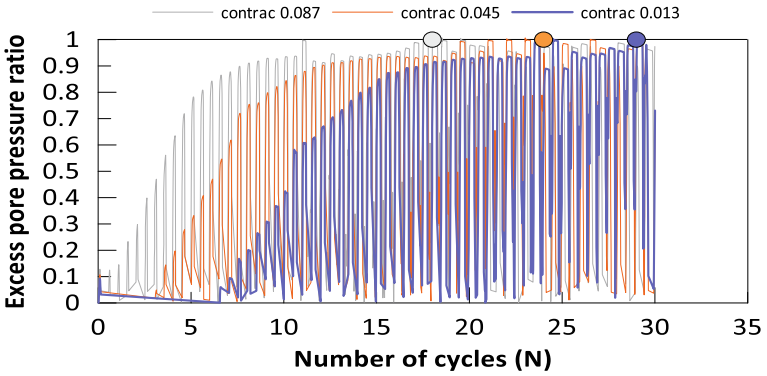

Fig. 5 Effect on Contraction1 parameter on excess PWP ratio

takes a greater number of cycles to get liquefied. Reduction in Dilate2 causes an increase in dilation; nonetheless, it is less sensitive than Dilation1. Khosravifar et al. [14] suggested to fix the Dilate2 parameter as constant; however, it can be varied between 3–0.3 for the soil specific calibration.

For Contrac3, Dilate3, and Liquefaction2 within the range of 100%, no change is observed in the output; hence, it can be called insensitive parameters. The liquefaction1 parameter has a significant effect on the development of excess PWP. It can be seen from Fig. 7 that the increase in this parameter results in the faster development of the excess PWP.

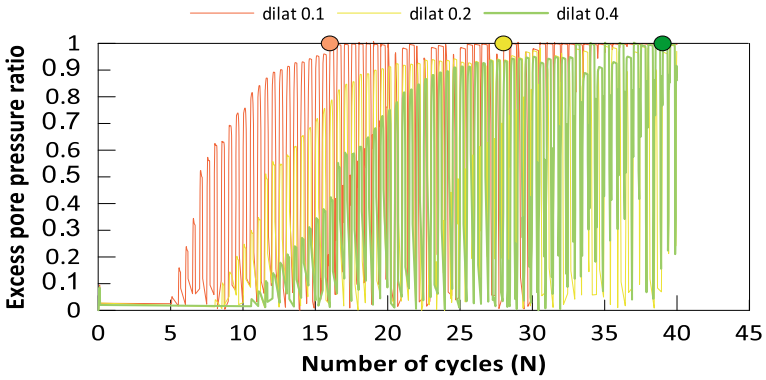

Fig. 6 Effect of Dilation1 parameter on excess PWP ratio

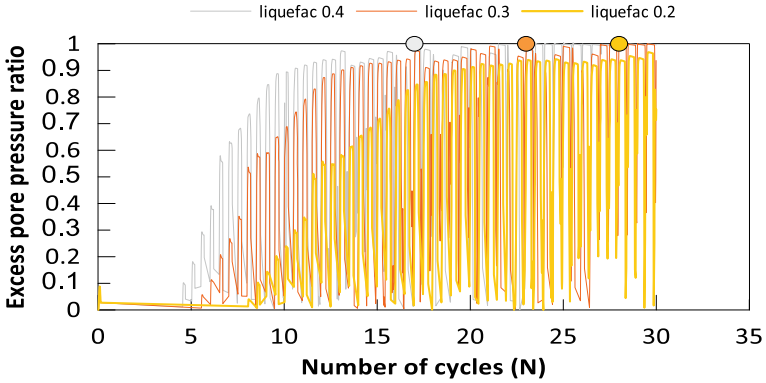

Fig. 7 Effect of Liquefaction1 on excess PWP ratio

4 Conclusions

From the above study carried out using a 2D finite element analysis, reasonably good agreement is found between the experimental and finite element results. Sensitivity analysis is also carried out to understand the trend of the input parameters used in the model. It can be concluded that Dilate1, Dilate2, and Liquefac1 are the most sensitive, whereas Contrac3, Dilate3, and Liquefac2 are the least sensitive parameters. The sensitivity of parameters can vary depending upon the output selected for the analysis. Based on this study, calibration of a numerical model for the liquefaction triggering of fly-ash could be convenient with good computational efficiency. The critical assessment of the sensitivity will empower the geotechnical engineers in utilizing the numerical model with confidence in the evaluation of liquefaction induced deformation behavior of ash-dykes.

References

1. Boominathan, A., Hari, S.: Liquefaction strength of fly ash reinforced with randomly distributed fibers. Soil Dyn. Earthq. Eng. **22**(9–12), 1027–1033 (2002)
2. Jakka, R.S., Datta, M., Ramana, G.V.: Liquefaction behavior of loose and compacted pond ash. Soil Dyn. Earthq. Eng. **30**(7), 580–590 (2010)
3. Mohanty, B., Patra, N.R., Chandra, S.: Cyclic triaxial behavior of pond ash. In: GeoFlorida 2010: Advances in Analysis, Modeling & Design, pp. 833–841 (2010)
4. Kim, B., Prezzi, M.: Evaluation of the mechanical properties of class-F fly ash. Waste Manage. **28**(3), 649–659 (2008)
5. Vijayasri, T., Patra, N.R., Raychowdhury, P.: Cyclic behavior and liquefaction potential of Renusagar pond ash reinforced with geotextiles. J. Mater. Civ. Eng. **28**(11), 04016125 (2016)
6. Zand, B., Tu, W., Amaya, P.J., Wolfe, W.E., Butalia, T.S.: An experimental investigation on liquefaction potential and post-liquefaction shear strength of impounded fly ash. Fuel **88**(7), 1160–1166 (2009)
7. Jakka, R.S., Ramana, G.V., Datta, M.: Seismic slope stability of embankments constructed with pond ash. Geotech. Geol. Eng. **29**(5), 821–835 (2011)
8. Chattaraj, R., Sengupta, A.: Dynamic properties of fly ash. J. Mater. Civ. Eng. **29**(1), 04016190 (2017)
9. Rahitya, S., Patra, N.R.: Effect of gradation on dynamic response of pond ash embankment
10. Vijayasri, T., Raychowdhury, P., Patra, N.R.: Numerical simulation of the dynamic behavior of Renusagar pond ash embankment in India using a fully coupled nonlinear approach. Discovery **40**, 20–26 (2015)
11. Vijayasri, T., Raychowdhury, P., Patra, N.R.: Seismic response analysis of Renusagar pond ash embankment in Northern India. Int. J. Geomech. **17**(6), 04016141 (2017)
12. Mohanty, S., Patra, N.R.: Dynamic response analysis of Talcher pond ash embankment in India. Soil Dyn. Earthq. Eng. **84**, 238–250 (2016)
13. https://opensees.berkeley.edu/wiki/index.php/PressureDependMultiYield02_Material
14. Khosravifar, A., Elgamal, A., Lu, J., Li, J.: A 3D model for earthquake-induced liquefaction triggering and post-liquefaction response. Soil Dyn. Earthq. Eng. **110**, 43–52 (2018)

Seismic Performance of Open Ground Floor Tall Buildings on Flexible Ground

R. K. Niranjan and S. K. Prasad

1 Introduction

Earthquakes are the most destructive calamities causing huge casualties, injuries and economic loss. Earthquake risk assessment is needed for disaster management and emergency preparedness. Many urban tall buildings in India have open ground floor as an unavoidable feature. This is primarily being adopted to accommodate parking or reception lobbies with reduced infill in the ground floor, and hence the lateral stiffness of this floor is less than 70% of upper floors or less than 80% of the average lateral stiffness of the three floors above (IS: 1893 Part1 2016). Soft storey collapse during earthquakes is certainly one of the most significant failures. It has been found that the soft storey at ground level is the most vulnerable location from seismic performance view point. Acute shortage of land in urban areas, the economic considerations, functional requirements and the necessity of vertical growth have forced the construction of tall buildings with soft storey on relatively poor ground.

It has been well understood that open ground storey has phenomenal influence on seismic behaviour of structures. Thickness and stiffness of overburden soil are likely to influence the seismic behaviour of structure. Soft soil is one which has very low stiffness; hence, most buildings will be more vulnerable on these soils. For the purpose of presenting performance of soft storey building, a three storey (tall) building has been considered in which the ground storey is made soft storey. Pushover analysis has been effectively used in the past to study the performance of irregular structure under lateral loading [1, 2]. The primary objective of this paper has been to study the vulnerability of soft storey (open ground storey) resting on soft

R. K. Niranjan
J.S.S. Science & Technology University, Mysuru 570006, India

S. K. Prasad (✉)
Vidyavardhaka College of Engineering, Mysuru 570002, India

C. N. V. Satyanarayana Reddy et al. (eds.), *Dynamics of Soil and Modelling of Geotechnical Problems*, Lecture Notes in Civil Engineering 186,
https://doi.org/10.1007/978-981-16-5605-7_32

ground, which is attained by using ATC40 and FEMA356. For this purpose, [3] has been used. However, recent guidelines such as ASCE41 are expected to give similar results.

2 Pushover Analysis

Pushover analysis captures the nonlinear behaviour of the building subjected to lateral load effectively and hence can trace the behaviour of the structure progressively up to failure. Pushover analysis can provide the most effective measure of global behaviour of structures in terms of base shear capacity and displacement ductility of the structure. Pushover analysis can also define the performance of the structure for a given level of earthquake intensity. One of the challenging tasks associated with seismic analysis of buildings is the quantification of the relative influence of various parameters on the seismic performance of structures. In this study, this challenge is accomplished by analytical vulnerability assessment of the structure. This method is an effective way to quantify the seismic risk associated with the structure with due considerations to the uncertainties associated with structural behaviour as well as ground motion characteristics. By subjecting a structure to a monotonically increasing load (or deformation) and monitoring the base shear and roof top displacement at each step, the pushover curve is plotted to represent the seismic capacity of the structure. The response spectrum corresponding to the seismic zone, soil type and damping level of the structure forms the demand curve. The intersection of these two curves is the performance point of the structure (see Fig. 1).

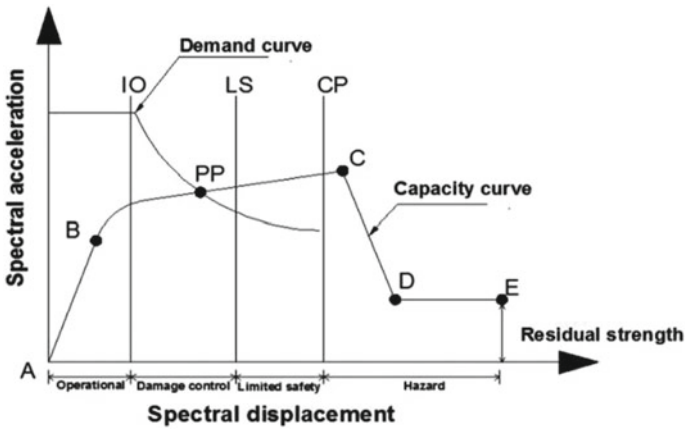

Fig. 1 Capacity and demand curves during a pushover analysis. IO: Immediate occupancy, LS: Life safety, CP: Collapse prevention, C: Collapse

Vulnerability index is obtained by multiplying the probability of exceedance of damage state developed by the fragility curves with the cost fraction associated with the damage states [4, 5].

3 Problem Definition

This paper presents the vulnerability of open ground floor tall structures on soft ground to seismic loading. For this purpose, RC framed structures are modelled (see Fig. 2). The lateral loading distribution is taken as triangular variation and analysed considering displacement controlled non-linear pushover analysis and properties of reinforced concrete frames considered in the analysis are detailed in Table 1. Gazetas approach [6] has been used to model the ground with varying stiffness as detailed in Table 2.

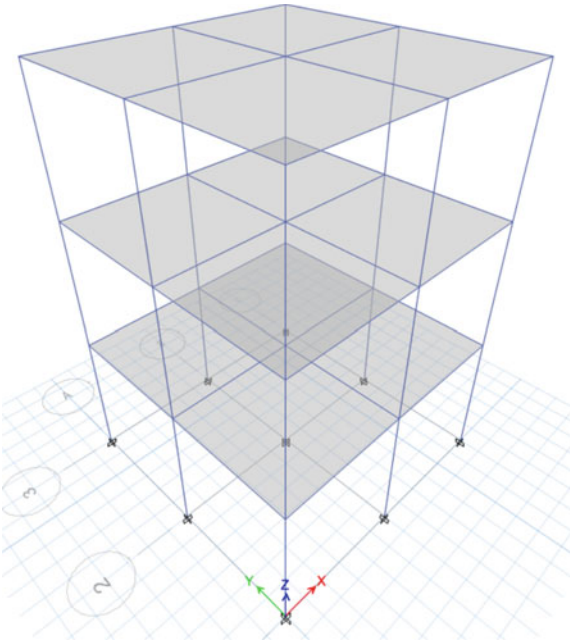

Fig. 2 Frame considered for analysis

Table 1 Design details of frame considered

Type of structure	Special RC moment resisting frame
Grade of materials	M20 and Fe415
Beam section	230 × 300 mm
Thickness of slab	150 mm
Column section	300 × 300 mm
Storey height	3 m
Bay width	3 m
Earthquake zone	III
Soil type	Medium
Floor finish	1 kN/m^2

Table 2 Ground stiffness's for different ground types

Ground type	Ground stiffness in MPa
1	1
2	10
3	1000
4	10,000
5	100,000
6	Fix support

4 Results and Discussion

Pushover curves resulting from the analysis of RC framed elements are compared to study the effect of analytical parameters on the pushover analysis. Base shear carrying capacity and displacements of the structures are considered for the comparison.

Figure 3 presents the variation of base shear with roof top displacement of frame considered with different soil stiffness. The range of stiffness of soil considered is from E = 1 MPa to E = 10 GPa to cover wide range of soils. When E = 10 GPa, it indicates solid rock; on the other hand, E = 1 MPa is for extremely soft soil, either when cohesionless soil is in the process of liquefaction during earthquake or when there is an extremely soft clay close to its liquid limit encountered. It can be seen that base shear increases with increase in soil stiffness and roof top displacement decreases with increase in soil stiffness. Further, base shear carrying capacity of frame on stiff soil is much higher than that on softer soil. The decrease in soil stiffness results in bearing capacity failure or excessive settlement or uneven settlement. All these are responsible for additional pressure on the structure and results in the failure of structure.

Figure 4 is plotted to identify the performance point. Performance point locates the intersection of capacity curve with demand curve in spectral acceleration and spectral displacement space. This point indicates the overall status of the building under earthquake shaking of Zone III. It suggests the base shear carrying capacity,

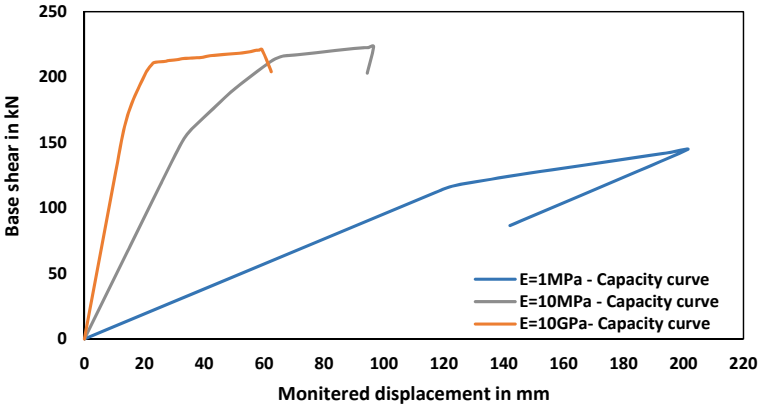

Fig. 3 Base shear versus roof top displacement for building on different soil types

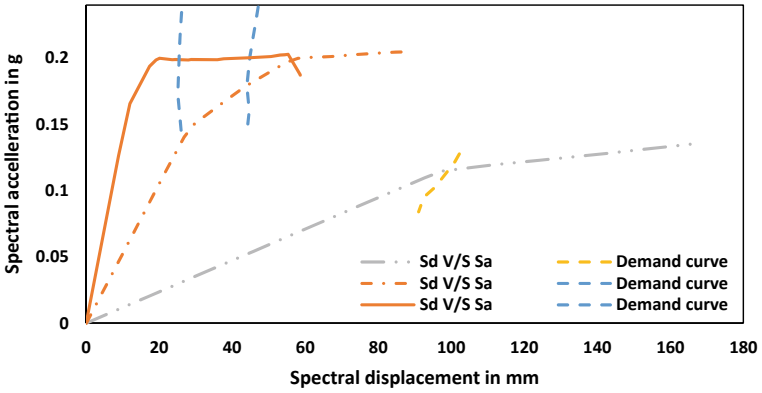

Fig. 4 Pushover curves and performance points for building on different soil types

ductility, and region in which the building lies (such as elastic, immediate occupancy (IO), life safety (LS), collapse prevention (CP), collapse (C) as per ATC-40 and FEMA-273) [4, 5]. It can be seen that the performance point shifts towards right when the frame is located on less stiff soil, indicating the increased vulnerability of the building.

Figure 5 indicates variation of vulnerability index of frame with varying soil stiffness from less stiff to very stiff conditions. It can be seen that the vulnerability index is more for frame on soft soil compared to that on hard soil.

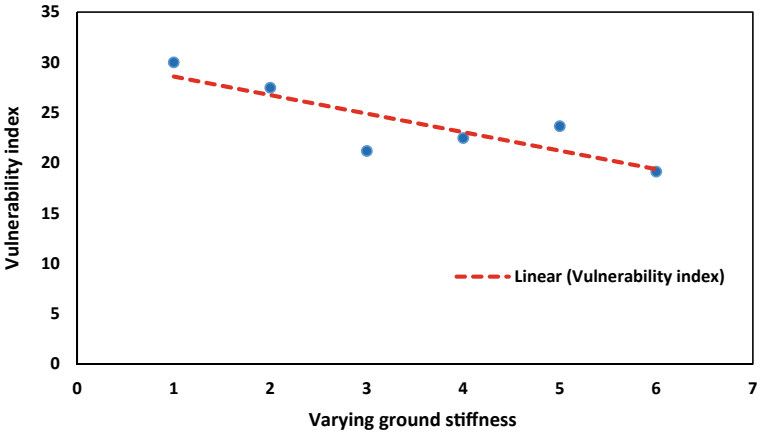

Fig. 5 Vulnerability index versus varying ground stiffness

5 Conclusions

The major inference from this study is that frames with open ground floor are vulnerable during earthquakes, and frames with open ground floor resting on soft soil are even more vulnerable to the earthquakes of same intensity. In the present paper, the vulnerability is identified based on the base shear carrying capacity, ductility characteristics and vulnerability index.

References

1. Kalibhat, M.G., Kumar, A.Y., Kamath, K., Prasad, S.K., Shetty, S.: Seismic performance of RC frames with vertical stiffness irregularity from pushover analysis. J. Mech. Civil Eng, **2**, 61–66 (2014)
2. Rajesh, M.N.: Influencing parameters on seismic performance of RC structures from pushover analysis. M. Tech thesis, Visvesvaraya Technical University, Belagavi (2014)
3. ETABS: analysis reference manual, computers and structures. Berkely, California, USA, (2016)
4. Comartin, C.D., Niewiarowski, R.W., Freeman, S.A., Turner, F.M.: Seismic evaluation and retrofit of concrete buildings: a practical overview of the ATC 40 Document. Earthq. Spectra **16**(1), 241–261 (2000)
5. Council, B. S. S. NEHRP guidelines for the seismic rehabilitation of buildings. FEMA-273, Federal Emergency Management Agency, Washington, DC, pp. 2–12 (1997)
6. Gazetas, G.: Formulas and charts for impedances of surface and embedded foundations. J. Geotech. Eng. **117**(9), 1363–1381 (1991)

A Review on Ground Improvement with Surcharge in Addressing Liquefaction Mitigation

Anurag Chafale and Madan Kumar Annam

1 Introduction

1.1 General

Development of oil and gas industry related infrastructure is major growing facilities in India. Storage structure like mounded storage vessels (MSV), spheres, and tanks are very sensitive to found on liquefaction prone subsoils. Soil liquefaction has been a major source of damage to such structures during past earthquakes (e.g., 1964 Alaska earthquake, 1995 Kobe earthquake, and 2001 Bhuj earthquake). In order to build foundations for such critical structures in similar environment, it is necessary to provide optimal foundation technique to meet their performance requirements. Various ground improvement methods, namely, deep vibro techniques, impact methods, blasting techniques, cement/admixture stabilization, etc. are generally practiced improving clean cohesionless soils for mitigation of liquefaction [1–3]. However, densification of silty soil with fines content greater than 20 percent requires special attention [1]. Silty soils with high fine content and intermediate permeability shows a complex behavior in seismic conditions [4, 5]. Use of vibro stone columns with surcharge to mitigate the liquefaction in such silty soil is studied in this paper.

A. Chafale (✉)
Keller Ground Engineering India Pvt Ltd, Mumbai 400059, India
e-mail: anuragchafale@kellerindia.com

M. K. Annam
Keller Ground Engineering India Pvt Ltd, Chennai 600024, India
e-mail: madankumar@kellerindia.com

C. N. V. Satyanarayana Reddy et al. (eds.), *Dynamics of Soil and Modelling of Geotechnical Problems*, Lecture Notes in Civil Engineering 186,
https://doi.org/10.1007/978-981-16-5605-7_33

1.2 Motivation and Objective

The structures like MSV and storage tanks can be effectively founded over ground improvement using vibro stone columns and have long proven track record [6, 7]. Application of surcharge over treated ground to enhance time rate of consolidation controlling post treatment settlements. Optimal foundation accompanied by progressive design and time convenience by means of application of full or partial surcharge can provide cost effective solution. Considering limited space in active bottling plant and execution feasibility partial surcharging corresponding to 60% of design load was done. The objective of this paper is to highlight performance of ground improvement using vibro stone columns with surcharge in mitigating liquefaction potential of subsoil. Performance of ground improvement was monitored by application of large scale zone load test in this project.

2 Project and Site Conditions

2.1 Details of MSVs

Mounded storage facility consisting of 3 no's of bullets was proposed in active.

LPG plant is in North India. Loading and performance requirements are given below:

- Loading intensity: 100 kPa
- Post construction settlement: $\leq$50 mm
- Seismic Parameters: Zone-IV, PGA = 0.24 g and EM = 7.5

2.2 Soil Data and Geotechnical Concerns

Confirmatory soil investigation via 2 boreholes was executed within the footprint of MSV. The maximum depth of exploration is about 25 m below the existing ground level (EGL). The subsoil conditions reveal that alternate layers of clayey silt and sandy silt up to 4 m followed by sandy silt up to the depth of 13 m below EGL. This layer is followed by clayey sandy silt with presence of gravels up to the 18 m below EGL.

Beyond 18 m depth, the subsoil comprises of dense silty sand with presence of gravels followed by very dense silty sand up to the depth of exploration. Ground water table was encountered at 5–7 m below EGL during the time of investigation. Pre SPT-N vs depth and gradation analysis is shown in Fig. 1. Mitigating liquefaction and limiting post construction settlement was required to be addressed considering the existing soil conditions.

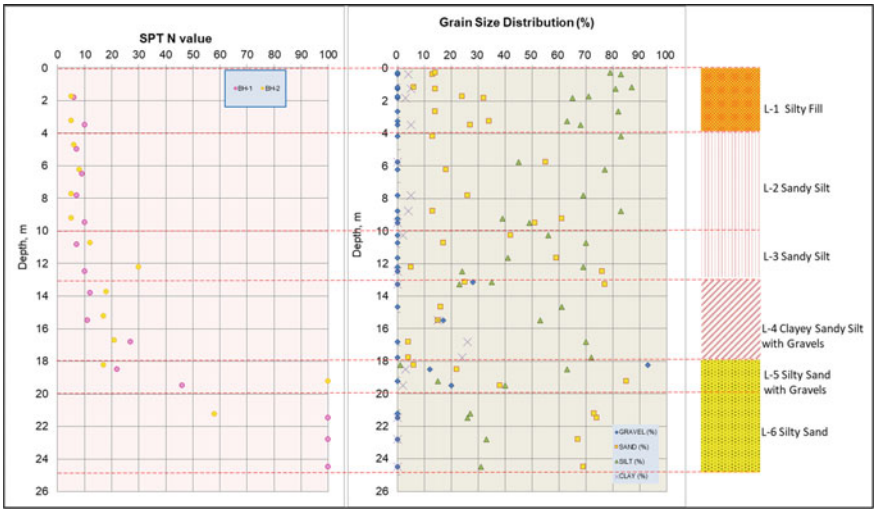

Fig. 1 Plot showing SPT-N, grain size distribution versus depth

The project location falls in earthquake zone IV and subsoil being loose sandy silt up to 12–13 m depth, and it was assessed soil get liquified. Liquefaction potential of sandy silts was evaluated using NCEER guidelines [8].

3 Need for Ground Improvement

3.1 Background

As the subsoil at the proposed site being loose silt with clay to a depth of 13 m, it will undergo excessive long-term settlements due to superimposed structural loads. Also, it will not have required bearing capacity to support the foundation of the MSV. In addition, the project location falls under seismic zone IV which might prone to be liquefaction, in event of earthquake.

Densification of silty soil may not immediately be obtained by ground improvement. The rate of settlement shall need to be accelerated by surcharging the treated ground. This process will not only help in densification of subsoil to reduce the liquefaction risk but also elude the excess post construction settlement.

3.2 Ground Improvement Technique

Ground improvement using vibro stone columns with surcharge was proposed to address the geotechnical concerns and introduces a coarse-grained material as load bearing elements and drainage element. Usually these coarse-grained materials consisting of gravel or stone aggregate as a backfill medium. Improvement of subsoil is mainly due to replacement of loose silty soil by strong aggregates and densification of soil in-between the columns. The densification occurs at slow rate over long period of time. Hence, densification of loose silty soils is further enhanced by applying surcharge over treated ground.

3.3 Improvement Scheme

Ground improvement design is carried out according to Priebe's design methodology [9, 10] using an in-house program "Keller Improvement Designer" (KID) by employing soil design parameters.

3.4 Surcharge Over Treated Ground

The aim of the surcharge placement works is to preload the treated ground to attain effective stress that exceeds the pressure due to the design load. Determination of surcharge level is dependent upon the expected settlement and the future load. A more acceptable way of surcharging for such a project is to place a thickness equivalent to a multiplier of the predicted settlement to compensate for the shortfall resulting from the remaining degree of consolidation. Hence, partial surcharging corresponding to 60% of design load was placed which will not only address the issue of limited space and execution feasibility but also elude the excessive settlement.

Rate of surcharge filling maintained at site was in the range of 0.4 to 0.5 m/day. Construction monitoring and placement of surcharge over the treated ground was done on observational methodology during execution phase. Figure 2 shows the typical schematics of construction stages for mounded storage vessel.

4 Post-performance

About seven settlement plates were installed over treatment to monitor the settlement during loading and unloading of surcharge. Further post-performance investigation was done using bore holes and stone column load tests. Summary of post-performance analysis is discussed in next sections.

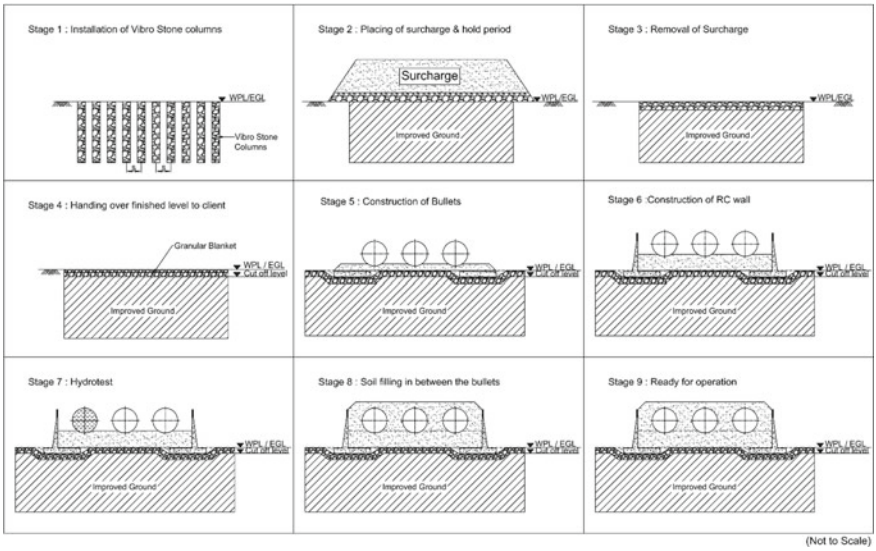

Fig. 2 Construction stages of mounded storage vessels

4.1 Settlements During Surcharge

The settlement readings of each plate were recorded daily using total station**.** Figure 3 shows the time vs settlement plot for known increment of surcharge loading. Following are key points:

- Total settlement experienced by the plates was in the range of 25–35 mm after reaching full surcharge height.
- Rate of settlement was nearly stabilized after 3 days waiting period under full surcharge height and remained constant for almost 7 days. Total waiting period under full surcharge height was about 10 days.

Load increment was held until average 90% of the ultimate consolidation was achieved, using Asaoka's method [11]. In this method final settlement was determined by plotting settlement at time (t-1) as the ordinate and settlement at time (t) as the abscissa. The ordinate of the point of intersection of the aforesaid plot and a 1:1 line gives the ultimate settlement from which the degree of consolidation at the present stage can be determined. The expected ultimate settlement under surcharge load using Asaoka's method is summaries in Fig. 4. Average degree of consolidation based on this observational method is around more than 90%.

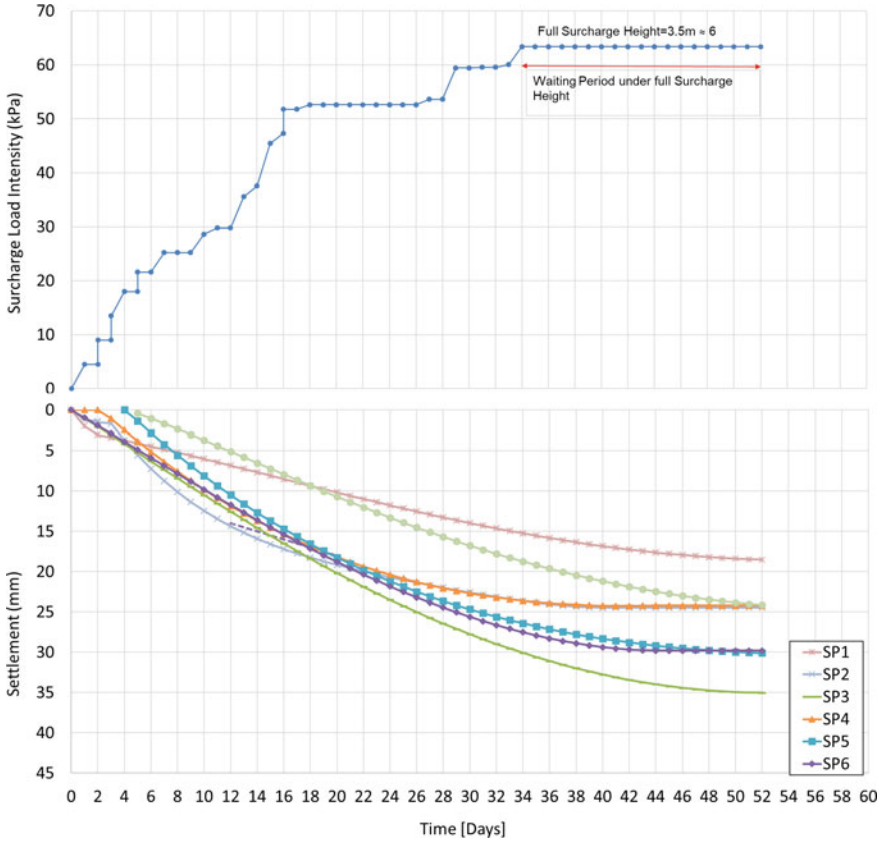

Fig. 3 Plot showing surcharge load intensity and settlement of plates w.r.t. time

4.2 Post Treatment Soil Investigation

Post ground improvement soil investigation using boreholes was conducted after removal of surcharge. Considerable improvement is observed in the subsoil stiffness due to densification of the silty soil in between the columns. Figure 5 shows the SPT-N vs depth plot for pre and post improvement. It can be noticed that there is improvement in the stiffness of the subsoil.

Liquefaction analysis was carried out using post SPT-N values using NCEER guidelines [8]. The results indicate the considerable improvement in Factor of Safety (FOS) against liquefaction (see Fig. 5). Hence, it can be concluded that proposed treatment scheme has considerably reduced the risk of liquefaction in the event of earthquake.

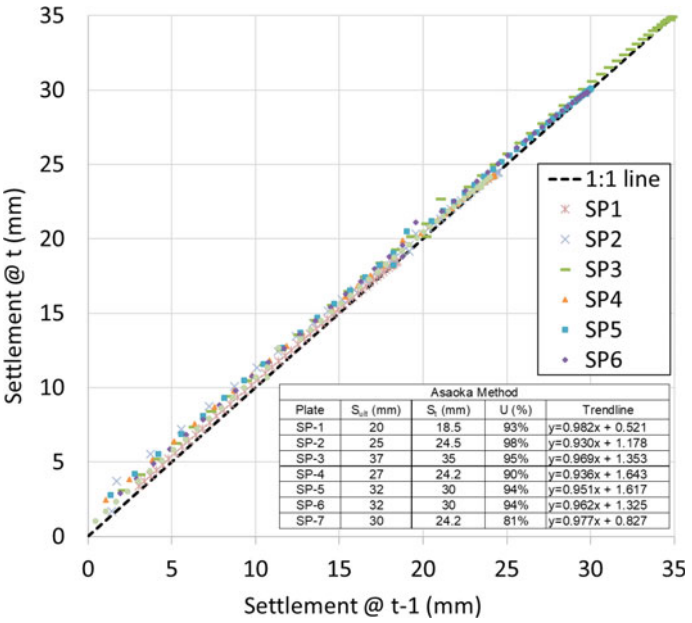

Fig. 4 Plot showing estimation of ultimate settlement using Asaoka's method

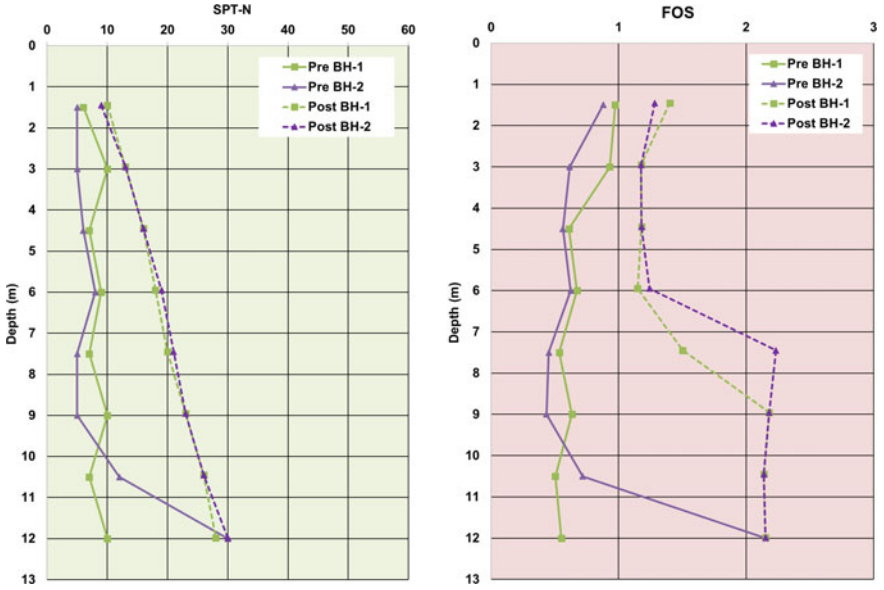

Fig. 5 Pre and post SPT-N values versus depth and FOS against liquefaction

4.3 Observations

Based on the post-performance results, it is observed that total settlement experienced due to surcharge over treated ground falls within the range of 25–35 mm during loading of surcharge. In addition, there is an improvement in the stiffness of the subsoil by approximately twofold in comparison to the estimated value.

5 Conclusions

Vibro stone columns have been effectively used to accomplish the required ground improvement in mitigating liquefaction and improving bearing capacity requirements. Pre and post soil investigation including large area zone load test is conducted to verify reflection of ground improvement. In addition to improving shear strength and compressibility parameters of soft soils, vibro stone columns ensure effective drainage paths to guarantee rapid consolidation prompting gain in shear strength of in-situ soils. Thus, the treatment with surcharge offered intense acceleration in the overall construction schedule and enabled the project completed within the stipulated time. Careful design installation of stone columns with real time monitoring for quality control and post construction monitoring ensured stable foundation for the proposed structure resting on improved ground using vibro stone columns.

References

1. Adalier, K., Elgamal, A., Meneses, J., Baez, J.I.: Stone columns as liquefaction countermeasure in non-plastic silty soils. Soil Dyn. Earthq. Eng. **23**(7), 571–584 (2003)
2. Raju, V.R., Sondermann, W.: Ground improvement using deep vibro techniques. Ground Improv. Case Hist. **3**, 601–638 (2005)
3. Towhata, I.: Developments of soil improvement technologies for mitigation of liquefaction risk. In: Pitilakis K.D. (eds.) Earthquake Geotechnical Engineering. Geotechnical, Geological and Earthquake Engineering, vol. 6, pp. 355–383 (2007)
4. Shenthan, T., Nashed, R., Thevanayagam, S., Martin, G.R.: Liquefaction mitigation in silty soils using composite stone columns and dynamic compaction. Earthq. Eng. Eng. Vib. **3**(1), 39–50 (2004)
5. Mitchell, J.K.: Mitigation of liquefaction potential of silty sands. From Res. Pract. Geotech. Eng. **1**, 433–451 (2008)
6. Bhushan, K., et al.: Ground improvement by stone columns and surcharge at a tank site. In: Fifth International Conference on Case Histories in Geotechnical Engineering, New York, USA, (2004)
7. Bohn, C., Lambert, S.: Case studies of stone columns improvement in seismic areas, 3ème Conférence Maghrébine en Ingénierie Géotechnique (3ème CMIG'13), Alger, Algeria, (2013).
8. Youd, T.L., et al.: Liquefaction resistance of soils: summary report from the 1996 NCEER and 1998 NCEER/NSF workshops on evaluation of liquefaction resistance of soils. J. Geotech. Geoenvironmental Eng. (2001)
9. Priebe, H.J.: The Design of Vibro Replacement. Ground Engineering (1995)

10. Priebe, H.J.: Vibro replacement to prevent earthquake induced liquefaction. Ground Engineering (1998)
11. Asaoka, A.: Observational procedure of settlement prediction. Soil Found. **18**(4), 89–101 (1978)

Probabilistic Seismic Response of Soil-Pile Foundation-Structure System: A Substructure Based Analysis

Rajat Banik and Rajib Saha

1 Introduction

Seismic soil structure interaction (SSI) analysis offers collective response of whole structural system. SSI modelling under seismic loading seems to be a prime factor which has a significant influence on accurate prediction of the seismic response of the structure. Though it was well evidenced that direct modelling approach renders solution with higher degree of accuracy, but this approach was not popular due to computational cost and inefficiency. While, sub-structure approach has an advantage towards SSI modelling and computational efficiency in order to predict the seismic response of structure. However, this approach was found to be limited to linear behaviour of soil-foundation system. On the other hand, several other factors, such as variability in subsoil properties, modelling and load uncertainty, have led the problem further complex. In this context, present study is attempted to carry out probabilistic seismic analysis of pile foundation supported building structure embedded in in-homogenous soft clay modelled through computationally efficient and simplified substructure based modelling approach. Monotonic pushover analysis is performed on soil-pile group foundation system which is modelled using beams on nonlinear Winkler foundation (BNWF) approach and subsequently stiffness of equivalent pile-soil impedance springs are calculated. Then frequency dependent dynamic stiffness of the foundation is also obtained by the help of [1] guidelines. At last, seismic response of the superstructure idealized as SDOF oscillator is calculated incorporating equivalent impedance springs with application of six [2] spectrum consistent artificial ground motions and two real ground motions at base and 5% of critical damping (dashpot) which is reasonable for concrete structures. Monte Carlo simulation (MCS) is adopted to perform the probabilistic analysis incorporating material

R. Banik (✉) · R. Saha
Department of Civil Engineering, National Institute of Technology Agartala, Tripura 799046, India

C. N. V. Satyanarayana Reddy et al. (eds.), *Dynamics of Soil and Modelling of Geotechnical Problems*, Lecture Notes in Civil Engineering 186,
https://doi.org/10.1007/978-981-16-5605-7_34

(i.e., soil properties) and load variability. The outcome of the study helps to assess the influence of variability of system parameters on seismic response of pile supported structure in a relatively simplified manner.

2 Statement of the Problem

A representative structure with fundamental period of 0.6 s resemble a six storied reinforcement cement concrete building supported on pile foundation consisting of 2×3 bays with plan area 22.5×15 m and elevation 22.5 m situated in very soft clay soil medium is considered in the present study. The size of each bay is 7.5×7.5 m. The total load is calculated by considering the live load of 7.2 kN/m^2 acting at each floor along with dead load. The superstructure weight is calculated as 15,364.35 kN, and the load acting on each central column is calculated as 1097.45 kN. Hence, the present study idealizes a 2×2 pile group of size 4×4 m, thickness of the pile cap 0.5 m, length of the pile 18 m, diameter of the pile 0.8 m with *L/d* ratio of 22.5 and spacing to diameter, i.e., *s/d* ratio of 2.5 under one of the central column by the help of BNWF SSI approach and developed an identical substructure based SSI model for the same pile group (Figs. 1, 2, 3, 4, 5, 6 and 7).

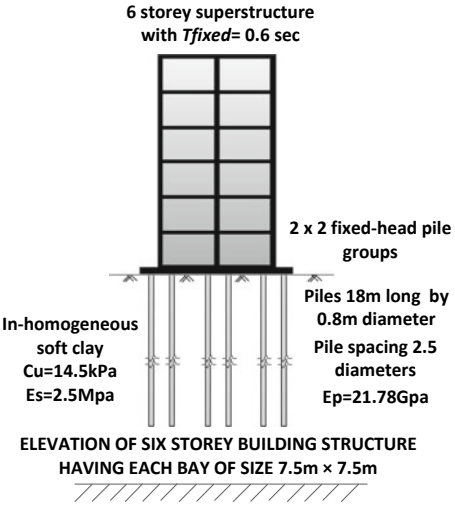

Fig. 1 Prototype structure

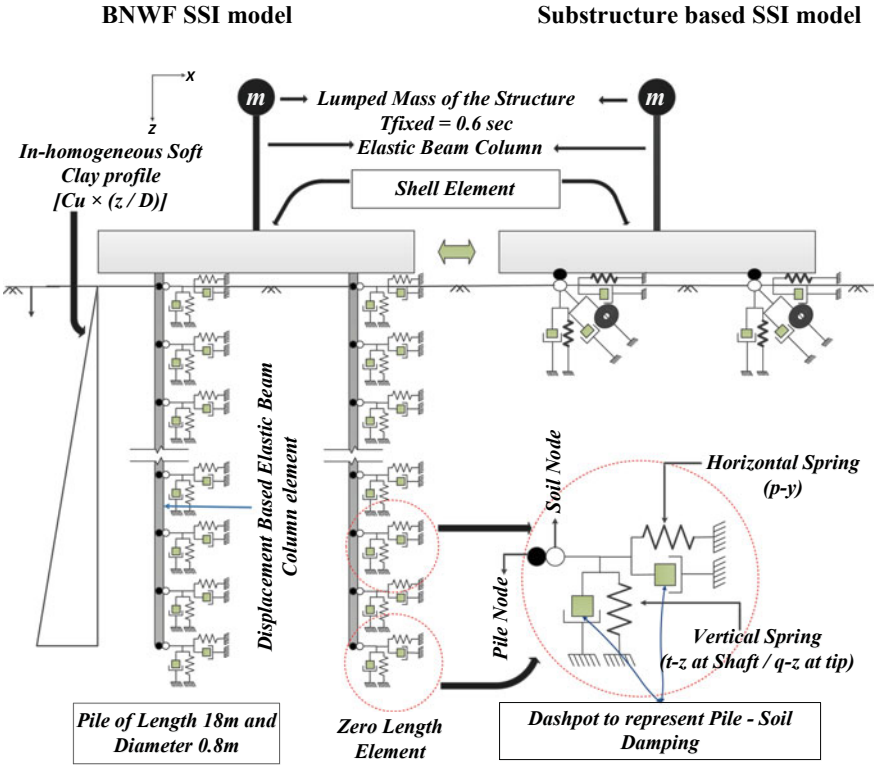

Fig. 2 Idealized of soil-pile foundation structure BNWF model and substructure based SSI model

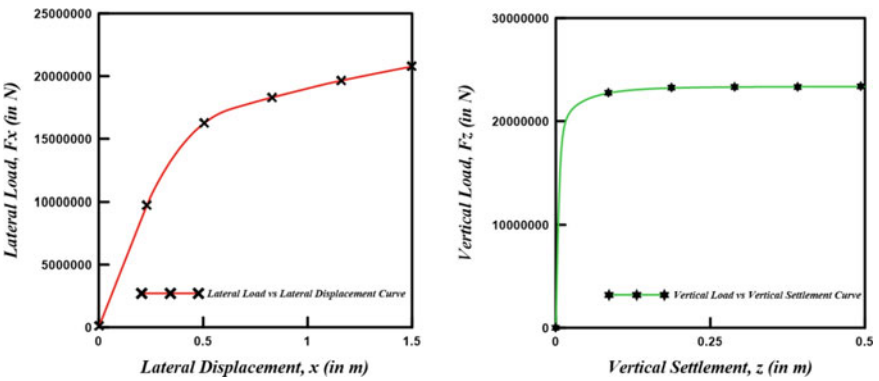

Fig. 3 Static-pushover curves for lateral load versus displacement and vertical load versus settlement

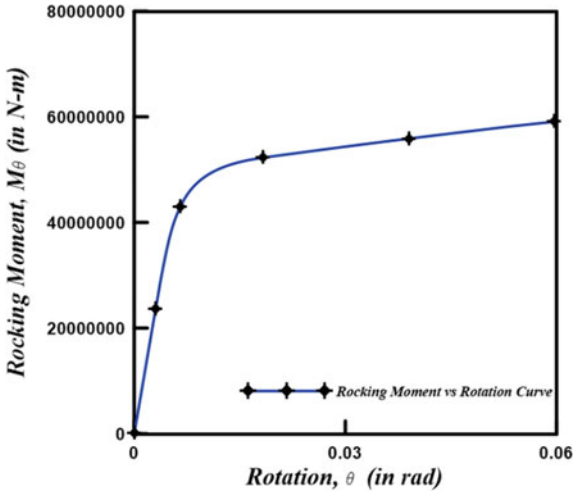

Fig. 4 Static-pushover curves for rocking moment versus rotation

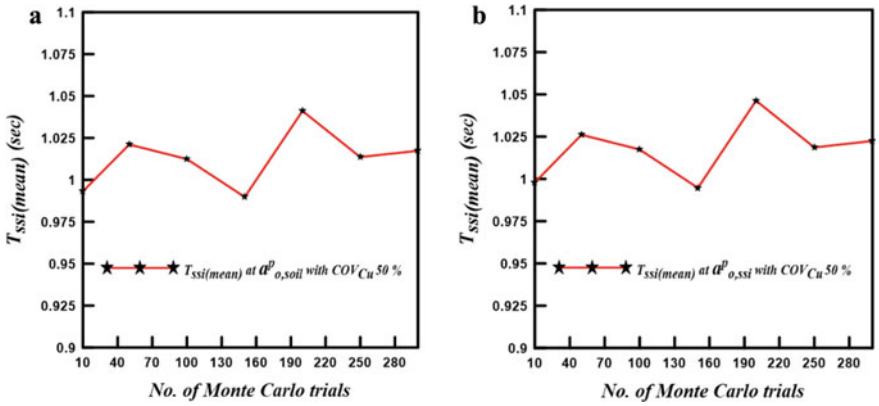

Fig. 5 Variation of time period of the substructure based SSI model with respect to the number of MCS trials $T_{fixed} = 0.6$ s: **a** for $a^p_{0,soil}a^p_{o,soil}$ and **b** for $a^p_{0,ssi}a^p_{o,ssi}$ with COV_{Cu} 50%, respectively

3 Idealization and Modelling of Structural System

3.1 Superstructure-Pile Foundation-Soil Modelling

Beams on nonlinear Winkler foundation (BNWF) model as adopted elsewhere are used to model the dynamic pile soil interaction behaviour. Modelling of pile is performed by using elastic beam column element. In fact, as per modern design codes, piles are not designed to remain linear elastic, especially under the MCE

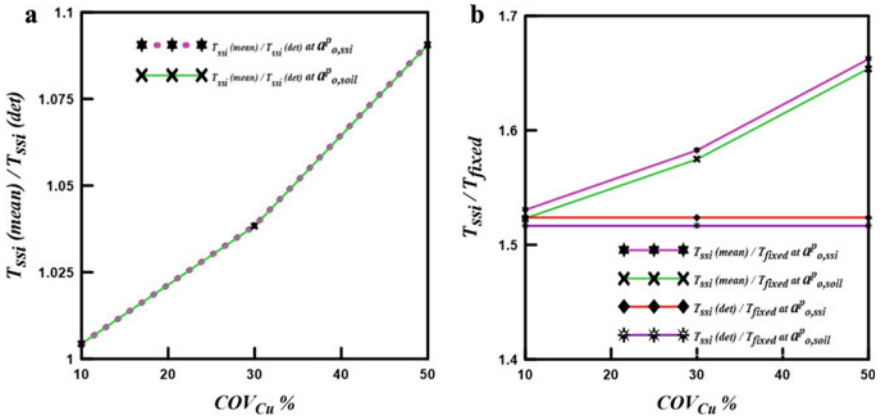

Fig. 6 Variation of the probabilistic normalized time period of the substructure based SSI model with respect to COV_{Cu} of 10, 30, 50% in case of very soft clayey soil: **a** T_{ssi} *(mean)*/T_{ssi} *(det)* w.r.t deterministic analysis and **b** T_{ssi} *(mean)*/T_{fixed} and T_{ssi} *(det)*/T_{fixed} w.r.t fixed base analysis for $a^p_{o,soil}$ frequency and for $a^p_{o,ssi}$ frequency

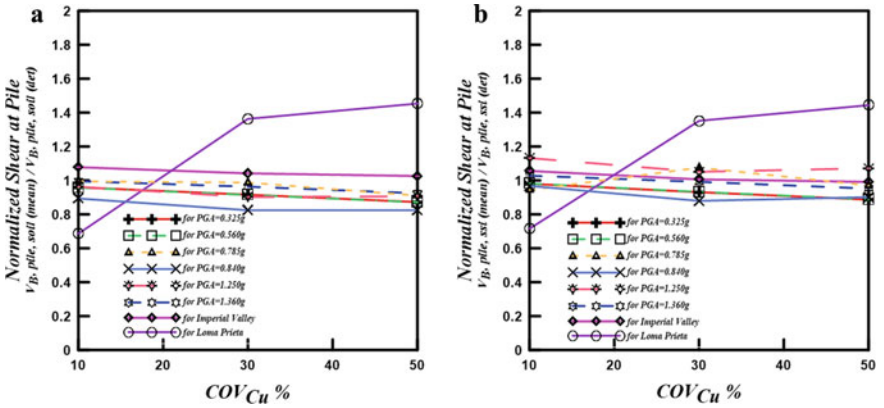

Fig. 7 Variation of the probabilistic normalized shear force at pile with respect to COV_{Cu} of 10, 30, 50% in case of very soft clayey soil: **a** for $a^p_{o,soil}$ frequency and **b** for $a^p_{o,ssi}$ frequency

earthquake level. Hence, nonlinear pile behaviour may be considered as future scope of study. Based on a convergence study, pile is discretized into 20 elements and the discredited length of each pile element is 0.9 m. The embedded pile length is 18 m. Six translational degrees of freedom are considered at each node of the pile. The mass acting on the central column is presumed to be lumped at the top of free head of the column. The equivalent soil springs are attached at each node of the pile in all translational directions (equal degree of freedom) which incorporates pile-soil interaction in all three directions. The pile is assumed to be embedded in in-homogeneous very

Table 1 Properties of pile and soil

Pile data	Soil data (clay)
Diameter, d (m), 0.80	Soil consistency, Very soft
Length, L (m), 18.00	Un-drained cohesion, Cu (kN/m^2), 14.50
Young's modulus, Ep (kN/m^2), 21.78 $\times$ 10^6	Saturated density, γ_{sat} (kN/m^3), 17.00
Poisson's ratio, 0.17	Young's modulus, Es (kN/m^2), 2500.00
	Poisson's ratio, 0.40

Table 2 Dynamic stiffness modifier (α_j^p) for different modes of vibration by NIST [3]

Dimensionless frequency	Dynamic stiffness modifier		
	α_X^p	α_Z^p	α_θ^p
$a_{o,ssi}^p$	0.98606886	1.192217825	1.00 (assumed)
$a_{o,soil}^p$	0.998511756	1.117703207	1.00 (assumed)

Table 3 Dynamic stiffness of group piles for different modes of vibration by NIST [3]

Dimensionless frequency	Dynamic stiffness		
	$K_X^{Dynamic}$	$K_Z^{Dynamic}$	$K_\theta^{Dynamic}$
$a_{o,ssi}^p$	41,720,891.21	3,280,679,160	7,747,000,000
$a_{o,soil}^p$	42,247,354.15	3,075,633,950	7,747,000,000

soft clayey soil medium. The nonlinear spring behaviour is modelled using dynamic nonlinear $p-y$, $t-z$ and $q-z$ curves for clay (Tables 1, 2 and 3).

3.2 Proposed Soft Clay Soil Modelled

In many studies, the design of pile foundation is given by considering the homogeneous soil medium (that means soil strength parameter does not vary with depth i.e. constant) beneath the structure which is unrealistic for soft clay as compared to stiff clay. Gazetas [4] proposed three soil models in his study of seismic response of end bearing single piles, and these are $E = Es \times (z/D)$ [linearly varying in-homogeneous soil medium], $E = Es \times \sqrt{(z/D)}$ [parabolic in-homogeneous soil medium], $E = Es$ $E = Es$[homogeneous soil medium], where Es = Young's modulus of soil, z = depth of the soil medium from the ground surface, and D= diameter of the pile and shown the comparison between them. On the other hand, Budhu and Davis [5] showed that field data suggest a linear relation between un-drained shear strength (Cu) and vertical effective stress (σ_z) for very soft (normally consolidated) clays as $Cu = 0.3 \times \sigma_z Cu = 0.3 \times \sigma_z$. For many practical cases, it is observed that

results are much more correlated by considering the Gazetas [4] linearly varying in-homogeneous soil medium. So, in this study, we consider linearly varying in-homogeneous soil medium proposed by Gazetas [4] as $E = Es \times (z/D)$ and considering linear relationship among Cu and Es, we proposed linearly varying in-homogeneous soil profile for clay as $Cu \times (z/D)$ which is more realistic for actual situation. Also show the comparison between homogeneous soil medium, linearly varying in-homogeneous soil medium of Gazetas [4] and Budhu and Davis [5].

3.3 Pile-Soil Interaction Model in Clay

The spring properties are modelled by nonlinear *p-y* behaviour under cyclic loading proposed by American Petroleum Institute [6].The ultimate resistance for nonlinear spring in case of very soft clay is found out using the following parameters:

$$Pu = 3C + \lambda H + J \times (CH/D) \quad for \quad H < H_R \tag{1}$$

$$Pu = 9C \quad for \quad H \geq H_R \tag{2}$$

$$H_R = 6D/\{(\lambda D/\{(+J\} \tag{3}$$

where P_u= ultimate resistance in (lbs/in or kN/m), C = un-drained shear strength (lbs/in^2 or kN/m^2), λ = Effective soil weight in (Ib/in.^{3}or kN/m^3), H = depth in (m), H_R= depth below soil surface to bottom of reduced resistance zone in (m), J = 0.25–0.5 (dimensionless empirical constant) and D = average pile diameter from surface to depth in (m). However, the final ultimate resistance in lbs or kN for clayey soil is calculated as follows:

$$Pu \;\; final = (Pu \times element \;\; length) \tag{4}$$

Further, in case of clay the displacement relationship is presented for 50% of ultimate resistance as follows:

$$Y_{50} = 2.5\varepsilon_{50} D \tag{5}$$

$$\varepsilon_{50} = \left(\frac{0.1796}{log_{10}^{Cu}}\right)^{(1/1.1841)} \tag{6}$$

where Y_{50} parameter is expressed as a function of un-drained cohesion (Cu) based on the suggested experimental relationship between ε_{50} and Cu as presented by Evans et al. [7] D = average pile diameter from surface to depth in (m).

Furthermore, many seismic codes (e.g. Indian seismic design guideline, IS 1893-Part -I 2002) suggest that 5% of critical damping is reasonable for concrete structures. Therefore, to strike a balance between rigour and accuracy, 5% of critical damping in each mode of vibration of pile-soil and superstructure system is considered for deterministic analysis regardless of structural support condition.

3.4 Nonlinear Pushover Analysis of Pile Foundation

By performing monotonic pushover analysis, it generates different static-pushover curves which plot different strength-based parameters against deformations. Here, strength-based parameters are lateral load, vertical load, and rocking moment and corresponding deformations are lateral displacement, vertical settlement and rotation, respectively. From these curves, it also generates three different stiffness curves against deformation, and these are lateral stiffness, vertical stiffness and rocking stiffness curve.

3.5 Uncertainty Modelling and Probabilistic Analysis [8, 9]

Probabilistic analysis is performed using Monte Carlo simulation (MCS) technique. The probability distribution function, PDF, is taken as log-normally distributed function. The range of variation is selected based on the suggested range for *COV* of un-drained cohesion (*Cu*), (10–50%) as proposed by Phoon and Kulhawy [10]. The soil parameters used in deterministic analysis is considered as mean parameter in case of variability modelling.

The log-normally distributed random field is given by

$$Cu(\widetilde{x_i}) = exp\{\mu_{lnCu}(\widetilde{x_i}) + \sigma_{lnCu}(x).G_i(\widetilde{x})\} \tag{7}$$

where *Cui* are the *i*th realization of *Cu* and *Gi* is a zero mean, unit variance Gaussian random number, μ_{lnCu} and $\sigma_{lnCu}\sigma_{\ln C_u}$ are described as

$$\sigma^2_{lnCu} = ln\left(1 + \frac{\sigma^2_{Cu}}{\mu^2_{Cu}}\right) = ln\left(1 + COV^2_{Cu}\right) \tag{8}$$

$$\mu_{lnCu} = lnCu - 0.5\sigma^2_{lnCu} \tag{9}$$

where $COV_{Cu} = \sigma_{Cu}/\mu_{Cu}$ is the coefficient of variation of *Cu* and μ_{Cu} and σ_{Cu} are the sample mean and standard deviation of *Cu*, respectively. Present study considers COV_{Cu} as 10, 30 and 50%. It is to be noted that the stiffness of soil springs are

estimated from the realizations of *Cu*. It is assumed that stiffness of the soil springs follow log-normal distribution due to linear relationship among spring stiffness, *Cu*.

3.6 Ground Motions

Six IS [2] spectrum consistent artificial ground motions and two real ground motion are applied to the substructure based model in both deterministic and probabilistic SSI analysis to obtain moment, shear force and displacement at various location of the SSI model. The artificial ground motions are generated by SeismoArtif 2018 software. These six ground motions are selected by taking 0.13 times, 0.22 times, 0.32 times, 0.34 times, 0.50 times and 0.54 times of the maximum PGA (Peak Ground Acceleration) of the IS spectra. Hence, the six different artificial ground motions are generated of PGA 0.325 g, 0.56 g, 0.785 g, 0.84 g, 1.25 g and 1.36 g covering low to high range of ground motion. Also two different real ground motions are applied. These are recorded when earthquake occurred at Loma Prieta, California (1989) [recorded station: Anderson Dam (L Abut)] and Imperial Valley, Mexico (1979) [recorded station: Cerro Prieto].

3.7 Dynamic Method of Analysis

Nonlinear dynamic analysis is performed to calculate the elastic and inelastic response of the structure and foundation under applied ground motion loading. In built algorithm available in OPENSees (version 3.2.0) is used to carry out the analysis [11]. The solution of equation of motion of the system for the analysis is done by using Newmark's β-γ step by step integration method. It involves consideration of constant average acceleration over each incremental time step. Modified Newton–Raphson method is employed to perform the iteration for each incremental step. Newmark's parameters are chosen as $\beta = 0.25$ and $\gamma = 0.5$ are adopted. This ensures unconditional stability. 1/5-1/20 (0.001 s) of the ground motion time step is taken as the time step of integration, which has been found to be suitable from a convergence study. The accuracy and correctness of the programs used has been validated in other cases and are available in literatures. (E.g. Chopra [12], Clough and Penzien [13]).

4 Results and Discussion

Results obtained from deterministic and probabilistic analysis performed by Monte Carlo Simulation (MCS) for different ground motions are presented in this study. Also, the effect of in-situ soil variability of soil design parameters on the dynamic characteristics, nonlinear load deformation behaviour of pile and soil under lateral

and dynamic loading (*p-y* behaviour) and response at various location of the pile foundation of different period of structures are primarily investigated in this chapter. The results presented for clayey soil will help to give a broad conclusion on the effect of in-situ variability on seismic design of structure supported by pile foundation in non-liquefiable clay (soft) soil.

4.1 Probabilistic Seismic Response of SSI Structure

A convergence study is performed to determine the number of sample realizations for MCS analysis. For instance, 300 realizations of soil springs stiffness are calculated considering 300 numbers of log-normally distributed randomly generated *Cu* values obtained from the above equations. Realizations of fundamental time period of the substructure based SSI system are obtained for different number of realizations of spring stiffness values considering COV_{Cu} 50%, $T_{fixed} = 0.60$ s and very soft clay ($Ep/Es = 8712$, $L/d = 22.5$ and $S/d = 2.5$) for $a^{p}_{o,ssi}$ and for $a^{p}_{o,soil}$ frequency respectively.

The mean and standard deviation of the fundamental time period of the entire system (T_{ssi}) is presented as a function of number of Monte Carlo simulations. It indicates that the fluctuation of (T_{ssi}) is marginal for number of trials beyond 280. Hence, a choice of 300 numbers of iterations is acceptable and adopted in this study for further analysis. However, 300 number of MCS may not be valid for nonlinear pile–soil system which may be considered as limitation of present study.

4.2 Influence of Shear Strength Variability of Soil on Fundamental Period of Structure

It is observed that the probabilistic normalized period $T_{ssi}\,(mean)/T_{ssi}\,(det)$ is varying with in a range of 1.0043–1.0908 (i.e., minimum to maximum range of variation of 0.43 to 9.08% w.r.t deterministic results) with respect to COV_{Cu} of 10% to 50% in case of very soft clayey soil. However, it is observed that the probabilistic normalized period $T_{ssi}\,(mean)/T_{fixed}$ is varying within a range of 1.53–1.67 (i.e., minimum to maximum range of variation of 53 to 67% w.r.t fixed base results) with respect to COV_{Cu} of 10 to 50% in case of very soft clayey soil. It is also observed that the probabilistic normalized period $T_{ssi}\,(det)/T_{fixed}$ is varying within a range of 1.51–1.53 (i.e., minimum to maximum range of variation of 51% to 61% w.r.t fixed base results) with respect to COV_{Cu} of 10 to 50% in case of very soft clayey soil. Hence, it is shown that by limiting the design (considering fixed base, not incorporating SSI and in-situ variability effect) of the structure, we actually eliminate time period effect which is more detrimental towards the structure. However, almost similar effects are observed for both the frequencies.

4.3 Influence of Shear Strength Variability of Soil on Shear at Pile

An identical response due to influence of shear strength variability of soil on shear force is observed between pile and superstructure. Here, also the results for $a^{p}_{o,soil}$ frequency and for $a^{p}_{0,ssi}$ frequency are almost same. Also the variation of responses of different ground motions and for different frequencies with respect to the COV_{Cu} are in between 0–20%. However, the probabilistic analysis of substructure based SSI model for Loma Prieta earthquake shows tremendous increase of shear force of about 40–60% for COV_{Cu} 30–50%. This issue needs to be studied in details with substructure based SSI model for more ground motions.

5 Summary and Conclusions

Summarily, in this present study, the fundamental time period estimated using two different modelling techniques (BNWF approach and substructure based approach) idealising different various soil profiles for validating proposed substructure model. They show a wide range of variation in normalized time period of pile supported structure due to incorporation of in-situ variability of soil parameters and modelling uncertainty which is idealized by consideration of certain range of *COV* of *Cu* with respect to the mean *Cu* used in deterministic analysis. Furthermore, the effect of in-situ variability of soil on different force and deformation parameters are also studied for different frequencies which also indicates that SSI modelling uncertainty may alter the design response of structure as well as pile foundation. These issues need to be studied in detail by considering a well-accepted statistical modelling of variability of soil, dynamic loading and SSI modelling uncertainty. However, this limited study shows the importance of reliability based design for piled supported heavy structures with an emphasis to carry out a detailed study in this direction.

References

1. Applied Technology Council, Seismic Evaluation and Retrofit of Concrete Buildings, vol. 1. California Seismic Safety Commission, California (1996)
2. IS: 1893 Part I: Indian Standard Criteria for Earthquake Resistant Design of Structures, Bureau of Indian Standards. Bureau of Indian Standards. NewDelhi, India (2016)
3. NIST GCR 12-917-21, Soil-Structure Interaction for Building Structures. U.S. Department of Commerce, National Institute of Standards and Technology Engineering Laboratory Gaithersburg, MD 20899 (2012)
4. Gazetas, G.: Seismic Response of End-Bearing Single Piles. Department of Ovil Engineering, Rensselaer Polytechnic Institute, Troy, New York 12181, USA (1984)
5. Budhu, M., Davies, T.G.: Analysis of laterally loaded piles in soft clays. ASCE J. Geotech. Eng. **114**(1) (1988)

6. API 2350: Overfill Protection for Storage Tanks in Petroleum Facilities. American Petroleum Institute (2005)
7. Evans, L.T., Duncan, G.M.: Simplified analysis of laterally loaded piles. University of California Berkeley, Rept. No. UCB/GT/82-04. (1982)
8. Phoon, K.K., Kulhawy, F.H.: Characterization of geotechnical variability. Can. Geotech. J. **36**, 210–238 (1999)
9. Phoon, K.K., Kulhawy, F.H.: Evaluation of geotechnical property variability. Can. Geotech. J. **36**, 625–639 (1999)
10. FEMA 440: Improvement of Nonlinear Static Seismic Analysis Procedures. Federal Emergency Management Agency, Washington, DC, U.S.A (2005)
11. Mazzoni, S., McKenna, F., Scott, M.H., Fenves, G. L.: OpenSees command language manual. In: Open System for Earthquake Engineering Simulation (OpenSees) (2006)
12. Chopra, A. K.: Dynamics of structures: Theory and applications to equation engineering, 2nd Ed., Prentice Hall, Englewood Cliffs, NJ (2007)
13. Clough, R.W., Penzien, J.: Dynamics of structures, 555–562. McGraw-Hili Book Co. Inc., New York (1975)
14. Gazetas, G., Anastasopoulos, I., Adamidis, O., Kontoroupi, T.: Nonlinear Rocking Stiffness of Foundation. National Technical University of Athens, Greece, Laboratory of Soil Mechanics (2013)

Impact of Vibrations on a High Rise RCC Structure Due to Blast Induced Demolition of Adjacent Building

Akhil Anil, S. S. Chandrasekaran, and A. Boominathan

1 Introduction

Rapid economic growth and the cost of increase of land has led to development of high rise residential and commercial building across urban India. When the buildings are constructed not much importance is given regarding the planning for deconstruction of the structure. As the high rise buildings are developed in prime location areas such as marine bays and water front properties the density of building will be very high and demolition of structures will be a major challenge. Demolition of structures is generally carried out when the life span of the building is over, or it has undergone severe damages due to corrosion, fire etc. or due to change of utility need in the locality or for removal of building which has legal violations.

Demolition can be defined as dismantling, razing, destroying or wrecking any building or structure or any part thereof by pre-planned and controlled manner. The demolition method is selected after pre-demolition works such as surveying, removal of hazardous material and stability analysis report. Implosion or explosion deconstruction is an effective and efficient method of deconstruction and can reduce both cost and time to bring dangerous multistorey structures to ground in comparison to conventional demolition methods. Implosion is the strategic placing of explosive material and timing of its detonation so that a structure collapses on itself in a matter

A. Anil (✉)
Geostructurals Pvt Ltd, Pullepaddy, Cochin, Kerala 682018, India

S. S. Chandrasekaran
Department of Structural and Geotechnical Engineering, School of Civil Engineering, Vellore Institute of Technology (VIT), Vellore, India
e-mail: chandrasekaran.ss@vit.ac.in

A. Boominathan
Department of Civil Engineering, Indian Institute of Technology Madras, Chennai, India

C. N. V. Satyanarayana Reddy et al. (eds.), *Dynamics of Soil and Modelling of Geotechnical Problems*, Lecture Notes in Civil Engineering 186,
https://doi.org/10.1007/978-981-16-5605-7_35

of seconds, minimizing the physical damage to its immediate surroundings. The technique weakens or removes critical supports so that the building can no longer withstand the force of gravity and falls under its own weight.

During the demolition by blasting techniques it is to be ensured that the impact of vibration induced by the touchdown of the collapsing structure does not adversely affect the safety of the buildings nearby and delayed detonation techniques is adopted for the same. In order to ensure that the execution happens as planned, vibration analysis studies are carried out. From the recorded time history of acceleration, the peak vertical acceleration and the duration of the ground vibrations can be determined. From the data collected the impact of the blast induced vibration on the neighbouring structure can be studied. Peak particle velocity (PPV) measured on the ground has been widely used to evaluate the ground motion caused by blasting demolition. Referring to the Sadov's Formula of blasting vibration and depend on observed data of chimney blasting demolition, several similar semi-theoretical formulas with empirical coefficients were developed [1] in order to predict the ground motion with vertical PPV. Response spectra, which is frequently used in earthquake engineering to evaluate strong ground motion [2, 3], caused by earthquakes, were also introduced to analyse the ground motion of blasting, but its application was still limited in the analysis of vibration caused by building collapse [4].

2 Project Description

The Secretary, Maradu Municipality, requested the Department of Civil Engineering Indian Institute of Technology, Madras, to carry out vibration measurements during the controlled demolition of apartment building as per the direction of the Honorable Supreme Court of India. Consequently, a team from IIT Madras carried out vibration measurement during the execution of controlled demolition of the buildings on 11th and 12th of January 2020.The Golden Kayaloram building was demolished in the afternoon of 12th January 2020. The vibration measurement was carried out at selected locations and was monitored at two stations. The data collected by the instruments were analysed and interpreted in terms of Peak Particle Acceleration and Peak Particle Velocity. A model for the structure Heera windfaire was developed on STAAD PRO V8i, and a comparative study was done subjecting it to the lateral loads generated due to the touchdown vibration, the lateral loads of earthquake as defined by IS1893 part 1 [5] and the model under the dead and live load condition.

2.1 Area Studied

Maradu is located just 7 km from Cochin Corporation. The Gram Panchayat, formed in 1953, was upgraded to a Municipality in 2011. The google map of the location is shown in Fig. 1.

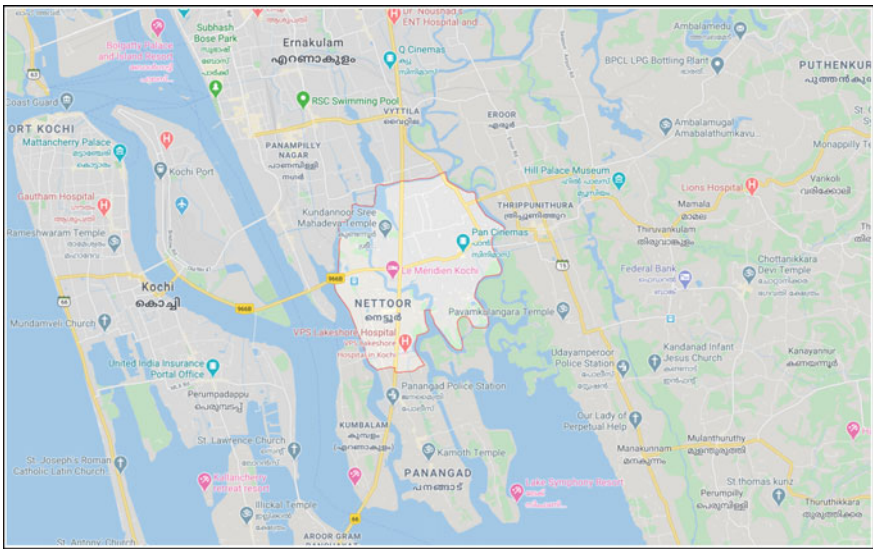

Fig. 1 The google map image of the location

2.2 *Typical Soil Profile of the Area*

The soil profile in the area comprise of top very loose sand followed by very soft marine clay extending up to a depth of 26 m with SPT value of 1 to 6. Below this, medium stiff laterite strata is noted up to 36 m followed by dense sand, medium stiff clay and very dense sand strata up to a depth of 58 m. Since the top soil consist of very soft marine clay extending up to 26 m, for the high rise structures in this locality bored cast in-situ piles of end bearing type are adopted. The piles are constructed by DMC method, and they are terminated at a depth of 40–48 m below the ground surface where very dense sandy strata were encountered.

2.3 *Structures Studied*

2.3.1 Golden Kayaloram Apartments

The Golden Kayaloram Apartment was a 17 storey apartment with a height of 54 m. Supreme Court had ordered the demolition of the building due to violation of coastal regulation zone. The Demolition of Golden Kayaloram apartments took place on 12th of January 2020 at 2 pm. This was the last building that underwent the controlled implosion with regards to the demolition order which was passed.

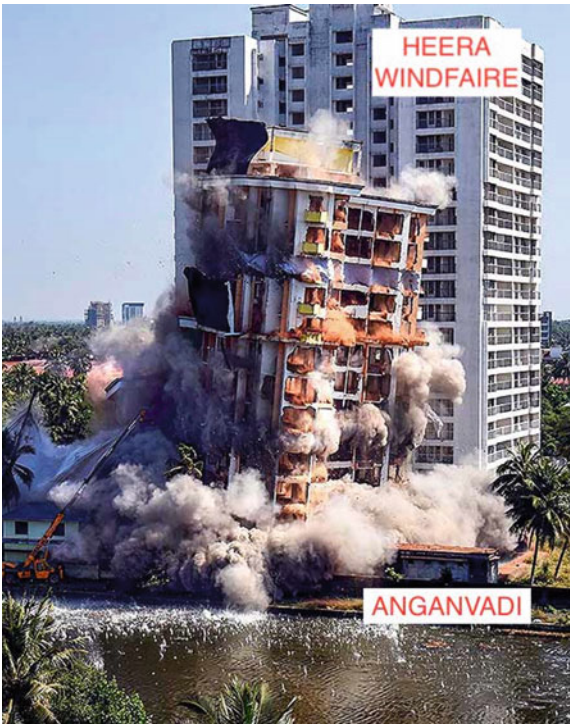

Fig. 2 Image of Golden Kayaloram apartment between heera windfaire and backwaters

The aspects that made the controlled implosion at this site challenging were the vicinity of an Anganvadi which was situated just 5 m away from the building boundary, Heera Windfaire apartments which is a 20 storeyed building located just 10 m away from Golden Kayaloram plot and the backwaters which was at a vicinity of 9 m to Golden Kayaloram. The relative locations of the structures are as shown in Fig. 2.

2.3.2 Heera Windfaire Apartment

Heera windfaire apartment is a 20 storeyed building with a floor area of 20,000 Sq.m and a height of 60 m. It was apprehended that since the space between the Golden Kayaloram Apartment and Heera Windfaire was very low, the touch down vibration induced during delayed detonation technology in controlled demolition process will impart serious damages to the structure. The apartment was evacuated before the demolition took place and instrumentations were carried out to understand the impact.

Table 1 The relation between the damage level of buildings and PPV

Damage level	Maximum velocity of mass point (mm/s)
None	35
Slight cracking/desquamation	55
Cracking	80
Severe cracking	115

3 Technical Specification and Design Approach

3.1 Peak Particle Velocity

Computing formula of vibration caused by dynamic compaction and heavy punching on earth advanced by Lü Shuran, Yang Jun and Liu Guozheng of Beijing Institute of Technology (2010):

$$v = K\left(\frac{\sqrt[3]{MgHC^2}}{R}\right)^a$$

where, C is the velocity of longitudinal wave of Strata media; K, a are modulus, decided by dynamic compaction experiment. The formula can be applied to predict the vibration velocity caused by the collapsed building part. M is the mass quantity of the collapsed body; H is the height of the mass centre. Table 1 shows the relation between the damage level of the buildings and vibration velocity [6].

3.2 Surveying and Measurement of Ground Vibration

A proper surveying of the blast location, Golden kayaloram was done and the position to place the equipment's was decided based on the wire length availability. The control station was fixed under a cover so that there would not be any direct debris fall contact. Vibrations generated due to the demolition of buildings were measured with a help of piezoelectric type accelerometers fixed directly on the concrete blocks embedded in the grounds as shown in Fig. 3a. In addition, inductive type acceleration transducers were fixed on to beams and columns of Heera windfaire apartments as shown in Fig. 3b. The vibration signals received from the accelerometers is connected to a multi-channel digital carrier frequency amplifier system to amplify the received signals. Two data acquisition systems consisting of multi- channel digital carrier frequency amplifier system of Hottinger Baldwin Messtechnik (HBM) make (model: MGC plus and QuantumX), and a CATMAN Easy program installed on to a Laptop were used to monitor and record the vibrations as digital data as presented in Figs. 3c and d.

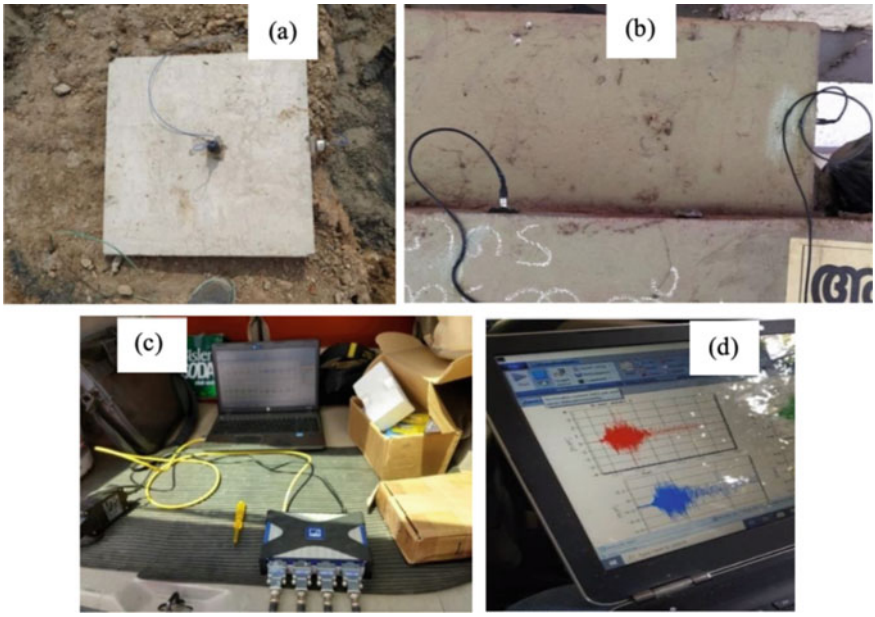

Fig. 3 Placement of accelerometers and measurement of vibrations

The time history of vertical acceleration during the controlled demolition operations was continuously recorded and stored. The recorded vibration data are processed using Catman AP software to arrive at peak particle acceleration (PPA), Peak particle velocity (PPV), frequency content and duration of ground vibration. The accelerometers were placed between 45–150 m from the building, PPV ranges from 0.93 to 105.43 mm/s and PPA ranges from 0.27 m/s^2 to 3.65 m/s^2. For the purpose of analysis of model of Heera Windfaire apartment the PPA value selected at the accelerometers positioned within the premises and building was taken. The acceleration time history recorded is shown in Fig. 4 and velocity time plot is indicated in Fig. 5.

The frequency content of the ground vibrations was determined from the Fourier Spectra obtained from the measured time history of acceleration using Seismosignal

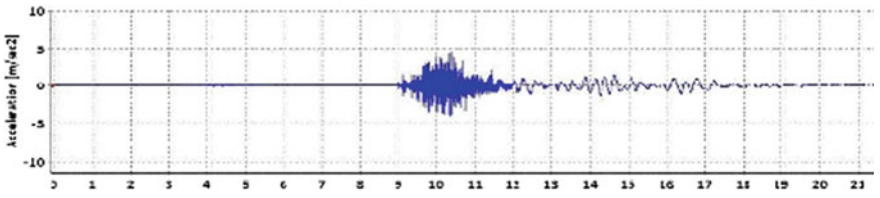

Fig. 4 Acceleration-time history recorded during the demolition of Golden Kayaloram at Heera windfaire

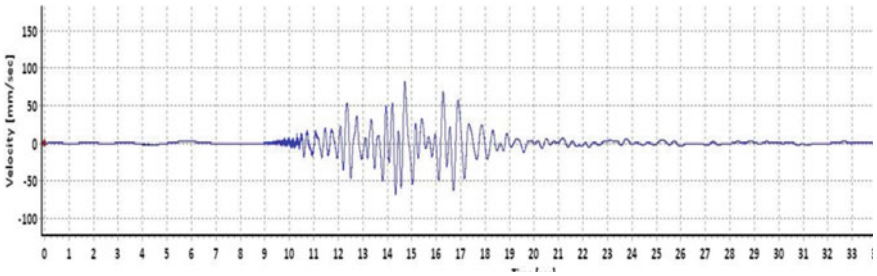

Fig. 5 Velocity–time plot recorded during the demolition of Golden Kayaloram at Heera windfaire

2020 software. The frequency content of the motion was found to consist of both low frequency (2–10 Hz) and high frequency (50–150 Hz) components likely due to blasting and sequential collapse of buildings.

3.3 Development of Heera Windfaire Model

Heera windfaire apartment was considered for the study, since being a high rise building and very close to the demolished building site the touch down vibration was expected to create considerable damages on the structure. The framed structure of the building with columns, beams, slabs and shear walls were developed using STAAD software. The loads were assigned to the building based on IS 875-1987 Part1 and 2 (7) and the blast induced loads were provided based on site measurement data. Figure 6a shows the image of Heera windfaire apartment during the demolition of Golden Kayaloram Apartments, and Fig. 6b shows the STADD Model of the structure.

3.4 Parameters Defined for the Study Process

The model that was developed has been analysed and studied based on selected parameters. The parameters used were (i) comparison of the A_h, S_a/g values for X and Z direction induced by both Touchdown vibration (TDV), Earthquake vibration (EQV) seismic activities, (ii) Exemplification of the maximum displacement when both X and Z transitional loads have been applied under TDV, EQV and DL (Dead + Live) conditions, (iii) A comparative study of the storey drift in EQV and TDV in X and Z direction lateral loads were studied and (iv) base shear caused by the lateral load of EQV and TDV were studied.

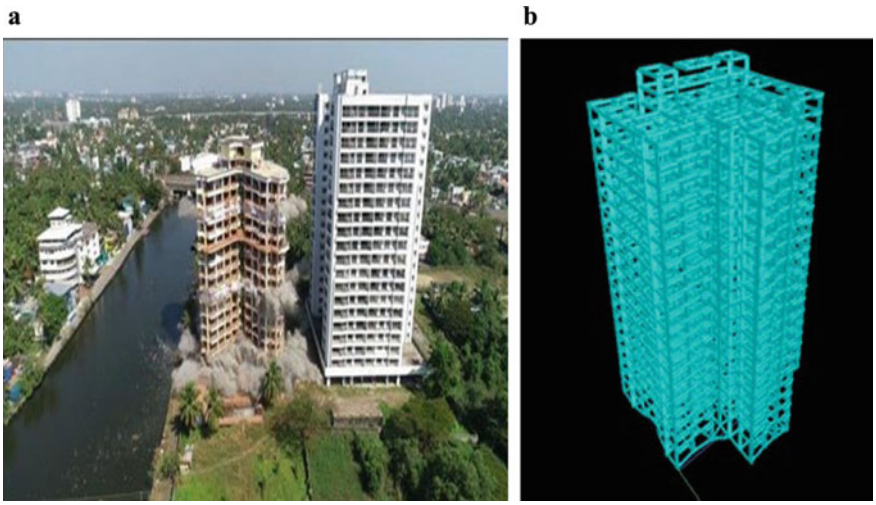

Fig. 6 **a** Image showing Heera windfaire apartment Fig. 6 **b** STADD model of the structure during demolition of Golden Kayaloram

4 Results and Discussions

4.1 Results from Vibration Studies Conducted

From the recorded time history of acceleration, the peak vertical acceleration was identified and it varies from 0.27 m/s^2 to 3.65 m/s^2. The duration of the ground vibrations recorded was 38 s. In the present case, the bracketed duration of ground vibration is considerably short and was varying from 0.91 s to 8.28 s, with widely varying frequency content and hence its damage potential may not be significant.

4.2 Results from Structural Analysis and Design of Heera Windfaire Apartments

After completing of the study of the model under three condition that model under are (i) Dead load and live load alone, (ii) Touchdown vibration (TDV) and (iii) Under Earthquake vibration (EQV) as defined by Indian Standard code 1893, Comparisons of various parameters were taken into consideration and results were drawn.

4.2.1 Comparison of Time Period and Horizontal Seismic Coefficient

From the output result obtained the Time period for X for earthquake and vibration was found to be 3.62 s and Time period of Z axis is found to be 3.46 s. The Sa/g value obtained for the seismic activities was 0.372 and 0.376 for touchdown vibration and earthquake vibration respectively along X direction. The Sa/g value obtained for the seismic activities were 0.372 and 0.396 for touchdown vibration and earthquake vibration respectively along Z direction. The A_h values for seismic activities were 0.0069 and 0.0116 for touchdown vibration and earthquake vibration respectively along X direction. The A_h values obtained for the seismic activities were 0.0069 and 0.0122 for touchdown vibration and earthquake vibration respectively along Z direction. From the results it can be noted that the design horizontal seismic coefficient ($A_{h)}$ for a TDV induced lateral load is much lesser than compared to the lateral load imposed by EQV and the average response acceleration coefficient (S_a/g) is higher for EQV induced than TDV induced lateral load. The critical impact is noted in the Z direction.

4.2.2 Maximum Deflections

The maximum deflection for X transitional load observed in the case of dead load and live load alone is 20.786 mm, with TDV load added to it is 71.780 mm and when the EQV was applied it is found to be106.613 mm. The maximum deflection for Z transitional observed in the case of dead load and live load alone is 25.109 mm, with TDV load added to it is 72.147 mm and when the EQV was applied it is found to be 108.523 mm. The maximum permissible deflection under seismic loading as per the coded provisions is 256 mm and the deflection of the structure is within the permissible limits. Figure 7 shows the 3D deflected image of structure under TDV and EQV.

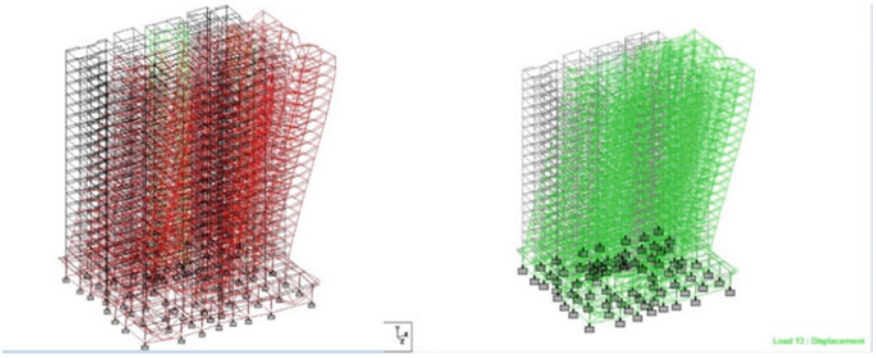

Fig. 7 3D deflection image of structure under TDV and EQV

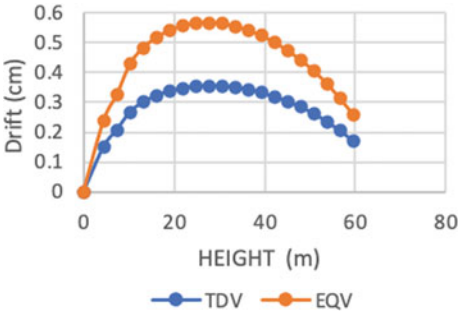

Fig. 8 Variation of storey drift in X direction between TDV and EQV

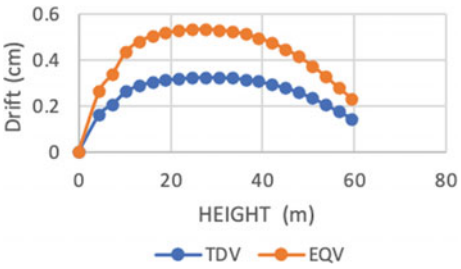

Fig. 9 Variation of storey drift in Z direction between TDV and EQV

4.2.3 Comparative Study of Storey Drift of the Building in TDV and EQV

Storey drift is the lateral displacement of one level relative to the level above or below. Storey drift ratio is the storey drift divided by the storey height and the according to IS1893 the storey drift ratio is 0.004. The storey drift of the structural model is studied, and a graph is plotted.

Storey drift in X- direction.

As the height of the building increases the storey drift is found to increase and as it reaches 30 m it starts decreasing. The storey drift of the TDV in both cases X and Z is found to be comparatively lesser than the storey drift due to the EQV in X and Z direction and the variation with height is shown in Figs. 8 and 9. Maximum value of storey drift of 3.547 mm and 5.652 mm was noted in X direction and 3.228 mm and 5.286 mm was noted in Z direction for TDV and EQV loadings respectively. The permissible storey drift as per coded provision is 11.6 mm.

Storey drift in Z-direction

4.2.4 Comparative Study of Storey Shear Variation of the Building in EQV and TDV

Base shear is an estimate of the maximum expected lateral force on the base of the structure due to seismic activity. The seismic activities in this situation that is applied

to the model are EQV and TDV. From the data given in Table 2 and from Fig. 10, it was observed that the storey shear is found to increase as the height increases, the dip in the graph at a 60 m height and in the value of the force in both EQV and TDV cases is due to the presence of the elevator shaft extending to the top of terrace of the

Table 2 Storey shear variation due to TDV and EQV

Height	TDV	EQV
4.5	2.619	4.409
7.4	3.574	6.016
10.3	6.914	11.637
13.2	11.356	19.113
16.1	16.894	28.433
19	23.528	39.599
21.9	31.258	52.61
24.8	40.085	67.465
27.7	50.008	84.166
30.6	61.027	102.412
33.5	73.142	123.103
36.4	86.354	145.339
39.3	100.662	169.419
42.2	116.066	195.345
45.1	132.566	223.116
48	150.163	252.732
50.9	168.855	284.193
53.8	188.645	317.499
56.7	209.53	352.65
59.6	159.608	268.63
TOTAL	1632.854	2747.886

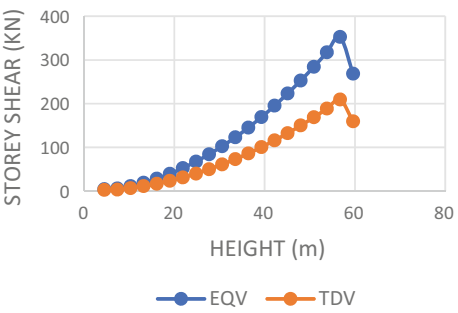

Fig. 10 Comparison of base shear with height between TDV and EQV

building. The storey shear values along the height of the building for EQV under the IS1893 conditions is found to be more than the storey shear values along the height of the building for TDV. The total base shear found in TDV is 1632.854 KN and EQV is 2748.186 KN.

5 Conclusions

From the study conducted about various type of demolition and from the field application, it is found that controlled implosion with delayed detonation technique can be successfully used for demolition of high rise structures in urban area with considerable speed and cost efficiency without damaging the adjacent structures. It is noted that the forces induced due to the blast induced vibration is lesser than the earthquake forces and since the structure was designed for taking care of earthquake, the building was capable to withstand blast induced loading without any damages other than minor cracks due to impact of flying debris.

References

1. Zhou, J.H.: Discussion on the Formulas for Calculating Falling Vibration Velocity of Blasting Demolition Buildings. Project Blasting, Chinese Academy of Sciences, Institute of Mechanics, Beijing 100190, China (2009)
2. Liu, A.W., Yu, Y.X., Fu, C.H., Lü, H.S., Chen, K., Zhao, J.S., Zhou, Z. H., Wang, W.: Explosion and Shock Waves, vol. 30, no.1, pp. 21–26 (2010)
3. Wang, Y.S., Li, X.J.: Analysis of strong ground motion caused by blasting demolition of a 22-story RC building. J. Appl. Mech. Mater. (2012)
4. Chen, M., Zhang, J., Lu, W., Yan, P., Deng, K.: Influence of basting vibration on young concrete bridge: a case study of Yesanhe Super large bridge, J. Shock. Vib. (2017)
5. IS1893 part 1: criteria for earthquake resistant design of structures
6. Lu, W., Fan, Y., Yang, J., et al.: Development of a model to predict vibrations induced by transient release of in-situ stress. J. Vib. Control (2015)
7. IS 875–1987 part 1 and 2: code of practice for design loads